NUREG/CR-7262

State-of-the-Art Reactor Consequence Analyses Project

Uncertainty Analysis of the Unmitigated Short-Term Station Blackout of the Surry Power Station

Office of Nuclear Regulatory Research

AVAILABILITY OF REFERENCE MATERIALS IN NRC PUBLICATIONS

NRC Reference Material

As of November 1999, you may electronically access NUREG-series publications and other NRC records at the NRC's Library at www.nrc.gov/reading-rm.html. Publicly released records include, to name a few, NUREG-series publications; *Federal Register* notices; applicant, licensee, and vendor documents and correspondence; NRC correspondence and internal memoranda; bulletins and information notices; inspection and investigative reports; licensee event reports; and Commission papers and their attachments.

NRC publications in the NUREG series, NRC regulations, and Title 10, "Energy," in the *Code of Federal Regulations* may also be purchased from one of these two sources:

1. **The Superintendent of Documents**
   U.S. Government Publishing Office
   Washington, DC 20402-0001
   Internet: www.bookstore.gpo.gov
   Telephone: (202) 512-1800
   Fax: (202) 512-2104

2. **The National Technical Information Service**
   5301 Shawnee Road
   Alexandria, VA 22312-0002
   Internet: www.ntis.gov
   1-800-553-6847 or, locally, (703) 605-6000

A single copy of each NRC draft report for comment is available free, to the extent of supply, upon written request as follows:

Address: **U.S. Nuclear Regulatory Commission**
Office of Administration
Digital Communications and Administrative Services Branch
Washington, DC 20555-0001
E-mail: distribution.resource@nrc.gov
Facsimile: (301) 415-2289

Some publications in the NUREG series that are posted at the NRC's Web site address www.nrc.gov/reading-rm/doc-collections/nuregs are updated periodically and may differ from the last printed version. Although references to material found on a Web site bear the date the material was accessed, the material available on the date cited may subsequently be removed from the site.

Non-NRC Reference Material

Documents available from public and special technical libraries include all open literature items, such as books, journal articles, transactions, *Federal Register* notices, Federal and State legislation, and congressional reports. Such documents as theses, dissertations, foreign reports and translations, and non-NRC conference proceedings may be purchased from their sponsoring organization.

Copies of industry codes and standards used in a substantive manner in the NRC regulatory process are maintained at—

The NRC Technical Library
Two White Flint North
11545 Rockville Pike
Rockville, MD 20852-2738

These standards are available in the library for reference use by the public. Codes and standards are usually copyrighted and may be purchased from the originating organization or, if they are American National Standards, from—

American National Standards Institute
11 West 42nd Street
New York, NY 10036-8002
Internet: www.ansi.org
(212) 642-4900

Legally binding regulatory requirements are stated only in laws; NRC regulations; licenses, including technical specifications; or orders, not in NUREG-series publications. The views expressed in contractor prepared publications in this series are not necessarily those of the NRC.

The NUREG series comprises (1) technical and administrative reports and books prepared by the staff (NUREG–XXXX) or agency contractors (NUREG/CR–XXXX), (2) proceedings of conferences (NUREG/CP–XXXX), (3) reports resulting from international agreements (NUREG/IA–XXXX),(4) brochures (NUREG/BR–XXXX), and (5) compilations of legal decisions and orders of the Commission and the Atomic and Safety Licensing Boards and of Directors' decisions under Section 2.206 of the NRC's regulations (NUREG–0750).

DISCLAIMER: This report was prepared as an account of work sponsored by an agency of the U.S. Government. Neither the U.S. Government nor any agency thereof, nor any employee, makes any warranty, expressed or implied, or assumes any legal liability or responsibility for any third party's use, or the results of such use, of any information, apparatus, product, or process disclosed in this publication, or represents that its use by such third party would not infringe privately owned rights.

NUREG/CR-7262

U.S.NRC
United States Nuclear Regulatory Commission
Protecting People and the Environment

State-of-the-Art Reactor Consequence Analysis Project

Uncertainty Analysis of the Unmitigated Short-Term Station Blackout of the Surry Power Station

Manuscript Completed: June 2019
Date Published: December 2022

Prepared by:
Severe Accident Analysis Department
Sandia National Laboratories
P.O. Box 5800 MS-0848
Albuquerque, NM 87185-0748

S. Tina Ghosh, NRC Project Manager

Office of Nuclear Regulatory Research

Sandia National Laboratories is a multi-program laboratory managed and operated by Sandia Corporation, a wholly owned subsidiary of Lockheed Martin Corporation, for the U.S. Department of Energy's National Nuclear Security Administration under contract DE-AC04-94AL85000.

ABSTRACT

The State of the Art Reactor Consequence Analyses (SOARCA) project published best estimate analyses for select accident scenarios at the Peach Bottom Atomic Power Station and Surry Power Station in 2012. This work was followed by an integrated uncertainty analysis (UA) performed on the unmitigated long-term station blackout (LTSBO) scenario for Peach Bottom, a draft UA on the unmitigated short-term station blackout (STSBO) scenario for Surry, and a UA on the unmitigated STSBO scenario for Sequoyah. The approach developed for the Peach Bottom UA was further enhanced for application to the subsequent UAs. Consequently, the current Surry UA not only benefits from additional knowledge gained since the original Surry SOARCA best-estimate calculation but also the other UAs. The UA projects include an integrated Monte Carlo analysis using the MELCOR and MACCS codes. Regression analyses and separate sensitivity analyses were conducted to understand the contributions of uncertain input parameters to the uncertainty in key figures of merit, such as radionuclide release to the environment and individual latent cancer fatality risk to the offsite public. Single realizations were analyzed to investigate individual parameter effects, typically associated with the extreme bounds, and to confirm phenomenological explanations of variations in system behavior and results. Consistent with the previous UAs, rank regression, quadratic regression, recursive partitioning, and multivariate adoptive regression splines (MARS) techniques were used to identify the importance of the input parameters regarding the uncertainty of the results. Using the insights gained from the previous UAs including the draft Surry UA and their respective ACRS reviews, the Surry model, the uncertain parameter definitions, and the uncertainty characterizations were revised for the UA documented in this report. Like the previous UAs, the analyses herein corroborate the conclusions of the original SOARCA study and further extend the body of knowledge on severe reactor accidents.

TABLE OF CONTENTS

LIST OF FIGURES

LIST OF TABLES

EXECUTIVE SUMMARY

The evaluation of accident phenomena and potential offsite consequences of severe nuclear reactor accidents has been the subject of considerable research by the NRC and its contractor, Sandia National Laboratories, over the last several decades. As a result of this research, the capability exists to conduct more detailed, integrated, and realistic analyses of severe accidents at nuclear power reactors. A desire to leverage this capability to address conservative aspects of previous reactor accident analyses was a major motivating factor in the State-of-the-Art Reactor Consequence Analyses (SOARCA) project. Through the application of modern analysis tools and techniques, the SOARCA project [1] developed a body of knowledge regarding the realistic outcomes of theoretical severe nuclear reactor accidents with best estimate analyses of selected accident scenarios at the Peach Bottom Atomic Power Station (Peach Bottom) and the Surry Power Station (Surry). The SOARCA project continued with an integrated uncertainty analysis (UA) of the unmitigated long-term station blackout (LTSBO) at Peach Bottom [2], integrated deterministic and uncertainty analyses of station blackouts at the Sequoyah nuclear plant station [7], and, documented in this report, the uncertainty analysis of an unmitigated short-term station blackout at Surry.

The SOARCA project [1] analyzed selected scenarios, first assuming the events proceeded without the 10 CFR 50.54(hh) mitigation measures (i.e., unmitigated), and then assuming that the 10 CFR 50.54(hh) mitigation measures were successful (i.e., mitigated). While these analyses have generally met the SOARCA project objectives, certain additional severe accident consequence analyses were warranted to expand upon the body of knowledge developed in SOARCA and to support and inform other NRC activities including the Site Level 3 Probabilistic Risk Assessment (PRA) project and the lessons learned from the Fukushima accident. These additional analyses are discussed in SECY-12-0092, “State-of-the-Art Reactor Consequence Analyses – Recommendation for Limited Additional Analysis,” [4], where NRC staff recommended performing a UA for a severe accident scenario at Surry. The UA insights would inform the NRC’s Site Level 3 PRA project. The Commission’s Staff Requirements Memorandum in SECY-12-0092 further noted that the ongoing SOARCA studies should support post-Fukushima regulatory activities including Tier 3 items [4].

An integrated UA on the unmitigated LTSBO at the Peach Bottom [2] boiling water reactor (BWR) with a Mark I containment was completed in 2015. The Peach Bottom study provided a quantitative analysis of the robustness of the deterministic calculations, and in the process, demonstrated the feasibility of producing integrated uncertainty results. The ability to implement an integrated UA permitted consideration of epistemic uncertainty in parameters, and to some degree aleatory uncertainty, across accident progression, release, and consequence modeling domains. The uncertainty aspect included sampling severe accident model parameters over defined distributions and performing regression analyses to identify the importance of the input parameters with regard to the uncertainty of the results. The Peach Bottom UA yielded interesting insights for an unmitigated LTSBO at a BWR with Mark I containment and staff thought it would be valuable to conduct a UA for the Surry plant too. After the Peach Bottom UA, a draft UA was performed for Surry based on the unmitigated short-term station blackout (STSBO) [8]. The draft Surry UA was reviewed by members of the NRC’s Advisory Committee on Reactor Safeguards (ACRS) cognizant subcommittee who offered suggestions for improvement. For programmatic reasons, a UA was performed for the Sequoyah nuclear power plant [7] before updating the draft Surry UA. The Sequoyah UA was also based on the unmitigated STSBO but had a particular emphasis to evaluate uncertainty of the ice condenser containment response. The ACRS also reviewed the Sequoyah UA. The current report is a

refinement of the lessons learned in the Peach Bottom UA, the Sequoyah UA, and the draft Surry UA. Like the previous studies, the quantitative results are dependent on the specific reactor design, the accident scenario, and site-specific characteristics.

The Surry UA followed the approach developed from the previous UAs. Lessons learned from the previous Peach Bottom, Sequoyah, and draft Surry UAs and the feedback from the ACRS were considered, as well as additional knowledge gained since the original Surry SOARCA calculations [3]. An objective of the Surry UA was to quantify the robustness of the Surry SOARCA analysis. However, since the completion of the Surry SOARCA study [3], there have been many enhancements and updates to the state of the art in modeling severe accidents. Nonetheless, this UA provided a comparison of the results of the Surry best estimate analysis [3] with the current, more advanced, severe accident modeling systems applied in an uncertain framework. Additional objectives included:

- determining whether the Surry UA results corroborate the general conclusions and insights from the original SOARCA best estimate study,

- developing insights into the overall sensitivity of results to uncertainty in selected modeling inputs,

- identifying influential input parameters contributing to accident progression and offsite consequences through application of an uncertainty analysis methodology, and

- informing the NRC's Site Level 3 PRA and post-Fukushima activities including Tier 3 items [4].

Figures of merit were selected to support the analysis and investigation of results. The accident progression and source term (MELCOR) figures of merit were the environmental release masses of cesium and iodine, the in-vessel hydrogen production, and the accident-induced steam generator tube creep failure. The consequence (MELCOR Accident Consequence Code System [MACCS]) figures of merit were the individual latent-cancer fatality (LCF) risk and the individual early fatality risk at specified distances.

The Surry SOARCA unmitigated STSBO was selected as the accident scenario in part because of the importance of station blackout scenarios and in part because the accident progression occurs relatively quickly under the postulated conditions. The relatively quick accident progression provides a basis to assess the effect of offsite response parameters while the release is potentially underway. Of the scenarios selected for Surry in the SOARCA best estimate study, the unmitigated STSBO with an induced steam generator tube rupture (SGTR) was also one of the two scenarios with the highest conditional individual LCF risk [1].

To meet the objective of developing insights into the overall sensitivity of SOARCA results to uncertainty in selected modeling inputs, the project team chose a reasonable number of parameters important to the figures of merit being assessed. Many of the parameters for a severe accident consequence analysis are basic input, such as reactor and containment geometry, population distributions, etc., with little uncertainty. However, the severe accident phenomenological models and associated processes have uncertainty. The selection of uncertain parameters was an iterative process to identify those expected to influence the results. The current UA was especially impacted by the ACRS member comments on the safety valve and steam generator tube failure models [150].

Most of the parameters characterized epistemic uncertainty and a few characterized aleatory uncertainties. Based on the findings of the previous UAs, some uncertain parameters were discarded where their impact was not influential. The range of the many uncertain parameter distributions encompassed the best estimate value used in the original analysis. However, when additional or new knowledge was available, this information was considered, and this resulted in the range of some parameters being different than the SOARCA best estimate value [3]. Examples of larger deviations from the SOARCA best-estimate values include the valve failure characteristics, the inclusion of gaseous iodine, the inclusion of steam generator tube flaws, variable times in the fuel cycle, and the incorporation of aerosol aerodynamic shape factors.

As a new approach for this study, the results from UA realizations (i.e., the MELCOR calculations) were processed to identify two reference realizations that closely represented the median results of the key figures of merit (i.e., iodine and cesium release to the environment, in-vessel hydrogen production, and containment failure timing).[1] The results from two reference realizations illustrate the median responses with and without a SGTR. The selection process of the reference realizations using the UA results provided insights into the parameter settings that generated median results rather than vice versa.

The state-of-the-art for this UA has progressed in three ways since the original SOARCA work. First, the MELCOR, MelMACCS, and the MACCS computer codes are continually enhanced, updated, and maintained as part of the NRC research program. Consequently, the code used in this UA includes new improvements. Second, some key input model corrections and changes were made that are documented in Appendix A of the draft Surry UA report [8]. Finally, the state of knowledge has changed since the original SOARCA study, which led to new modeling approaches. The new modeling approaches are documented in Appendix A of the draft Surry report and further improved in the current report (i.e., see Section 3.1 and Section 4) also impact the results.

The selection of the uncertain parameters and their associated distributions was expanded and updated for this UA study. Some of the key uncertain parameter updates or additions since the draft Surry UA include:

- The primary and secondary safety valve failure characteristics include a higher likelihood of the valve failure to close on the first demand versus subsequent demands. The valve failure data rely on actual plant data rather than test data;

- The primary and secondary safety valves are expected to fail in a slowly leaking or fully open position rather than in a partially open position;

- The steam generator tube flaw depth is based on an integration of results from the historical Surry steam generator tube inspection reports and fleet-wide data for less severe flaws not quantified in the inspection reports;

- The time at cycle was discretely sampled for 14 times from 0.5 days to 550 days to obtain the MELCOR and MACCS required inputs for radionuclide inventories and associated decay heat;

---

[1] The uncertain parameter inputs for the realizations that best matched the median of the key figures of merit were also reviewed to ensure they were close to the mode of their distributions.

- The gaseous iodine fraction was sampled with distributions that varied with the time at cycle. The remaining iodine mass was used to specify the cesium iodide mass. The remaining cesium mass was allocated based on the sampled cesium chemical form. Consequently, each realization had unique cesium and iodine mass distributions;

- The containment design leakage uncertainty distribution used recent data following the industry's implementation of the revised containment testing criteria as outlined in NUREG-1493, "Performance-Based Containment Leak-Test Program" [9]; and

- Three in-vessel steam-zircaloy oxidation models were sampled to examine uncertainty in the in-vessel hydrogen production.

Sandia's high-performance computing clusters were used to execute a Monte Carlo simulation of 1200 MELCOR runs. There was a 96% (1147 realizations) simulation completion success rate to 72 hours.[2] Each MELCOR run was identified with a unique realization number. In the 1147 successful realizations (i.e., MELCOR calculations), the key results are as follows:

- A SGTR occurred in 144 realizations (12.5% of realizations). Although SGTRs were calculated to occur inside and outside of the hot thermal plume regions, most of the SGTRs occurred from deep flaws in the colder region of the steam generator (SG)[3];

- There was no rupture of an unflawed SG tube in any UA realization;

- A hot leg nozzle rupture occurred in all but one realization[4];

- In every realization that predicted a SGTR, a hot leg nozzle rupture also occurred that subsequently reduced the direct release of radionuclides through the SGTR from the high pressure primary system;

    - The median timing between a SGTR and hot leg failure was 31 min.
    - The largest cesium release occurred in a realization with 2 SGTRs, which had a delayed hot leg failure 87 min later.

- A failure of one or more reactor coolant system (RCS) secondary side safety valves (SV) to close occurred in 373 realizations (32% of realizations); and

- One or more pressurizer SVs failed to close in 121 realizations (10% of the realizations); 10 of the realizations had 2 SV failures; and no realizations had 3 SV failures;

---

[2] There was a small portion (<5%) of the calculations that had convergence problems that caused an early termination before completing the 72-hr transient. The completion percentage was judged to be very good. The parameter distributions from the successful calculations were reviewed. There was no evidence that the convergence failures diminished the intended range and shape of the parameter uncertainty distributions.

[3] The SGTR flaw sampling was apportioned by the size of the regions inside and outside of the hot plume region entering the steam generator. The cooler region of the steam generator was three times the size of the hot plume region and assumed to be three times more likely to sample a deep flaw. However, for a given flaw depth, the tubes in the hot plume region were more likely to fail a steam generator tube than the cooler region.

[4] The broad scope of UA calculations suggested hot leg failure was almost certain. However, one realization with a partially stuck-open pressurizer SV achieved enough primary system depressurization and intermittent but prolonged accumulator injection to prevent hot leg failure.

- The steel containment liner yielded and tore in 1091 realizations (95% of realizations) while 56 realizations (5%) had no containment failure prior to 72 hr[5]; and

- The containment rebar yielded (and the concrete fractured) in 16 realizations (1.3% of realizations).

The uncertainty analyses produced sets of time-dependent results referred to as horsetail plots which were used in the analysis. Figure ES-1 shows the horsetails for Cs release over the 72-hour analysis period. The non-SGTR and SGTR reference realizations are highlighted as well as coloring for the non-SGTR and SGTR results. There are significant differences in the non-SGTR and SGTR results. The SGTR realizations have a rapid, higher release of cesium to the environment following the SGTR but flatten after the hot leg fails. The rapid depressurization of the primary system through the failed hot leg initially stops the outflow through the SGTR until the primary and secondary system pressures equilibrate. The subsequent release of radionuclides from the core primarily goes out the failed hot leg into the containment. Although there is continued containment and SGTR leakage after the hot leg failure, the magnitude of the releases is small relative to the initial release.

The non-SGTR realizations show the start of the release starting before 4 hours due to the nominal intact containment leakage. However, as the containment continues to pressurize, the liner failures start at 34 hr with a median failure timing of 50 hr. The cesium releases to the environment are predicted to increase at this time but benefit from considerable gravitational settling time and dilution in the containment. Consequently, the median non-SGTR cesium releases are almost two orders of magnitude less than the SGTR results as shown in Table ES-1 and ES-2, respectively.

[5] The realizations without containment failure had low decay due to an early sampled time at cycle (i.e., 0.5 days).

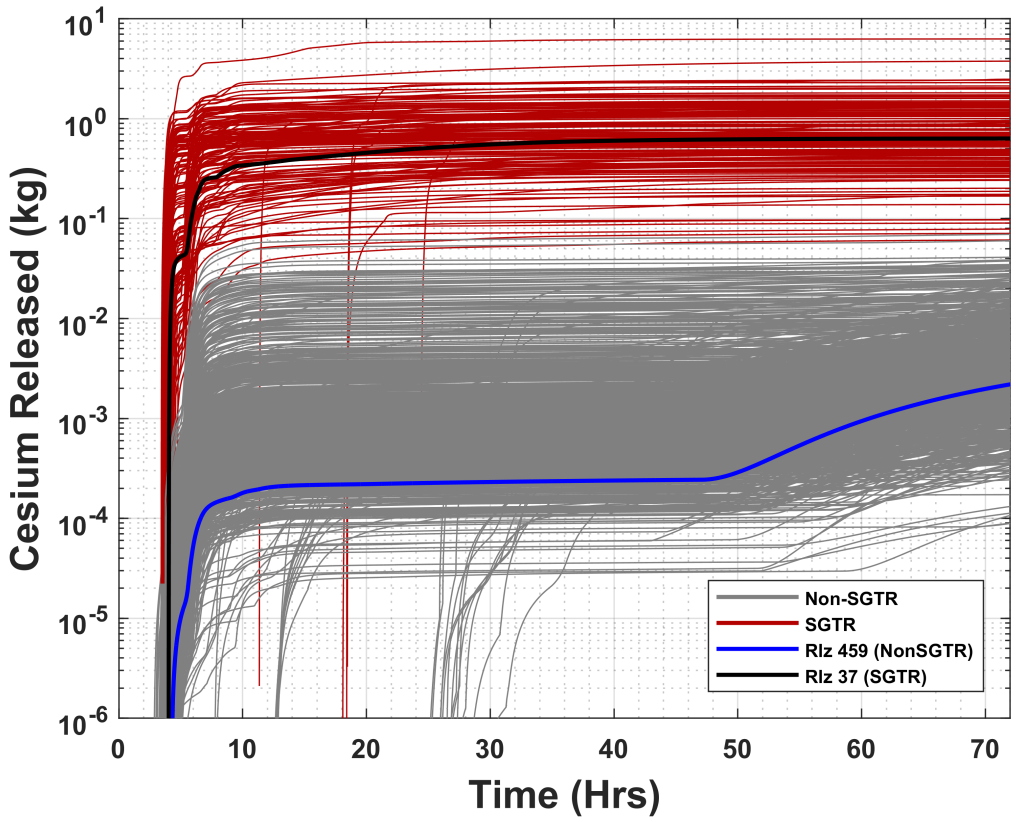

Figure ES-1 Non-SGTR and SGTR Cesium Mass Released to the Environment Over 72 Hours and the Respective Reference Realizations

Table ES-1 Cs Release to the Environment by 72 hr (SGTR)

	Released Cs fraction	Released Cs (kg)
Minimum	1.06E-03	0.24
5th Percentile	3.78E-03	0.80
Median	1.15E-02	2.15
Mean	1.32E-02	2.52
95th Percentile	2.45E-02	4.71
Maximum	7.30E-02	11.46

Table ES-2 Cs Release to the Environment by 72 hr (Non-SGTR)

	Released Cs fraction	Released Cs (kg)
Minimum	7.29E-06	1.00E-03
5th Percentile	1.22E-05	1.89E-03
Median	3.65E-05	7.18E-03
Mean	7.05E-05	1.38E-02
95th Percentile	3.29E-04	6.53E-02
Maximum	9.21E-04	1.34E-01

Figures ES-2 and ES-3 show the non-SGTR iodine and cesium environmental release masses as compared to the original Surry SOARCA non-SGTR calculation [3]. The original SOARCA calculation initially compares well with the new realizations until the containment failure at 25 hr. The SOARCA calculation is subsequently higher due to a combination of modeling changes and corrections that were described in the draft Surry UA (Appendix A of Reference [8]). The two largest impacts were the incorrect specification of limestone concrete in the reactor cavity in the original study and changes to the containment failure modeling in the current UA. The high non-condensable gas generation from the core-concrete interactions in the limestone concrete promoted larger releases in the original SOARCA calculation than the current UA realizations. The containment liner failure in the current UA occurred between 35 hr to >72 hr and had smaller leakage rates due to significantly lower non-condensable gas generation from the basaltic concrete.

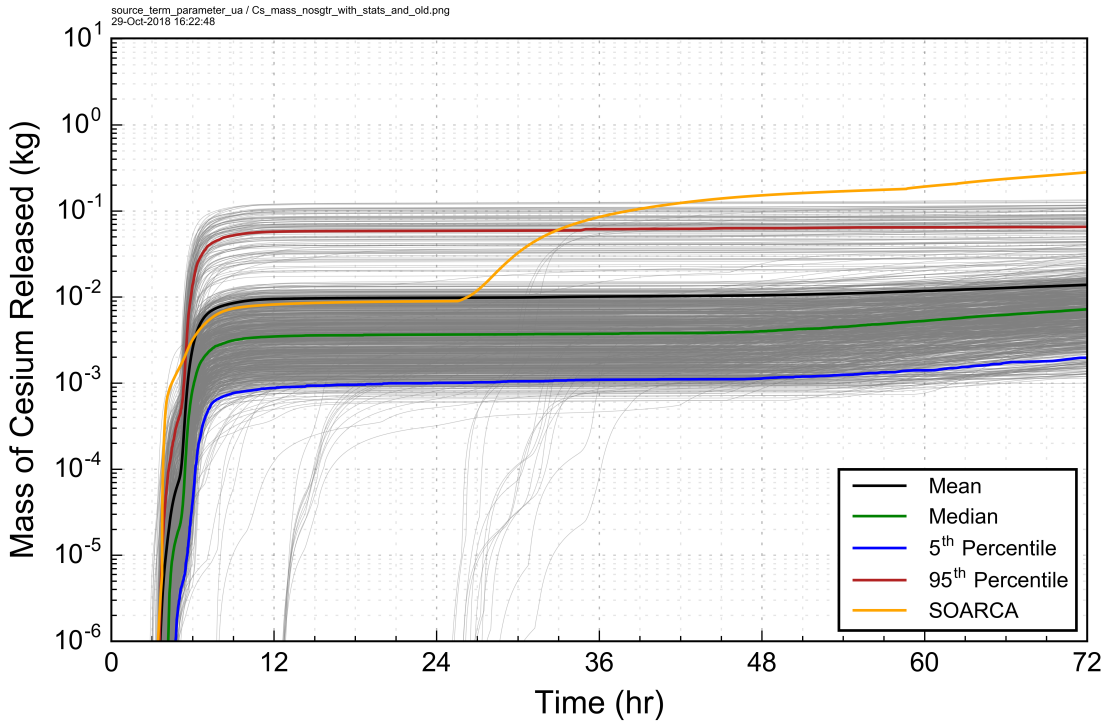

Figure ES-2 Non-SGTR Cesium Mass Released Over 72 Hours as Compared to Original SOARCA Calculation

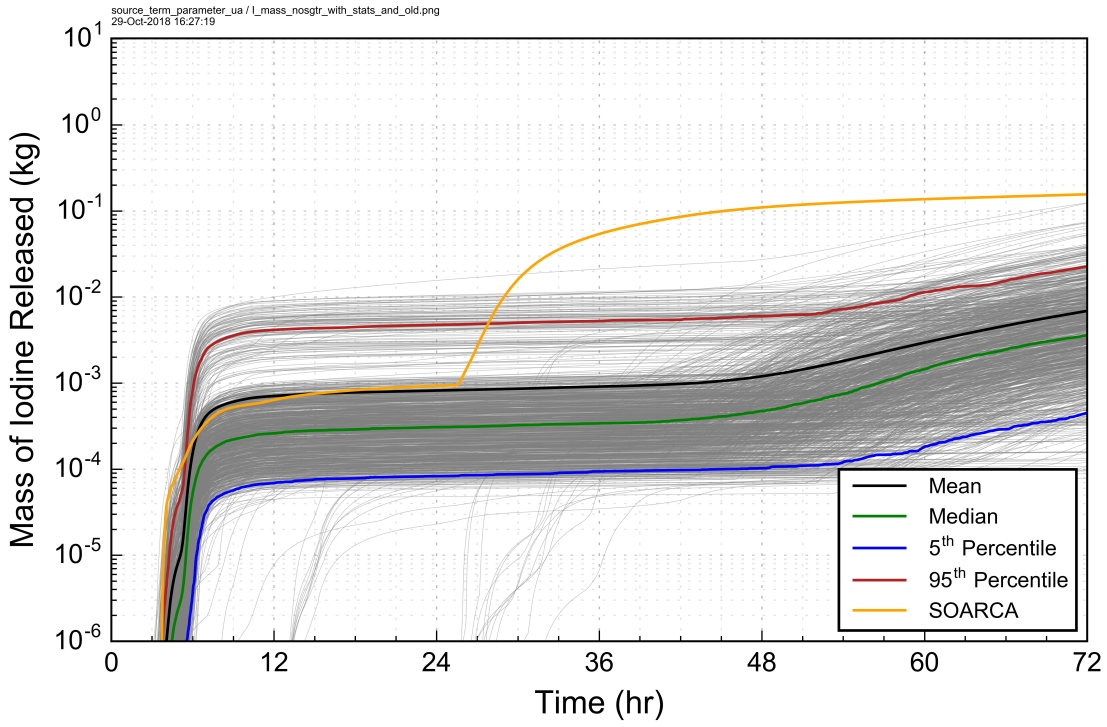

Figure ES-3 Non-SGTR Iodine Mass Released Over 72 Hours as Compared to Original SOARCA Calculation

Additional insights related to accident progression were obtained through investigation of selected single realizations to identify phenomena affecting the Cs and I releases to the environment and the in-vessel hydrogen production. The key parameters and phenomena identified in the MELCOR single realization analysis affecting the accident progression and source term include:

- The largest non-SGTR release of cesium to the environment had a high sampled containment leakage rate that is characteristic of an isolation failure;
- The largest overall (i.e., SGTR and non-SGTR realizations) release of cesium to the environment occurred in a realization with 2 SGTRs;
- The earliest release of 1% of the gaseous iodine to the environment occurred with a SGTR after but near the time of the cladding gap failures;
- The latest release of 1% of the gaseous iodine to the environment among realizations with a 1% release occurred with a high sampled containment failure pressure with low containment leakage and no SGTR;
- The realization with the largest in-vessel hydrogen production (i.e., 777 kg) occurred with the earliest time at cycle (i.e., 0.5 days). The slower heatup allowed for more hydrogen production before the core collapsed and became less supportive of significant hydrogen generation.

- The chemical form of the cesium was ranked in the regression analysis as a less important parameter to explain the magnitude of the cesium release. The containment leakage rate was the most important parameter, which was significantly more important than the volatility differences between cesium molybdate and cesium hydroxide. However, the individual realizations showed some correlation with the following expected trends,

    - The smallest cesium release to the environment occurred with a high cesium molybdate fraction, which has lower volatility than other forms of cesium.
    - The largest releases of cesium occurred with a lower cesium molybdate fraction.

- The earliest SGTR occurred when the maximum possible flaw depth was sampled in the cold region. Due to the higher number of tubes in the cold region of the steam generator, the most severe flaw was more likely to be there. However, the cold region required a very severe flaw to generate a SGTR relative to the hot upflow and hottest tube regions.

- The earliest RPV lower head failure occurred when the combined seal leakage from all three pumps was very high. A high RCP leakage rate also combined with a small leakage rate in a stuck-open pressurizer SV to cause the earliest hot leg rupture; and

- The realizations with a non-dimensional stuck-open pressurizer SV area fraction >0.36 led to the pressurizer relief tank (PRT) boiling dry in 54 of the 56 realizations. The subsequent heat up and revaporization of the cesium hydroxide and cesium iodide (i.e., the non-chemisorbed portion) initially retained in the PRT water could increase the environmental source if the dryout timing occurs near or after the containment liner failure.

Separate regression analyses were performed on the UA source term (i.e., MELCOR) and the consequence (i.e., MACCS) results. In the analysis in the source term regressions, the realizations with a SGTR dominated the regression results due to their **s**ubstantial impact on the higher early radionuclide release behavior (e.g., see Figure ES-1).[6] Consequently, it was difficult to sort the important parameters impacting key figures of merit. Table ES-3 summarizes the regressions used to identify and describe the key parameters influencing the MELCOR source term figures of merit. By isolating the non-SGTR realizations, the important parameters impacting the released cesium and iodine to the environment could be evaluated without the dominating influence of the SGTR results. After a review of the in-vessel hydrogen production regressions for non-SGTR, SGTR, and all realizations separately, there was not an appreciable difference in the results. Consequently, all realizations were used for the in-vessel hydrogen production regression. Finally, the impact of uncertain parameters on the SGTRs was focused on their occurrence. Eight separate creep parameter regressions were performed for the SGTR realizations (i.e., separate regressions for SG A and B for four types of tubes). The SGTR realization regressions for the released cesium and iodine to the environment were also reviewed. However, the small number of SGTR realizations relative to the number of uncertain inputs led to poorer quality regression results. Consequently, no SGTR regression results are discussed for the released cesium and iodine to the environment. Instead, the SGTR discussion focused on their occurrence.[7]

---

[6] Regression analyses are used to determine which inputs, amongst those that are uncertain, are driving the output uncertainty.

[7] The results of the SGTR regressions of the iodine and cesium release to the environment are archived in Appendix E.

Table ES-3 Surry UA Realizations Used in MELCOR Regression Analyses for each Figure of Merit

Figure of Merit Regression Summary						
Released Cesium	Released Iodine	In-vessel Hydrogen Production	SGTR Tube Creep (SG A & B)			
Non-SGTR	Non-SGTR	All	Cold Flawed	Hot Up Flow Flawed	Hottest Flawed	Hottest Unflawed

The source term regression analysis was performed for results obtained at the end of the 72 hr MELCOR realizations, which included the important accident progression phenomena of the core degradation, vessel failure, and containment liner plate yield.[8] The results from each regression technique for the individual contribution of a parameter and the conjoint influence[9] of a parameter on the results are calculated. The overall influence of a parameter is reported as an average of the influence suggested by the four regression techniques.

As shown in Tables ES-4 and ES-5, the most influential parameters contributing to cesium and iodine environmental release fractions for non-SGTR realizations varied (i.e., non-SGTRs are 87% of the completed realizations). The cesium release to the environment was most strongly impacted by the time at cycle (ORIGENDay) and the design containment leakage rate (designLeakLA). In addition to those parameters, the iodine release to the environment was also impacted by the gaseous iodine fraction (I2GasGapFraction) and the containment rupture pressure (rupture).

The cesium release was impacted by the nominal containment leakage rate (designLeakLA) prior to containment failure due to the higher containment airborne concentration during the earlier core degradation phase. Due to the relatively late timing of containment failure and the corresponding lower airborne concentration of cesium aerosols, the containment failure pressure (rupture) was less impactful on the total environmental release. The aerosol form of iodine was impacted in a similar manner.

The time at cycle (ORIGENDay) impacted the cesium and iodine inventories in different ways but was the second most important parameter in both regressions. Although iodine reached an equilibrium concentration in the fuel before 100 days and was relatively constant thereafter, the sampled concentration of gaseous iodine increased with the time at cycle. The amount of gaseous iodine was very important to the environmental release because it does not settle and would eventually leak. The build-up of iodine was also important when the time at cycle was less than 100 days. However, the time at cycle had a lower impact than the design containment leakage rate for cesium releases and the

---

[8] The Surry UA extended the duration of the calculations to 72 hr, which is adequate to capture key accident progression phenomena and the evacuation phase for all but the 0.5 day time at cycle realizations. The 0.5 day time at cycle realizations had a signficantly slower containment pressurization that did not challenge the containment integrity until much later than 72 hr and days after the end of the evacuation phase. The post-Fukushima Daichii accident, the SOARCA Sequoyah analyses, and the Containment Protection and Release Reduction analyses documented in NUREG-2206 also use a 72-hr simulation timeframe.

[9] Conjoint influence is the influence of two or more input parameters acting together, which may have synergistic effects that would not be uncovered by studying the influence of each parameter separately and individually.

gaseous iodine gap fraction for iodine releases. In contrast to the relatively constant iodine inventory after 100 days, the cesium inventory continuously increases throughout the cycle and therefore corresponded to more cesium released from the fuel and more available for environmental release. This was the second highest parameter affecting the non-SGTR cesium release to the environment.

The failure pressure of the containment (rupture) had a small importance on iodine release. Unlike cesium, which is in aerosol form in the containment and can settle, a portion of the iodine is gaseous. The timing of the containment rupture dictated how long gaseous iodine could release at a higher rate before the end of the calculation. A lower containment rupture pressure corresponded with a longer time between the start of enhanced containment leakage until 72 hr.

Table ES-4 Regression Analysis of Cesium Release Mass in Non-SGTR Realizations

	Rank Regression		Quadratic		Recursive Partitioning		MARS		Main Contribution	Conjoint Contribution
Final R^2	0.82		0.96		0.94		0.97			
Input	R2 contr.	SRRC	Si	Ti	Si	Ti	Si	Ti		
designLeakLa	0.50	0.70	0.94	0.96	0.96	0.99	0.92	0.96	0.800	0.027
ORIGENDay	0.21	0.46	0.02	0.04	0.02	0.04	0.02	0.06	0.068	0.024
rupture	0.05	-0.22	---	---	0.00	0.01	0.00	0.01	0.015	0.005
shapeFactor	0.03	0.18	0.01	0.02	---	---	0.01	0.01	0.011	0.005
Cs2MoO4Fraction	0.03	-0.16	---	---	---	---	0.01	0.01	0.008	0.000
Zr_brkout_T	0.00	-0.04	0.00	0.01	---	---	---	---	0.000	0.005

** highlighted if main contribution larger than 0.02 or conjoint contribution larger than 0.1*

Table ES-5 Regression Analysis of Iodine Release Mass for Non-SGTR Realizations

	Rank Regression		Quadratic		Recursive Partitioning		MARS		Main Contribution	Conjoint Contribution
Final R^2	0.81		0.94		0.81		0.93			
Input	R2 contr.	SRRC	Si	Ti	Si	Ti	Si	Ti		
I2GasGapFraction	0.20	0.48	0.44	0.61	0.82	0.89	0.54	0.72	0.444	0.131
ORIGENDay	0.49	0.54	0.11	0.21	0.07	0.10	0.14	0.25	0.193	0.077
rupture	0.07	-0.26	0.05	0.09	0.02	0.09	0.07	0.12	0.049	0.046
designLeakLa	0.04	0.20	0.05	0.08	0.03	0.03	0.08	0.13	0.045	0.029
EU_melt_T	0.00	0.06	0.01	0.07	---	---	0.01	0.04	0.004	0.032
RCP_Leak	---	---	0.00	0.16	---	---	0.00	0.02	0.001	0.054
secSVfrac1	0.00	0.07	---	---	---	---	---	---	0.001	0.000
priSVfrac	---	---	0.00	0.10	---	---	---	---	0.001	0.031

** highlighted if main contribution larger than 0.02 or conjoint contribution larger than 0.1*

The calculated mean and median of the in-vessel hydrogen production distribution at 72 hours were lower in magnitude than the original Surry SOARCA calculation [3] (see Figure ES-4). The differences in the results are attributed a number of factors including an important code change and the UA uncertain parameter settings. The code change concerned the fuel quench modeling following the accumulator discharge at hot leg failure (see Appendix D, Reference [7]). Earlier code versions often predicted high stainless-steel oxidation after the accumulator discharge that contributed to higher total in-vessel hydrogen amounts. The UA uncertain parameter modeling included realizations with lower fuel eutectic melting temperatures and lower molten zircaloy breakout temperatures, which tend to lower total in-vessel hydrogen

production (i.e., see hydrogen regression parameters in Table ES-6).[10] Nevertheless, the original SOARCA hydrogen results were relatively consistent with the new UA results and not significantly higher than the mean or the median.

The regression results for in-vessel hydrogen generation in all realizations is shown in Table ES-6. Five parameters were identified as being important to hydrogen generation. The time at cycle (ORIGENDay) was the most important parameter, which led to higher in-vessel hydrogen generation earlier in the time at cycle. The lower amount of decay heat earlier in the cycle contributed to a slower heatup before core degradation and more time for high-temperature hydrogen generation. Similarly, the hydrogen production increased when the fuel melted at a higher temperature (EU_melt_T) and the molten zircaloy inside the fuel cladding oxide shell was released at a higher temperature (Zr_brkout_T). In the reverse trend, significantly less hydrogen was generated when the fuel melting temperature approached the zircaloy cladding melting temperature or the molten zircaloy released at a lower temperature. The primary system SV failure area (priSVfrac) and the pump seal leakage (RCP_Leak) had weak influences that slightly increased hydrogen production with a larger SV failure area or more pump seal leakage.

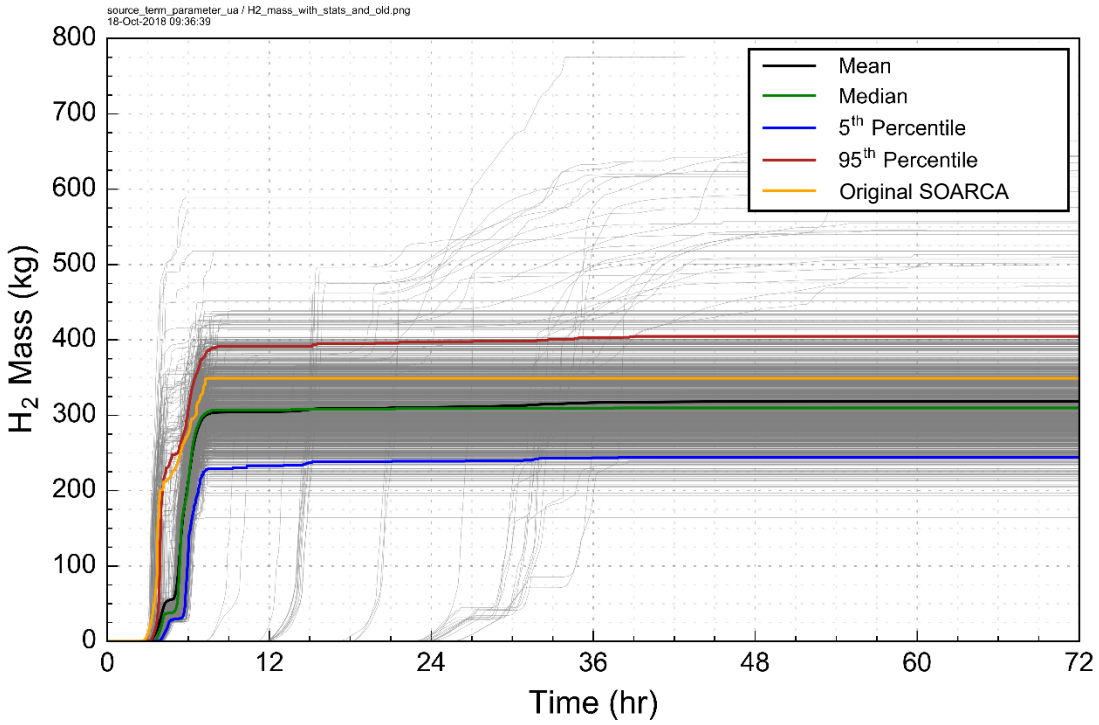

Figure ES-4 Non-SGTR In-Vessel Hydrogen Generation Over 72 Hours as Compared to SOARCA

[10] A lower time at cycle increases the in-vessel hydrogen production, especially at the lowest time at cycle (i.e., 0.5 days). This parameter does not explain the lower in-vessel hydrogen production in the UA.

Table ES-6 Regression Analysis of Hydrogen Production in All Realizations

	Rank Regression		Quadratic		Recursive Partitioning		MARS		Main Contribution	Conjoint Contribution
Final R^2	0.40		0.44		0.76		0.61			
Input	R2 contr.	SRRC	Si	Ti	Si	Ti	Si	Ti		
ORIGENDay	0.02	-0.14	0.27	0.27	0.51	0.53	0.42	0.43	0.195	0.006
EU_melt_T	0.23	0.46	0.34	0.39	0.20	0.31	0.26	0.30	0.172	0.043
Zr_brkout_T	0.10	0.29	0.11	0.14	0.05	0.16	0.08	0.11	0.057	0.038
priSVfrac	0.03	0.33	0.10	0.12	0.05	0.06	0.10	0.10	0.043	0.007
RCP_Leak	0.00	0.08	0.10	0.10	0.02	0.03	0.07	0.08	0.026	0.004
Zr_drn_rate	0.02	-0.14	0.02	0.02	0.01	0.05	0.03	0.03	0.013	0.011
Ox_model	0.01	0.09	---	---	0.00	0.02	0.01	0.01	0.003	0.005
tubeHotA_NFD	---	---	---	---	0.01	0.01	0.00	0.01	0.002	0.003

** highlighted if main contribution larger than 0.02 or conjoint contribution larger than 0.1*

The SGTR regressions were handled in two manners and focused on the magnitude of the tube damage rather than the environmental source term. First, regressions were performed on the cold tube, the hot upflow tube, and the hottest tube using the flawed tube creep damage parameter as the primary figure of merit. The results were dominated by the flaw depth for the particular location being evaluated (e.g., SG A cold tube creep is dominated by the Cold Tube A flaw depth). The flaw depth analysis revealed the following:

- The likelihood of a SGTR from a cold tube flaw significantly increased when the non-dimensional flaw depth is >0.80;
- The likelihood of a SGTR from a hot upflow tube flaw significantly increased when the non-dimensional flaw depth is >0.68; and
- The likelihood of a SGTR in the hottest tube significantly increased when the non-dimensional flaw depth is (a) >0.42 or (b) >0.31 with a maximum normalized hot plume temperature >0.48 (i.e., >75th percentile of the maximum normalized plume temperature distribution).

The individual steam generator cold and hot upflow tube regression analyses also showed that the magnitude of the main steam isolation valve (MSIV) leakage and the flow area of a stuck-open pressurizer SV are factors influencing the cold tube creep but significantly less important relative to the flaw depth. A large MSIV leakage increased the pressure difference across the tube to increase creep whereas a larger failed pressurizer SV area decreased the pressure difference to decrease creep.

The regression on the hottest tube also showed that the maximum normalized plume temperature is important (see Table ES-7). The normalized plume temperature is interpreted from detailed computational fluid dynamics (CFD) simulations to identify the maximum sustained plume temperature. It is applied as a boundary condition for the hottest tube calculation to predict conditions for the most thermally vulnerable tube. It was the second most important parameter but significantly less important relative to the flaw depth. The MSIV leakage rate was also an important parameter for the hottest tube but the pressurizer SV failure area was slightly below the criterion for high importance.

Table ES-7 Regression Results for the Hottest Tube Creep in SG A

	Rank Regression		Quadratic		Recursive Partitioning		MARS		Main Contribution	Conjoint Contribution
Final R2	0.59		0.88		0.77		0.85			
Input	R2 contr.	SRRC	Si	Ti	Si	Ti	Si	Ti		
tubeHotA_NFD	0.18	0.72	0.64	0.89	0.78	0.97	0.70	0.90	0.485	0.179
ThotA_norm	0.19	0.42	0.03	0.16	0.03	0.20	0.02	0.27	0.063	0.152
msiv_leak_a	0.14	0.39	0.01	0.09	0.00	0.02	0.00	0.00	0.038	0.029
priSVfrac	0.05	-0.47	0.01	0.05	---	---	0.02	0.02	0.016	0.012
secSVfrac1	0.03	0.31	0.00	0.02	---	---	0.00	0.02	0.007	0.009
RCP_Leak	0.02	0.15	0.00	0.05	---	---	---	---	0.005	0.014

** highlighted if main contribution larger than 0.02 or conjoint contribution larger than 0.1*

The second SGTR regression technique was handled in a non-intuitive manner. When the flawed tube creep parameter is the figure of merit, the corresponding flaw depth overwhelmed all other parameters. By considering an unflawed tube creep parameter as the figure of merit, the regressions were independent of the flaw depth. Since no unflawed tubes failed in the realizations, the unflawed tube creep magnitude also has the advantage of being more continuous. The attributes of the important parameters from the unflawed tube regressions can be used to identify factors that increase the likelihood of a consequential tube failure.

Separate unflawed tube regressions were performed for the hottest tube creep parameter in SG A and B. The comparison of results between steam generators shows the same phenomenology for tube damage and the same important parameters. Table ES-8 shows the regression results from SG A. As expected, the hot tube flaw depth is missing. However, the order of the top three parameters in Table ES-8 is the same as parameters two through four in Table ES-7. Consequently, the unflawed analysis confirms the importance of the next most important parameters. The key new insight is the stronger influence of the hot tube maximum normalized plume temperature on the unflawed creep magnitude of the hottest tube versus the flawed tube creep evaluation.

Table ES-8 Regression Results for an Unflawed Hottest Tube Creep in SG A

	Rank Regression		Quadratic		Recursive Partitioning		MARS		Main Contribution	Conjoint Contribution
Final R2	0.56		0.79		0.81		0.76			
Input	R2 contr.	SRRC	Si	Ti	Si	Ti	Si	Ti		
ThotA_norm	0.29	0.52	0.62	0.73	0.60	0.60	0.62	0.76	0.435	0.120
msiv_leak_a	0.18	0.44	0.15	0.23	0.17	0.17	0.16	0.29	0.139	0.103
priSVfrac	0.04	-0.44	0.05	0.08	0.01	0.01	0.05	0.08	0.032	0.017
RCP_Leak	0.02	0.18	0.03	0.06	---	---	0.03	0.03	0.017	0.013
secSVfrac1	0.03	0.32	0.00	0.01	---	---	0.00	0.01	0.007	0.009

** highlighted if main contribution larger than 0.02 or conjoint contribution larger than 0.1*

Consequence Results

The consequence results for individual, latent cancer fatality (LCF) risk were estimated based on the assumption of linear, no-threshold (LNT) dose response. All consequence results in this study are presented as conditional risks, which are the risks assuming that the accident occurs. They do not account for the very small likelihood that the assumed accident might occur.

The emergency phase used in this analysis is seven days following the beginning of release to the environment. An intermediate phase duration of 1 year and then a long-term phase of 50 years follows the emergency phase. Results for the LNT dose-response show that the large

majority of the LCF risk is from the intermediate and long-term phases at all five distance intervals evaluated, even for the realizations with SGTR. The mean values of the fraction of risk from the emergency phase are 1 percent within 10 miles and about 15 to 17 percent at distances beyond 10 miles. Only a handful of realizations have emergency-phase contributions that exceed the intermediate and long-term phase contributions to LCF risk.

Like the original SOARCA study and all other subsequent UAs, the Surry UA demonstrates that early fatality risks are negligible, essentially zero. LCF risks are somewhat lower than those evaluated in the original SOARCA study for Surry. Table ES-9 shows that the mean LCF risks from this uncertainty analysis, conditional on the occurrence of a STSBO scenario at Surry, are about 3×10^{-5} within 10 miles of the site and that the risk diminishes at longer distances. This mean value includes the 12.5 percent of the realizations with induced SGTRs. For comparison, this value is about a factor of three lower than the SOARCA unmitigated STSBO risks (which exclude the occurrence of SGTRs, cf., Table 7-4 in [3]). The 95th percentile LCF risk from this UA is about one-third less than the mean risk for the unmitigated SOARCA STSBO with induced SGTR (cf. Table 7-6 in [3]). This is a meaningful comparison because the top 12.5 percentile of the results from this UA represent SGTR realizations. Within 50 miles of the site, the LCF risks are similar but slightly less than the comparable values from the original SOARCA study.

Table ES-9 Mean, Individual LCF Risks using LNT Dose Response, Conditional on Surry Unmitigated STSBO Occurring (per event) at Different Radial Distances

	0-10 miles	10-20 miles	0-50 miles
UA Mean	3.2E-05	1.8E-05	9.0E-06
UA Median	2.2E-06	7.1E-07	3.4E-07
UA 5th percentile	3.2E-07	1.2E-07	5.4E-08
UA 95th percentile	2.1E-04	1.2E-04	6.3E-05
Original SOARCA estimate, STSBO	9.4E-05	N/A	1.5E-05
Original SOARCA estimate, STSBO with SGTR	3.2E-04	N/A	6.5E-05

Regression analyses of the UA results were performed to determine the uncertain inputs that most affect the LCF risks. No regression analyses were performed for early fatality risks because only one realization estimates a risk greater than zero and even this risk is extremely small.

Table ES-10 provides the regression results for the complete set of realizations (including SGTR and non-SGTR). The highlighted values under the column labeled “Main Contribution” are the ones considered to be significant. They are ordered from largest to smallest, so the most influential of the uncertain parameters appear at the top of the list. Highlighted values under the column labeled “Conjoint Contributions” indicate parameters that have a significant influence on LCF risk in conjunction with one of the other parameters.

The top three parameters are all measures of SGT flaw depths in different regions of the steam generators, and these directly influence the likelihood of a SGTR. Risk increases with all three of these measures of flaw depth. The next most important input parameter is the containment leakage area, which is proportional to containment leakage rate prior to containment failure.

This parameter is more influential when a SGTR does not occur, but it plays a role even when a SGTR does occur. The next most influential parameter represents the long-term groundshine shielding factor. Overall, groundshine is the most important dose pathway in this analysis and long-term groundshine doses are proportional to this parameter. The last of the highlighted contributions is the day during the operating cycle that the accident is modeled to occur. This parameter plays a dual role in that it affects the level of decay heat in MELCOR and it affects the isotopic inventory in MACCS. Both contributions tend to increase LCF risk when the accident occurs later in the operating cycle.

Table ES-10 Mean, Individual, LCF Risk (LNT Dose Response) Regression Results within a 50-mile Circular Area for all Realizations

	Rank Regression		Quadratic		Recursive Partitioning		MARS		Main Contribution	Conjoint Contribution
Final R^2	0.48		0.60		0.48		0.65			
Input	R^2 contr.	SRRC	S_i	T_i	S_i	T_i	S_i	T_i		
tubeColdA_max	0.01	0.09	0.23	0.35	0.40	0.52	0.30	0.32	0.133	0.049
tubeUpflowA_NFD	---	---	0.09	0.15	0.21	0.24	0.08	0.19	0.070	0.039
tubeColdC_max	0.00	0.07	0.10	0.15	0.11	0.11	0.18	0.39	0.058	0.057
designLeakLa	0.15	0.38	---	---	0.00	0.03	---	---	0.039	0.005
GSHFAC_2	0.11	0.34	0.02	0.08	---	---	0.01	0.05	0.033	0.020
ORIGENDay	0.09	0.28	---	---	---	---	0.02	0.07	0.024	0.011
tubeHotC_NFD	---	---	0.00	0.03	0.04	0.05	0.03	0.03	0.012	0.008
CFRISK_8	0.03	0.19	0.00	0.13	0.00	0.12	0.02	0.22	0.011	0.088
VDEPOS_1	0.01	0.10	0.01	0.03	0.04	0.04	---	---	0.009	0.004

** highlighted if main contribution larger than 0.02 or conjoint contribution larger than 0.1*

As shown in Table ES-11, the most important of the uncertain input parameters is the MACCS parameter representing long-term groundshine shielding factor for realizations with a SGTR. Two cancer fatality risk factors, for residual and colon cancers, are next in importance. These are proportional to the risks of the corresponding cancer types, which are the two types with the largest risk factors. Next is the MELCOR parameter for dynamic shape factor of the aerosols. A larger value of this factor causes less deposition to occur in the reactor coolant system and containment, thus increasing the environmental release. This parameter also biases the aerosol size distribution to be larger, and this enhances deposition in the environment. The last of the highlighted parameters is the containment leakage area, which is proportional to the containment leakage rate prior to containment failure. Also, notice that two parameters have a significant conjoint influence. One of these, which also has a significant main contribution, is the cancer fatality risk for residual cancers, which are the set of cancers not specifically treated in the consequence analysis. The conjoint influence is with the dose and dose-rate effectiveness factor for residual cancers. This conjoint influence results from the fact that these two parameters appear in the equation for residual cancers, one in the numerator and one in the denominator.

Table ES-11 Mean, Individual, LCF Risk (LNT Dose Response) Regression Results within a 50-mile Circular Area for Realizations with a SGTR

	Rank Regression		Quadratic		Recursive Partitioning		MARS		Main Contribution	Conjoint Contribution
Final R^2	0.59		0.93		0.54		0.62			
Input	R^2 contr.	SRRC	S_i	T_i	S_i	T_i	S_i	T_i		
GSHFAC_2	0.35	0.61	0.07	0.11	0.29	0.39	0.20	0.21	0.173	0.032
CFRISK_7	0.07	0.27	0.06	0.10	0.44	0.48	0.34	0.49	0.143	0.049
CFRISK_8	0.11	0.35	0.05	0.40	0.13	0.22	0.21	0.34	0.088	0.155
shapeFactor	0.06	0.27	0.01	0.02	0.01	0.02	0.10	0.10	0.035	0.002
RCP_Leak	---	---	0.08	0.21	---	---	0.00	0.01	0.024	0.041
SGTRB_loc	---	---	0.03	0.35	---	---	0.01	0.02	0.010	0.101
SGTRC_loc	---	---	0.03	0.04	---	---	---	---	0.008	0.005
CWASH1	---	---	0.02	0.21	---	---	---	---	0.005	0.060
msiv_leak_c	---	---	0.01	0.06	---	---	0.00	0.02	0.004	0.019

** highlighted if main contribution larger than 0.02 or conjoint contribution larger than 0.1*

For the realizations without a SGTR, the most important of the uncertain input parameters are design leakage area of the containment, long-term groundshine shielding factor, the day the accident occurs during the operating cycle (time at cycle), and the cancer fatality risk factor for residual cancers. The reasons that these parameters are important are the same as those described in the preceding paragraphs.

Table ES-12 Mean, Individual, LCF Risk (LNT Dose Response) Regression Results within a 50-mile Circular Area for Realizations without a SGTR

	Rank Regression		Quadratic		Recursive Partitioning		MARS		Main Contribution	Conjoint Contribution
Final R^2	0.77		0.94		0.74		0.95			
Input	R^2 contr.	SRRC	S_i	T_i	S_i	T_i	S_i	T_i		
designLeakLa	0.27	0.50	0.45	0.78	0.57	0.88	0.53	0.80	0.404	0.265
GSHFAC_2	0.17	0.43	0.07	0.23	0.06	0.38	0.08	0.20	0.089	0.166
ORIGENDay	0.15	0.37	0.02	0.03	0.02	0.03	0.03	0.04	0.055	0.006
CFRISK_8	0.04	0.20	0.04	0.13	0.00	0.04	0.03	0.12	0.026	0.064
rupture	0.04	-0.18	0.01	0.02	0.00	0.00	0.00	0.03	0.011	0.014
DDREFA_8	0.01	-0.12	0.01	0.07	0.00	0.14	0.01	0.04	0.008	0.064

** highlighted if main contribution larger than 0.02 or conjoint contribution larger than 0.1*

Sensitivity studies were conducted to determine the relative importance of the different chemical groups. Results were generally similar for source terms with and without a SGTR. For a SGTR, the cesium group contributes about 88% of the risk, mostly from groundshine exposures during the intermediate and long-term phases. Of the 88%, about 64% is from Cs-137 and the remainder is mostly from Cs-134. Next, the tellurium group contributes about 4.5% of the LCF risk, and most of that is from Te-132. Most of the tellurium contribution is from exposures during the emergency phase. Third in importance is the molybdenum group, which contributes about 4.0% of the risk, and the major contributor to that group is Nb-95. Exposures from the molybdenum group are more from the intermediate and long-term phases (2.5%) than from the emergency phase (1.5%). Fourth is the iodine group, which contributes about 2.6%. The majority of that is from I-131, but I-133 also contributes significantly. Most of the exposures from iodine occur during the emergency phase. Other isotopes, Ru-106, Mo-99, Kr-88, Ba-140, Xe-133, and Xe-135 combined, contribute about 1% to the overall risk, and this is almost exclusively from exposures during the emergency phase.

For the non-SGTR source term, about 84.5% of the LCF risk is from the cesium group, 5.5% is from the iodine group, 3.4% is from the tellurium group, 3.3% is from the xenon/krypton group, and 2.2% is from the molybdenum group. An evaluation of the contributors at the level of the individual isotopes was not performed for the non-SGTR source term, but the contributions are expected to be similar to those for the SGTR source term, as described in the preceding paragraph. The barium and ruthenium groups contribute a combined total of 1.1%. The other two groups cerium and lanthanum, do not contribute to LCF risk to the precision of this calculation.

The largest difference between the SGTR and non-SGTR realizations is that the noble gases contribute significantly more when the source term is small. This is because the noble gases are generally released in large fraction even when other chemical groups are not. Thus, the relative contribution of the noble gases is greater for smaller source terms.

Summary

As described above, the Surry UA includes distributions for parameter values that previously were modeled with fixed values and applies multiple regression techniques to support an understanding of the results. Such an analysis produces substantial information, which is described in detail in this document. A summary of important accident progression and source term insights is provided below:

- SGTRs occur in 12.5 percent of the UA realizations and have iodine and cesium release masses one to two orders of magnitude larger than the non-SGTR realizations. The most influential parameters are the SG tube flaw depth and flaw location followed by the magnitude of the MSIV leakage and whether a pressurizer SV sticks open.

- The original Surry SOARCA [3] iodine and cesium environmental release fractions were similar to the mean or median of the UA realizations until the containment failure at 25 hr. An incorrect specification of the reactor cavity concrete composition in the original SOARCA calculation caused faster containment pressurization during the ex-vessel CCI, an earlier containment failure, a larger containment failure leakage rate, and higher post-containment failure radionuclide releases to the environment.

- The most influential parameters impacting the cesium and iodine environmental releases for the non-SGTR realizations (i.e., 87% of realization outcomes) are slightly different. The cesium release to the environment is most strongly impacted by the time in the operating cycle when the postulated accident occurs and the design containment leakage rate. The iodine release to the environment includes those parameters but is also impacted by the gaseous iodine fraction and the containment rupture pressure.

The consequence portion of the uncertainty analysis considers a set of uncertain source terms from MELCOR in conjunction with other consequence-analysis-specific inputs. Most historical consequence analyses have modeled these parameters to be fixed and considered, at most, a set of source term groups to quantify the types of accidents that might occur and a set of weather trials to capture weather variability. A summary of the most important offsite consequence conclusions and insights from this Surry UA is provided below:

- Mean (over epistemic uncertainty and weather variability), individual, LCF risks, conditional on the occurrence of an accident, estimated in this uncertainty analysis of the Surry STSBO are very low, approximately 3×10^{-5} within 10 miles and lower at longer distances.

- Most of the mean risks (about 99% within the 10-mile emergency planning zone (EPZ) and 83% to 85% beyond 10 miles from the plant) are from intermediate and long-term exposures following the emergency phase.

- Early fatality risks for this scenario are essentially zero, as they were in all the other SOARCA studies.

- MELCOR parameters that determine the likelihood of a SGTR, primarily flaw depths for various groups of steam generator tubes, are the most influential parameters for latent cancer fatality risks overall. Containment leakage area is also important, especially for the subset of realizations that do not result in a SGTR.

- The most influential MACCS-specific parameters are the long-term groundshine shielding factor, the day during the operating cycle that the accident occurs, and two of the cancer fatality risk factors, those for residual and colon cancers.

The Surry UA project informed the Level 3 PRA project by including staff in Surry parameter development meetings, presenting Level 3 PRA staff early Surry UA results, and interacting with Level 3 PRA staff on key issues of interest. In addition, like the SOARCA Peach Bottom UA [2] and the SOARCA Sequoyah UA, the results of this Surry UA corroborate the conclusions from the SOARCA project [1]:

- Latent cancer and early fatality risks from severe nuclear accident scenarios modeled are smaller than those projected in NUREG/CR-2239.

- The delay in releases calculated provides more time for emergency response actions (such as evacuating or sheltering).

- “Essentially zero” absolute early fatality risk is projected.

ACKNOWLEDGMENTS

The Surry Uncertainty Analysis SOARCA project document is the result of the efforts of many NRC staff and the staff of its contractor, Sandia National Laboratories. The co-leads, S. Tina Ghosh, NRC, and Douglas M. Osborn, Sandia, gratefully acknowledge the contributions from the following individuals in preparing this document:

Jonathan Barr	U.S. Nuclear Regulatory Commission
Keith Compton	U.S. Nuclear Regulatory Commission
Hossein Esmaili	U.S. Nuclear Regulatory Commission
Salman Haq	U.S. Nuclear Regulatory Commission
Alfred Hathaway	U.S. Nuclear Regulatory Commission
Patricia A. Santiago	U.S. Nuclear Regulatory Commission

Nathan Bixler	Sandia National Laboratories
Dusty Brooks	Sandia National Laboratories
Jeffrey Cardoni	Sandia National Laboratories
Matthew Dennis	Sandia National Laboratories
Matthew Denman	Sandia National Laboratories
Christopher Faucett	Sandia National Laboratories
Aubrey Eckert-Gallup	Sandia National Laboratories
Troy Haskin	Sandia National Laboratories
Larry Humphries	Sandia National Laboratories
Randall Gauntt	Sandia National Laboratories
Patrick Mattie	Sandia National Laboratories
Katherine McFadden	Sigma Software, LLC
Kyle Ross	Sandia National Laboratories
John Reynolds	Sandia National Laboratories
Rodney Schmidt	Sandia National Laboratories
Kenneth C. Wagner	Sandia National Laboratories
Fotini Walton	Sandia National Laboratories

The co-leads would also like to thank the support provided by the staff of the Surry Nuclear Plant, Dominion Power, the State of Virginia's Emergency Management Agency, members of the NRC's Advisory Committee on Reactor Safeguards who provided comments on an earlier draft during the February 2016, and during the May 2016 and June 2017 subcommittee meetings on the Sequoyah UA, and staff who have since retired from NRC and Sandia.

ABBREVIATIONS AND ACRONYMS

AC	Alternating Current
ACRS	Advisory Committee on Reactor Safeguards
ANS	American Nuclear Society
ARP	Automatic Rapid Processing
ARTIST	Aerosol Trapping in a Steam Generator
atm	Atmosphere
BEIR	Biological Effects of Ionizing Radiation
BOC	Beginning of Cycle
BWR	Boiling Water Reactor
CCDF	Complementary Cumulative Distribution function
CCI	Core Concrete Interactions
CDF	Cumulative Distribution Function
CEA	Atomic Energy and Alternative Energies Commission
CFC	Containment Fragility Curve
CFRISK	Cancer Fatality Risk
CRAC	Calculation of Reactor Accident Consequences
CV	Control Volume
DC	Direct Current
DCF	Dose Conversion Factor
DDREFA	Dose and Dose Rate Effectiveness Factor
DEGB	Double-Ended Guillotine Break
DF	Decontamination Factor
EAS	Emergency Alert System
ECCS	Emergency Core Cooling Systems
ECST	Emergency Condensate Storage Tank
EOC	End of Cycle
EPA	Environmental Protection Agency
EPRI	Electric Power Research Institute
EPZ	Emergency Planning Zone
ETE	Evacuation Time Estimate
FGR	Federal Guidance Report
FP	Flow Path
FPT	Fission Product Tests
FTC	Failure to Close
FTO	Failure to Open
gpm	Gallons Per Minute
GSDE	Ground Shine Deposited Energy
Gy	Gray
HPS	Health Physics Society
HTC	Heat Transfer Coefficient
IPE	Individual Plant Examination

LCF	Latent Cancer Fatality
LET	Linear Energy Transfer
LEU	Low Enriched Uranium
LHS	Latin Hypercube Sampling
LNT	Linear No Threshold
LTSBO	Long-Term Station Blackout
LWR	Light Water Reactor
m	Meter
MAAP	Modular Accident Analysis Program
MACCS	MELCOR Accident Consequence Code System
MARS	Multivariate Adaptive Regression Splines
MOC	Middle of Cycle
mph	Miles Per Hour
MSIV	Main Steam Isolation Valve
MSL	Main Steam Line
mSv	Millisievert
NCG	Non-Condensable Gas
Nu	Nusselt Number
ORO	Offsite Response Organization
PAG	Protective Action Guide
PAR	Protective Action Recommendation
PDF	Probability Density Function
PRA	Probabilistic Risk Assessment
PRT	Pressure Relief Tank
PRY	Per Reactor Year
PSV	Pressurizer Safety Valve
PWR	Pressurized Water Reactor
RCP	Reactor Coolant Pump
RCS	Reactor Coolant System
RLZ	Realization
ROP	Reactor Oversight Program
RPV	Reactor Pressure Vessel
RRC	Rank Regression Coefficient
SAE	Site Area Emergency
SBO	Station Blackout
scfh	Standard Cubic Feet Per Hour
SG	Steam Generator
SGTR	Steam Generator Tube Rupture
SME	Subject Matter Expert
SNL	Sandia National Laboratories
SOARCA	State of the Art Reactor Consequence Analyses
SPAR	Standardized Plant Analysis Risk
SRRC	Standardized Rank Regression Coefficient
SRS	Simple Random Sampling
SRV	Safety Relief Valve

SSE	Sum Of Square Error
STSBO	Short-Term Station Blackout
SV	Safety Valve
SVV	Code Safety Valve
TAF	Top of Active Fuel
TDAFW	Turbine Driven Auxiliary Feedwater
UA	Uncertainty Analysis
USBGR	U.S. Background

1 INTRODUCTION

The evaluation of accident phenomena and potential offsite consequences of severe nuclear reactor accidents has been the subject of considerable research by the NRC over the last several decades. As a result of this research, the capability exists to conduct more detailed, integrated, and realistic analyses of severe accidents at commercial nuclear power reactors. A desire to leverage this capability to perform more realistic analyses to address conservative aspects of previous reactor accident analyses was a major motivating factor in the State of the Art Reactor Consequence Analyses (SOARCA) project (NUREG-1935). Objectives of the SOARCA project included: (1) evaluating the potential benefits of post-9/11 mitigation improvements, (2) updating the quantification of offsite consequences found in earlier NRC publications, such as the 1982 Siting Study (NUREG/CR-2239 [5]), and (3) enabling the NRC to better communicate severe accident related aspects of nuclear safety to stakeholders, including Federal, State, and local authorities, licensees, and the public (NUREG/BR-0359). Through the application of modern analysis tools and techniques, the SOARCA project [1] developed a body of knowledge regarding the realistic outcomes of theoretical severe nuclear reactor accidents for selected accident scenarios at the Peach Bottom Atomic Power Station (Peach Bottom) and the Surry Power Station (Surry). The SOARCA project continued with an integrated uncertainty analysis (UA) of the unmitigated long-term station blackout (LTSBO) at Peach Bottom [2], the Sequoyah Integrated Deterministic and Uncertainty Analyses [7], and the Surry integrated UA of the unmitigated short-term station blackout (STSBO) presented herein.

The original SOARCA project [1] analyzed selected scenarios, first assuming the events proceeded without the 10 CFR 50.54(hh) mitigation measures (unmitigated), and then assuming that the 10 CFR 50.54(hh) mitigation is successful (mitigated). While these analyses have generally met the SOARCA project objectives, certain additional severe accident consequence analyses were warranted to expand upon the body of knowledge developed in SOARCA and to support and inform other agency activities including the Site Level 3 Probabilistic Risk Assessment (PRA) and Fukushima lessons learned projects. These additional analyses are discussed in SECY-12-0092, “State-of-the-Art Reactor Consequence Analyses – Recommendation for Limited Additional Analysis,” dated July 5, 2012 [4], where staff recommended performing a UA for a severe accident scenario at Surry; the insights from which would inform the Site Level 3 PRA. The Commission’s Staff Requirements Memorandum on SECY-12-0092 further noted that the ongoing SOARCA studies should support post-Fukushima activities including Tier 3 items [4].

MELCOR and the MELCOR Accident Consequence Code System (MACCS) are the NRC developed codes for analysis of severe accidents and their consequences. These codes were used in all the SOARCA calculations. The SOARCA analyses show that successful implementation of existing mitigation measures can prevent reactor core damage, or delay, or reduce offsite releases of radioactive material [1]. All SOARCA scenarios [1], even when unmitigated, progress more slowly and release much less radioactive material than in earlier studies (e.g., NUREG/CR-2239, commonly referred to as the 1982 Siting Study [5]). The SOARCA analyses show that emergency response programs, implemented as planned and practiced, would reduce the scenario-specific risk of health consequences among the public during a severe reactor accident at the plants evaluated [1]. As a result, the calculated risks of public health consequences from severe accidents modeled in SOARCA are very small.

In 2013, an integrated UA was completed on the unmitigated LTSBO for Peach Bottom [2]. This first-of-a-kind UA study provided a quantitative analysis of the robustness of the deterministic

SOARCA calculation [1], and in the process, demonstrated the feasibility of producing integrated uncertainty results. The Peach Bottom UA results are informative; however, the analysis was conducted for the unmitigated LTSBO scenario for a boiling water reactor (BWR). As with the Surry UA presented herein, the application of the results must be tempered with the understanding of the reactor type, containment type, scenario for which results were produced, and site-specific characteristics. This UA of the unmitigated STSBO at the Surry Power Station continues the SOARCA work.

The Surry UA followed the approach developed for the Peach Bottom UA. The unmitigated STSBO was selected as the accident scenario for the Surry UA, in part because of the importance of station blackout (SBO) scenarios and because SBO accident progression provides opportunity to assess the offsite response parameters while the release is potentially underway under the postulated conditions. The unmitigated LTSBO analyzed in the Peach Bottom UA [2] showed that battery life is important in delaying the start of releases. For the Surry UA, the short-term variant on the SBO was selected to investigate the potential for early release and greater consequences. Of the scenarios selected for Surry in the SOARCA study, the unmitigated STSBO with induced SGTR was also one of the two scenarios with the highest conditional individual LCF risk [1]; the Surry UA effort considers induced SGTR. As an unmitigated scenario, a few operator actions were considered to be attempted, but were not successful as described in Section 2.1. Lessons learned from the Peach Bottom UA and feedback from the NRC's Advisory Committee on Reactor Safeguards (ACRS) on the Peach Bottom, draft Surry, and Sequoyah UAs were included, as well as additional knowledge gained since the publication of NUREG/CR 7110 Volume 2 [3] (also referred to as the original SOARCA or Surry SOARCA throughout this study) and the integrated deterministic and UA for the Sequoyah Nuclear Plant (Sequoyah) [7].

For this UA, epistemic uncertainty was explored by randomly sampling distributions for selected parameters. In NUREG/CR 7110 Volume 2, the only uncertainty considered was that associated with weather conditions at the time of the accident, which is aleatory [3]. In NUREG/CR 7110 Volume 2, the reported offsite consequence values represented the mean value (arithmetic average) for a large number of these aleatory weather trials. This best practice approach [6] to weather uncertainty was also applied for the Surry UA.

A distribution was developed for each varied parameter with the intent of representing the degree of belief in the expected range. Often, the mode (most likely value) of the distribution corresponded to the best estimate value used in the original SOARCA analysis [3]. Each of the probability distributions were applied in the respective MELCOR and MACCS models (e.g., the specific Surry model). For MELCOR, this often required enhancing the model to accept the distributions. When final runs were ready to be executed, the most current MELCOR and MACCS code versions available at the time were used. These changes to the codes made it very difficult to make a direct comparison of results to understand the precise robustness of the original SOARCA calculation; particularly for MELCOR, because MELCOR Version 1.8.6, used in the original SOARCA study, is no longer maintained. The MELCOR accident progression and a comparison of the MELCOR Version 1.8.6 and Version 2.1 results are presented in the draft Surry UA documentation [8]. However, the present work used MELCOR Version 2.2 and a comparison between results presented in the draft Surry UA documentation[8] and this work was not conducted.

1.1 Background on SOARCA

The NRC, the US nuclear power industry, and the international nuclear energy community have devoted considerable research over the last several decades to examining severe reactor accident phenomena and offsite consequences. These updated analyses incorporate the wealth of accumulated research and use the most detailed, integrated, and best estimate modeling to date. An insight gained from post-9/11 security assessments was that the NRC needed updated analyses of severe reactor accidents to better reflect realistic estimates of the more likely outcomes; considering the current state of plant design, plant operation, and the advances in understanding of severe accident behavior [1].

The NRC initiated the SOARCA project in 2005, and in the original phase completed in 2012, developed best estimates of the offsite radiological health consequences for potential severe reactor accidents at Peach Bottom and Surry. Peach Bottom is a U.S. operating reactor using the General Electric boiling-water reactor (BWR) design with a Mark I containment. Surry is a U.S. operating reactor using the Westinghouse pressurized-water reactor (PWR) design with a large, dry (sub-atmospheric) containment [1].

Preparations for SOARCA [1] included extensive cooperation from the licensees to develop high-fidelity plant system models, define operator actions (including the most recently developed mitigation actions at the time), and develop models for simulation of site-specific and scenario-specific emergency response. In addition to input for model development, licensees provided information on accident scenarios from their PRAs. Through tabletop exercises of the selected scenarios with senior reactor operators, PRA analysts, and other licensee staff, licensees provided input on the timing and nature of the operator actions to mitigate the selected scenarios. The licensee input for each scenario was used to develop assumed timelines of operator actions and equipment configurations for implementing available mitigation measures which include mitigation measures beyond those routinely credited in the licensee's current PRA models. A human reliability analysis was not performed for SOARCA, but instead tabletop exercises, plant walkdowns, simulator runs, and other inputs from licensee staff were employed to ensure that operator actions and their timings were correctly modeled [1].

Updated and benchmarked standardized plant analysis risk (SPAR) models and available plant-specific external events information were used in the SOARCA scenario selection process [1]. Scenarios common to both Peach Bottom and Surry included the STSBO and LTSBO. Both types of SBOs involve a loss of all alternating current (AC) power. For Surry, the STSBO also involves the loss of turbine-driven systems through loss of direct current (DC) control power or loss of the condensate storage tank, and therefore proceeds to core damage more rapidly (hence "short term"). The STSBO has a lower core damage frequency than the LTSBO since it requires a more severe initiating event and more extensive system failures. SOARCA assumed that a SBO is initiated by a seismic event, since this is the most extreme accident sequence in terms of both the timing and amount of equipment that fails [1]. SBO scenarios are commonly identified as important contributors in PRA because of the common cause failure for both reactor safety systems and containment safety systems.

1.2 Objectives

The overall objective of the SOARCA project was to develop a body of knowledge regarding realistic outcomes of theoretical severe nuclear reactor accidents. The UAs further expand this body of knowledge. The objectives of the Surry UA include:

1. Evaluate the robustness of the NUREG/CR 7110 Volume 2 SOARCA Surry deterministic results [3].

2. Determine whether the Surry UA results corroborate the general conclusions and insights from the original SOARCA study [1].

3. Develop insights into the overall sensitivity of SOARCA results to uncertainty in selected modeling inputs.

4. Identify influential input parameters contributing to accident progression and offsite consequences through application of an uncertainty analysis methodology.

5. Inform the NRC's Site Level 3 PRA and post-Fukushima activities including Tier 3 items.

Regarding informing the Level 3 PRA, this was accomplished by including NRC Level 3 PRA staff in Surry UA meetings, beginning early in the project. This continued through parameter development and as early results became available.

1.3 Scope

The scope of the Surry UA was to produce a state of the art UA that achieves the objective of evaluating the robustness of the original SOARCA analysis and provides insights into the overall uncertainty of the best estimate results and conclusions. This required the following:

- Developing distributions for selected parameters;
- Implementing MELCOR and MACCS model enhancements to accommodate distributions;
- Implementing additional enhancements to improve selected features of the MELCOR model;
- Performing the severe accident and offsite consequence analyses;
- Performing regression analysis;
- Conducting sensitivity analyses and investigating single realizations; and
- Examining results to identify parameter importance and severe accident insights.

To achieve the scope within a reasonable level of effort, project limitations were necessary. Each sampled parameter in MELCOR and MACCS required extensive research, and in some cases model enhancements; therefore, a reasonable number of parameters was selected. The scope of this project does not include model uncertainty or completeness uncertainty.

1.4 Methodology

A methodology for the integrated investigation of uncertainties in MELCOR accident progression and MACCS offsite consequence analyses was developed in the Peach Bottom UA [2]. The methodology for the Surry UA generally followed the same approach. Like Peach Bottom, the accident scenario was selected, followed by identification of parameters of interest to be varied in the analyses, specific to a PWR reactor type. A minor departure from Peach Bottom was that some sensitivity analyses and 'one-off' calculations[11] were performed earlier in the process to help inform some of the parameter distributions [8]. This approach was suggested during the ACRS review of the Peach Bottom study. The Surry UA also applied the insights from the

[11] MELCOR analysts run periodic analyses to view the effects on model performance or results of a specific parameter.

Sequoyah UA [7], and expanded and enhanced selected project activities based on lessons learned. Thus, the Surry UA is continuing the advancement of the state of knowledge and understanding relevant to severe accident analyses.

The Surry UA team conducted a lessons-learned meeting to identify the processes and applications that worked well for the Peach Bottom UA [2] and the Sequoyah UA [7], and applied those that could have worked better. The lessons learned, a few of which are described below, are addressed throughout the report.

- Better parameter documentation. For the Surry UA, a storyboard approach was implemented to justify and defend the parameter distributions early in the effort. A 'storyboard' is simply a specified format for each author to document key parameter information.

- The results of the sensitivity analyses could have been useful in informing the selection of parameters for investigation. For the Surry UA, some sensitivity analyses were completed early in the process to better inform the overall effort.

- MACCS output volume was very high causing post processing to take longer than planned. For the Peach Bottom UA, the amount of data to be post-processed overwhelmed the capabilities of MACCS and was addressed on an ad hoc basis. For the Surry UA, the code was modified to resolve the issue.

- While the quality assurance (QA) of the Peach Bottom UA model inputs was implemented, it was not systematic or documented. For the Surry UA, a systematic and rigorous QA of the MELCOR and MACCS inputs and model enhancements was performed; including legacy values when appropriate (e.g., dose coefficients).

2 UNCERTAINTY ANALYSIS APPROACH

The approach implemented for the Surry UA generally followed that applied with the Peach Bottom UA [2] and the Sequoyah UA [7]. The major activities included:

- Selecting the accident scenario;
- Selecting input parameters and developing distributions;
- Model modifications and enhancements;
- Analysis; and
- Investigation of results.

To meet the objective of developing insights into the overall sensitivity of SOARCA results to uncertainty in selected modeling inputs, the modeling inputs important to the figures of merit being assessed, were identified. The MELCOR figures of merit for the uncertainty analysis are environmental releases of cesium and iodine, and the in-vessel hydrogen production. Due to the differences in the early radionuclide response, the figures of merit for the realizations with steam generator tube ruptures are discussed separately. The MACCS figures of merit are individual latent-cancer fatality (LCF) risk and individual early fatality risk at specified distances. The accident scenarios and parameter selection process are described below. The code modifications, analysis, and investigation of results are described in subsequent sections.

2.1 Accident Scenario

The Surry SOARCA unmitigated STSBO [3] was selected as the UA accident scenario in part because of the importance of station blackout scenarios to nuclear power plant risk, and because accident progression occurs relatively quickly under the postulated conditions. The relatively quick accident progression provides an opportunity to assess the offsite response parameters while the release is potentially underway. of the scenarios selected for the SOARCA Project, the Surry unmitigated STSBO with induced SGTR was also one of the two scenarios with the highest conditional individual LCF risk [1]. This scenario, as detailed in the Surry SOARCA study [3], is initiated by an earthquake (0.5–1.0g peak ground acceleration) and has an estimated frequency of $1x10^{-6}$ to $2x10^{-6}$ per reactor year (pry). System failures were specified in the Surry SOARCA calculation [3] based on the type of event.

The seismic event causes a loss of offsite power and failure of onsite emergency AC power resulting in a SBO where neither onsite nor offsite AC power are recoverable. All systems dependent on AC power are unavailable, including all active emergency core cooling systems (ECCSs) and the containment engineered safety systems (e.g., the containment sprays and fan coolers). The reactor coolant system (RCS) and containment are undamaged, and the containment is isolated. No instrumentation is available.

Additionally, significant auxiliary structural damage outside containment is judged to have occurred, including structural failure of the turbine building and loss of access to the condenser blow down valves [3]. Also, this seismic event causes a failure of the emergency condensate storage tank (ECST), which is the source of water for the turbine driven auxiliary feedwater (TDAFW) system making this a STSBO rather than a LTSBO.

The available systems include the passive ECCS accumulators, as well as unused mitigative equipment including portable power supplies, portable air bottles, and portable high-pressure

(Kerr) and low-pressure (Godwin) diesel driven pumps. The containment spray and firewater piping are assumed to remain intact, but these systems were not active in the unmitigated analysis.

Although mitigative actions would be recommended and attempted throughout an emergency, the unmitigated STSBO in this analysis assumes no mitigative actions are successful. The mitigated response, analyzed for Surry SOARCA [3] included successful implementation of mitigative actions, which are intended to prevent the accident from progressing, termination of core damage (if it begins), maintenance of the integrity of the containment (as long as possible), and minimizing of the effects of offsite releases. As described in NUREG/CR 7110 Volume 2 [3], an expected National level response to a severe nuclear power plant accident provides a basis for truncating the environmental release to no later than 48 hours after the accident begins. Past studies, including NUREG-1150 [16], typically truncated releases after 24 hours. Consistent with the SOARCA Project [1], the Peach Bottom UA [2] also considered a 48-hour truncation timeframe. Consistent with more recent analyses post-Fukushima, such as the Containment Protection and Release Reduction technical basis (NUREG-2206) and the SOARCA Sequoyah analyses [7], and due to the inclusion of relatively low beginning of cycle decay heat which suggest a 48-hour timeframe may not be appropriate, a 72-hour truncation time is considered for environmental releases in this UA.

2.2 Selection of Uncertain MELCOR Parameters

MELCOR uses thousands of input parameters and sensitivity coefficients in the evaluation of the equations and algorithms embedded in its constituent models. Many parameters are basic well-known inputs, e.g., core inventory, material properties, sizes and lengths of piping. However, there are many input parameters for which the base values were established through comparison to experiments. Additionally, some input parameters were established long ago by subject matter experts (SMEs) and were assumed reasonable for the present application.

The extensive investigation into parameters for the Peach Bottom UA [2] and Sequoyah UA [7] were leveraged for the Surry UA; as well as, insights from previous Surry UA draft work [8]. The Peach Bottom UA input parameters were used as the starting point in the review of this work because they were initially chosen by collective expert judgment, and due to their proposed impact on key portions of accident progression, such as in-vessel melting. Although some of the input parameters used in this work did not show importance in either the Peach Bottom UA or the Sequoyah UA results, the parameters were maintained for further investigation because they could be important for a different reactor type, different containment type, and different scenario. A suite of common input parameters was kept at this stage primarily because in the Peach Bottom analysis, the overwhelming importance of a handful of parameters in determining whether the accident progressed to main steam line (MSL) rupture, which in turn was a large determinant of release magnitude, could mask parameters that are important for other scenarios and reactor types. However, the Peach Bottom UA input parameters specific only to BWRs were removed from consideration, such as parameters related to drywell refueling dome leakage.

The chosen set of input parameters is not an exhaustive list of all parameters important for MELCOR analyses nor was a phenomena identification and ranking table (PIRT) conducted. There are many alternative parameters that could represent the phenomenology of interest, and a practical subset was chosen to capture important aspects of modeling without introducing unnecessary complications, such as the need to extensively specify correlations.

Developing the input parameter list was a multi-step and iterative process. An initial input parameter list was prepared and reviewed jointly by Sandia and NRC staff early in the project. These meetings included brainstorming sessions where additional input parameters were discussed and added to the list. Next was a more comprehensive team review from a systems approach with detailed consideration of the following:

- Sequence issues,
- In-vessel accident progression,
- Ex-vessel accident progression,
- Containment response, and
- Radionuclide behavior.

During these reviews, the Sandia analysts described the phenomenology and characteristics of each system and discussed why the input parameters should be considered candidates for the UA. After the systems review, the candidate input parameter list was updated. At this point, identification of parameters through expert judgment had been completed and the parameter list was relatively complete.

Next, a phenomenological based review was conducted of the MELCOR Reference Manual [14] rather than a mechanistic review of parameters in the MELCOR User's Guide [15], because a review of the User's Guide, which contains thousands of parameters and inputs, was not practical. In fact, experience from other UAs suggested more insights could be determined from a small set of uncertain parameters.

First, the uncertain physics or phenomenological parameters were discussed. The notes from the review meeting as a function of the MELCOR physics packages are listed below.

- Burn Package
  - Consider variations in the hydrogen flammability limit.
  - Consider uncertainty in flammability limits based on uncertainty in the initial propagation direction.

- Cavity Package
  - Consider addressing uncertainty in the amounts of gasses generated by molten core-concrete interaction by sampling the proportions of common sand and aggregate in the concrete.

- Condenser Package
  - Not applicable. The Surry units do not have isolation condensers or a passive containment cooling system.

- Core Package
  - Consider uncertainty in the core blockage user input
  - Address uncertainties in core degradation including fuel collapse
  - Address uncertainties in core material eutectic melting temperature
  - Address uncertainties in the oxidation kinetics

- Control Volume Hydrodynamics-Flow Path Packages
  - No related parameters identified as potentially significant.

- Decay Heat Package
  - Address variation in decay heat dependent on where the core is in its lifecycle when the accident occurs.

- Fan Cooler Package
  - This is a SBO scenario, and without AC power the fan coolers would not be operating.

- Fuel Dispersal Package
  - This parameter is only important if the analysis shows a high-pressure ejection. After the initial set of MELCOR uncertainty runs were complete, the results were reviewed and confirmed the fuel dispersal package parameters did not require investigation.

- Heat Structures Package Manual
  - Condensation was identified as a potential parameter. The effect of the presence of non-condensable gas on condensation rate.

- Material Properties Package Manual
  - Eutectic temperatures for zircaloy oxide and uranium oxide

- Non-condensable Gas and Water Package
  - No uncertainty modeling suggested here.

- Passive Autocatalytic Hydrogen Recombiner Package Manual
  - Not applicable because there are no passive autocatalytic hydrogen recombiners at US reactors.

- Radionuclide Package
  - Model uncertainty in dynamic shape factor
  - Chemical form (CHEMFORM) of cesium and iodine

- Containment Sprays Package
  - Not applicable. Containment sprays are not available in the SBO scenario.

In addition to uncertainties in the severe accident phenomenology, the following sequence-related parameters were considered for inclusion. Sequence-related parameters included hardware failures and possible operator actions (i.e., parameters not related to the physics models). The notes on the sequence-related parameters are listed below.

- Valve behavior
  - Consider uncertainty in stochastic failure of the pressurizer and steam generator safety valves to open or close
  - Consider uncertainty in thermal failure of the pressurizer and steam generator safety valves to open or close
  - Consider uncertainty in failure area when a valve does not close
  - Consider uncertainty in the main steam isolation valve leakage area

- Pump seal leakage
  - Consider uncertainty in pump seal failure and the resultant leakage rate

- Steam generator tube rupture
    - Consider uncertainty in the depth and location of steam generator tube flaws
    - Consider uncertainty in the temperature and flowrate of the hot thermal plume entering the steam generator

- Containment performance
    - Consider uncertainty in the containment nominal leakage rate
    - Consider uncertainty in the containment failure criteria (pressure, temperature, and leakage area)

- Operator actions
    - Consider availability of firewater injection systems at different times
    - Consider availability of power for relief valve flow at different times

The merits of various parameters that could be used to characterize uncertainties in the various MELCOR physics models and sequence-parameters were debated. The list of parameters has evolved through the insights from the previous uncertainty assessments [2][7][8]. As knowledge was gained on the importance of parameters from the other uncertainty assessments, the list of parameters was adjusted. In response to ACRS member comments, the parameters used to characterize the uncertainty varied. The final list of parameters is summarized in Table 2-1.

Although operator actions were discussed, the scope of the effort was limited to an unmitigated accident. This allowed a more in-depth investigation of phenomenological and hardware-related parameters without the complications of operator and mitigative actions that can radically alter the accident progression.

The next step in the uncertain parameter development included the rationale for the parameter selection. To facilitate development of parameter justification and rationale, a storyboard process was implemented. Figure 2-1 illustrates the form that was created to identify the parameter, technical justification for uncertainty, type of distribution, rationale for the distribution, and which related parameters were considered and rejected for inclusion (discussed further in Section 2.2.1 below). The intent was to capture, in a concise format, specific information regarding each parameter from which the detailed technical bases could ultimately be developed.

The storyboards were reviewed internally where analysts explained and defended each parameter. The team challenged the technical leads to explain the basis and defend the appropriateness of supporting data. This approach often resulted in the need for additional research to support the rationale. When significant changes were required to a storyboard, the parameter was again reviewed internally. Once a set of storyboards was ready, Sandia coordinated a joint review meeting with NRC staff SMEs to review and critique the parameter distributions and rationale.

The storyboards were presented in ACRS subcommittee meetings to solicit input on the parameter selection process. A frequent ACRS member comment was for the technical team to clearly identify the point of departure from a known technical basis, at which use of professional judgment begins. Such judgment was often required in the development of parameters and has been identified, where applicable, within this project. Another area of interest in the ACRS members' review was the level of detail of the technical justification for the uncertainties assigned to each parameter and the rationale for the type of distribution used to characterize the uncertainty.

Table 2-1 Surry MELCOR Model Uncertain Input Parameters

MELCOR Input Parameters
Sequence
Primary safety valve (SV) stochastic failure to close
Primary SV open area fraction
Secondary SV stochastic failure to close
Secondary SV open area fraction
Reactor coolant pump seal leakage
Normalized temperature of hottest steam generator (SG) tube
Steam generator non-dimensional flaw (NDF) depth
Main steam isolation valve (MSIV) leakage
In-Vessel Accident Progression
Zircaloy melt breakout temperature (SC1131(2))
Molten clad drainage rate (SC1141(2))
Effective temperature at which the eutectic formed from zircaloy oxide (ZrO_2) and uranium oxide (UO_2) melts
Decay heat based on time within the fuel cycle
Oxidation kinetics model
Containment Response
Hydrogen ignition criteria (H_2 LFL)
Containment design leakage rate
Containment fragility curve (CFC)
Containment convection heat transfer coefficient
Radionuclide behavior
Chemical form of iodine (CHEMFORMion[1]
CHEMFORM cesium fraction
Dynamic shape factor
Secondary side decontamination factor (ARTIST)

[1] This parameter is also informed from the Decay Heat section.

Parameter Name:	Type of Distribution:
Technical justification for the uncertainties:	
Rationale for type of distribution:	
Were similar or related parameters considered and rejected.	
Graphic: (plot of the distribution)	

Figure 2-1 Key Information Evaluated in the Uncertain Parameter Storyboards

2.2.1 MELCOR Parameters Considered but not Included

The process described above included multiple review steps, each of which provided an opportunity to add parameters or justify why further consideration of a parameter was not needed. The parameters below represent some of those that were considered but not included in the analysis.

Other Primary SV Failure Modes
SV reseat pressure (the pressure at which a SV closes, lower than the opening condition) was considered, but was omitted from further investigation based on insights from the Peach Bottom UA [2] and because SV dynamics are well represented in the Surry analysis [3]. The Peach Bottom UA identified that the SV setpoint drift will produce analogous results to the distributions considered for SV stochastic failure to close (FTC) [1]. A delay in the SV stochastic FTC will be representative of those sequences within the Surry analysis that have long SV cycle periods prior to stochastic failure. These long SV cycle periods will produce sequence results similar to what would be expected from uncertainty in the SV reseat pressure.

In the draft Surry UA [8], the valve failure to open (FTO) mode was included. However, a FTO of all three primary SVs was not sampled due to the very low probability. The subsequent Sequoyah UA [7] includes an analysis that shows the probability of all three valves FTO is almost three orders of magnitude lower than the probability of that at least one SV stochastic FTC. Based on this very low probability, the FTO mode was not included in this UA.

The draft Surry UA [8] included passing water through the SV as uncertain variable. The subsequent Sequoyah UA [7] documents discussions with nuclear valve testing personnel and Idaho National Laboratory Licensee Event Report (LER) data base specialists identified passing water is not necessarily threating to a SV but passing ‘cold water’ is a problem (cold being relative to valve design conditions). The conditions that promote water flow through the pressurizer SV during the STSBO is when the fluid is heated near saturated conditions (i.e., much different than the historical problem of cold condensed water in the loop before the valve). Consequently, the uncertainty of SV failure due to passing water is not included.

The draft Surry UA [8] included thermal failure of the primary SV FTC as uncertain variable. The accident progressions during the draft Surry UA did not reach high SV temperatures where thermal failures would be likely (i.e., unlike the responses observed in the Peach Bottom UA [2]). Consequently, the uncertainty of SV FTC failure due to passing high temperature gases is not included.

Concrete Properties
Core-concrete interaction (CCI) is an important phenomenon in ex-vessel accident progression where uncertainty is expected. Varying CORCON parameters was considered but was not included. The team considered the potential for varying the aggregate quantity of the concrete mix, which could affect gas generation. A sensitivity analysis on concrete aggregate was performed in the draft Surry UA [8], which provided the insights on the impact of the concrete properties.

Reactor Pressure Vessel (RPV) Lower Head Penetration Failure
SOARCA and ACRS reviewers have commented that failure of instrument tube and other lower head penetrations (e.g., RPV drain line) should be considered in addition to gross lower head failure. For example, an analysis of the margin to failure of the TMI-2 vessel suggests competing failure mechanisms of instrument tube rupture, instrument tube ejection, global vessel failure, and localized vessel failure [11]. Post-accident examinations of the TMI-2 lower head from the Vessel Integrity Program (VIP) revealed that several of the instrument nozzles were severely ablated. Similarly, Reference [12] describes detailed methodologies for estimating the likelihood of an earlier penetration failure that are not currently modeled in the MELCOR code. The numerical evaluation of penetration is dependent upon multi-dimensional heat transfer, core melt flow physics, the weld strength and geometry, and the composition and temperature of the debris adjacent to the lower head, which is beyond the current capabilities of MELCOR.

The impact of this limitation was considered in the Sequoyah UA [7] and determined to be most important for the timing of an early containment failure (i.e., hydrogen deflagrations which failed containment). It would also be particularly important for mitigated accidents that include injection recovery after core damage. However, the impact of the penetration failure was judged to be less important to the magnitude of the source term for the unmitigated Surry STSBO, which always progresses to containment failure well after vessel failure. Due to the lack of an adequate mechanistic model and lower importance for this study, this vessel failure mode was not further considered.

Secondary Decontamination Factor
The Aerosol Trapping in a Steam Generator facility (ARTIST) built at the Paul Scherrer Institute (PSI) in Switzerland hosted a series of tests to try to determine the amount of decontamination that occurs within a steam generator following a steam generator tube rupture (SGTR) [13]. An alternative to implementing the ARTIST approach was reviewed and would have included turning on MELCOR models for aerosol capture and settling on the secondary side. For this to be a reasonable alternative, significant effort would have to be made to model all possible deposition structures on the secondary side, and there is uncertainty regarding whether such an approach would produce a more physical result due to MELCOR limitations (e.g., lack of a particle bounce model). Because of this, the total secondary decontamination factor (DF) (ARTIST approach) was selected.

Radial Solid and Molten Debris Relocation Rate
MELCOR uses relocation time constants to specify the radial movement of solid and molten debris from ring to ring. This is one of a few MELCOR parameters, which could be modified to influence uncertainty to in-vessel debris movement. Although many experiments exist to inform axial fuel relocation, there is a decided lack of data available to inform radial debris relocation. The main reason for this is because the test facilities, such as Phebus and CORA, were too small in scale to really observe the effects of radial relocation. he MELCOR default for the radial solid relocation constant (360 s) and the radial molten debris relocation constant (60 s) are

used, which were used for the original SOARCA calculations [3] and the Sequoyah UA [7]. These parameters lack a good technical basis for their uncertainty range and were not identified as an important parameter in the Peach Bottom UA [2] and draft Surry UA [8]. Consequently, these parameters were not selected as uncertain parameters and the defaults are used.

2.3 Selection of Uncertain MACCS Parameters

There are also potentially thousands of input parameter values that could be varied in MACCS. Therefore, an early effort was to select a reasonable number of parameters important to the figures of merit being assessed. The figures of merit for MACCS are LCF risk and early fatality risk at specified distances. The project team again began with a review of the MACCS parameters in the Peach Bottom UA [2], the draft Surry UA [8], and the Sequoyah UA [7]. There was no compelling reason to remove any of the parameters from consideration. Furthermore, the plant type and accident scenario differences could show a different priority of importance of the Peach Bottom parameters when applied in the Surry analysis. Therefore, the full list of MACCS parameters used in the Peach Bottom UA was the starting point.

A complete review of MACCS parameters identified in Appendix D, “Glossary of Input File Variables,” of NUREG/CR-6613 [80] was conducted. The following parameter sets were included in the analysis with each set consisting of multiple individual input parameters;

- Deposition,
- Dispersion,
- Shielding,
- Early Health Effects,
- Latent Health Effects, and
- Emergency Response.

Both epistemic and aleatory uncertainty exists for many MACCS parameters, and the combined effect adds complexity when developing the uncertainty distributions. Furthermore, for some MACCS parameters, compromise values were necessary when a large number of different situations (e.g., weather trials and time of day) exist, but only one input value may be assigned. The specified values selected were deemed the most appropriate to use for these situations. As a result, the epistemic uncertainty distributions for these parameters attempt to characterize the uncertainty of the most appropriate values.

Aleatory uncertainty in weather is treated in MACCS. Weather conditions that would apply in the case of a potential accident at some time in the future cannot be known in advance. MACCS accounts for weather variability by analyzing a statistically significant set of weather trials, and the modeled results are ensemble averages of weather trails that represent the full spectrum of meteorological conditions. This sampling strategy was chosen to represent the statistical variations of the weather and is consistent with MACCS best practices [6].

The MACCS input parameters varied in the analysis are listed in Table 2-2. The storyboard process described in Section 2.2 was also implemented for MACCS parameters. Some of the parameters in Table 2-2 are actually groups of individual parameters; for example, the CFRISK is actually a set of eight organ-specific risk factors (discussed further in Section 4.2).

Table 2-2 Surry MACCS Model Uncertain Input Parameters

Epistemic Uncertainty
Deposition
Wet Deposition Coefficient (CWASH1)
Dry Deposition Velocities (VDEPOS)
Shielding Factors
Groundshine Shielding Factors (GSHFAC)
Inhalation Protection Factors (PROTIN)
Early Health Effects
Early Health Effects LD_{50} Parameter (EFFACA)
Early Health Effects Exponential Parameter (EFFACB)
Early Health Effects Threshold Dose (EFFTHR)
Latent Health Effects
Dose and Dose Rate Effectiveness Factor (DDREFA)
Lifetime Cancer Fatality Risk Factors (CFRISK)
Long Term Inhalation Dose Coefficients
Dispersion
Crosswind Dispersion Linear Coefficient (CYSIGA)
Vertical Dispersion Linear Coefficient (CZSIGA)
Emergency Response
Evacuation Delay (DLTEVA)
Evacuation Speed (ESPEED)
Hotspot Relocation Time (TIMHOT)
Normal Relocation Time (TIMNRM)
Hotspot Relocation Dose (DOSHOT)
Normal Relocation Dose (DOSNRM)
Aleatory Uncertainty
Weather Trials

2.3.1 MACCS Parameters Considered but Not Included

As with the MELCOR input parameters, the MACCS storyboard process included multiple review steps, each of which provided an opportunity to add parameters or justify why further consideration of a parameter was not needed. The parameters below represent some of those that were considered but not included in the analysis.

Risk of Early Injury
Parameters to estimate the risk of an early injury, specifically pneumonitis, were made uncertain in the Peach Bottom UA [2]. However, early injuries were not reported in the Peach Bottom study, so there was little value to treating this uncertainty. Early injuries are not commonly reported because they are not life threatening and are of relatively less concern than fatalities. Therefore, for the Surry UA, the parameters for early injuries were set to the values used in the original SOARCA Surry study [3].

Ingestion Pathway
The ingestion pathway was not treated in the SOARCA project [1] because it does not contribute to individual LCF and early fatality risks, the SOARCA figures of merit. In addition, uncontaminated food and water supplies are abundant within the United States, and it is judged unlikely that the public would eat radioactively contaminated food [3].

Habitability
The habitability criteria is considered to be an important uncertain parameter, but was not included with the Surry UA because a detailed sensitivity analysis was performed with the Peach Bottom UA [2]. The Peach Bottom UA showed, as would be expected, that when the dose truncation models were used, the LCF risks within the emergency planning zone (EPZ) were orders of magnitude lower when the habitability criteria were below the dose truncation level. Beyond the EPZ, the habitability criteria still showed an important, though smaller, effect on the overall LCF risk when a dose truncation model was applied.

Non-Evacuees
Evacuation research has documented that some residents refuse to evacuate [85][86] and the fraction of this population is uncertain. MACCS does not have a capability to reapportion population fractions in an uncertain application. It was determined the code modifications to support varying population fractions could not be completed during the course of this effort, and the non-evacuating cohort fraction was kept at a single point estimate.

Wet Deposition
The wet deposition model parameters include CWASH1 and CWASH2. CWASH1 was selected to vary because there is considerable research and data available to support development of the uncertainty distribution. The same is not true for CWASH2. Although this would be a reasonable parameter to evaluate, it was not considered because there are insufficient data to support development of a defensible distribution. Furthermore, CWASH1 captures the effect of wet deposition sufficiently, such that it was not necessary to evaluate CWASH2 as an 'exploratory' uncertain parameter.

Cloudshine Shielding Factor
The cloudshine shielding protection factor (CSFACT) was included in the Peach Bottom UA [2]. However, in the storyboard process for the Surry UA, it was discovered that there was an error in the reference from which the cloudshine distribution was taken. There was no other source found to inform an accurate distribution for this parameter. Since this was not identified as an important parameter in the Peach Bottom UA and the team lacked a basis for specifying an uncertainty distribution for this parameter, a single point estimate was used.

3 DESCRIPTION OF CODES AND REGRESSION ANALYSIS

The NRC severe accident codes were applied in this UA, and regression analyses were conducted on the results. The codes and techniques applied in this study were the same as those used in the Peach Bottom UA [2] and Sequoyah UA [7]. Some updates have been implemented in both the codes and in the regression approach since the Peach Bottom UA; these are described below.

3.1 Severe Accident Analysis Codes

MELCOR, MelMACCS, and MACCS are the three primary codes used in the integrated analysis. These codes are continually enhanced, updated, and maintained as part of the NRC research program. Version control numbers are assigned to each code throughout this process. The codes were designed to work in conjunction with one-another with the outputs from one code becoming inputs for the next code, making deterministic analyses easier. The codes have been integrated for use in analyzing uncertainty in the same manner as implemented for the Peach Bottom UA [2], as illustrated in Figure 3-1. The full Surry UA analysis also uses the MELCOR uncertainty engine and an external macro that creates appropriate unique RN inventories based on the time at cycle and other uncertain radionuclide sampling inputs. A brief description of each code is shown below.

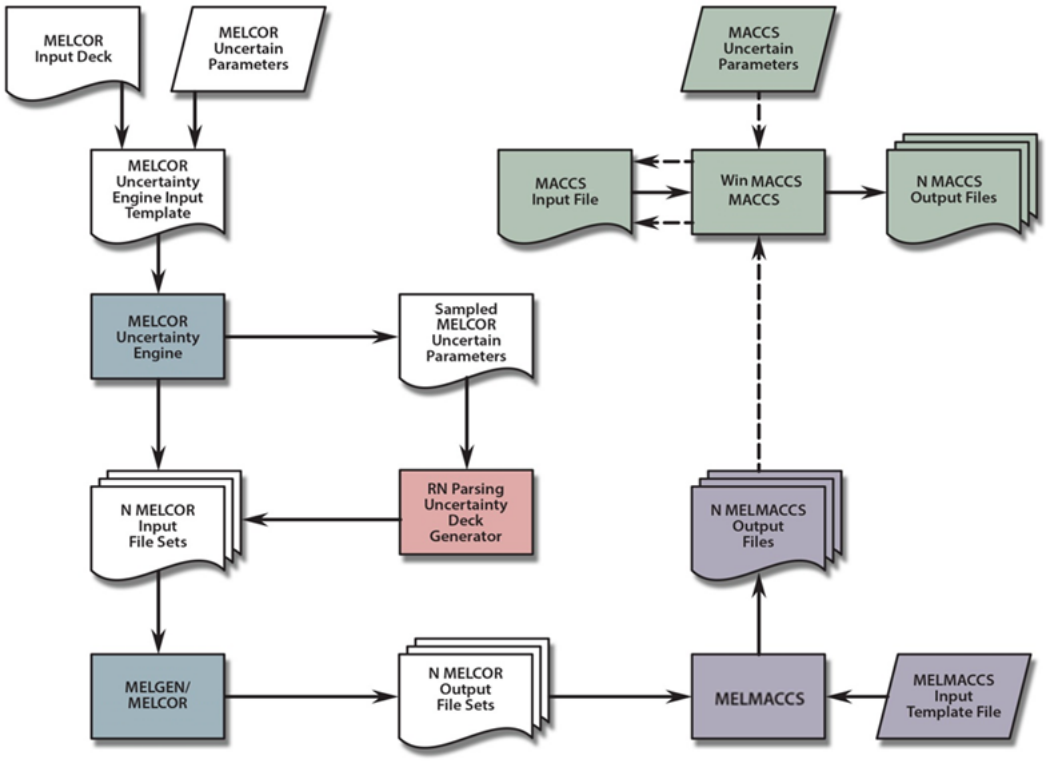

Figure 3-1 Diagram of the UA Framework and Information Flow

The MELCOR uncertainty engine implements two processes, illustrated in the vertical path on the left of Figure 3-1. Based on the desired number of uncertainty calculations, 'N', the uncertainty engine software creates a base set of 'N MELCOR input file sets' that define the Surry model and the transient specifications (i.e., often described as the input *.gen files). Included in each set of realization files are the unique set inputs based on the sampled uncertainty parameters, which are specific to each MELCOR run. It is at this point in the process where the uncertainty parameter 'time at cycle' is used to additionally vary the radionuclide inventory. Additionally, based on the selection of the uncertain radionuclide uncertainty parameters, radionuclide distributions are created using supporting scripts, which are discussed in Section 4.1.4.

3.1.1 MELCOR

MELCOR is a fully integrated, engineering level computer code that models the progression of severe accidents in nuclear power plants [14]. A broad spectrum of severe accident phenomena in both boiling and pressurized water reactors is treated in MELCOR in a unified framework. This includes the thermal-hydraulic response in the reactor coolant system, the reactor cavity, the containment, and the confinement buildings; the core heatup, degradation, and relocation; the core-concrete attack; the hydrogen production, transport, and combustion; and the fission product release and transport behavior. An illustration of applying MELCOR in an uncertain framework is provided in Figure 3-2.

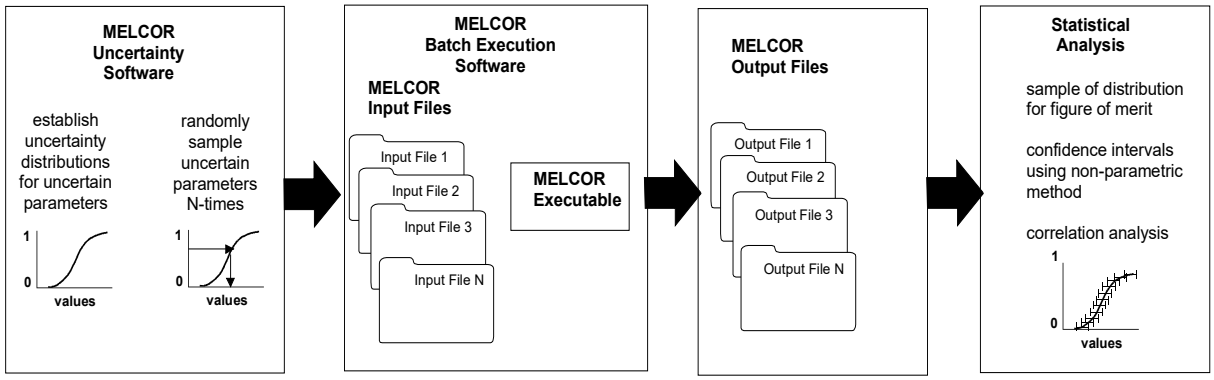

Figure 3-2 MELCOR Source Term UA Framework

The MELCOR SOARCA Surry analysis in NUREG/CR 7110 Volume 2 was performed with MELCOR 1.8.6 YV3780 [3] circa 2007. A code modernization effort initiated in early 2000 resulted in the conversion of the source code from Fortran 77 (MELCOR 1.8.6) to FORTRAN 95 (MELCOR 2) that changed the input deck structure but not the underlying models. MELCOR 2.2 is current code version and the earlier versions of the code are no longer maintained (e.g., Version MELCOR 1.8.6). This uncertainty analysis was performed using MELCOR 2.2, Revision 10479 dated February 26, 2018.

A direct comparison of newly performed MELCOR 2.2 runs to the MELCOR 1.8.6 runs performed for the original MELCOR SOARCA Surry analysis [3] is not straightforward. There have been many code enhancements and improvements between MELCOR 1.8.6 and MELCOR 2.2. In addition, there have been improvements in the state-of-the-art severe accident modeling as well as some input corrections. Appendix A of the draft version of the current

analysis documents the impact of the code enhancements, model improvements, and model corrections [8].

Since 2007, the STSBO model used in NUREG/CR 7110 Volume 2 has continued to be advanced to support other non-SOARCA activities. Therefore, the first MELCOR activity for the Surry UA was to reconcile the SOARCA STSBO model with the most recent Surry model. Once this was complete, the SOARCA MELCOR 1.8.6 model was converted to MELCOR 2.1 input format. A limited set of additional enhancements were then implemented to improve areas of the model known to be weak or under represented. The model corrections and enhancements are described in Appendix A of Reference [8]. The key changes are listed below:

- New ex-vessel, core-concrete interaction (CCI) models to improve debris to concrete heat transfer;
- A refined steam generator nodalization on the inlet side to better predict the hot plume heat transfer (illustrated in Figure 3-3);
- Addition of the hottest steam generator tube representations for each loop;
- Added igniter logic to H_2/CO burn modeling;
- RCS hot leg nozzle creep rupture input was modified to:
    - Reflect that both the carbon and stainless steels of the nozzle need to fail for the pipe to rupture and that the carbon steel will fail first;
    - Consider whether the carbon steel of the nozzle has failed when determining the stress on the nozzle (realizing that the stress would increase markedly when the carbon steel failed); and
    - Reflect that the nozzles are clad (on the inside) with 1/8” stainless steel and that the wall thickness of the nozzles is 2½” inclusive of cladding;
- Identified the appropriate heat structure nodes to be examined for temperature dependencies in the creep failure logic; and
- Implemented the Surry core inventory, as described in Appendix A of Reference [8].

During the model enhancements and parameter research, several errors in the Surry SOARCA model [3] were identified and corrected. These errors include:

- Errant vapor pressure coefficients for control rod materials silver, indium, and cadmium were corrected.
- The chemical composition of the aggregate in the concrete in the Surry reactor cavity was corrected from limestone (used in the SOARCA study [3]) to a basalt-based aggregate. The SOARCA study [3] modeled a limestone-based aggregate, which was used in the Surry Modular Accident Analysis Program (MAAP) model. However, during research related to the UA, the team identified that the individual plant examination (IPE) model had specified a

basalt-based aggregate. Sandia obtained copies of the concrete test results from the University of Virginia which confirmed that basaltic based aggregate was used.

- Errant particle density function was corrected.

- Steam drains were not isolating.

Following the completion of the initial set of calculations in 2015 [8], the results were reviewed by the responsible subcommittee of the ACRS. In addition, a separate uncertainty study was performed based on the Sequoyah plant [7]. The Surry model was subsequently revised using the insights from the ACRS reviews and the Sequoyah UA study to include the following improvements.

- The H_2/CO burn modeling was updated to reflect improvements included in the Sequoyah analyses [7]. This included error corrections in the draft Surry UA that were previously assessed to have a small impact. The combustion model was also modified to require an ignition source from hot debris in the reactor cavity or from hot plumes above the auto ignition temperature exiting the reactor coolant system. The potential for hot plumes was monitored at the hot leg rupture, the PRT rupture disk, and the pump seal leakage pathways.

- The pressurizer relief tank modeling was updated to include three heat structures that separated regions for gravitational settling versus the sides and the top of the tank. Convective and radiative heat transfer from the tank to the containment were also implemented. The wall thickness of the tank was corrected.

- The steam generator tube creep failure models were updated to include thick-walled stress calculations for the hottest tube, the hot upflow region, and cold region of each steam generator. The stress calculations were moved to formula control functions to support uncertainty sampling based on the flaw depth in the steam generator tubes (see Appendix B).

- Non-flawed tube creep rupture calculations were added for the hottest tube, the hot upflow region, and the cold region of the steam generator. The non-flawed creep evaluations provide the margin between flawed and non-flawed tubes in each location.

- Revision and addition of many External Data File (EDF) outputs to monitor accident progression variables in the MELCOR calculations.

- Implemented updates per the recommendations found in NUREG-1922 for natural circulation flow splits in the steam generator, recirculation ratio, and hot leg drag coefficient [52]. The MELCOR counter-current flow (CCF) model was implemented for the natural circulation exchange in the hot leg.

- The solid and molten radial relocation constants were set to the default constant values (i.e., rather than being a sampled variable).[12]

---

[12] After review of the findings from the draft Surry UA and discussion with the ACRS, these parameters were excluded from the uncertainty evaluation. The two parameters had low importance in the parameter regressions.

- Updated RCP seal leakage to sample each loop independently.[13]

- Containment leakage was altered to be a flow multiplier of the allowable mass leakage.

- The lowest opening pressure safety valve on each SG was updated to allow uncertainty sampling on the FTC.

Finally, the following uncertainty parameter definitions and/or distributions were refined since the draft evaluation of the Surry uncertainty assessment [8]. These uncertain parameters are more fully discussed in Section 4.1.

- The primary and secondary safety valves FTC distributions were updated to follow the approach in the Sequoyah UA [7]. Following the draft Surry UA, the SV failure attributes were changed based on discussions with nuclear valve testing personnel and closer examination of Licensee Event Reports. The SV behavior was updated to reflect the expert judgment that the probability of the FTC on the first challenge is weighted differently than subsequent challenges.

- The primary and secondary safety valves failure area distributions were also updated to follow the approach in the Sequoyah UA [7]. The discussions with nuclear valve testing personnel and closer examination of Licensee Event Reports indicated a higher likelihood of either a slowly leaking (mostly closed) or a mostly open failure position.

- The steam generator tube flaw distribution was reevaluated based on historical Surry steam generator inspection reports and results in the NRC consequential steam generator tube rupture study [10].

- The Zircaloy steam oxidation kinetics correlation was added as an uncertainty parameter to be consistent with the Sequoyah UA [7].

- The nominal or design containment leakage uncertainty distribution was redefined to reflect industry and Surry improvements from performance-based testing [9].

- Fourteen decay heat and initial radionuclide inventories were calculated to span the operating cycle of the plant. The uncertainty algorithm samples uniformly on the time in the cycle and then selects from the closest decay heat profile and associated radionuclide inventory.

- The uncertainty parameters for the cesium speciation and the initial iodine gas mass are used to apportion the radionuclide masses from the appropriate radionuclide inventory results identified in the previous bullet. The apportioning algorithm conserves the radionuclide masses when assigning them to the various radionuclide classes identified in the uncertainty sampling (see Appendix D).

A comparison of the results from the direct conversion of the MELCOR 1.8.6 model to the MELCOR 2.1 model is described in Appendix A of Reference [8]. The comparison was

[13] Surry has upgraded their reactor pump seals to low leakage, Flowserve N-9000 seals [151]. The model for the higher leakage seals was retained in the UA, which allows comparison to the other UAs and an assessment of the parameter importance on the key figures or merit.

performed in two steps. First the original SOARCA results were compared to the MELCOR 2.1 results (i.e., a straight conversion with no input model changes). The thermal-hydraulic responses are very similar prior to the hot leg creep rupture. After the hot leg creep rupture failure, the MELCOR 2.1 accident progression proceeds slightly more slowly than the original MELCOR 1.8.6 calculation. However, the key timings to lower core plate failure, the vessel lower head failure, and the containment failure were within 1 hr of each other. Considering the complex physics after the hot leg failure, the agreement between the two calculations was judged relatively good.

The second step compared a reference UA input model[14] to the converted SOARCA model. Whereas the first comparison assessed the impact of the code changes for the same input model, the second comparison assessed the changes in the input model using the same code version. In contrast to the relatively close agreement in the first comparison step, the second comparison step revealed significant changes in the response due to new assumptions on the decay heat power, the reactor coolant pump seal leakage, the steam generator and pressurizer safety valve failure timing, the effective fuel eutectic melting temperature, the containment leakage and failure modeling, the containment reactor cavity concrete composition, the speciation of cesium, the inclusion of iodine gas, the aerosol aerodynamic shape factor, and the lower flammability limit for hydrogen. These changes led to a significantly new trajectory for the accident progression and a significant decrease in the source term at 48 hr. The most significant impact to the source term was the slower containment pressurization from the ex-vessel CCI with basaltic concrete versus the limestone concrete used in the UA study (i.e., corrected for the UA study, see discussion above). The slower containment pressurization from CCI with basaltic concrete delayed containment liner plate failure until after 41 hr versus 26 hr in the SOARCA analysis with limestone concrete.

[14] The reference model was defined using approximately median settings for the uncertain parameters used in the draft Surry UA study [8].

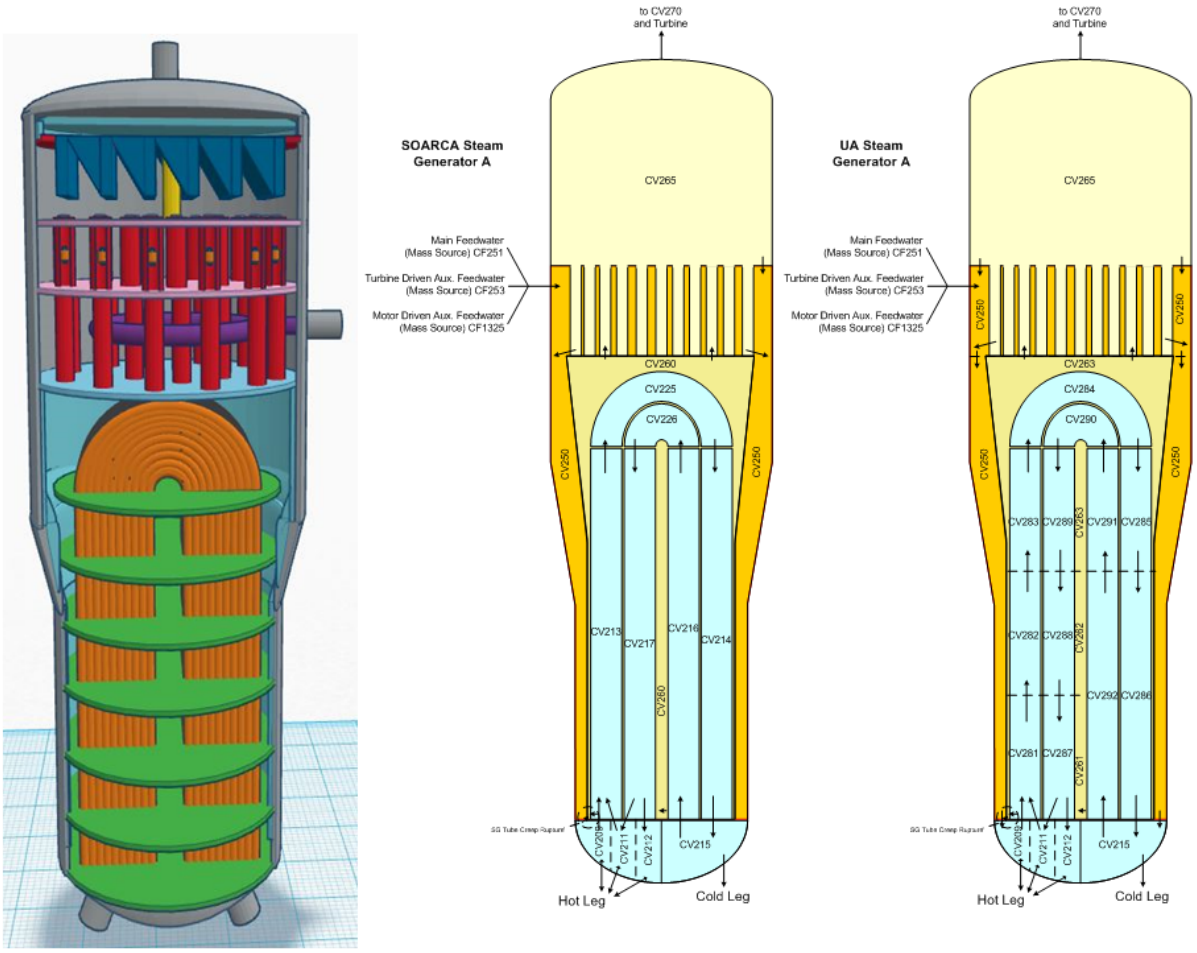

Figure 3-3 Comparison of the SOARCA and the UA Steam Generator Nodalizations

3.1.2 MELMACCS

MACCS requires isotopic breakdowns of the RN classes present in the MELCOR source term output and obtains these breakdowns from a pre-processing program called MelMACCS, which takes as input masses and activities for nuclides separated by ORIGEN-S output libraries (i.e. light elements, actinides, and fission products) and reactor model type. MELMACCS requires both nuclide mass and activity because it does not contain nuclear decay data, such as decay constants. The activity and mass of the radionuclides is specified as a function of time from ORIGEN-S. Historically, nuclide masses were used to linearly scale the activities by comparing the appropriate MELCOR class mass (in the MELCOR plot file) to the class mass in MelMACCS, which is calculated by summing the applicable user-specified nuclide masses. The SNL process for automatic generation of consistent MELCOR and MACCS inventories directly from ORIGEN-S output supersedes the need for the scaling algorithm. This method is both more consistent and accurate.

MelMACCS Version 1.7.7 SVN-2575 was used in this analysis. Implementation of MelMACCS required additional inputs that are not direct outputs from MELCOR [6], including:

- a set of radionuclide inventory files to reflect fuel burnup and the type of reactor (PWR or BWR),
- time of accident initiation in the MELCOR time frame,
- grade (ground height) relative to the MELCOR coordinate system,
- building height and initial plume width and height for building wake calculations,
- parameters and choices used to estimate deposition velocities,
- mass-fraction thresholds for paths and plume segments to be considered, and
- time intervals for plume segments.

Version 1.5.1 was used in NUREG/CR-7110 Volume 2. A discussion of MelMACCS improvements from Version 1.5.1 to Version 1.7.0 is provided in Appendix C of NUREG/CR-7155 [1]. Major changes to MelMACCS from Version 1.7.0 to Version 1.7.7, important to the Surry UA, are described below.

The major change from Version 1.7.0 to 1.7.1 was the ability to read MELCOR plot files (.ptf) in Windows 7. Important changes from Version 1.7.1 to 1.7.2 included:

- The ability to edit and add radionuclide inventories (e.g., Surry BOC, MOC, and EOC inventories),

- The ability to read MELCOR 2.1 plot files (.ptf or .plt),

- The ability to leverage a computers dynamic memory for reading MELCOR plot files into MelMACCS,

- The addition of the user having to define the risk dominant plume segment (MAXRIS),

- An adjustment to the algorithm that chooses time of first mass release to start at the MELCOR time step just prior to the release to ensure all mass is captured, and

- An adjustment to the algorithm calculating gas density (PLMDEN) adjusting the lower bound of the integral to the time corresponding to the first nonzero temperature.

The only change from Version 1.7.2 to Version 1.7.3 was the change in 'MELCOR height associated with ground level' from 0 to 1000 meters to -1000 meters to 1000 meters. There were no major changes from Version 1.7.3 to Version 1.7.4 that affect the Surry UA. Major changes from Version 1.7.4 to Version 1.7.5 include:

- Added the core inventory scale factor (CORSCA),
- Allowed the manual adjustment of the plume release height for each release path,
- Changed the upper bound for surface roughness from 0.2 meters to 1.0 meters, and
- Changed the model setting lines in the MelMACCS output file to comment lines.

There were no major changes from Version 1.7.5 to Version 1.7.7 that affect the Surry UA.

3.1.3 MACCS

MACCS uses a Gaussian plume dispersion model and incorporates plume depletion, exposure pathway assessment, emergency response, and dose analysis. The MACCS Best Practices for SOARCA document [6] describes the code in detail and identifies the best practice approach for

implementation of the model. The MACCS application for the Surry UA was consistent with the best practices document except that recommended values were characterized as an uncertain distribution.

MACCS Version 2.5.0.0 was used in the Surry SOARCA study [3]. Version 3.10.0.0 SVN-2560 was used in this Surry UA. MACCS code changes made between Version 2.5.0.0 and Version 2.5.0.9 are described in software quality assurance documentation [17]. Changes between MACCS Version 2.5.0.9 and Version 3.6.2 used in the Peach Bottom UA are described in Section 3 of NUREG/CR-7155 [2]. Important changes from Version 3.6.2 to Version 3.10.0.0 are described below. None of these changes resulted in a significant difference in the results calculated. Changes include:

- Provide file locations on MACCS cyclical files (e.g., MelMACCS source term files) to provide enhanced traceability between inputs and results;
- Increased maximum plume segments (MAXNP) allowed from 200 to 500;
- Addition of simple random sampling as an uncertainty analysis input variable option;
- Implemented a lower plume density limit consistent with the MACCS User Manual;
- Change to a FORTRAN compiler compatible with the Windows 7 operating system;
- Correction of the NRC Regulatory Guide 1.145 plume meander model [10]. This feature was not used in the original SOARCA and was therefore not used in this UA. It likely would have had a minimal impact on the predicted doses because this model only affects the plume dimensions at relatively short distances [6];
- The allowable upper limit of the early phase (ENDEMP) was increased to 40 days to allow modeling of prolonged releases;
- The addition of a new dose-projection period for the emergency phase (DPPEMP) and intermediate phase (DPP_INTERPHAS); and
- The relocation times calculated in CHRONC for health effect risks were corrected to consider multiple cohorts (evacuation and non-evacuation cohorts) within the same grid space.

3.2 Uncertainty Quantification and Propagation

3.2.1 Introduction

The inclusion of uncertainty is an inherent part of any risk analysis of complex systems. The approach chosen for this Surry analysis is consistent with the methodologies used for the Peach Bottom analysis [2], with minor changes implemented based on the lessons learned.

3.2.2 Uncertainty Type

When analyzing a complex system, it is useful to classify the uncertainty under consideration into aleatory uncertainty and epistemic uncertainty [25]. Aleatory (or stochastic) uncertainty

refers to the (apparent) inherent randomness in the properties or behavior of the system. For example, the weather conditions at the time of a reactor accident are inherently random. Another example is the variability in the possible future environmental conditions to which a system component could be exposed. Alternative designations for aleatory uncertainty include variability, stochastic, irreducible, and type A.

Epistemic (or subjective) uncertainty derives from the lack of knowledge about a known, but usually fixed, quantity (or at least a quantity that has a fixed representative value in the context of the analysis). For example, the pressure at which a given reactor containment would fail for a specified set of pressurization conditions is fixed but not precisely known. This type of uncertainty is usually reducible by increasing the knowledge about the parameter or model under consideration[15]. The use of a probabilistic framework to characterize lack of knowledge uncertainty is not necessarily the best approach. Over several decades, multiple mathematical structures were developed to better represent this uncertainty type [26]. However, these methods are computationally intensive and lack the clarity of a simple probabilistic approach. Therefore, in this study, epistemic uncertainty is represented by the classical probabilistic approach. Alternative designations for epistemic uncertainty include state of knowledge, subjective, reducible and type B.

The main reason to separate aleatory and epistemic uncertainty is that it brings more insight to decision making [27][28]. Estimates can be made regarding which part of the uncertainty is irreducible, which part can be reduced with further study, and the relative and cumulative effects of both types of uncertainty. Regression analyses are used to determine which inputs, amongst those that are uncertain, are driving the output uncertainty, i.e., where to focus future work.

The analysis of complex systems typically requires answering the following four questions:

1. What can happen?
2. How likely it is to happen?
3. What are the consequences if it happens?
4. What is the confidence level in the answers to the first three questions?

The first three questions are referred to as the Kaplan-Garrick ordered triplet [21]. The separation of uncertainty with respect to aleatory and epistemic classifications allows for the definition of a formal mathematical framework in which aleatory uncertainty is used to answer the first two questions (as they deal with randomness in future events and the conditions at the time of the event that may affect the consequences). For this study, a STSBO is assumed and the first question relates to the amounts of release of hydrogen and radionuclides that are possible within that scenario. The second question pertains to the likelihoods of the possible release amounts. The third question is answered by the models, which estimate (deterministically) the consequence, given a fixed set of inputs. The consequences are the health effects associated with the release amounts. Epistemic uncertainty answers the fourth question (as confidence increases with the state of knowledge that directly depends on epistemic uncertainty), which is investigated with sensitivity and stability analyses.

---

[15] Epistemic uncertainty includes parameter, model, and completeness uncertainty. See NRC's Regulatory Guide 1.174, "An Approach for Using Probabilistic Risk Assessment in Risk-Informed Decisions on Plant-Specific Changes to the Licensing Basis," for a more complete discussion [19]. The scope of this project does not include model or completeness uncertainty.

While it is desirable to keep a separation between epistemic and aleatory uncertainty, this is not always possible in practice. First, the separation requires a simulation to include two embedded loops (see Section 3.2.4 for MACCS implementation). If high accuracy is necessary for both loops, the number of realizations may quickly become prohibitive. Second, while the definitions of aleatory and epistemic uncertainties are unambiguous, the characterization may be much more complex. It is not uncommon to find both an aleatory and an epistemic component in the uncertainty associated with a given input. See Section 4.1.1.1 for an example of a MELCOR parameter that embodies both epistemic and aleatory uncertain components.Section

3.2.3 Uncertainty Characterization

Each input that is considered uncertain in this analysis has its uncertainty represented with a probability distribution assigned to potential values of that input. The process through which the parameters are selected, and how the associated uncertainty is represented (via a probability distribution) is a crucial part of any probabilistic analysis, as the results will be strongly affected by the choices. The methodology developed to build the uncertainty distributions can be summarized as follows:

- Data and information was gathered and categorized based on relevance and reliability. For instance, observations and measurements were given more credit than expert judgment by itself. In the same spirit, data associated with the same mechanism or from Surry were considered more representative than proxies.

- Depending on the amount of data available, an appropriate selection of distribution representation was selected. The choice varied from simple distribution fitting when enough observations were available, to Bayesian updating, and to judgment when limited data was available.

- Consequent effort was made to document the rationale and assumptions to demonstrate the depth of the technical basis because the results are interpreted conditionally upon those assumptions.

3.2.4 Uncertainty Propagation for Source Term and Consequence Analysis

Monte Carlo methods were developed in the late 1940's [30] as an answer to a specific problem: how can a function of a large number of inputs be estimated numerically? The problem of dimensionality quickly led to an impractical number of runs. The Monte Carlo technique consists of covering the input space by randomly sampling a value in that input space. A dense coverage insures that the approximation of the function is close enough to reality so that the appropriate conclusion can be reached. Demonstrations showed that the Monte Carlo approach will converge to the true solution as the sample size increases. The Monte Carlo method is the core of any sampling-based approach, notably when the input space represents uncertainty with respect to the system. The original Monte Carlo method is characterized by sampling randomly in each direction and is sometimes called Simple Random Sampling (SRS).

Latin hypercube sampling (LHS) was developed in the 1970's [31] [33] to improve the Monte Carlo technique by stratifying each distribution in order to ensure a dense coverage throughout the input space. LHS reduces the variance in each estimate without introducing a bias. The technique can be effective at ensuring samples at the tails or low probability portions of the distributions. However, a limitation of LHS is that the stratification requires the sample size under consideration to be known at the beginning of the analysis. This limits the utility of LHS

when the sufficient sample size is unknown ahead of time or when realizations fail to converge (i.e., MELCOR realizations do not run to completion), resulting in a reduction of the pre-defined sample size and a change in the input space stratification.

These limitations of the LHS application resulted in the decision to use SRS in the present context. MELCOR is a complex code that requires a change in the time-stepping or discretization for some realizations to reach convergence. Some of these refinements are so demanding that they are computationally impractical. The Peach Bottom UA [2] showed that rejecting some of the realizations due to a lack of convergence did not invalidate the coverage of the input space and did not bias the results toward a specific region. Such an analysis is once again necessary considering that it is not practical to have convergence for all realizations. However, the cost of the removal of these non-convergent realizations is that the required pre-specified sample size for LHS to insure complete stratification of the input space is reduced post-sampling, resulting in incomplete stratification. Also, because the sample locations are dependent, an additional set of simulations cannot be used to replace the failed realizations. Thus, the use of LHS is not recommended and the SRS technique was used. MACCS is not affected by the same problem and each realization leads to a convergent result. Nevertheless, in order to maintain a consistent approach, the SRS technique was also used for the MACCS analysis.

The traditional method utilized to distinguish between aleatory and epistemic uncertainty is to use an inner loop for aleatory uncertainty and an outer loop for epistemic. The order of the loops could be reversed in theory, but a preference towards an inner aleatory loop and an outer epistemic loop is derived from what each uncertainty type represents. Aleatory uncertainty in the context of risk analysis is typically represented as a summary statistic (e.g., mean or median) or a distribution. For a given epistemic set (i.e., for a specific set of input parameter values in the outer loop), risk can be represented conditionally on the assumption that one would have perfect knowledge about the value of the parameter. Epistemic uncertainty is then represented as a distribution on the representative value (e.g., distribution of mean or median of aleatory outcomes) or a set of distributions showing confidence in the results given the current state of knowledge. The MACCS code was developed with this strategy in mind, and thus distinguishes between random inputs (mostly weather conditions) and epistemically uncertain inputs. This distinction is preserved and the outputs of interest (individual LCF risk and individual early fatality risk at various locations or areas) are estimated as expected values over aleatory uncertainty.

3.3 Analyzing Uncertainty Results

In the last step of a probabilistic approach, results are statistically analyzed (via uncertainty analysis) and the influence of input parameter uncertainty over the variance of each output under consideration is assessed (via regression analysis). Such analyses help to draw insights with respect to the results. Many techniques have been developed to perform such analyses, several of which are presented in Storlie, et al. [29].

3.3.1 Uncertainty Analysis

Uncertainty analysis usually refers to the determination of the uncertainty in the output of interest that derives from the uncertainty in the inputs. Its main purpose is to assess the extent of uncertainty in the results of interest given the uncertainty in the overall system. When a sampling-based approach is used to propagate uncertainty, a sample is generated for each

output under consideration. Uncertainty analysis thus corresponds to a statistical analysis of the results of interest.

Graphical representations, such as probability density functions (PDF) and cumulative or complementary cumulative distribution functions (CDF and CCDF), are usually used to visualize the extent of the uncertainty under consideration. Statistical measures such as moments (mean, standard deviations) and percentiles (e.g., median, 5^{th} and 95^{th} percentile) are used to summarize the distributions.

3.3.2 Regression Analysis

The purpose of the regression analysis was to determine the contributions of individual uncertain inputs to the uncertainty of the analysis results. Several techniques can be used to estimate the influence of each uncertain input on the output uncertainty. Some methods are qualitative while some are more quantitative and can assess the importance of each input relative to the others with respect to uncertainty [23].

The four regression techniques applied in the Peach Bottom UA [2] were also applied in this analysis to assess quantitatively the importance of uncertain inputs. The results of these four regressions are presented showing the influence of the uncertainty of each input parameter according to each of the techniques. The conclusions of these techniques are supported by the qualitative graphical representations of the relations using scatterplots.

Rank regression, quadratic regression, recursive partitioning, and multivariate adaptive regression splines (MARS) were the four regression techniques used in this analysis to estimate the importance of the input parameters on the uncertainty of the outputs. The use of a set of regressions, instead of a single technique, was demonstrated to be beneficial in the Peach Bottom analysis [2] and was motivated by the fact that there is no universal regression approach capable of capturing all possible relationships from a given sample. Some regression techniques (such as linear regression) have the advantage of being robust (in the sense that they will not overfit the model and lead to artificial R^2 values) but are unable to capture complex relationships (nonlinear and non-monotonic influences, conjoint influences). Other techniques are more flexible but may still include some assumptions on the nature of the relationship. Furthermore, such techniques can be less robust and might give importance to spurious relations. In particular, techniques considering conjoint influence can examine so many possibilities that they identify a combination that appears to drive the uncertainty of the output of interest when this is not the actually the case.

Using a suite of regression techniques allows for better coverage of potential relations between input uncertainty and output uncertainty, while also increasing the confidence that an influence is not spurious if it is captured by multiple regressions. The results of each regression were studied by professionals experienced in the physical phenomenon under simulation to confirm that the regression results were expected in the physical sense based on the variation of the related input values. Although the use of multiple regression techniques leads to a more complex interpretation of the results, it was considered a necessary step since the application of a single regression technique could lead to a misinterpretation and erroneous conclusions. A short description of each selected technique follows, and more detailed descriptions of the techniques can be found in [23], [24], and [27].

3.3.2.1 Rank Regression

The rank regression technique uses a rank transformation over the input and output variables under consideration. The smallest value of a variable is given a rank of one, the next a rank of two, and so on up to the largest value having a rank of *n* (i.e. sample size). A stepwise linear regression is then applied to the rank-transformed data. The model is linear and additive and is shown in the following form:

$$Y = a_0 + a_1X_1 + a_2X_2 + \cdots + a_nX_n + \varepsilon = a_0 + \sum_{i=1}^{n} a_iX_i + \varepsilon$$

Eq. 3-1

where ε represents (for this regression and the subsequent ones) the difference between Y and the regression estimate $\hat{Y}$ for Y.

The stepwise approach starts with trying to find the best fit with only one parameter by testing all possible input parameters. It then builds up from this initial fit by selecting the best fit with two parameters, conditional upon keeping the first parameter, and so on. A stopping criterion is set via a generalized cross validation approach. Rank regression is effective in capturing monotonic relationships between inputs and outputs. The non-parametric aspect makes it less sensitive to outliers. This technique is limited to additive models where no conjoint influences are considered and may perform poorly on non-monotonic relationships.

Two metrics are included for each input variable used to display rank regression results. One is based on the coefficient of determination, noted conventionally as R^2, which represents the amount of variance explained by the regression model. The coefficient of determination is a normalized value which varies between 0 (no variance explained) and 1 (all the variance explained).

- R^2_{cont} gives the incremental gain in R^2 when the i^{th} variable has been added compared to the model with $(i-1)$ variables. It is a good indicator of the contribution of this specific variable in explaining the variance of the output in consideration. The sum of all R^2_{cont} values is R^2.

- The rank regression coefficient (RRC) is an indication of the strength of the influence. An absolute value close to zero means that the parameter has a small influence, while an absolute value close to one indicates a very strong influence. The RRC also indicates the positive or negative direction of the influence of this input variable on the considered output. A negative sign represents negative influence in which high values of the input lead to low values of the output and low values of the input lead to high values of the output. A positive sign represents positive influence where high values of input lead to high values of the output and low values of the input lead to low values of the output. For notational consistency with results obtained in traditional linear regression, results obtained in rank regressions are often presented with standardized rank regression coefficients (SRRCs). However, when there are no ties in the data, RRCs and SRRCs are equal.

3.3.2.2 Quadratic Regression, Recursive Partitioning, and MARS Techniques

The three additional regression techniques (i.e., quadratic regression, recursive partitioning and MARS) are treated differently, as their models do not provide a direct estimate of the contribution to each individual input to the variance of the output. These regression techniques lead to analytical models that can quickly be run a large number of times (over the course of

seconds to minutes). Once the regression model is available, it can be used to generate a large number of realizations via a variance decomposition technique known as the Sobol' decomposition. The Sobol' decomposition is a technique that can estimate the contribution of each input and their potential interactions (i.e., conjoint influence) via an integral decomposition of variance [22]. However, this technique requires a large number of realizations (tens of thousands) to be accurate (within a few percentages) and cannot usually be applied directly to a computationally demanding model. Once the Sobol' decomposition is applied, the importance of each variable (according to its uncertainty) can be assessed given the regression model. For each of these models a coefficient of determination (R^2) is estimated for the entire regression technique and can be used as an indicator of how the regression performed. The answer is thus strongly dependent on the quality of the regression model and caution should be applied when the R^2 value is relatively low. In some situations, a regression technique may overfit and lead to an artificially high R^2. However, scatterplots can be used to confirm whether there is indeed a relation or not.

The Sobol' decomposition leads to different measures of effect than those used in stepwise linear regression. The two metrics selected for this analysis are described below:

- S_i represents the first order sensitivity index and characterizes how much of the variance of the selected output is explained by the input parameter under consideration by itself (i.e., without conjoint influence). This index therefore estimates the same quantity as R^2_{cont} for the rank regression technique and it is acceptable to compare these two quantities.

- The second measure, labeled T_i, characterizes how much of the variance of the selected output is explained by the input parameter alone plus its interaction with the other uncertain parameters (i.e., conjoint influence). It has no analogue in the rank regression model as the additive model does not capture conjoint influences. The difference between T_i and S_i provides an estimate of the conjoint influence for a single input on the output considered.

3.3.2.3 Quadratic Regression

Quadratic regression techniques apply the same approach as linear regression, including individual input variables, the square of these variables, and second order multiplicative interaction terms. The prediction model is of the form:

$$Y = a_0 + \sum_{i=1}^{n} a_i X_i + \sum_{i=1}^{n} b_i X_i^2 + \sum_{i=1}^{n} \sum_{j=i+1}^{n} c_i X_i X_j + \varepsilon$$

Eq. 3-2

Quadratic regression is not solely additive, as it can capture second order interactions. It can also capture the parabolic influence measured by the square of variables in the regression model. However, a complex relationship between variables and the output, like asymptotic behavior, may still be hard to capture with this technique and the method remains parametric, making it sensitive to outliers. Similar to traditional regression and rank regression, quadratic regression can be performed in a stepwise manner. As mentioned above, quadratic regression, like recursive partitioning and MARS, may overfit the data and lead to an artificially high R^2 value.

3.3.2.4 Recursive Partitioning

Recursive partitioning, also known as a regression tree, is a regression method that captures conjoint influences. A regression tree splits the data into subgroups of uncertain parameters that generate similar values of the figures of merit. The regression function is constructed using the sample mean of each subgroup. This approach results in a piecewise constant function over the input space under consideration. The predictive model is:

$$Y = \sum_{s=1}^{nP} (d_s I_s(X_i))_{i=1,\dots,n} + \varepsilon$$

Eq. 3-3

Recursive partitioning is well adapted to the present study as it strives to capture the effect of thresholds (e.g., a low value for one parameter and a high value for another parameter, or when a certain parameter reaches a threshold value). MELCOR includes many such threshold conditions to initiate key events or processes in its physical models. One of the drawbacks of this regression is that it examines such a high number of potential relations that it can overfit by capturing spurious correlations. Consequently, checking the relations only found by this regression using scatterplots is recommended and was performed. In addition, the tendency to overfit was discouraged by increasing the default number of realizations that must be in a subgroup in order for the model to attempt a split.

3.3.2.5 Multivariate Adaptive Regression Splines (MARS)

MARS is a combination of (linear) spline regression, stepwise model fitting and recursive partitioning. A regression with a single input starts with a mean-only model and adds basis functions in a stepwise manner while adding the overall linear trend first. Then, a second model using linear regression via least squares is fit to the data. This model is added to the basis functions in a way that reduces the sum of squared error (SSE) between the observations and predictions. A fourth basis function is then added to minimize the SSE again. This process is repeated until *M* (set by default at 200) basis functions have been added.

At this point, the MARS procedure will try to simplify the model using stepwise deletion of basis functions while keeping the y-intercept and linear trend. The $M - 2$ candidate leading to the smallest increase of SSE will be selected. This deletion will be applied until regressed to the original linear model.

Stepwise addition and deletion leads to the creation of two different $M - 2$ models. The “best” model is chosen using a generalized cross validation score which corresponds to a SSE normalized by the number of basis functions considered. With multiple inputs, the basis functions will consider main effects and multiple-way interactions. The options used for this analysis consider only two-way interactions to avoid the exponential cost of considering more interactions.

MARS usually leads to similar results as linear regression with a greater accuracy, and with the inclusion of non-monotonic effects and conjoint influences. However, it performs poorly with discrete inputs due to the use of splines.[16]

3.3.2.6 Ranking the Variables According to the Four Regression Techniques

A consequence of the use of multiple regressions is that the ranking of the inputs amongst themselves is not obvious when the different regressions disagree. A qualitative approach has been used in the past [1] based on the physics considered in the problem and expert knowledge, but such an approach introduces some subjectivity and is hard to document. A more quantitative approach for the current analysis was implemented, along with the continued understanding that such a quantitative ranking is an indicator and should be supported by expert opinion based on the physics of the problem.

Two effects of the uncertainty in the input on the output of consideration are estimated in the present study. The individual or "main" effect represents the influence of the uncertain input by itself and is estimated with R^2_{cont} in the stepwise regression and S_i for the other three regression techniques. Then the effect of the uncertain input from its interaction with other variables, which is ignored by the stepwise regression as it is an additive regression, is estimated with $T_i - S_i$ for the other three regressions.

The first effect of the uncertainty in the input was considered the most important, and a decision was made to rank the variables according to this main effect. Stepwise regression provides an estimate of the main effect for each variable directly. For the other regressions techniques, the real effect has to be adjusted by the efficacy of fit of the model (i.e. the R^2 value from the regression model). In order to accomplish this, each S_i value is multiplied by the R^2 value of the regression model. Finally, if a variable is not included in a given regression, it is supposed that its main effect is null, and the corresponding value is set to 0. This weighted average is represented by:

$$\text{Main influence} = \frac{R^2_{cont} + \sum_{j=1}^{3} R_j^2 . S_{i,j}}{4}$$

Eq. 3-4

where R^2_{cont} is from rank regression, j is the index of the three non-linear regression techniques, and R_j^2 is the final R^2 for each non-linear technique.

The conjoint influence is captured by estimating $T_i - S_i$ for each of the last three regressions, adjusted using the R^2 value as a weight. An average is taken again, represented by:

$$\text{Conjoint influence} = \frac{\sum_{j=1}^{3} R_j^2 * (T_{i,j} - S_{i,j})}{3}$$

Eq. 3-5

[16] A spline is a numeric function that is piecewise-defined by polynomial functions. Several uncertain parameters in Section 4 used discrete distributions (e.g., valve failure area, Section 4.1.1.2) that were driven by physical explanations and data for non-continuous distributions.

If the average value is greater than 0.1 (meaning 10 percent of the regression is explained via conjoint influence with this input), the T_i are emphasized to draw attention to a potential important conjoint influence. As the first order indices (i.e., S_i) and total order indices (i.e., T_i) are estimated numerically using a Sobol' decomposition, they are approximations. If no conjoint influence is present, it may happen that T_i is estimated slightly lower than S_i. This is an artifact of how the S_i and T_i are calculated. In such situations the confidence intervals around S_i and T_i were calculated and compared. Comparisons showed that the confidence intervals were the same, demonstrating no statistically significant difference between T_i and S_i and the value of $(T_i - S_i)$ was set to 0. These two metrics, main contribution and conjoint contribution, are added to the summary tables for the four regression results, as an indicator of the importance of the input uncertainty to the output uncertainty. This represents a best estimate of the input uncertainty influence on the uncertainty of the output considered.

The first four major columns in the regression tables presented in the analysis sections are labeled with the regression technique used to create the results. The last two columns contain average values of the main contribution of the parameter on the result metric and the conjoint influence of the parameter on the result metric. For ease of reading the regression tables which are presented with the results, highlighting is applied in the main contribution and conjoint contribution columns to identify the input parameters with potentially strong importance, based on the overall analysis. The cutoff for the main contribution effect was set at 0.02, and the cutoff for conjoint effect was set at 0.1. The reason for a difference in the contribution effects is that conjoint contribution influence looks at a larger range of possible interactions (for instance, with 20 inputs variables, the main contribution looks at 20 potential relations while conjoint influence of 2 inputs looks at 190 potential relations) and is more likely to identify spurious correlations. Therefore, an approach that concentrates on the larger contribution was considered appropriate. The threshold values of 0.02 and 0.1 were selected based on the knowledge acquired during Peach Bottom UA [2] and the regressions tables for the present analysis, such that important parameters would be acknowledged, and negligible influence would not be highlighted. In all cases, the highlighted and non-highlighted input parameters were plotted against the figure-of-merit to qualitatively verify that important parameters were identified.

3.3.2.7 *Testing for Potential Over-Fitting*

Higher order methods, such as quadratic regression and MARS may lead to an artificially high R^2. When a single regression technique identifies a strong relation, it is necessary to check for the validity of the relation found. An approach aimed at checking a relation's validity created a random output for each realization and used this to check on the result of the regression technique. Six random variables (three discrete, three continuous) were generated. The four regression techniques were then used with the same inputs to regress on these random outputs. The results can be used to infer whether the selected regression technique can be trusted or not. The tests showed that only recursive partitioning was likely to over fit; all other models consistently fit to random outputs with an R^2 less than 0.15. Recursive partitioning models had an R^2 of that varied between 0.24 and 0.43, with mostly conjoint influence captured (no high S_i values, only high T_i values). This suggests that high conjoint influences in the absence of significant main effects should be interrogated for overfitting and overfitting is most likely to occur with the recursive partitioning model whether the output is discrete or continuous. As a result, for any set of regressions leading to only T_i influence, the results of the regressions were verified using scatter plots and regression trees to identify the specific interactions and compare the behavior to known phenomenology.

3.3.2.8 Scatterplots

The use of scatterplots is a qualitative yet powerful technique that completes the suite of regression techniques applied in this analysis. Scatterplots display a set of points, one per realization, whose coordinates correspond to the value of one selected input for the x-axis and of the output considered on the y-axis. It confirms graphically that the relation estimated by any of the regression techniques is indeed present and not spurious.

3.3.2.9 Recursive Partitioning Tree

The quadratic, recursive partitioning, and MARS regression models all identify parameters with significant conjoint influences, but the regression results do not explicitly identify the parameter interactions that account for those influences. It is possible, for example, that a parameter has an important conjoint influence because it interacts in a small way with many other parameters. In this instance, the influence is likely spurious and not physically meaningful. For this reason, it is important when conjoint influences are significant that the specific contributors are identified. One technique for accomplishing this uses three-dimensional scatterplots, where the third dimension is either spatial (difficult to interpret in two-dimensional presentations) or represented using color. If the interaction is not easily identified, however, this process is inefficient. This UA utilized regression trees. These are the graphical presentations of the recursive partitioning model and explicitly depict the interactions included in the models. For each figure-of-merit, regression trees are presented and used to help explain the phenomenology responsible for the conjoint effects.

3.3.2.10 Regression Analysis of Failed Realizations

A certain number of MELCOR realizations fail to converge within a reasonable computational time for various reasons. An analysis is thus completed to determine whether there is a correlation between failed runs and a particular area of the input space. Such a situation would indicate that a particular value for one input (or combination of values for several inputs) would lead to failure, biasing the conclusion that could be drawn by only analyzing the successful runs. In order to detect a potential relation between input uncertainty and failure, a regression analysis (using the four regressions techniques described in Section 3.3.2) was performed, using an indicator function set to 0 when the realization failed to run to completion and 1 when it ran up to the end as the output of interest.

Another regression analysis was performed using a random permutation of the realization success indicator. The same regression techniques that were applied in the analysis of failed runs were used with the random permutation. Similar regression results for all three regressions indicated that the instance of realization failure is random with respect to the input space, showing that the completed realizations are representative and there is not a significant relationship between input values and realization completion.

The results indicated that the eutectic melt temperature may have a small contribution to realization failures. However, the impact was only identified by the recursive partitioning model using eight uncertain input parameters. The nature of the complex, multi-parameter technique suggested that the result was either a numerical artifact or limited to a small range of many input parameters. Since no strong correlation was identified in the other three regression methods and the there was a relatively small number of realization failures, the overall regression results were judged valid.

4 UNCERTAIN INPUT PARAMETERS AND DISTRIBUTIONS

The discussion of the uncertain parameters is separated into the accident progression and source term model uncertainty (i.e., the MELCOR modeling inputs) and the consequence model uncertainty (i.e., the MACCS modeling inputs). The various MELCOR and MACCS uncertain parameters are discussed in Sections 4.1 and 4.2, respectively. The quality steps taken to control the model inputs and implement the uncertain parameters are discussed in Section 4.3.

4.1 Source Term Model Uncertainty (MELCOR Inputs)

As discussed in Section 2.2, the MELCOR uncertain parameters were selected to cover the following issues of severe accident phenomenological areas:

- Sequence,
- In-vessel accident progression,
- Containment response, and
- Radionuclide behavior.

Table 4-1 lists the distributions and bounds related to each MELCOR parameter sampled in this analysis. The parameters and uncertainty distributions also used in the Sequoyah UA [7] are indicated in Table 4-1.[17] The sampling approach for many of the parameters is quite complex and is described in the following sections along with the rationale for each distribution, and justification for the upper and lower bounds. The basis for defining many distributions is strong where known physical or chemical phenomena are well understood. For some parameters, the technical basis for establishing the distribution was less defensible. In such cases, these distributions were considered exploratory and intended to inform the severe accident community on the effect of applying a distribution to these parameters. The bounds for exploratory parameters were generally based on professional judgment, and in some cases were based on sensitivity analyses conducted early in the course of this project.

Correlations of MELCOR parameters were considered but ultimately no direct parameter correlations were implemented. It was originally planned in the draft Surry UA [8] to correlate the molten Zircaloy breakout temperature, the eutectic melt temperature, and the time at temperature model. However, the sampling on the time at temperature was removed from consideration, and the sampling for breakout temperature and eutectic temperature were 85 percent exclusionary. Furthermore, any correlation relationship was uncertain and there was a desire to understand each parameter's uncertainty individually. Consequently, no parameter correlation was implemented. Correlation of radial relocation times for molten and solid debris was also considered in the draft Surry UA. These parameters were consistently shown to have little importance in past UAs and were not retained for the UA documented in this report.

Two parameters were indirectly correlated. The SV FTC parameters were effectively correlated by sampling according to a single model and appropriately using a single value of the epistemic parameter across all SV samples in a realization (see Section 4.1.1.1 for further discussion). The gaseous iodine fraction sampling was dependent on time at cycle. Based on the time at

[17] An emphasis of the Sequoyah UA was the ice condenser performance. Consequently, the selection of the UA parameters was different. The Surry UA also further refined some uncertain parameter distributions used in the Sequoyah UA based on feedback from the ACRS (e.g., the time at cycle sampling).

cycle, the gaseous iodine fraction was randomly sampled based on uncertainty range for the corresponding time at cycle fuel burn-up (see Appendix D). There were no other MELCOR parameters where correlation was determined necessary.

Table 4-1 MELCOR Sampled Parameters

Uncertain Parameter	Distribution type	Distribution Parameters		Lower Bound	Upper Bound
Sequence Parameters					
Primary SV stochastic FTC (-) (priSVcycle, Section 4.1.1.1) [SEQ]	Beta[1]	α: 17.5 β: 756.5		0	1
Primary SV open area fraction (-) (priSVfrac, Section 4.1.1.2) [SEQ]	Piecewise linear	Bin	Prob	0.01	1
		0.01 – 0.1	0.5		
		0.1 – 0.3	0.1		
		0.3 – 0.9	0.1		
		0.9 – 1.0	0.3		
Secondary SV stochastic FTC (-) (secSVcycle, Section 4.1.1.3) [SEQ]	Beta [1]	α: 17.5 β: 756.5		0	1
Secondary SV open area fraction (-) (secSVfrac, Section 4.1.1.3) [SEQ]	Piecewise linear	Bin	Prob	0.01	1
		0.01 – 0.1	0.5		
		0.1 – 0.3	0.1		
		0.3 – 0.9	0.1		
		0.9 – 1.0	0.3		
Reactor coolant pump seal leakage (gpm/RCP) (RCPSL, Section 4.1.1.4)	Discrete	Bin (gpm)	Prob.	21	480
		21	0.79		
		76	0.01		
		182	0.1975		
		480	0.0025		
Normalized temperature of hottest SG tube (-) (Hot Tube, Section 4.1.1.5)	Beta	α: 43.7 β: 54.9		0	1
SG tube NDF depth (-) (NDF Depth, Section 4.1.1.6)	Discrete [2]	Specified distributions		0.3	0.9
MSIV leakage (in^2) (MSIV, Section 4.1.1.6)	Uniform	-		0.01	1.0
In-Vessel Accident Progression Parameters					
Zircaloy melt breakout temperature (SC1131(2)) (K) (Breakout, Section 4.1.2.1) [SEQ]	Scaled Beta [3]	α: 3.83 β: 3		2100	2540
Molten clad drainage rate (SC1141(2)) (kg/m-s) (Zr Drain, Section 4.1.1.2) [SEQ]	Log triangular	Mode: 0.2		0.1	2
Effective melting temperature of the eutectic formed with UO_2 and ZrO_2 (K) (EU_melt_T, Section 4.1.2.3) [SEQ]	Normal	Mean: 2479 σ: 83		-	-
Time in the Cycle (-) (CYCLE, Section 4.1.2.4) [SEQ+]	Uniform [4]	-		0	550
	Discrete	Bin	Prob.	-	-
		UH (MELCOR default):	0.25		

Table 4-1 MELCOR Sampled Parameters (Continued)

Uncertain Parameter	Distribution type	Distribution Parameters		Lower Bound	Upper Bound
Oxidation kinetics model (Ox_Model, Section 4.1.2.5) [SEQ]		Leistikov-Schanz/ Prater-Courtright:	0.5		
		Cathcart-Pawel/UH	0.25		
Containment Behavior					
Hydrogen ignition criteria (%) (H2 LFL, Section 4.1.3.1) [SEQ]	Discrete	Bin	Prob.	~4% [6]	~9% [6]
		4%	0.33		
		6%	0.33		
		9%	0.33		
Containment design leakage rate multiplier (-) (designLeakLa, Section 4.1.3.2)	Log Uniform, Uniform	Bin	Prob.	0.1	10.0
		0.1 – 1.0	0.9		
		1.0 – 10.0	0.1		
Containment fragility curve (-) (CFC, Section 4.1.3.3)	Scaled Beta [3]	α: 5.6 β: 6.3		1.09	2.03
Containment convection heat transfer coefficient (-) (Section 4.1.3.4) [SEQ]	Triangular	Mode: 1.4		1.0	2.0
Radionuclide Behavior Parameters					
CHEMFORM iodine (-) (CHEMFORM I2, Section 4.1.4.1) [SEQ+]	Lognormal [5]	Various		0.0	-
CHEMFORM cesium (-) Fraction of Cesium as Cesium Molybdate (CHEMFORM Cs, Section 4.1.4.2) [SEQ+]	Beta	α: 9 β: 3		0.0	1.0
Dynamic Shape Factor (-) (Shape_Fact, Section 4.1.4.3) [SEQ]	Scaled Beta[3]	α: 1 β: 5		1.0	5.0
Secondary side rupture location and decontamination factor (-) (ARTIST, Section 4.1.4.4)	Discrete	Bin	Prob.	1	7
		1	0.02		
		2	0.03		
		3	0.05		
		4	0.08		
		5	0.14		
		6	0.25		
		7	0.43		

Table 4-1 MELCOR Sampled Parameters (Continued)

Notes:

SEQ = Same as the Sequoyah UA [7],
SEQ+ = Same parameter as the Sequoyah UA but modified for the Surry UA.

[1] The sampling scheme is more complicated than a simple Beta. The probability of failure conditional on demand is described by the given beta, but then is updated based on a distribution.
[2] The non-dimensional flaw depth for the steam generator tube uses specified profiles based on historical data. Two distributions. Separate distributions are used for the hottest tube versus the hot upflow and cold regions.
[3] A Beta distribution has bounds of 0 and 1. Any Beta with other bounds can be referred to as a Scaled Beta.
[4] This parameter impacts the decay heat power and the initial radionuclide inventory. Although the time in the cycle is uniformly sampled, the resultant values are discretely assigned to the nearest ORIGEN result (i.e., 0.5, 25, 50, 75, 100, 150, 200, 250, 300, 350, 400, 450, 500, and 550 days).
[5] A lognormal distribution based on the burnup at the time in the cycle is used to determine the gaseous iodine percentage. The lognormal distribution was developed by the French CEA from the scatter of gaseous iodine concentrations in the fuel cladding gap for LEU and mixed oxide fuel (see Section 4.1.4.1).
[6] The exact values of the lower flammability limit vary based on the local steam concentration but are approximately 4% and 9% for upward and downward flame progression, respectively.

4.1.1 Sequence

Following the draft Surry UA [8], the SV failure attributes were changed based on (a) discussions with nuclear valve testing personnel, (b) closer examination of Licensee Event Reports, and (c) review of the draft Surry UA results. Only the FTC was retained as an uncertain parameter. FTO, failure due to passing water, and thermal failure of the SV were not included for the reasons described next.

A FTO of all three pressurizer SVs was not sampled due to the low probability. The Sequoyah UA [7] includes an analysis that shows the probability of all 3 valves failing closed is almost three orders of magnitude lower than the probability that at least one SV would FTC. Consequently, the FTO mode was not included.

The valve testing specialists identified passing water isn't necessarily threating to a SV unless it was cold, which is not observed in the unmitigated STSBO. The conditions that promote water flow through the pressurizer SV is during level swells after the fluid is heated near saturated conditions (i.e., much different than the historical problem of cold condensed water in the loop before the valve). Consequently, the uncertainty of SV failure due to passing water is not included.

The STSBO accident progressions in the PWR UA calculations did not reach high temperatures where thermal valve failures would be likely. Unlike the Peach Bottom STSBO accident progression [2], the PWR SVs are located significantly further away from the degrading core. A

thermal failure of the SV was unlikely before some other breach of the reactor coolant system (e.g., hot leg or lower head failure). Consequently, the uncertainty of SV failure due to passing high temperature gases is not included.

Finally, the discussions with the valve specialists led to changes in the failure area following a FTC. The primary and secondary safety valves failure area distributions were also updated to follow the approach in the Sequoyah UA [7]. The discussions with nuclear valve testing personnel and closer examination of Licensee Event Reports indicated that the valve will fail in either a slowly leaking (mostly closed) or mostly open position. The primary and secondary SVs use the same approach for their respective FTC and failure open area uncertainty parameters. While the same distributions are used for the primary side and secondary side SVs, no correlations were assumed between these two sets of valves because the two locations use different types of valves and the valves are exposed to different environmental conditions (i.e., see Section 4.1.1.1).

The reactor coolant pump leakage parameter distribution is unchanged since the draft Surry UA [8]. The remaining sequence uncertain parameters address uncertainties contributing to a steam generator tube rupture, which was not evaluated in the Sequoyah UA. These parameters are the normalized temperature of hottest SG tube, the non-dimensional depths of the tube flaws in the steam generators, and the MSIV leakage area. The normalized temperature of the hottest SG tube is unchanged since the draft Surry UA [8]. However, the non-dimensional depth of the tube flaws in the steam generators was revised since the draft Surry UA to include consideration of the Surry tube inspection data. The MSIV leakage was included as an uncertain variable due to its importance in affecting the stress across the steam generator tubes.

4.1.1.1 *Primary SV Stochastic Failure*

The Surry pressurizer has three SVs with differing opening set-points. The spring-loaded valves open when primary system pressure rises to the set-point, which release steam to the Pressurizer Relief Tank (PRT). Once the primary system pressure reduces to 96 percent of the set-point, the valve re-seats. This is considered one “cycle” of the SV. Every opening and closing of the SV has a failure probability associated with the state transition.

In the Surry SOARCA analysis [3], the SV stochastic failure was modeled for the FTC failure mode of the lowest-set-point SV. The mean probability of failure per demand was to determine the number of SV demands at which failure occurred. Equations 4-1 and 4-2 show the probability distribution and cumulative distribution functions for the negative binomial distribution:

$$f(n|p) = P(N = n|p) = p(1-p)^{n-1}, 0 \le p \le 1, n \sim [1,2,3 \dots] \quad \text{Eq. 4-1}$$

$$F(n|p) = P(N \le n|p) = 1 - (1-p)^{n+1}, 0 \le p \le 1, n \sim [1,2,3 \dots] \quad \text{Eq. 4-2}$$

where.

p is the probability of a failed state for the SV per demand and
n is the number of valve cycles the SV experiences.

Once the distributions were defined, the SOARCA study used the mean of the number of SV demands at which failure occurred to define the number of cycles at which FTC occurs [3].

A new uncertainty characterization of stochastic SV failure was developed following the draft Surry UA and was also used in the Sequoyah UA [7]. The new SV FTC uncertainty characterization was informed by Table 20, Failure probabilities for PWR code safety valves (behavior after scrams), from NUREG/CR-7037 [35]. Table 20 reports on SV operation subsequent to scram events in operating nuclear reactors. Information is included for both main steam system (MSS) and RCS valves. The authors note that the MSS and RCS SVs are similar. Inquiries to SV testers revealed that these valves are similar but not identical, in that there are some physical and maintenance differences. However, there was significantly more data for MSS valve demands than the RCS valves (i.e., RCS valve demands are extremely rare). While there are differences between the MSS and RCS SVs, the following judgments were used to exclude the RCS valve data. First, the RCS data only consists of four data points with two valve failures. Only four data points are insufficient to draw representative conclusions about RCS valve failure. In contrast, NUREG/CR-7037 reports 769 MSS valve demands (i.e., including all failures). Second, a review of the Licensee Event Reports (LER) for the two failure-to-close events on the RCS SVs indicate that the failure mechanism in one of those two events (noted as the passing of relatively cold water from a loop seal ahead of the valve) does not exist at Surry nor at the majority of operating PWRs in the US. The cold water valve failure issue was addressed following an EPRI evaluation of problem and issuance of a recommendation in the mid-1990s [123]. Third, the lack of instrumentation or reporting in the LER has potentially left additional successful valve cycle demands undocumented, thus causing an attribution bias. As a result of these factors, the failure probability distribution for the RCS valves was calculated using the MSS valve data.

Recovered valve function (e.g., a previously stuck-open valve closing when pressure reduces) was not taken to be successful valve operation. In reviewing the Licensee Event Reports for the *recovered* SV events, there was typically no subsequent cycling demands reported on a recovered valve. Consequently, there was no information to assess the recovered valve performance.

The valve responses to scram events in the Main Steam System Code Safety Valves section of Table 20 [35] was used to develop the valve failure distribution. The value for all events reports zero failures to open and 15 failures to close in 769 demands considering all failures, recovered and non-recovered. The reported failure rates are derived from actual events at US plants. NUREG/CR-7037 (Table 22) also reports on failure rates in SV testing but the rates differ markedly from the rates evidenced by actual plant events suggesting that aspects of the testing were inconsistent with actual conditions experienced by an installed valve. Further inquiries on valve testing and review of testing requirements show that the focus of testing is to demonstrate that the valves will unseat at design pressures to relieve pressure during a design-basis overpressure event. The testing does not fully stroke a SV at pressure like an actual demand. In fact, no testing facility in the United States has the flow capacity to fully stroke a SV. As such, the testing data was not considered applicable for the purpose of this UA of a severe accident scenario.

The data collection for NUREG/CR-7037 ended in 2007. A new search was performed for the Sequoyah UA to identify additional valve operating events between 2007 and March 2016 using the methodology from NUREG/CR-7037. Most of the SV operating experience data comes from licensee event reports (LERs) to the NRC. LER data reporting, as described in NUREG-1022 [36], requires licensees to report valid emergency core cooling system signals or critical scrams,

but does not explicitly require reporting of relief valve actuations or demands. NUREG-1022 does, however, require reporting of SV failures thus leading to credible failure information. There were ~3,000 LERs in the initiating event database from calendar year 1987 to 2007. Each of these initiating event LERs was reviewed in the preparation of NUREG/CR-7037, and post-2007 LERs (i.e., through March 2016) to determine whether valves were actuated and/or demanded (observed lift) and whether they failed. Many LERs describing the plant response to scram report the operation of SVs, but a significant portion of the LERs just use phrases like, "All systems operated as expected." Hence, expert judgment must be used to interpret the information provided in the LERs, which may undercount actual demands. A handful of the operating experience data came from review of SV failures reported in the proprietary EPIX database.[18] The numbers in Table 4-2 reflect updated data compared to Table 20 in NUREG/CR-7037 [35], and is separated between initial demands and subsequent demandsTable .

The data from actual scram events is typically only for failures in a single SV cycle, so there may be some limitation in extrapolating to repeated valve cycles during a severe accident, but this is the best data available. There is sufficient resolution in the data, however, to separate it into two groups. The first group consists of all of the initial demands and the number of valve failures on initial demand. There were no valves that failed after the initial demand, so the second group consists of the number of cases in which a subsequent demand occurred, and the valve did not fail on subsequent demand. This separation of the data (Table 4-2, [35]) specifies two separate failure probability distributions: one for the probability of failure on the initial demand and another for the probability of failure on subsequent demands.

Table 4-2 SV FTC data (from actual scram events) and associated epistemic uncertainty distributions for probability of occurrence on demand

Demand	# Failures	# Demands	Distribution*
Initial	16	621	$\beta(\alpha = 16.5, \beta = 605.5)$
Subsequent	0	223	$\beta(\alpha = 0.5, \beta = 223.5)$

*Development of indicated distributions is described below.

A beta-binomial distribution is used to model cycles until a FTC event. However, the sampling includes uncertainty in the cycles-to-failure. For a FTC on the initial demand, the model consists of a beta distribution on the probability of a FTC event on initial demand and a binomial distribution on the cycles to failure given the sampled value for FTC probability. Similarly, for FTC on subsequent demand, the model consists of a beta distribution on the probability of a FTC event on subsequent demand and a negative binomial distribution on the subsequent cycles-to-failure. Hence, both for failure on the initial demand and failure on the subsequent demand, the beta-binomial model facilitates two stage sampling that incorporates both uncertainty in the probability of the valve failure-to-close-on-demand, and in the cycles-to-failure experienced by a valve given that probability of failure.

The beta distribution on the probability of FTC on initial demand is plotted in Figure 4-1a. For each realization, one sample of a FTC probability was taken from the distribution and used to

[18] http://nrcoe.inl.gov/resultsdb/RADS/

generate a binomial distribution. The binomial distribution was sampled once for each valve. If the value sampled was 1, then the valve failed on initial demand, otherwise the valve did not fail on initial demand. This sampling process leads to the distribution of FTC on initial demand in Figure 4-1b.

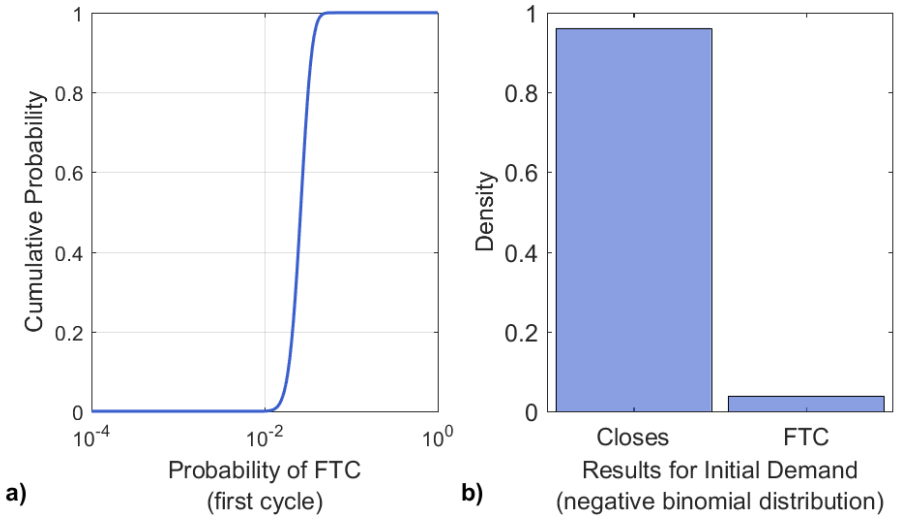

Figure 4-1 Cumulative Probabilities (per valve) of a FTC event on Initial Demand for the Pressurizer SVs (priSVcycles) and the Resulting Distribution of FTC on Initial Demand

For valves that did not fail on initial demand, the beta distribution for probability-of-failure on subsequent demand is plotted in Figure 4-2(a) with the corresponding negative binomial distributions on cycles-to-failure plotted in Figure 4-2(b) [19]. Each cycles-to-failure distribution in Figure 4-2(b) is the negative binomial distribution that results from a single sample of a failure probability from Figure 4-2(a). The development of these distributions is described further below.

[19] The same beta distribution was sampled for the SG SVs (secSVcycles).

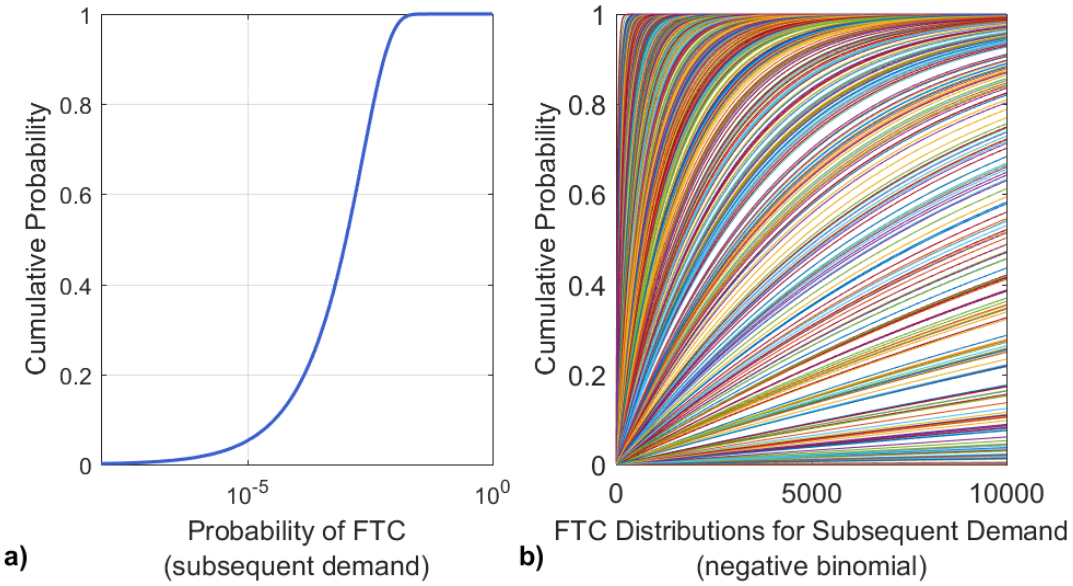

Figure 4-2 Cumulative Probabilities (per valve) of a FTC event on Subsequent Demand for the Pressurizer SVs (priSVcycles) and the Resulting Distributions of Cycles-to-Failure on Subsequent Demand

The beta-binomial distributions were derived to reflect the high level of uncertainty surrounding valve failure. To do this, the beta distributions were calculated by incorporating the data from Table 4-2 to refine a Jeffreys uninformed beta distribution[20]. The Jeffreys uninformed beta distribution, defined as $Beta(0.5\ 0.5)$, is commonly used as a prior distribution in Bayesian analysis with limited data [43]. The mean of the Jeffreys prior can be interpreted as roughly half a failure per trial, representing the lack of knowledge about the probability-of-failure. This methodology is preferable when the data is sparse because it allows sparse data to be used in informing a distribution without placing undue confidence on the data. For example, the point estimate based on the data in Table 4-2 for the probability-of-failure on subsequent demand is 0. However, due to the limited quantity and applicability of the data to the circumstances experienced by valves in a STSBO scenario, it is not reasonable to assume that the probability-of-failure is actually 0. Applying the data to a Jeffreys prior provides a robust method for incorporating the data while including a level of uncertainty commensurate with the limitations of the data. For a data set that consists of k FTC events out of n demands, the updated distribution for FTC probability is $Beta(0.5 + k, 0.5 + n - k)$. In particular, note that as n increases, the effect of the initial 0.5 parameters is lessened; the uncertainty around the failure probability represented in the distribution decreases as a function of amount of available data. This formula was used to calculate the posterior beta distributions for all of the failure probabilities, pictured in Figure 4-1b and Figure 4-2b.

The probability-of-failure on initial demand distribution[21] for the pressurizer SVs and the steam generator SVs is plotted in Figure 4-3 with the initial Jeffreys prior to illustrate the development of the distributions. There is a clear shift in the mean value and decreased variance due to the

[20] http://www.nrc.gov/reading-rm/doc-collections/nuregs/contract/cr6823/

[21] This distribution was also used for the SG SVs (secSVcycles).

incorporation of the data. Similarly, the probability-of-failure on subsequent demand distribution[21] for the primary SVs and the steam generator SVs is plotted in Figure 4-4 with the initial Jeffreys prior, again showing a shift in the mean due to incorporation of data, but maintaining a fairly high variance due to the smaller number of demands in the subsequent demand valve data set (see Table 4-2).

Probabilities from these beta distributions form families of negative binomial distributions for cycles-to-failure (one family for the initial demand and one family for subsequent demand). Thus, uncertainty in the probability-of-failure is incorporated into the uncertainty in cycles-to-failure. The beta distribution in Figure 4-2a represents the uncertainty in the failure probability, modified from a Jeffreys prior by including the data. Then each failure probability data point within that distribution gives rise to one of the negative binomial distributions seen in Figure 4-2b. Each individual negative binomial distribution characterizes the uncertainty in the cycles-to-failure and the whole family characterizes the uncertainty due to uncertainty in the failure probability.

To illustrate this connection between the beta and binomial distribution, consider the notional example in Figure 4-5. Notice that the median probability-of-failure in Figure 4-5(a) is approximately 0.01, implying that half of the time failure should occur by approximately 100 trials. This is reflected in the medians of the negative binomial distributions in Figure 4-5b which are centered on 100 trials. The medians of the negative binomial distributions vary around 100 trials, rather than falling precisely at 100 trials, due to uncertainty in the failure probability.

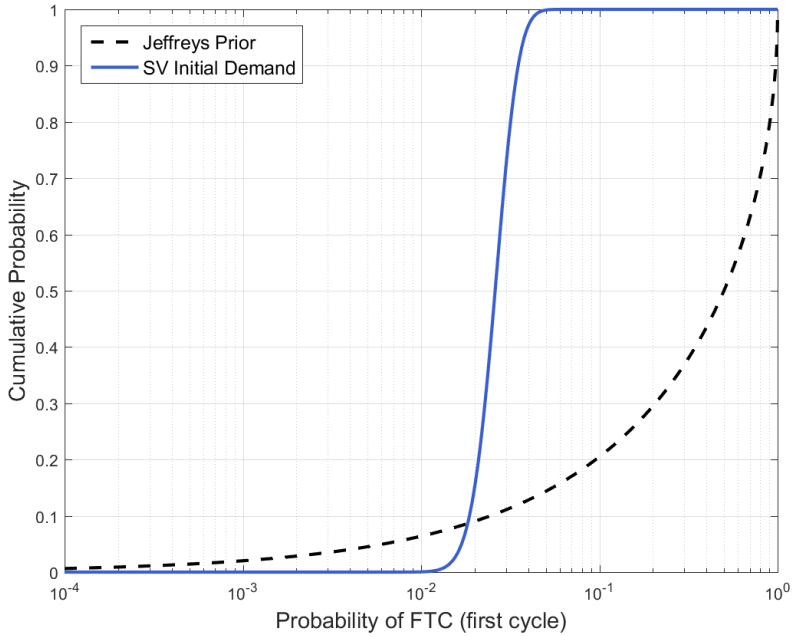

Figure 4-3 **Cumulative Probabilities (per valve) of a FTC Event on Initial Demand for the Pressurizer SVs (priSVcycles)**

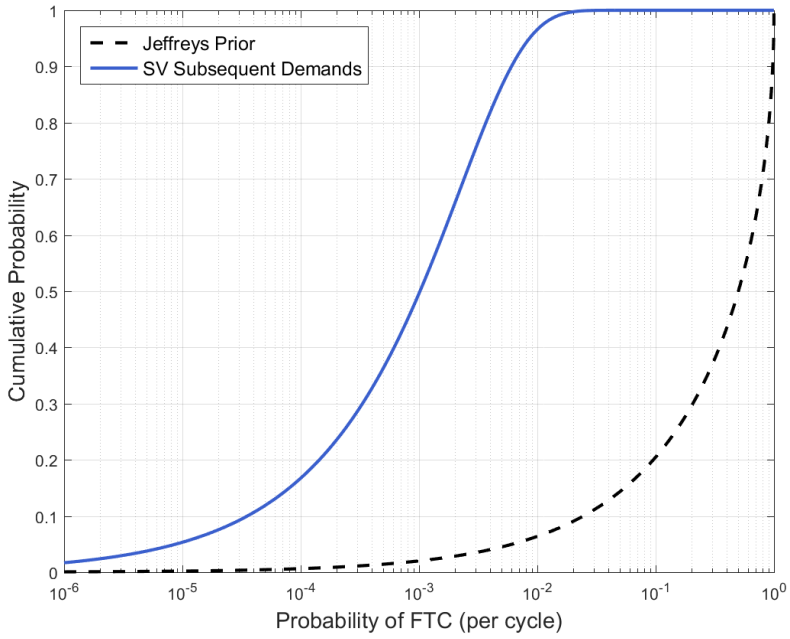

Figure 4-4 **Cumulative Distribution (per valve) of a FTC Event on Subsequent Demands for the Pressurizer SVs (priSVcycles)**

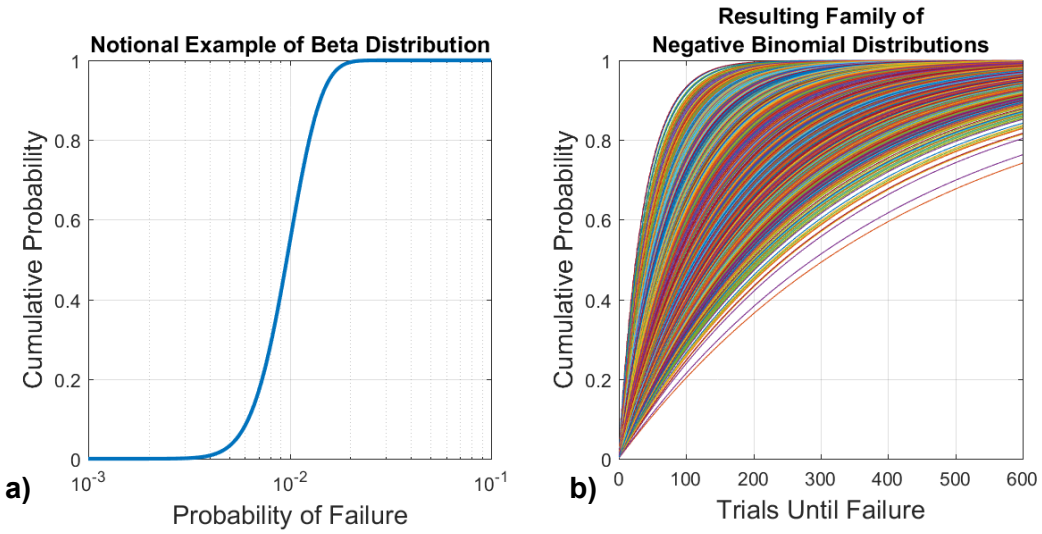

Figure 4-5 Notional Example Illustrating a Beta Distribution on a Failure Probability and the Family of Distribution in Trials until Failure that Results from the Uncertain Failure Probability

To determine the cycles-to-failure for this uncertainty input, the following two-stage sampling procedure was applied. First, for each realization, a probability of failure for the first cycle, p_1, and a probability of failure for subsequent cycles, p_{sub}, were both sampled from their beta distributions (Figure 4-1(a) and Figure 4-2(a) respectively). The sampling was performed such that the draws from each distribution would be obtained from the same quantile. In other words, if p_1 corresponded to the 95th percentile of its distribution, then p_{sub} corresponded to the 95th percentile of its distribution. The rationale for this correlated sampling is that the same valves are under consideration, so a valve that has a high probability of failing on the first cycle due to its construction or service experience would also have a high probability of failing on subsequent cycles due to its construction or service experience.

Second, for each sampled probability-of-failure, a cycles-to-failure distribution was created using that probability (Figure 4-1(b) and Figure 4-2(b)). Because p_1 only applies to one cycle, the distribution for cycles-to-failure on initial demand is a binomial distribution, $Binomial(p_1)$. For subsequent demands, the cycles-to-failure distribution is a negative binomial, which models the number of trials until failure given a specific failure probability. The distribution for cycles-to-failure on subsequent demand is $NegativeBinomial(1, p_{sub})$.

Third, one random draw was taken from each of the cycles-to-failure distributions for each valve. This means that each valve in the system has the same probability-of-failure on the initial demand, but not necessarily the same outcome. Similarly, each valve in the system has the same probability-of-failure on subsequent demands, but the actual number of cycles-to-failure is different for each valve. The draw from the binomial distribution for initial demand failure is either 0.0 or 1.0. If it is 1.0, the valve fails on initial demand so cycles-to-failure for that valve is assigned the value of 1.0. If it is 0.0, the valve does not fail on initial demand so cycles-to-failure for that valve is assigned the value sampled from the subsequent cycles-to-failure negative binomial distribution. A notional example of the sampled values and the corresponding MELCOR input is provided in Table 4-3. Note that the cycles-to-failure for each individual valve are sampled separately but they are sampled from the same distribution. This reflects the stochastic nature of valve failure but accounts for the failure probability shared by all three

valves in the system. In this notional example the first valve would fail on the 25th cycle, the second valve would fail on the initial demand, and the third valve would fail on the 124th demand. The actual number of cycles experienced by the valves may be less, but not more, than the sampled value if the system depressurizes before the sampled number of cycles is reached.

Table 4-3 Notional Example of a Sample and Corresponding MELCOR Input

	p_1	p_{sub}	Initial Failure [SV1 SV2 SV3]	Subsequent Cycles-to-failure [SV1, SV3, SV3]
Sample 1	0.0407	0.0057	$[0, 1, 0]$	$[25, 63, 124]$
MELCOR Input 1	--	--	--	$[25, 1, 124]$

This sampling scheme implements two types of uncertainty in the UA. First, the uncertainty in cycles-to-failure of the three valves within one realization is representative of the stochastic nature of valve failure (aleatory uncertainty), in that one cannot predict when a particular valve will fail even given a probability-of-failure. Second, the uncertainty in cycles-to-failure between different realizations is representative of the uncertainty induced by uncertainty in the probability-of-failure, state-of-knowledge or epistemic uncertainty stemming from not knowing the actual probability of failure-on-demand.

4.1.1.2 SV Open Fraction

The pressurizer SV FTC open area fraction is represented by the MELCOR uncertain variable priSVfrac. A piecewise-uniform distribution is used to represent uncertainty with a lower bound of 0.01 and an upper bound of 1.0. The distribution assigns a higher probability to open area fractions on the interval [0.01, 0.1] and the interval [0.9, 1] than on the interval [0.1, 0.9]. This allows for some samples in which the open area fraction is between 0.1 and 0.9 but only infrequently, as SMEs deem open area fractions in this range to be unlikely, though possible.

Each pressurizer SV uses a separate random failure area. The same failure area distribution is also used for the lowest pressure SV on each main steam line, which is also randomly selected for each valve (see Section 4.1.1.3). The Sequoyah UA [7] used the same SV open area fraction uncertainty distribution.

Rationale for Distribution

Small open area fractions that do not lead to depressurization and large open area fractions that causes rapid depressurization are judged the most likely events. This suggests that the distribution on open area fraction should result in more sampling at the extremes of the interval than in the middle of the distribution. The lower end of the distribution with small open areas represents a leaking valve, something observed in failure events during operations [123]. The higher end with large open areas represents a valve that energetically opens fully and suffers a mechanical deformation of internal parts that prevents re-closure. There are no substantiated failure mechanisms observed to result in the middle part of the distribution for open areas, and hence these open areas are judged less likely. However, given the sparse data on SV failures during actual operating events, the intermediate areas are still assigned a non-zero probability. The lower end was truncated at 0.01; though small open area fractions are possible, by definition a valve cannot fail to close and also have an open area fraction of 0.0. The value of 0.01 was chosen so if all three valves fail to close and all three valves have small open area fractions, the combined open area fraction of all three valves will still fall within a realistic range for a FTC mode.

A piecewise-uniform distribution between 0.01 and 1.0 with four sub-regions was selected to measure the potential effects of a FTC event on accident progression. The sub-regions are the intervals of open area fraction from 0.1% to 10%, from 10% to 30%, from 30% to 90%, and from 90% to 100%. All of the open area fractions within a sub-region have the same probability. However, the first and last sub-regions are more likely to be sampled than the middle sub-regions reflecting expert opinion that valves are likely to either leak or to fail full open. The region 10% to 30% was assigned a slightly higher probability than the region 30% to 90% because for one of the 16 failure-to-close events on which the SV failure probability is based, the event description indicated a ~20% flow area. The density function[22] that illustrates the sub-intervals is plotted in Figure 4-6. The cumulative distribution[23] is shown in Figure 4-7. A comparison of (a) the density function and (b) cumulative distribution of priSVfrac for this effort (blue line) and the draft UA [8](orange line) is presented in Figure 4-8.

[22] This density function was also used for the SG SVs (secSVfrac).

[23] This cumulative distribution was also used for the SG SVs (secSVfrac).

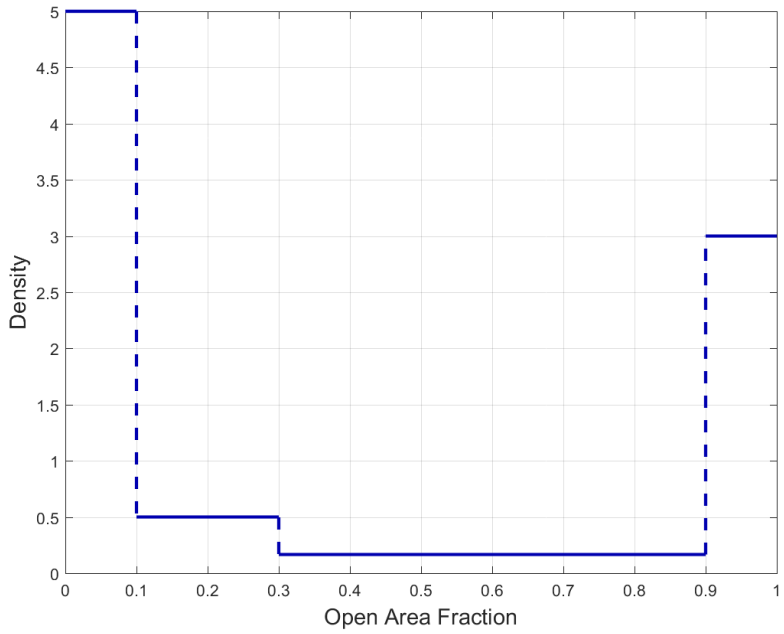

Figure 4-6 **The Density Function for SV Open Area Fraction (priSVfrac) for each Pressurizer SV**

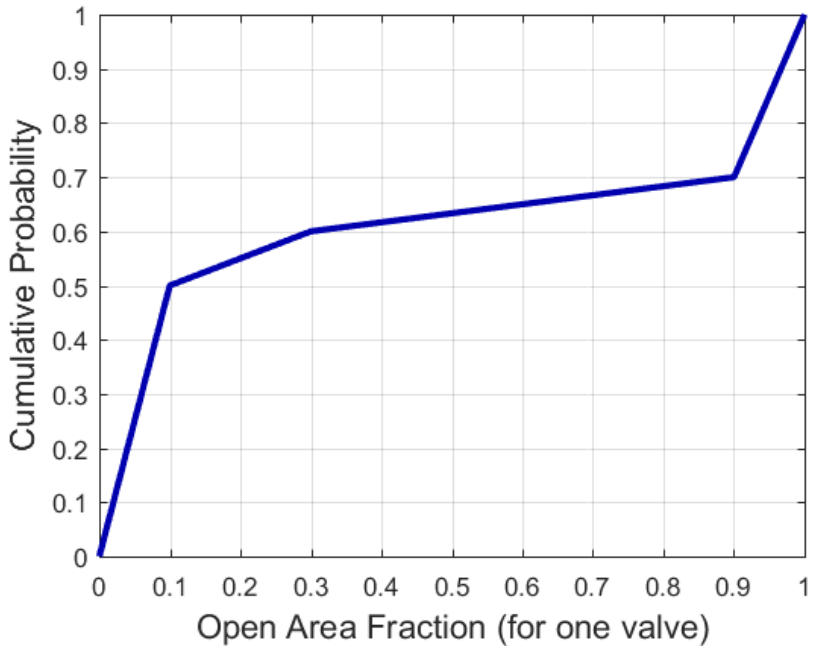

Figure 4-7 **CDF for the Pressurizer SV FTC Open Area Fraction (priSVfrac)**

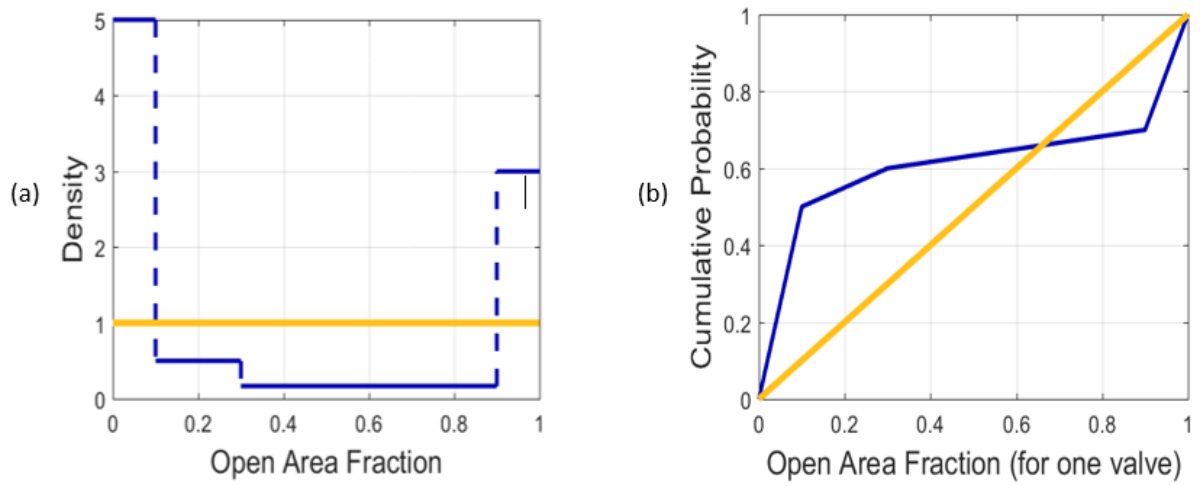

Figure 4-8 Pressurizer SV FTC Open Area Fraction (priSVfrac) Comparison between Current UA and Draft UA

4.1.1.3 Secondary SV Stochastic Failure to Close and Open Area Fraction (secSVcycles and secSVfrac)

The SG SV FTC cycles-to-failure and open area fraction are represented by the MELCOR variables secSVcycles and secSVfrac respectively. The data and subsequent sampling distributions for stochastic FTC are taken from the MSS valve data in Reference [35], which is the same approach used in the Sequoyah UA [7]. The FTC open area fraction distribution used for the pressurizer SVs is also used for the SG SVs, which is also the same approach used in the Sequoyah UA [7]. The sampling was only conducted on the lowest opening pressure SV for each of the three recirculation loops. The remaining SVs are treated as cycling as designed (i.e., no additional SV failures). While the same distributions are used for the primary side and secondary side SVs, no correlations were assumed between these two sets of valves because the two locations use different types of valves and the valves are exposed to different environmental conditions. Conversely, the samples from the first and subsequent distributions on the number of cycles until valve failure and between the steam generators within a given realization are correlated (as described for the pressurizer SVs in the previous section) because the same class of valves are being analyzed.

4.1.1.4 Reactor Coolant Pump Seal Leakage (RCPSL)

The reactor coolant pump seal leakage rates upon loss of seal cooling system are represented by RCPSL parameter. Specifically, the potential for above nominal leakage 13 minutes into the accident transient is sampled. A discrete distribution is used to represent uncertainty of 4 different leakage rates. The uncertainty in the flow rate of reactor coolant pump (RCP) seal leakage can change the evolution of an accident scenario by precluding failure of the SVs. As observed in the Surry SOARCA STSBO analysis [3], when the RCP seal leak rate increases above 21 gpm, the primary depressurizes at a sufficient rate that there is no longer a demand on the SVs.

Under normal operating conditions, cooling water is supplied to the RCP seals at a higher pressure than the primary. As a result, the water keeps the RCP seals cool while preventing any primary coolant from flowing up the RCP shaft and contaminating areas outside the primary system boundary. When a loss of AC power occurs, the RCP seal cooling system no longer

supplies cooling water. The primary coolant begins leaking along the RCP shaft through the mechanical seals at a nominal rate of 21 gpm per RCP at the nominal operating system pressure (based on calculations from a Westinghouse Owners Group model [40]). The RCP seal leakage begins at 21 gpm per pump for all sequences following the loss of AC power [47]. However, the mechanical seals may thermally or mechanically fail as the primary system heats up. Depending on the seal component failures, the higher leak rates are estimated at 76 gpm, 182 gpm, or 480 gpm per RCP as described in NUREG-1953, Table 13 [49]. Any increased leakage is specified to occur at 13 min, which is the time required to fill the RCP seal cavity with the hot primary system water [40]. The leakage rates described with this parameter are identified relative to the nominal flow at the normal primary system operating pressure. However, the MELCOR UA leakage model will adjust the leakage as the primary system pressure and temperature conditions change.

The SOARCA analysis specified an initial leakage rate of 21 gpm per RCP but transitioned to 182 gpm per RCP once the primary system fluid near the pump approached saturation conditions [3]. While the seals are more likely to fail when leaking saturated or two-phase water, the Westinghouse Owners Group model is judged to better characterize the probability of higher seal leakage.

Rationale for Distribution

There are four discrete leak rates specified in Table 13 of NUREG-1953. The probability of occurrence for each leak rate is also taken directly from Table 13 and is based on work done by the Westinghouse Owners Group [48]. If the seal is sampled to fail, the increased RCP leakage occurs at 13 minutes after the RCP seal cavity fills with the hot primary system water. A summary of the various leak rates and their probabilities are given in Table 4-4. While there will be a very limited number of realizations with leakage of 76 or 480 gpm per RCP, there is no technical justification to adjust these probabilities.

Since the original SOARCA work, Surry installed the Flowserve N-9000 pump seals as part of their post-Fukushima safety enhancements [151]. The N-9000 seals have dramatically improved leakage characteristics. Consequently, the seal leakage in a STSBO would be very small (i.e., <<21 gpm/RCP). However, the older RCP seal uncertainty distribution was retained to provide comparison with the Sequoyah UA [7] and the previous SOARCA work [3]. The higher leakage seal parameter also adds insights to other plants without the pump seal enhancements.

Table 4-4 RCP Seal Leak Probabilities at Operating Pressure

Time = 0 min	Time ≥ 13 min	Probability
21 gpm/RCP	21 gpm/RCP	0.79
21 gpm/RCP	76 gpm/RCP	0.01
21 gpm/RCP	182 gpm/RCP	0.1975
21 gpm/RCP	480 gpm/RCP	0.0025

4.1.1.5 Normalized Temperature of the Hottest Steam Generator Tube

The NRC and industry have been studying SG tube ruptures for decades because of their importance in maintaining the RCS pressure boundary [37][38]. In particular, a tube failure during a severe accident has the potential for radioactive release to the environment that

bypasses the containment. At high temperature conditions during a severe accident, natural circulation flow patterns are established where high temperature gases from the core circulate into the hot leg and SG. The effectiveness of the high temperature gases to heat the SG tubes is an important factor in determining their failure. The NRC and industry performed 1/7th scale experimental tests to characterize the natural circulation flows between the vessel and the steam generator [39][40]. The tests were studied using computational fluid dynamics techniques [50]. The computational fluid dynamic techniques were subsequently scaled to full plant geometry and severe accident conditions. NUREG-1922 developed recommended modeling parameters to characterize the natural circulation for lumped parameter codes [52]. The specific recommendations included (a) the hot leg discharge coefficient, (b) the SG mixing fraction, (c) the ratio of the hot leg flow to the SG recirculation flow, (d) the percentage of tubes involved in up-flow versus the circulatory return flow, (e) the maximum normalized temperature of the hottest tube, and (f) the hot and cold stream flow split into the surge line. The computational fluid dynamics calculations included sensitivity studies that estimate the variation in these parameters under a variety of conditions and assumptions [52]. The following conclusions were drawn from the NUREG-1922 sensitivity studies.

a. the hot leg discharge coefficient remained relatively constant with maximum variations of less than 8 percent,

b. the SG mixing fraction was found to vary by only a few percent over the range of conditions considered,

c. the recirculation ratio is not sensitive to the secondary side temperature,

d. the hot tube fraction was difficult to predict with confidence because some of the tubes change direction. However, the hottest tube region was not significantly affected by changes in the overall size and shape of the hot tube region,

e. the normalized temperature of gases entering the hottest tube is an important parameter because it refers to the portion of the tube bundle where the thermal loading is most severe. The sensitivity of this parameter to changes in the modeling parameters was significant.

f. the tube bundle heat-transfer rate was found to impact the recirculation ratio in previous work. However, the reasonable variations around best-estimate heat transfer conditions are well characterized by a recirculation ratio of 2.4.

Based on these conclusions, the normalized inlet temperature (T_n) of the hottest tube was selected as the most significant parameter for use in this uncertainty study. The observed variation of T_n in the computational fluid dynamics calculations is partly due to variations in the recirculation ratio and the SG mixing fraction. Hence, the variability in T_n is somewhat representative of the variability in the mixing and recirculation ratio parameters. The normalized temperature is defined below as:

$$T_n = \frac{T_{ht} - T_{ct}}{T_h - T_{ct}}$$

Eq. 4-3

where:

T_n	Normalized hot tube temperature
T_{ht}	Hottest tube temperature
T_h	Hot leg hot stream temperature
T_{ct}	Cold tube temperature

An example computational fluid dynamics temperature distribution is shown in Figure 4-9 [52] where T_h is the red portion of the flow leaving the vessel and T_{ct} is the dark blue return flow to the SG inlet plenum. Both T_h and T_{ct} are calculated internally by MELCOR. By sampling the normalized hot tube temperature T_n, the temperature of the hottest tube T_h can be calculated using Equation 4-3. The time-dependent temperature is imposed as a boundary condition to the single-tube models, which was a MELCOR model enhancement implemented for this project.[24] The single tube model is used to evaluate the potential for creep rupture at the hottest tube location in each SG.

[24] The single tube models (i.e., one for each SG) monitor conditions in the system model to evaluate the potential for a SGTR at the hottest tube inlet conditions. The single tube models are incorporated into each realization calculation. The single tube model only simulates the inlet section of the hottest tube using time-evolving boundary conditions from the system model and the sampled value of the normalized inlet temperature of the hottest tube.

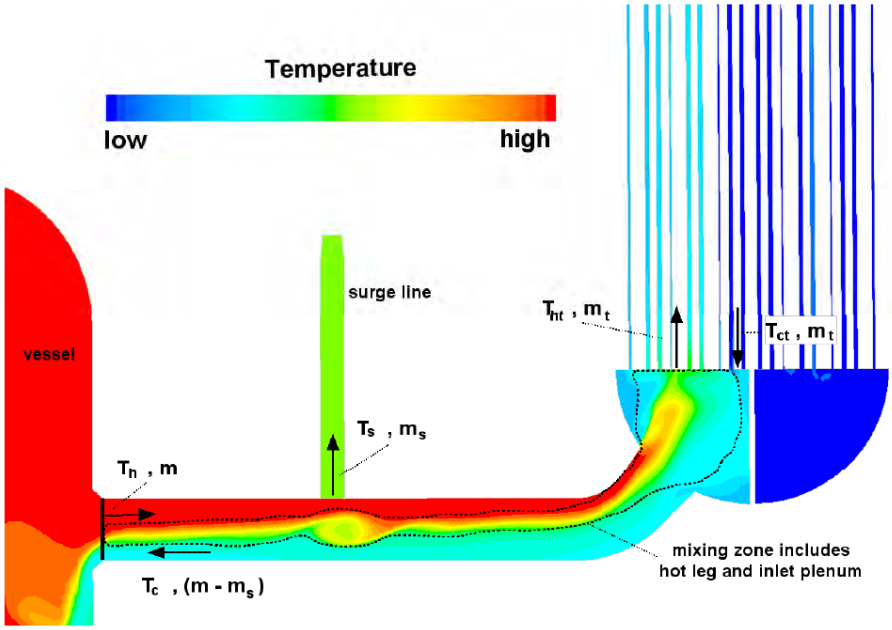

Figure 4-9 CFD Predictions Indicating Expanded Mixing Region

Rationale for Distribution

Two methodologies were applied in NUREG-1922 [52] to evaluate the hottest tube temperatures, and the CDF created is based on data from both methodologies. First, the normalized temperature range was divided into 20 subranges (0.0-0.05 up to 0.95-1.0) and the fraction of tubes within each range was obtained for each of the 140 data sets in the base case prediction. The data from the normalized temperature groupings ranged from 0.0 to 0.7. The data in the upper three ranges (i.e., 0.55-6, 0.6-65, and 0.65-0.7) represented less than a single tube in the computational fluid dynamics model and were considered insignificant. Even the data in the 0.5-0.55 range only represented an average of 0.6 percent of the tubes, which is two tubes in the computational fluid dynamics model. The location of the two tubes in the 0.5-0.55 range also varied with time.

With the second methodology, the hottest tubes were considered individually. A mass-weighted, average normalized temperature was determined for each tube in the model. The single hottest tube over the 140 data sets was described with a normal distribution with a mean of 0.43 and standard deviation of 0.1. The data was broken down into seven groups containing 20 data sets each, which yielded 7 normalized temperature predictions ranging from 0.38 to 0.51. The author notes that these predictions may slightly under predict the prototypical hottest temperature, due to the enlarged size of the tubes (i.e., the computational fluid dynamics model uses one tube to represent nine prototypical tubes) but the impact is expected to be small.

The CDF was created using data from both methodologies, which recognizes the uncertainty in the computational fluid dynamics results (e.g., one computational fluid dynamics tube corresponds to 9 tubes). A 90 percent confidence, based on analyst judgment, was applied to the seven averaged normalized temperatures from the second methodology (i.e., the second method was recommended for lumped parameter calculations by NUREG-1922). Each of the

seven values from the data set were considered equally likely. The seven points were ordered by increasing temperature and assigned equal relative probabilities from 0.0 to 0.9 on the CDF.

The CDF was completed using the three highest data sets from the first method. These three values were weighted with the remaining 10 percent confidence (i.e. defining the CDF from 0.9 to 1.0). The three values had higher normalized tube temperatures than the specific tube method (i.e., the second methodology), but with low reliability (i.e., unsteady at a particular tube location and low frequency of occurrence). The probabilities of the highest temperatures confidence interval were weighted by their relative frequency of occurrence.

In summary, the seven data points from the second methodology with the maximum sustained temperature at a specific tube were combined with the three data points from the first methodology with the maximum sustained temperature at any tube. The 10 discrete points comprising the CDF were fit with a beta distribution due to the irregular intervals, which is shown in Figure 4-10. The beta distribution has parameters of α=43.7 and β=54.9. The lower and upper bounds were taken to be the physical limits of 0.0 and 1.0, although almost all samples will be in the 0.3-0.6 range.

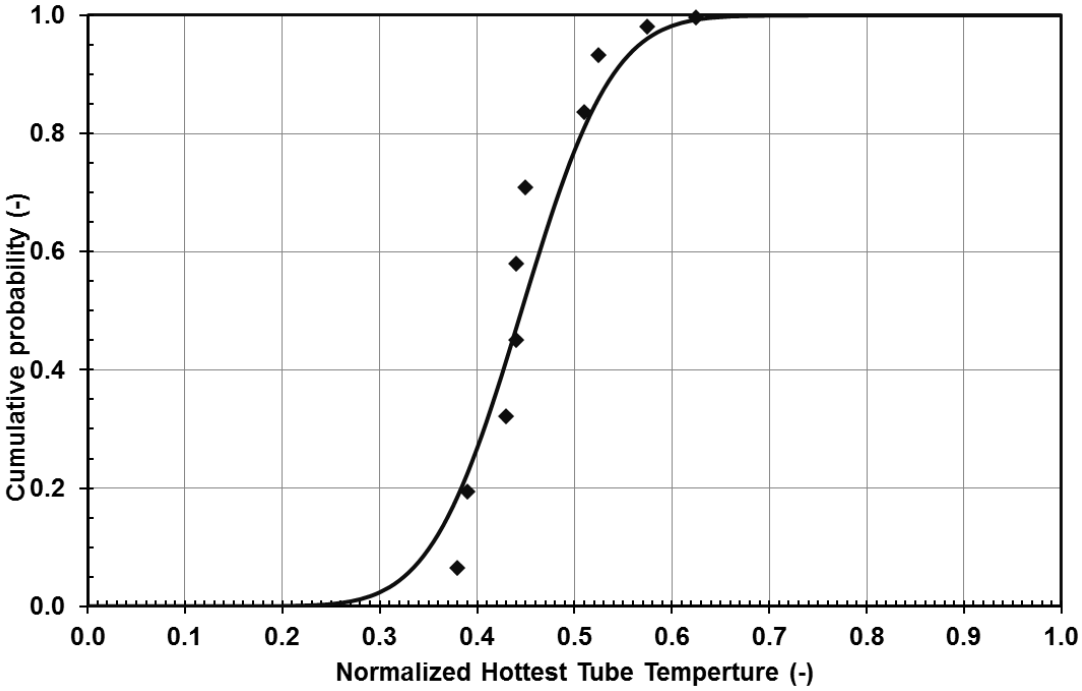

Figure 4-10 CDF of Normalized Hottest Tube Temperature

The normalized SG tube temperature distribution is used to determine the inlet temperature to the hottest tube.[25] Since the calculation for the hottest tube inlet temperature is dependent on the hot stream and cold tube temperatures from the system model, the temperature changes

[25] The normalized SG tube temperature is calculated using the hot leg and cold tube temperatures (see Eq. 4-3). A normalized fraction of 1 means the peak tube inlet temperature is equal to the hot leg gas temperature (i.e., no mixing with cooler gases). A normalized fraction of 0 means the cooler gas exiting the SG returns back into the hottest tube (i.e., no hot gases from the hot leg enter the SG).

dynamically during the accident progression. Hence, the hottest tube temperature evaluation is dynamically coupled to the overall system calculation through the gas temperature used in the normalized hottest tube evaluation (i.e., see Eq. 4-3).[26] For example, pressurizer SV cycling can disrupt natural circulation flow while the valve is open, which impacts the hot stream and cold tube temperatures. The single tube model is only used to calculate the potential for creep rupture in the hottest tube and is not part of the overall system energy balance.

4.1.1.6 Steam Generator Tube Flaw Depth

In the original Surry SOARCA analysis [3], a SGTR induced by creep rupture was only predicted after prescribing a stuck-open secondary SV in the model and lowering the creep rupture failure criterion on the tube. This approach was necessary due to limitations in the MELCOR input model. Due to the importance of a SGTR bypass release path on the total environmental release, the prediction of the SGTR was improved for the Surry UA. The new modeling uses separate single steam generator tube models for each loop, which run concurrently with the full steam generator models. The separate tube models specify the response of the maximum plume temperature entering the steam generator tubes based on NRC CFD analysis [52]. In particular, the hot tube model monitors the developing conditions and uses the normalized scaling results from Ref. [52] to specify the sampled maximum SG tube inlet temperature (i.e., see Section 4.1.1.5 for a description). The hot tube model is combined with the limiting tube flaws in this region. Since a SGTR creep failure is dependent on the local temperature and the tube thickness, the new hot tube representation better predicts the most vulnerable tube location in the steam generator. If a steam generator tube creep rupture failure is predicted in the tube model, then a leak path is opened in the full model. Steam generator tube creep rupture is also monitored in two other locations, which are representative of the hot upflow region and the cooler regions in the steam generator. Consequently, three locations are monitored for creep rupture in each steam generator.

Tube Modeling

The calculation of a creep rupture failure depends on the tube temperature and stress. The temperature variation is impacted as described above using the hot plume sampled temperature described in Section 4.1.1.5. The calculation for circumferential or hoop stress (σ_θ) can be estimated using the differential pressure (ΔP), the tube radius (r), and the tube wall thickness (t) according to the equation:

$$\sigma_\theta = \frac{\Delta P r}{t} \qquad \text{Eq. 4-4}^{27}$$

The differential pressure (ΔP) across the tube is influenced by accident conditions. The Surry UA includes modeling of SG safety valve failures and MSIV leakage that usually results in a low secondary side pressure by the time of the core damage. However, the primary system pressure may also be low due to the sampling of the pressurizer SV failure, which could also impact the calculated stress. The tube radius (r) can change if a tube balloons; however, any

---

[26] The single tube model also uses the system model pressure and fluid composition (e.g., void, gas composition) as boundary conditions.

[27] The simplified thin-walled formula for hoop stress is shown for discussion purposes. The uncertainty evaluation uses the more accurate thick-walled hoop stress evaluation. The more complex thick-walled evaluation can account for flaws on inside, outside, or both sides. In this analysis, it is assumed that the flaw only erodes the outer radius. The maximum difference is approximately 10% (see Appendix B).

change in the radius is not expected to be significant. The remaining variable, the tube thickness (t) of a flawed tube is a sampled parameter for the stress calculation. The degradation in the tube thickness can also be equated to a stress multiplier, which is often used in other studies (e.g., [38]).

First the bounds of the flawed tube distribution were determined. An estimate of the lower limit for the wall thickness is the thickness at which the yield strength of the material (Inconel 600) would be exceeded at normal operating conditions. The tube hoop stress must be lower than the yield strength. A representative yield strength for Inconel 600 is 45,000 psi. Using the normal operating differential pressure across the tube of 1426 psi, the bounding analysis indicates that the minimum tube thickness is 0.312 mm. This corresponds to a through-wall flaw of 75 percent or a maximum stress multiplier of 4. The minimum thickness was not strictly enforced in the final UA distribution but presented here as a reasonable bounding flaw.[28]

The upper limit is guided by previous NRC research that showed stress multipliers of 1.5 (i.e., a flaw through-wall depth of 0.35) is needed for a tube rupture prior to hot leg failure [38]. The minimum flaw depth needed to result in tube rupture prior to hot leg failure ranges between 0.3 and 0.4 in NUREG-2195, so only flaws deeper than 0.3 are considered. Less severe flaws are not considered because they are not predicted to cause a tube failure prior to another thermally-induced failure of the reactor coolant system (e.g., hot leg or the surge line) in severe accident conditions.

Consideration of Surry Plant Data

NUREG-1771 [125] and NUREG-2188 [126] summarize the results of the Surry ISI reports since their steam generator replacements in 1980 and 1981 until December 2013. The most recent Surry SG inspection reports were also reviewed [130][131][132][133][134][135]. By 2016, Surry Units 1 and 2 had 111 (1.1%) and 99 (1%) tubes plugged over 334 and 333 Effective Full Power Months (EPFM) of operation since the first in-service inspection, respectively. NUREG-2188 reports that only 2,734 tubes (1.0 percent) of the 281,262 thermally treated Alloy 600 tubes placed in service at 18 units between 1980 and 2013 have been plugged. Consequently, Surry is typical of the plants with thermally treated Inconel 600 tubes.

Surry adopted Technical Specification Task Force 449 (TSTF-449) in 2007 and adopted TSTF-510 in 2013 [126]. The technical specifications require developing a steam generator program to maintain steam generator tube integrity for the operating interval between tube inspections. The technical specifications define what constitutes tube integrity through the establishment of performance criteria. The specifications require monitoring primary-to-secondary leakage, inspecting tubes periodically, assessing the condition of the tubes relative to the performance criteria, and defining criteria for plugging tubes. The requirements in the technical specifications are largely performance based; however, they are supplemented with some prescriptive requirements. Since Surry adopted TSTF-449 in 2007, they inspect 100% of the tubes every two refueling outages.

Detailed information is provided in the NUREG-1771 and NUREG-1988 from the Surry's ISI reports that summarizes the inspection results. The ISI reports include a table summarizing the

[28] The flaw distribution described from actual plant in-service inspection reports guided the bounds limits. Bounding limits were used to limit the maximum depth flaws that would fail at normal operating conditions (described further later in this section).

wear observed at the Anti-Vibration Bars (AVBs) at the top of the tube bundle, a known location for tube wear that is carefully monitored. In the six most recent inspection reports, the maximum tube degradation at the monitored locations was less than 25%. The Surry ISI experience is consistent with the other units with Inconel 600 tubes. Approximately 42 percent of the plugged tubes were plugged because of wear at a support structure (e.g., an anti-vibration bar) for the 18 units with thermally-treated Inconel 600 tubes. The wear at these locations generally increases at a predictable rate and can be managed effectively in the ISI program. For example, Surry 2 reported the AVB wear rate is approximately 1.5 percent through-wall per cycle in 2005 [126].

The second most common reason for plugging thermally-treated Inconel 600 tubes is due to damage by loose parts. The ISI reports include detailed information on every tube plugging not due to AVB wear, which includes loose parts damage. Surry also had some problems with sludge build-up in the bottom of the steam generator from a chemistry excursion occurring because of an issue with the condenser. The lancing equipment used to clean out the sludge caused damage to sixteen tubes, which led to their plugging in 2003.

The Surry ISI report includes the tube location, the outage when plugged, the reason for plugging, and the measured flaw depth if that was the reason for plugging. The measured flaw depth is provided for all the tubes damaged from loose parts or maintenance activities. The flawed tube data were extracted for all the steam generators from both Surry units since their installation (circa 1980) through the Fall of 2016. The non-dimensional flaw depths ranged from 0.10 to 0.98 (see Table 4-5). There were 76 tubes with reported flaws. 56 of the plugged tubes were located on the inlet side of the steam generator, which is more susceptible to creep rupture failure in a severe accident than flaws on the outlet side. 46 of the plugged tubes with flaws on the inlet side of the steam generator occurred between the tube sheet and the second grid support. Figure 4-11 shows the locations of the flaws on the inlet side of the SG with color coding for the non-dimensional flaw depth. Since the flaw results from all three steam generators from both units are shown, some of the indicated flaw locations have multiple flaws.

Table 4-5 Surry Tube Flaw Depth Distribution

Non-dimensional Flaw Depth	Stress Multiplier	Number of Tubes
0.0 to 0.1	1.0 to 1.1	0
0.1 to 0.2	1.1 to 1.3	9
0.2 to 0.3	1.3 to 1.4	15
0.3 to 0.4	1.4 to 1.7	11
0.4 to 0.5	1.7 to 2.0	21
0.5 to 0.6	2.0 to 2.5	9
0.6 to 0.7	2.5 to 3.3	5
0.7 to 0.8	3.3 to 5.0	2
0.8 to 0.9	5.0 to 10	1
0.9 to 1.0	10 to ∞	3

Figure 4-11 also shows the likely locations for the hot plume during a severe accident [52]. The hot leg piping connects in an asymmetric manner to the inlet plenum. Since the orientation of the hot leg connection is unknown, both possible hot plume locations are shown in the figure. However, it is believed that the tube columns start numbering from the hot leg inlet side.

Consequently, the left-hand plume region would have the hottest tubes in a severe accident. Only two flawed tubes are identified in either plume region.

There are two interesting findings from the historical Surry tube flaw locations. First, 70% of the tube flaws were located on the hot inlet side of the steam generator. In fact, 61% of the flaws were located between the tube sheet and the second grid support. The higher occurrence of flaws on the inlet of the hot side of the steam generator is significant because the hot gas plume enters the steam generator on the inlet side [52]. Second, many of the flawed tubes were plugged due to unexpected loose parts damage. The loose parts damage has occurred regularly through the Surry steam generator life cycle. The loose parts damage almost always occurs near the bottom of the steam generator. When located on the inlet side of the steam generator, the loose parts-induced flaws near the tube sheet are more susceptible to failures due to higher inlet temperatures during a severe accident. The potential failure of a steam generator tube due to creep rupture is strongly influenced by the heating from the hot plume.

The Surry ISI reports show some very severe tube defects in Unit 1 during the 1984 RFO (i.e., tubes with 89% and 96% through-wall degradation) and in Unit 2 during the 2005 RFO (i.e., tubes with 90% and 98% through-wall degradation). The hoop stress is 2.5 times design yield strength of Inconel 600 at a through-wall thickness of 0.9. Based on the minimum tube thickness calculations in the Tube Modeling section, tubes with flaws greater 0.75 would not be expected to remain intact at normal operating conditions. It is believed that the discrepancy is due to the simplifying assumptions in the interpretation of the flaw depth. In particular, it is assumed that the flaw causes a uniform circumferential radius reduction. In fact, Surry MELCOR model testing with these severe flaws using a uniform radius reduction resulted in tube failures at normal operating conditions. The actual characteristics of the flaw shape (length, width, depth, etc. in all radial directions) with more detailed structural models are needed to improve the failure prediction. The MELCOR tube failure model only addresses strain accumulation with a one-dimensional thick-walled hoop stress evaluation. Alternate modes of failure and multidimensional effects are expected to be important for asymmetric flaws, especially at lower temperatures.

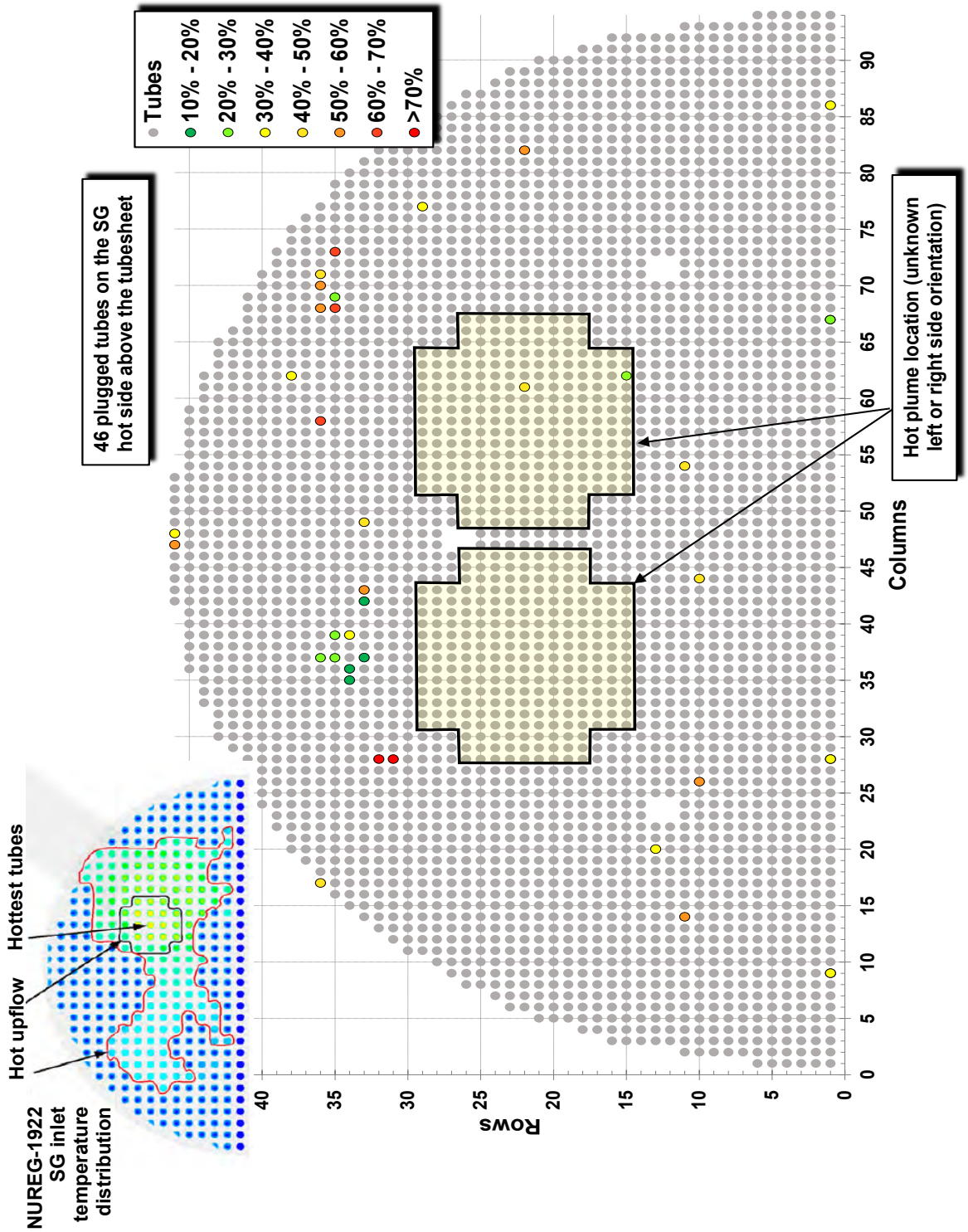

Figure 4-11 **Summary of the Flaw Depths in the Surry Unit 1 and 2 Plugged SG Tubes**

The MELCOR thick-walled stress and Larson-Miller creep models were parametrically varied to identify a reasonable minimum thickness using the simplifying assumption of a uniform circumferential radius reduction. Figure 4-12 shows the tube failure timing responses from MELCOR Larson-Miller Inconel Tube creep rupture correlation as a function of the flaw depth and the tube temperature. As shown in the figure, the tube response is highly sensitive to very deep flaws. When there is a deep flaw (e.g., Surry reported values to 0.98), the Larson-Miller creep rupture model fails the tube during the steady state prior to the STSBO. Based on the results in Figure 4-12, the maximum tube depth of the 3 deepest flaws is limited to the range of 0.8 to 0.9. A flaw depth of 0.9 will fail in ~3 min at a temperature of 700 K at a maximum pressure difference, which is just above normal operating conditions. Consequently, limiting the maximum flaw depth to 0.9 still results in a very severely degraded tube that could fail very early in the core heatup.

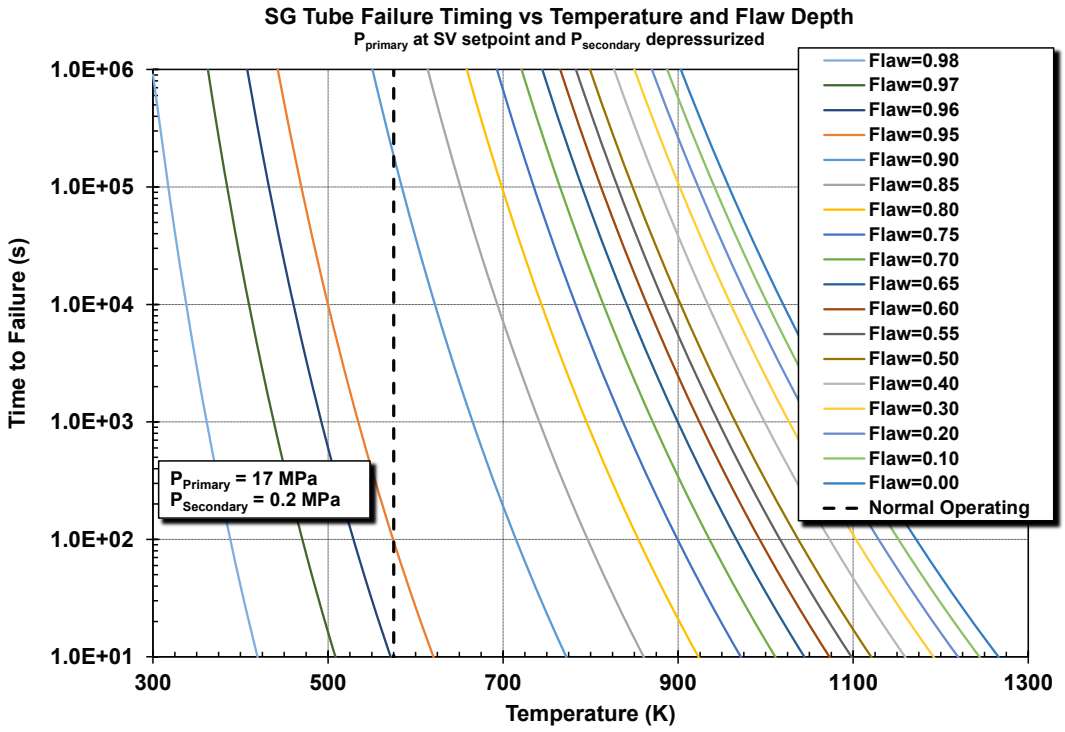

Figure 4-12 Summary of the SG Tube Failure Timings Versus Temperature and Flaw Depth

Application of NUREG-2195 Methodology

A recent NRC study (NUREG-2195) for the evaluation of consequential SGTRs was reviewed for generic guidance on flaw distribution [10]. NUREG-2195 includes a database of recorded flaws from SG inspections. The database provides the probability of the flaw depth and length for thermally treated Inconel 600 and 690 tubes in both pressurized water reactor plant types with U-tube steam generators (i.e., Westinghouse and Combustion Engineering plants) based on detected flaws. Table 4-8 shows the size distributions for the detected flaw depths, the associated stress multipliers, and the probability of occurrence.

The final column in Table 4-8 shows the expected number of tubes with flaws in each of Surry's steam generators following the example described in NUREG-2195. The following steps were performed to determine the number of tubes with flaws. Surry has 3 SGs with 3342 tubes in each. The expected number of flaws is identified at k EFPYs for three types of flaws: volumetric/wear, circumferential cracks, and axial cracks. The equation is defined below (Equation 6-2 from Reference [129]).

$$NFlaws = (\#\text{tubes})(\#\text{SGs})[1 - \exp[-0.5\mu k^2 + \Omega k]] \quad \text{(Eq. 4-5)}$$

The coefficients for each flaw type are defined below (and in Table 6-2 in Reference [10]).

Table 4-6 Parameters from NUREG-2195 for Estimating the Number of Flaws of each Flaw Type

	Wear/Volumetric Flaws	Axial. Crack Flaws	Circ. Crack Flaws
Ω	0.0013236	0.0002	0.0001
μ	0.000064166	0	0

Applying this equation to a single SG at Surry at 36 EFPYs results in an estimated 285.29 volumetric/wear flaws, 23.98 axial flaws, and 12.01 circumferential flaws. Surry has a 1.5-year fuel cycle and completes a 100% inspection of the tubes every two refueling cycles. Consequently, new flaws could appear for up to 3 years. If it is assumed that the previous inspection was three years ago, then the total number of new flaws would be the difference between the estimated number of flaws at 36 EFPYs and at 33 EFPYs.[29] The total number of flaws and the estimated number of new flaws are summarized in Table 4-6.

Table 4-7 Number of New Flaws Expected by 36 EFPYs

Age	Wear/Volumetric Flaws	Axial Crack Flaws	Circ. Crack Flaws	Total
33 EFPYs	252.68	21.99	11.01	285.68
36 EFPYs	285.29	23.98	12.01	321.28
Difference:	32.61	1.99	1	35.6

Consequently, is estimated that there are 321 flawed tubes per steam generator predicted at 36 EFPYs. By accounting for the SG inspection schedule at Surry, 35.6 new flaws appear between the 33 and 36 EFPYs.

The SG flaw size distribution from all plants with thermally-treated Inconel 600 and 690 SG tubes is summarized in Column 3 in Table 4-8 (from Table 7-3 [10]). The number of tubes with flaws depths between 0.0 and 0.3 are multiplied by 321 tubes/SG, or the expected lifetime accumulation of flaws. The number of tubes with flaws depths between 0.3 and 0.9 are

[29] The number of new flaws for any SG conservatively assumes 3 years of new flaw development to the 24th RFO on the 36th EFPY of operation. The number of new flaws could be smaller because the UA considers accidents throughout the entire fuel cycle (i.e., not just at the end of the cycle), which would reduce the estimated number of new flaws accordingly. In addition, Surry typically performs a 100% tube inspection of either one or two SGs each RFO. Consequently, the tubes inspected at the last RFO would have 1.5 years less of new flaw development than the tubes inspected at the prior RFO.

multiplied by the number of new flaws (i.e., 35.6 tubes/SG) by the 36th EFPYs of operation.[30] The estimated flaw distribution as a function of flaw depth in each Surry SG at 36 EFPYs is presented in Column 4 of Table 4-8.

Previous analysis with SCDAP/RELAP5 shows a stress multiplier of about 1.5 (i.e., through-wall depth of approximately 0.35) is needed for a tube failure prior to hot leg failure [38]. The timing of the tube failure relative to a hot leg failure or some other primary system depressurization mechanism (i.e., SV FTC) is critical for determining the occurrence of a tube rupture. Once the primary system depressurizes, the tube stress drops below a value where a tube failure would be expected. Consequently, only more deeply flawed tubes (i.e., >0.35 through-wall depth) have a likelihood of failing prior to a primary system depressurization. Table 4-8 shows a cumulative total of 4.27 flawed tubes with a through-wall depth >0.3.

Table 4-8 Probability of Flawed Tubes as a Function of Flaw Depth from NUREG-2195

Non-dimensional Flaw Depth	Stress Multiplier	Probability [129]	Number of Tubes with Flaws[31]
0.0 to 0.1	1.0 to 1.1	7.78E-02	3
0.1 to 0.2	1.1 to 1.3	5.29E-01	170
0.2 to 0.3	1.3 to 1.4	2.73E-01	88
0.3 to 0.4	1.4 to 1.7	8.78E-02	3.126
0.4 to 0.5	1.7 to 2.0	2.41E-02	0.858
0.5 to 0.6	2.0 to 2.5	6.08E-03	0.216
0.6 to 0.7	2.5 to 3.3	1.46E-03	0.052
0.7 to 0.8	3.3 to 5.0	3.39E-04	0.012
0.8 to 0.9	5.0 to 10	7.70E-05	0.003

The NUREG-2195 statistical analysis is based on flaws that are detected. The 321 flawed tubes per steam generator does not account for the hidden flaws that are not detected during in-service inspections. The larger and deeper the flaw, the higher will be the probability of detection (POD). NUREG-2195 cites NUREG/CR-6791 [137] as providing techniques for evaluating the POD and judges the impact is relatively small. In consideration of other uncertainties in this analysis and the relatively small number of deep flaws identified in the replacement SGs at Surry, it is assumed that the hidden flaws would not substantially change the expected size distribution or the total number of flaws.

For prediction of the tube failure characteristics, there are three distinct regions of interest. NRC Computation Fluid Dynamics (CFD) analysis of natural circulation flow patterns during severe accidents [52] can be used to identify the region of the hottest tube, the broader hot upflow region, and the remainder of the steam generator. The fraction of the flaws in the three regions are identified as follows,

---

[30] The NUREG-2195 methodology assumes more severe flaws (i.e., >0.3) are plugged when discovered. Consequently, only the new flaws each year contribute to the flaw depth range greater than 0.3.

[31] The total number of flaws in all three steam generators.

$X_{hot} = (0.41)*(0.13)*(0.61) = 0.032$
$X_{upflow} = (0.41)*(1 - 0.13)*(0.61) = 0.22$
$X_{cold} = 1 – (X_{hot} + X_{upflow}) = 0.75$

where,

41% of the steam generator tubes are in hot upflow during natural circulation
13% of the hot upflow region has the hottest tubes
Surry ISI reports show 61% of the flaws are on the inlet side of the SG

NRC CFD analysis of natural circulation through the steam generator [52] estimates that only 41% of the tubes have upflow from the steam generator inlet plenum. The hottest tubes are located in 13% of the hot upflow region, which had the most sustained inflow from the hottest part of the plume (i.e., the region modeled in the single hot tube model). The hot upflow and hot zone regions from Reference [52] are shown in the upper left-hand side of Figure 4-11. The hot tube region is removed from the hot upflow region to just represent the remainder of the tubes outside the hottest location. The cold zone is assigned to all the other regions of the steam generator. Table 4-9 summarizes the results of the flawed tubes in the three regions of the SG. Only flawed tubes with through-wall damage greater than 0.3 are shown based on findings from NUREG/CR-6995 [38].

Table 4-9 Number of Flawed Tubes in the Three SG Regions Based on NUREG-2195

Non-dimensional Flaw Depth	Number of Tubes with Flaws in the Hottest Zone[32]	Number of Tubes with Flaws in the Hot Upflow Zone[33]	Number of Tubes with Flaws in the Cold Zone[34]
Zone Factors	0.032	0.22	0.75
0.3 to 0.4	1.01E-01	6.75E-01	2.35E+00
0.4 to 0.5	2.77E-02	1.85E-01	6.45E-01
0.5 to 0.6	6.98E-03	4.67E-02	1.63E-01
0.6 to 0.7	1.68E-03	1.12E-02	3.91E-02
0.7 to 0.8	3.89E-04	2.61E-03	9.07E-03
0.8 to 0.9	8.84E-05	5.92E-04	2.06E-03
Total	1.377E-01	9.212E-01	3.208E+00

The Surry tube flaw depths reported in the ISI reports were also used to predict the likelihood of various depth tube flaws. Most of the flaws appeared without warning between inspections due to loose parts damage. Although the location of the flaws on the hot side of the generator were generally outside of the hottest plume region, many flaws could be within the broader hot upflow region, which is also exposed to relatively hot gases (Figure 4-11). For the purposes of this analysis, the flaws were assumed to be uniformly spread across all tubes in the steam generator but 61% of the flaws are specified on the inlet side versus the outlet side of the generator based on observations from the Surry ISI reports.

---

[32] Column 2 shows the expected number of flawed tubes per steam generator in the hot zone region. The multipliers for the hot zone flaw depths of 0.3 to 0.9 are calculated using (11 tubes/SG)*(0.41)*(0.61)*(0.13)*(3 years)*(flaw depth probability from Column 3 of Table 4-8).

[33] The calculations for the upflow zone is identical to the hot zone except without the 0.13 multiplier for the hot zone is replaced with (1-0.13) for the region in upflow outside of the hot zone.

[34] The calculations for the cold is the remaining regions of the SG times the flaw depth probability from Column 3 of Table 4-8.

UA Distribution for Tube Flaw Depth

Similar to the NUREG-2195 discussion, the Surry flawed tube data were scaled per unit, per steam generator, and per inspection period. There were 76 flawed tubes identified and plugged over 24 fuel cycles from the operation of the six steam generators in the two units. 52 of those tubes had flaw through-wall depths greater than 0.3.[35] Since the adoption of TSTF-449, Surry completes a 100% inspection of all SG tubes over two consecutive refueling outages. Based on the Surry ISI reports, 0.72 flawed tubes with a through-wall depth >0.3 are currently predicted in the Surry SG.[36]

Table 4-10 Number of Flawed Tubes in the Three SG Regions Based on Surry ISI Reports

Non-dimensional Flaw Depth	Number of Plugged Tubes	Number of Tubes with Flaws in the Hottest Zone[37]	Number of Tubes with Flaws in the Hot Upflow Zone[38]	Number of Tubes with Flaws in the Cold Zone[39]
	Zone Factors	0.032	0.22	0.75
0.3 to 0.4	11	4.93E-03	3.30E-02	1.15E-01
0.4 to 0.5	21	9.41E-03	6.30E-02	2.19E-01
0.5 to 0.6	9	4.03E-03	2.70E-02	9.40E-02
0.6 to 0.7	5	2.24E-03	1.50E-02	5.22E-02
0.7 to 0.8	2	8.96E-04	6.00E-03	2.09E-02
0.8 to 0.9	4	1.79E-03	1.20E-02	4.18E-02
Total	52	2.330E-02	1.559E-01	5.430E-01

Comparing Table 4-9 and Table 4-10 shows a relatively large difference in the number of flawed tubes in each region. The difference in the number of flawed tubes from the two approaches is in the lower portion of the flaw range. The reason for the differences is attributed to the large size of the NUREG-2195 database and its inclusion of unplugged tubes with through-wall depths less than 0.4. Conversely, the number of more deeply flawed tubes (i.e., >0.5) are in good agreement between the two data sets.[40] For example, NUREG-2195 predicts 0.8% of the flawed tube depths are greater than 0.5, which corresponds to 0.26 deeply flawed tubes per SG.

$$N_{\text{NUREG-2195, flaw >0.5}} = 3.96 \text{ tubes/SG} * 0.008 = 0.32 \text{ tubes}$$

Similarly, the Surry ISI reports have 20 tubes over the lifetime of the replacement SGs in the two units with through-wall depths of 0.5, which corresponds to 0.28 deeply flawed tubes per SG.

---

35 The tube flaw depths greater than 0.9 were included in the range between 0.8 and 0.9, as discussed previously.

36 (52 flawed tubes) / [2 units x 3 SGs/unit x 24 fuel cycles/(2 fuel cycles per inspection)] = 0.72 flawed tubes per inspection period.

37 Column 2 shows the expected number of flawed tubes per steam generator in the hot zone region. The multipliers for through-wall depths are calculated using (0.72 tubes/SG)*(0.41)*(0.61)*(0.13)*(3 years)*(number in the range/52 tubes with flaws >0.3). The multipliers for through-wall depths 0.9 are calculated using (0.72 tubes/SG)*(0.41)*(0.61)*(0.13)*(3 years)* (number in the range/52 tubes with flaws >0.3).

38 The calculations for the upflow zone is identical to the hot zone except without the 0.13 multiplier for the hot zone is replaced with (1-0.13) for the region in upflow outside of the hot zone.

39 The calculations for the cold is the remaining regions of the SG times 0.72 tubes/SG.

40 The depth flaws (i.e., >0.5) are where MELCOR has predicted tubes failures prior to hot leg failure [16].

$$N_{Surry,\ flaw\ >0.5} = 0.72 \text{ tubes/SG} * (20 \text{ tubes} >0.5/52 \text{ tubes} >0.3) = 0.28 \text{ tubes}$$

Using the NUREG-2195 distribution as the basis for the number of flawed tube per steam generator, the number of flaws expected in the hot, hot upflow, and cold regions are,

$$N_{hot} = N_{NUREG-2195} * X_{hot} = (4.27)*(0.032) = 0.14 \text{ tubes}$$
$$N_{upflow} = N_{NUREG-2195} * X_{upflow} = (4.27)*(0.22) \approx 1 \text{ tube}$$
$$N_{cold} = N_{NUREG-2195} * X_{cold} = (4.27)*(0.75) \approx 3 \text{ tubes}$$

The UA flaw distribution is specified by using the total number flawed tubes from the NUREG-2195 distribution in Table 4-8 between 0.3 and 0.5. As described above, the total number of flawed tubes with flaw depths above 0.5 through-wall is similar between the two methods but the Surry ISI reports include more severe flaws with through-wall depths greater than 0.7. Consequently, the Surry flaw distribution is used for tubes with through-wall flaw depths between 0.5 and 0.9. As shown in Table 4-11, the relative probability of each flaw range is calculated using the combined flawed tube distributions.

Table 4-11 Number of Flawed Tubes in the Three SG Regions Based on Surry ISI Data

Non-dimensional Flaw Depth	NUREG-2195 Total Flawed Tubes per SG	Surry Data Total Flawed Tubes per SG	Surry Data & NUREG-2195	Relative Probability
0.3 to 0.4	3.126	Not included	3.126	7.33E-01
0.4 to 0.5	0.858	Not included	0.858	2.01E-01
0.5 to 0.6	Not included	0.125	0.125	2.93E-02
0.6 to 0.7	Not included	0.069	0.069	1.63E-02
0.7 to 0.8	Not included	0.028	0.028	6.52E-03
0.8 to 0.9	Not included	0.056	0.056	1.30E-02
Total	3.98	0.278	4.26	1.00E+00

For each realization, five flaw samples are randomly selected. The maximum of three of the samples will be used for the cold region flaw depth as only the most severely flawed tube in this region will be modeled. Another sample will be used for the hot upflow region. The fifth flaw sample will be used for the hot zone flaw. The cumulative flaw distribution for the hot region is specified so that the sampled flaw is used 14% of the time and there is no flaw 86% of the time. The cumulative distribution function versus flaw depth and the effective stress multiplier used in the UA are shown in Figure 4-13 and Figure 4-14, respectively. Both figures include the corresponding scaled cumulative probability for the hot zone. The five probabilities cited in Table 4-11 are used for the hot zone but are scaled to occur within the final 14% of the cumulative probability distribution. The effective stress multipliers range from 1.4 to 10. The resultant cumulative probability distributions are summarized in Table 4-12.

Table 4-12 Cumulative Flaw Distributions for Hottest, Cold, and Hot Upflow SG Regions

Non-dimensional Flaw Depth	Effective Stress Multipliers	CDF for Flaws in the Cold and Hot Upflow Regions	CDF for Flaws in the Hottest Region
0.0	1.0	0.000E+00	8.600E-01
0.1	1.1	0.000E+00	8.600E-01
0.2	1.3	0.000E+00	8.600E-01
0.3	1.4	0.000E+00	8.600E-01
0.4	1.7	7.335E-01	9.653E-01
0.5	2.0	9.348E-01	9.915E-01
0.6	2.5	9.641E-01	9.953E-01
0.7	3.3	9.804E-01	9.975E-01
0.8	5.0	9.870E-01	9.983E-01
0.9	10.0	1.000E+00	1.000E+00

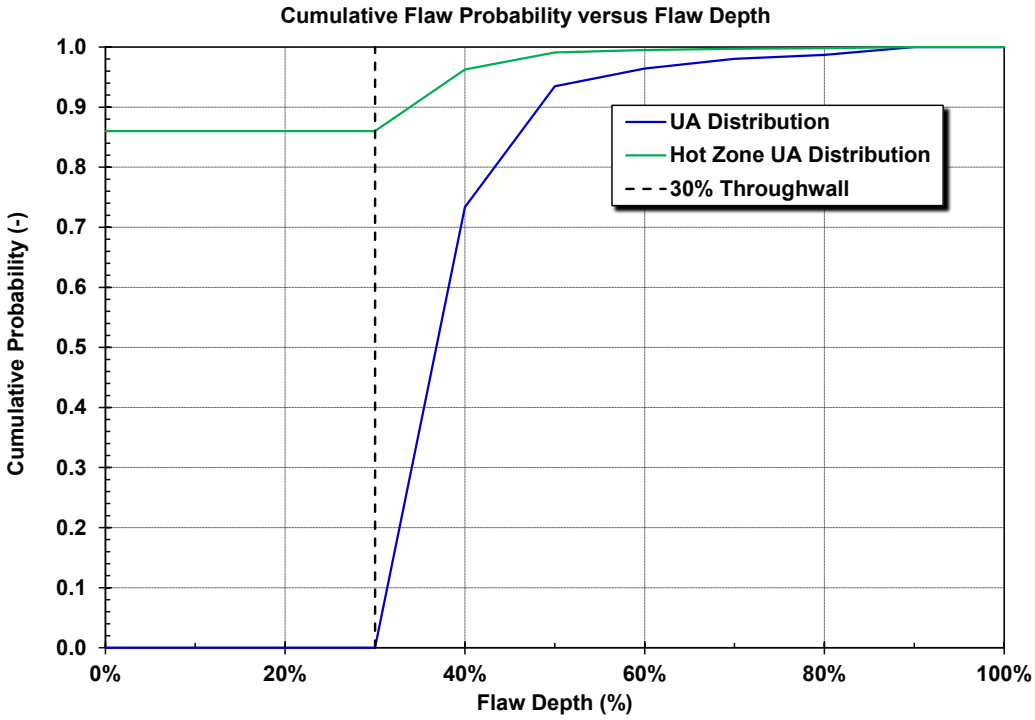

Figure 4-13 CDF of Flaw Depth

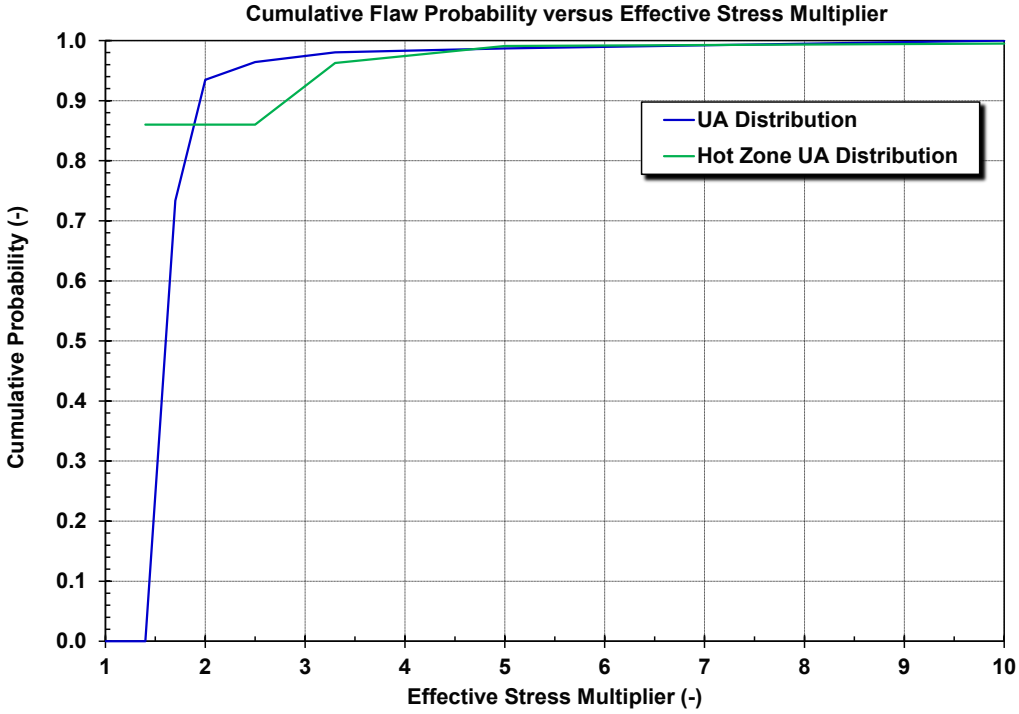

Figure 4-14 CDF of Effective Stress Multiplier

Rationale for Distribution

The UA tube flaw distribution was developed from two sources, NUREG-2195 and the Surry SG ISI reports. The NUREG-2195 study represents a much larger database of flaws than the Surry SG ISI reports and includes all reactors with thermally-treated Inconel 600 and 690 tubes. Using the NUREG-2195 methodology, the total number of more severe flaws in each Surry steam generator was calculated using the total number of flaws based on the Surry replacement SG's EFPYs age[41] times the probability of the flaws having a through-wall depth greater than 0.3. The results of this evaluation predicted 4.27 flawed tubes with a through-wall depth greater than 0.3 in each steam generator and 0.28 tubes with a flaw depth greater than 0.5 through-wall.

The Surry ISI reports show 76 incidences of tube plugging due to flaws during the replacement steam generator's lifetimes. 61% of the identified flaws that led to tube plugging were located between the tube sheet and the second grid support, or close to the hot side of the steam generator inlet. Most of the flaws occurred due to loose parts or damage from a lance during sludge maintenance near the top of the SG tube sheet. The higher occurrence of flaws near the inlet of the hot side of the steam generator is significant because this location is susceptible to the highest temperatures during a severe accident [52]. The potential failure of a steam generator tube due to creep rupture is strongly influenced by the temperature of the tube. These insights were incorporated into the hottest and hot upflow region sizes.

Similar to the NUREG-2195 analysis, the Surry ISI reports were used to predict the number of flawed tubes in each steam generator. The total number of flaws was calculated by accounting for per unit (i.e., both Surry 1 and 2 flawed tube data were used), per steam generator, the number of RFOs, and Surry's pattern of two RFOs to inspect 100% of the tubes. The results of this evaluation predicted 0.72 flawed tubes with a through-wall depth greater than 0.3 in each steam generator and 0.28 tubes with a flaw depth greater than 0.5.

Although the expected number of flawed tubes with through-wall flaw depths greater than 0.5 are similar for the two methods discussed, the expected likelihood of flawed tubes is much different below that value. In particular, the number of plugged tubes at Surry between through-wall depths of 0.3 and 0.5 is more limited than the NUREG-2195 distribution. The NUREG-2195 distribution has many more samples of unplugged tubes with through-wall depths between 0.3 and 0.5 (i.e., the Surry ISI reports were limited to only plugged tubes). The number of flawed tubes in each flaw range were combined to use the larger database from NUREG-2195 for the flaws with depths below 0.5 through-wall and the Surry ISI distribution for flaws with depths above 0.5 through-wall. The total number of flawed tubes with flaw depths above 0.5 through-wall is similar between the two methods but the Surry distribution had a greater likelihood of a severely flawed tube with a through-wall flaw depth greater than 0.7. Consequently, the probability of a flawed tube uses a combination of plant-specific findings for the more severe flaws and the larger NUREG-2195 database from all reactors with thermally treated Inconel 600 and 690 tubes for the less severe flaws.

The NUREG-2195 statistical analysis and the Surry ISI reports are based on flaws that are detected. The number flawed tubes from the two approaches does not account for the hidden flaws that are not detected during in-service inspections. The larger and deeper the flaw, the

---

[41] From Equation 6-2 in Reference [10], 35.6 new flaws/SG are expected between the 33 and 36 EFPYs at Surry. The number of new flaws is applied to the probabilities of flaws greater than 0.3 as described in the NUREG-2195 methodology.

higher will be the probability of detection (POD). NUREG-2195 cites NUREG/CR-6791 [137] as providing techniques for evaluating the POD and judges the impact is relatively small for deep flaws. In consideration of other uncertainties in this analysis and the relatively small number of deep flaws identified in the replacement SGs at Surry, it is assumed that the hidden flaws would not substantially change the expected size distribution or total number of flaws.

4.1.1.7 MSIV Leakage (MSIV)

The MSIVs on a PWR are located on the secondary side of the system, off the steam generators' main steam lines. There is the potential that seal failures could lead to MSIV leakage, which would depressurize the secondary side. The resulting larger pressure difference between the primary to the secondary system increases the stress across the steam generator tubes and increases the likelihood of their failure. The occurrence of a SGTR, along with the MSIV leakage, provides a release path for radionuclides to bypass containment and reach the environment. A major improvement to the MELCOR model for the Surry UA is the improved modeling of a potential steam generator tube rupture by monitoring multiple locations and flawed tubes. Due to the importance of the primary to secondary pressure difference for the tube creep failure, the uncertainty in secondary side depressurization is an important factor.

To inform the uncertainty range for MSIV leakage, it was desirable to have the technical specification for a PWR. An in-depth search was conducted, both in-house and at NRC. This including checking the FSAR and plant data book for Surry, a search of licensee testing reports, and a discussion with a former PWR operator who is now with the NRC. Although the PWR MSIV performance is controlled by technical specifications for closure timing, there is no requirement for leak-tightness. No direct information was obtained for measured leakage of PWR MSIVs.

The guidance for this uncertain parameter was obtained from several sources. First, the BWR MSIV performance was reviewed. These values are available since the BWR MSIV leakage is controlled by technical specifications as a primary barrier of the reactor vessel for containment isolation (i.e., steam generator tubes alleviate the need in a PWR). Sandia reviewed the impacts of MSIV leakage in BWRs with both Mark-I and Mark-III containments [149]. A typical specification for BWR MSIV leakage is 11.5 scfh (standard cubic feet per hour) maximum when tested at 25 psig. This value is confirmed by a 1976 letter from Monticello (a BWR) to the NRC informing them of the failure of 3 of 8 MSIVs to meet the technical specification during initial outage testing. One MSIV had leakage as high as 33.26 scfh. Observation evidence by in-house experts has also shown that MSIV leakage is much higher than the technical specifications during initial testing and significant machining has to be done to meet the required leakage.

Next, parametric MELCOR calculations were performed to examine the secondary depressurization rate for a range of leak sizes. The hot leg failure of the reactor coolant system occurs at ~4 hr in the Surry STSBO. Consequently, the secondary pressure at 4 hr has the most significance in the competition between a hot leg failure and a steam generator tube failure. After the hot leg failure, the primary system depressurizes and there is no more threat of a tube rupture. Figure 4-15 shows that leakages less than 0.025 in^2 do not show any significant depressurization within 4 hr whereas a leak of 0.2 in^2 or greater depressurizes the secondary below 1 MPa by 4 hr. Consequently, a range of 0.25 in^2 to 0.2 in^2 has the most significance for this parameter, albeit not informative to the likely amount of leakage.

Finally, Licensing Event Reports (LERs) on PWR MSIV problems since 2000 were reviewed (see Appendix C). The PWR LERs document problems associated with MSIV testing and their performance. The SMEs were encouraged that regular performance testing is done on the MSIVs but concerned about the noted failures in the LERs. In particular, there are several LERs that report failure of the MSIVs to close on demand. There was no mention of leakage testing in the LERs, which is not required for the MSIV closure timing technical specification. The SMEs believed that large leakages could be observed in the testing, which would lead to repairs.

The specification of the distribution was influenced by the lack of knowledge on PWR MSIV leakage, BWR technical specifications, PWR LERs, and information from MELCOR calculations on the range of leak rates affecting the likelihood of a tube rupture. To put the BWR technical specification into perspective, 0.1 in^2 and 0.5 in^2 leakages correspond to approximately 4600 and 23,000 scfh, respectively, which is very large compared to the BWR technical specification of 11.5 scfh. In fact, Reference [149] notes 33 scfh as a large reported failure. These observations are offset by the lack of required testing for PWRs and the large number of LERs. After considerable debate, the MSIV leakage was specified to span from 0.01 in^2 to 1 in^2 using a uniform distribution.[42]

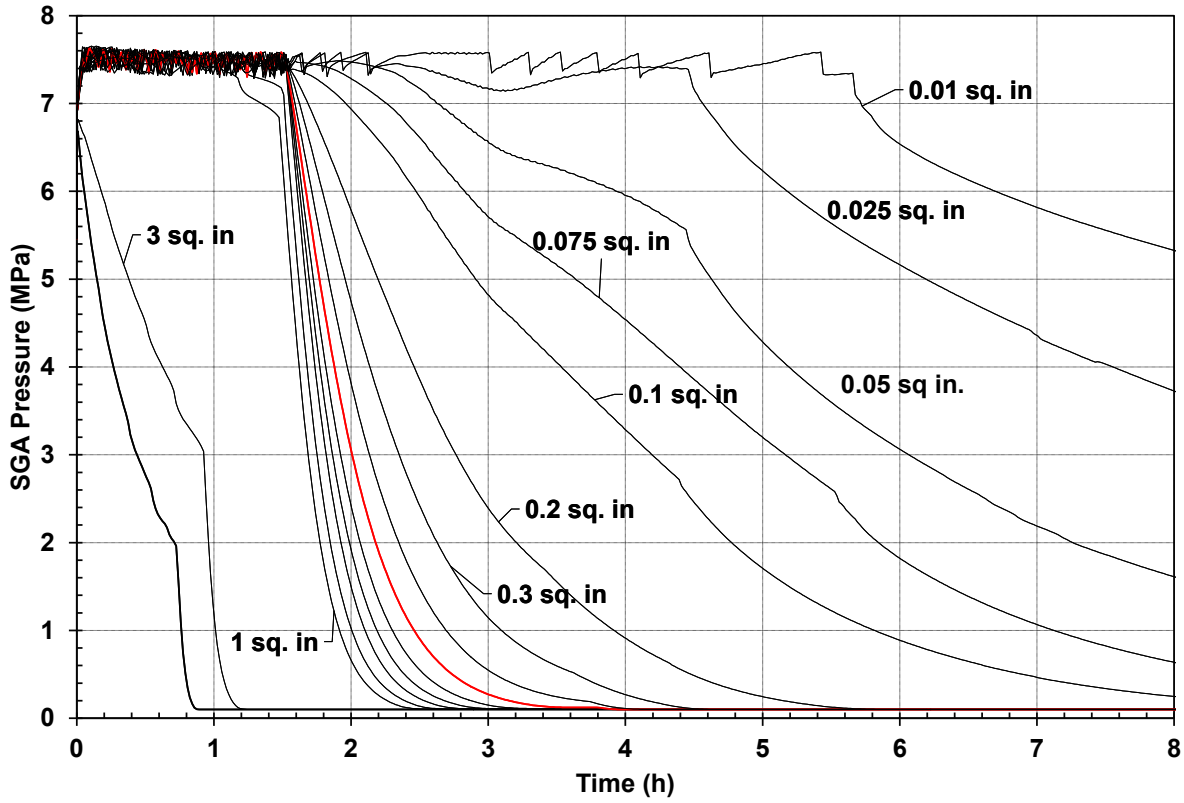

Figure 4-15 SG A Pressure as a Function of MSIV Leakage Size

[42] The focus of the Sequoyah UA was containment response and did not include MSIV leakage as an uncertain parameter. However, the Sequoyah UA used 0.1 in^2/SG [7], which is within the Surry UA parameter range.

Rationale for Distribution

The only available values for MSIV leakage are BWR specific. Although a PWR only has one MSIV on each steam line, as opposed to the two in series on a BWR, the two on a BWR quickly equilibrate and therefore the leakage rates should be directly applicable. However, this ignores any specific MSIV design differences between BWRs and PWRs, which may be significant. The specification of the distribution was influenced by the lack of knowledge on PWR MSIV leakage. A range of 0.01 in^2 to 1 in^2 using a uniform distribution is specified, which reflects very low leakage that does not depressurize the secondary within 4 hr to a large leakage that fully depressurizes the secondary. The uniform distribution conservatively biases the results toward depressurizing the secondary system. However, there will be several samples with small leakage to assess its impact. It should be noted that previous studies that investigated the potential for SGTRs included leakages of 0.5 in^2 [38], which is the median of the range used in this study.

4.1.2 In-Vessel Accident Progression

The in-vessel accident progression includes three parameters related to the core degradation, (1) the Zircaloy melt breakout temperature, (2) the molten clad drainage rate, and (3) the effective temperature at which the eutectic formed from UO_2 and ZrO_2 melts. These uncertain parameters are unchanged from the draft Surry UA [8] and are the same as the Sequoyah UA [7]. The next in-vessel accident progression uncertain parameter concerns the time in the cycle. In the draft Surry UA [8] and the Sequoyah UA [7], the time in cycle addressed three discrete times in the operating cycle. The time in cycle was updated for the final Surry UA by considering a more continuous evaluation of time in cycle using 14 distributed times. The time in cycle also specifies the initial radionuclide inventory. The last uncertain parameter concerns the in-vessel hydrogen product via the steam-Zircaloy oxidation correlation. The uncertainty evaluation of the oxidation kinetics modeling is the same approach as the Sequoyah UA [7].

4.1.2.1 Zircaloy Melt Breakout Temperature (SC1131(2))

The Zircaloy melt breakout temperature and its associated distribution characterize the uncertain properties that determine the temperature at which the ZrO_2 shell releases underlying molten Zircaloy, which can occur for two reasons, both captured by this parameter. First, the outer oxide shell can crack due to physical stresses from the extreme environment, and second the molten Zircaloy can chemically reduce the oxide, leading to localized failures. The oxide shells have a high melting temperature relative to that of unoxidized cladding and, as shown in the Phebus experiments [54], can maintain fuel geometry as Zircaloy interior to the shell melts and drains away. Uncertainty is represented by a beta distribution (α: 3.83; β: 3) with a lower bound of 2100 K and an upper bound of 2540 K.

The fuel rod cladding ruptures and releases fission products from the fuel-cladding gap once the temperature reaches 1173 K (i.e., the MELCOR default). However, the fuel rods remain standing and form an oxide shell (i.e., ZrO_2) as the steam oxidizes the hot cladding. After 2100 K, the zirconium that does not fully oxidize forms an α-phase ZrO fluid which is held up by the ZrO_2 shell. The ZrO also migrates through the fuel pellet cracks and forms a $(U,Zr)O_{2-x}$ mixture through slow dissolution of the irradiated UO_2 fuel. The thickness of the ZrO_2 is primarily a function of:

- Steam supply of oxygen to the α-ZrO, thus increasing the ZrO_2 shell thickness.

- Oxygenation of the α-ZrO from the ZrO_2 shell, thus decreasing the shell thickness (does not occur below 2273 K [57]).

- Rod temperatures, which heavily influence reaction rates (i.e., a higher temperature yields faster reactions).

It is noted that the α-ZrO can also extract oxygen from the UO_2 pellet. Schematic representations of the zirconium melt breakthrough process can be seen in Figure 4-16 and Figure 4-17. An approximation of the oxygen content in the α-ZrO can be seen in Figure 4-17. When zirconium-melt breaks through the ZrO_2 shell, it also removes some dissolved uranium and fission products and stops the heat generation from the zirconium oxidation reaction. This dissolution process is simulated in SOARCA by assuming 0.2 kg of UO_2 (via COR_CMT) is dissolved for every 1 kg of Zr melt generated by the candling process.

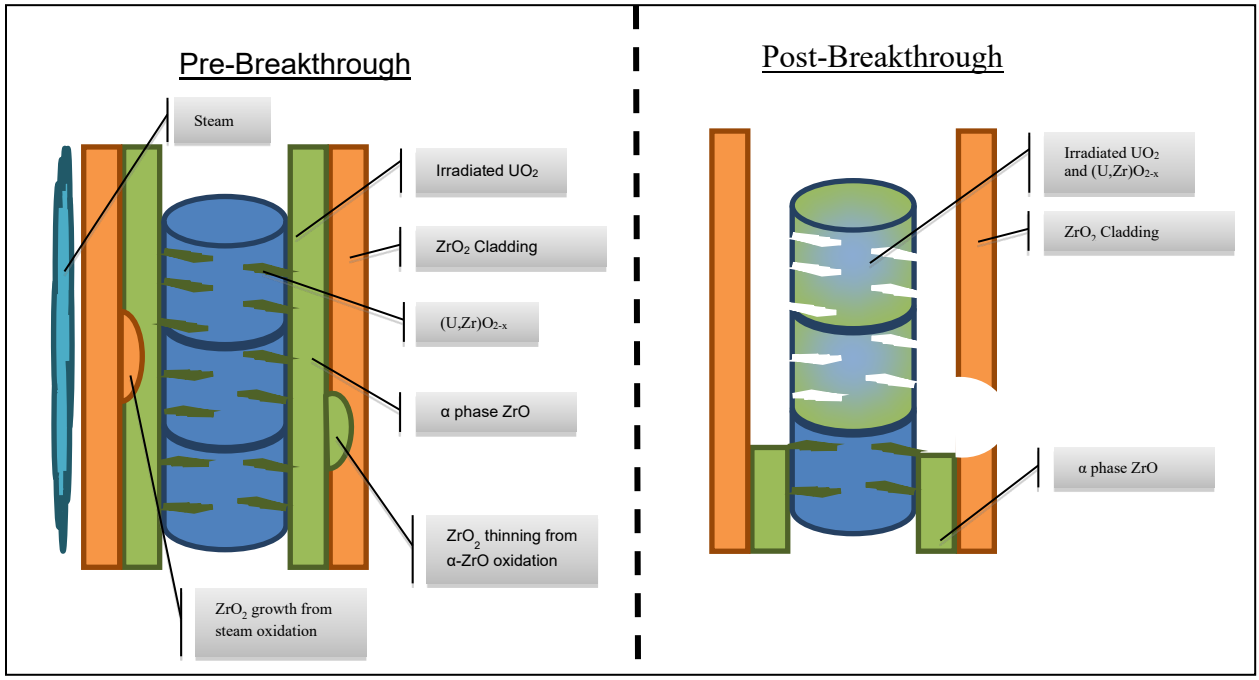

Figure 4-16 Schematic of Zirconium Melt Breakthrough

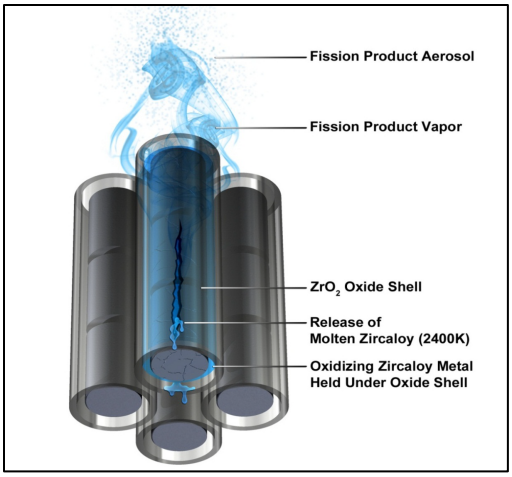

Figure 4-17 Depiction of the Fuel Rod Degradation

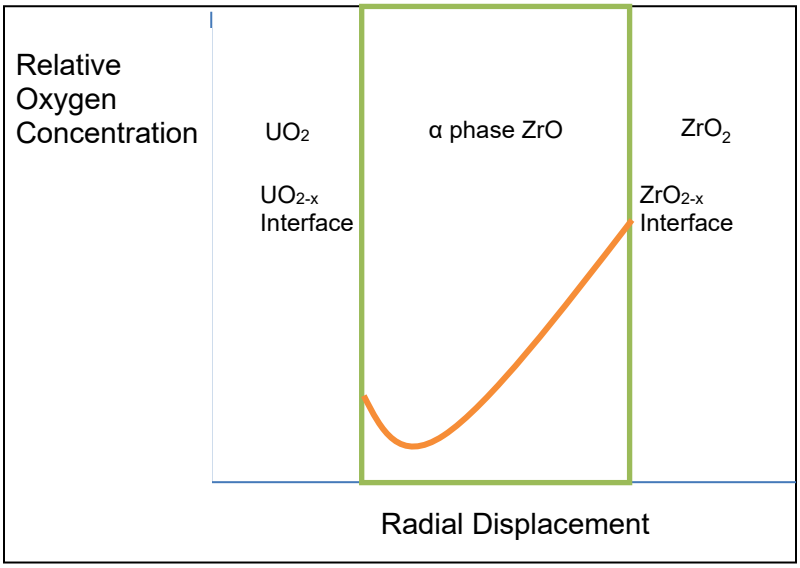

Figure 4-18 Qualitative Oxygen Concentration in the α-ZrO Region

It has been shown, using structural models of the oxide shell, that the high temperature failure (a.k.a., flowering) of the ZrO_2 shell can occur through two primary failure modes. The first occurs when the oxide shell grows too thick under intermediate rate temperature ramps:

$$\left\{\sim 3\frac{K}{s} < \frac{dT}{dt} < \sim 6\frac{K}{s}\right\}$$

Eq. 4-6

where K is temperature in Kelvin, s is time in seconds, T is temperature, and t is time. This results in the surface stress exceeding the flexural limits. The stress causes cracks in the ZrO_2 shell, which are filled with melt. The melt then oxidizes, causing more cracks. Eventually, the

oxide shell expands to the point where the incompressible melt applies enough internal pressure to rupture the oxide shell.[43] Simulations with the code S/Q [57] have been conducted. The second failure mode occurs when the oxide shell erodes and is too thin under rapid temperature ramps to contain the melt:

$$\left\{\frac{dT}{dt} > \sim 6\frac{K}{s}\right\}$$

Eq. 4-7

This thinning of the oxide shell is caused by internal erosion from the melt.

The last possibility of failure that is beyond flowering occurs when the oxide shell completely oxidizes the melt. This is predicted to occur under extremely slow temperature ramps:

$$\left\{\frac{dT}{dt} < \sim 3\frac{K}{s}\right\}$$

Eq. 4-8

It is noted that the CORA experiments suggest that the temperature ramps allowing for complete oxidation of the melt are closer to 0.3K/s [104].

The breakout temperature initiates the downward drainage of molten Zircaloy on a ring and axial level basis in the MELCOR simulation and can act in terminating or decreasing oxidation reaction rates in the originating core cell. Previous SNL studies [55][56], determined that at the "breakout temperature" oxidizing molten Zircaloy is relocated to cooler regions at a time when the oxidation rate is at its maximum value. Fuel temperatures are increasing rapidly (~10K/s) at this time, hydrogen generation rate is locally at a maximum, and fission product release rates are large. The relocation of the oxidizing melt has the effect of terminating the intense local fuel heating, since the chemical heating source has relocated to a cooler region of the vessel. This should affect release rate for volatile fission products and total localized releases of low-volatile species.

Rationale for Distribution

This distribution for Zircaloy melt breakout temperature is created by Bayesian updating the Peach Bottom Zircaloy Melt Breakout Temperature (prior distribution) with the S/Q simulation results [57] provided in Table 4-13. A binomial likelihood function was used to update a scaled version of the prior distribution and then rescale the posterior distribution to the appropriate range.

Table 4-13 Zircaloy Melt Breakthrough Temperature Estimates from S/Q Simulations of Two ZrO_2 Failure Modes

Failure Mode	*Temperature*	*Assigned Weight*
#1-Surface stress exceeds the flexural limits.	2393 K	0.5

[43] Small variations in pellet diameter can dramatically change the predicted failure temperature.

#1-Surface stress exceeds the flexural limits.	2223 K	0.5
#2-Oxide shell erodes and is too thin.	2372 K	1

The prior distribution was defined as a triangular distribution. The lower bound value is the Zircaloy melting temperature of 2100 K. The value of 2100 K also corresponds to fragile outer oxide shells that are incapable of retaining molten Zircaloy. The upper value of 2540 K was selected in the original hydrogen uncertainty study based on fuel rod failure in 15 minutes using the time at temperature model (precluding failure by Zircaloy breakout), which in turn is based on qualitative consideration of the alpha-Zr(O) phase diagram and observations/analyses of the Phebus experiments [54]. The mode is default value in MELCOR (2400 K), which was used in the Sequoyah UA [7] and the SOARCA analysis [3]. The selection of a triangular distribution suggests that a most probable value for the uncertain parameter is recommended (mode), with decreasing likelihood for values away from the most probable. The CDF is presented in Figure 4-19.

Two simulations were conducted for failure mode #1 to show variability due to pellet diameter uncertainties that result because individual pellets have differential thermal expansions during reactor operation. During the updating process, the two failure modes were assigned equal weight, and the two variability simulation results were assigned equal weight. To ensure that the weights are additive in the product likelihood function, the updating equation shown in Eq. 4-9 was used.

$$\pi(Temp|E) = \frac{1}{c}\pi(Temp)\prod_{i=1}^{N}\left\{L\left(E^i\middle|Temp\right)\right\}^{w^i}$$

Eq. 4-9

In Eq. 4-9, $\pi(Temp)$ represents the state of knowledge of the values for the Zircaloy melt breakout temperature (SC1131(2)) without simulation estimates, $\pi(Temp|E)$ represents the state of knowledge for SC1131(2) given the estimates in Table 4-13, $L\left(E^i\middle|Temp\right)$ is the likelihood that if the actual value for SC1131(2) was Temp, the ith evidence (E^i) would be observed, w^i is the weight of the ith evidence as defined in Table 4-13, and c is a normalization constant. The likelihood function was assumed to be proportional to the binomial function if the evidence was transformed to fall within 0 to 1, given zero represented the lower bound of the distribution (2100K) and one represents the upper bound of the distribution (2540K).

Because the MELCOR uncertainty engine cannot sample from user specified distributions, a maximum likelihood estimate fit (beta distribution) of the posterior distribution was sampled. The shape parameters of that distribution are α = 3.83 and β = 3.0 with upper and lower bounds set the same as the prior triangular distribution [2100.0, 2540.0].

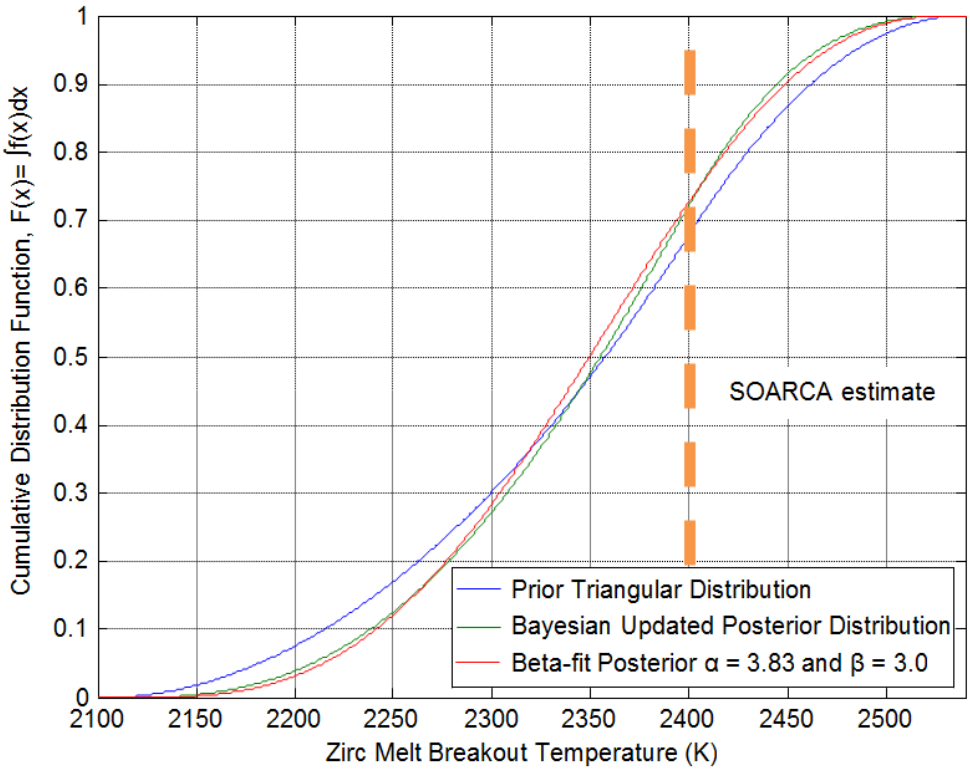

Figure 4-19 Zircaloy Melt Breakout Temperature Cumulative Distributions

The Zircaloy melt breakout temperature showed importance in the Peach Bottom UA [2]. Intuitively, it is suspected that molten Zircaloy breakout must occur before ZrO_2 and UO_2 eutectic reactions (and other chemical reactions) cause local fuel failure, which is supported by experimental observations of fuel oxidation and failure. The temperature at which the eutectic formed from UO_2 and ZrO_2 melts is another uncertain parameter in this Surry UA and correlation between the two was considered. However, it was calculated, that with the distributions for the two parameters, Zircaloy breakout would occur before fuel failure by eutectic reactions in 85 percent of the sampled realizations. By not correlating the two parameters, the sequence of events that is intuitively expected and experimentally supported, will occur the majority of the time, but some samples will allow for the exploration of the alternative scenario.

4.1.2.2 Molten Clad Drainage Rate (SC1141(2))

MELCOR uses sensitivity coefficients SC1141(1) and SC1141(2) to control the candling model when molten material has just been released after holdup by an oxide shell or by a flow blockage (crust) [15]. The sensitivity coefficient (SC1141(2)) is defined as the maximum melt flow rate per unit width after breakthrough (with units of kg/m-s) and is described herein as the molten clad drainage rate. The molten clad drainage rate is an uncertain input in MELCOR that influences the in-vessel accident progression. A log triangular distribution was implemented with a mode of 0.2 kg/m-s, a lower bound of 0.1 kg/m-s and an upper bound of 2 kg/m-s.

In MELCOR, when molten material has just been released after holdup by a flow blockage or oxide crust, the assumption built into the candling model of constant generation of melt over the timestep is no longer valid. Behavior of the model related to the amounts of mass refrozen in

lower core cells would thus be highly dependent on the size of the current timestep. Therefore, for those situations involving the sudden release of a large mass of molten material built up over perhaps several previous timesteps, application of the candling model is modified slightly. In order to eliminate dependencies on molten pool mass and timestep size, SC1141(1) is a constant timestep used for the breach of an oxide shell, while SC1141(2) is the maximum flow rate (per unit surface width) of the molten pool after breakthrough of a flow blockage, which is used to calculate a timestep according to:

$$\Delta t_{contact} = max\left[\Delta t, \quad \frac{M_m\,\Delta z}{\Gamma_{max}\,A_s}\right]$$

Eq. 4-10

Where $\Delta t_{contact}$ is the timestep used after failure of a flow blockage holding up a molten pool, Δt is the nominal MELCOR timestep, Γ_{max} is the maximum flow rate, M_m is the mass of molten material, Δz is axial cell height and A_s is the surface area available for flow.

In other words, a large molten pool is allowed to discharge at a maximum rate of Γ_{max}, (SC1141(2)), and the amount refreezing onto structures below (candling) will be a linear function of the total mass of the pool. This effect can be visualized as the melt pool moving axially down a fuel rod in the open space between 4 closest fuel rods in the square assembly lattice.

The release timestep and the maximum melt flow rate affect subsequent code calculations for heat transfer, refreezing, core degradation kinetics, and overall in-vessel accident progression.

Rationale for Distribution

A log triangular distribution is used for SC1141(2) with a mode of 0.2 kg/m-s and 0.1 and 2.0 kg/m-s respectively for the lower and upper bounds. The mode of 0.2 kg/m-s is the current MELCOR best practice [58] and was used in the SOARCA analysis [3]. It was determined by observing video of the CORA-13 experiment showing movement of molten material following the breakthrough of a flow blockage and calculating the flow rate. There is no citable technical basis to inform the bounds of the distribution, making the uncertainty of this parameter exploratory. For an exploratory study, an approximate order of magnitude uncertainty range was desired to allow investigation of a large amount of uncertainty. Had the regression results indicated high importance for this parameter, the distribution would have been revisited.

The selection of a log-triangular distribution suggests that a most probable value for the uncertain parameter is the recommended value (i.e., the mode), with decreasing likelihood for values away from the most probable. A triangular distribution would give too much weight to sampling near the bounds. Since the parameter represents the maximum possible flow rate, it is more beneficial to sample larger values (i.e., smaller rates below the prescribed maximum specified by this parameter may occur naturally during the MELCOR runs). Additionally, the historical default value for MELCOR was 1 kg/m-s and it is beneficial to analyze some runs at and above this value. Because of these two reasons and the desire to have an approximate order of magnitude range, an upper limit of 2.0 kg/m-s and lower limit of 0.1 kg/m-s were selected. This selection gives approximately 10 percent of samples above the previous default of 1 kg/m-s, while keeping the majority of samples near the mode. The CDF is presented in Figure 4-20.

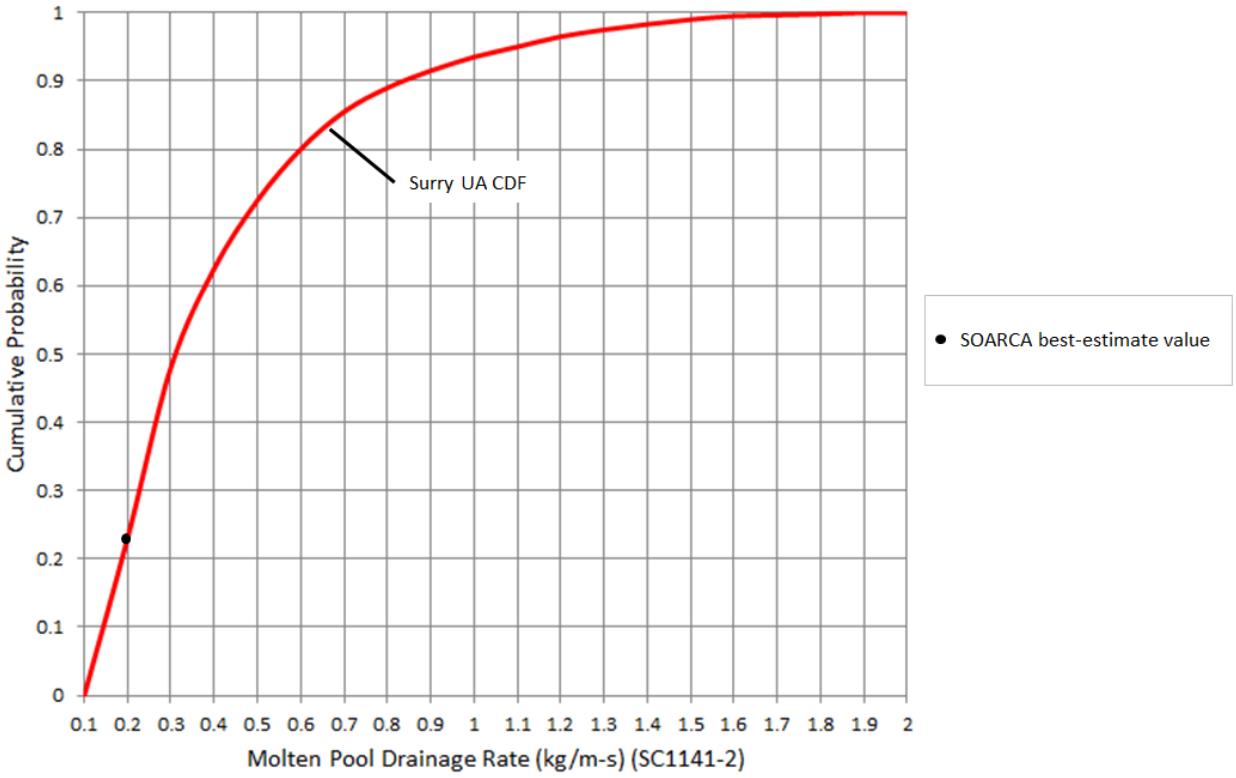

Figure 4-20 CDF of Molten Pool Drainage Rate

The corresponding timestep size following rupture through an oxide shell is not considered. Although it is also an uncertain parameter that affects subsequent code calculations, only the variation of the maximum molten pool flow rate after breach of a blockage is considered in the Surry UA. The maximum molten pool drainage rate parameter is a carryover from the Peach Bottom UA.

4.1.2.3 Effective Temperature at which the Eutectic Formed from Zircaloy Oxide and Uranium Oxide Melts (SC1132)

This parameter represents the temperature at which the eutectic formed from UO_2 and ZrO_2 melts. Within MELCOR this is input as a eutectic sensitivity coefficient (SC1132) and a melting temperature. By including the temperature of the eutectic reaction between ZrO_2 and UO_2 as a sampled parameter, general fuel failure of when the fuel collapses and when it becomes molten is affected. There are other failure mechanisms and possible eutectic reaction[44] between core materials, some of which are described in more detail in the related parameters section within Section 4.1.2.1.

The binary phase diagram for ZrO_2/UO_2 suggests the melting point for equilibrium conditions is approximately 2800 K for a 50/50 molar mixture; hence this was the historical MELCOR default

[44] It is noted that the pure UO_2/ZrO_2 system has only a melting point, not a eutectic point. High burnup pins have complex intermetallic effects which are referred to as eutectic reactions in the VERCORS [56] experiments and the MELCOR users guide. This nomenclature is maintained for this analysis.

value. Any liquefaction below this temperature accounts for the effect of molten Zircaloy metal or alpha-Zr(O) 'wetting' the oxide surfaces. Observations of the Phebus and VERCORS experiments suggest that irradiated fuel and oxidized cladding exhibit eutectic liquefaction at significantly lower temperatures; thus, the MELCOR default was subsequently modified to 2500 K. Following significant local cladding oxidation, the effective liquefaction of ZrO_2 and UO_2 mixtures results in local rod collapse as molten material, rather than as rubble or debris. The parameter treatment for this work attempts to approximate the combined uncertainties associated with burnup, eutectic composition, material properties, and non-equilibrium effects on ZrO_2/UO_2 eutectic reactions.

The fuel melt associated with this parameter is a localized effect. This means that MELCOR evaluates the temperature independently for each core cell and allows the fuel in that specific cell to melt when it reaches a failure temperature, such as the temperature at which the eutectic formed from UO_2 and ZrO_2 melts. Thus, the entire core will not fail at once when the hottest region reaches the sampled temperature. It is possible that melting of a core cell can cause the subsequent failure of fuel above in the same radial ring that was previously supported by the failed cell. However, this is a physical effect and still only affects a section of a single ring, hence keeping it a localized effect.

In MELCOR, eutectic reactions are approximated by user-modification of melting and failure temperatures in model input. Thus, to effectively represent the temperature at which the eutectic formed from UO_2 and ZrO_2 melts, the user must modify:

1. The sensitivity coefficient SC1132(1), which defines the cladding temperature resulting in rod collapse without Zr-metal cladding remaining (discussed further in Section 4.1.2.1), and

2. The melting temperatures of both UO_2 and ZrO_2 in the input deck (MP_PRC records).

Rationale for Distribution

Six experimental data points for eutectic induced core collapse are readily available from the VERCORS experiments to help inform the uncertainty distribution [56]. Table 4-14 shows the VERCORS test results along with the mean and standard deviation.

Table 4-14 VERCORS Test Results for Collapse Temperature

Test	Collapse Temperature (K)
T1	2525
HT1	2550
HT2	2400
HT3	2525
V_6	2525
RT6	2350
Mean	2479
Standard Deviation	83

In selecting this experimental data, observed core slump is projected to a eutectic reaction. This was strongly indicated by the test results but cannot be definitively confirmed due to a lack of instrumentation.

The selection of a specific distribution is complicated by the lack of detailed experimental data over ranges of severe accident conditions and reactor operation (e.g., high burnup). While the VERCORS testing matrix does not provide randomly distributed evidence of eutectic formation temperatures, these tests do provide a range of temperatures over which eutectics were significant enough to cause core collapse. A normal distribution fitted to the data in Table 4-14 was used to assess uncertainty in the average core collapse temperature for higher burnup fuel. The simple parameter treatment is not intended to rigorously quantify eutectic effects on severe accidents and core degradation; such treatment is impossible when the MELCOR eutectic model is not activated. Rather, the proposed treatment roughly evaluates the influences that the physical state of the core debris has on core degradation kinetics and subsequent severe accident progression. A lower temperature for this parameter results in an increased generation of molten pools in the RPV during core disassembly. Alternatively, a higher temperature for this parameter results in a decreased generation of molten pool formation for ZrO_2 and UO_2 debris. The relocation and cooling of molten pools after formation are treated by several other models and parametric inputs in MELCOR; hence the eutectic parameter only affects the initial creation of molten pools for ZrO_2 and UO_2 immediately upon rod collapse.

Even though the testing data was derived from independent, identical tests, a normal distribution was fitted to the VERCORS data in order to describe the general range of potential collapse temperatures for the varying environmental conditions (i.e., see Figure 4-21). This normal distribution has a mean of 2479 K and a standard deviation of 83. The red star in Figure 4-21 represents the 2800 K value used in SOARCA. Even left unbounded, the probability of sampling beyond these bounds is effectively *de minimis*, thus the bounds should not affect the results of this work.

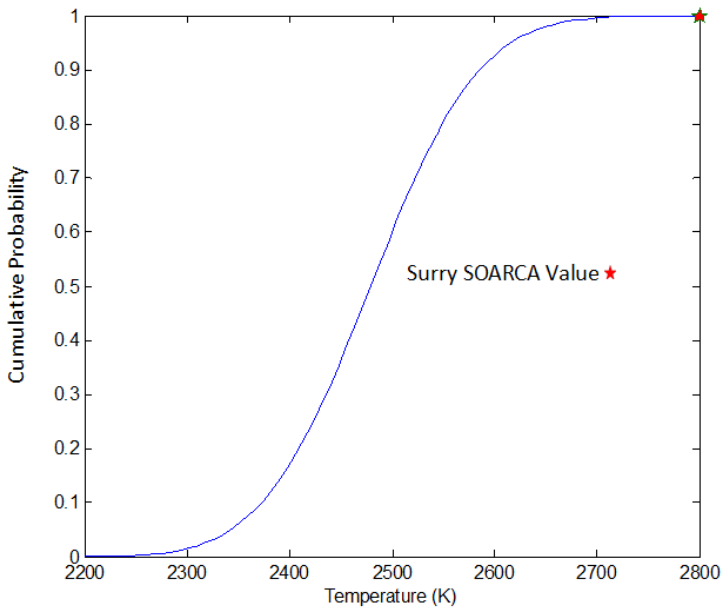

Figure 4-21 CDF of Eutectic Melting Temperature

4.1.2.4 Time of the Cycle

The time in cycle parameter was included to understand the extent to which the fuel burnup influenced simulation results. This was accomplished by including an uncertain parameter named CYCLE, which identifies the point during the fuel burnup cycle at which the accident occurs. The time in cycle is discretely assigned to 14 decay heat and radionuclide inventory evaluations across the 550-day operating cycle to characterize the parameter distribution. The fourteen points within the cycle are taken as 'representative' times to constrain the problem. One of fourteen corresponding radionuclide inventories is assigned once the time in the cycle is selected.

The CYCLE parameter directly affects the MELCOR source term calculation through the decay heat and affects the MACCS consequence analysis through the fission product inventory. The inventories of shorter lived isotopes increase with burnup only until secular equilibrium is established. However, the inventories of longer lived isotopes, like Cs-137 which grows monotonically throughout the cycle, can nearly double from the beginning to end of the fuel burnup cycle. Because the longer-lived isotopes have an effect on LCF risk, especially in the long-term phase, this parameter is significant to the predicted results.

In the Sequoyah UA [7], the cycle was represented using three point estimates: the beginning (BOC), the middle (MOC), and the end of cycle (EOC). The BOC and EOC results occurred at 7 days and 505 days in the cycle, which were biased towards the beginning and the end of the cycle, respectively. There is a markedly lower decay heat at BOC (within a few hours after shutdown) due to short recent irradiation time, which results in lower inventory of the shorter-lived nuclides that dominate decay heat a few hours after shutdown. Similarly, the radionuclide inventory at 505 days was near the maximum activity of the long-lived isotopes during the cycle, which will dominate the decay power for longer decay time. The inability to characterize the continuous variation from the start to the end of cycle with only three points was identified a weakness in the original approach.

Thus, from a decay heat perspective, using representative days at 14 points throughout the cycle rather than three allows for more precise examination of higher decay heat later within the accident scenario which could be important for RPV lower head response, ex-vessel behavior, and long-term containment response. Additionally, the motivation for differentiating between time in the burnup cycle, and especially days after the beginning of cycle, is the long-lived radionuclide inventory that affects the MACCS consequence analysis for LCF risk. The activity levels of the inventories for short-lived isotopes increase with burnup only until secular equilibrium is established. However, the activity levels of the inventories for long-lived isotopes grow monotonically throughout the cycle, and nearly double over the course from beginning to end of cycle (see Figure 4-22).

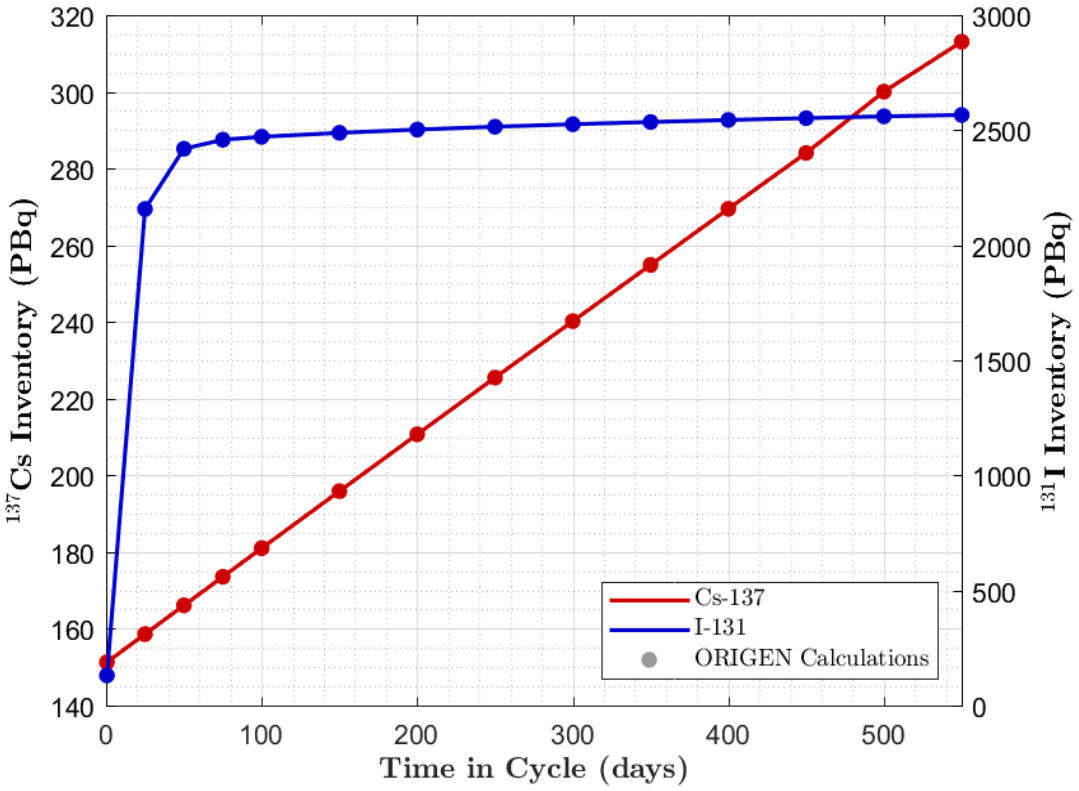

Figure 4-22 Activity Levels for I-131 and Cs-137 with Respect to Time in Cycle

The decay heat power from ORIGEN calculations for the fourteen times in the cycle were integrated through 4 hours (see Figure 4-23). The integrated power during the first four hours (i.e., the core degradation phase of the STSBO accident) rapidly changes at the start the cycle. The delineation between the startup phase of the cycle is about 100 days before the integrated decay heat is relatively constant. Although the integrated decay heat stabilizes after ~100 days, the radionuclide inventories continue to change (e.g., see Cs-137 in Figure 4-22).

The discrete points in the cycle for the uncertainty evaluation were selected to characterize the initial buildup of the short-lived isotopes and decay heat power as well as the steady increase in long-lived isotopes through the length of the cycle. A finer discretization of days was used towards the beginning of cycle to capture the initial rapid increase in decay heat over the first 100 days with a broader time interval for the remaining days. This defines two regions for sampling: one region on [0,100] with a representative ORIGEN calculation every 25 day and one region on [100,550] with a representative ORIGEN calculation every 50 day. This results in ORIGEN calculations for 0.5, 25, 50, 75, 100, 150, 200, 250, 300, 350, 400, 450, 500, and 550 days. Note that 0.5 days is used as a more reasonable initial day than 0 in order to capture the effects of a very early accident.

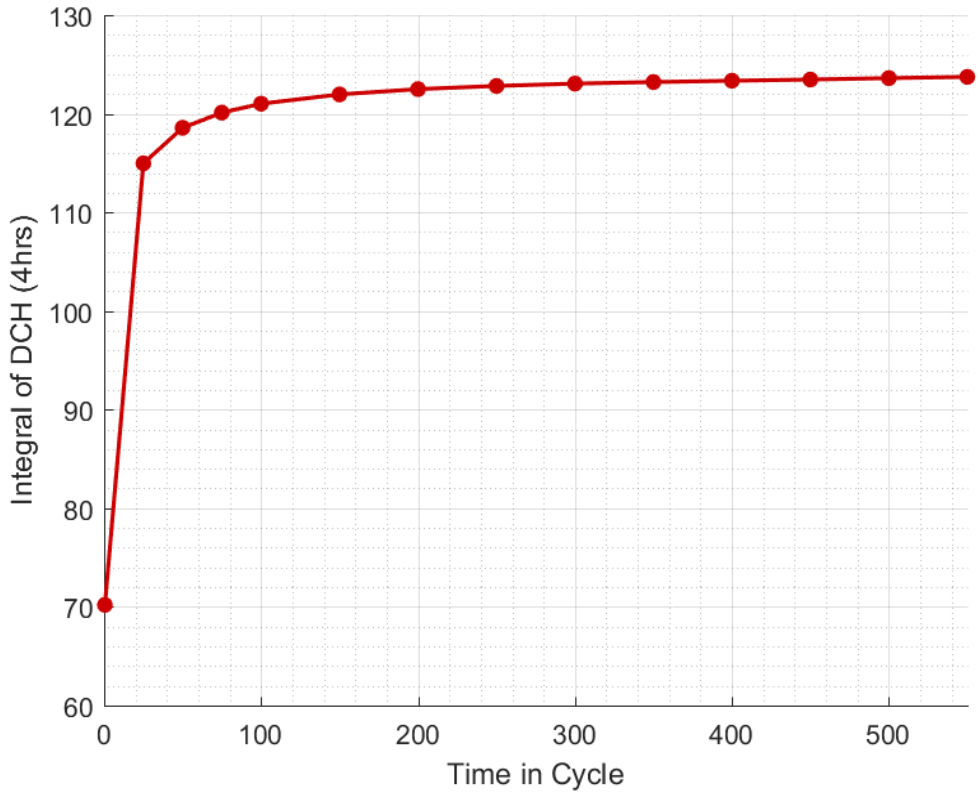

Figure 4-23 Plot of the integrated decay heat for ORIGEN calculations used in the Surry UA

Because the new ORIGEN calculation days are evenly distributed within each of the two regions, sampling for UA realizations is facilitated by with 218 samples uniformly on the first region $(1200 \text{ samples x} \frac{(100 \text{ days} - 0 \text{ days})}{(550 \text{ days})})$and 982 samples uniformly on the second region $(1200 \text{ samples x} \frac{(550 \text{ days} - 100 \text{ days})}{(550 \text{ days})})$. For each sampled day, the nearest ORIGEN calculation is used. Note that this implementation enforces that precisely the correct proportion of realizations is sampled in each of the two regions.

The scatter plot in Figure 4-24a shows the realization number (1 to 1200) and the corresponding sampled day (integer between 0 and 550). Figure 4-24b shows this distribution of samples when each of the sampled day is assigned to the nearest-neighbor ORIGEN calculation. Both plots illustrate the randomness of Time in Cycle with respect to the realization. A comparison of the plots demonstrates that the discretization by ORIGEN calculations is a reasonable approximation to the continuous distribution. This is also demonstrated in the empirical CDFs of these samples in Figure 4-25.

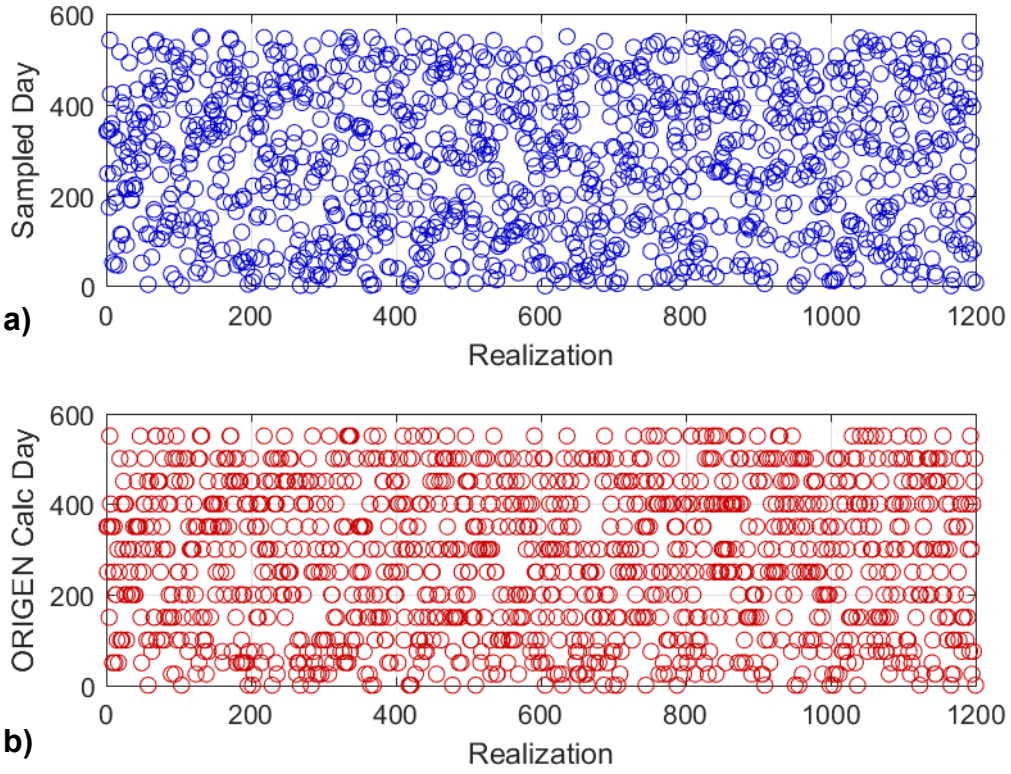

Figure 4-24 Results of the Sampling for Time in Cycle Showing the Discretization of Days by ORIGEN calculations

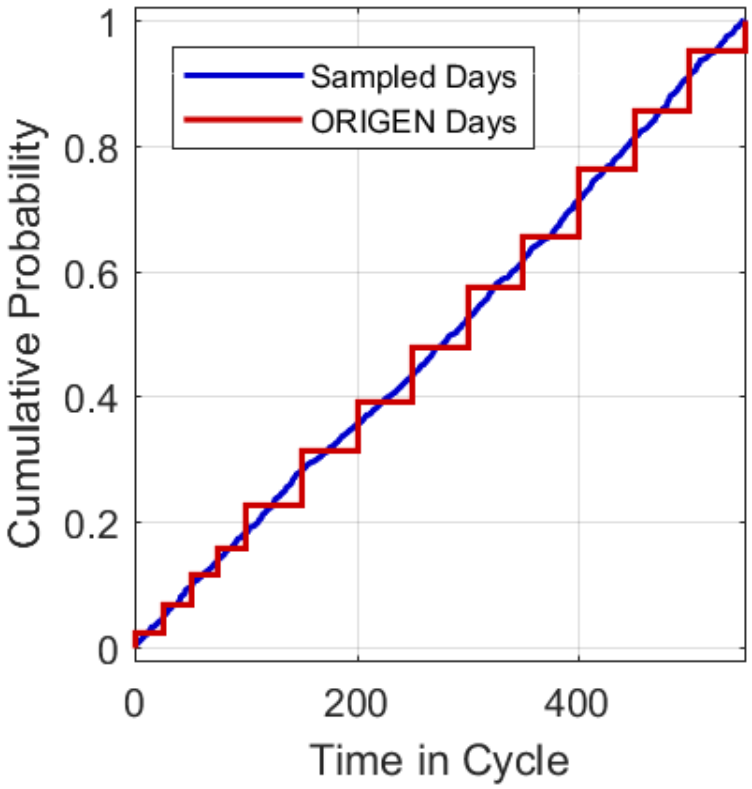

Figure 4-25 Empirical CDFs for the 1200 Samples of Days and the Discretization by ORIGEN Calculation Days

Rationale for Distribution

Varying the decay heat and inventory entails a large amount of data reduction and input generation for MELCOR and MACCS, which SNL has automated in support of similar efforts for Fukushima-related research [99]. Using plant-specific data, ORIGEN-S/ARP calculates decay heat and inventory, and a post-processing tool directly generates consistent MELCOR inputs of decay heat and lumped RN-class inventories (including class specific decay heats), along with consistent detailed nuclide input for MACCS.

The timing of the accident initiator relative to the last operating cycle (assumed to be cycle 20) is treated as inherently random; thus the first step of the decay heat uncertainty analysis involves uniform sampling of the time of reactor shutdown with assignment to closest of 14 pre-chosen times (see Figure 4-24). The corresponding decay heat and radionuclide inventory from the 14 points in the cycle survey the initial build-up of short-lived isotopes and the long-term increase of the long-lived isotopes (e.g., see Figure 4-22). The CYCLE parameter uniformly surveys the entire range of the fuel cycle from 0 to 550 days with consistent values of decay heat and radionuclide inventory.

The time of the cycle for the MELCOR run is seamlessly transferred to the MELMACCS code for consequence calculations. Consequently, the specific radionuclide inventory selected for the MELCOR realization is used in the subsequent MACCS calculation.

The draft Surry UA only used 3 points in the operating cycle [8], which did not continuously survey the range of the decay heat or radionuclide activity. The results showed a bifurcation in the response from the earliest time in the cycle to the latter two times. For example, no BOC results showed a containment liner overpressure failure within the simulation duration whereas nearly all the MOC and EOC results had or were trending to containment liner failure. The uncertainty in the decay heat was considered at the three specific times in the cycle in the draft study but only one radionuclide inventory was used for each time. The new methodology has a more continuous evaluation of results that improves the evaluation of the time in the cycle on the key response and consequence measures. It was not practical to incorporate uncertainty in the decay heat and radionuclide inventory at a specific cycle time. However, the results from the draft UA suggest this uncertainty is most important at the beginning of the accident (i.e., <100 sec). The 14 distributed times of the decay heat and radionuclide inventories from 0.5 days (i.e., the calculated earliest time) to 550 days (i.e., the latest calculated time) in new study is judged to be a practical and improved approach to characterize the operating cycle parameter.

4.1.2.5 *Oxidation Kinetics (Ox_Model)*

The Sequoyah UA realizations [7] showed a high sensitivity of the early containment failure timing to the amount of hydrogen released to the containment prior to the first ignition. Whereas the amount of hydrogen released to the containment prior to ignition is strongly influenced by the pressurizer SV failure characteristics, the uncertainty in the oxidation rate also impacted early containment failure. Four aspects of the oxidation modeling were considered for possible inclusion as uncertainty variable(s). The four aspects were: (1) the oxidation rate correlation used in the steam-Zircaloy parabolic kinetics model, (2) the oxidation rate correlation used in the steam-steel parabolic kinetics model, (3) the fuel collapse modeling, and (4) the fuel quenching model.

After review of the four aspects effecting oxidation, only the oxidation rate correlation used in the Zircaloy parabolic kinetics model was selected as an important uncertainty in the Sequoyah study. The other parameters were dismissed due to their lower importance in the peak combustion magnitude in the initial hydrogen burns. The remaining uncertainty variable is steam-Zircaloy oxidation kinetics. The draft Surry UA [8] used the default Urbanic and Heidrick steam-Zircaloy oxidation kinetics model in MELCOR [14]. It is a two-temperature region oxidation model that uses parabolic kinetics with appropriate rate constant expressions for Zircaloy oxidation-limited gaseous diffusion. The solid-state diffusion of oxygen through an oxide layer to unoxidized metal is represented by the parabolic rate equation:

$$\frac{d(W^2)}{dt} = K(T) \qquad \text{Equation 4-1}$$

where W is the mass of metal oxidized per unit surface area and K(T) is a rate constant expressed as an exponential function of surface temperature, *T*, [14]. The Urbanic and Heidrick model uses a low region temperature rate constant correlation through 1853 K and a separate high temperature correlation above 1873 K. The high temperature regime is characteristic of an open oxide structure that greatly increase the oxidation kinetics. The low and high temperature Urbanic and Heidrick steam-Zircaloy oxidation rate coefficients are shown in Figure 4-26. The rate constant is interpolated between the low- and high-temperature regions. As shown in the figure, the oxidation rate constant grows rapidly with temperature and especially increases after the transition to the high temperature region.

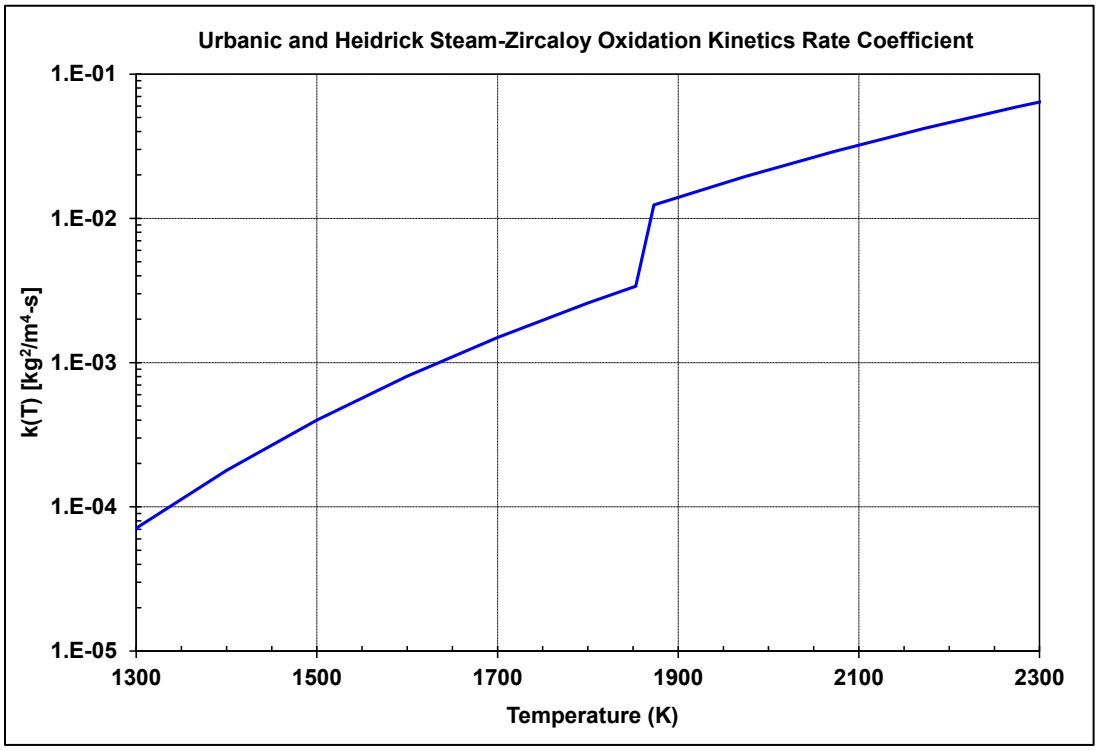

Figure 4-26 Urbanic and Heidrick Steam-Zircaloy Kinetics Rate Coefficient

The Paul Scherrer Institute (PSI) of Switzerland recently developed a new model for air and steam oxidation that were incorporated into MELCOR 2.1 [138]. While the most significant enhancements were for air oxidation, multiple steam oxidation correlations are included from well-referenced correlations including the default Urbanic and Heidrick model.

With respect to the other correlations included in the new PSI model, the Sokolov correlation was developed for VVER E110 cladding which includes niobium [139]. It was discarded as not being prototypical to PWR fuel. Similarly, a newer VVER E110 oxidation correlation by Grosse was not included because it is not prototypical to PWR fuel. Finally, two options are available in the PSI model that use the Leistikov and Schanz correlation. The Leistikov and Schanz correlation was developed based on data through 1600°C and therefore not appropriate for the very high temperature range [140]. The option of Leistikov-Schanz combined with Prater-Courtright was included because Prater-Courtright addresses the high temperature region. However, the PSI option of the Leistikov and Schanz that did not include a high-temperature correlation was dismissed. After dismissing the VVER correlations and the Leistikov and Schanz without a high-temperature correlation, the remaining correlations built into the MELCOR code are shown in Figure 4-27.

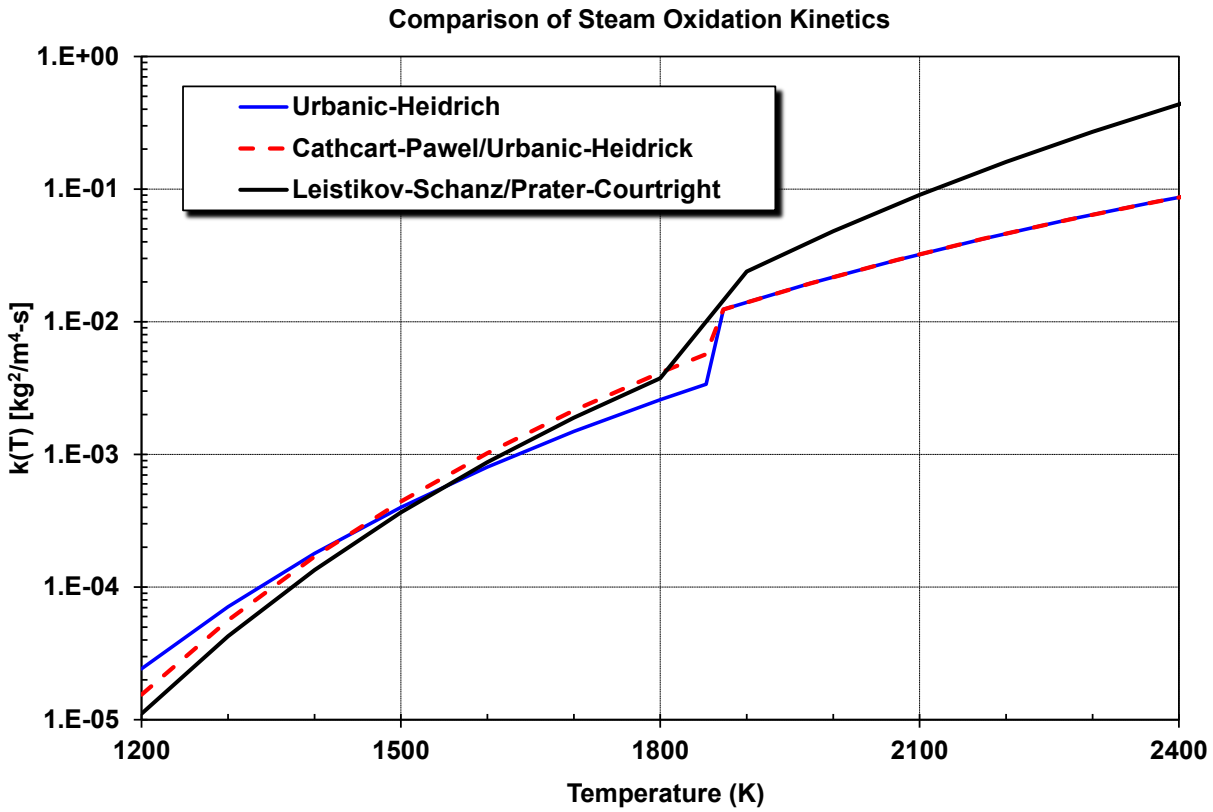

Figure 4-27 Oxidation Rate Coefficient Correlations used for Sampling

Rationale for Distribution

While reviewing comparisons to experiments (e.g., [138][140][141]) and other computer code defaults (e.g., [142]), the Cathcart-Pawel correlation is often cited as providing best oxidation comparisons up to the high temperatures. At high temperatures, the Prater-Courtright correlation is benchmarked against high temperature data from ORNL data [143]. For example, Reference [144] showed better predictions at temperatures above 1800 K using the Prater-Courtright correlation than the Urbanic and Heidrick correlation. However, it is noted that the differences of the three correlations below the transition at ~1900 K were smaller than above.

Three correlations commonly used in the literature were selected for the uncertainty analysis. The Urbanic-Heidrich correlation is historically important due to its use in MELCOR analysis, including the original SOARCA analysis [1] and the previous Peach Bottom UA [2]. The Cathcart-Pawel correlation is identified for wide-spread citations in the literature and for default code settings [142]. The Leistikov-Schanz correlation is the only correlation in MELCOR that is coupled with the Prater-Courtright correlation [14]. All three correlations had similar values below the high-temperature transition point near 1900 K. Two of the correlations used the rate constants from the Urbanic-Heidrich correlation above 1900 K, which was significantly lower than the Prater-Courtright correlation. To equally survey the two different high-temperature rate correlations, a 50%, 25%, and 25% distribution is used (see Figure 4-28). A 50% probability is assigned to the correlation that included the high-temperature Prater-Courtright correlation and 25% each to the correlations with Urbanic-Heidrich high-temperature correlation.

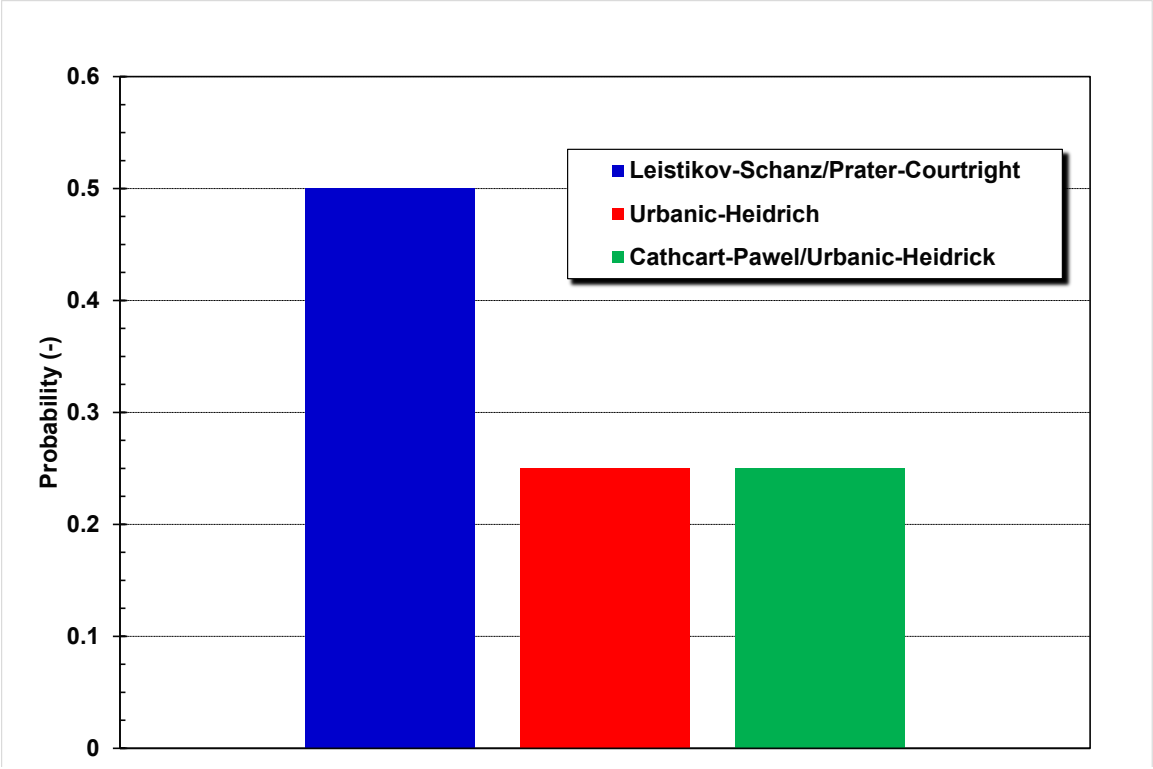

Figure 4-28 Probability Assigned to each Oxidation Kinetics Rate Constant Correlation

4.1.3 Containment Response

There are four containment response uncertain parameters. The first parameter addresses hydrogen combustion in the containment, the next two uncertain parameters address containment leakage and failure, and the final parameter addresses containment heat transfer. The hydrogen ignition criteria has been changed from the draft Surry UA [8] to only allow ignition with an active source, which is the same approach as the Sequoyah UA [7]. However, the hydrogen ignition uncertainty parameter distribution is the same. The containment leakage uncertain parameter is updated for the final Surry UA to recognize industry and Surry-specific efforts to improve containment leak tightness [9]. The remaining two uncertain parameters for the containment fragility curve and containment heat transfer are unchanged from the draft Surry UA [8].

4.1.3.1 Hydrogen Ignition Criteria

The hydrogen ignition criteria determine the ignition location for a hydrogen deflagration and the corresponding flammability limit (volume percent of hydrogen). The uncertainty parameter is characterized using upward, horizontal, or downward propagation from the ignition source. This is accomplished by sampling on the location of the ignition source in each MELCOR control volume representing containment compartments. A discrete distribution was chosen with an equal probability for each of three bins that represent ignition location and corresponding flammability limit.

Hydrogen combustion has uncertainties in the ignition location, ignition timing, flammability limits, and combustion intensity. Ignition timing uncertainty includes both known sources like hot leg creep or presence of random ignition sources (not modeled in this study). The implementation of the hydrogen ignition criteria supports examination of two of these uncertainties (ignition location and flammability limits). The previous SOARCA calculations [3] included combustion at the default limit for spontaneous ignition (10% hydrogen concentration within the atmosphere). The presence of steam and other diluents precluded combustion in the containment during the unmitigated STSBO scenario except upon the initial release of hydrogen-rich gas following hot leg creep rupture failure. The hydrogen ignition criteria are selected to explore the uncertainty in the lower limits of flammability for possible combustion at other times. A key uncertainty in the lower limit for combustion is the location of the ignition source relative to the reactants. The flammability, or propagation, limits are greatly influenced by the initial direction of propagation from the ignition source. For example, the limits for hydrogen-air mixtures for upward, horizontal, and downward initial propagation of the flame are approximately 4, 6, and 9 percent hydrogen, respectively, demonstrating the effect of buoyancy [59].

The sampling is performed on upward, horizontal, and downward propagation direction when there is an identifiable ignition source. The identifiable ignition sources include hot gas jets from a hot leg failure, the PRT rupture disk, and the reactor coolant pump seals. The ex-vessel debris in the reactor cavity is also an active ignition source. Although there are defined ignition sources, the ignition propagation is assumed to occur randomly within a compartment (i.e., upward, downward, or horizontally). When gas concentrations are within the sampled flammability limits and there is an active ignition source, the burn will begin at the ignition source, propagate from there into a deflagration. It is assumed that the ignition sources in these three categorizations of ignition location/propagation direction characterize the lower flammability possibilities for a large-scale burn throughout a compartment.

Rationale for Distribution

The variable flammability limit approach was initially conceived for random ignition in the draft Surry UA [8]. The sources of ignition were assumed to be present throughout the compartmentalized containment such that the location(s) where hydrogen would ignite and the direction(s) the flame(s) would need to propagate would be uncertain and random. The current Surry UA follows the same approach as the Sequoyah UA [7], which only allows ignition when with well-defined sources of ignition. Consequently, combustion only occurs with an active ignition source (i.e., hot gas jets or ex-vessel debris) and the control volume gas concentration satisfies the sampled flammability limit.[45]

The current UA and the Sequoyah UA maintain uncertainty sampling on the initial direction of the flame propagation. Although there is an active ignition source, the direction for the flame propagation is assumed to be uncertain. For example, the source of the hot jet or ex-vessel debris may be located at the bottom of the compartment, but the ignition may originate near the top of the compartment after mixing with the room air. The discrete thresholds for upward and downward propagation are supported by experimental information [59]. A uniform weighting of the three discrete initial propagation directions and their corresponding flammability limits is assumed.[46] Figure 4-29 shows the discrete distribution for initial propagation direction; each is equally likely.

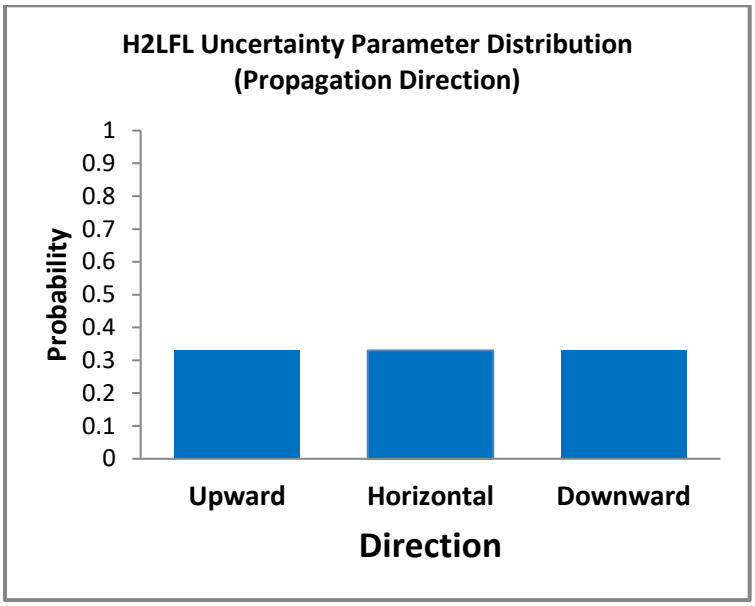

Figure 4-29 Uncertainty Distribution for Ignition Propagation Direction

4.1.3.2 Containment Design Leakage Rate (designLeakLa)

Prior to containment overpressure failure, radionuclide releases through nominal leakage tends to be relatively small (0.1% air volume per day at an overpressure ratio [P/P_{Design}] of 1). As an

[45] The combustion evaluation checks for adequate oxygen, the sampled value of hydrogen or carbon-moxoide, and the limiting steam and carbon-dioxide concentration.

[46] Independent of the initial ignition location and propagation arguments, it was also desirable to have three thresholds that sampled a weaker but more likely ignition threshold (i.e., upward or 4%), a middle value (i.e., horizontal or 7%), and a less likely but more powerful deflagation (i.e., downward or 9%). Consequently, the updarwd, horizontal, and downward framework was retained.

example, release fractions are less than 10^{-4} of the core inventory (excluding noble gases) in the unmitigated SOARCA STSBO scenario (see Figure 5-36 in NUREG/CR-7110 Volume 2 [3]) before containment overpressure failure near 26 hours. Releases due to design leakage remained low and steady for about 20 hours before containment rebar failure in the SOARCA STSBO, after which release fractions increased by several orders of magnitude due to containment functional failure (CFC parameter). Consequently, the designLeakLa parameter can have an effect on population dose during the first day of the accident, the containment failure timing, cumulative release, and consequences during evacuation.

Nuclear power plant control of containment leak tightness is governed by the Code of Federal Regulations Appendix J. Appendix J specifies containment leak-testing requirements, including the types of tests required. For each type of test required, Appendix J specifies the leak-rate acceptance criteria, how such tests should be conducted, the frequency of testing, and reporting requirements. Appendix J requires the following types of containment leak tests:

- Measurement of the containment integrated leak rate (Type A tests, often referred to as ILRTs).
- Measurement of the leak rate across each pressure-containing or leakage-limiting boundary for various primary reactor containment penetrations (Type B tests).
- Measurement of containment isolation valve leak rates (Type C tests). Type B and C tests are referred to as local leak rate tests (LLRTs).

The NRC implemented an initiative to allow performance-based requirements to replace prescriptive requirements of Appendix J with only a marginal impact on safety. NUREG-1493 provided the technical bases for the NRC's rulemaking to revise leak-testing requirements for nuclear power reactors [9]. The most significant change in the performance-based requirements was to reduce the Type A testing interval in place of Type B and C testing. NUREG-1493 concludes that the ILRTs identify only a few potential containment leak paths that cannot be identified by Type B and C testing, and the leaks that have been found by Type A tests have been only marginally above existing requirements.

In response to the performance-based update to Appendix J, the Nuclear Energy Institute (NEI) developed performance-based testing to extend the Intervals of Type A, B, and C testing. The NRC in Regulation Guide (RG) 1.163 accepted the NEI proposal with some limitations extending Type A test intervals up to 15 years and extending Type C test intervals up to 75 months. The ACRS recently noted in a review of RG 1.163 that 94 operating reactors were given one-time 15-year ILRT interval approval [145]. Approximately 75 reactors have completed 15-year Type A tests and no test failures have been reported. Furthermore, ACRS noted that the performance results from the extended test intervals that have been applied to date do not indicate that any new failure modes have been missed. The ACRS endorsed a revision to RG 1.163 that allowed continual extension of extended testing intervals without requiring new approvals every 15 years.

A publicly available report from EPRI on Type B and C testing by 26 units from 1996 to 2010 was reviewed [146]. The study reports on 349 plant-years of experience with 8529 Type C LLRTs on 2055 valves. 148 valve failures were reported. Seven instances of failures involved redundant valves in single penetrations, which is approximately 4.7% of the 148 failed tests. The maximum failure leakage rates were 0.22 (i.e., 22%) of the allowable leakage rate (La) and within the acceptance criteria. None of the reported Type C tests exceeded the 0.6 La criterion.

NRC review of Surry the Unit 2 application for extension of LLRT testing to 15 years noted that the last three ILRTs have been successful. The as-found leakage rates ranged from 0.061 La to 0.728 La and are shown in Table 4-15 [147]. Based on this performance and their ongoing containment surveillance program, the NRC approved an extension to 15-year testing on the ILRT.

Table 4-15 Surry Unit 2 ILRT Results

Test Date	November 1986	May 1991	October 2000	Acceptance Criteria
Total As-Found Leakage	0.728 La	0.452 La	0.061 La	1.0 La
Total As-Left Leakage	0.638 La	0.418 La	0.06 La	0.75 La

La = 0.1 percent by weight of containment air per 24 hours at calculated peak pressure (Pa)

The previous discussion supported a maximum leakage rate less than 1.0 La to be consistent with Appendix J requirements. However, SMEs for this UA believed that consideration of isolation failure was needed. A historical review of ILRTs prior to risk-informed testing was consulted. NUREG/CR-4220 concluded that a 30% unavailability of the containment due to leakage in the 1.0 to 10.0 La range [148]. While such a high unavailability is not supported by current results, it provides an upper bound based on historical findings.

The containment leakage rate was sampled assuming uncertainty in the parameter can be reasonably represented having lower and upper bounds of 0.1 La to 10.0 La, respectively. The recent testing data at Surry and across the fleet supports most of the distribution being less than 1.0 La. A piecewise distribution is used to represent the parameter from 0.1 to 10.0. A uniform logarithmic distribution is used from 0.1 to 1.0 and a linear distribution is used from 1.0 to 10.0 (see Figure 4-30 for semi-log scale and Figure 4-31 for linear scale). The distribution assigns a higher probability to leakage rates on the interval [0.1, 1.0] than on the interval [1.0, 10.0]. The selected distribution allows for some samples in which the leakage area is between 1.0 and 10.0 but only infrequently, as SMEs deem leak rates in this range to be unlikely, though possible.

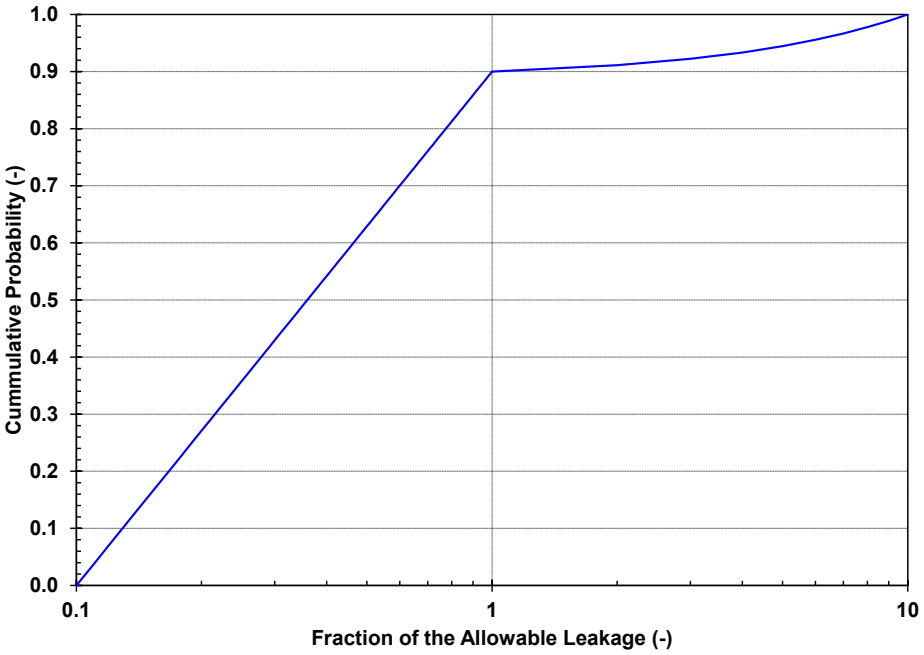

Figure 4-30 CDF for the Non-Dimensional Containment Leakage Rate (DLEAK) Semi-Log Scale

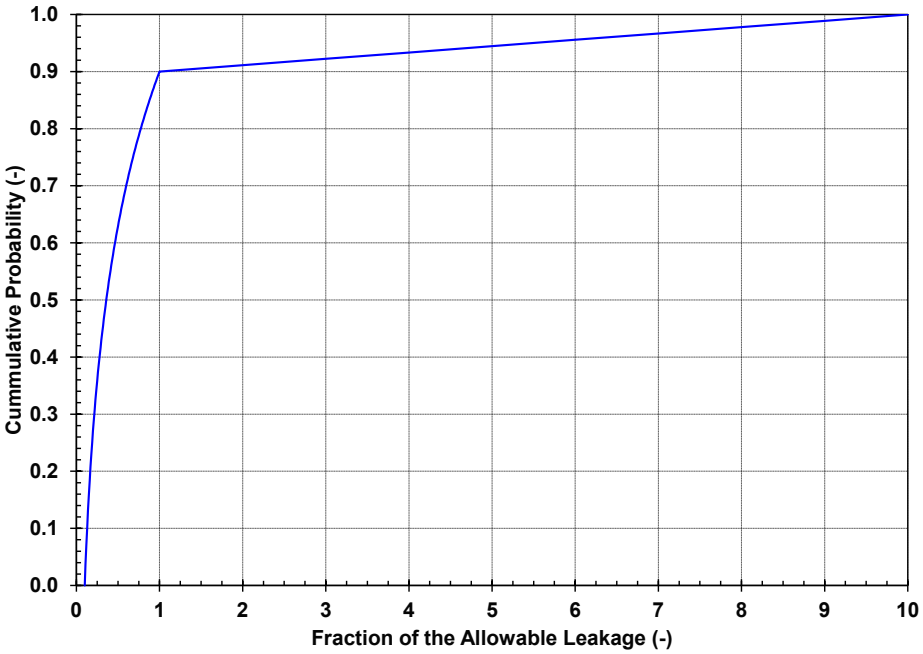

Figure 4-31 CDF for the Non-Dimensional Containment Leakage Rate (DLEAK) Linear Scale

Rationale for Distribution

The results of the performance-based containment leakage testing program has been very successful. The program reports 75 successful ILRTs from the adoption of performance-based testing and no failures. Similarly, an EPRI study shows successful results from Type B and C testing. The three most recent Surry Unit 2 ILRTs have been successful with leakages ranging from 0.061 La to 0.728 La with a trend for improvement.

Leakage in excess of 1.0 La is certainly possible. However, it is a violation of the technical specifications, which results in corrective actions to shorten the time between the testing intervals. The draft Surry UA study explored leakage to 10 La and found this parameter to be significant on several consequence metrics [8]. It was concluded that the extension beyond 1 La is interesting (in part because NUREG-1493 cites low risk significance[47]). The SMEs believed that consideration of isolation failure was needed. Consequently, the range of DLEAK is extended to 10 times the allowable leakage to consider possible but unlikely isolation failures, which is assigned a 10% chance. A uniform semi-log scale was used from 0.1 to 1.0 La to increase the number of samples at smaller leakage, which is consistent with Surry 2's most recent ILRT. A linear scale is used for La greater than one due to the high uncertainty of the leakage rate within this range.

The base value for containment design leakage was implemented into the MELCOR Surry model by defining a flow path that is limited by a choked flow condition. The flow path

[47] This difference may be due in part to the UA's focus on a single unmitigated scenario, versus NUREG-1493's reliance on PRAs considering a variety of different scenarios to construct an overall risk profile.

accommodates a 0.1 percent volume per day flow of air at P/P_{Design}=1. A continuous logarithmic DLEAK distribution is sampled from the piecewise CDF shown in Figure 4-30. The sampled DLEAK parameter is implemented into the MELCOR model as a discharge coefficient on the choked flow model.

4.1.3.3 Containment Fragility Curve (CFC)

The Containment Fragility Curve (CFC) refers to a set of containment pressure ratios at which failure modes occur and leakage increases. The ratio at which the lowest point in the curve, liner plate yield, occurs is sampled and the remainder of the data points can potentially shift, depending on the sampling. Uncertainty in liner plate yield was represented with beta distribution (α: 5.6; β: 6.3) with a lower bound of 1.09 and an upper bound of 2.03 for P/P_{Design} (45 psig).

For accident scenarios without containment bypass, enhanced containment leakage due to overpressure is the dominant release path for radionuclides in the Surry MELCOR model used in SOARCA. The SOARCA model for containment overpressure failure is based on over 25 years of research. This research included both experimental and advanced computational efforts, such as the scaled PWR containment experiments at SNL (particularly the 1:4 for pre-stressed concrete and 1:6 for reinforced concrete) and nonlinear finite element simulations. These tests show that upon pressurization, PWR concrete containments exhibit significantly increased leakage before failing catastrophically due to the physically redundant arrangement of the steel-liner enclosed in a concrete shell. Large leakage effectively precludes catastrophic containment rupture for reasonable pressurization rates. Leakage following overpressure is most likely to occur near equipment hatches and other penetrations through the containment; these are regions of material and geometric discontinuities that cause high local stresses.

The SOARCA model for containment overpressure uses experimental data from the SNL 1:6 scaled experiments, since the Surry containment is reinforced concrete, in conjunction with a very simple NRC method to reconcile scale and the idealized nature of the experimental models. Specifically, the test data for normalized mass flow rate is used in the SOARCA MELCOR model while a set of very simple stress calculations provides the internal pressures at key stages of containment pressurization. This process yields tabular data of containment pressure vs. enhanced mass leak rate. Informed by the experimental observations, the hand-calculations estimate the internal containment pressures associated with the following events:

- Liner plate yield: 82.1 psig. Liner yield is defined to be the onset of enhanced containment leakage and is associated with a leak rate that exceeds design leakage by an order of magnitude.

- Rebar yield: 119.36 psig

- 2 percent global containment strain: 126.71 psig.

In SOARCA, each of the calculated internal pressures was conservatively reduced 15 percent to roughly embody the large uncertainties associated with the rudimentary nature of the hand calculations, as well as uncertainties in material properties.

The SOARCA model for containment overpressure is uncertain for several reasons. The scaled tests for containment overpressure were performed at ambient temperature with nitrogen and

did not consider the effects of high temperature steam, which could be saturated or superheated due to generation of non-condensable gases (from in-vessel oxidation and/or CCI). The experimental models were non-prototypical with respect to aging, corrosion, and the arrangement of penetrations. Finally, the SOARCA hand-calculations for pressure at the various stages of containment overpressure are very simple and are reduced 15 percent for conservatism. Therefore, the Surry UA treats the containment pressure at which to initiate the fragility (failure) curve as an uncertain parameter, and the treatment is informed by SOARCA, the 1:6 scale experiments, and finite element simulations for degraded containments [107].

Rationale for Distribution

The data points shown in Figure 4-32 reflect leak rate data collected from the 1:6 scale experiments [62] and associated with NRC supplemental calculations of pressure for each stage of containment overpressure. These data points were generated in SOARCA to help inform the Surry containment leakage model. The three calculated pressures were all reduced 15 percent in SOARCA for conservatism; a fourth data point (liner plate yield shown at 1% volume / day in Figure 4-32) is adopted directly (both pressure and leak rate) from experimental data, but again with the pressure reduced 15 percent. The original SOARCA model [3] implemented a 3rd order polynomial through these data points and neglected the liner yield point; thus overpressure leakage before rebar yield was assumed to be subsumed by design leakage, and early enhanced leakage was assumed insignificant for calculation of integral releases. The Surry UA modeling approach was slightly different to facilitate uncertain parameter treatment of containment failure by overpressure and to maintain consistency with experimental observations. The Surry UA model considers functional failure to begin at liner plate yield, which is associated with a 1.0 percent mass/day leak rate (i.e., 10 times the original design leak rate, which is now an acceptable design basis leak rate under 10CFR50 Appendix J). This approach provides a model reflecting containment yield-before-rupture which was confirmed by the structural experts involved in the 1/6th scale reactor containment tests [108] as more realistic. Also, simple linear interpolation is used between the four data points of the fragility curve instead of a polynomial fit. The liner yield point is taken to be the sampled quantity from the CDF of overpressure ratio for the start of effective containment failure created in this work, and this is appropriate since past research has determined it to be the onset of significantly increased containment leakage.

After review of the containment research which documents finite element simulations for significant corrosion at mid-height of the containment [107][108], methodologies considered for severe accidents in NUREG/CR-6433 [109] and recent severe accident analyses in NUREG/CR-7149 [110], a CDF was created for the liner plate yield point of the CFC and is shown as the blue line in Figure 4-33. This CDF was also informed by discussions with containment experts and engineering judgment. It places the SOARCA pressure for liner plate yield ($P/P_{Design} \approx 1.55$) significantly below the 50th percentile of the CDF, which reflects the conservatism introduced by the 15 percent reduction in the calculated pressure for liner plate yield. The majority of sampled values are between the SOARCA [3] value and the original experimental data point without conservatism of about 1.75. This reflects the best current state of knowledge about the most probable value to start overpressure leakage. The bounds of the distribution are set based on physical limits. The lower limit of P/P_{Design} of 1 is because while it would be possible to have containment degradation to the point of damage at atmospheric pressure, leakage below design pressure would be detected during outage testing. The upper limit is simply set to about the experimental point of rebar yield, which is an advanced damage state.

The CDF for the Surry UA differs from other CDFs (e.g., Surry IPE and NUREG/CR-6920), but is used to create sampled values for the liner yield pressure, which initiates overpressure leakage at a relatively low pressure and leak rate. Additionally, the CDF allows investigation into the interplay due to the effect of severe containment degradation with MACCS evacuation parameters (i.e., potential early release frequency consequence analyses).

The data points beyond liner plate yield (rebar yield and beyond) with higher leak rates are lowered appropriately for P/P_{Design} according to the sampled P/P_{Design} for the liner plate yield data point along the CDF in Figure 4-33. However, these over pressure data points (rebar yield and beyond) are not raised for a subsequently higher liner plate yield data point along the CDF. The rebar yield (~2.25 P/P_{Design}) and beyond data points in Figure 4-32 are considered the maximum value since they are based on experimental data and are considered fixed within structural mechanics (rebar yield and 2% global strain). While it could be envisioned that these data points could be reduced (e.g., corroded rebar), there is no justification to raise these data points within the current understanding of severe accident containment response.

As an example, consider the 20^{th} and 80^{th} percentile data from Figure 4-33. These percentiles translate to a P/P_{Design} of 1.45 and 1.75, respectively, for the liner plate yield data point in Figure 4-32. For the 20^{th} percentile, the subsequent data points (rebar yield and beyond) are reduced for P/P_{Design} by ~0.1 (e.g., 2.155 for the rebar yield data point) and these new data points are linearly interpolated between the data points for the containment functional failure model in MELCOR. For the 80^{th} percentile, the subsequent data points (rebar yield and beyond) remain at the same P/P_{Design} (e.g., 2.255 for the rebar yield data point) and the new liner plate yield data point is linear interpolated with the original subsequent data points to produce the containment functional failure model in MELCOR.

Uncertainty in the leak rates are neglected since estimations of experimental error are not readily available for the Surry UA. It is assumed that most of the uncertainty lies in the pressure associated with each of the four data points representing increasing leak rates, which were estimated by simple hand calculations informed by the experiments.

For compatibility with the MELCOR uncertainty engine, a beta distribution was fit to the CDF described above and shown in Figure 4-33. This distribution has the parameters: LB = 48.9 psi (P/P_{Design}=1.09), UB=103.6psi (P/P_{Design}=2.03), $\alpha = 5.6$, $\beta = 6.3$.

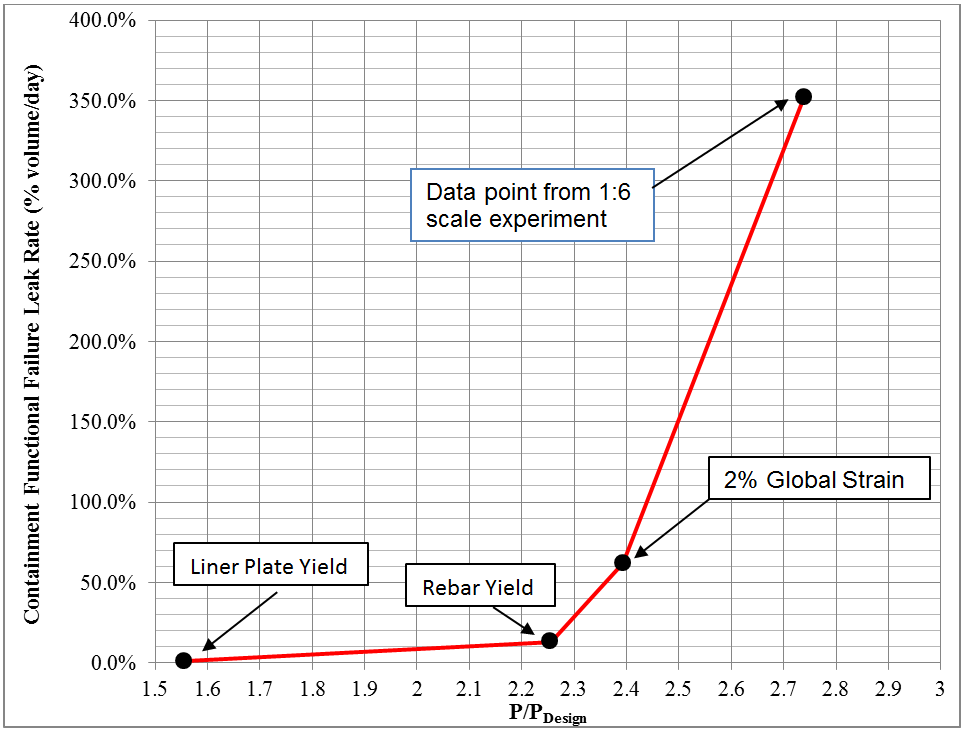

Figure 4-32 Containment Functional Failure Leakage

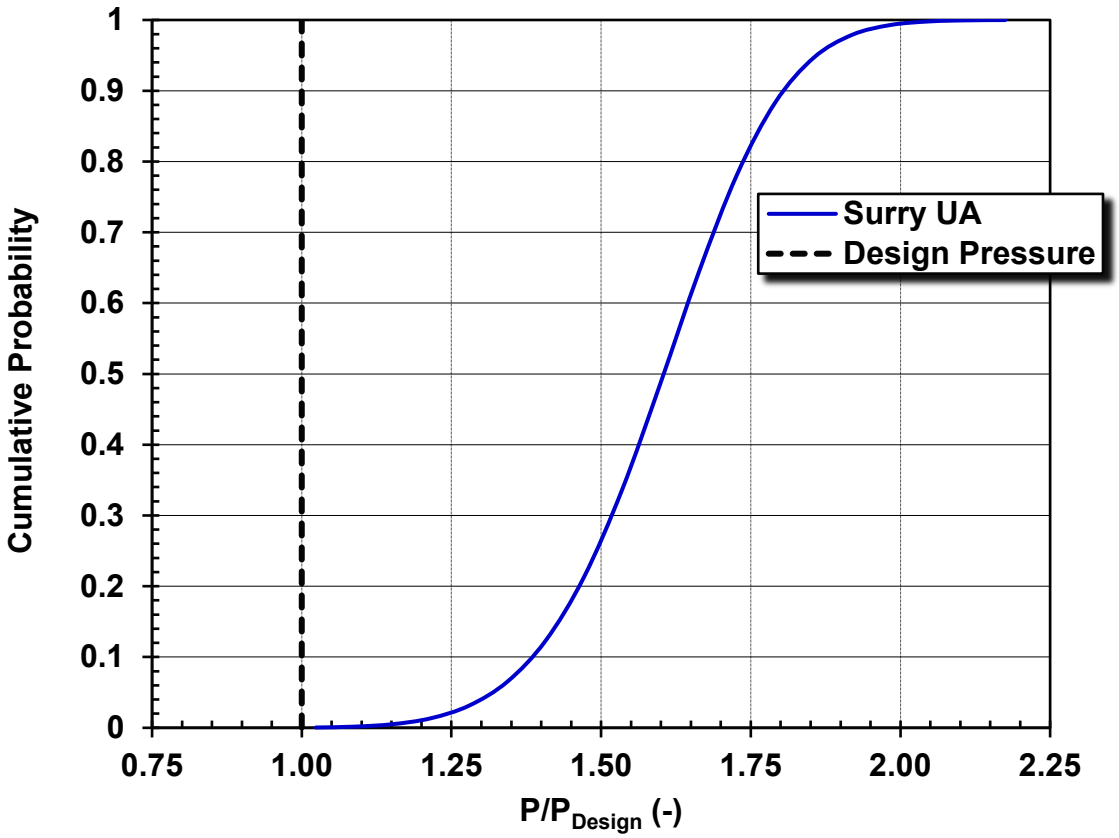

Figure 4-33 CDF for Containment Overpressure Ratio for Liner Plate Yield

4.1.3.4 Containment Convection Heat Transfer Multiplier

To address uncertainty in containment convection heat transfer, a multiplier (defined as XHTFCL in MELCOR) is modified for containment wall heat structures. The uncertainty in the unitless multiplier was represented by a triangular distribution with a mode of 1.4, a lower bound of 1.0 and an upper bound of 2.0. This parameter is identified as CONDENS in the regression tables in Section 6.1.

The heat deposited in concrete and steel in containment is significant in a MELCOR severe accident simulation and the rate at which the heat is deposited has associated uncertainty. Greater heat deposition rates relate to slower containment pressurization. Important to heat deposition rate (or heat transfer rate) is heat transfer coefficient (HTC). The calculation of HTC in MELCOR involves determining Nusselt number (Nu) as it does in the CONTAIN computer code [111]. Increasing the leading coefficient in the relation for Nu from 0.10 (default in MELCOR) to 0.14 (CONTAIN default) has historically been found to give more realistic results in comparisons with applicable experimental data [114]. Nu is a multiplier in the relation for HTC and increasing the leading coefficient in the relation for Nu from 0.1 to 0.14 increases HTC by 40 percent. The value of 0.14 is only applicable to laminar natural circulation so its use in other accident sequences or models may require a new distribution.

Rationale for Distribution

HTC can be increased in MELCOR by increasing the leading coefficient in the relation for Nu, just as in CONTAIN. Doing so, however, globally affects all heat structures in the model. A different means of increasing HTC is to increase the HTC multiplier XHTFCL individually associated with each heat structure. This was done for each heat structure representing a wall of containment. The uncertainty in HTC was represented by employing a triangular probability distribution for the multiplier with mode 1.4, lower bound of 1.0 and upper bound of 2.0. The same specific multiplier was applied to all the containment walls in a given realization. The mode of 1.4 reflects the 40 percent increase reported as beneficial in the CONTAIN work. The value of 1.0 assigned to the lower bound is the default value of the multiplier. The value of 2.0 assigned to the upper bound reflects a doubling of the HTC MELCOR would assign on its own.

MELCOR documentation recommends that the XHTFCL and mass transfer (i.e., condensation and evaporation) coefficient multiplier XMTFCL not be modified independently to avoid computational difficulties [11] (Section 2.6). Consequently, the XHTFCL and XMTFCL multiplier have been defined together as the same value in each realization. The associated PDF and CDF for the heat transfer coefficient and mass transfer multipliers are shown in Figure 4-34 and Figure 4-35, respectively.

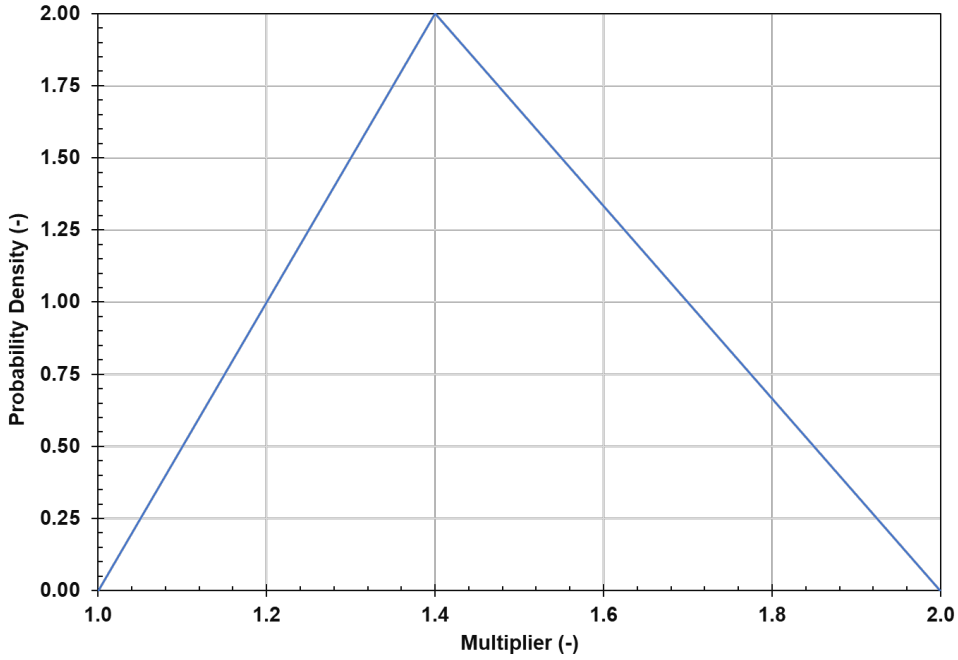

Figure 4-34 PDF of Heat Transfer Coefficients and Mass Transfer Multipliers

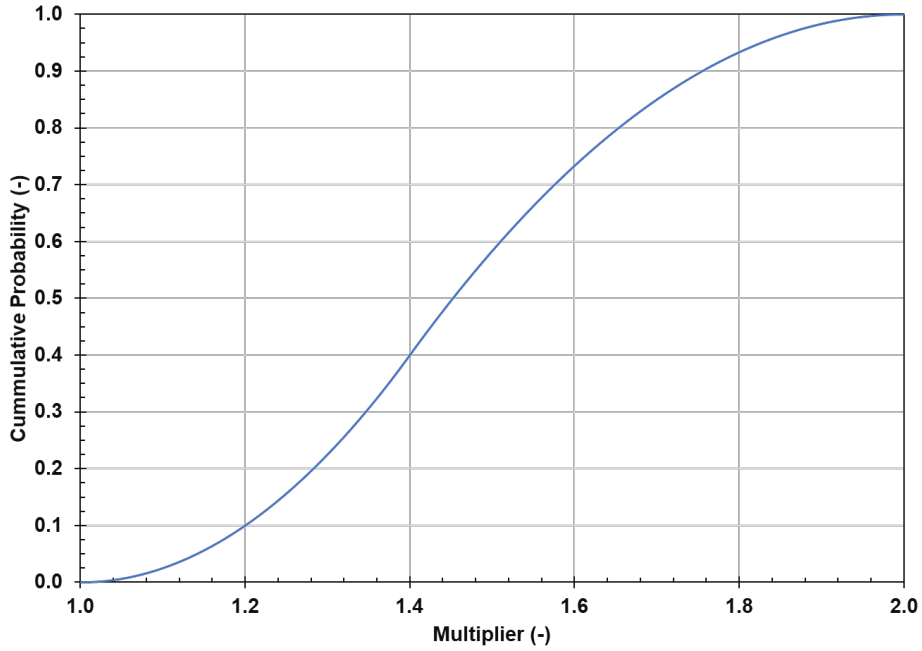

Figure 4-35 CDF of Heat Transfer Coefficients and Mass Transfer Multipliers

4.1.4 Radionuclide Behavior

The final grouping of uncertain parameters includes those addressing uncertainty in the radionuclide behavior. The first two parameters address uncertainties in the speciation of iodine and cesium released from the fuel. Although the uncertainty distribution is unchanged from the draft Surry UA [8] and the approach in the Sequoyah UA [7], a new UA implementation of the fractional specifications for the various iodine and cesium chemical compounds was automated to generate separate chemical class inventories for each of the 14 times in the cycle (see Section 4.1.2.4).

The third uncertain parameter addresses the dynamic shape factor of the airborne aerosols. This parameter is unchanged from the previous UAs. The final parameter addresses the retention of radionuclide aerosols released to the secondary side of the steam generator following a SGTR.

4.1.4.1 Chemical Form of Iodine

The Surry Uncertainty Analysis considers a distribution of gaseous iodine fractions and a compatible set of CsI fractions. The fraction of gaseous iodine versus an aerosol form of iodine is based on data that was acquired by Sandia National Laboratories from the Atomic Energy and Alternative Energies Commission (CEA) detailing fraction of fission gas released to the fuel-cladding gap as a function of burnup. Figure 4-36 summarizes data provided by the CEA from French reactors for low enriched uranium (LEU) and mixed oxide fuel.[48] The fuel was removed from operating reactors, and the cladding was punched to determine the gases present in the gap. The uncertainty in the measured gap gas mass (i.e., represented as a fraction of the total iodine inventory) at a particular burn-up from the CEA data is the sampling distribution for the gaseous iodine mass (see Figure 4-36). The sampled fraction for each realization is assumed to reside in the gap and released when the cladding fails.

For each of the specified times selected during the Surry fuel cycle in Section 4.1.2.4, there is an associated ORIGEN simulation. The ORIGEN simulation gives a burnup for each fuel assembly and thus a closed interval of burnup values to consider. For each of the ORIGEN calculations, the range of burnup values is identified. The relevant CEA data is fit to a log-normal distribution, and the gaseous iodine fraction is sampled from that distribution. The sampled fraction of the total iodine inventory is applied uniformly across the entire core. For each of the fourteen times in the cycle where ORIGEN inventories are calculated, a log-normal distribution is defined for the gaseous iodine sampling (i.e., a separate iodine distribution for each of the fourteen ORIGEN runs).

The gaseous iodine distributions used for the ORIGEN runs are shown in Figure 4-37 through Figure 4-40. The data is represented with the empirical curve and the sampled range for the particular time in the cycle is shown with the fitted curve. The all data curve shows how the selected time in the cycle compares to all the data, including burnup values outside the range of ORIGEN calculations. A comparison of fitted data curve to all data curve illustrates the effect of restricting the sampled distribution to the specified time in the cycle.

---

[48] The cladding gap gas data was obtained from Sandia interactions with CEA and is not available in referenceable material.

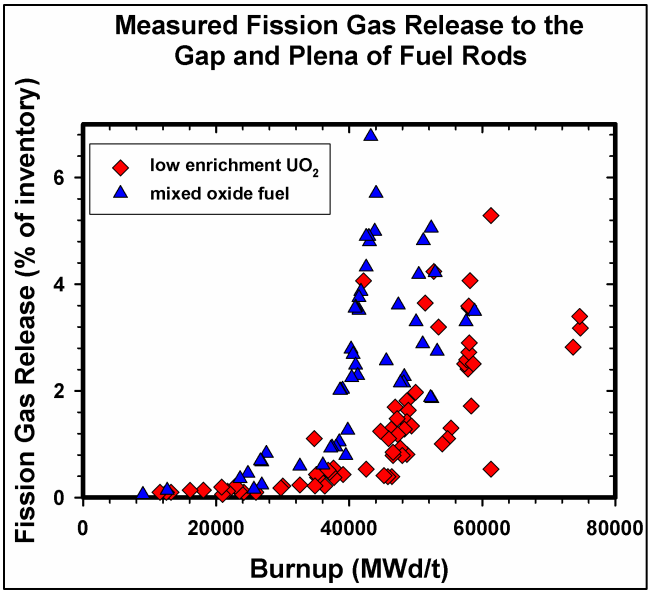

Figure 4-36 French Measured Fission Gas Release to the Fuel/Cladding Gap

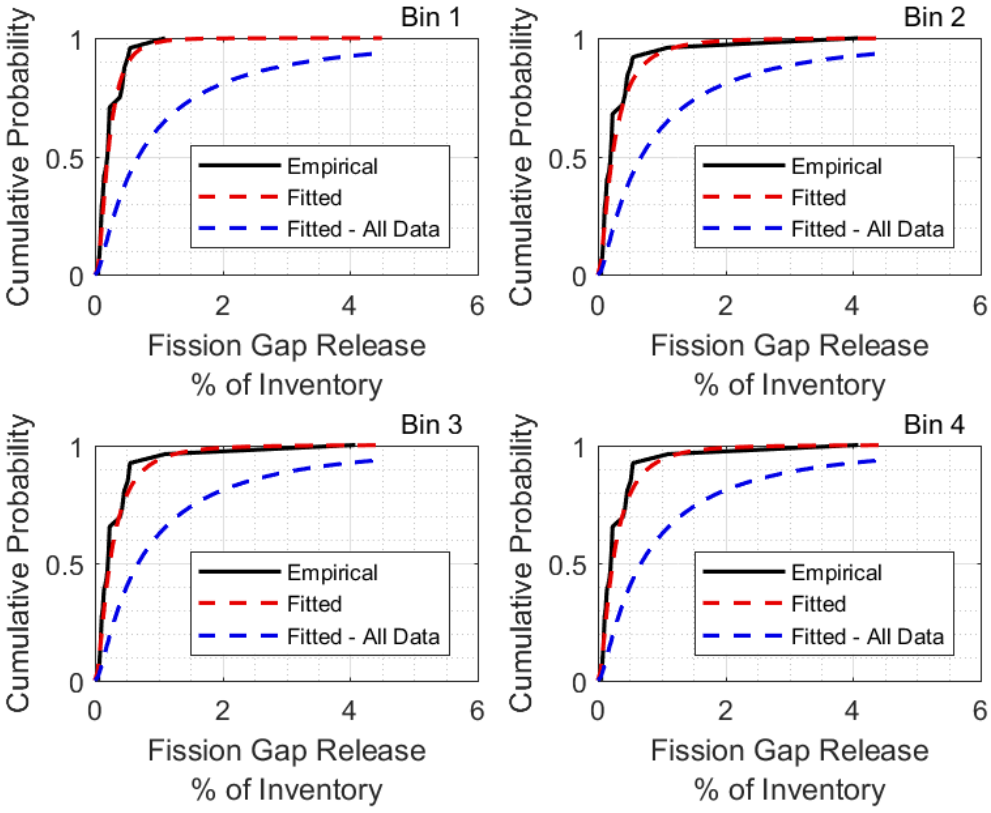

Figure 4-37 Distributions for ORIGEN Runs to 0.25, 25, 50, and 75 Days - (Bins 1, 2, 3, and 4, Respectively)

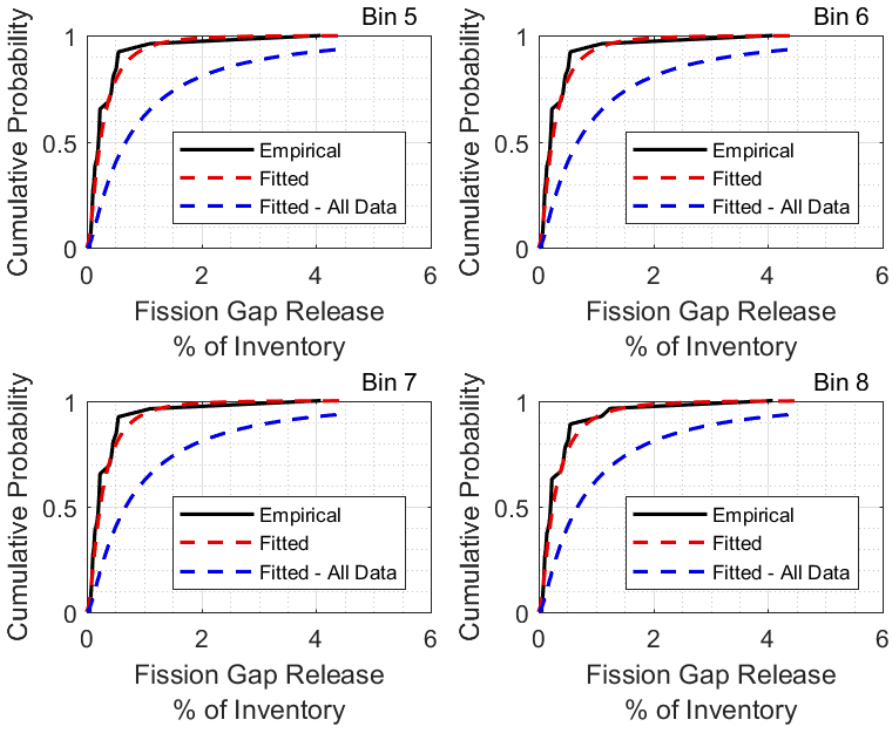

Figure 4-38 Distributions for ORIGEN Runs to 100, 150, 200, and 250 Days - (Bins 5, 6, 7, and 8, Respectively)

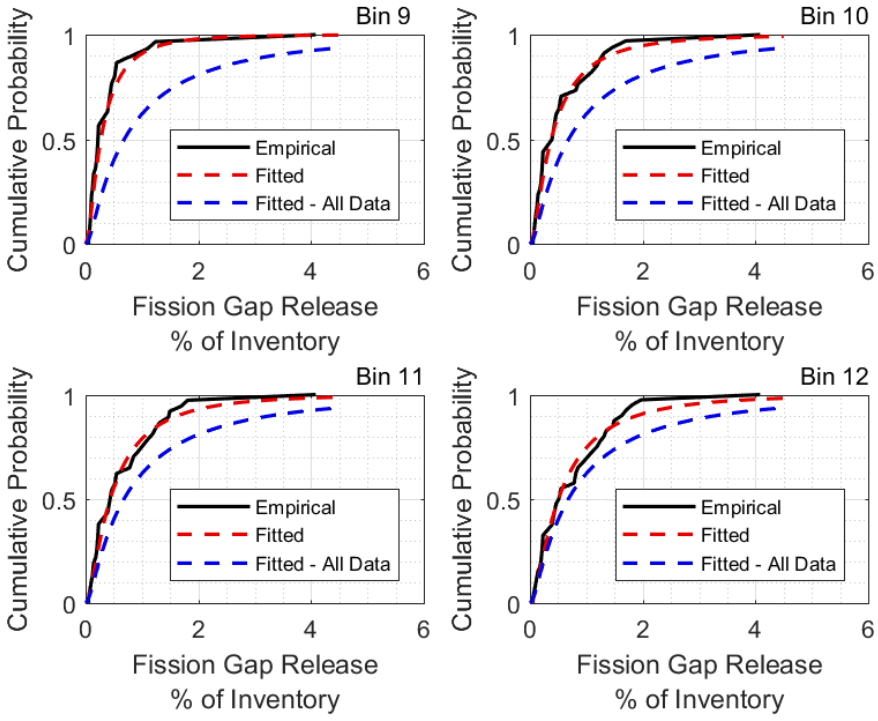

Figure 4-39 Distributions for ORIGEN Runs to 300, 350, 400, and 450 Days - (Bins 9, 10, 11, and 12, Respectively)

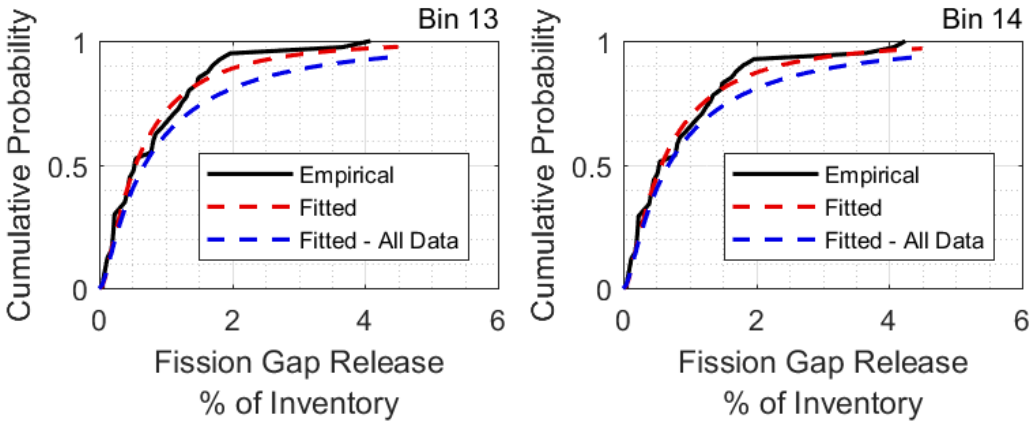

Figure 4-40 Distributions for ORIGEN Runs to 500 and 550 Days - (Bins 13 and 14, Respectively)

Rationale for Distribution

Gaseous iodine can greatly influence the source term magnitude due to its high mobility and immediate release upon cladding failure. The Surry SOARCA analysis [3] assumed all released iodine combines with cesium to form cesium iodide (CsI) [3]. However, past radionuclide release studies, such as NUREG-1465 [121], have assumed that as much as 5 percent of the total

iodine inventory is released as gaseous iodine. The current revision of NUREG-1465, ongoing at Sandia, has maintained this 5 percent gaseous iodine fraction as of the publication of this study. Additionally, recent experiments at the Phebus facility show that gaseous iodine is found within containment [54]. With the different core make-ups of the various Phebus tests, the percentage of iodine in the containment that is gaseous has varied from as low as 0.2 percent to as high as 7 percent. Understanding the uncertainty regarding the chemical form of iodine is important because the iodine chemical behavior affects the amount and timing of iodine release from containment to the environment.

Because there is a lack of understanding on gaseous iodine behavior from the Phebus tests, the recommended approach is that fission gas release to the fuel/cladding gap be used as a surrogate for the gaseous iodine fraction. This is an applicable surrogate because past research performed for reports such as WASH-1400 [82] (pg. IX-5) and NUREG/CR-7003 [83] (pg. 2-4) has shown that (i) the percentage of iodine released to the gap relative to the total inventory is similar to the corresponding percentage for noble gases like xenon and (ii) iodine and xenon have about the same diffusion coefficient. Second, analysis of used fuel rods has shown that iodine in the gap is gaseous. Finally, the consensus based on multiple severe accident experiments is that the iodine retained in the fuel rod and not transported to the gap will later be released in the form of CsI. Therefore, it is assumed that all gaseous iodine is located within the fuel/clad gap at essentially the same percentage as all fission gas.

4.1.4.2 *Chemical Form of Cesium*

CHEMFORM Cs determines the fraction of total cesium that is not bound to iodine that becomes Cs_2MoO_4, with the remainder as CsOH. Results from the Phebus test facility indicated that cesium deposited into containment as cesium hydroxide (CsOH) and Cs_2MoO_4 with a smaller fraction as CsI. Analysis of the results further indicated that late-term reactions between the Cs_2MoO_4 and steam led to revaporization of the cesium as CsOH. While the UA's CsI fraction is modelled to be stoichiometrically limited by the initial non-gaseous iodine mass, the initial fraction of the remaining cesium mass in the fuel rod that is Cs_2MoO_4 versus CsOH is uncertain.

Phebus data showed an 80:20 ratio of Cs_2MoO_4 to CsOH in containment. However, MELCOR has no model for the creation of CsOH from steam reactions with CsI and Cs_2MoO_4. Consequently, the long-term transformation to CsOH must be addressed through the initial inventory specifications of CsOH and Cs_2MoO_4.

The fractional distribution of elemental Cs as Cs_2MoO_4 is a beta distribution with shape parameters α equal to 9 and β equal to 3 (see Figure 4-41). The beta distribution is naturally bounded between zero and one, which makes it well-suited for a fractional sampling. Further, the shape parameters give a mode of 80% Cs_2MoO_4, to agree with Phebus data, while also possessing a noticeable amount of negative skewness to explore the effects of higher CsOH concentrations upon release.

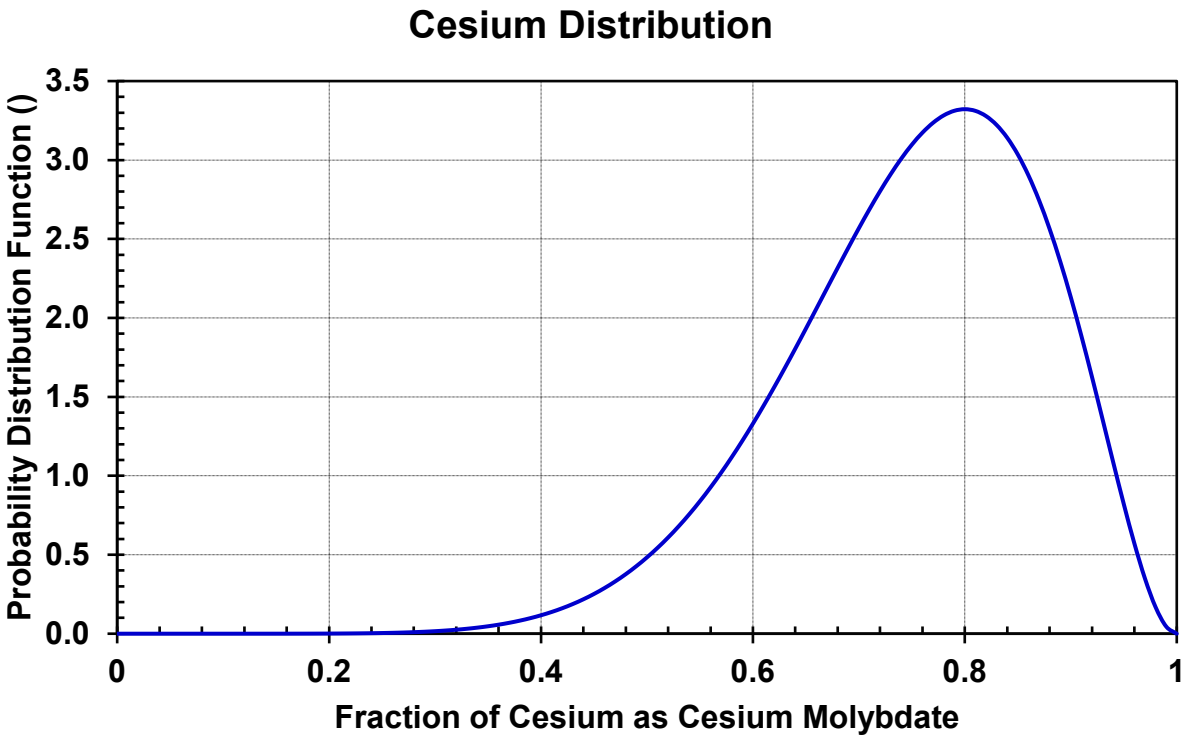

Figure 4-41 The Beta Distribution used to Sample the Fraction of Cesium as Cesium Molybdate

Once the uncertain parameters for the time in the cycle (Section 4.1.2.4) and chemical forms of cesium and iodine (Section 4.1.4.1) are identified, Appendix D describes the process for calculating the specific amounts of each compound.

Rationale for Distribution

The predominant next speciation of cesium described in the Surry SOARCA analysis [3] was based on detailed chemical analysis of the deposition and transport of the volatile fission products in the Phebus facility tests. The chemical analysis revealed molybdenum combined with cesium and formed cesium molybdate (Cs_2MoO_4). This is based on cesium and molybdenum having been found deposited in the same locations that were at temperatures too high for cesium hydroxide to remain deposited. However, there was also evidence from the Phebus tests that cesium is revaporized at temperatures consistent with the cesium hydroxide chemical form. It is presumed that reactions between cesium molybdate and steam cause cesium hydroxide to form after release from the fuel. Prior to the Surry SOARCA analysis [3], the MELCOR default chemical form of remaining cesium (beyond the creation of CsI) was 100 percent cesium hydroxide. Understanding the uncertainty regarding chemical form of cesium is important because cesium chemical behavior affects the amount and timing of the cesium release from containment into the environment (e.g., late phase revalorization of cesium).

The parameter being sampled is the fraction of cesium that becomes Cs_2MoO_4 and so there are clear limits at 0.0 and 1.0. These limits include the ‘best practice’ for cesium in past work for

SOARCA [3] with 100 percent cesium molybdate (Cs_2MoO_4) and prior to SOARCA where the best practice was 100 percent cesium hydroxide (CsOH). A beta distribution is used to approach the bounds of the previous 'best-practice'.

The best estimate for cesium partitioning based on examination of Phebus results indicates that outside of the primary system (and in containment) cesium will have a speciation of 80 percent Cs_2MoO_4 and 20 percent CsOH. This may not represent the cesium distribution at the time of release from fuel, but within MELCOR there is no model for the cesium chemistry within the fuel and its subsequent release, so the environmental release forms need to be initialized within the fuel.

Partitioning the initial core inventory of cesium among certain allowable chemical forms for release and transport is managed within MELCOR input files that define the initial spatial mass distribution of each chemical species and its associated decay heat. Changes to the mass fractions assumed for a particular chemical group directly affect the mass fractions of other chemical groups, and hundreds of individual input records within the MELCOR model for Surry. A script was written that takes input from the sampled continuous distribution and pre-creates the necessary MELCOR files. Fixed partition fractions are used to preserve mass balances.

Again, it should be noted that this distribution of cesium is applied to the amount of cesium remaining after it reacts with iodine to form CsI and after 4.65 percent of remaining cesium beyond form CsI is introduced to the fuel gap as CsOH, since there is no significant molybdenum within the fuel gap.

4.1.4.3 Dynamic Shape Factor

The dynamic shape factor is defined as "the ratio of the actual resistance force of the non-spherical particle to the resistance force of a sphere having the same volume and velocity" [117]. This unitless dynamic shape factor is used to account for the stringing out of aerosol agglomerates in a linear or complex manner as opposed to growing as a perfect sphere. The dynamic shape factor is sampled directly, and the uncertainty of it is represented with a scaled beta distribution with the parameters of $\alpha=1$ and $\beta=5$ and bounds of 1.0 and 5.0.

A value of 1.0 is a perfect sphere and it is the lower limit for the dynamic shape factor. This value is also the default value in MELCOR and was used in the Surry SOARCA analysis [3].

Rationale for Distribution

The MAEROS model in MELCOR is used to determine the mass concentration evolution of aerosols in a spatially homogenous volume, as well as deposition on surfaces and injection/removal from volumes. One of the critical assumptions of this model is that non-spherical particle effects are adequately parameterized with the dynamic shape factor, the collision shape factor, and the effective material density. The importance of these parameters is demonstrated in several uncertainty analyses of the MAEROS aerosol model performed in support of the development of the MELCOR program [112][113]. To determine the uncertainty of this model, the uncertainty of the dynamic shape factor is addressed.

Kasper et al [116] (Tables 9 and 10), experimentally measured values for the dynamic shape factor for linear chains with their long axis either parallel or perpendicular to the settling direction, as shown in Figure 4-42. As seen in Figure 4-42, the shape factor is reasonably linear with respect to the number of spheres. This data supports an upper bound of 2.8, with a

weighting toward values less than 2.0. Compiled data from Hinds [117] (pg. 48) also supports a range of 1.0 to 2.04. However, Brockmann, J. E., et al. [118], compiled data and models that yield a range of 1 to 10 for the dynamic shape factor. The same report includes a correlation for loosely-packed spheres which calculates dynamic shape factors will be in the range of 1 to 5 for void volumes ranging from 26 to 99 percent. Based on these sources, a range of 1 to 5 is reasonable and is the range used for this project.

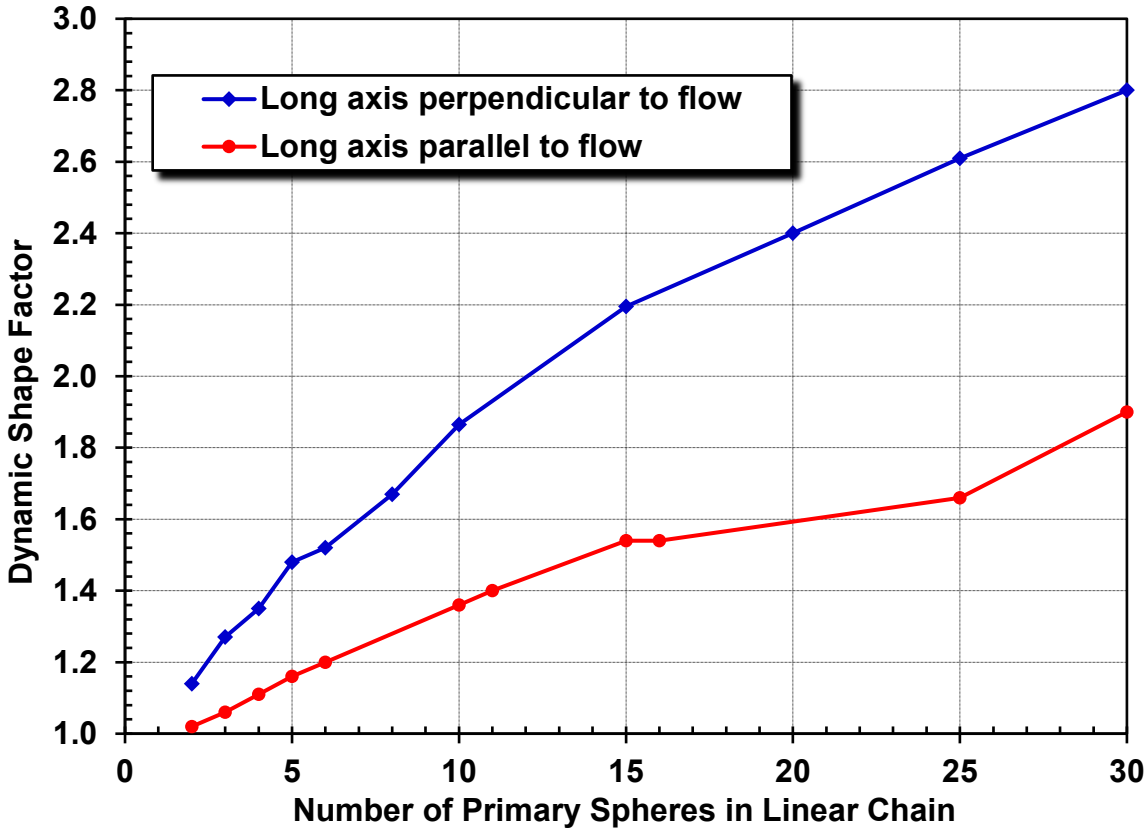

Figure 4-42 Dynamic Shape Factor Compared to Number of Spheres within a Chain

Although the bounds of the distribution were informed by the experiments described, these works cannot inform the shape of the distribution since they do not contain information on the normal shape of aerosols during a severe accident. Kissane [119] compiled information on aerosols from a number of nuclear accident experiments, including the Phebus fission product tests (FPT). The report concluded, “Concerning particle shape, relatively compact particles without branching chain-like structures appear to be typical in the RCS;” although a visual inspection of post-test deposition images did show slight evidence of aerosol chains. Since a compact, spherical particle has a shape factor of 1.0, the distribution is weighted more heavily toward the lower end of the range (1.0). Additionally, most references support weighting more heavily in the 1.0 to 2.0 range. Because of this weighting, a beta distribution is used, with the parameters of $\alpha=1$ and $\beta=5$, and the CDF of the distribution is shown in Figure 4-43. The α parameter yields a function that has a peak as close as possible to the lower bound of 1.0, while the β parameter gives the desired shape to the PDF and yields about 75 percent of samples between 1.0 and 2.0 while still allowing some samples at physically possible values up to 5.0.

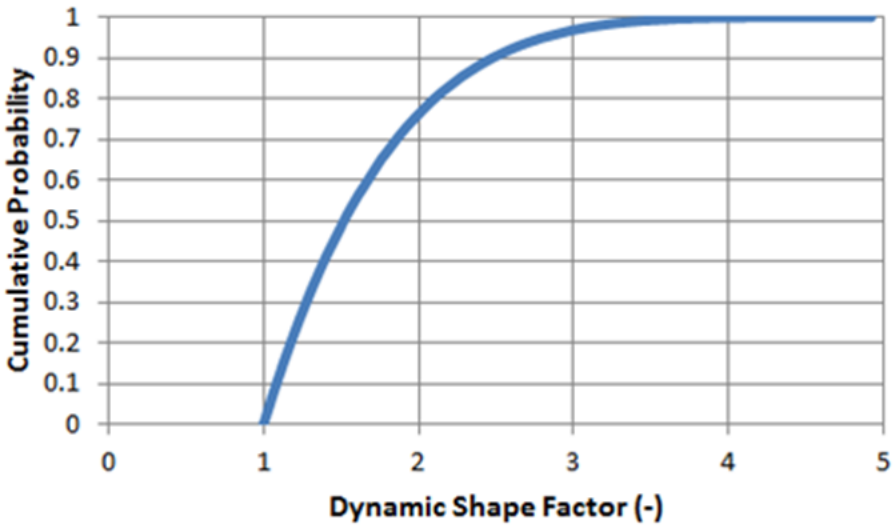

Figure 4-43 CDF of the Dynamic Shape Factor

Additionally, there is a fundamental MELCOR limitation for aerosols in that the dynamic and collision shape factors and density are set globally at the beginning of the run and cannot be updated as the accident progresses. This means that the dynamic shape factor chosen from the uncertainty distribution cannot be changed during the accident progression.

4.1.4.4 Secondary Side Decontamination Factor (SGTRLOC)

The ARTIST SGTRLOC parameter determines the number of steam generator stages traversed by radionuclides following a SGTR, which is used to calculate decontamination factors in the secondary side of the steam generator. There is a total of seven stages, and a discrete distribution is used with an assigned probability to each of seven bins representing number of stages. This parameter is identified as SGTRLOC in the regression tables in Section 6.1.

Following a SGTR in a severe accident scenario, there is some portion of the radionuclide inventory that would be transported from the primary system to the secondary side and subsequently to the environment. However, there is a tortuous path through the steam generator that would result in a deposition of radionuclides; significantly reducing the total environmental release. A series of tests were performed in the ARTIST facility to determine the amount of decontamination that occurs within a steam generator following a SGTR under various conditions. The results were extracted and interpreted from the ARTIST final report. The majority of the deposition occurs due to inertial impaction of large particles in the bends and obstacles. In contrast, the smaller aerosols smaller particles can follow the flow stream and are not captured. The total DF drops to one (i.e., no decontamination) at lower particle sizes instead of slowly, asymptotically approaching one.

The ARTIST results are broken out into a DF per steam generator stage[49] and are shown in Figure 4-44, as well as a separate DF for just the steam dryer and separator as shown in Figure 4-45. The applicable ARTIST results for the Surry scenario modeled in this work

[49] A PWR steam generator includes support grids to align the tubes. The tube region between the grids is described as a stage. There are seven grids or stages in the Surry steam generator.

included three aerosol particle sizes and three measurement techniques (although not all types of measurement were conducted with every ARTIST test). Functions were fit to these results which were implemented into the Surry UA model. The shape of the correlation between data for the various measurement methods and particle sizes for the steam separators and dryers in Figure 4-45 is consistent with decontamination by inertial impaction, but reflects the 'bounce' of large particles that prevent surface retention. The correlations produce a DF that is applied to the each aerosol section (i.e., size range) exiting the SGTR to the secondary side. The normal MELCOR aerosol capture and settling models on the secondary side are disabled.

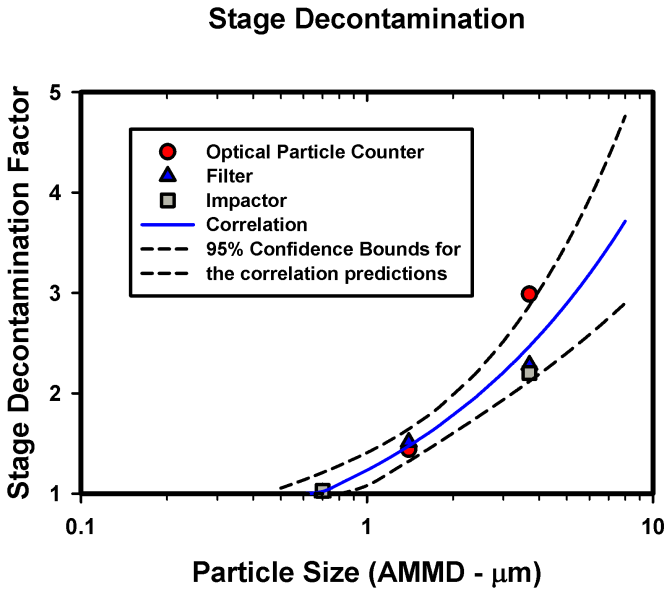

Figure 4-44 Decontamination Factor per Steam Generator Stage Versus Particle Size and Associated Confidence Bounds

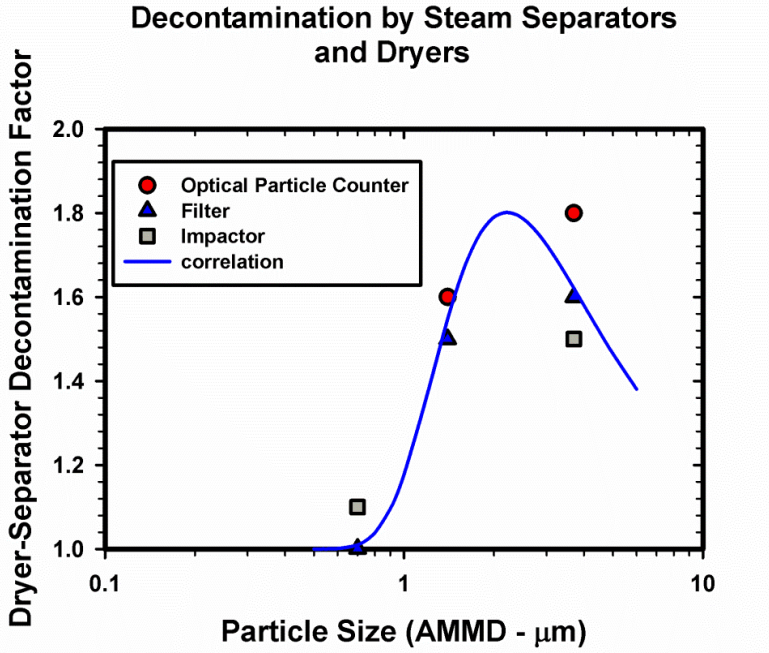

Figure 4-45 Decontamination Factor from the Separator and Dryer Versus Particle Size

The total DF for mono-dispersed particles is dependent on the DF per stage to the power of the number of stages in the flow path; thus, the uncertainty in tube rupture location dominates uncertainty from the ARTIST experiment (shown by the dotted lines in Figure 4-44). As Surry has seven steam generator stages, a discrete distribution will be sampled for *N*; where *N* is the number of stages traversed.

The median particle size in each aerosol section (i.e., size range) is used to determine two DFs based on the functions for a single steam generator stage and for the steam dryer and separator. The DF for a single stage is raised to the N^{th} power, where *N* is the number of steam generator stages between the SGTR and the steam dryer and separator. *N* was sampled in this work to determine the axial temperature on the steam generator tube for input into the MELCOR control logic for a SGTR. The calculated total DF for the tube section will be multiplied by the DF from the steam dryer and separator function to yield a total DF for that aerosol section (i.e., size range).

The ARTIST tests were done with flow conditions and particles chosen to be representative of conditions in reactor accidents [13]. However, the ARTIST results require some scaling to match the calculated flow conditions in the MELCOR simulations (i.e., time-varying versus the steady values in the ARTIST tests). The effective particle size calculated and used in the two DF correlations. Assuming that the dominant retention mechanism is inertial impaction, the test results can be scaled by preserving the Stokes number. The effective particle diameter, d_{eff}, was related to the actual particle diameter, d_p, by:

$$d_{eff} = d_p \left[\frac{U_{acc}}{U_{test}} \frac{\rho_{acc}}{\rho_{test}} \frac{\mu_{test}}{\mu_{acc}} \frac{1}{\chi_{acc}}\right]^{1/2} = 1.4x10^{-4} d_p \sqrt{\frac{U_{acc}\rho_{acc}}{\mu_{acc}\chi_{acc}}}$$

Eq. 4-11

where, U_{acc} and U_{test} are the superficial gas velocities (m/s) through the steam generators in the accident and in the test, respectively, ρ is density, μ is gas viscosity, and χ is the aerosol dynamic shape factor.

Rationale for Distribution

The number of stages through which a particle travels is an integer value and represented with a discrete distribution. Surry has seven steam generator stages, giving seven discrete bins. The probability of a SGTR in a particular stage was determined based on the axial temperature distribution Figure as predicted using computational fluid dynamics [51]. The creep function is a strong function of temperature and the pressure difference across the tube. At any given time during the severe accident phase, the pressure variation in the tube is negligible. However, there is a very strong axial temperature variation. The axial temperature profile from the computational fluid dynamics work was axially normalized. Seven points are selected from a curve fit to the data, based on the locations of tube supports within the Surry steam generators. The distribution of temperatures is directly taken as the probability of failure in each location. This creates the discrete PDF distribution in Figure 4-46. Since temperatures are higher closer to the primary side inlet of the steam generator, there is a much greater probability at those locations (i.e., N=7 in Figure 4-46), but there will still be a significant number of samples throughout all seven tube locations.

The distribution for the SGTR location did not include the insights from the Surry ISI flaw locations, especially the loose parts locations near the tubesheet. Furthermore, the sampling does not reflect the relatively flat temperature cold zone (see Section 4.1.1.6). No further sophistication was applied as the current approach included conservatisms of a lower a DF from fewer stages (i.e., the SGTR at a higher location). Due to the shape of the stage DF correlation, the large aerosols are effectively captured, and the small aerosols pass through the steam generator to the environment. The natural circulation processes during the core degradation generate small aerosols. Consequently, the stage number had a smaller impact than expected.

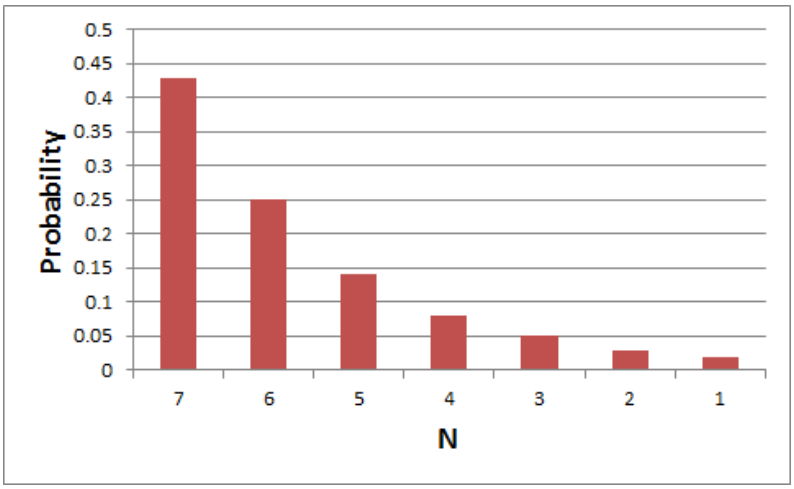

Figure 4-46 PDF for Number of Stages Traversed After SGTR

4.2 Consequence Model Uncertainty (MACCS Inputs)

The MACCS consequence model (Version 3.10.0.0 SVN-2560) was used in this analysis to calculate offsite doses and their effect on members of the public. Since the publication of NUREG/CR-7110 Volume 2 [3], MACCS and MELCOR have continued to be updated and improved, making a direct comparison with the Surry SOARCA analysis [3] not practical. To allow some comparison, the Surry SOARCA analysis [3] site file, which includes demographics, was maintained. The early fatalities are those expected to occur within a relatively short period from the time of exposure (deterministic early health effects), and the latent cancer fatalities are those expected to occur over the lifetime of the exposed individuals [120]. The MACCS figures of merit were LCF risk and early fatality risk at specified distances.

Many of the uncertain MACCS parameters have both epistemic and aleatory contributions, and the combined effect adds complexity when developing the distributions. The focus of this UA is on epistemic uncertainty; however, some of the distributions developed for the uncertain inputs include aleatory uncertainty as well. For example, some of the evacuation parameters include the effects of weather, which is considered aleatory uncertainty. While the effects of adverse weather on evacuation speed are partially accounted for in the model, they are not fully accounted for and this leads to some uncertainty in the input parameters resulting from weather uncertainty. No effort was taken to deconvolve aleatory and epistemic uncertainties when they both contribute to individual parameters; instead, a simple approach is taken where weather is considered to be aleatory in nature, and all other uncertainties are considered to be epistemic in nature. A total of 622 parameters were sampled for the MACCS portion of the analysis. These parameters are described as parameter groups in Table 4-16.

Weather conditions that would apply in the case of a potential accident at some time in the future cannot be known in advance. In this analysis, MACCS accounts for weather variability by analyzing a statistically significant set of weather trials, and the modeled results are ensemble averages of weather that represent the full spectrum of meteorological conditions. This sampling strategy was chosen to represent the statistical variations of the weather and is consistent with MACCS best practices [6]. Emergency response to a potential accident cannot be predicted in advance either, because it is dependent on source term magnitude, time of day, weather, and site-specific characteristics. Modeling of emergency response includes the timing of response actions related to protecting the public health and safety. MACCS represents protective action response activities through movement and sheltering of cohorts. A cohort is defined as a segment of the population with unique response characteristics. The cohorts established in the best estimate analysis [3] were maintained for this UA and are listed below.

Cohort 1 represents the majority of the public residing within the 10 mile EPZ.
Cohort 2 represents the shadow evacuation population of 20 percent.
Cohort 3 represents the schools within the EPZ.
Cohort 4 represents the special facilities residents within the EPZ.
Cohort 5 represents the evacuation tail for the 0 to 10 mile public.
Cohort 6 represents the small fraction of the public within the EPZ that does not evacuate.

As described in Section 2, MACCS parameters expected to be important to the figures of merit were selected as uncertain inputs. Table 4-16 lists the distributions and bounds related to each

parameter. For many of these parameters, the sampling approach is quite complex and is described in detail later in this section.

Several of the parameter distributions selected for this analysis are based on expert elicitation data captured in NUREG/CR-7161, “Synthesis of Distributions Representing Important Non-Site-Specific Parameters in Off Site Consequence Analysis” [73]. The United States and the Commission of European Communities conducted a series of expert elicitations to obtain distributions for uncertain variables used in health consequence analyses related to accidental release of nuclear material. The distributions reflect degrees of belief for non-site specific parameters that are uncertain and are likely to have significant or moderate influence on the results. The methodology in reference [73] used a resampling of the expert values and equal weights of the expert opinions.

Table 4-16 Uncertain MACCS Parameters Applied in the Analysis

Uncertain Parameter		Distribution type		Mode	Lower Bound	Upper Bound
Wet Deposition (CWASH1) (Section 4.2.1)		Log uniform			10^{-6}	10^{-4}
Dry Deposition Velocities (VDEPOS, m/s) (Section 4.2.2)		Triangular	1	0.000405	0.000128	0.00128
			2	0.000373	0.000118	0.00118
			3	0.000488	0.000154	0.00154
			4	0.000823	0.00026	0.0026
			5	0.00161	0.000509	0.00509
			6	0.00329	0.00104	0.0104
			7	0.00636	0.00201	0.0201
			8	0.0104	0.0033	0.033
			9	0.013	0.0041	0.041
Groundshine Shielding Factors (GSHFAC)* (Section 4.2.3.1)	Evacuation for All Cohorts	Piecewise Linear		N/A	0.0415	1
	Normal Activity for All but Cohort 4 andLong Term Activity for Entire Population			N/A	0.0265	0.8820
	Sheltering for All Cohorts and Normal Activity for Cohort 4			N/A	0.0075	0.4965
Inhalation Protection Factors (PROTIN)* (Section 4.2.3.2)	Evacuation for All Cohorts	Piecewise Linear		N/A	0.9	1
	Normal Activity for All but Cohort 4 and Long Term Activity for Entire Population			N/A	0.336	0.896
	Sheltering for All Cohorts and Normal Activity for Cohort 4			N/A	0.098	0.699
Early Health Effects LD_{50} Parameter (EFFACA)* (Section 4.2.4.1)	Hematopoietic	Piecewise Uniform		5.6	2.0	16.5
	Pulmonary			20.1	10.0	76.5
	Gastrointestinal			10.3	4.8	30.0
Early Health Effects* Exponential Parameter (EFFACB) (Section 4.2.4.2)	Hematopoietic	Piecewise Uniform		6.0	2.4	16.0
	Pulmonary			4.8	3.7	21.7
	Gastrointestinal			4.4	3.2	19.9
Early Health Effects Threshold Dose (EFFTHR)* (Section 4.2.4.3)	Hematopoietic	Piecewise Uniform		2.18	0.67	8.55
	Pulmonary			12.0	5.3	37.5
	Gastrointestinal			6.5	2.0	15.0
Dose and Dose Rate Effectiveness Factor (DDREFA)* (Section 4.2.5.1)	Breast	Continuous		N/A	1	3
	Other	Piecewise Continuous		N/A	1	8
Lifetime Cancer Fatality Risk Factors (CFRISK) (Section 4.2.5.2)	Multiple organs	Truncated Log normal		Varies by organ	Varies by organ	Varies by organ
Long Term Inhalation Dose Coefficients (Section 4.2.5.3)	Multiple organs and radionuclides	Log normal		Varies	Varies	Varies
Crosswind Dispersion Linear Coefficient (CYSIGA, m)	A/B	Continuous Log triangular		0.7507	0.3002	1.8768
	C			0.4063	0.1625	1.0158

Table 4-16 Uncertain MACCS Parameters Applied in the Analysis (Continued)

Uncertain Parameter		Distribution type	Mode	Lower Bound	Upper Bound
(Section 4.2.6.1)	D		0.2779	0.1112	0.6948
	E/F		0.2158	0.0863	0.5395
Vertical Dispersion Linear Coefficient (CZSIGA, m) (Section 4.2.6.2)	A/B	Continuous Log triangular	0.0361	0.0144	0.0903
	C		0.2036	0.0814	0.509
	D		0.2636	0.1054	0.659
	E/F		0.2463	0.0985	0.6158
Evacuation Delay (DLTEVA, hr) (Section 4.2.7.1)	Cohort 1	Triangular	2	1	4
	Cohort 2		3	1	4
	Cohort 3		2.75	0.5	4
	Cohort 4		5	3	10
	Cohort 5		4	1	10
Evacuation Speed (ESPEED, mph) (Section 4.2.7.2)	Cohort 1	Triangular	1	0.5	12
	Cohort 2		5	0.5	15
	Cohort 3		1	0.5	15
	Cohort 4		5	0.5	20
	Cohort 5		10	0.5	20
Hotspot Relocation Time (TIMHOT, hr) (Section 4.2.7.3)		Uniform	N/A	12	30
Normal Relocation Time (TIMNRM, hr) (Section 4.2.7.4)		Uniform	N/A	16	48
Hotspot Relocation Dose (DOSHOT, rem) (Section 4.2.7.5)		Triangular	5	1	7.5
Normal Relocation Dose (DOSNRM, rem) (Section 4.2.7.6)		Triangular	1	0.5	2
Weather Trials - Aleatory Uncertainty (Section 4.2.8)		N/A			

*Multiple values, refer to specific parameter section for discussion

4.2.1 Wet Deposition Model (CWASH1)

CWASH1 is a linear factor in the expression for the wet deposition rate for aerosols. A log uniform distribution was used to represent uncertainty with a lower bound of 10^{-6} and an upper bound of 10^{-4}. Under rain conditions, wet deposition is very effective and rapidly depletes the plume. This process can produce concentrated deposits on the ground and create what is often referred to as a hotspot (i.e., an area of higher radioactivity than the surrounding areas) [84]. The epistemic uncertainty associated with CWASH1 is potentially important in reactor accident consequence calculations because increasing values for CWASH1 result in increased local concentrations of radionuclides deposited by rainfall events. In turn, such increased local radionuclide concentrations can have two opposing effects on radiation exposure and resulting health effects. First, high local radionuclide concentrations can increase early individual exposure and resulting early health effects. Second, high local radionuclide concentrations can increase the total fraction of a radionuclide release that is interdicted, and thus decrease long term population exposure and resulting latent health effects. This happens because the localized, high-concentration area created by the rain is likely to be interdicted, reducing the

exposures to the residents in the long-term. Populations at longer distances receive less exposure because most of the plume has been washed out by the rain.

Rationale for Distribution

The model used in MACCS for wet deposition of aerosols over a unit area for a time interval [t_i, t_{i+1}] is formally given by

$$\mathrm{d}C(t)/\mathrm{d}t = -\lambda C(t) = -c_1 R^{c_2} C(t),$$

Eq. 4-5

where t = time (units: s), $C(t)$ = vertically integrated aerosol concentration in the plume at time t (units: Bq/m^2), $\lambda = c_1 R^{c_2}$ = fractional removal rate for aerosols (units: 1/s), R = rainfall rate (units: mm/hr), and C_1 (units: $1/\mathrm{s}(\mathrm{mm/hr})^{c_2}$) and C_2 (units: dimensionless) are constants used in the definition of λ. In turn,

$$\begin{aligned} D(t_i, t_{i+1}) &= C(t_i) - C(t_{i+1}) \\ &= C(t_i) - C(t_i)\exp\left[-\lambda(t_{i+1} - t_i)\right] \\ &\cong \lambda(t_{i+1} - t_i) C(t_i) \end{aligned}$$

Eq. 4-6

is the estimated aerosol deposition (units: kg/m^2) that takes place over the time interval [t_i, t_{i+1}].

In the computational implementation of aerosol deposition in MACCS, the rainfall rate R changes hourly for each rainfall event; however, the same values for C_1 and C_2 are used for all rainfall events. Although rainfall rate is taken into account in the definition of λ, it is well known that many additional properties of a rainfall event affect aerosol deposition, including (i) distribution of aerosol size, (ii) chemical and physical properties of aerosols, (iii) distribution of rain drop size, (iv) different aerosol removal rates within clouds (i.e., rainout) and below clouds (i.e., washout), and (v) short-term temporal variations in rainfall rate that are lost in reported hourly rainfall rates [60][64][65][66][67].

Given that MACCS uses fixed values for C_1 and C_2 for all rainfall events over the course of one year, the indicated range of properties that can affect aerosol deposition presents a major challenge in defining uncertainty distributions for C_1 and C_2. Specifically, the values used for C_1 and C_2 in MACCS are compromise values that are used for a large number of different rainfall situations, while being the most appropriate values to use for only a few of these situations. As a result, the epistemic uncertainty distributions for C_1 and C_2 should characterize the uncertainty in the locations of the most appropriate values to use for C_1 and C_2 given that a single value for C_1 and a single value for C_2 are used for all rainfall events. Given the manner in which C_1 and C_2 are used in MACCS, care must be taken to avoid using distributions for C_1 and C_2 that are intended to characterize the variability in C_1 and C_2 over the range of individual rainfall events, as the use of such distributions may produce unrealistic uncertainty analysis results. For example, the results of the expert elicitations for the wet deposition of aerosols in Appendix A of [68] appear to be for aleatory uncertainty over individual rainfall events.

The strategy adopted here to quantify the epistemic uncertainty associated with values for C_1 and C_2 chosen for universal use (i.e., for all rainfall conditions in a year of weather data) was first to look at the results of a number of studies that obtained values for C_1 and C_2 from data for real rainfall events or from computational models that incorporate effects that are difficult to quantify for observational data (e.g., [60], Tables 10 and 11; [65], Tables 7-11; [66], Table 3; [67], Equations (16) and (21); [69], Table 1; [70], Equations (1) and (2); [71], Figures 2 and 3; [72], Table 9). Next, choose a range of possible values for C_1 and C_2 that is representative of these values, while avoiding extreme values. The outcome of this effort was a range of [10^{-6}, 10^{-4}] for C_1 and a fixed value of 0.7 for C_2. A fixed value for C_2 was selected because, given a potential range of perhaps [0.6, 0.8] for C_2, the effects of the much larger range for C_1 should dominate the effects of the uncertainty associated with C_2. Given the absence of a reason to assign a particular distribution to the possible values for C_1, a log-uniform distribution is specified for the indicated range of [10^{-6}, 10^{-4}] so that each order of magnitude is assigned the same probability (i.e., 0.5). The CDF is presented in Figure 4-47. C_1 and C_2 in the above discussion correspond to CWASH1 and CWASH2 in the MACCS framework, respectively.

As noted above, the CWASH2 parameter was also considered, but there are insufficient data to support development of a defensible distribution. Furthermore, CWASH1 captures the effect of wet deposition sufficiently such that it was not necessary to evaluate CWASH2 as an exploratory parameter.

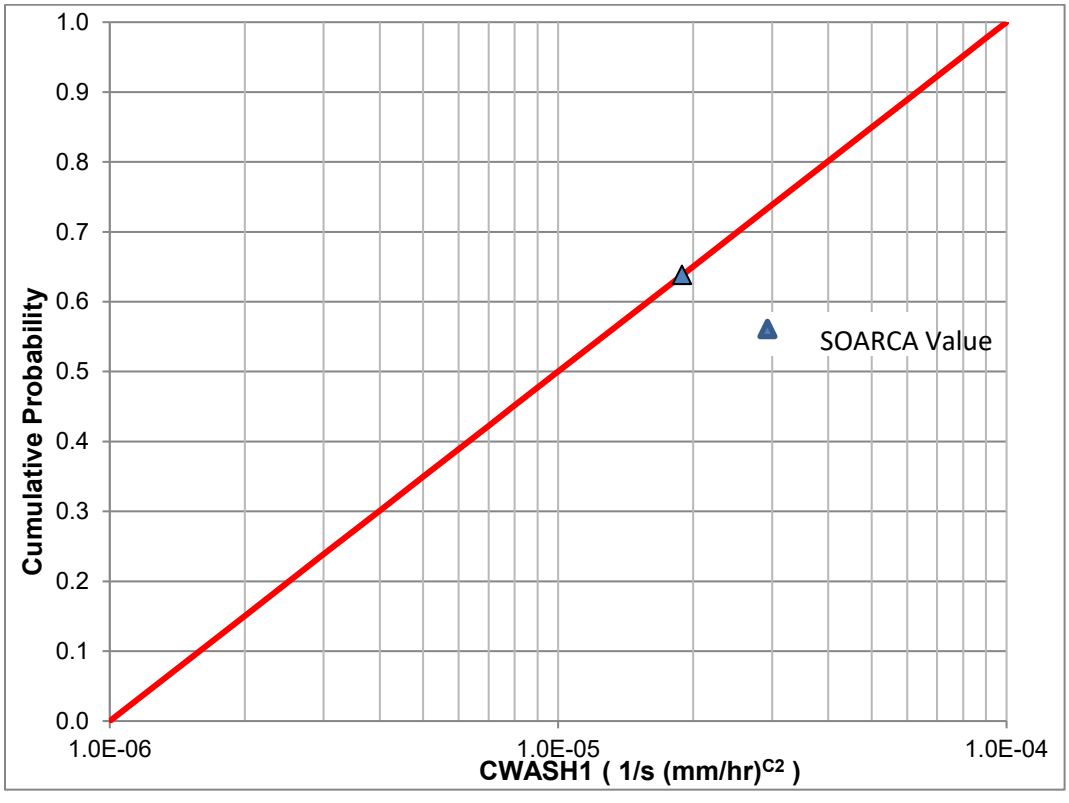

Figure 4-47 CDF of the Linear Coefficient CWASH1

4.2.2 Dry Deposition Velocities (VDEPOS)

Dry deposition velocities are established by aerosol bins to represent the dependence of deposition velocity on particle size. A triangular distribution is used to represent uncertainty in each of nine aerosol particle sizes. Dry deposition is the only mechanism for deposition onto the ground for more than 90 percent of the hours of the year at Surry (i.e., the hours during which precipitation does not occur). Since long-term exposures usually contribute more than 50 percent of the overall exposure, deposition is important because deposited material is the only source of exposure during the long term. Furthermore, the PB UA indicated that dry deposition velocity is the most important parameter of all those considered for individual latent cancer risk.

Dry deposition involves a variety of mechanisms that cause aerosols to deposit, including gravitational settling, impaction onto surface irregularities, including buildings and other manmade structures, and Brownian diffusion. Dry deposition is a much slower process than wet deposition, but occurs continuously, whereas, wet deposition occurs intermittently. Larger values of dry deposition velocity result in larger long-term doses at shorter distances and smaller doses at longer distances. The converse is also true that smaller values of dry deposition velocity result in smaller long-term doses at shorter distances and larger doses at longer distances.

Rationale for Distribution

As a starting point, the distributions for dry deposition velocity use the expert elicitation data in NUREG/CR-6244 [68]. These expert data are evaluated in *Synthesis of Distributions Representing Important Non-Site-Specific Parameters in Off-Site Consequence Analysis* [73], Section 3. The expert data show uncertainty ranges of nearly five orders of magnitude for small particles (0.1 μm) and about three orders of magnitude for large particles (10 μm). These ranges seem larger than should be expected for representative values that are to be applied to an entire year of weather trials. In reviewing the expert elicitation documents, it is likely that the experts interpreted the uncertainty to represent instance by instance uncertainties rather than representative values for a large set of weather trials to represent one year of weather data.

In NUREG/CR-4551, Vol. 2, Rev.1, Part 7, pp. 2-18 to 2-20 [74] the authors describe the uncertainty in deposition velocity for NUREG-1150 [16]. In that study, a single deposition velocity was used to characterize the entire range of aerosol sizes that would be released into the atmosphere during a reactor accident. The best estimate, based on empirical equations and physical models, was that deposition velocity is 0.3 cm/s and that the reasonable range of uncertainty is 0.03 to 3 cm/s, a range of a factor of 100. This range accounts for uncertainties in aerosol size, wind speed, surface roughness, and aerosol density. Of these uncertainties, aerosol size is explicitly accounted for in the current study, but uncertainty in the other three parameters should have an effect on the overall uncertainty in deposition velocity. This reasoning should lead to an uncertainty range for a specific aerosol size that is less than two orders of magnitude, which is clearly narrower than the range provided in the expert elicitation study. Another parameter not discussed in the NUREG-1150 documentation is aerosol shape factor, but this should have a relatively minor contribution to uncertainty in deposition velocity.

Estimation of the importance of wind speed, surface roughness, and aerosol density can be made from Eq. 4-14, which is equation 3.1 in [73]. The coefficients *a* through *f* were chosen to be 50th percentile values from Table 3-1 in the same reference. For establishing a range of deposition velocities considering uncertainties in surface roughness and wind speed, the important parameters in the equation are *e* and *f*, which are respectively 1.061 and 0.169 in the

table. By examining the meteorological data file for Surry, a representative range for wind speed is 1 to 10 m/s, with 2.2 m/s being the annual mean wind speed at Surry. From Equation 4-14, this range in wind speed leads to about a factor of 5 in deposition velocity. A representative range for surface roughness at Surry is 0.1 to 0.6 m [3]. Based on Equation 4-14, this range in surface roughness leads to about a factor of 2 in deposition velocity. Aerosol density has a significant effect for larger particles and a negligible effect for small particles, as can be seen from Figure 2-13 in [74]. For larger particles, a range of 4 in particle density corresponds to a range of about 2 in deposition velocity. For small aerosols, particle density has almost no effect on deposition velocity and for that reason it is not included here. From this discussion, assuming that the influences of wind speed and surface roughness are independent, which is reasonable, then the uncertainty range in deposition velocity to account for these effects should be about a factor of 10.

$$ln(v_d) = a + b\left(\ln d_p\right) + c\left(\ln d_p\right)^2 + d\left(\ln d_p\right)^3 + e \cdot z_0 + f \cdot V$$

Eq. 4-714

Where

$d_p = hydrodynamic\ particle\ diameter, (\mu m)$
$z_0 = surface\ roughness, m$
$v_d = deposition\ velocity, cm/s$
$V = wind\ speed, m/s$
$a, b, c, d, e, f =$ correlation coefficients

The above discussion corresponds to the following equation, which is simply the difference in Eq. 4-14 evaluated at an upper bound and a lower bound set of values:

$$ln(v_d)_{UB} - ln(v_d)_{LB} = \ln\left(\frac{(v_d)_{UB}}{(v_d)_{LB}}\right) = e \cdot [(z_0)_{UB} - (z_0)_{LB}] + f \cdot [(V)_{UB} - (V)_{LB}]$$
$$= 1.061 \cdot (0.6 - 0.1) + 0.169 \cdot (10 - 1) \quad \text{Eq. 4-15}$$

where

UB indicates an upper bound value

LB indicates a lower bound value

Solving Eq. 4-15 for the ratio of the upper bound to the lower bound value of deposition velocity produces a factor of about 8. This value is rounded up to a factor of 10 to account for variations in particle size and density within a bin.

To construct distributions to be used in this study for each aerosol size, the 50th percentile values from the expert elicitation are used as the modes of a set of triangular distributions. These values were chosen because, although the distributions from the expert elicitation process are considered too wide, the median values from these distributions should represent best estimates from the group of experts. The lower and upper bounds of triangular distributions are chosen to be the mode divided and multiplied by the square root of 10, respectively. The 50th percentile values from the expert elicitation (modes of the triangular distributions) are evaluated from Eq. 4-14 with choices for surface roughness to be 0.22 m (based on the newer

approach to estimating surface roughness, as described in [7]) and wind speed to be the mean Surry wind speed, 2.2 m/s. The distribution parameters are tabulated in Table 4-17 and shown in Figure 4-48.

Table 4-17 Dry Deposition Velocities

Triangular Distributions	Deposition Velocity (m/s)		
Representative Aerosol Diameter (μm)	Lower Bound	Mode	Upper Bound
0.15	1.46E-04	4.62E-04	1.46E-03
0.29	1.34E-04	4.24E-04	1.34E-03
0.53	1.76E-04	5.55E-04	1.76E-03
0.99	2.96E-04	9.36E-04	2.96E-03
1.8	5.79E-04	1.83E-03	5.79E-03
3.4	1.18E-03	3.75E-03	1.18E-02
6.4	2.28E-03	7.22E-03	2.28E-02
12	3.75E-03	1.18E-02	3.75E-02
22	4.72E-03	1.49E-02	4.72E-02
41	1.63E-02	5.15E-02	1.63E-01

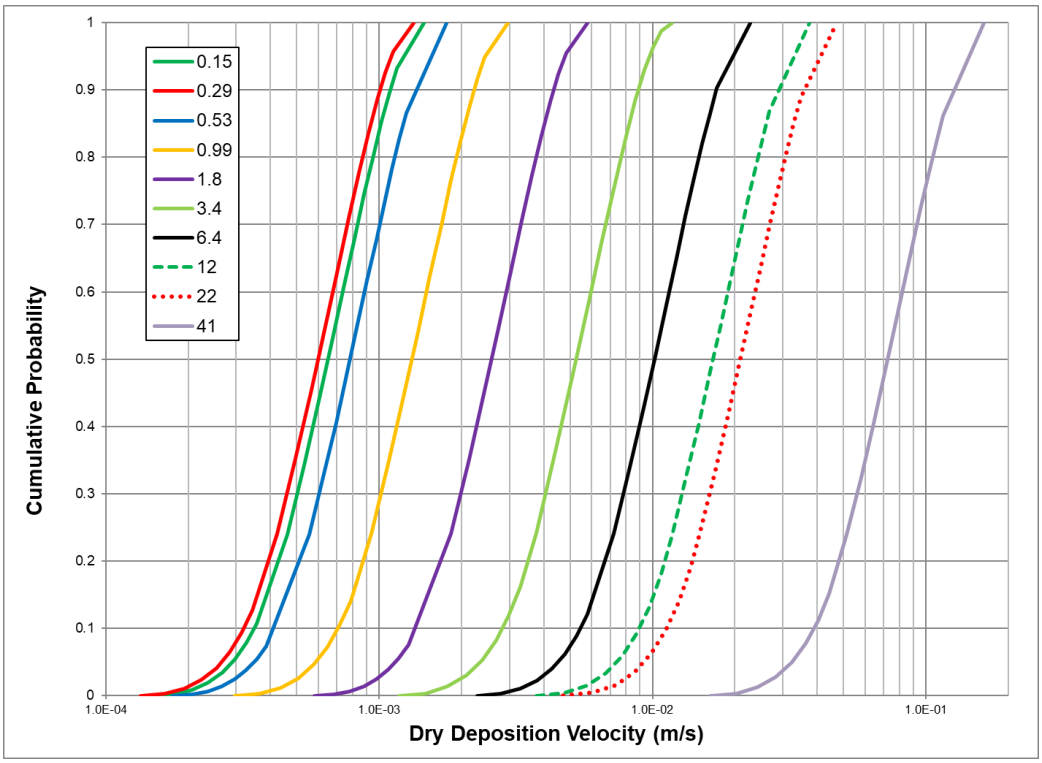

Figure 4-48 CDF of Dry Deposition Velocities for Mass Median Diameters Representing MACCS Aerosol Bins

VDEPOS is assumed to be perfectly rank-order correlated across aerosol sizes. This prevents small aerosols from depositing faster than large aerosols, which would contradict our understanding of aerosol physics. Rank-order correlation is the most commonly used method of computing a correlation coefficient using the rank order of the sampled values between two variables, rather than the absolute value sampled from the distribution.

4.2.3 Shielding Factors (GSHFAC and PROTIN)

As described in the MACCS code manual [80], in general the dose equation for an early exposure pathway in a given spatial element is the product of the radionuclide concentration, dose conversion factor, duration of exposure, and a shielding or protection factor. For the cloud inhalation exposure pathway, the quantities are the ground-level air concentration within a spatial element, inhalation dose conversion factor, duration of exposure, and inhalation protection factor. For the groundshine pathway, the quantities are the ground concentration, groundshine dose conversion factor, duration of exposure, and groundshine shielding factor. MACCS calculates groundshine dose as though an individual were located on an infinite flat plane onto which deposition occurs, consistent with Federal Guidance Report (FGR) 12 [80]. The shielding factor accounts for effects of surface roughness and shielding offered by a building or set of buildings that block a portion of the gamma radiation.

The shielding or protection factor is a unitless quantity used to reduce the radiation dose to account for protection provided by a given protective action or mitigating environmental condition. Shielding or protection factors are specified by the user for the cloudshine, inhalation, groundshine, and skin dose exposure pathways, and for three activity types (evacuation, normal activity, and sheltering) [80]. A shielding factor of unity represents the limiting case of a person

receiving the full dose (i.e., standing outdoors and completely unprotected from exposure), and a shielding factor of zero represents the limiting case of complete shielding from the exposure. As part of the SOARCA project, Dr. Keith Eckerman provided an updated technical basis and methodology for radiation dose and health risk estimation [76]. This reference provided much of the basis for the shielding factors, as described below, and other risk factors discussed within this study.

During the investigation of the cloudshine shielding factor, CSFACT, issues were identified regarding the source data, which was an unpublished internal Sandia document "Recommendations for MACCS2 Parameter Uncertainty Distributions," prepared by Heames, et al. in 2003. The internal Sandia report was an attempt to use data from expert elicitation to create distributions for MACCS parameters, and was based on an earlier Sandia letter report [75]. However, while the distributions in Gregory [75] for inhalation and groundshine are identical to Heames, there is no distribution in Gregory [75] for cloudshine and no supporting discussion. Physically, cloudshine shielding and inhalation protection are completely different. Protection from cloudshine represents the fraction of radiation from a plume external to a structure is able to reach the interior of the structure; inhalation protection is the fraction of the external concentration that leaks into a structure and is able to be inhaled. Because physically the two distributions should not be identical and because there is no discussion in either source regarding the basis for a distribution for cloudshine shielding factor, a point value was used in the UA. Since the cloudshine pathway is typically a small contributor to overall dose in MACCS analyses, using a point value for the shielding factor should have a minor effect on the estimated uncertainties.

4.2.3.1 Groundshine Shielding Factors (GSHFAC)

The values of GSHFAC are important because the doses received from groundshine are directly proportional to these factors and groundshine is usually the most important of the long-term dose pathways. Uncertainty exists in factors that affect GSHFAC, such as indoor residence time, household shielding value, and departures from the infinite flat plane assumptions. There are additional contributions to uncertainty in the energy deposited within a human organ for a specified incident radiation, which is represented by the groundshine deposited energy (GSDE) scaling factor. GSDE is a dimensionless scaling factor used to account for the amount of ionizing radiation energy deposited within various human organs from external radiation emanating from the ground. These uncertainties of the deposition in individual organs stem from age, height, and weight variations of the exposed population and are incorporated into GSDE uncertainty; but GSDE is not a specific MACCS input. So the uncertainty in GSDE is incorporated into GSHFAC uncertainty distribution, as explained below. The two mechanisms, shielding from structures and energy deposition into organs, are independent and so are treated as being uncorrelated.

Rationale for Distribution

Piecewise uniform distributions (normal activity, sheltering, and evacuation) for the combined GSHFAC and GSDE uncertainty were implemented in MACCS as an overall uncertainty for GSHFAC. Construction of this distribution function is described in the following paragraphs.

The piecewise uniform values used in GSHFAC represent a combination of uncertainty derived from NUREG/CR-6526 [77] and uncertainty in GSDE. Gregory et al. [75] evaluated the expert data to derive distributions for groundshine from NUREG/CR-6526. In Gregory et al. [75], three

types of activity, normal, sheltering, and evacuation, are evaluated for the groundshine dose pathway, resulting in three sets of shielding factors, shown on Figure 4-49.

Regarding GSDE, to simplify the implementation of uncertainty in the energy deposited within a human organ for a specified incident radiation, Eckerman [76] recommends that a single triangular distribution be applied as a multiplicative factor for all radionuclides and for all organs. Eckerman [76] recommends a triangular distribution with a minimum of 0.5, a peak (mode) of 0.8, and a maximum of 1.5 which incorporates variations in ionizing radiation energy and human body variations from age, sex, height, and weight. The triangular distribution used to represent uncertainty in the dose coefficients for GSDE is shown in Figure 4-50.

Furthermore, Eckerman [76] suggests that the uncertainties in organ-specific groundshine dose conversion factors are highly correlated. As a result, this UA combines the uncertainty in GSHFAC and the uncertainty in the dose coefficients (i.e., through the GSDE uncertainty distribution) into a single uncertainty factor, which can be implemented as an overall uncertainty in the GSHFAC input for MACCS. The uncertainties in the GSHFAC and the groundshine dose coefficients are treated as uncorrelated, since they have no relation (i.e., the shielding from a building (GSHFAC) does not bear upon variations in organ geometry or variations in ionizing radiation energy).

Table 4-18 shows the combination of uncertainty in GSHFAC and GSDE for all cohorts considered. For long-term groundshine exposure, the distribution is assumed to be the same as for normal activity. GSHFAC is specified to be the same for each of the six cohorts in this UA, with one exception. Cohort 4, which is the population in special facilities, uses the same shielding factors for normal activity as for sheltering because this cohort is normally indoors and resides in fairly stout concrete structures that provide better shielding than typical housing.

The distributions for normal activity and evacuation are uncorrelated, i.e., a rank correlation coefficient of 0.0. The distributions for normal activity and sheltering are correlated with a rank correlation coefficient of 0.8 because both represent fractions of time spent indoors. The distributions for sheltering and evacuation are taken to be uncorrelated. The distributions for normal activity and long-term groundshine shielding factors are considered perfectly rank correlated (RRC is 1.0). No correlation is assumed between GSHFAC and inhalation protection factors (PROTIN).

Figure 4-51 shows the final piecewise uniform distributions used for GSHFAC. The Surry SOARCA [3] values are also provided for the normal, sheltering, and evacuation activities and long-term activity. The long-term shielding factor is taken to be identical to the value for normal activity during the emergency phase.

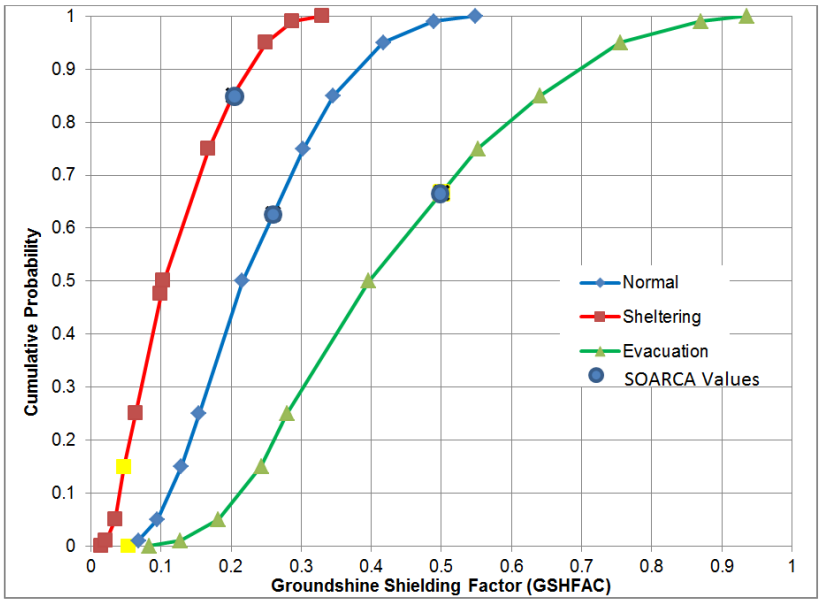

Figure 4-49 Cumulative Distribution Functions of GSHFAC for Normal Activity, Sheltering, and Evacuation Based on Expert Elicitation Data

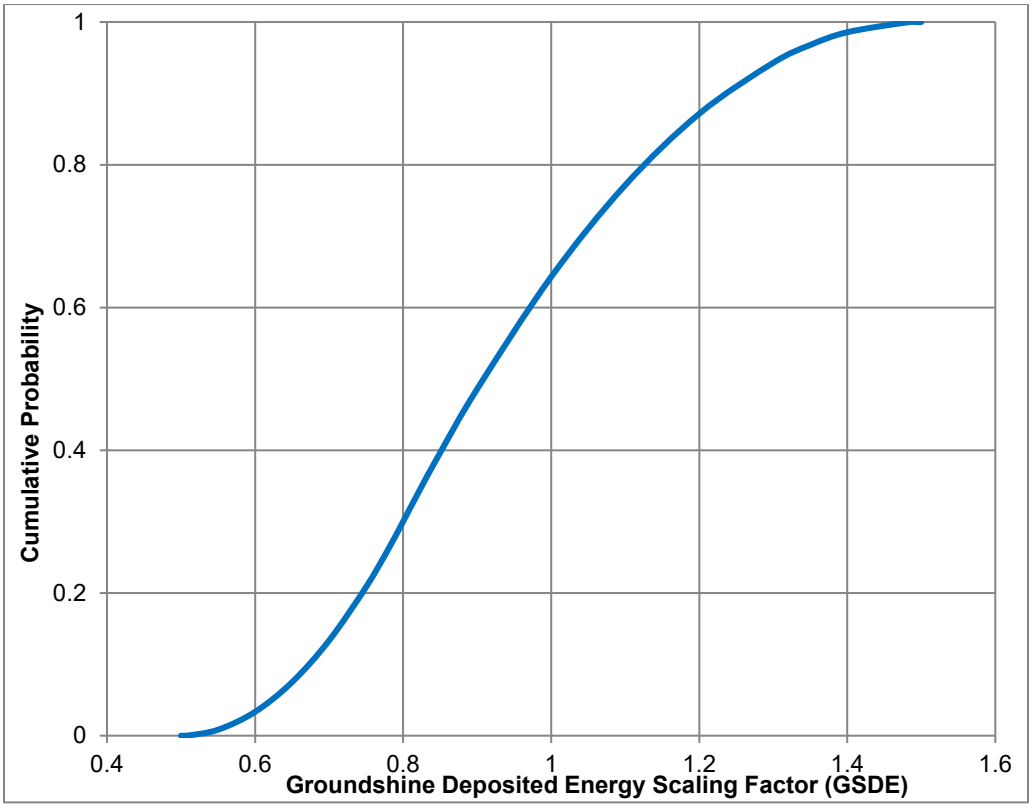

Figure 4-50 Cumulative Distribution Function of GSDE

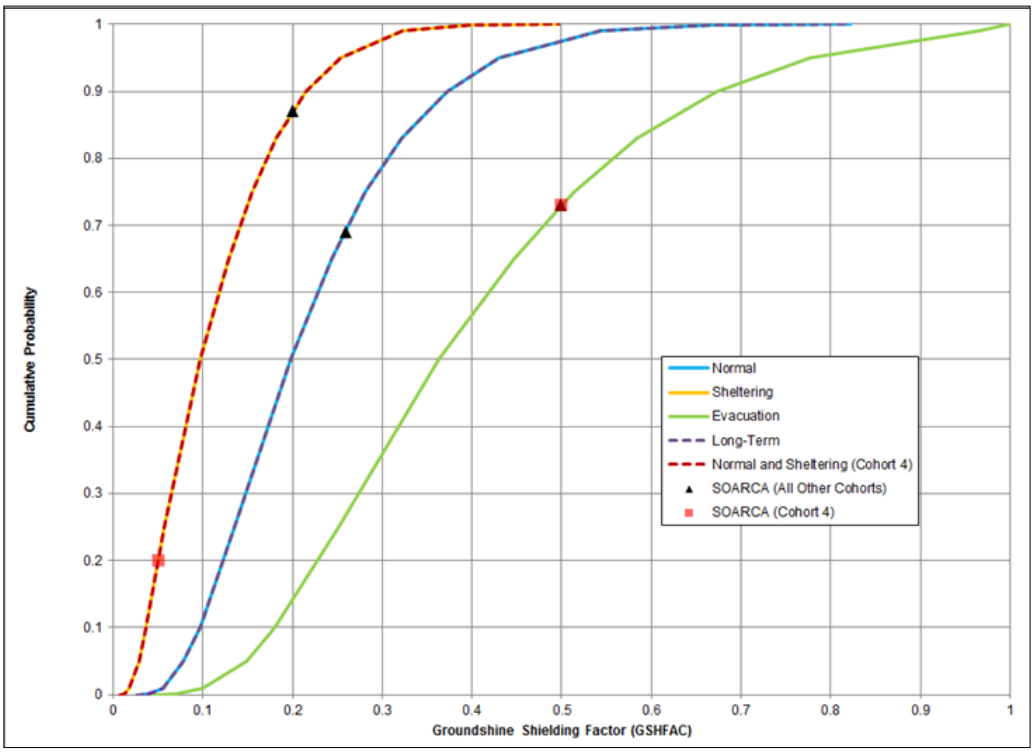

Figure 4-51 CDF of GSHFAC accounting for uncertainty in GSDE

Table 4-18 Groundshine Shielding Factor Distribution Parameters. A Value of Unity Represents Full Groundshine for a person standing on an Infinite Flat Plane with Uniform Concentration; a Value of Zero Represents Complete Shielding

Continuous Linear Distributions	Groundshine Shielding Factor (-)		
Quantile Value	Evacuation for All Cohorts	Normal Activity for All but Cohort 4 and Long-Term Activity for Entire Population	Sheltering for All Cohorts and Normal Activity for Cohort 4
0	0.0415	0.0265	0.0075
0.001	0.0692	0.0394	0.0120
0.01	0.1001	0.0552	0.0179
0.05	0.1491	0.0784	0.0286
0.1	0.1804	0.0967	0.0361
0.25	0.2504	0.1354	0.0563
0.5	0.3635	0.1979	0.0969
0.65	0.4464	0.2433	0.1288
0.75	0.5146	0.2816	0.1549
0.83	0.5843	0.3211	0.1818
0.9	0.6717	0.3719	0.2148
0.95	0.7768	0.4297	0.2533
0.99	0.9665	0.5441	0.3226
0.999	N/A	0.6660	0.3975
1	1.0000	0.8220	0.4965

4.2.3.2 Inhalation Protection Factors (PROTIN)

The inhalation dose protection factor is represented by PROTIN. Population dose is reduced through the PROTIN inhalation protection factor based on the activity the population is engaged in, such as sheltering, evacuating, or performing normal activities. The inhalation shielding factors used in the MACCS calculation are important because the doses received from inhalation are directly proportional to these factors and dose is a key metric in this analysis. The distributions used in this UA are derived from NUREG/CR-6526 [77] which collected data from an expert elicitation panel on deposited material and external doses. The expert data indicates that there is a large range of uncertainty in expert best estimates on the inhalation protection factor.

Rationale for Distribution

Gregory et al. [75] evaluated the expert data in [77] to derive distributions for the inhalation protection factor. Three distributions were derived, one each for normal activity, sheltering, and evacuation. Only data from the U.S. expert were used to determine the time spent in various structures (outdoors, vehicles, and low-, medium-, and high-shielded buildings). These data provided the needed information for the normal activity type. The times were shifted towards outdoors in vehicles for evacuation and shifted towards high shielded buildings for sheltering. To determine the final distributions from all the experts, the air concentration ratios (indoors/outdoors) were considered for both normally ventilated buildings and buildings with all windows closed.

In reviewing these distributions, it appears that the ranges of the distributions are too large, especially for sheltering and evacuation, with the protection factor for sheltering skewed toward too little protection and evacuation skewed toward too much protection. The experts seemed to be answering the question of what are the maximum and minimum possible protection factors for any individual person in the zone, whereas for this work, a representative value for all people in the zone is needed.

To verify that these judgments are correct, the Gregory distributions were compared to distributions for inhalation protection factor given in NUREG/CR-4551 [74], which were prepared for NUREG-1150. This source recommended a uniform distribution from 0.15 to 1.0 for normal activity, a uniform distribution from 0.1 to 0.4 for sheltering, and a constant value of 1.0 (no protection) for evacuation.

The recommended distribution for normal activity is similar to the distribution in [75]; whereas, the distribution for sheltering has a significantly smaller range because it only allows for relatively high amounts of protection, indicating sheltering is in stouter building structures. In practice sheltering may be enforced wherever people currently are (shelter in place), so the higher values in [75] are plausible for some individuals but not for an entire cohort.

Thus, the decision was made to use the ranges for sheltering and normal activities from [75], except with a truncation at the 0.2 and 0.8 quantiles of each CDF to be representative of cohorts instead of a single member of a cohort. New CDFs were drawn, using the 0.2 and 0.8 quantile values as the upper and lower bound with an additional 0.5 quantile value anchor. The distributions are defined to be piecewise-uniform. Figure 4-52 also shows the SOARCA values as black triangles, which were obtained from the NUREG-1150 defaults [16].

The single inhalation protection factor of 1 for evacuation [74] is significantly different than the values from the distribution in [75], which includes low values for PROTIN that are difficult to defend. Additionally, the SOARCA default for evacuation of 0.98, which came from NUREG/CR-6953, Volume 1 [78], is still considered the best estimate. Therefore, the best judgment was to create a uniform distribution from 0.9 to 1.0, which allows for a limited uncertainty investigation in PROTIN for evacuation but doesn't include high amounts of protection indicated in Gregory that do not seem physically possible for an entire cohort.

The distribution for the long-term inhalation protection factor is assumed to be the same as the distribution for normal activity during the emergency phase. PROTIN must be specified for each cohort (population group) in a MACCS analysis. In the Surry SOARCA analysis [3], shielding values for Cohorts 1, 2, 3, 5, and 6 are identical. Cohort 4 represents special facilities, which had different shielding values in the Surry SOARCA analysis [3]. Because normal activity for Cohort 4 would be approximately the same as sheltering due to the robust nature of the special facility buildings, the distribution for normal activity was chosen to be the same as for sheltering for Cohort 4. These distributions are shown in Figure 4-52 as dashed lines overlaying the base distributions.

The distributions for normal activity and sheltering are correlated with a rank correlation coefficient of 0.75, based on the assumption that the majority of normal activity is indoors. Therefore, if sheltering is sampled with a lower value, normal activity should also be a lower value. The distributions for normal activity and long-term inhalation are also perfectly rank correlated. No correlations are assumed between PROTIN and the groundshine shielding factor (GSHFAC) for any of the three activity types, evacuation, normal activity, and sheltering.

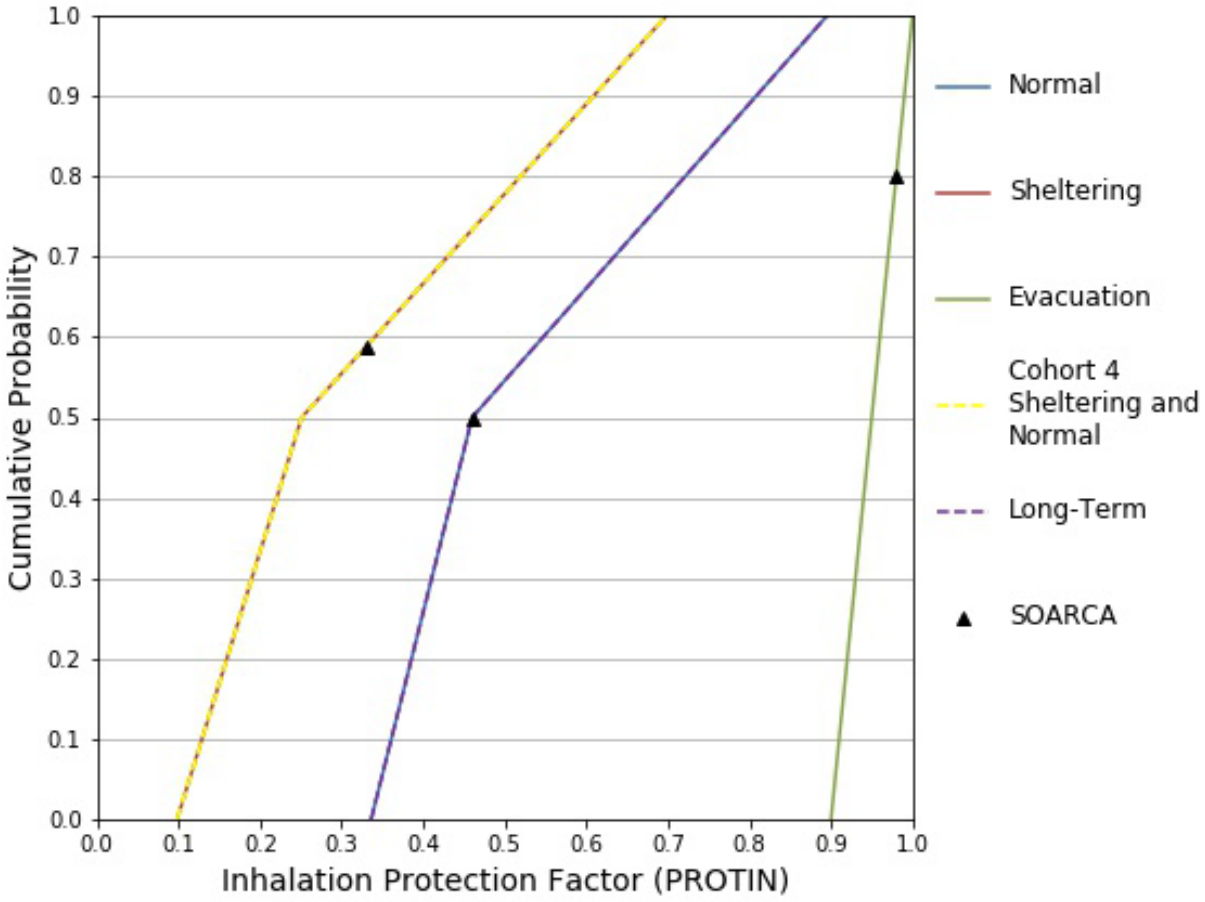

Figure 4-52 CDFs of PROTIN for Normal Activity, Sheltering, and Evacuation

Table 4-19 Inhalation Protection Factor Distribution Parameters. A Value of Unity Represents Direct Inhalation from a Passing Plume; a Value of Zero Represents Complete Protection

	Inhalation Protection Factor (-)		
	Implemented as a Uniform Distribution	Continuous Linear Distributions	
Quantile Value	Evacuation for All Cohorts	Normal Activity for All but Cohort 4 and Long-Term Activity for Entire Population	Sheltering for All Cohorts and Normal Activity for Cohort 4
0	0.9	0.336	0.098
0.5	N/A	0.460	0.251
1	1.0	0.896	0.699

4.2.4 Early Health Effects (EFFACA, EFFACB, EFFTHR)

When radioactive material is inhaled and retained in the respiratory system, an individual may continue to receive a radiation dose for long periods of time after the material was inhaled. Depending on particle size and chemical form, clearance mechanisms may remove the material

from the body or transport it from the respiratory system to other organs of the body. The MACCS early health effects model accounts for dose protraction from radioactive material inhaled and retained within the body and calculates an effective acute dose, i.e., a one-day dose that would induce the same effects as the protracted dose [80]. External radiation is only received during the exposure period, so dose protraction is not usually an issue.

The individual risk of an early fatality is modeled in MACCS using a three-parameter hazard function, expressed in Eq. 4-16 for specified target organs (i.e., red bone marrow, lungs, and stomach) with an acute dose threshold. The early health effects parameters represented in the equation include:

- Early Health Effects LD50 Parameter (EFFACA),
- Early Health Effects Exponential Parameter (EFFACB), and
- Early Health Effects Threshold Dose (EFFTHR).

The Weibull function contains the EFFACA parameter for the lethal dose to 50 percent of the population (LD_{50}), EFFACB as an exponential parameter that defines the steepness of the dose-response function, and a threshold dose defined by EFFTHR.

$$H = 0.693 \left(\frac{DOSE}{EFFACA}\right)^{EFFACB}$$

Eq. 4-16

Where:

H =	hazard function for individual risk of an early fatality (unitless)
DOSE =	effective acute dose (Gy) to a target organ. DOSE is set to zero when it is below the threshold, EFFTHR
EFFACA =	LD_{50} (Gy) for a specific health effect
EFFACB =	the exponential parameter in the hazard function (unitless)

All three of the variables used to determine the individual risk of early fatality in Eq. 4-16 are treated as uncertain. Furthermore, there are three values for each of the parameters for the three organs listed above. A dose to each of the organs is associated with a specific type of early fatality, as follows: (1) an acute dose to the red bone marrow is used to assess occurrences of the hematopoietic syndrome, (2) an acute dose to the lungs is used to assess occurrences of the pulmonary syndrome, and (3) an acute dose to the stomach is used to assess occurrences of the gastro-intestinal syndrome.

When estimating early health effects, it is appropriate to use gray (Gy) as the unit of measure for doses. Doses measured in gray and Sieverts (Sv) are the same for low linear energy transfer (LET) radiation (gamma and beta), but different for high LET radiation (alpha). Doses in Sieverts are based on a standard radiation weighting factor for high LET radiation of 20; doses from high LET radiation in units of gray are based on either a value of unity or a nonstandard value for radiation weighting factor. In the case of latent health effects, a Sievert captures the biological effects of radiation in terms of the risk of cancer induction. In the case of early health effects, a nonstandard radiation weighting factor of 10 is used for acute doses. This difference is because high LET radiation has a different biological impact for early health effects than it does for latent health effects.

4.2.4.1 Early Health Effects LD_{50} Parameter (EFFACA)

The EFFACA parameter represents LD_{50}, the lethal dose to 50 percent of the population, in the hazard function for a target organ [80]. The effective acute dose commitment period is up to one year for inhaled radionuclides. The EFFACA distribution is based on data provided for the estimation of four types of early health effects, hematopoietic syndrome, gastrointestinal syndrome, pulmonary syndrome, and pneumonitis [73]. The first three of these early health effects are potentially fatal and are included in the documented results. Pneumonitis is generally nonfatal, and was not reported.

Rationale for Distribution

The EFFACA distribution for the three target organs considered are piecewise uniform and are based on linear interpolation between data points taken from Table 6-1 of NUREG/CR-7161, Bixler et al. [73]. The basis for the EFFACA distribution are uncertain characteristics associated with estimation of four types of early health effects, and are taken directly from Bixler et al. [73] and are derived expert elicitation values provided in NUREG/CR-6545. The parameter distributions and SOARCA values associated with the three fatal, early health effects are shown on Figure 4-53. The upper and lower bounds of each of the distributions incorporate the entire range of the expert elicitation data [73].

Bixler et al. [73] recommended that EFFACA be correlated with the early health effects threshold parameter (EFFTHR) for the same health effect using a 1.00 rank correlation coefficient [73].

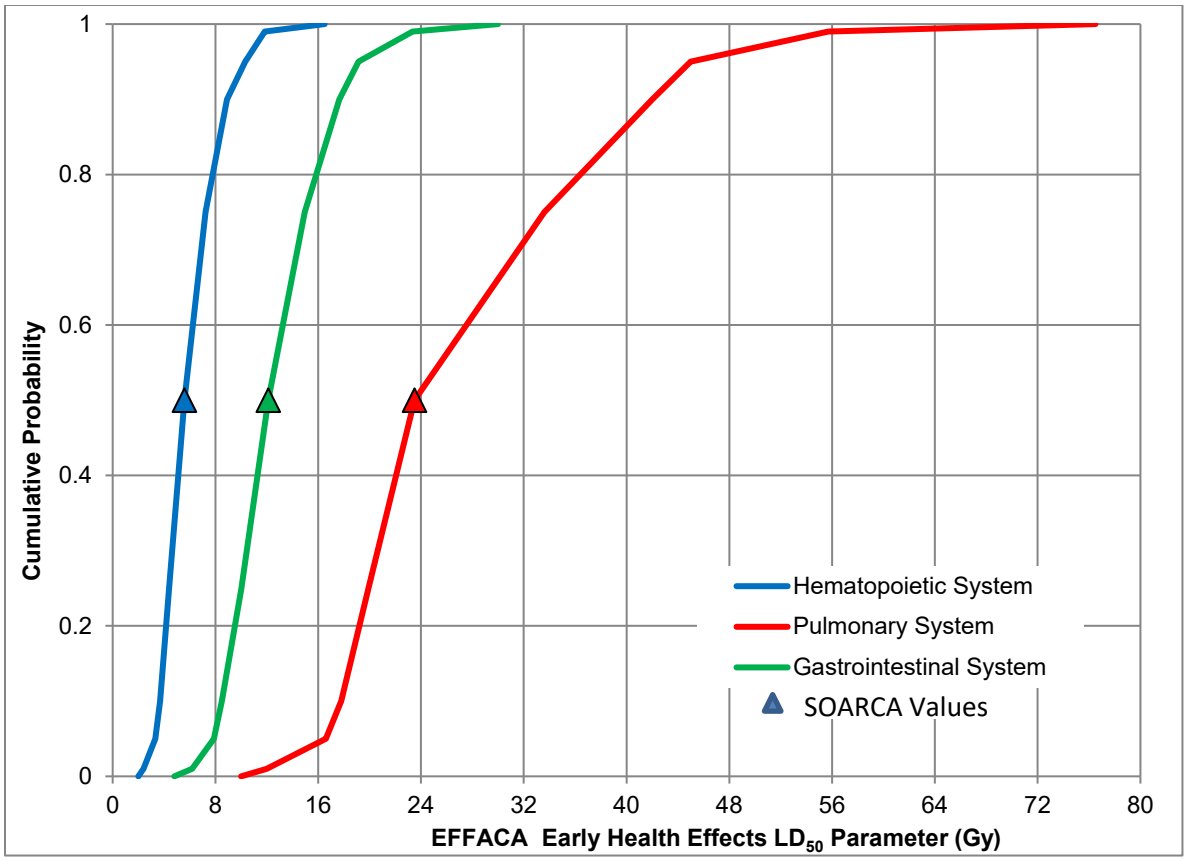

Figure 4-53 CDFs of EFFACA for Specified Health Effects

4.2.4.2 Early Health Effects Exponential Parameter (EFFACB)

The EFFACB parameter represents the exponential or shape factor in the hazard function for the target organ [80]. The same target organs identified with EFFACA are considered here. Again, pneumonitis is nonfatal, was not included as an uncertain parameter, and does not contribute to any reported results.

Rationale for Distribution

The EFFACB distribution for all three target organs considered are piecewise uniform, and are based on linear interpolation between data points taken from Table 6-1 of Bixler et al. [73]. The basis for the EFFACB distributions is derived from NUREG/CR-6545 and evaluated by Bixler et al. [73]. The parameter distributions and SOARCA values associated with these three potentially fatal early health effects for EFFACB are shown on Figure 4-54. The Surry SOARCA values [3] are the median values from these distributions, as shown in the figure. The upper and lower bounds of each of the three distributions incorporate the entire range of the expert elicitation data [73].

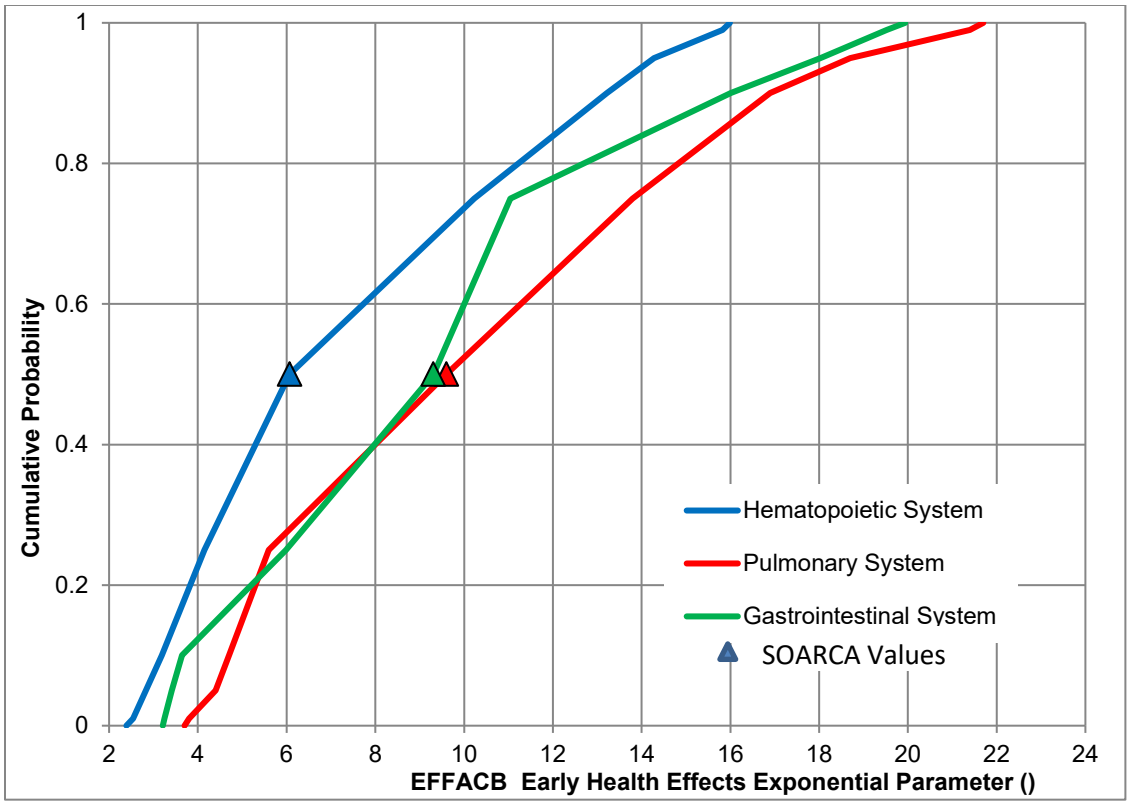

Figure 4-54 CDFs of EFFACB for Specified Health Effects

4.2.4.3 Early Health Effects Threshold Dose (EFFTHR)

The EFFTHR parameter represents the threshold dose associated with the target organ [80]. The same target organs identified with EFFACA and EFFACB are considered here. Pneumonitis is not included for the reasons discussed above.

Rationale for Distribution

The EFFTHR distribution for all three target organs considered are piecewise uniform, and are based on linear interpolation between data points taken from Table 6-1 of Bixler et al. [73]. The EFFTHR distributions are derived from NUREG/CR-6545 and evaluated by Bixler et al. [73]. The parameter distributions and SOARCA values associated with these three potentially fatal early health effects for EFFTHR are shown on Figure 4-55. The Surry SOARCA values [3] were chosen to be the medians of these distributions. The upper and lower bounds of each of the three distributions incorporate the entire range of the expert elicitation data [73].

For each health effect, EFFTHR is correlated with the early health effects LD_{50} parameter (EFFACA) for the same health effect using a rank correlation coefficient of 1.00 [73].

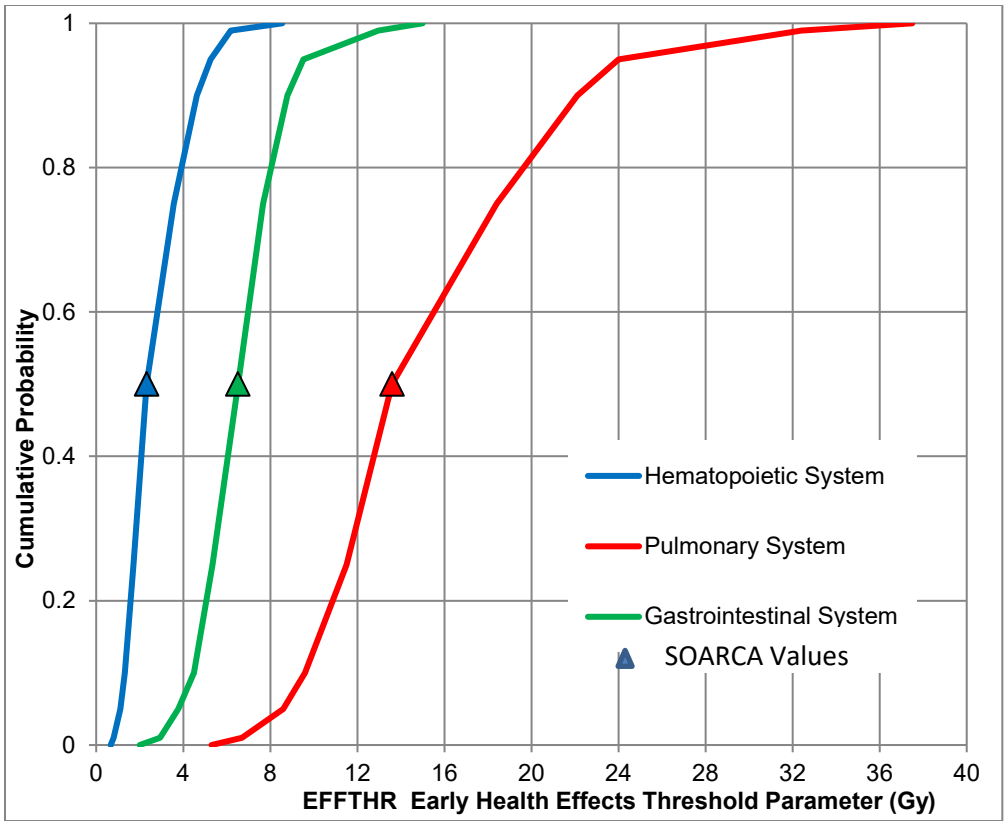

Figure 4-55 CDFs of EFFTHR for Specified Health Effects

4.2.5 Latent Health Effects (DDREFA, CFRISK, Long-Term Inhalation Dose Coefficients)

4.2.5.1 Dose and Dose Rate Effectiveness Factor (DDREFA)

The dose and dose rate effectiveness factor (DDREFA) is a dimensionless dose- and organ-dependent reduction factor. Epidemiological studies used in the development of radiation exposure risk models involved subjects who experienced high radiation doses delivered in a relatively short time period [76]. There is evidence that indicates that the biological response per unit dose at low doses may be an overestimation if one extrapolates from observations made with high, acutely delivered doses [76]. The degree of overestimation is commonly expressed in terms of a dose and dose rate effectiveness factor. DDREFA is used in MACCS to modify the organ-specific lifetime cancer fatality risk factors (CFRISKs) in order to distinguish between low and high dose exposures incurred during the early phase. There is significant uncertainty in DDREFA because there is a large amount of scatter in dose-response data at lower dose levels.

For this analysis, low dose is defined as 0.2 Gy (20 rad) or less and low dose rate is defined as 0.1 mGy/min (600 mrad/hr) or less [76]. MACCS only considers dose and not dose rate in the implementation of DDREFA. In MACCS, doses received during the emergency phase are divided by DDREFA when the committed dose is less than 0.2 Gy. Doses received during the

long-term phase are assumed to be controlled by the habitability criterion to be well below 0.2 Gy, so these doses are always divided by DDREFA in the calculation of latent health effects.

Rationale for Distribution

Age- and gender-averaged cancer mortality risk uncertainties were developed for SOARCA [3][76]. Additionally, Eckerman [76] recommends a PDF specific for breast cancer and all other types of cancer for low LET radiation. However, the PDFs provided did not integrate to unity; therefore, the PDF equations were normalized as shown in Figure 4-56. An upper limit of DDREFA is 3.0 for breast and 8.0 for other cancers [76].

Eckerman recommended that high LET radiation be assigned a DDREFA of unity (1.0) with no uncertainty [76]; however, the distinction between low and high LET radiation to an organ cannot be distinguished within the MACCS framework; therefore, the PDFs suggested for low LET radiation are applied to all types of radiation. To implement the uncertainty in DDREFA, the CDF was segmented into equally spaced quantiles to construct a piecewise uniform distribution as shown in Figure 4-57. The SOARCA values are represented in Figure 4-57 by the blue triangles.

The value of DDREFA for each organ is independent of the other organs and so they are not correlated [76]. The DDREFA for each organ has a corresponding CFRISK parameter, and these parameters are also uncorrelated.

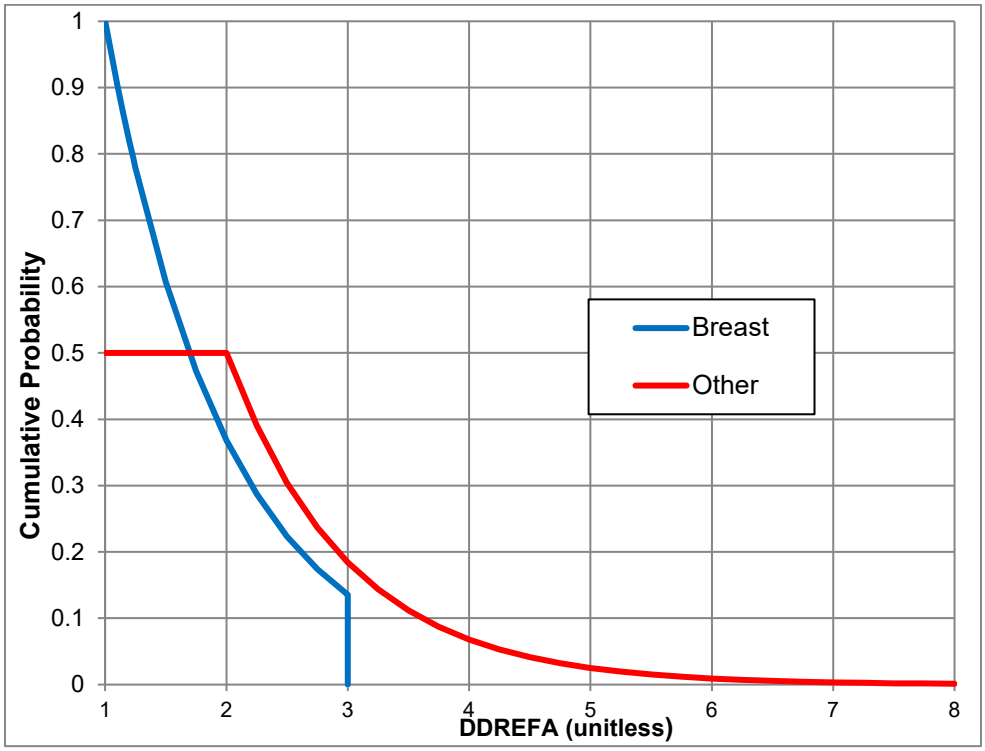

Figure 4-56 Normalized PDFs for DDREFA for Breast and Other Cancers

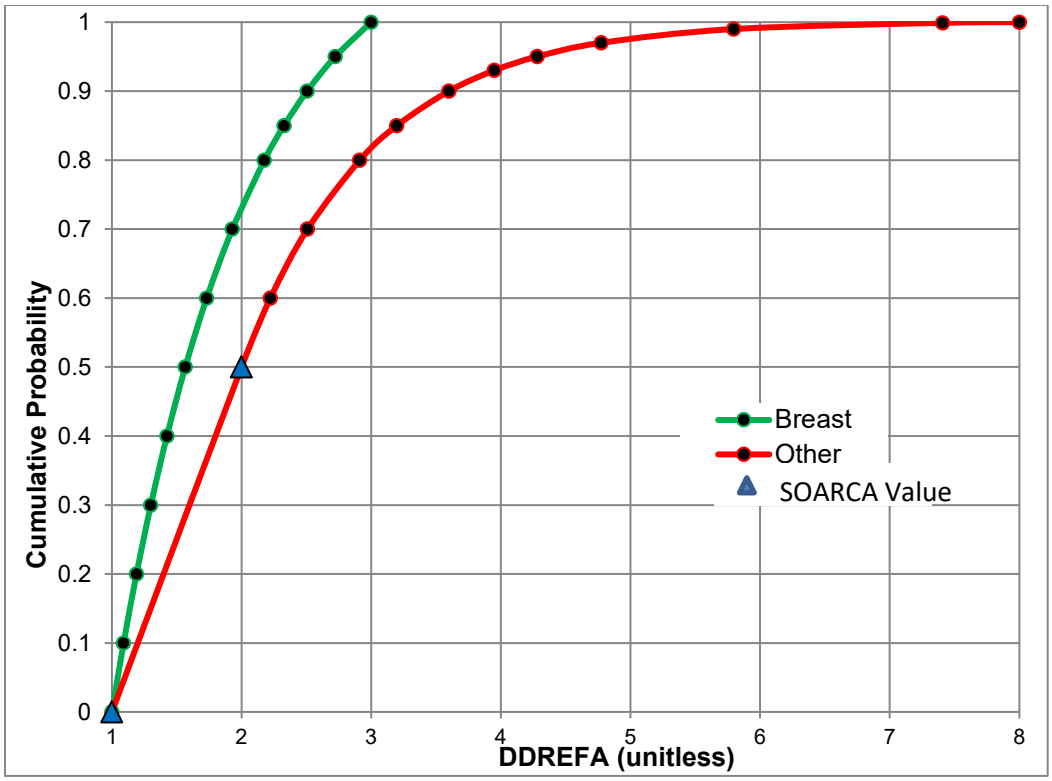

Figure 4-57 CDFs of DDREFA for Breast and Other Cancer Types

4.2.5.2 Lifetime Cancer Fatality Risk Factors (CFRISK)

The lifetime cancer fatality risk factors (CFRISK) are based on a 50-year lifetime dose commitment to specified target organs (risk/Sv). The probability of a lifetime cancer fatality is calculated separately for each cancer syndrome related to each target organ and is based on the technical approach described in the National Academy of Sciences / National Research Council Biological Effects of Ionizing Radiation (BEIR) V report. The BEIR V risk models are used in FGR-13.

Radiation dose to organs and tissues of the body are involved in the decision to allow the evacuated population to return and in the estimation of the potential health effects in the population. Return of the population falls within the scope of radiation protection and uses the standard dosimetric quantities of radiation protection, i.e., effective doses. Estimation of health effects involves calculating doses to specific organs and applying cancer risk factors to estimate the number of excess cancer fatalities in a population. Both the dose coefficients (Section 4.2.5.3) and risk factors are uncertain. Uncertainties in the cancer fatality risk factors are evaluated in this section.

Rationale for Distribution

Truncated log-normal distributions were selected for the cancer fatality risk factors based on guidance from Keith Eckerman [76]. Estimates of the gender and age averaged uncertainty in CFRISK for each of the organs used for latent health effects were obtained from Eckerman [76]; whereas, the estimates used in the earlier Surry SOARCA analysis were from BEIR V (the blue triangles in Figure 4-58) in [3].

The uncertainty distributions provided by Eckerman [76] indicate that cancer risk for leukemia seems to be relatively well quantified; lung, breast, colon, and residual (cancer sites not explicitly identified – esophagus, stomach, skin, ovaries, bladder, kidney, etc.) are moderately well quantified; and thyroid, liver, and bone are relatively poorly quantified. Eckerman [76] concluded this based on the premise that inconsistency in expert judgment is a valid measure of uncertainty in CFRISK.

Each log normal distribution is truncated at ±3 sigma for each distribution. This represents a truncation at quantile 0.001 and 0.999. CFRISK for each organ is considered independent of the other organs and therefore the risk factors are not correlated [76].

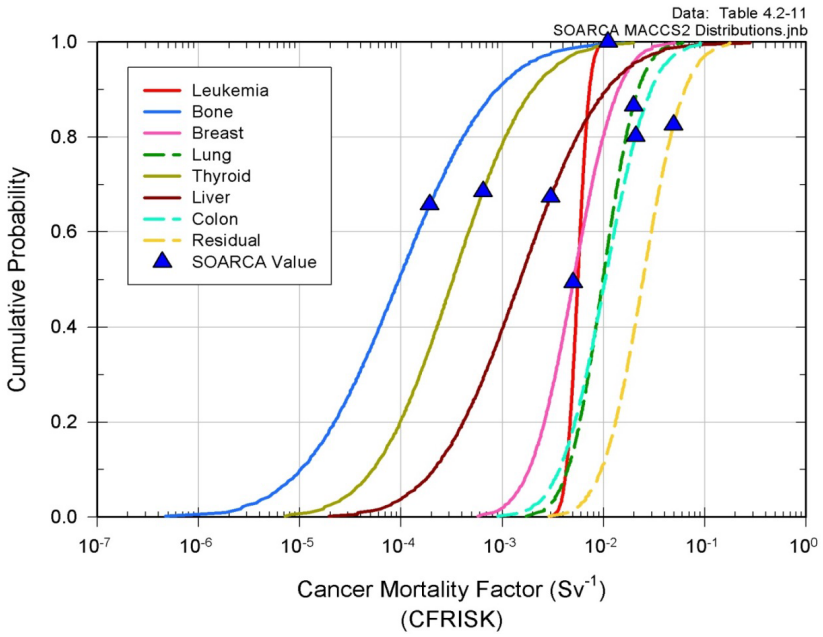

Figure 4-58 CDF for CFRISK for each of the Organs Included in the Analysis

4.2.5.3 Long-Term Inhalation Dose Coefficients

The long-term inhalation dose coefficients are used to calculate the committed organ-specific equivalent dose or the committed effective dose (Sv) from the inhalation of 1 Bq of a radionuclide over a 50-year commitment period. Uncertainties in inhalation dose coefficients were examined by Pawel et al. [79] to evaluate the uncertainties in the cancer risk coefficients of FGR-13. Based on the Eckerman report for SOARCA [1], the assignment of uncertainty distributions to long-term inhalation dose coefficients for individual radionuclides is difficult because these values are the end products of complex calculations. These calculations involve a collection of uncertain biokinetics and dosimetric coefficients and assumptions, which Pawel et al. [79] determined to be the largest uncertainty for most risk coefficients.

The LCF risk factors in MACCS are based on the technical approach described in BEIR V in which long-term inhalation dose coefficients are part of that approach. The assessment of the uncertainty in dose is evaluated on the basis of sensitivity analyses in which various combinations of plausible biokinetics and dosimetric models are used to generate alternative dose coefficients, such as those discussed in Pawel et al [79], and Eckerman report [76].

Rationale for Distribution

For the long-term dose coefficients related to the inhalation pathway, Eckerman [76] recommends that the uncertainty distributions for the coefficients be treated as truncated log normal distributions with the geometric means and standard deviations for the 58 radionuclides listed in Table 4-9. The upper and lower values used to create the distributions are assumed to represent the 90 percent confidence interval for each dose coefficient.

For an individual radionuclide, the long-term inhalation dose coefficients are treated as correlated with a rank correlation coefficient of 1.0 for all of the organs except the lung. The lung is correlated with a rank correlation coefficient of -1.0 with the dose coefficients of all of the other organs (red bone marrow, bone, breast, thyroid, liver, colon, and 'residual'). This, in effect, means that only one input is sampled independently (e.g., long-term inhalation dose coefficient for the red bone marrow) to represent all organ-specific long-term inhalation dose coefficients uncertainty. The logic behind this is that the inhaled radionuclides may spend more or less time (residence time) in the lungs, depending on the chemical form of the radionuclide and its solubility, and subsequently after departing from the lung, the radionuclide is carried through the blood stream to other systemic tissues. Thus, the longer the time spent in the lungs, the greater the dose in the lungs and the less the dose to the other systemic tissues. The shorter the time spent in the lungs, the smaller the dose in the lungs and the greater the dose to the other systemic tissues. MACCS uses the bone as the corresponding organ to correlate the other organ-specific long-term inhalation dose coefficients.

There are 69 radionuclides considered in the Surry SOARCA analysis [3]. Of those, only 58 radionuclides have nonzero dose coefficients for inhalation. In this UA, these 58 radionuclides, listed in Table 4-20, are assigned uncertain long-term inhalation dose coefficients for each of the eight organs used in this analysis, which are lung, red bone marrow, bone, breast, thyroid, liver, colon, and residual. The residual[50] dose coefficient represents the collection of organs that are not specifically represented and that are important for cancer induction.

Figure 4-59 and Figure 4-60 provide examples of the truncated log normal distributions for two radionuclides, Cs-137 and Pu-241, for the eight different organs included in this analysis. Uncertainties in the acute inhalation dose coefficients (used to estimate the early health effects discussed in Section 4.2.4) were considered to be less important and were not included in this UA.

SOARCA did not include the ingestion dose pathway and neither does this UA. Uncertainty in groundshine dose coefficients is treated through uncertainty in the groundshine shielding factors, as explained above. Cloudshine uncertainty is not treated because it is a relatively unimportant dose pathway, compared with groundshine and inhalation.

[50] The version of MACCS used in this analysis was limited to eight organs.

Table 4-20 Radionuclides Treated as having Uncertain Inhalation Dose Coefficients

Radionuclides							
Co-58	Y-90	Nb-97	Te-127	I-132	Ba-140	Pr-144	Cm-242
Co-60	Y-91	Mo-99	Te-127m	I-133	La-140	Nd-147	Cm-244
Rb-86	Y-91m	Tc-99m	Te-129	I-134	La-141	Np-239	
Rb-88	Y-92	Ru-103	Te-129m	I-135	La-142	Pu-238	
Sr-89	Y-93	Ru-105	Te-131	Cs-134	Ce-141	Pu-239	
Sr-90	Zr-95	Ru-106	Te-131m	Cs-136	Ce-143	Pu-240	
Sr-91	Zr-97	Rh-103m	Te-132	Cs-137	Ce-144	Pu-241	
Sr-92	Nb-95	Rh-105	I-131	Ba-139	Pr-143	Am-241	

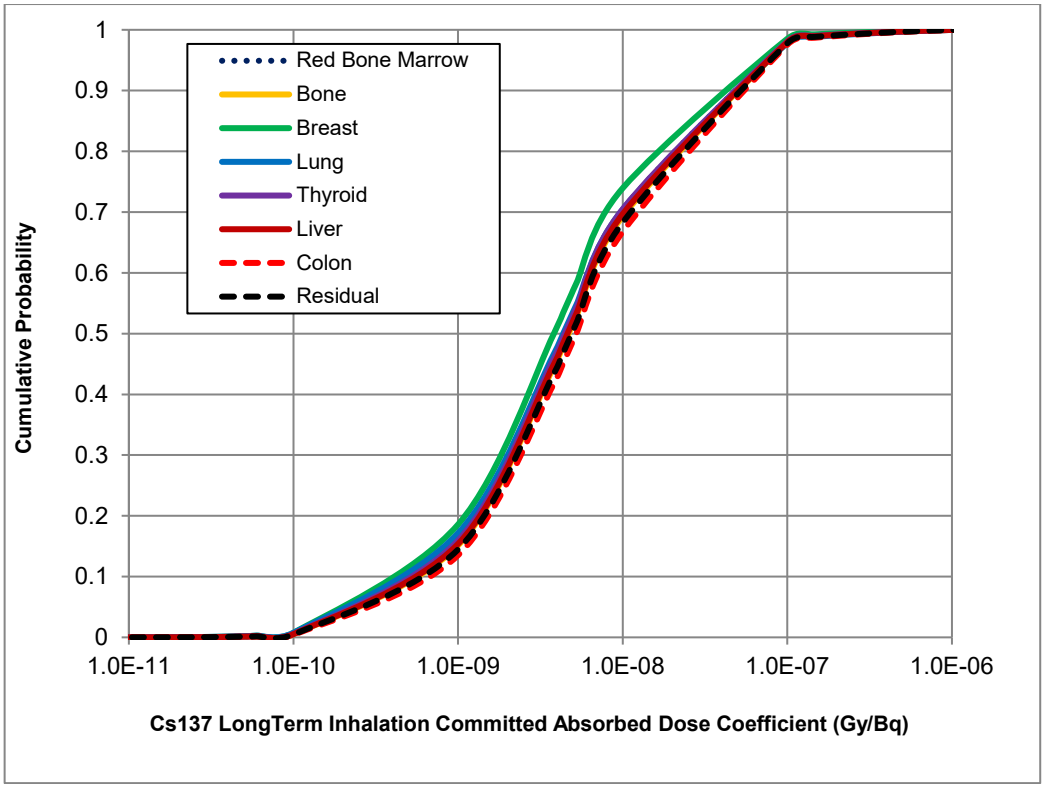

Figure 4-59 Cs-137 Lifetime Inhalation Dose Coefficient Distributions for Organs Included in the Consequence Analysis

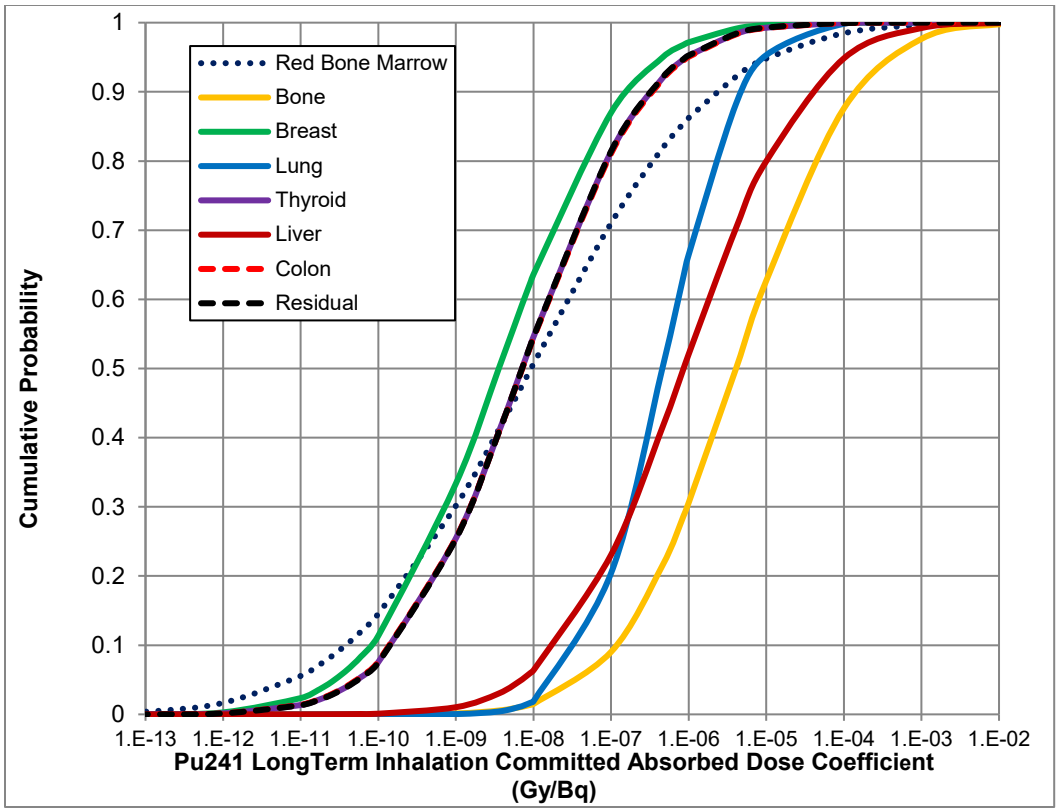

Figure 4-60 Pu-241 Long-Term Inhalation Dose Coefficient Distributions for Organs Included in the Consequence Analysis

4.2.6 Dispersion (CYSIGA, CZSIGA)

Dispersion of a radioactive plume following a severe accident directly affects doses to members of the population and resulting health effects. Thus, the dispersion parameters used to estimate atmospheric dispersion are important to the outcome of the calculation. The coefficients used to calculate dispersion were chosen to be the median values from an expert elicitation [73], but there is significant uncertainty in these values.

In terms of predicted health effects, these parameters tend to have a non-linear effect when using the linear, no-threshold (LNT) hypothesis for estimating latent health effects because dispersion influences the amount of land that is interdicted. Dispersion has an even greater influence on estimated health effects when truncation is used in the dose-response model because a smaller dose to an individual can reduce a nonzero risk to zero and, conversely, a larger dose can raise a zero risk to be nonzero.

Within MACCS, plume dispersion is calculated using the Gaussian plume model, shown in Eq. 4-17 for the simple case of an unbounded plume.

$$\chi(x,y,z) = \frac{Q}{2\pi\,\bar{u}\,\sigma_y\,\sigma_z}\exp\left[-\frac{1}{2}\left(\frac{y}{\sigma_y}\right)^2\right]\exp\left[-\frac{1}{2}\left(\frac{z-h}{\sigma_z}\right)^2\right]$$

Eq. 4-17

where $\chi(x,y,z)$ is the air concentration at a downwind location (x,y,z), Q is the source strength, $\bar{u}$ is the mean wind speed, h is the release height, and σ_y and σ_z are the standard deviations of the normal crosswind and vertical concentration distributions, respectively. Q and h are determined by the accident sequence, while $\bar{u}$, σ_y, and σ_z are functions of weather. Uncertainty in σ_y is used to capture the uncertainty in crosswind dispersion. The function used to define σ_y is given in Eq. 4-18.

$$\sigma_y = CYSIGA \cdot x^{CYSIGB}$$

Eq. 4-18

where x is the downwind distance and CYSIGA and CYSIGB are empirical constants chosen to fit observed results. A value for both of the constants must be entered for each of the six Pasquill-Gifford stability classes (A-F).

In this work, it was beneficial to only sample one of the two constants to simplify the specification of uncertainty. Bixler et al. [73] characterized the uncertainty as an uncertainty in CYSIGA and this characterization is used here.

4.2.6.1 *Crosswind Dispersion Linear Coefficient (CYSIGA)*

The crosswind dispersion linear coefficient is represented by CYSIGA. The SOARCA best estimate values for CYSIGA were chosen to be the median of the results of an expert elicitation [73]. Distributions were fit to the expert data and these were roughly lognormal. The median of the distributions is considered to be a reasonable best estimate value for this parameter; however, the distributions created from the elicitation are not used in this analysis. The expert data indicate about one order-of-magnitude uncertainty within the 90 percent confidence interval and about two orders of magnitude at the 100 percent confidence interval.

In retrospect, it appears that the experts considered the question: what is the uncertainty in the dispersion at a specific point in time, i.e., for a specific weather instance. The appropriate question for this UA is: what is the uncertainty in dispersion that is representative of a year of weather data? The second question leads to a narrower distribution because a single set of dispersion parameters is selected to represent a whole year of weather variability.

There are a number of other sources for CYSIGA, three of which are given as examples in the MACCS User's Guide [80]. These values were compared to the best estimate values from expert elicitation. It was found that two thirds of the values were within a factor of 3 of the best estimate value and were about evenly distributed between larger and smaller. These historic values (from 1977, 1979, and 1989) were used by multiple experts in constructing their distributions, showing they continue to be regarded as reasonable bases to estimate dispersion.

Additionally, NUREG/CR-6853 [81], compared results from MACCS (a Gaussian plume code) with 3 other codes for transport and dispersion and found that the results from the 4 codes were within a factor of 2 for compass averaged concentrations and 3 for sector specific concentrations. This factor can be considered to be an approximation of the uncertainty in transport and dispersion. As a first-order approximation at short distances, the uncertainty in plume concentration is inversely proportional to the uncertainty in σ_y multiplied by the

uncertainty in σ_z. Accounting for an uncertainty in concentration of a factor of three above and below the median corresponds to a range of uncertainty in CYSIGA from 1/1.73 to 1.73 times the median assuming that both cross-wind and vertical dispersion have the same ranges of uncertainty. If this range is considered to be the uncertainty at the 90 percent confidence level, the entire range of uncertainty is reasonably chosen to be bounded by factors of 1/2.5 and 2.5 on the median value for CYSIGA.

Rationale for Distribution

The 50th percentile of the distribution from the expert elicitation [73] is a reasonable and defensible choice for the best estimate value to use for CYSIGA. Expert elicitation results are based on a combined category for stability classes A and B and a combined category for stability classes E and F, yielding 4 distributions for A/B, C, D, and E/F. Based on the previous discussion, the bounds of the distribution are set to be a factor of 2.5 higher and lower than the best estimate value for each weather class. All calculated values are found in Table 4-21.

In the previous Peach Bottom UA, a piecewise log-uniform distribution was used for CYSIGA because the expert elicitation data were approximately lognormal [2]. Since the range of uncertainty was chosen to be different for this analysis, a simpler log-triangular distribution was chosen. This choice is consistent with a most likely value at the center of the distribution and a likelihood that decreases as the bounds are approached. A log-triangular distribution was used instead of a triangular one because it gives equal sampling weight on either side of the mode when using a multiplicative factor for the lower and upper bounds.

Table 4-21 Log-Triangular Values for Dispersion Parameter CYSIGA for each Stability Class

Class	Lower Bound	Mode	Upper Bound
A/B	.3002	.7507	1.8768
C	.1625	.4063	1.0158
D	.1112	.2779	0.6948
E/F	.0863	.2158	0.5395

CYSIGA and CZSIGA are perfectly rank correlated across the four stability classes. These values are also perfectly rank correlated with the values of CZSIGA, the vertical dispersion parameters discussed below. This indicates that uncertainty in CYSIGA is partially caused by changing weather conditions that would result in an increase or decrease in both the crosswind and vertical dispersion together. It also ensures that the order between the stability classes is preserved. The CDF is presented in Figure 4-61.

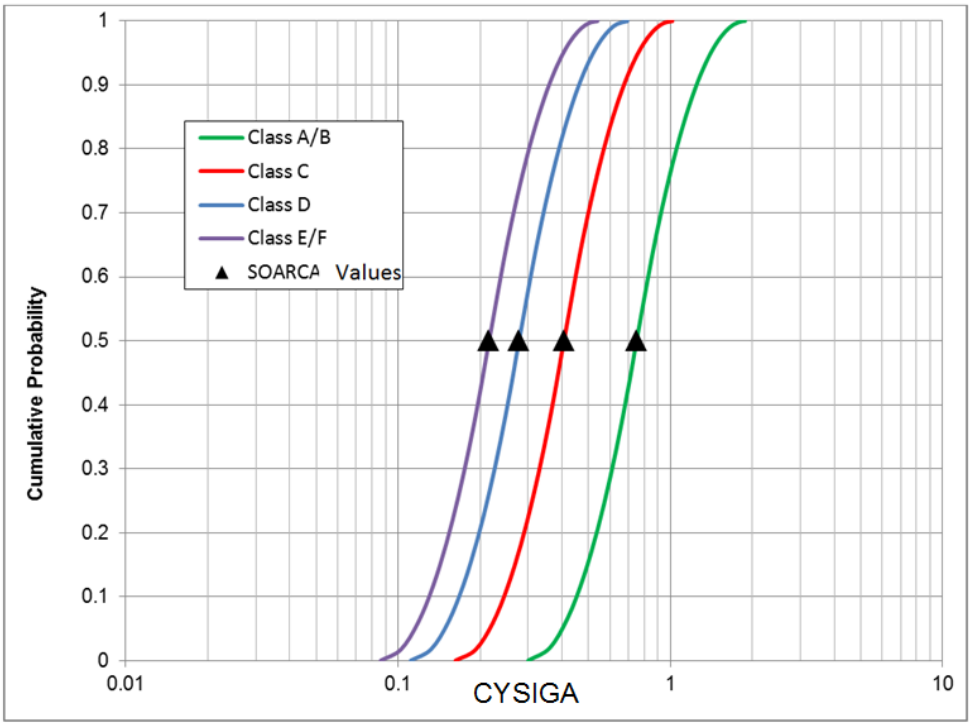

Figure 4-61 CDFs of CYSIGA for Individual Stability Classes

4.2.6.2 Vertical Dispersion Linear Coefficient (CZSIGA)

The SOARCA best estimate values for CZSIGA were also based on the results of an expert elicitation [73]. Distributions were fit to the expert data, which were again roughly lognormal. The best estimate values used in SOARCA were chosen to be the 50th percentile of the distributions, and that value is appropriate as a median value in the UA for Surry. However, the distribution for CZSIGA has the same issues as the one for CYSIGA described above, so a narrower distribution is developed and used in this work. The same approach described in the previous section leads to distribution bounds on CZSIGA that are also factors of 2.5 above and below the median value for each stability class.

Rationale for Distribution

The 50th percentile of the distribution from the expert elicitation [73] is a reasonable and defensible choice for the best estimate value for CZSIGA. Based on the previous discussion, the bounds are set at a factor of 2.5 higher and lower than the best estimate value for each stability class. The distribution parameters are provided in Table 4-22.

CZSIGA distributions are perfectly rank correlated with each other and across the weather stability classes. They are also rank correlated with the crosswind coefficients (CYSIGA). This indicates that uncertainty in CZSIGA is partially caused by changing weather conditions that would result in an increase or decrease in both the crosswind and vertical dispersion together. It also ensures that the order between the stability classes is preserved. Figure 4-62 shows the CDFs of a log-triangular distribution for each of the four SOARCA stability class groupings.

Table 4-22 Log-Triangular Values for Dispersion Parameter CZSIGA for each Stability Class

Class	Lower Bound	Mode	Upper Bound
A/B	.0144	.0361	.0903
C	.0814	.2036	.509
D	.1054	.2636	.659
E/F	.0985	.2463	.6158

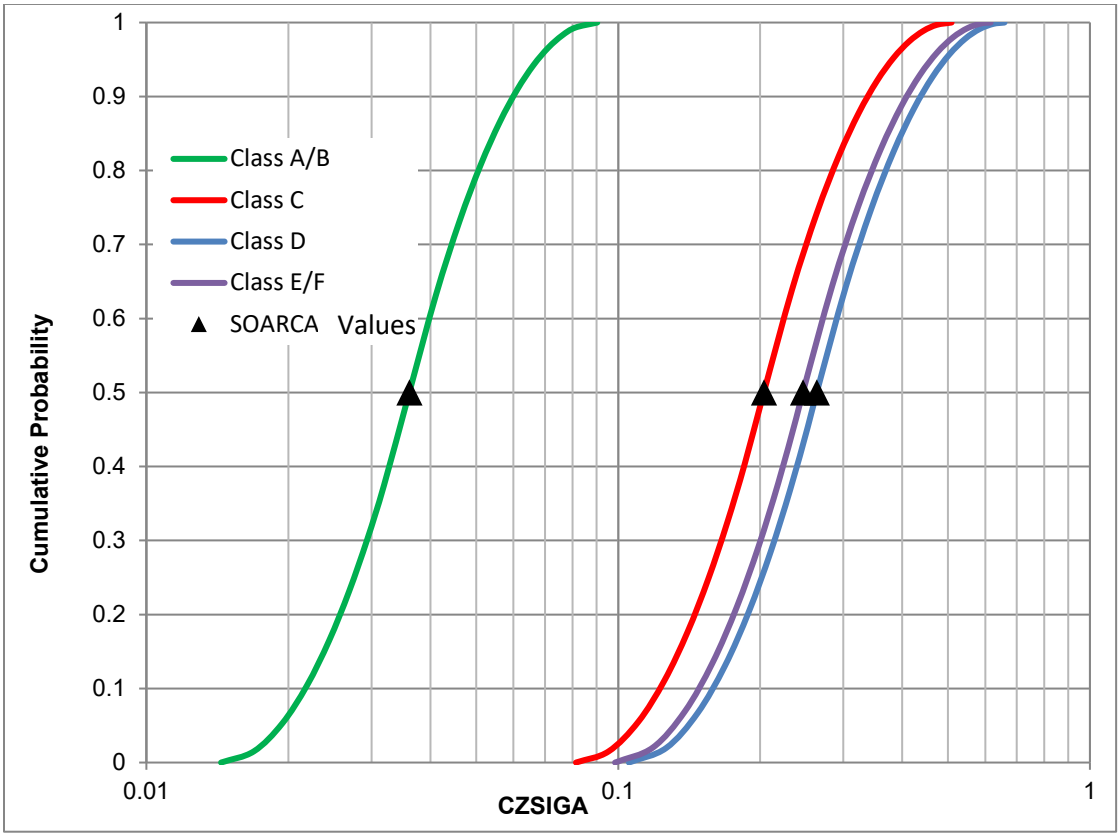

Figure 4-62 CDFs of CZSIGA for Individual Stability Classes

4.2.7 Emergency Response (Evacuation and Relocation)

MACCS input parameters related to emergency response and evacuation were developed primarily from the 2012 Surry Evacuation Time Estimate (ETE) study [86]. The ETE provided the mobilization times, travel times for cohorts, and evacuation route information. Licensees are required under Appendix E, "Emergency Planning and Preparedness for Production and Utilization Facilities," to 10 CFR Part 50 and 10 CFR 50.47, "Emergency Plans," to estimate the time to evacuate the EPZ. Appendix E.IV.3 to 10 CFR 50 provides that nuclear power reactor licensees shall use ETEs in the formulation of protective action strategies. Therefore, it may be expected that the information in the ETE report will be used in the response decisions.

In the Surry SOARCA analysis [3], information from the 2001 Surry ETE was used to develop these response times [3]. NRC has since published updated guidance for developing ETEs in

2005 and 2011 [90][91]. The 2012 Surry ETE [86] follows the current guidance and includes detailed demographic information and measures of effectiveness that were useful in developing the delay and speed parameter values for each cohort. The cohorts established in the Surry SOARCA analysis [3] were maintained for this UA and are described below.

Cohort 1 represents the public residing within the 10-mile EPZ. One cohort was used to represent the entire public within the EPZ (with the exception of the evacuation tail described as Cohort 5, and the non-evacuating fraction described as Cohort 6). Current analyses [97] separate the public into smaller population segments, creating additional cohorts to represent the response of the public. Expanding the number of cohorts was a new advancement in MACCS when SOARCA was initiated, and due to concerns over computer run time, which never materialized, it was determined at the time that a maximum of 6 cohorts should be used.

Cohort 2 represents the shadow evacuation which was defined as 20 percent of the population within the area 10 miles beyond the EPZ. A shadow evacuation typically occurs after widespread news of a nearby emergency is broadcast, and residents outside the official evacuation zone begin to evacuate. The area of 10 to 20 miles was specific to SOARCA. More current research [20] and ETE guidance [90] suggests that 20 percent of the population of the area extending 5 miles beyond the evacuation area is appropriate. However, to maintain a consistent demographic population distribution for risk comparisons, the Surry SOARCA [3] approach of 20 percent of the public from the area 10 to 20 miles beyond the EPZ was maintained.

Cohort 3 represents the schools within the EPZ. The 2012 Surry ETE report identifies sufficient resources for a single wave evacuation with enough buses to serve all of the schools [86].

Cohort 4 represents special facilities residents within the EPZ and includes ambulatory, wheelchair bound, and bedridden patients. Special facilities can take longer to evacuate than the general public because special transportation resources must be mobilized and loading patients must be done with care. The facilities evacuate individually following facility-specific evacuation plans [87].

Cohort 5 represents the evacuation tail for the 0 to 10 mile public. The evacuation tail is the last 10 percent of the general public and as such follows the general public evacuation [88]. The initial speed of the tail is the same as the final speed of the general public, but because the tail enters the roadway network late in the event, the roadways begin to clear, and the tail eventually has a faster evacuation speed [88].

Cohort 6 represents a small fraction of the public assumed to refuse to evacuate. A value of 0.5 percent was used in NUREG-1150 and has been applied in subsequent studies, including SOARCA [3]. This value is supported through recent research which included a survey of evacuees by Mitchell, et al. that identified 98.4 percent of the public evacuated in response to the Graniteville chemical spill [93][94]. Thus, 1.6 percent of the public did not evacuate in this event. The EPZ has a siren system and backup capabilities to alert the public, and the EPZ population receives emergency response information at least annually; therefore, response from the EPZ public may be expected to be more efficient than the ad hoc evacuation for Graniteville. Additionally, as identified in a national telephone survey of EPZ residents, the public has a good understanding of

the emergency response expectations [20]. The speed and delay parameters are not applicable to this cohort, but the relocation parameters apply.

Figure 4-63 shows a typical response timeline as implemented in MACCS.

Figure 4-63 General Response Timeline Representing MACCS Activities

For each cohort, MACCS uses the following duration and travel speed parameters:

- Delay to shelter (DLTSHL) represents the duration of time from the accident initiation until the population becomes aware of the emergency and begins sheltering. During this period, shielding parameters are applied assuming normal activity.

- Delay to evacuate (DLTEVA) represents the duration of time from the start of sheltering to the start of evacuation. During this period, shielding parameters are applied assuming sheltering.

- Duration of beginning phase (DURBEG) of evacuation is the first of three emergency response time periods in MACCS and is typically used to represent the time from start of travel until evacuees are in the evacuation queue. This phase begins when the sheltering period ends. During this phase, a travel speed (ESPEED1) is applied for each cohort. For each of the three evacuation phases, shielding parameters are applied for evacuation.

- Duration of middle phase (DURMID) of evacuation is typically used to represent the time of travel after DURBEG until the cohort travels beyond the EPZ. This period begins when DURBEG ends. During this phase a second travel speed (ESPEED2) is applied for each cohort.

The third and final phase of evacuation is defined as the period of time from the end of DURMID to the end of the early phase, which is 7 days from the time of the first radiation release in this analysis and in SOARCA [1]. During this phase, a third travel speed (ESPEED3) is used to represent the travel speed beyond the EPZ. The population travels at ESPEED3 until they have reached a distance of 30 miles from the plant, at which point they are modeled to receive no further early phase radiation exposure. As distances increase radially beyond the EPZ, the roadway network becomes more expansive providing increased capacity which facilitates greater speeds.

It is not necessary to make each of the above parameters uncertain. In determining which parameters to select, it was decided that one delay parameter and one speed parameter would adequately represent the uncertainty of the set. Because DURBEG and ESPEED1 represent the early part of the evacuation (only 15 minutes for most cohorts), assessing the uncertainty for this duration would be of less interest than assessing the middle phase which comprises most of

the travel time inside the EPZ. The third phase occurs primarily beyond the EPZ and at faster speeds and would also be of less interest. Therefore, ESPEED2 was selected to be uncertain because this occurs during the middle phase when congestion within the network is at its greatest, and vehicles are slowly moving out of the EPZ.

When a General Emergency is declared, licensees have 15 minutes to make a declaration and provide a protective action recommendation (PAR) to the offsite response organizations (OROs). After receipt of the accident declaration, OROs make a protective action decision, activate sirens, and issue an Emergency Alert System (EAS) message. The data used in Surry for this time period was developed from exercise information. A sensitivity analysis was conducted on delaying notification in the Surry SOARCA analysis by one hour [3]. The results showed there was little effect from this delay [3].

The effect of weather is partially addressed in emergency response. An evacuation speed multiplier was used to reduce travel speed when precipitation is occurring, as indicated from the meteorological data file. This multiplier is used to address adverse weather, consisting of rain, ice, or snow, any of which can affect the response. The evacuation speed multiplier was set at 0.7, which reduces the ESPEED values to 70 percent of the fair weather travel speed.

In addition to speed and delay, relocation parameters are sampled to reflect uncertainty in post-evacuation activities. Relocation was first introduced in the CRAC model [82] to instantaneously remove the public from areas that exceed specified dose limits at a specified time after plume arrival. This evolved into the MACCS hotspot and normal relocation parameters. Following a release of radioactive material, levels of deposition can vary resulting in areas with elevated dose rates called hotspots [84] which may warrant the relocation of residents from affected areas. These areas of elevated contamination would typically be identified after the initial evacuation, but still during the early phase, based on dose projections from state, utility, and federal agency computer modeling and field measurements.

The U.S. Environmental Protection Agency (EPA) protective action guides (PAGs) for evacuation are typically used in MACCS as the dose thresholds at which the public would be relocated. When these thresholds are exceeded, OROs would be expected to relocate individuals from the affected areas. This application is typically considered for residents beyond the EPZ, but also applies to residents within the EPZ who may have refused to follow the initial evacuation orders. It is assumed these individuals will relocate when they understand a release has occurred, and they are informed they are located in elevated dose areas. MACCS implements relocation with the hotspot and normal relocation parameters, which are specific to the MACCS model.

Hotspot and normal relocation are determined in MACCS based on the total effective dose commitment projected to be received by an individual who remained in place for the entire emergency phase period while engaging in normal activity. The pathways used for calculating the total effective dose commitment are cloudshine, groundshine, direct inhalation, and resuspension inhalation. The reference time for the relocation dose criteria is plume arrival. Relocated individuals are removed from the problem for the duration of the emergency phase and receive no additional dose during this phase [6].

4.2.7.1 Evacuation Delay (DLTEVA)

The evacuation delay (DLTEVA) defines the duration of the sheltering period that occurs immediately before evacuation. Lengthy delays could increase the potential for receiving dose.

However, there are reasons for expecting such delays to be limited; for example, there is high confidence in the alert and notification system used to warn the public. Sirens are tested at least monthly and the performance characteristics for siren systems are maintained under the Reactor Oversight Process (ROP). The ROP data for Surry showed a 99.9 percent performance indicator at the time of the Surry SOARCA analysis [3]. Furthermore, research has found that EPZ residents understand actions that may be expected during an emergency and are well prepared, with 20 percent of EPZ residents having go-bags and are ready to leave promptly [20]. Wolshon et al. [88] found that delay is not uniform with most of the evacuees experiencing a smaller delay (e.g., 90 percent of the public evacuates in about 60 percent of the response time). The variation in public response makes this a good candidate for the UA. Information used to develop the DLTEVA distribution was obtained from the ETE report [86].

Rationale for Distribution

A triangular distribution is used to represent DLTEVA uncertainty because there is some confidence in the mode which was based on a site specific telephone survey conducted to support the ETE [86]. Delays can occur for many reasons, and this is represented by the bounds. Delays can increase due to a slow response to the evacuation order, a need to wait for the return of commuters, a need to wait for public transportation, a need to shut down operations prior to leaving work, etc. Likewise, those members of the public with go-bags may respond rapidly, with little or no delay. Because delays vary individually, they would not apply to the entire cohort. However, MACCS moves cohorts as a whole based on population fraction; therefore, compromise values, based on the ETE data, are used to represent the entire cohort response.

The DLTEVA parameter is applied at the cohort level. Response timing is sampled for each cohort. Cohort 1 represents the first 90 percent of the 0-10 mile general public (the EPZ). The SOARCA baseline DLTEVA value was 1 hour [3]. A mode of 2 hours represents the expected time, which is taken as an approximate average of the mobilization time for residents with and without commuters as presented in the ETE report [86]. A lower bound of 0 hours would indicate there is no delay after the public has been notified. Such conditions could occur as demonstrated in spontaneous evacuations where some people leave when they observe an emergency, such as a fire, but prior to receiving evacuation orders [92]. However, it would not be realistic that the entire cohort would leave immediately. With a mode of 2 hours and understanding that there are situations where the public may become aware of a need to evacuate prior to receiving formal notification, 1 hour was judged to be reasonable for the lower bound of the entire cohort. With regard to the upper bound, the ETE report shows the longest the general public cohort (the first 90 percent of the public) is expected to take 4 hours [86] in the case of residents waiting for commuters to return home during snow, and this was used for the upper bound.

Cohort 2 represents the shadow evacuation in the 10 to 20 mile area. The size of the shadow evacuation can be influenced by communication during the emergency. The timing and content of messaging can cause the shadow to increase or decrease and can cause residents to leave earlier or later in the event depending on the perceived risk of the residents [92]. The shadow evacuation typically begins shortly after the general evacuation begins. The lower bound for Cohort 2 is established as 1 hour, which allows time for the general evacuation to get underway. The 1 hour value was based on analyst judgment and review of emergency evacuation information [85]. A value of 5 hours was judged to be reasonable for the upper bound. A mode of 3 hours was judged reasonable to reflect this cohort usually follows the evacuees from the hazard area (e.g., the general public cohort).

Cohort 3 represents the schools within the EPZ. When the SOARCA project [1] was initiated, it was decided at the time to select a winter weekday scenario that includes school evacuation. Although this scenario only occurs on weekdays over a range of a few hours, it challenges the response agencies with additional logistics and responsibilities. For this scenario, the Virginia Department of Emergency Management would notify schools when a Site Area Emergency (SAE) is declared [3]. This notification triggers activities to mobilize buses and evacuate the schools. The baseline SOARCA DLTEVA was 1 hour based on the 2001 ETE, which assumed that transportation resources were immediately available. The ETE report [86] identifies sufficient resources for a single wave evacuation, indicating there are enough buses to serve every school at the same time. A lower bound of 0.5 hours was judged reasonable for this cohort. This includes time for OROs to notify the schools and assumes the evacuation occurs in the morning at the beginning of school or in the afternoon at the end of school when buses are already mobilized. The 2012 ETE report provides school bus mobilization times that range from 145 minutes to 180 minutes [86]. An upper bound of 4 hours was established to account for the mobilization time and potential delay in notification, communication with drivers, delay in travel due to weather or other impediments, etc. A mode of 2.75 hours was selected to represent an average of the mobilization times presented in the ETE [86].

Cohort 4 represents the special facilities within the EPZ and was modeled in SOARCA [3] with a DLTEVA of 11 hours based on the 2001 ETE. There are 12 special facilities identified in the 2012 Surry ETE [86], and these facilities would evacuate as resources are available. It is not necessary, to model each facility individually; therefore, special facilities are modeled as a group. The departure was set later in the evacuation with a time that represents an average of when the facilities may depart. The 2012 ETE report identifies 3 hours as the average time for buses to arrive at the facilities. Additional time was estimated for loading the residents prior to beginning the evacuation [86]. It is unlikely resources for all facilities could be obtained and mobilized much faster than 3 hours, because the ETE report identifies there are insufficient ambulances to complete the evacuation in a single wave, making a second wave necessary. Therefore, 3 hours was judged reasonable for the lower bound. A mode of 5 hours was judged reasonable to reflect the vehicle mobilization time, lack of transportation resources to mobilize in a single wave, and the time to load residents. A factor of 2 was applied to the mode providing a value of 10 hours. The factor of 2 was based on analyst judgment which considered there are cooperative agreements with neighboring counties to acquire additional resources. This gives confidence that resources would eventually become available. However, additional time would be needed to acquire these resources, and for such an event, there could be competing priorities with the cooperative agreement counties. The upper bound may also represent a potential delay in availability of transportation resources, communication with drivers, delay in travel due to weather, or other impediments.

Cohort 5 represents the evacuation tail for the 0 to 10 mile public. The SOARCA [3] DLTEVA value was 11 hours, based on the 2001 ETE. In the 2012 ETE [86], Scenario 6 represents the midweek winter day good weather evacuation, which is similar to the SOARCA scenario. The 2012 ETE report shows that 90 percent of the general public completes their evacuation in about 4 hours, which is the time the tail would begin. The evacuation ends at about 6 hours. A lower bound of 3 hours was judged reasonable to reflect efficient evacuation of the general public. An upper bound of 10 hours was judged reasonable to reflect a range of potential delays that contribute to the tail, such as waiting for commuters, shutting down equipment, and other delays. A mode of 4 hours was selected based on the ETE [86] which represents the expected time for this scenario.

Table 4-23 provides a listing of the cohorts and the values used in the triangular distribution. The cohort sampling approach is shown in Figure 4-64. Evacuation delays are sampled independently for each cohort. Although it was intended the evacuation tail be correlated with the public, because the tail leaves after the public, the modeling was not implemented in this manner. This modeling error would likely have a negligible effect on the results. For each cohort the timing of evacuation is specified independently at each radial distance in the grid (a ring). These values are rank correlated so that the entire cohort begins to evacuate at approximately the same time.

Table 4-23 MACCS Uncertain Parameters – Evacuation Delay

Parameter	SOARCA Value	Mode	Bounds
Cohort 1 (0-10 Public)	1.0	2.0	LB = 1.0 hr. UB = 4.0 hr.
Cohort 2 (10-20 Shadow)	1.0	3.0	LB = 1.0 hr. UB = 4.0 hr.
Cohort 3 (Schools)	1.0	2.75	LB = 0.5 hr. UB = 4.0 hr.
Cohort 4 (Special Facilities)	11	5.0	LB = 3.0 hr. UB = 10.0 hr.
Cohort 5 (Evacuation Tail)	11	4.0	LB = 1.0 hr. UB = 10.0 hr.

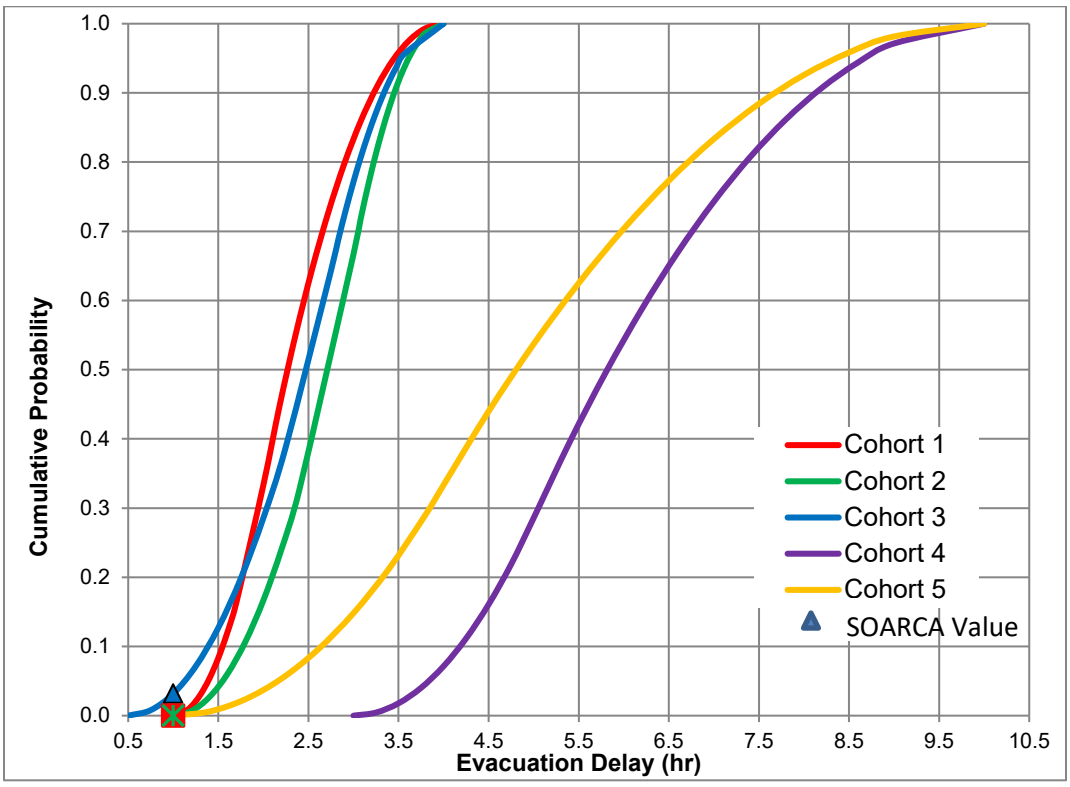

Figure 4-64 CDF of DLTEVA for each Cohort

(*Note:* Cohort 4 and 5 SOARCA values fall outside of their respective CDFs)

4.2.7.2 Evacuation Speed (ESPEED)

The ESPEED2 parameter represents the speed for each of the evacuating cohorts for the duration of the middle phase. As mentioned earlier, the Surry SOARCA analysis [3] values were based on the Surry ETE report dated 2001. The current Surry ETE report [86] includes additional detail, measures of effectiveness, and updated time estimates.

Rationale for Distribution

A triangular distribution was used to represent uncertainty because there is confidence that the mode derived from the ETE report is the most likely value. The ETE report was developed following NRC guidance and reviewed by NRC staff. Average speeds for the entire roadway network and for select evacuation routes are provided in the ETE [86]. These speeds can vary by cohort depending on the evacuation routes selected by each cohort, the location of the cohort within the EPZ (e.g., schools may be near the edge of the EPZ), and the time the cohort enters the roadway.

For Cohort 1 (the 0-10 mile public) the Surry SOARCA [3] speed was 1 mph based on the 2001 ETE report and accounted for MACCS loading the entire public cohort at one time. In reality, evacuating residents would load the roadway network over a longer period of time and travel at different speeds based on congestion at the time they enter the roadway network. The current ETE identifies an average network speed of about 12 mph for the duration of the evacuation [86]. This average speed includes the beginning, middle and late phases in MACCS, and includes areas west of the James River, which experience a faster free flow speed (i.e., unimpeded traffic flow) and areas east of the river, which experience congested flow as illustrated in Chapter 7 of the ETE report [86]. Because the speed is being sampled for the middle phase duration, a lower bound of 0.5 mph is judged reasonable and reflects a potential for congestion and impediments to the evacuation. Such impediments can range from drivers stopping to ask emergency personnel questions to power outages that affect stoplights or infrastructure damage that requires alternate routes. An upper bound of 12 mph was judged reasonable to represent the average speed identified in the ETE report, which represents evacuation under normal conditions. A mode of 1 mph was judged reasonable, again accounting for MACCS loading the entire public cohort at one time and accounting for the fact that the parameter is ESPEED2 which occurs during the congested period. The current ETE shows speeds of less than 2 mph on several evacuation routes under normal conditions [86].

Cohort 2 represents the 10 to 20 mile shadow evacuation which is travelling on different roadways than the EPZ population, thus the speeds are not directly related to the EPZ evacuees. The speed was set at 1 mph in the Surry SOARCA analysis [3] because most of the shadow population is located in the densely populated areas east of the James River. The lower bound is established at 0.5 mph. Although shadow evacuations occur in response to emergencies, the effect of the shadow evacuation on the evacuees from the EPZ is seldom significant. This is quantified in Appendix M of the ETE study [86] which shows that an increase in the shadow population to 25 percent of the public has no effect on the ETE, and an increase to 60 percent, only has a 25 minute increase on the ETE. The upper bound of 15 mph was judged reasonable to account for limited traffic congestion and increased roadway capacity beyond the EPZ. A mode of 5 mph was judged reasonable to reflect these evacuees are beyond the congested EPZ when they begin their travel.

For Cohort 3 (schools), a speed of 10 mph was used in the Surry SOARCA analysis [3] because schools are notified directly, allowing them to begin evacuation prior to the general public. For this accident scenario, schools are assumed to receive orders to evacuate after declaration of the SAE, which is about 2.5 hours prior to the general public [3]. The 2012 ETE shows the schools require approximately 3 hours to mobilize buses. This puts the school cohort on the evacuation route during periods when traffic congestion is building. The current ETE report shows average speeds for the school evacuation ranging from 1.1 mph to 33 mph. The school speeds largely depend on the proximity to the EPZ boundary and the level of congestion on the evacuation routes travelled. The school with a 33 mph speed is located about 0.5 miles from the southeast edge of the EPZ; thus, this school evacuates ahead of the rest of the population on uncongested roadways and is not typical of other schools. Most of the average speeds for schools were estimated at less than 10 mph [86]. A lower bound of 0.5 mph was judged reasonable to account for congestion and potential impediments to the evacuation. An upper bound of 15 mph was judged reasonable based on the potential for less congestion due to evacuation early in the event, which could occur in the mornings or afternoons while buses are already mobilized. A mode of 1 mph was chosen based on the speeds used for the general public and the current ETE which shows the schools evacuating with the general public [3].

Cohort 4 represents the special facilities within the EPZ which were modeled in the Surry SOARCA analysis [3] as starting evacuation later in the event, near the end of the peak traffic congestion. The lower bound of 0.5 mph was judged reasonable to represent these evacuees entering the roadway network during heavy congestion. These facilities evacuate individually, and the potential exists to enter the roadway network when traffic congestion is heavy. The upper bound of 20 mph was judged reasonable to represent evacuating late in the event when roadways are less congested. This would be consistent with sheltering for an extended period until specialized vehicles arrive to support the evacuation. A mode of 5 mph was judged reasonable reflecting facilities that evacuate independently, on average, are likely to enter the roadway network while some congestion exists.

Cohort 5 represents the evacuation tail for the EPZ public, which begins evacuation at the end of the general public evacuation. The initial speed of the tail is the same as the general public because they enter the roadway immediately behind the general public. As evacuees exit the EPZ, the roadways begin to clear and the evacuation speed of the tail increases [88]. The lower bound was set at 0.5 mph because the tail enters the roadway network at the end of the peak congestion, which is represented by the lower bound for Cohort 1. The upper bound of 20 mph represents roadways that are relatively free of congestion once the majority of vehicles have left the area. A mode of 10 mph was judged reasonable to reflect that in most instances, the tail has left late enough that there is less congestion.

Table 4-24 provides a listing of the cohorts and the values used in the triangular distribution. Cohorts are sampled as shown on Figure 4-65. Evacuation speeds are perfectly rank correlated between cohorts.

Table 4-24 MACCS Uncertain Parameters – Evacuation Speeds

Cohort	SOARCA Value	Mode (mph)	Bounds (mph)
Cohort 1 (0-10 Public)	1 mph	1.0	LB = 0.5 UB = 12.0
Cohort 2 (10-20 Shadow)	1 mph	5.0	LB = 0.5 UB = 15.0
Cohort 3 (Schools)	10 mph	1.0	LB = 0.5 UB = 15.0
Cohort 4 (Special Facilities)	10 mph	5.0	LB = 0.5 UB = 20.0
Cohort 5 (Evacuation Tail)	10 mph	10.0	LB = 0.5 UB = 20.0

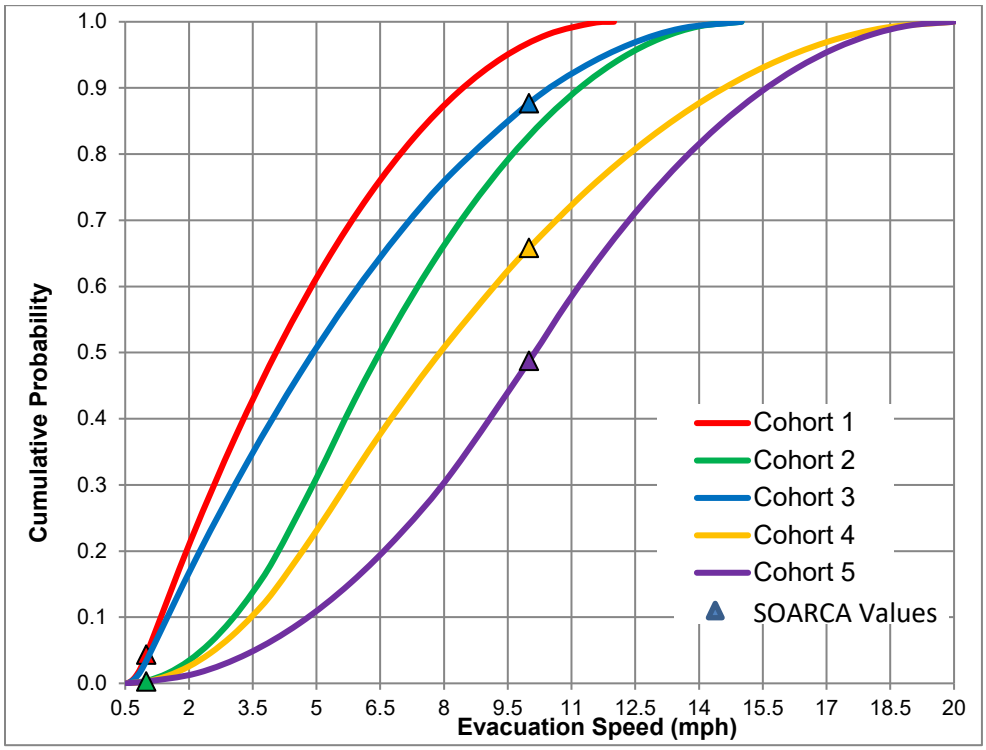

Figure 4-65 CDFs of ESPEED for each Cohort

4.2.7.3 Hotspot Relocation Time (TIMHOT)

The hotspot relocation time (TIMHOT) is the estimated time needed to relocate residents from areas that exceed the hotspot dose threshold (DOSHOT). This user specified time is implemented in MACCS after plume arrival. The relocation time should include all temporal elements that contribute to the relocation activities. This includes time for OROs to define the affected areas, develop messaging and initiate the EAS to notify the public. This also includes time for the public to prepare to leave and travel out of the affected area. Each of these elements can be influenced by factors such as size of the affected area, number of affected

residents, location of residents when the warning is received, available resources to coordinate the relocation, clarity of data, weather, etc. Notification may be augmented by route alerting (which is identified in the state emergency plan), Reverse 911®, or other communication methods [85].

MACCS implements this parameter by removing the entire affected population from the dose equation at point in time, the time specified by TIMHOT after plume arrival. Because relocation occurs over a period of time, this was developed as an average for the affected population. Establishing a distribution to account for a range of source terms, population densities, and other characteristics that influence relocation is challenging.

Rationale for Distribution

A uniform distribution was used to represent uncertainty, because the potential influences in activity duration during the emergency make any value within the range described below possible. Few of the time contributing activities can be estimated with confidence prior to an event, such as the affected area, affected population, available transportation infrastructure, need for traffic control, and plume travel speed. There are no empirical data available related to prompt relocation of residents. NUREG/CR-7110 Volume 2 [3] used a relocation time of 24 hours.

Relocation is expected to occur after evacuation is complete. This approach allows emergency responders who were supporting the evacuation to transition to relocating residents, and helps limit extra traffic in areas where the evacuees are travelling. The lower bound was developed based on an optimal relocation implemented promptly after plume arrival. Capabilities exist to project hotspot areas, and OROs could request the public make preparations to leave, prior to the release. Relocation could then begin promptly once it is determined the plume has passed. Assuming the public is prepared to leave, the final time element is travel out of the affected area. A review of the SOARCA results from NUREG/CR-7110 Volume 2 [3] shows that the release fraction of cesium for the STSBO scenario may only exceed the hotspot dose threshold in a few areas up to 5 miles beyond the EPZ. Therefore, the affected area may be small and associated population for hotspot may represent only a small fraction of the population. From SecPop [87], the 2010 population within the radial area 5 miles beyond the EPZ (i.e., 10 to 15 miles from the plant) is about 150,000. The Surry emergency response scenario includes an assumption that 20 percent of the population in this area evacuates as a shadow evacuation, which reduces the number of people potentially affected by hotspots [3]. It is assumed 20 percent of the remaining residents may need to be relocated due to exceeding the hotspot criteria. Considering the number of people potentially affected and the need for authorities to notify these people and support the relocation, a lower bound value of 12 hours after plume arrival was judged reasonable.

The upper bound represents conditions in which there is a delay in relocation, which could occur for many reasons. For example, OROs may decide to wait until the morning, rather than trying to mobilize families at night. Loss of communication, infrastructure damage, or OROs focused on activities within the EPZ or having other conflicting priorities could contribute to such a delay. Because relocation is based on projected dose over the emergency phase, it may not have the same priority as other urgent requirements. It is also possible that response officials may choose to shelter in place for a period of time. A value of 30 hours after plume arrival was judged reasonable for the affected area. The CDF is presented in Figure 4-66.

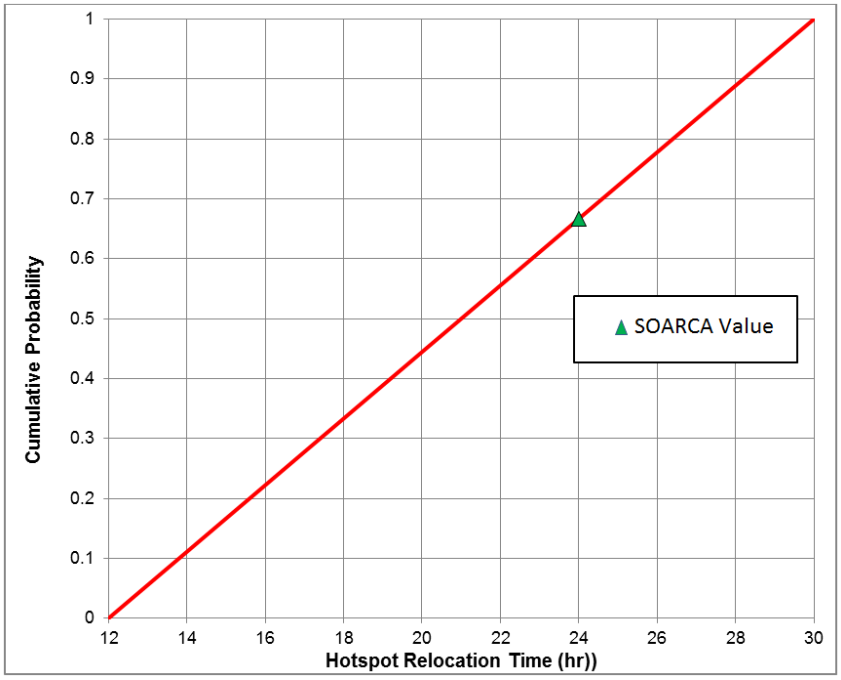

Figure 4-66 CDF of TIMHOT

4.2.7.4 Normal Relocation Time (TIMNRM)

The normal relocation time (TIMNRM) is the time to relocate residents from areas that exceed the normal dose threshold (DOSNRM). This user specified time is relative to plume arrival. The time includes the elements described for the hotspot relocation time (TIMHOT). In addition, time may be needed to allow clearance of residents relocated due to the hotspot criteria. Again, establishing a distribution to account for a range of source terms, population densities, and other characteristics that influence relocation is challenging. Furthermore, because DOSNRM is a relatively low dose threshold, the size of the area could be large and could have a correspondingly large population. MACCS implements this parameter by removing the entire affected population from the dose equation at a point in time, the specified TIMNRM after plume arrival. As with TIMHOT, a compromise time is developed by considering the influencing factors.

Rationale for Distribution

A uniform distribution is used to represent uncertainty in TIMNRM because the potential influences in activity duration during the emergency make any value within the range described below possible for the same reasons described with TIMHOT. However, normal relocation has a lower dose threshold and may not be implemented with the same urgency as hotspot relocation. No empirical data related to prompt relocation of residents after an evacuation was identified. This lack of data also supports use of a uniform distribution. NUREG/CR-7110 Volume 2 [3], used a normal relocation time of 36 hours.

Similar to TIMHOT, the lower bound is developed based on an optimal response where OROs relocate residents promptly after plume arrival. A review of the SOARCA reference realization results [3] shows that the release fraction of cesium could exceed the normal dose threshold over most of the area 5 miles beyond the EPZ. From SecPop [87], the 2010 population within

the radial area 5 miles beyond the EPZ is about 150,000. The Surry scenario includes an assumption that 20 percent of this population evacuates as a shadow evacuation [3], and it is assumed another 20 percent of the public are relocated under the hotspot criteria. Thus for this analysis, about 95,000 residents remain in the area and could potentially be relocated (this assumes the entire remaining population in this area is relocated). Early notifications can be accomplished via EAS messaging, but route alerting would still be necessary and would take a few hours. For this size of population, traffic control would likely be established to support a relocation effort. Because the compromise time reflects the entire affected population, which is dispersed throughout the 5 mile radial area beyond the EPZ (approximately 400 square miles), a lower bound of 16 hours after plume arrival was judged reasonable.

The upper bound represents conditions where OROs are focused on activities within the EPZ or have other conflicting priorities which delay relocation activities. Furthermore, they may delay relocation until daylight hours. Because this relocation is due to a 1 rem dose projected over the emergency phase, it may not have the same priority as other urgent requirements. An upper bound of 48 hours after plume arrival was judged reasonable. The CDF is presented in Figure 4-67.

TIMNRM is perfectly rank correlated with the hotspot relocation time (TIMHOT) because MACCS requires TIMNRM be less than TIMHOT.

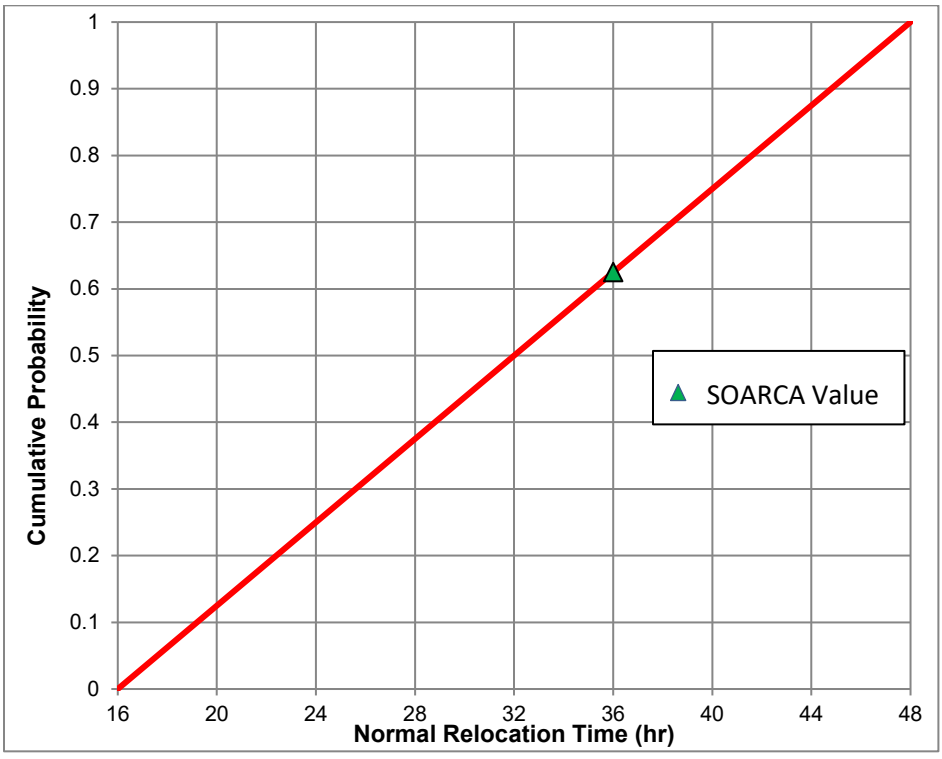

Figure 4-67 CDF of TIMNRM

4.2.7.5 Hotspot Relocation Dose (DOSHOT)

The hotspot relocation dose (DOSHOT) is a projected dose used to initiate hotspot relocation. If the total dose to individuals exceeds DOSHOT, those people are relocated (i.e., removed from the analysis) at a user specified hotspot relocation time (TIMHOT) [80] in the early phase.

DOSHOT is often [3][6] represented as the upper bound of the projected dose range provided in the EPA PAG Manual (Table 1-1. Planning Guidance and Protective Action Guides for Radiological Incidents) [89]. This should not be confused with the EPA PAG Manual criteria for relocation, which is specified for the intermediate phase [89].

Rationale for Distribution

A triangular distribution is used to represent the uncertainty in DOSHOT because the mode is considered to be the most likely value (5 rem) based on the EPA PAGs [89]. For the Surry SOARCA analysis [3], 5 rem projected over the emergency phase was used based on the upper evacuation bound in the EPA PAG Manual [89]. The range was developed recognizing that ORO decisions are influenced by many factors that could result in a higher or lower value.

The EPA PAG Manual provides a range of 1 to 5 rem for implementing protective actions and explains that under normal conditions, evacuation should be implemented if residents are expected to receive 1 rem over a 4 day emergency phase [89]. The upper bound for this distribution was increased 50 percent above the EPA PAG to 7.5 rem, based on analyst judgment. The lower bound was set at 1 rem, which is the mode of the normal relocation criteria (DOSNRM) as described in Section 4.2.7.6. The CDF is presented in Figure 4-68.

DOSHOT is perfectly rank correlated (i.e., coefficient of 1.0) with the normal relocation dose (DOSNRM) because MACCS requires DOSNRM to be less than DOSHOT.

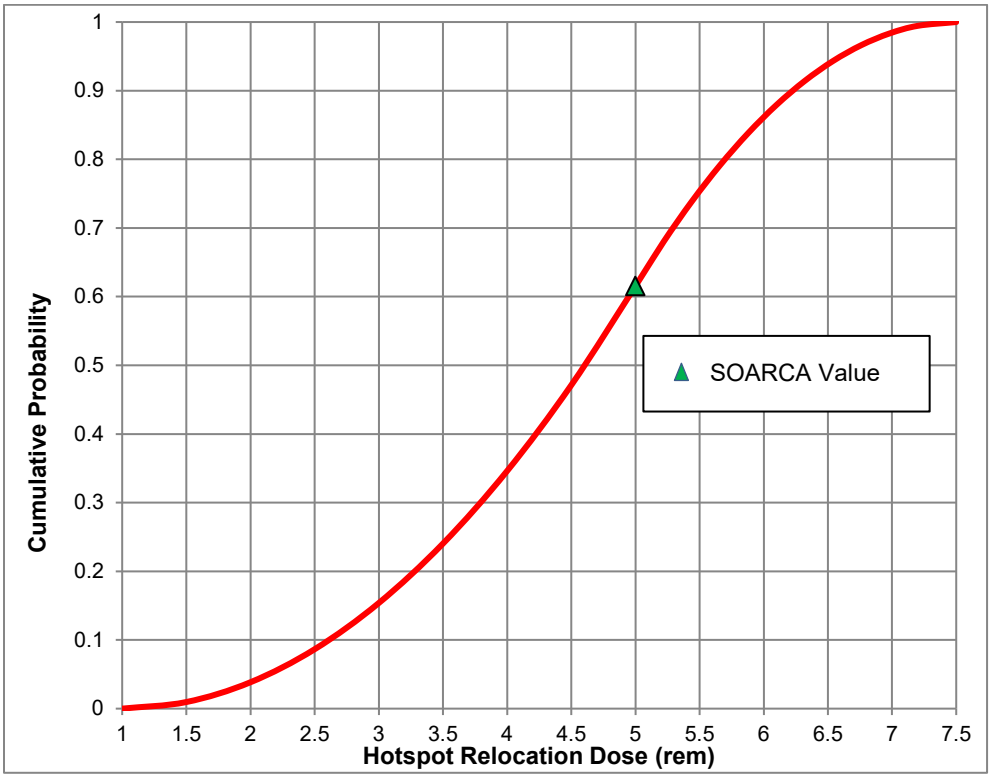

Figure 4-68 CDF of DOSHOT

4.2.7.6 Normal Relocation Dose (DOSNRM)

The normal relocation dose (DOSNRM) is a projected dose used to initiate normal relocation. If the total dose to individuals exceeds DOSNRM, those people are relocated (i.e., removed from the analysis) at a user specified normal relocation time (TIMNRM) [80] in the early phase. DOSNRM is typically [3][6] represented as the lower bound of the projected dose range provided in Table 1.1 of the EPA PAG Manual [89].

Rationale for Distribution

A triangular distribution is used because the mode (1 rem) is considered to be the most likely value based on EPA PAGs. For the Surry SOARCA analysis [3], a projected dose of 1 rem was used based on the lower evacuation bounds in Table 1.1 of the EPA PAG Manual [89]. A range was developed because OROs may implement a higher or lower value.

It is assumed that OROs would attempt to meet the EPA PAG barring unforeseen circumstances. Therefore, using judgment, the upper bound for this distribution was increased by a factor of two over the mode to 2 rem. The lower bound of 0.5 rem was judged reasonable. A low threshold value causes the size of the affected area to increase, which would increase the number of people requiring relocation. The number of people affected would likely influence ORO decisions on the lower threshold value. The CDF is presented in Figure 4-69.

DOSNRM is perfectly rank correlated with the hotspot relocation dose (DOSHOT) because MACCS requires DOSNRM to be less than DOSHOT.

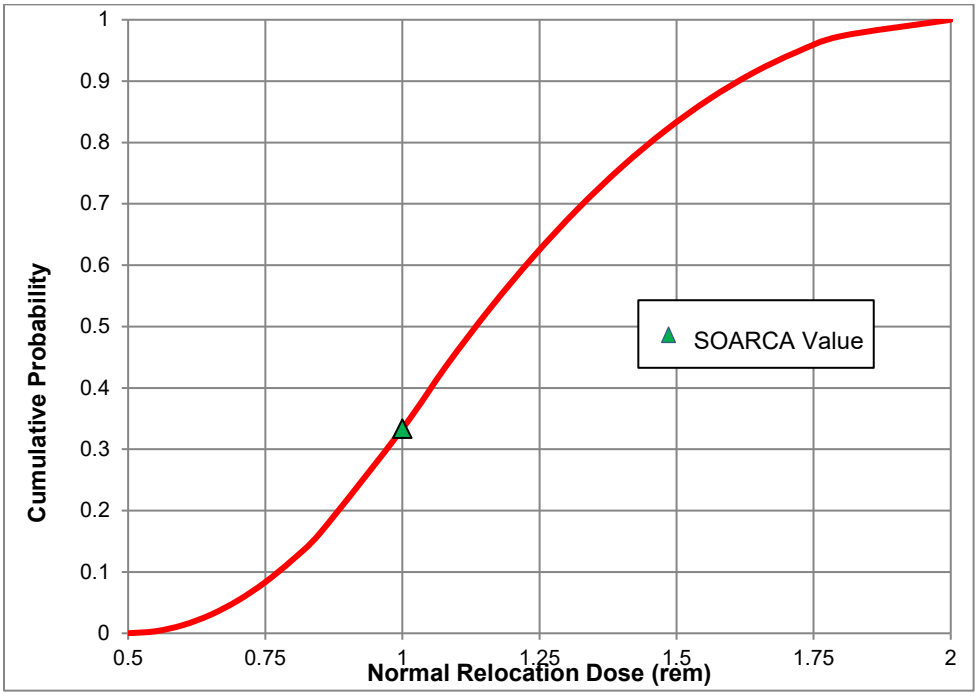

Figure 4-69 CDF of DOSNRM

4.2.8 Weather

Weather binning approach is used to categorize similar sets of weather data based on wind speed, stability class, and the occurrence of precipitation. For the non-uniform weather-bin sampling approach used for SOARCA, the number of trials selected from each bin was the maximum of 12 trials and 10 percent of the number of trials in the bin. Some bins contain fewer than 12 trials. In those cases, all of the trials within the bin are used for sampling. This strategy results in roughly 1,000 weather trials for the Surry weather data used in this analysis.

The best estimate offsite consequence values are the expected (mean) value of the probability distribution obtained from a large number of weather trials. The UA uses the same weather-sampling strategy adopted for SOARCA, as reported in the MACCS SOARCA Best Practices document, and also applied in the Peach Bottom and Sequoyah UAs [2][6][7].

One or more years of archived weather data from a reactor site is the starting point for evaluating the variability in consequences that can result from uncertain weather at the time of a future, hypothetical, atmospheric release of radioactive material. The inherent assumption in using historical data to quantify the consequences of a future event is that future weather data will be statistically similar to historical data. This has been a good assumption from past experience, as established by the body of work created when plants perform consequence analyses to support license extension applications.[51] That work looks specifically at two consequence measures: population dose and economic losses. For those results, the general observation has been that mean consequence values have been the same when evaluated for different individual years within five, usually consecutive, weather years to within about ±10 percent. The expectation is that this observation will be equally valid for future weather, although the variation could be larger for specific consequence measures.

Consequence analysis using MACCS is based on one year of archived data from a single weather tower. Most commonly, the weather tower is on the actual site of the nuclear power plant and is fairly close (less than a kilometer) to the location from which a source term would be emitted, were an accident to occur. This is the case for the Surry consequence analysis. Two years of archived weather data were obtained from the site and one of those years, 2004, was selected for this consequence analysis. Measurable precipitation (at least 0.01 in.) occurred during 6.9% of the hours of 2004. More details about the weather data used for Surry are provided in NUREG/CR-7110 Vol. 2 [3].

Meteorological data are measured at two elevations on a single weather tower and those measurements are used to construct four, hourly values to characterize the influence of weather. The hourly values represent integral or averaged values over hour-long intervals for each hour of a 365-day year (a total of 8760 data points). The hourly values in the meteorological data file are (1) wind direction, (2) wind speed, (3) stability class, and (4) precipitation rate. Wind direction and wind speed are measured at a fine time resolution (e.g., every 5 s) and averaged over the one-hour intervals. Stability class is constructed from temperatures measured at two elevations and evaluated according to criteria in Reg. Guide 1.23 [98]. One parameter in the meteorological data file, mixing layer height, is recorded as a seasonal average rather than an hourly value. The mixing layer heights serve as upper boundaries for vertical dispersion of a plume. There are eight values for mixing layer height, and

---

[51] See SAMA analyses in supporting Environmental Reports and Environmental Impact Statements (https://www.nrc.gov/reactors/operating/licensing/renewal/applications.html).

these are for morning and afternoon, averaged over each of the four seasons. A morning value generally corresponds to the minimum of the mixing layer height over a 24-hour period; the afternoon value generally corresponds to the maximum of the mixing layer height over a 24-hour period. All of these eight values are used to analyze a set of weather trials that represent the entire year and every hour of the day.

MACCS has several options for treatment of meteorological data, which include the ability to directly input weather data, or the ability to sample weather data from an external input file. Sampling options include a strategy that uses meteorological bins defined by the user (weather binning), or one or more random samples from each day of the weather file. Weather binning is a type of importance sampling used to categorize similar sets of weather data based on wind speed, stability class, and the occurrence of precipitation. With regard to wind direction, the assumption is that sampling within each weather bin is sufficient to adequately represent the wind rose, i.e., the likelihood of the wind blowing in each compass direction, for that bin. Accounting for the fact that each plume segment travels in its own direction, as explained below, this assumption should be satisfied.

The weather sampling strategy adopted for SOARCA and this Surry UA uses the weather-binning approach in MACCS. The weather binning structure is the same as the one in NUREG-1150 [16], which consists of 16 predefined bins for combinations of stability class and wind speed and 20 user-defined bins for rain occurring before the plume travels 32 km (20 miles). The rain bins differentiate rain intensity and the distance the plume travels before rain begins. Each hour of weather in the meteorological data file is placed into one of the weather bins, with the rain bins taking priority over the wind-speed/stability-class bins. The definition of these weather bins is provided in the Table 4-25. The probability of weather in each weather bin is proportional to the number of hours of data that go into that bin, and thus the weather bins are not equally probable. The probability of a sample (weather trial) drawn from a weather bin is accounted for in the sampling method. A weather trial uses a selected hour from one of the bins as the initial hour of weather corresponding to a release into the atmosphere. Subsequent hours of a weather trial follow the sequence of data from the weather file, as explained below.

Table 4-25 Rain Bins and Wind Speed and Stability Class Bins

	Rain Bins			
Rain Distance (miles)	Rain Intensity (mm/hr)			
	0 - 2	2 - 4	4 - 6	> 6
< 2 miles	Bin 17	Bin 18	Bin 19	Bin 20
2 - 3.5 miles	Bin 21	Bin 22	Bin 23	Bin 24
3.5 - 7 miles	Bin 25	Bin 26	Bin 27	Bin 28
7 - 13 miles	Bin 29	Bin 30	Bin 31	Bin 32
13 - 20 miles	Bin 33	Bin 34	Bin 35	Bin 36
> 20 miles	Not a rain bin – use wind speed and stability class binning			

	Wind Speed and Stability Class Bins					
Stability Class	Wind Speed u (m/s)					
	0 - 1	1 - 2	2 - 3	3 - 5	5 - 7	> 7
A/B	Bin 1			Bin 2		
C/D	Bin 3	Bin 4	Bin 5	Bin 6	Bin 7	Bin 8
E	Bin 9	Bin 10	Bin 11	Bin 12		
F/G	Bin 13	Bin 14	Bin 15	Bin 16		

The number of weather trials selected from each bin was the maximum of 12 trials and 10 percent of the number in the bin. Some bins contain fewer than 12 trials. In those cases, all of the trials within the bin are used in the set of weather trials. This strategy results in roughly 1,000 weather trials to represent the 8,760 hours of data in a 365-day year for the Surry UA. A sensitivity study conducted for the Peach Bottom UA [2] showed that this sampling strategy matched the mean results that would have been obtained by choosing every hour in the weather file (8760 samples) within 3% for health risks evaluated with the linear, no-threshold (LNT) dose-response assumption and within 12% for health risks evaluated with the two non-LNT dose-response assumptions. Since the same sampling strategy was chosen for Surry as Peach Bottom, the expectation is that the accuracy should be similar.

A weather trial in MACCS is significantly more complex than if it were modeled with just a point value of weather data. A weather trial is defined by the starting hour of weather data from the meteorological data file. However, the weather trial uses as much data from the meteorological data file as required to transport plume segments through and out of the computational grid. An overall atmospheric release (source term) for the Surry UA is described by 50 to 100 plume segments, depending on the occurrence of steam generator tube rupture. Each plume segment represents the quantity of radionuclides released over a one-hour period from a specific release path (e.g., leakage through a failed steam generator tube). Each plume segment can travel in a different direction, and it is affected by the hourly data, i.e., wind speed, stability class, and precipitation rate, taken from the weather file starting with the hour of its release from the source location until it exits the computational grid.

An illustration of the way plume segments move through the grid is shown in the following two snapshots from a plume animation. Figure 4-70 shows four consecutive plume segments, where the tail of one segment happens to align in distance traveled, but not in direction, with the head of the next. The plume segments are colored purple, green, yellow, and red in order of increasing radius in the first snapshot. The wind is shifting from northwest to northeast, as indicated by the directions of the segments. Figure 4-71 also shows four plume segments, where each has moved outward along its centerline toward the edge of the grid. One plume segment has disappeared off the grid and a new one has been created in an even more easterly direction than the previous segments. Each segment has its own width, depending on the amount of dispersion that has occurred as it experiences varying weather conditions along its path. Each segment also has a unique length, depending on the speed of the wind during its release.

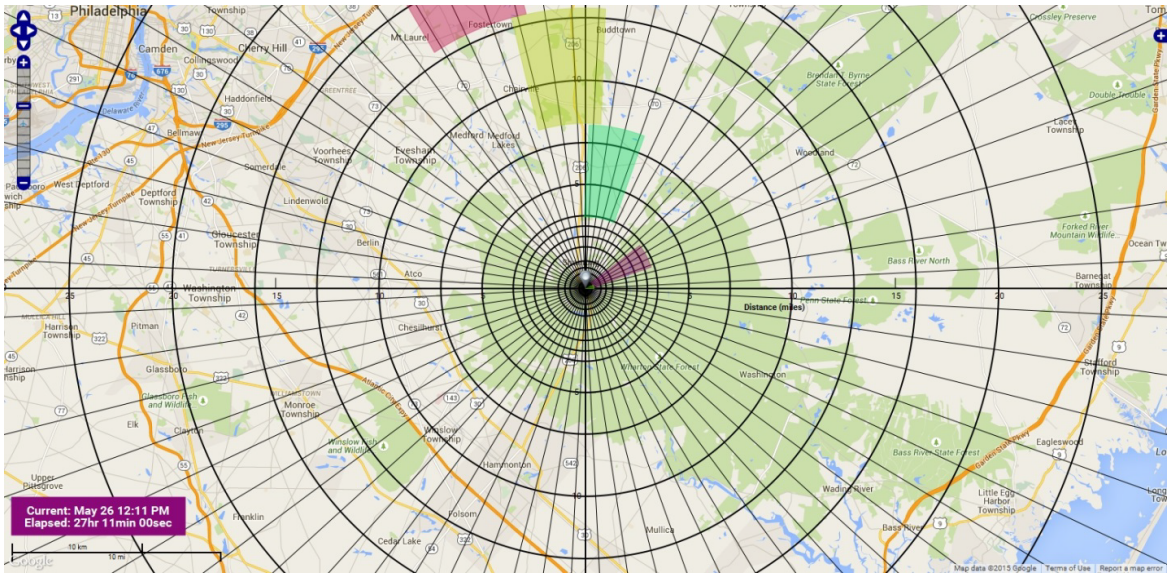

Figure 4-70 Illustration of Four Consecutive Plume Segments, where the tail of One Segment Aligns in Distance Traveled, but not in Direction, with the Head of the Next Segment

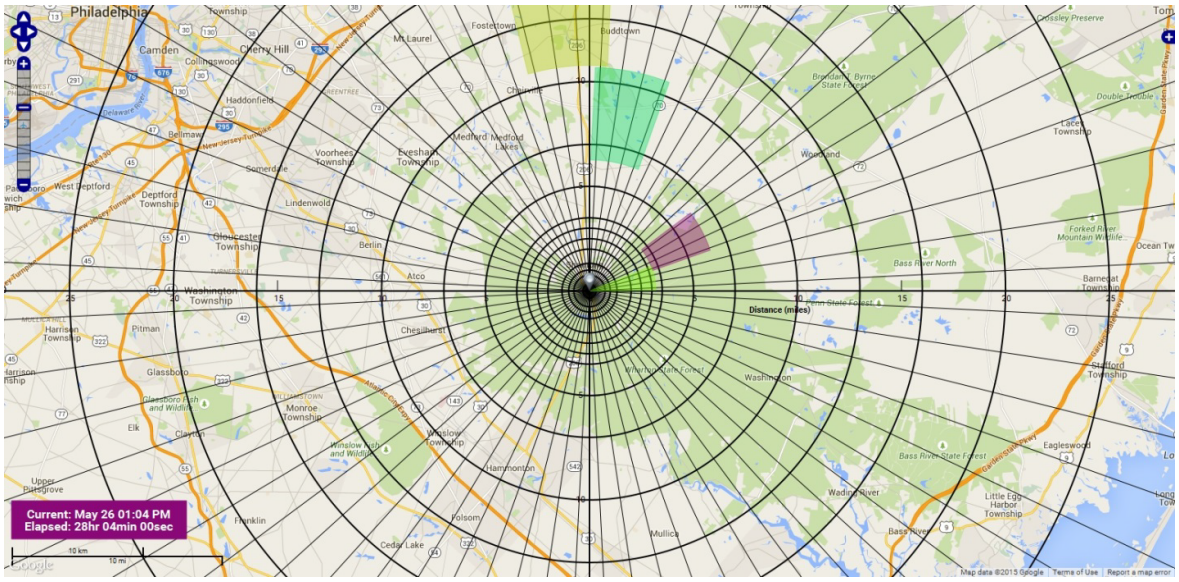

Figure 4-71 Illustration of Four Consecutive Plume Segments with tails that do not Align

4.2.9 MACCS Correlated Parameters

Many of the parameters in the analysis have correlations. Some of these are perfectly rank ordered and others have rank correlation coefficients between -1.0 and +1.0. Unless specified in Table 4-26 below, parameters are not correlated.

Table 4-26 MACCS Correlated Parameters

Input Parameter	Perfectly Rank-Order Correlated with	Comments
PROTIN(2)	LPROTIN	Long-term is tied to normal activity
GSHFAC(2)	LGSHFAC	Long-term is tied to normal activity
TIMHOT	TIMNRM	HOT is always less than NRM
DOSHOT	DOSNRM	HOT is always greater than NRM
EFFTHR(1)	EFFACA(1)	Red bone marrow
EFFTHR (2)	EFFACA (2)	Lungs
EFFTHR (3)	EFFACA (3)	Stomach
CYSIGA(1)	CYSIGA(2-6)	All weather conditions
CYSIGA(1)	CZSIGA(1-6)	All weather conditions
ESPEED(2)-1	ESPEED(2)-(2-5)	Middle Phase of Espeed for all Cohorts evacuating
VDEPOS(1)	VDEPOS(2-10)	All particle size bins
Co-58_ICH(1)	Co-58_ICH(2,4-9)	Lifetime inhalation dose coefficient
Co-60_ICH(1)	Co-58_ICH(2,4-9)	Lifetime inhalation dose coefficient
Rb-86_ICH(1)	Co-58_ICH(2,4-9)	Lifetime inhalation dose coefficient
Rb-88_ICH(1)	Co-58_ICH(2,4-9)	Lifetime inhalation dose coefficient
Sr-89_ICH(1)	Co-58_ICH(2,4-9)	Lifetime inhalation dose coefficient
Sr-90_ICH(1)	Co-58_ICH(2,4-9)	Lifetime inhalation dose coefficient
Sr-91_ICH(1)	Co-58_ICH(2,4-9)	Lifetime inhalation dose coefficient
Sr-92_ICH(1)	Co-58_ICH(2,4-9)	Lifetime inhalation dose coefficient
Y-90_ICH(1)	Co-58_ICH(2,4-9)	Lifetime inhalation dose coefficient
Y-91_ICH(1)	Co-58_ICH(2,4-9)	Lifetime inhalation dose coefficient
Y--91m_ICH(1)	Co-58_ICH(2,4-9)	Lifetime inhalation dose coefficient
Y-92_ICH(1)	Co-58_ICH(2,4-9)	Lifetime inhalation dose coefficient
Y-93_ICH(1)	Co-58_ICH(2,4-9)	Lifetime inhalation dose coefficient
Zr-95_ICH(1)	Co-58_ICH(2,4-9)	Lifetime inhalation dose coefficient
Zr-97_ICH(1)	Co-58_ICH(2,4-9)	Lifetime inhalation dose coefficient
Nb-95_ICH(1)	Co-58_ICH(2,4-9)	Lifetime inhalation dose coefficient
Nb-97_ICH(1)	Co-58_ICH(2,4-9)	Lifetime inhalation dose coefficient
Mo-99_ICH(1)	Co-58_ICH(2,4-9)	Lifetime inhalation dose coefficient
Tc-99m_ICH(1)	Co-58_ICH(2,4-9)	Lifetime inhalation dose coefficient
Ru-103_ICH(1)	Co-58_ICH(2,4-9)	Lifetime inhalation dose coefficient
Ru-105_ICH(1)	Co-58_ICH(2,4-9)	Lifetime inhalation dose coefficient
Ru-106_ICH(1)	Co-58_ICH(2,4-9)	Lifetime inhalation dose coefficient
Rh-103m_ICH(1)	Co-58_ICH(2,4-9)	Lifetime inhalation dose coefficient
Rg-105_ICH(1)	Co-58_ICH(2,4-9)	Lifetime inhalation dose coefficient
Te-127_ICH(1)	Co-58_ICH(2,4-9)	Lifetime inhalation dose coefficient
Te-127m_ICH(1)	Co-58_ICH(2,4-9)	Lifetime inhalation dose coefficient
Te-129_ICH(1)	Co-58_ICH(2,4-9)	Lifetime inhalation dose coefficient
Te-129m_ICH(1)	Co-58_ICH(2,4-9)	Lifetime inhalation dose coefficient
Te-131_ICH(1)	Co-58_ICH(2,4-9)	Lifetime inhalation dose coefficient
Te-131m_ICH(1)	Co-58_ICH(2,4-9)	Lifetime inhalation dose coefficient
Te-132_ICH(1)	Co-58_ICH(2,4-9)	Lifetime inhalation dose coefficient
I-131_ICH(1)	Co-58_ICH(2,4-9)	Lifetime inhalation dose coefficient

Table 4-26 MACCS Correlated Parameters

Input Parameter	Perfectly Rank-Order Correlated with	Comments
I-132_ICH(1)	Co-58_ICH(2,4-9)	Lifetime inhalation dose coefficient
I-133_ICH(1)	Co-58_ICH(2,4-9)	Lifetime inhalation dose coefficient
I-134_ICH(1)	Co-58_ICH(2,4-9)	Lifetime inhalation dose coefficient
I-135_ICH(1)	Co-58_ICH(2,4-9)	Lifetime inhalation dose coefficient
Cs-134_ICH(1)	Co-58_ICH(2,4-9)	Lifetime inhalation dose coefficient
Cs-136_ICH(1)	Co-58_ICH(2,4-9)	Lifetime inhalation dose coefficient
Cs-137_ICH(1)	Co-58_ICH(2,4-9)	Lifetime inhalation dose coefficient
Ba-139_ICH(1)	Co-58_ICH(2,4-9)	Lifetime inhalation dose coefficient
Ba-140_ICH(1)	Co-58_ICH(2,4-9)	Lifetime inhalation dose coefficient
La-140_ICH(1)	Co-58_ICH(2,4-9)	Lifetime inhalation dose coefficient
La-141_ICH(1)	Co-58_ICH(2,4-9)	Lifetime inhalation dose coefficient
La-142_ICH(1)	Co-58_ICH(2,4-9)	Lifetime inhalation dose coefficient
Ce-143_ICH(1)	Co-58_ICH(2,4-9)	Lifetime inhalation dose coefficient
Ce-144_ICH(1)	Co-58_ICH(2,4-9)	Lifetime inhalation dose coefficient
Pr-143_ICH(1)	Co-58_ICH(2,4-9)	Lifetime inhalation dose coefficient
Pr-144_ICH(1)	Co-58_ICH(2,4-9)	Lifetime inhalation dose coefficient
Nb-147_ICH(1)	Co-58_ICH(2,4-9)	Lifetime inhalation dose coefficient
Np-239_ICH(1)	Co-58_ICH(2,4-9)	Lifetime inhalation dose coefficient
Pu-238_ICH(1)	Co-58_ICH(2,4-9)	Lifetime inhalation dose coefficient
Pu-239_ICH(1)	Co-58_ICH(2,4-9)	Lifetime inhalation dose coefficient
Pu-240_ICH(1)	Co-58_ICH(2,4-9)	Lifetime inhalation dose coefficient
Pu-241_ICH(1)	Co-58_ICH(2,4-9)	Lifetime inhalation dose coefficient
Am-241_ICH(1)	Co-58_ICH(2,4-9)	Lifetime inhalation dose coefficient
Cm-242_ICH(1)	Co-58_ICH(2,4-9)	Lifetime inhalation dose coefficient
Cm-244_ICH(1)	Co-58_ICH(2,4-9)	Lifetime inhalation dose coefficient
Linear correlation coefficients		
Input Parameter	**Rank-Order Correlated With**	**Correlation Coefficient**	**Comments**
PROTIN(2)	PROTIN(3)	0.75	Applies to all evacuation cohorts for normal activity and sheltering inhalation protection factors
GSHFAC(2)	GSHFAC(3)	0.8	

4.3 Quality Assurance Review of Input Parameters

4.3.1 MELCOR QA Review

Each uncertain MELCOR parameter was input into the Surry SOARCA model using a combination of existing MELCOR input records, new control and tabular, the .mapped and .vars files, and external data files. To confirm that the implementation of the parameters was done correctly, a QA review for each parameter was performed using the first set of fifty uncertainty runs along with select one-off sensitivities.

The QA involved multiple activities. First, the created input files and associated MELCOR output variables were checked to ensure that the proper values were used. Second, plots of key results were checked to see that they matched with expectations based on certain values of the parameters. If there was not a run in the uncertainty set that used a needed value for a parameter, a sensitivity analysis was run where that value was manually selected.

This general QA approach was implemented for each of the uncertain MELCOR parameters. Other single sensitivities were conducted, such as varied containment liner yield pressure, a secondary SV sticking open, and primary SV1 failing closed. A number of errors were found, both in the sampling of values and in the model enhancements done for their implementation. All of the identified errors were corrected before the final uncertainty realizations were run.

4.3.2 MACCS QA Review

Dose coefficients were an important element of the QA review. A comprehensive table of mean dose coefficients and variances for eight organs was created using data from a report developed by Keith Eckerman to support SOARCA [76]. The dose coefficients were calculated by taking the natural log of the inhalation dose coefficients from Appendix B of Eckerman's report. Appendix B tabulates dose coefficients for the eight cancer sites and represents their uncertainties in terms of a log-normal distribution. The variance was calculated by also taking the natural log of the standard deviation values found in Table B-2 of Eckerman's report. The natural log of both the dose coefficient and variance were reviewed individually from the MACCS run. Of the 928 values reviewed, 7 values were found incorrect and were corrected for Surry.

5 MELCOR ACCIDENT PROGRESSION – OVERALL RESULTS AND SELECT REALIZATIONS

The MELCOR accident progression results are presented in two ways. First, Section 5 presents the results of individual realizations to provide background and context of the uncertainty results that are presented in Section 6.1. Whereas the results presented in Section 6.1 focus on the overall importance of various accident progression uncertainties on the key metrics of merit, the results presented in this section characterize the accident progression of individual realizations. First, Section 5.1 provides some overall statistics on the UA realizations, including key observations about realizations with a SGTR versus ones without. Next, Section 5.2 presents the results of two reference realizations to illustrate the accident progression with and without a SGTR. Finally, Section 5.3 examines individual realizations that had interesting or minimum/maximum responses from the uncertainty study (e.g., minimum or maximum cesium source term, maximum in-vessel hydrogen production, etc.). Using the context of the individual realization responses allows a better understanding of the uncertainty results presented in Section Section 6.1.

5.1 Overall MELCOR Uncertainty Analysis Results

1,200 realizations were initiated with varying combinations of values for the uncertain variables described above. Of these 1,200 realizations, 1,147 of them were successful to 72 hr relating to a success rate of 96%.[52] Various first-order statistics and results are presented below.

5.1.1 SGTR Occurrences

In the 1,147 successful UA realizations, there were 144 realizations with SGTRs. 6 of the 144 realizations with SGTRs had 2 SGTRs. The tube ruptures occurred in all three SGs and in all three distinct regions defined within the tube bundles. The three regions are:

- the hottest tube temperatures (referred to below as the hottest region),
- the reminder of the hot upflow region (referred to as the hot upflow region), and
- the remainder of the steam generator including the cooler return flow tubes (referred to as the cold region)

Table 5-1 presents the distribution of SGTRs between SGs and region. Notice that most tube ruptures occurred away from the hotter and even the hottest tubes. This is because of the dominant influence that major flaws had on tube stress and the greatest possibility of a major flaw location being in the least hot (“cold”) region of the tube bundle.[53]

All three locations (hottest, hot upflow, and cold regions) in each of the three steam generators were monitored for the potential of a tube failure in an unflawed tube. However, there were no rupture of an unflawed tube in any UA realization.

---

[52] See section 3.3.2.10 for a discussion of the regression analysis of failed realizations.

[53] The flaws were assumed to be randomly located across all tubes. Since the cold zone contains 75% of the tubes with only 3% and 22% in the hottest and hot upflow regions, respectively, it was more likely to have a deep flaw in the cold zone. The accident progression and assoiated thermal response determined whether a less flawed tube failed in the hotter region or a more severely flawed tube failed in the cold region. The tube flaw assumptions are discussed in Section 4.1.1.6 (e.g., see Table 4-10).

Table 5-1 SGTR Occurrences by SG and Region

SG	SGTR region			Total
	Cold	Hot	Hottest	
SG A [54]	39	19	8	65
SG B	24	18	4	45
SG C	26	10	8	41
Combined	89	47	20	150

5.1.2 SG Tube Creep Damage

The creep damage suffered by SG tubes in the UA realizations is illustrated in Figure 5-1. Unity creep values are indicative of tube rupture. Notice in this figure that the rate of creep damage is quite steep during the initial core damage phase. The accumulation of creep damage was interrupted by either a SGTR (i.e., creep damage index is equal to 1) or creep rupture of a hot leg nozzle. Consequently, the hot leg rupture timing was critical. Any significant delay (e.g., 1 hr) on average in the time to hot leg rupture would have markedly increased the number of tube ruptures in the UA. Figure 5-1 includes results for only SG-A, but the results for SG-B and SG-C are similar. The creep damage plateaus either when a hot leg ruptures or the steam generator tube ruptures.

[54] The Monte Carlo samples of tube flaws randomly left more deep flaws in SG A that caused more SGTRs. The randomness of the flaw algorithim was confirmed by generating a successively larger flaw samples, which generated more uniform profiles across the three steam generators. Since the regressions focused on a single SG, it was advantageous to have one steam generator with a larger number of realizations with SGTRs. Consequently, the random seed was not changed.

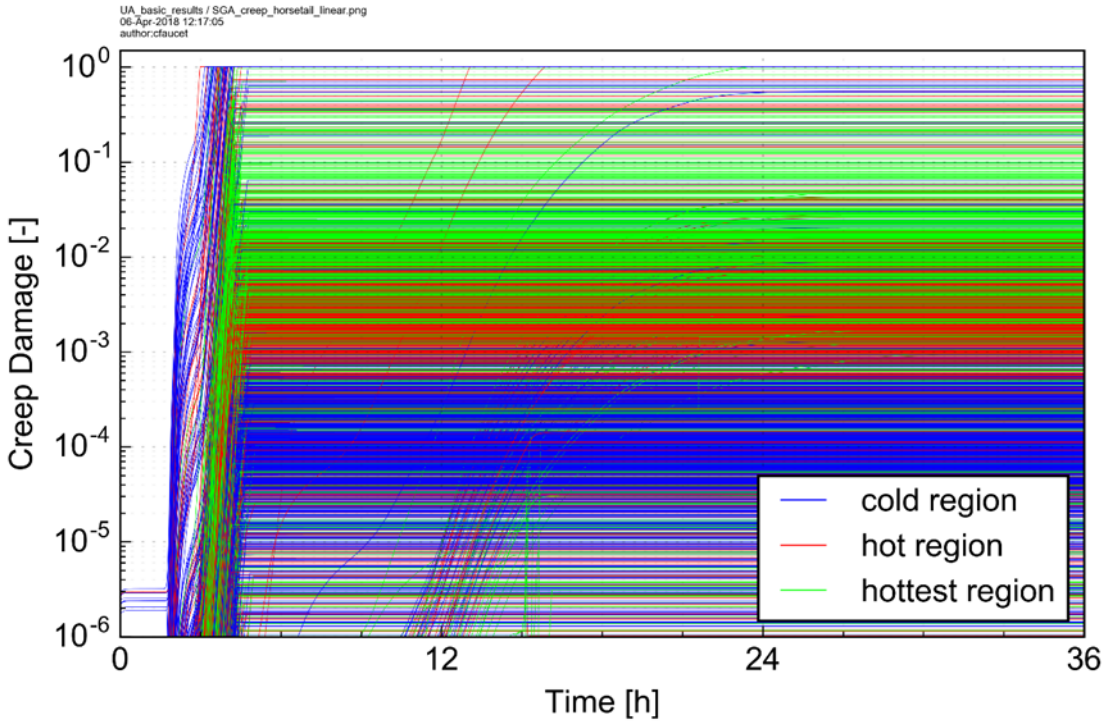

Figure 5-1 SG-A Tube Creep Damage History

The sampled normalized flaw depth was the largest factor relating to whether a tube ruptured. If a tube wasn't flawed at the onset of a MELCOR calculation, it did not rupture. The temperature to which a tube was subjected, i.e., the location of the tube in the tube bundle, was also an important factor relating to whether the tube ruptured with hotter regions leading to greater creep damage. The dependencies of tube creep damage on normalized flaw depth and region can be seen in Figure 5-2. Figure 5-3 shows further the dependency on region but with a somewhat different creep damage consideration, that being the creep damage to unflawed tubes, i.e., the creep damage to tubes having a nominal as-manufactured wall thickness. The creep damage to unflawed tubes in the UA was helpful to eliminate the sometimes-overwhelming influence of the sampled nominal flaw depth. This allowed lesser but still important influences of other parameters to be recognized. Notice the strong striations in Figure 5-3 associated with the different regions in the tube bundle. Figure 5-2 and Figure 5-3 include results for only SG A but results for SGs B and C are similar.

Clearly evidenced in Figure 5-2 is that maximally compromised tubes could rupture without being exposed to the hotter temperatures developed in a tube bundle (i.e., the relatively coolest temperatures being sufficient to rupture a more severely flawed tube).

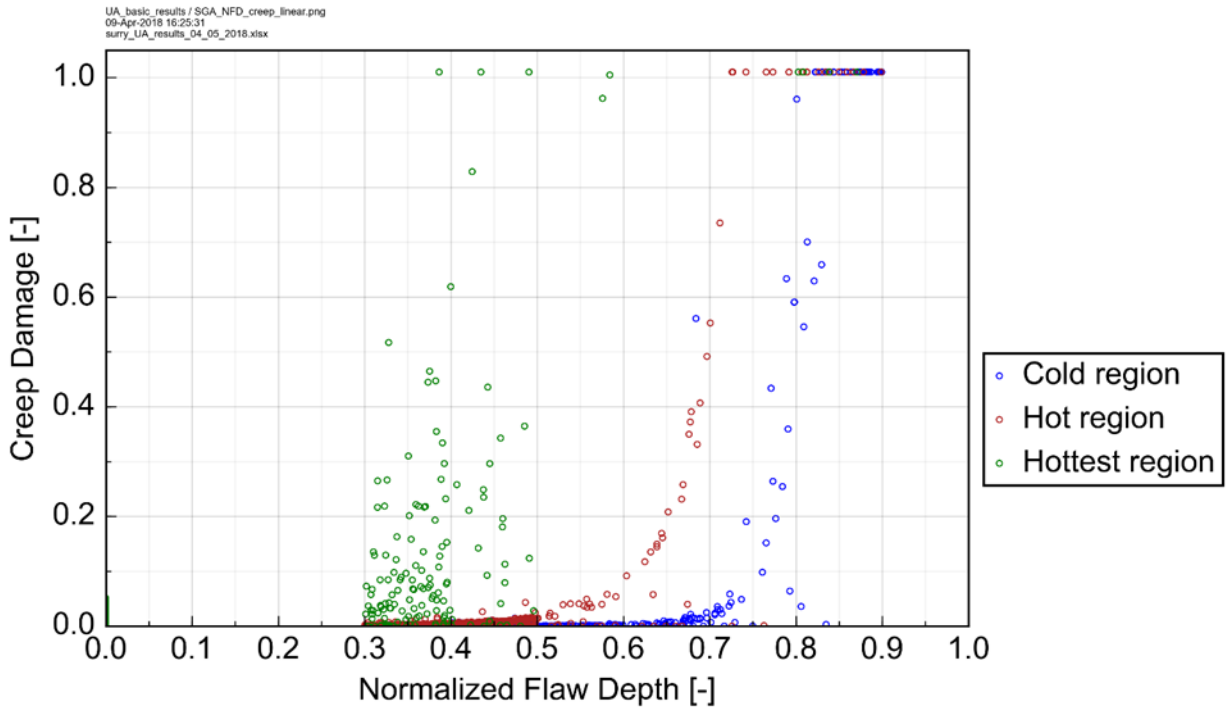

Figure 5-2 SG-A Tube End-State Creep Damage by Flaw Depth and Bundle Region

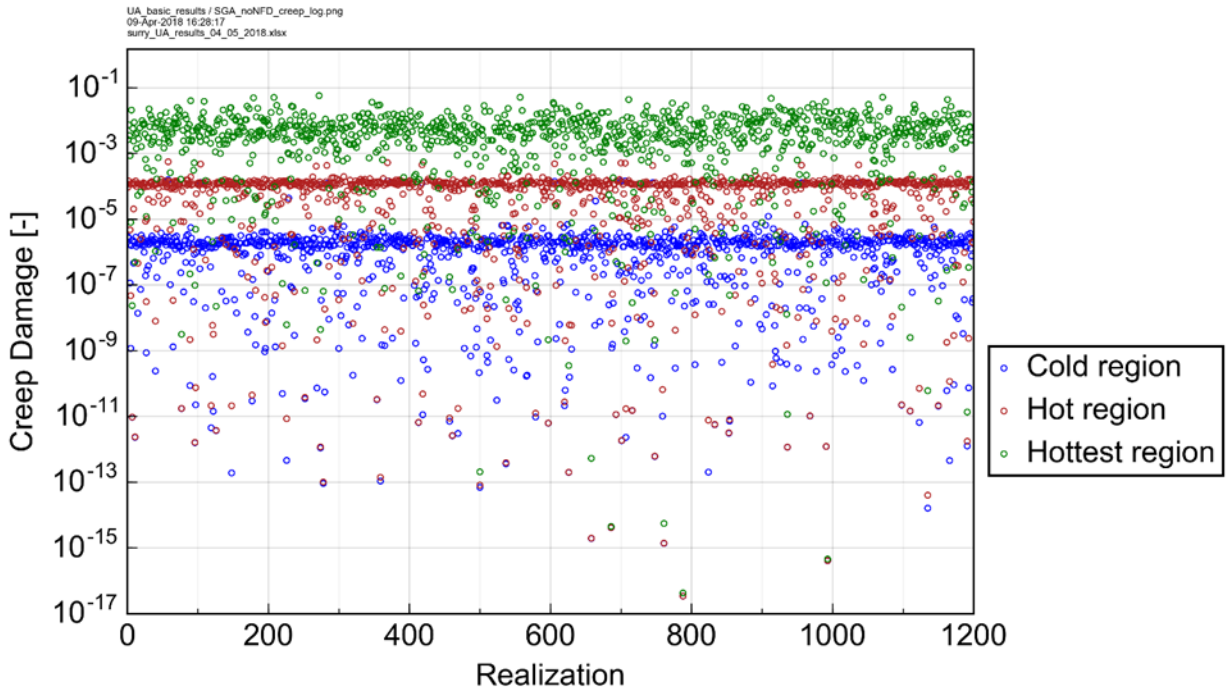

Figure 5-3 SG-A Unflawed Tube End-State Creep Damage by Bundle Region and Realization

5.1.3 Cesium Release to the Environment

Fundamentally important with respect to the amount of cesium released to the environment in the UA realizations was whether a SGTR occurred. A SGTR allowed fission products to bypass containment in releasing to the environment. Table 5-2 and Table 5-3 present basic statistics of the cesium releases to the environment in the UA realizations that did and did not experience a SGTR, respectively.

Table 5-2 Cs Release to the Environment by 72 hr (SGTR)

	Released Cs fraction	Released Cs (kg)
Minimum	1.06E-03	0.239
5th Percentile	3.78E-03	0.803
Median	1.15E-02	2.147
Mean	1.32E-02	2.516
95th Percentile	2.45E-02	4.712
Maximum	7.30E-02	11.456

Table 5-3 Cs Release to the Environment by 72 hr (Non-SGTR)

	Released Cs fraction	Released Cs (kg)
Minimum	7.29E-06	1.00E-03
5th Percentile	1.22E-05	1.89E-03
Median	3.65E-05	7.18E-03
Mean	7.05E-05	1.38E-02
95th Percentile	3.29E-04	6.53E-02
Maximum	9.21E-04	1.34E-01

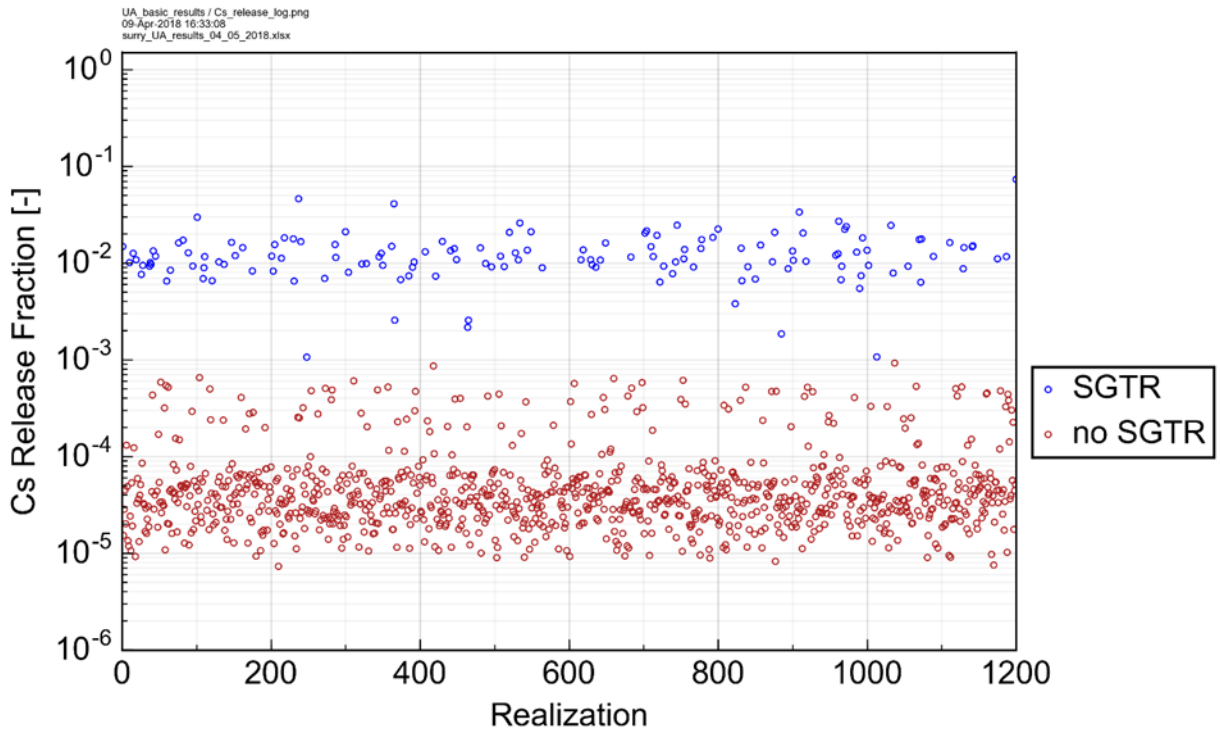

Figure 5-4 Cs Release to the Environment by Realization

5.1.4 Iodine Release to the Environment

Similar to the cesium releases, the amount of iodine released to the environment in the UA realizations was strongly dependent whether a SGTR occurred. Table 5-4 and Table 5-5 present basic statistics of the iodine releases to the environment in the successful realizations that did and did not experience a SGTR, respectively.

Table 5-4 Iodine Release to the Environment by 72 hr (SGTR)

	Released I fraction	Released I (kg)
Minimum	2.50E-03	1.95E-04
5th Percentile	5.91E-03	6.55E-04
Median	1.79E-02	3.25E-01
Mean	1.99E-02	3.40E-01
95th Percentile	3.92E-02	8.53E-01
Maximum	7.84E-02	2.33E+00

Table 5-5 Iodine Release to the Environment by 72 hr (Non-SGTR)

	Released I fraction	Released I (kg)
Minimum	9.57E-06	3.57E-05
5th Percentile	4.67E-05	6.72E-04
Median	2.73E-04	5.42E-03
Mean	4.64E-04	2.68E-02
95th Percentile	1.41E-03	4.87E-02
Maximum	8.47E-03	9.44E-01

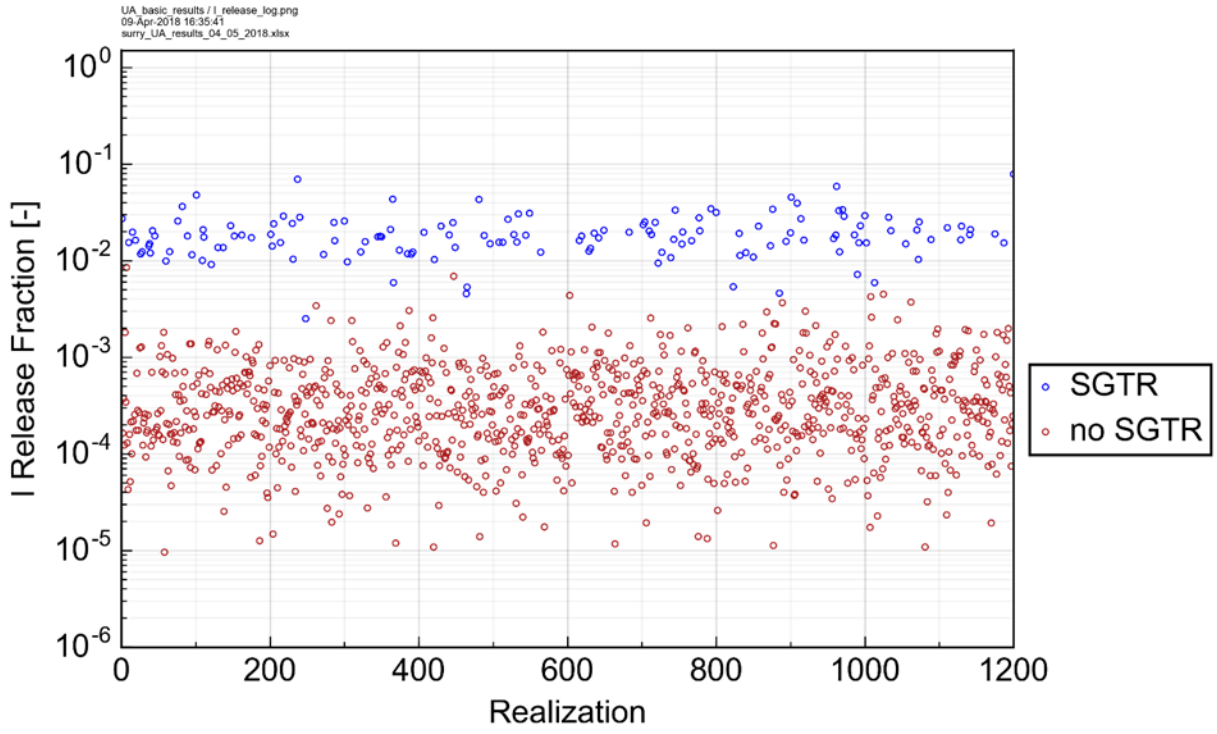

Figure 5-5 Iodine Release to the Environment by Realization

5.1.5 Timing of 1% Release of Elemental Gaseous Iodine (I_2) to the Environment

The time from the onset of the SBO to when the release of elemental gaseous iodine to the environment exceeds 1% of the initial gaseous iodine in the core-wide interstitial volume of the fuel pins was defined as a relative measure of fission product release timing in the UA. Table 5-6 and Figure 5-6 present the results associated with this metric.

Table 5-6 Timing of 1% Release of Elemental Gaseous Iodine (I_2) to the Environment

	Timing of 1% I_2 release (hr)
Min	3.511
Mean	49.104
Median	55.591
Max	71.983

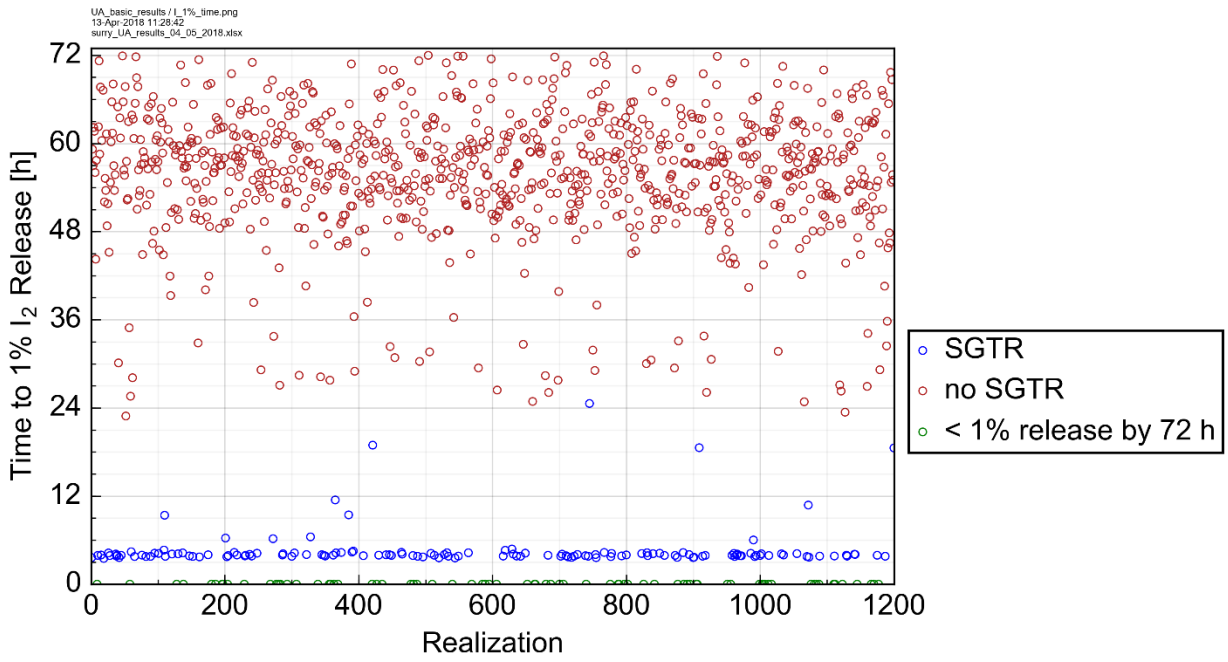

Figure 5-6 Timing of 1% Release of Elemental Gaseous Iodine (I_2) to the Environment by Realization

5.1.6 In-Vessel Hydrogen Production

Basic statistics in the UA realizations of hydrogen produced in the reactor vessel by fuel cladding and steel oxidation reactions are presented in Table 5-7. Figure 5-7 shows in-vessel hydrogen production by realization.

Table 5-7 In-Vessel Hydrogen Production

	H_2 produced (kg)
Mean	318.2
Median	309.7
Min	164.0
Max	777.0

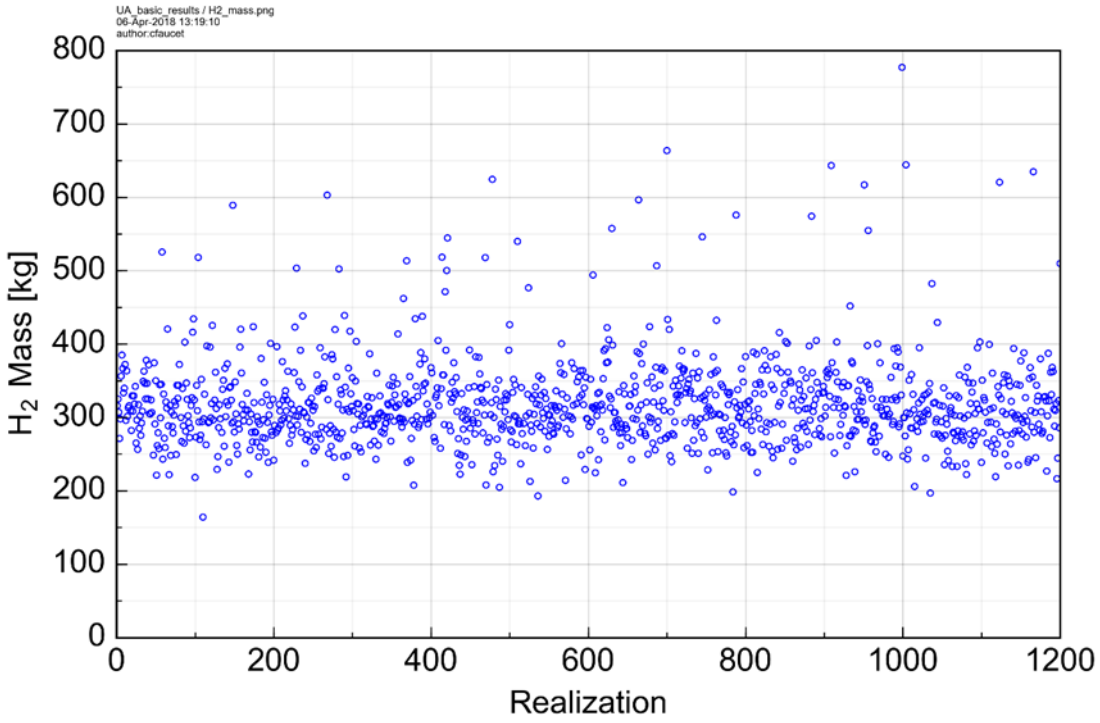

Figure 5-7 In-Vessel Hydrogen Production by Realization

5.1.7 Pressurizer SV FTC Statistics

Various FTC statistics on the pressurizer SVs in the UA realizations are presented in Table 5-8 while Figure 5-8 shows the combinations of valve cycles to failure and open area fraction given failure that were and were not associated with a SGTR. For a tube rupture to occur, the pressurizer SVs needed to function per design, i.e., not fail to close, or fail to close with a small open area fraction.

Table 5-8 Pressurizer SV FTC Statistics

	SV-1	SV-2	SV-3
FTC occurrences	120	10	0
Mean cycles to FTC	17.667	5.800	-
Median cycles to FTC	11	5.5	-
Min cycles to FTC	1	1	-
Max cycles to FTC	63	15	-
Mean FTC open fraction	0.384	0.661	-
Median FTC open fraction	0.092	0.773	-
Mean time of FTC (hr)	2.468	2.512	-
Median time of FTC (hr)	2.204	2.295	-
Earliest FTC time (hr)	1.876	2.042	-
Latest FTC time (hr)	4.122	3.728	-

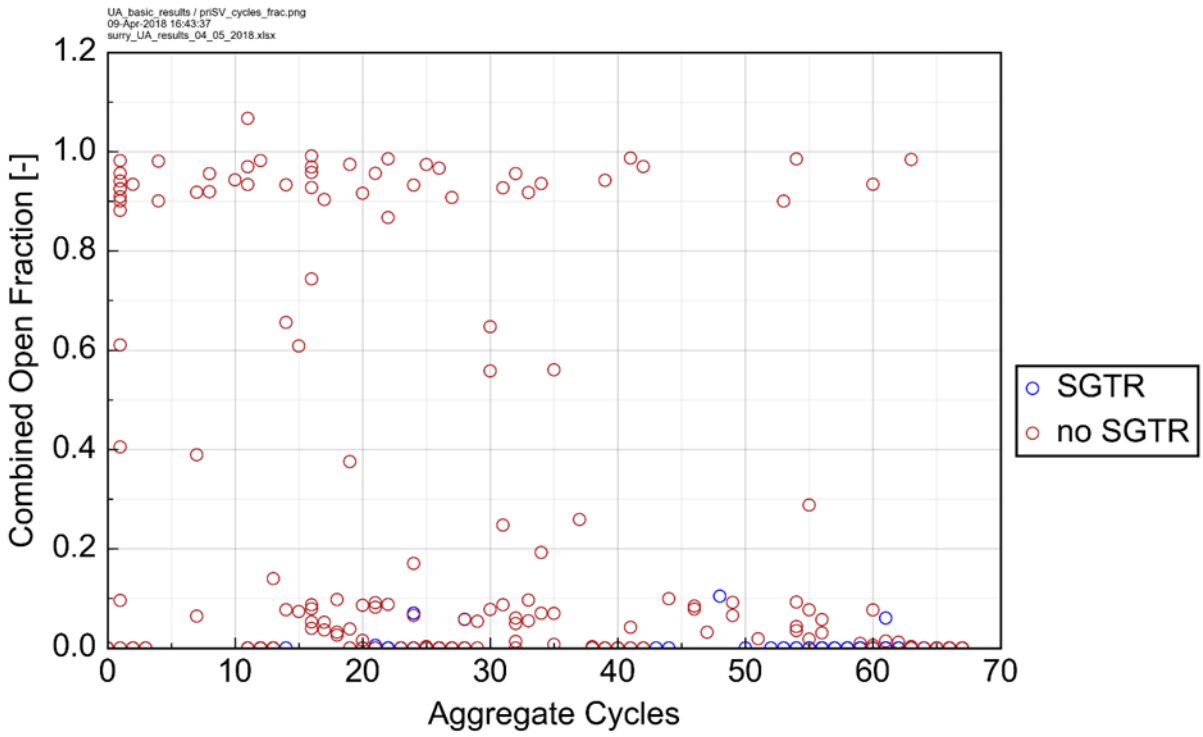

Figure 5-8 Aggregate Pressurizer SV Cycles and End-State Open Fraction

Notable with respect to pressurizer SV failure in the UA realizations is that there were no indicated overheating threats to the valves. The elevated temperature of the fluid passed by a SV that would threaten the valve was sampled and tracked. The monitored thermal failure temperature was not reached in any realization. The sampling was between 840 K and 1,258 K with a mean and median of 1,005 K.

5.1.8 MSL SV FTC Statistics

FTC statistics on the main steam line SVs in the UA realizations are presented in Table 5-9. Figure 5-9 shows the combinations of valve cycles to failure and open area fraction given failure by realization.

Table 5-9 MSL SV FTC Statistics

	MSL A	MSL B	MSL C
FTC occurrences	116	127	130
Mean cycles to FTC	26	26	23
Median cycles to FTC	24.5	19	15
Min cycles to FTC	1	1	1
Max cycles to FTC	102	93	92
Mean FTC open fraction	0.325	0.380	0.398
Median FTC open fraction	0.087	0.181	0.176
Mean time of FTC (hr)	0.617	0.644	0.490
Median time of FTC (hr)	0.563	0.537	0.309
Earliest FTC time (hr)	0.042	0.043	0.040
Latest FTC time (hr)	1.827	4.350	1.507

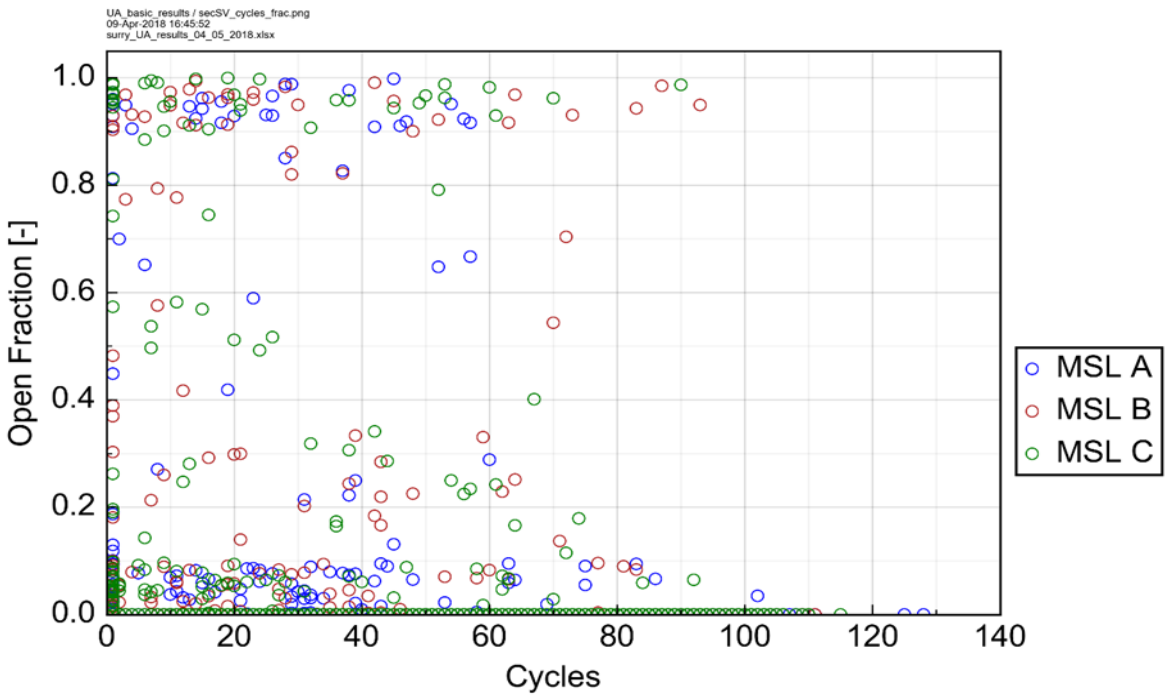

Figure 5-9 MSL SV Cycles and End-State Open Fraction

5.1.9 Timing of PRT Drying Out

In the 1,147 successful UA realizations, the PRT dried out 54 times. Table 5-10 presents statistics of the timing of the PRT dryout in the 54 realizations with dryout. The dryout of the PRT is important because the fission products captured in the water are susceptible to re-vaporization once the tank dries out. The impact of the revaporized fission products is most significant when it occurs near or after the timing of the containment failure.

The water depth in the PRT at 72 hr in the UA realizations is shown in Figure 5-10. The initial water level is 2.3 m. Most of the final PRT water levels fell into three groups: (1) 2.3 m or higher, (2) ~1.75 m, and (3) dried out. The realizations with significant pump seal failures (i.e., >500 gpm)[55] had limited pressurizer SV cycling and the rupture disk remained intact. The PRT level increased in the first group due to water density changes from external heating as the containment pressurized. The PRT rupture disk did not open in these realizations. In the second group of realizations with a PRT water level near ~1.75 m, the rupture disk opened after heating and pressurizing (i.e., most realizations). The water level settled at ~1.75 m after the rupture disk opened. All flow to the PRT terminated after the hot leg failure. The drop in inventory occurred when some water was expelled during the PRT depressurization when the rupture disk opened. The final group of realizations where the PRT dried out included a stuck-open pressurizer SV that discharged a large mass of fission products to the PRT. The decay heat from the fission products boiled the PRT dry.

Table 5-10 Timing of the PRT Dryout in in the Realizations with Dryout

	PRT dryout time (hr)
Mean	12.712
Median	10.116
Min	7.373
Max	66.212

[55] Realizations with the earliest time at cycle (i.e., 0.5 days) did not have any pressurizer cycling with lower amounts of pump seal leakage (e.g., Realization 196 with 224 gpm to RRCP pump leakage).

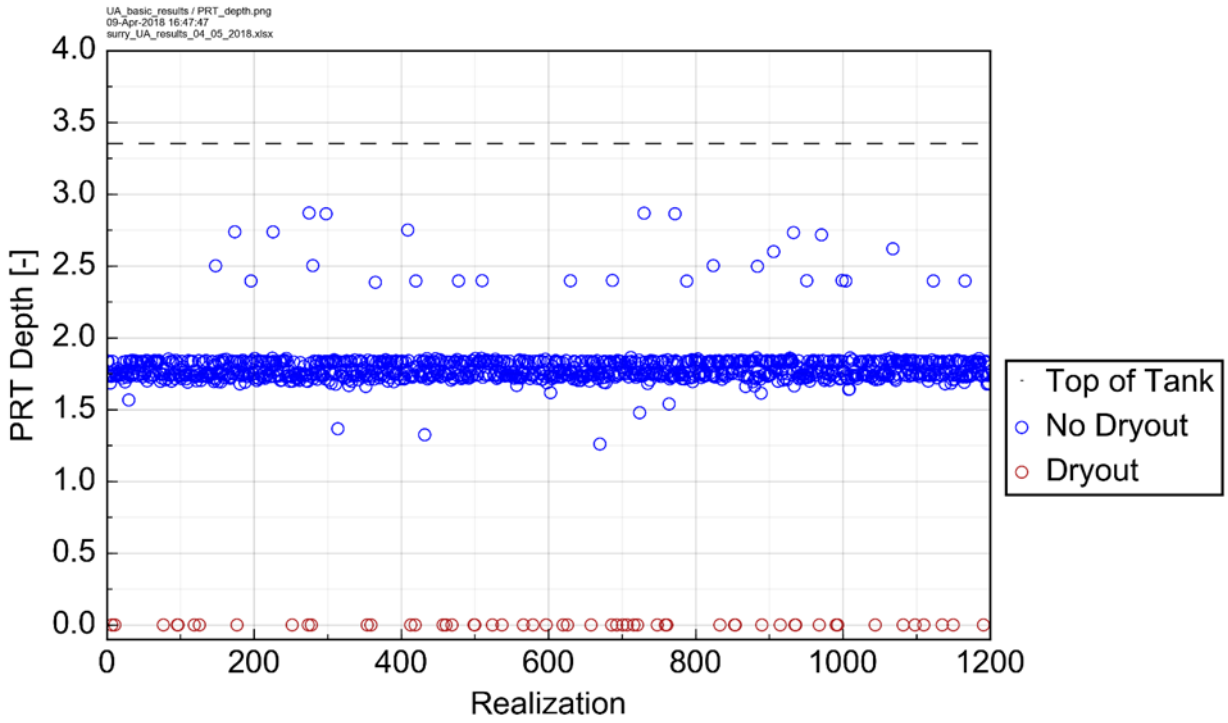

Figure 5-10 End-State Water Depth in the PRT by Realization

5.1.10 Hot Leg Rupture Timing

In all but one of the successful UA realizations, there was a rupture of a hot leg nozzle. Table 5-11 presents timing and location statistics of the ruptures. The lone realization that did not suffer a hot leg rupture by 72 hr (Rlz 935) is addressed in Section 5.3.

Table 5-11 Timing and Location of Hot Leg Nozzle Ruptures

	All hot legs	Hot leg A	Hot leg B	Hot leg C
Number of ruptures	1146	10	4	1133
Mean rupture time (hr)	4.714	10.236	9.340	4.648
Median rupture time (hr)	4.253	4.623	4.748	4.251
Min rupture time (hr)	3.713	4.401	4.371	3.713
Max rupture time (hr)	>72	27.168	23.493	31.278

The strong propensity for the hot leg rupture to occur at the loop C nozzle is due to the pressurizer being connected to loop C. As core damage proceeds and the RCS vents through the pressurizer SVs, hot gasses flow through the loop C hot leg nozzle. This venting flow is larger than the hot leg natural circulation flows experience by all the loops. Consequently, the heat stress on the loop C nozzle is generally greater than on the loop A and loop B nozzles.

Noteworthy is that creep damage to the pressurizer surge line nozzle was never significant (always <0.01) in the UA realizations.

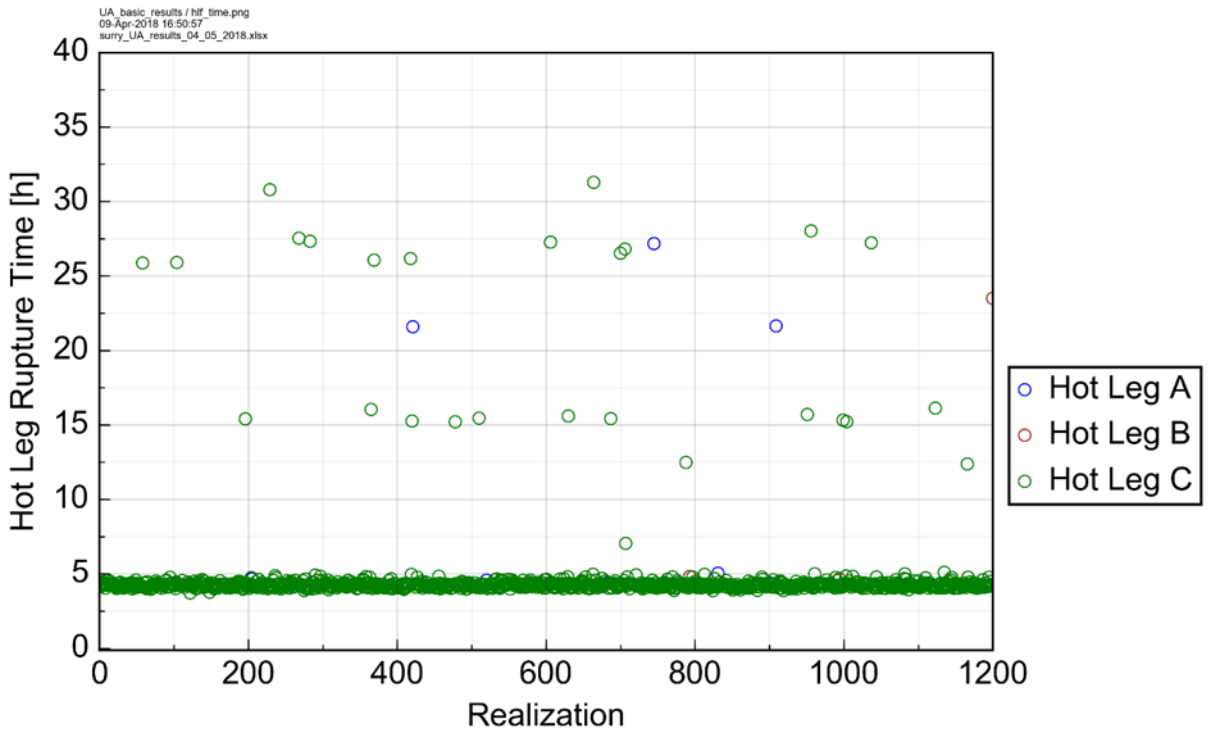

Figure 5-11 Hot Leg Nozzle Rupture Time by Loop and Realization

5.1.11 Reactor Lower Head Failure Timing

There were 5 realizations in the UA where the reactor lower head did not fail by 72 hr. The lower head failure timing statistics for all other realizations with a reactor lower head failure less than 72 hr are presented in Table 5-12. The lower head failure time by realization is presented in Figure 5-12.

Table 5-12 Reactor Lower Head Failure Timing

	Lower head failure time (hr)
Mean	10.207
Median	9.220
Min	7.541
Max	70.063

Most of the reactor vessel failures between 7.5 to 2 hr. The five reactor vessel failures shown in Figure 5-12 at 0 hr actually corresponded to a failure time after 72-hr. All of the realizations with reactor failure after 35 hr used the earliest sampled time at cycle. The earliest time at cycle had significantly lower decay heat than the other sampled times (see Section 4.1.2.4) that resulted in a much slower accident progression relative to all other time at cycle realizations (i.e., see Figure 4-23). Section 5.3 provides additional discussion on the non-typical reactor vessel failure timings.

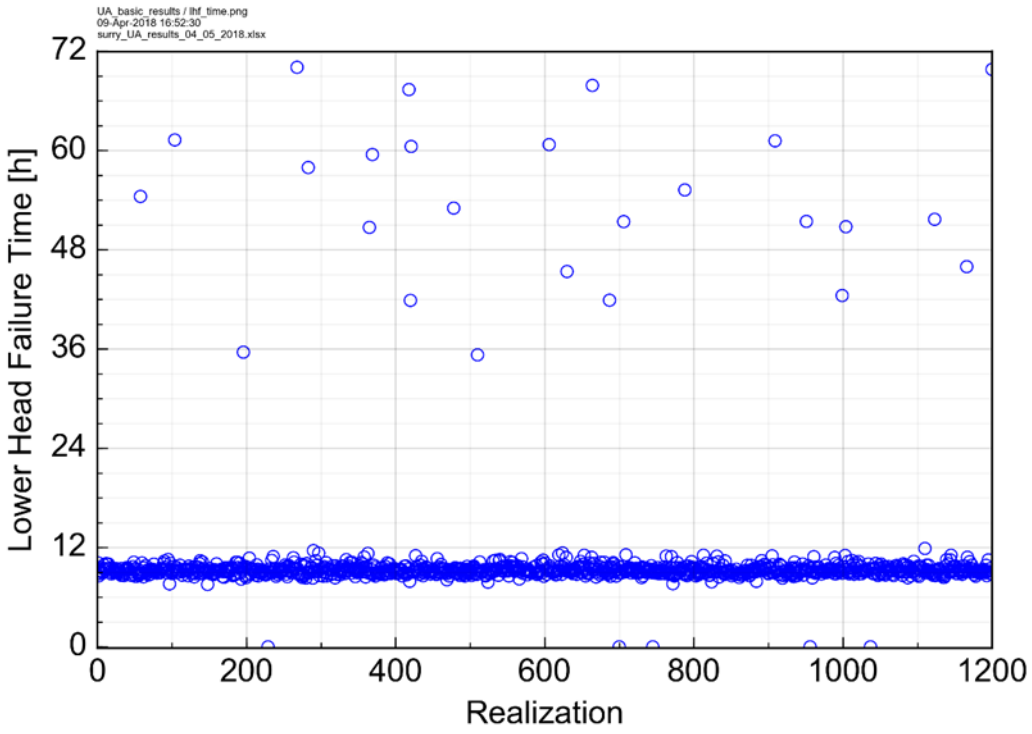

Figure 5-12 Reactor Lower Head Failure Timing by Realization

5.1.12 Containment Failure Timing

In the 1,147 successful UA realizations, there were 1,091 liner failures and 16 rebar failures within 72 hr (see Section 4.1.3.3 for a discussion of liner and rebar failure). There were also 56 realizations without a containment failure within 72 hr. Table 5-13 and Figure 5-13 present the timing of the containment failures. All the failures resulted from gradual monotonic pressurizations of containment (i.e., there were no containment ruptures due to pressurizations following a hydrogen deflagration). Although hydrogen deflagrations occurred in the realizations, they generally occurred following the failure of the hot leg and none were threatening to over-pressurize the containment. The SGTRs decreased the rate of the containment pressurization as evidenced in the horsetails in Figure 5-14. This influence, addressed further in Section 5.2.2, is attributable to the additional containment leakage pathway through the SGTR and an unsealed (leaky) MSIV.

The low pressure horsetails in Figure 5-14 are the 0.5-day time at cyle realizations (i.e., very early in core life after refueling). The decay power for the 0.5-day time at cycle is significantly lower than the other times at cycle (see Figure 4-23) and isn't sufficient to significantly pressurize the containment within 72 hr.

Table 5-13 Containment Failure Timing

	Liner failure time (hr)
Mean	50.785
Median	50.058
Min	34.489
Max	71.915

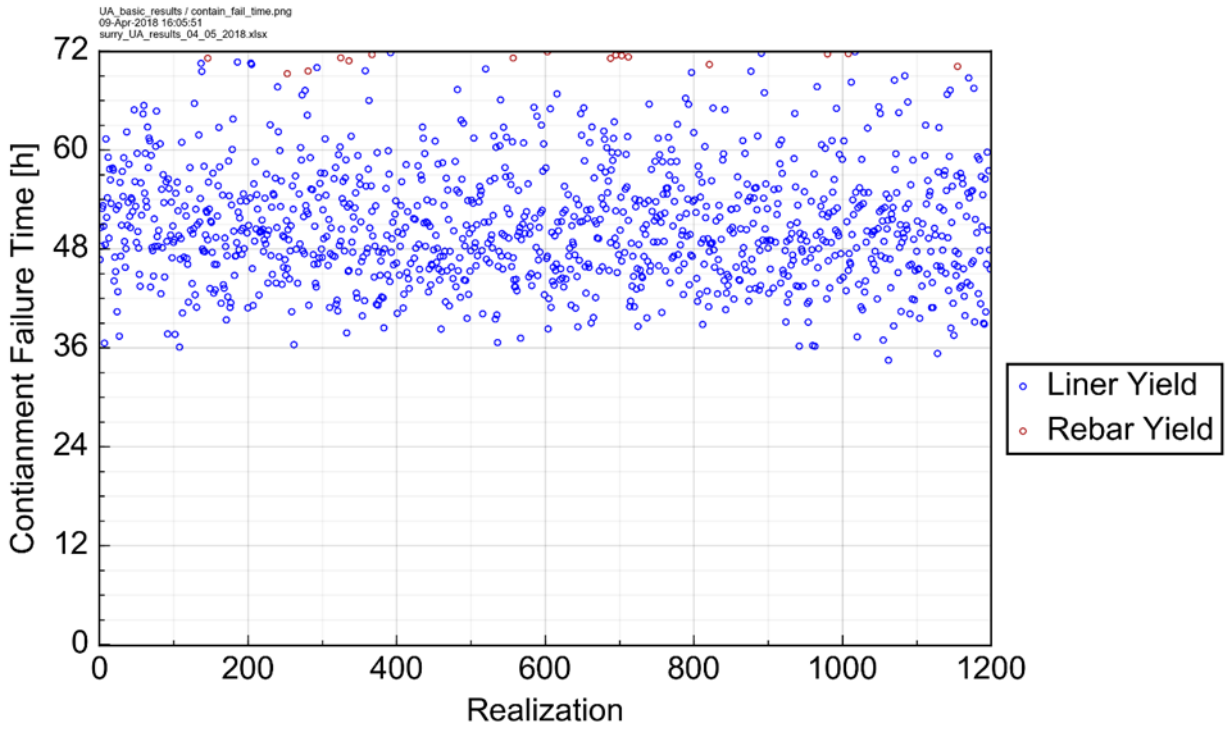

Figure 5-13 Containment Failure Timing by Realization

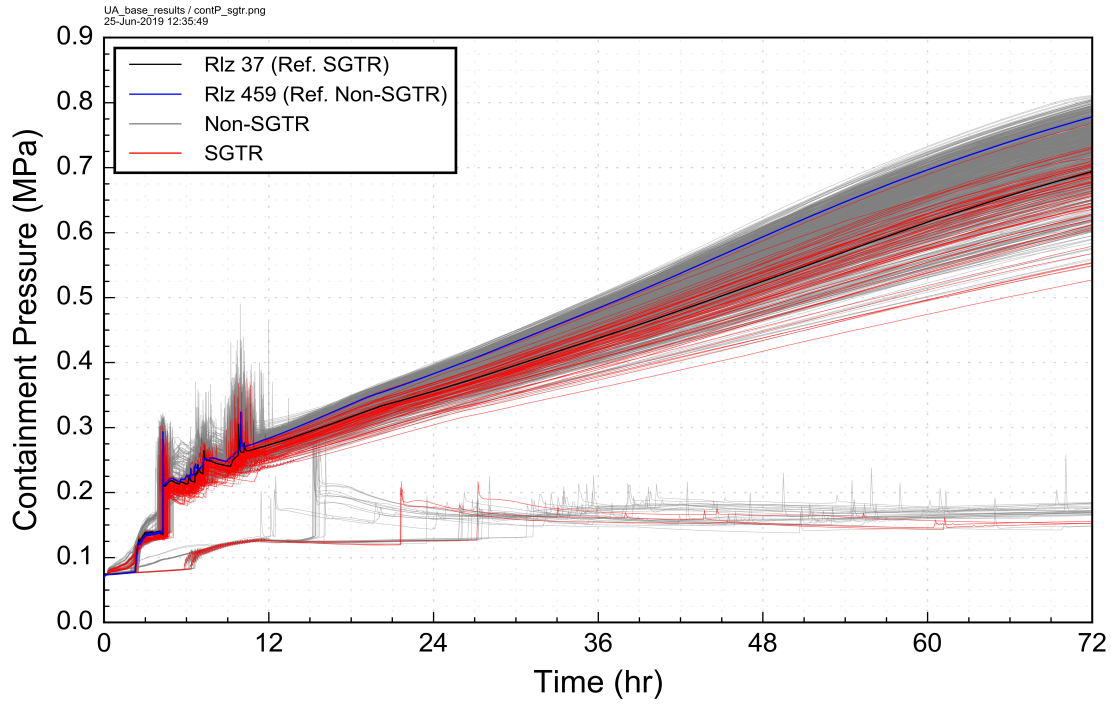

Figure 5-14 Containment Pressure for the SGTR and Non-SGTR Realizations

5.1.13 RCS Primary and Secondary Drying Out Times

Differing sampled values of RCP seal leakage, cycles to pressurizer SV FTC and time in the life of the fuel led to a large spread in the time taken in the UA realizations to dry out the RPV. Sampled MSIV leakage and cycles to MSL SV FTC resulted in some spread in the time taken to dry out the SGs. Basic statistics on RPV and SG drying out times are presented in Table 5-14.

Table 5-14 RPV and SG Drying Out Times

	RPV dryout (hr)	SG A dryout (hr)	SG B dryout (hr)	SG C dryout (hr)
Mean	8.425	1.532	1.524	1.479
Median	7.858	1.517	1.514	1.476
Min	5.398	0.448	0.438	0.427
Max	>72	3.691	3.568	3.592

5.2 Reference MELCOR Realization Analyses

The MELCOR realizations performed for the UA that are presented in Section 6.1 were generated with an updated version of the MELCOR Surry SOARCA STSBO model that included the modeling attributes identified in Sections 3.3.1 and 4.1.[56] Following the completion of the MELCOR UA calculations, the results were reviewed to identify reference realizations that gave the closest median response for specific attributes of interest. The attributes selected to identify the reference realizations were (a) the cesium release to the environment, (b) the iodine release to the environment, (c) the timing of the containment liner yielding (or the SGTR if calculated to occur), and (d) the containment pressure at the end of the calculation. The first three parameters characterize the magnitude and the timing of the source term, which is the focus of the SOARCA. The containment pressure was included in this evaluation to reflect the median hydraulic condition for long-term releases from the containment.

The reference realizations were selected by separating the realizations with and without a SGTR into two groups. The medians for the four reference attributes were calculated for each group. Using equal weighting of the four cited parameters, two realizations were selected that had the closest responses to the median for all four criteria. The selected realizations were subsequently reviewed to ensure their specified uncertain parameter values did not deviate substantially from the uncertain parameter median or mean. The values of the key uncertain parameters are listed in Table 5-15.

Noteworthy aspects that apply to both the reference non-SGTR and the reference SGTR realizations include:

- No over-cycling FTC SV occurred on any of the SGs.
- No over-cycling FTC occurred on the pressurizer SV.

---

[56] Appendix A of the draft version of this analysis [8] presents a description of the model and response changes from the original Surry STSBO calculation using MELCOR 1.8.6 [1][3] and the draft version of this analysis using MELCOR 2.1. The appendix examines the change in response due to model corrections, model enhancements, and a newer code version. The information presented in the Appendix A of the draft report is largely for historical and archival purposes and not repeated in this report.

- No RCP pump seal failures, which is the most likely outcome from the uncertainty distribution.

- The hot leg nozzle rupture occurred on Loop C where the pressurizer surge line connects. Loop C heated faster due to the cycling pressurizer SV, which led to the preferential failure on this loop.

- Hydrogen deflagrations occurred in containment after the hot leg failure, but they did not pose a significant over-pressure challenge to the containment boundary.

- The containment design pressure and the pressure associated with liner yield were both exceeded. However, the containment pressure was below the rebar failure pressure at 72 hr.

- Although the containment pressure associated with rebar yield was not reached by 72 hr, the pressure was expected to exceed this value shortly thereafter.

- The long-term containment pressurization was due to the continuous heating and vaporization of water on the containment floor (i.e., discharged from the RCS into the containment) and the non-condensable gas generation from core-concrete interactions.

- The SGTR significantly increased the release to the environment. The non-SGTR reference realization released 0.028% and 0.003% of the iodine and cesium inventory, respectively. However, the SGTR reference realization released 1.42% and 0.92% of the iodine and cesium inventory, respectively.

- The concrete ablation from core-concrete interaction had not slowed by the end of the MELCOR realization at 72 hours. The concrete erosion rate and non-condensable gas generation was relatively constant after the start of the core-concrete interaction.

Sections 5.2.1 and 5.2.2 show the results for Realizations 459 and 39 for the non-SGTR and SGTR reference realizations, respectively.

Table 5-15 Key Uncertain Parameter Values for the Reference Realizations

Description	UA Variable	Realization 459 (Non-SGTR)	Realization 39 (SGTR)
Total Reactor Coolant Pump Seal Leakage for all three RCPs, (gpm)	totalRCP_leak	63	63
SG A Cold Tube Flaw Depth, (-)	maxColdA_NFD	0.6741 (Note a)	0.8526
SG A Hot Upflow Tube Flaw Depth, (-)	tubeUpflowA_NFD	0.4364 (Note a)	0.4087
SG A Hottest Tube Flaw Depth, (-)	tubeHotA_NFD	0.0000 (Note a)	0.0000
Hot SG A Tube Temperature Multiplier, (-)	ThotA_norm	0.415 (Note a)	0.334
Zircaloy melt breakout temperature (SC1131(2)), (K)	Zr_brkout_T	2411.2	2307.3

Table 5-15 Key Uncertain Parameter Values for the Reference Realizations (Continued)

Description	UA Variable	Realization 459 (Non-SGTR)	Realization 39 (SGTR)
Material Properties: temperature at which the eutectic formed from ZrO_2 and UO_2 melts (ZrO_2/UO_2), (K)	EU_melt_T	2391.5	2560.4
Molten clad drainage rate (SC1141(2)), (kg/m-s)	Zr_drn_rate	0.13	0.48
Containment design leakage multiplier, (-)	designLeakLa	0.221	0.166
Containment Fragility Curve (CFC) Rupture, (-)	Rupture	1.56	1.71
Burn direction, (-)	burn_dir	1	1
Secondary side decontamination factor – N represents number of stages after SGTR, (-)	SGTRA_loc	2 (Note a)	7
Aerosol Dynamic Shape Factor, (-)	shapeFactor	1.95	1.12
Containment condensation rate multiplier, (-)	condensation_X	1.72	1.43
Oxidation model, (-)	Ox_model	1	1
Time in the cycle, (days)	ORIGEN Day	400	300
Gaseous iodine fraction, (-)	I2 Gas Gap Fraction	0.00151	0.00188
Cesium fraction, (-)	Cs2MoO4 Fraction	0.890	0.762
MSIV leakage rate, (-)	msiv_leak_a	0.317	0.576

Note a. These SGTR-specific parameters for Realization 459 did not lead to a SGTR and are not relevant to the accident progression.

5.2.1 Reference STSBO Realization without a SGTR

The key event times for reference realization 459, which progressed without a SGTR are listed in Table 5-16. The settings of the key uncertain parameters are summarized in Table 5-16. The key calculated responses of the Realization 459 accident progression are summarized in Figure 5-15 through Figure 5-37. The attributes of the figures are discussed next.

Table 5-16 Key Event Timing in the Reference STSBO Realization without a SGTR

Event	Time (hh:mm)
STSBO – loss of all AC and DC electrical power, AFW unavailable	00:00
Reactor trips Main steam isolation valves (MSIVs) close RCP seal leakage initiates at 21 gpm/pump *(these events occur shortly after the loss of power)*	00:00+
SG dryout	01:32
PRT rupture disk breaks	02:16
RPV water level reduces to TAF	02:46
First fission product gap release	03:44
Loop C hot leg nozzle rupture	04:17
Accumulators begin discharging	04:17
Accumulators empty	04:19
Core debris mass exceeds 5%	05:33
1st hydrogen burn	06:01
Core plate failure	06:22
RPV lower head breach	08:58
End of containment hydrogen burns	09:57
Containment pressure reaches design (45 psig)	27:35
Containment liner yields	47:04
Release of noble gases to the environment exceeds 1.0%	55:49
Release of elemental iodine to the environment exceeds 1.0%	57:01
End of calculation	72:00

The primary system pressurizer pressure for the non-SGTR reference realization is shown in Figure 5-15. The SGs cooling influence on the primary system pressure exists while there is water in the SGs after the initial pressurization at the start of the transient (i.e., through 1.5 h). Full-loop single phase water natural circulation removes the fission product decay heat from the core to the SGs. Following the SG dryout, the primary system pressurizes until the pressurizer SVs open. The primary system pressure cycles as the pressurizer SVs open and close until 4 hr 17 min when the hot nozzle fails by creep rupture. Due to the fluid loss during the pressurizer cycling, the vessel water level fell below the top of the core, which led to the natural circulation of hot gases from the core to the SGs. The hot leg nozzle failed by creep rupture due to the high temperature and pressure conditions during the natural circulation phase. The primary system was fully depressurized when the lower head vessel failed at 8 hr 58 min.

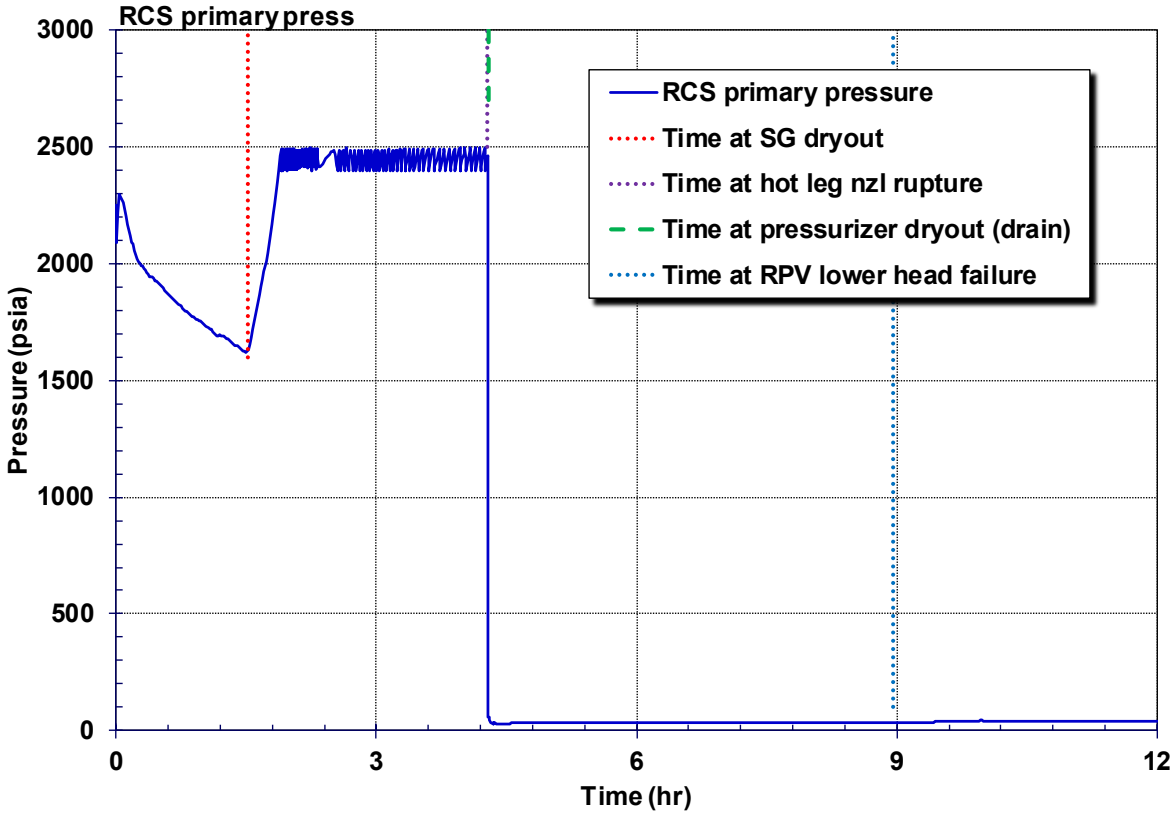

Figure 5-15 RCS Primary Pressure (Non-SGTR Reference Realization)

Figure 5-16 shows SG pressure history. The SG pressure rises quickly to the SV setpoint following the closure of the MSIVs and termination of the feedwater flow. It was this initial heatup to near saturated conditions in the SGs that corresponded to the brief primary system pressurization prior subsequent cooldown. The secondary system pressure cycles with the SV openings and closings to remove heat transferred from the primary system to the secondary. Following the dryout of the SGs at 1.5 hr due to venting steam out the cycling SVs, the system pressure begins to slowly decrease. The pressure response following the dryout is primarily controlled by leakage past the MSIVs. While not shown in Table 5-15, the differences in the depressurization rates following the SG dryout are attributed to the various sampled leakages (i.e., 0.31, 0.25, and 0.80 in^2 for the MSIVs on SGs A, B, and C, respectively).

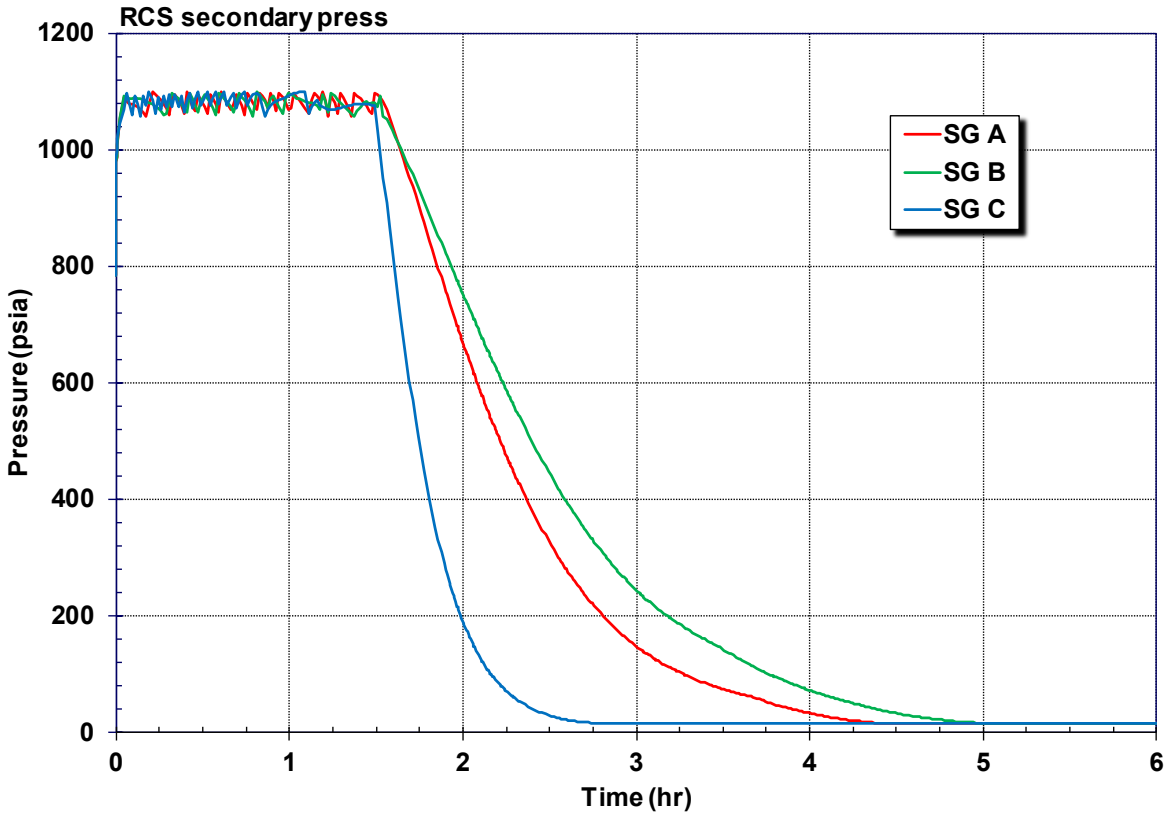

Figure 5-16 RCS Secondary Pressure (Non-SGTR Reference Realization)

The RCS reactor and pressurizer level responses are shown in Figure 5-17. Even though the hot leg is dry, this figure shows that there is water holdup in the pressurizer due to counter-current flow limiting (CCFL) in the surge line prior to the sharp primary system depressurization following the hot leg failure. The accumulator injection following the hot leg failure is evident in the vessel response at 4 hr 17 min. Following the debris relocation to the vessel lower head, the remaining water in the bottom of the vessel is boiled away by 8 hr. The lower head heats and fails due to a creep rupture at 8 hr 58 min.[57]

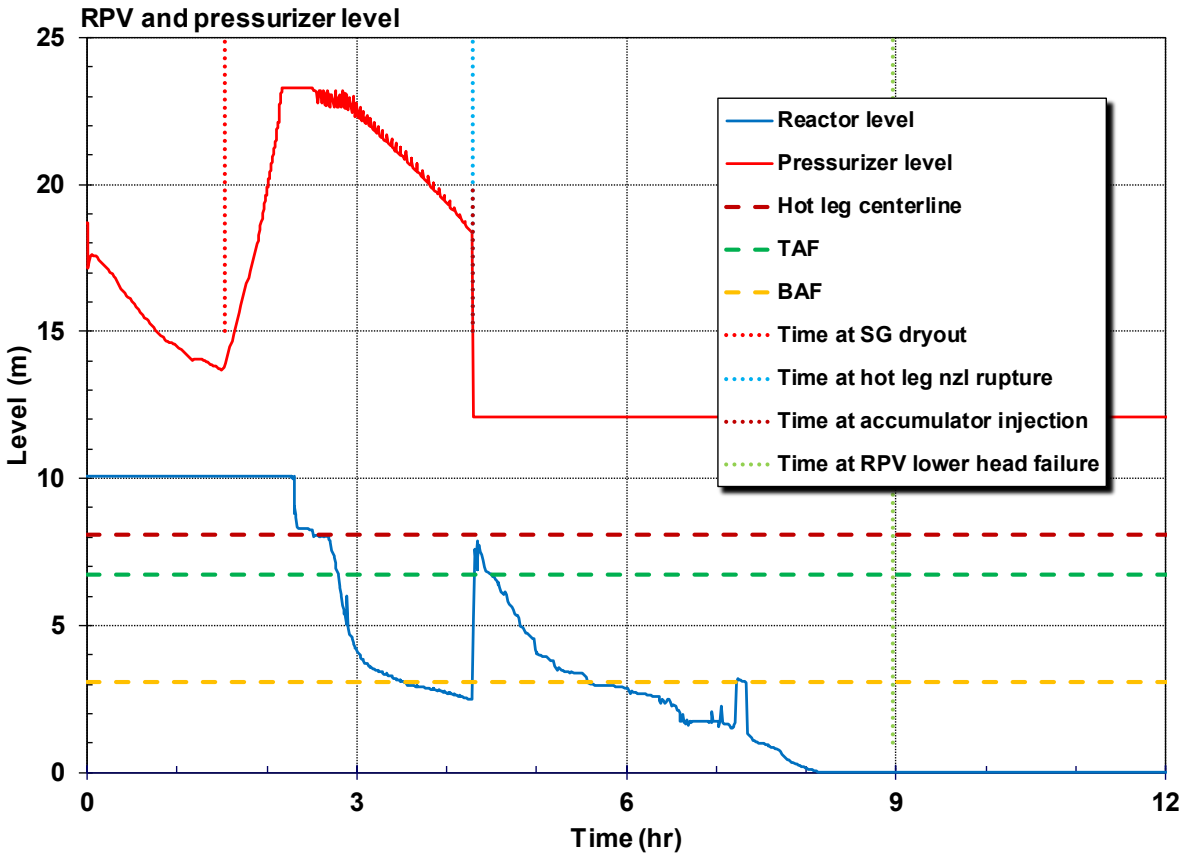

Figure 5-17 RCS Primary Level (Non-SGTR Reference Realization)

[57] The mode of vessel failure was assumed to be creep rupture of the lower head using a Larson-Miller relationship. A potentially earlier failure of the instrument penetrations was not considered, see Section 2.2.1.

Figure 5-18 shows the combined and individual pump leakage from the RCS through the RCP seals. There are no seal failures in these two reference realizations. The seals simply continue to leak at the nominal amount of 21 gpm/pump (at normal operating pressure and fluid temperature conditions). However, the actual flow rate is a function of the system pressure and water phase. As the primary system fluid heats toward saturated conditions, the flowrate decreases. Following the system depressurization after the hot leg nozzle failure due to creep rupture, the total RCP pump flow rate decreases to less than 1 gpm.

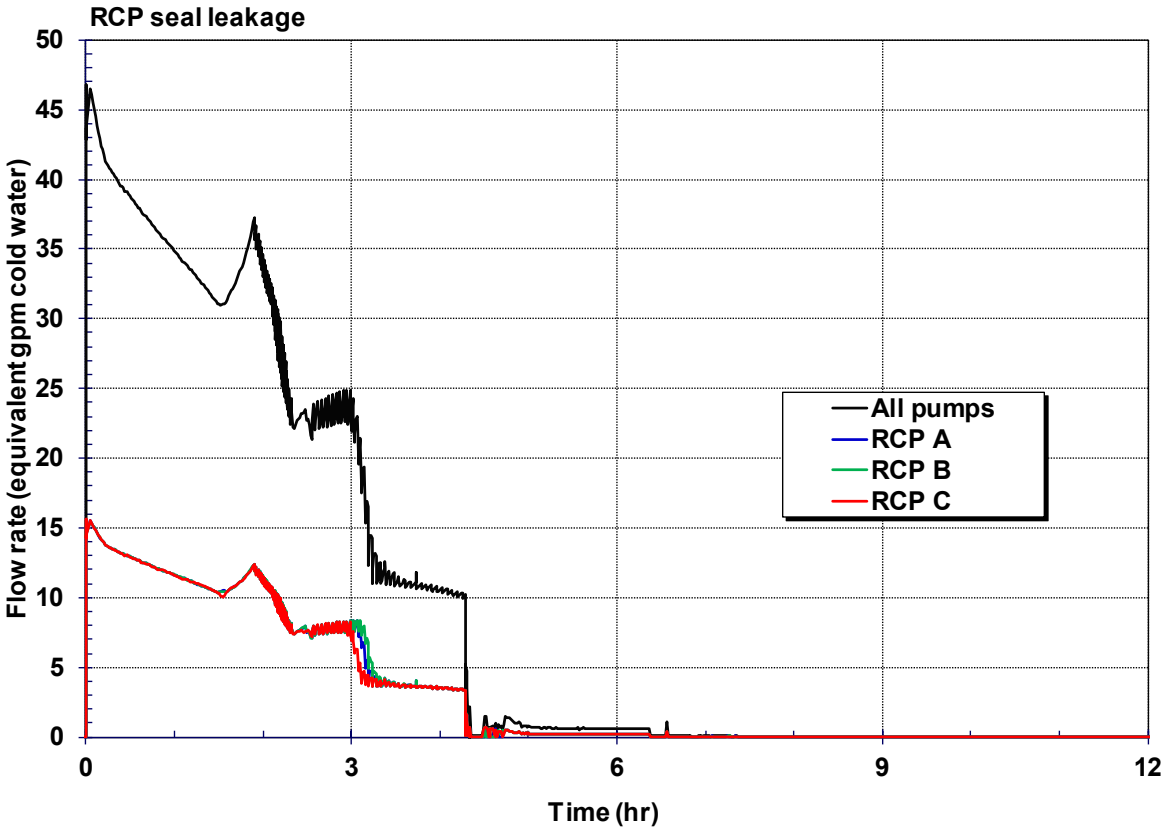

Figure 5-18 RCP Seal Leakage (Non-SGTR Reference Realization)

The SG level response is shown in Figure 5-19. All three SGs have essentially the same water level trend. The water level decreases continuously as the initial inventory is boiled away following the loss of all feedwater at the initiating station blackout event. All the SGs are dry at approximately 1 hr 30 min.

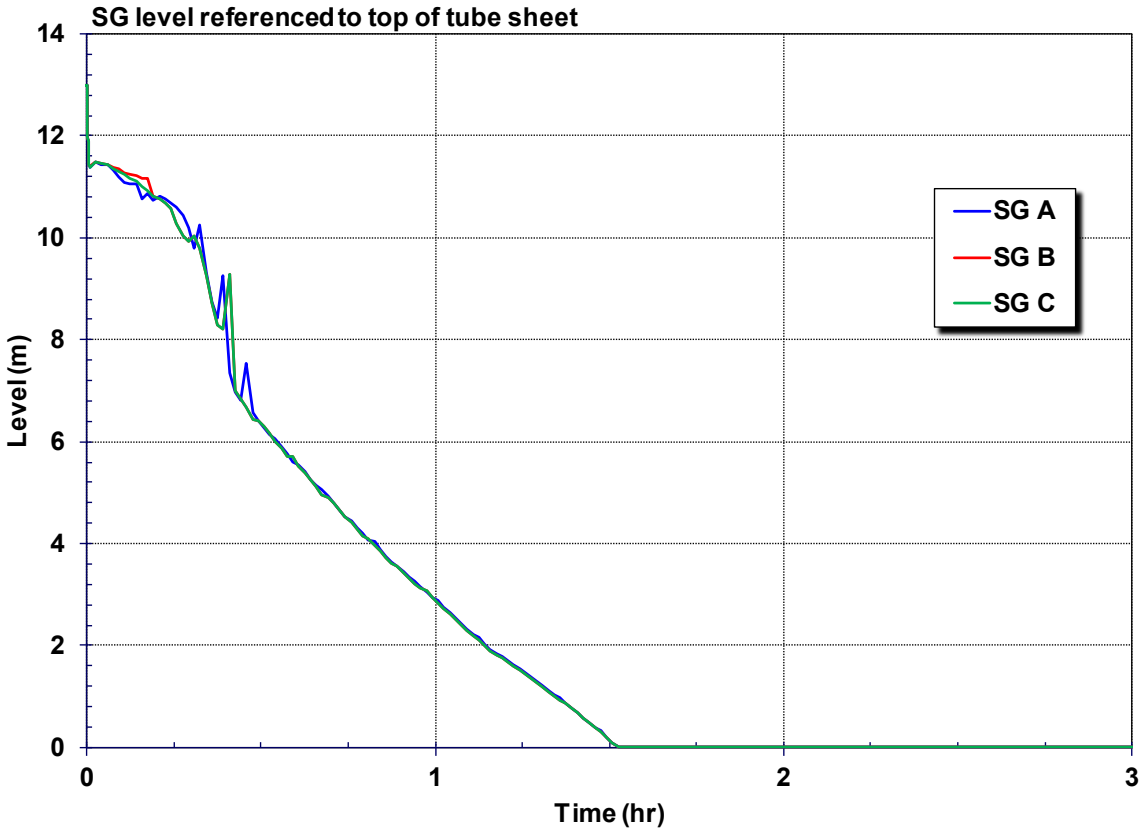

Figure 5-19 SG Level Referenced to Top of Tube Sheet (Non-SGTR Reference Realization)

Figure 5-20 shows the hydrogen produced inside the RPV through oxidation of the fuel cladding and interior steel structures. The figure shows the total hydrogen production is dominated by zircaloy oxidation rather than steel oxidation. The large surface area of the zircaloy cladding on the fuel rods dominates oxidation reactions until after the fuel degrades into debris geometry. There is about 20 kg of steel oxidation after the collapse of the core. The total hydrogen production initially increases until the hot leg nozzle failure, which depressurizes the primary system and discharges the accumulator water into the core. There is only 36 kg of hydrogen produced at the time of the hot leg failure. After the injected water boils away, the second heatup of the core creates approximately 300 kg of hydrogen. The hydrogen production slows after the core starts degrading into debris geometry. At the time of lower head failure, all the core debris is rapidly discharged to the containment (see Figure 5-21) and the in-vessel oxidation phase is over.

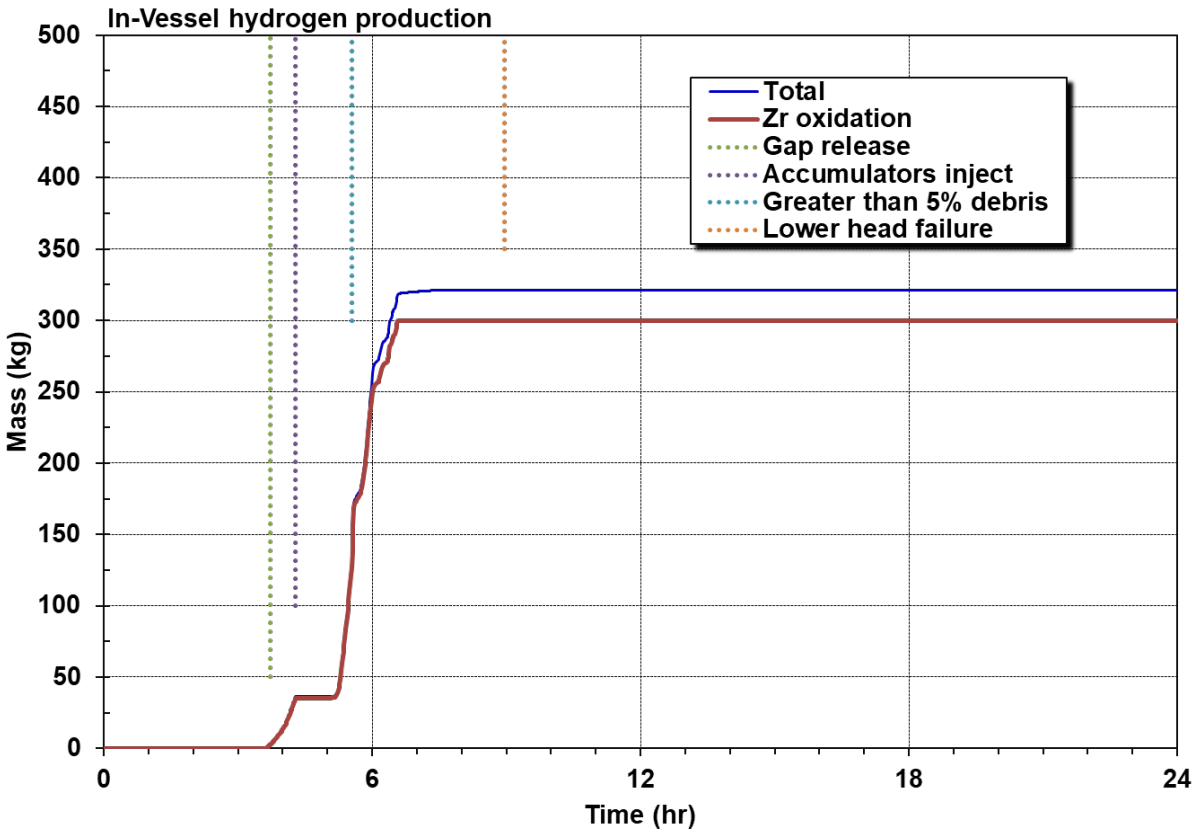

Figure 5-20 In-Vessel Hydrogen Production (Non-SGTR Reference Realization)

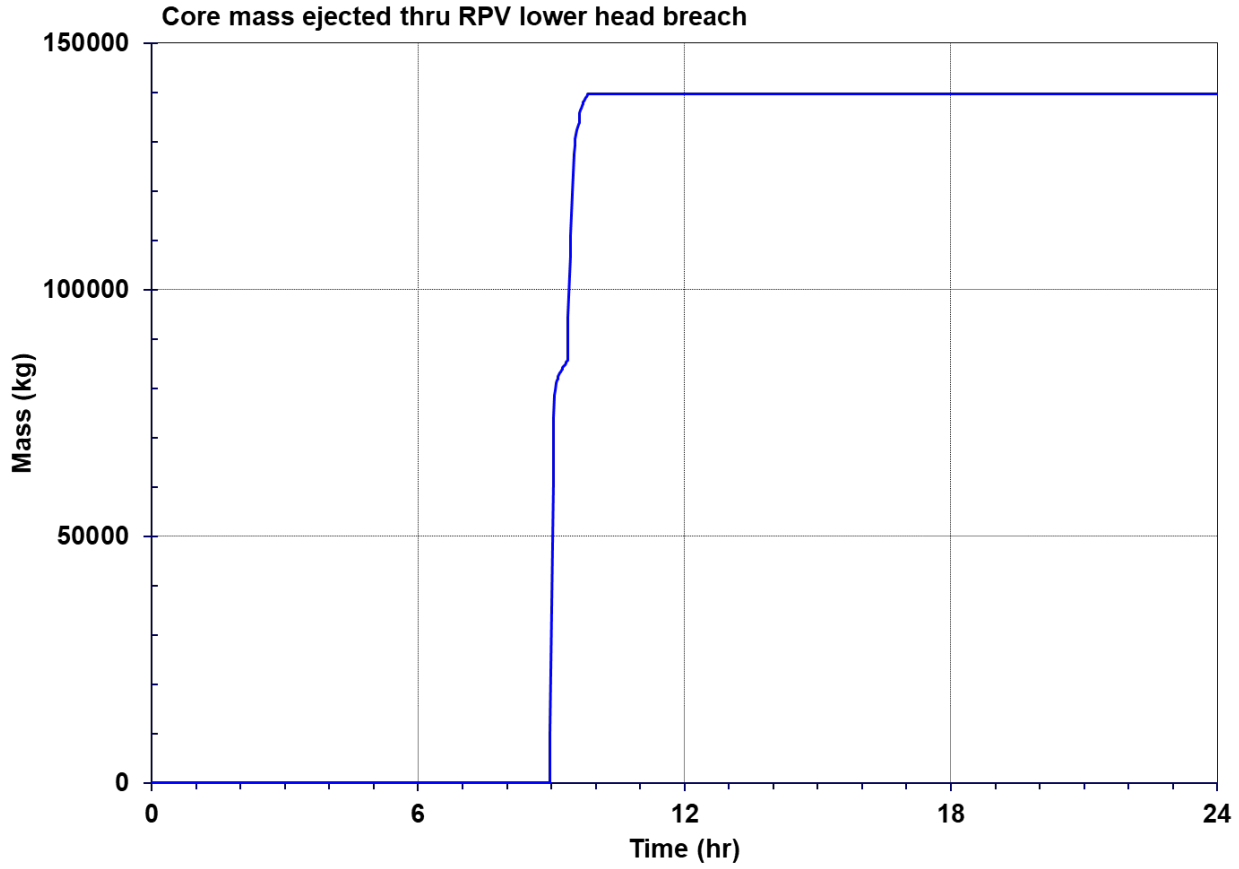

Figure 5-21 Core Mass Relocated to the Reactor Cavity (Non-SGTR Reference Realization)

Figure 5-22 shows the containment pressure response. The pressure starts off at a sub-atmospheric pressure consistent with the Surry containment design. The containment quickly pressurizes following the loss of heat removal systems with the initiating event. Once the SGs dry out, the RCS inventory heats to near saturated conditions and the RCS pressure increases. The lowest set-point SV on the pressurizer opens to vent the system to the PRT. Once the energy absorbing capacity of the PRT is reached, the rupture disk on the tank opens at 2 hours 16 minutes. The containment pressure jumps when the PRT depressurizes into the containment. Following the PRT rupture disk opening, the subsequent pressurizer SV openings discharge steam through the saturated PRT pool and into the containment. The next rapid pressure rise occurs when the hot leg nozzle on Loop C ruptures, which immediately and fully vents the RCS primary system fluid to containment. There was relatively little hydrogen produced at the time of the hot leg failure, so the first burn does not occur until roughly 2 hr later at 6 hr. Some small burns are evident in the pressure trace between 6 to 10 hr. The last burn propagated to the containment dome and shows the largest hydrogen-induced pressure spike.

There is no significant pressure rise at the time of the vessel lower head failure, while the core debris relocates into the containment and begins ablating the concrete. The containment pressure steadily increases as the debris heats the containment atmosphere and produces non-condensable gases from concrete ablation. The corresponding pressure rise is a combination of the heating and gas generation. The design pressure of containment is

exceeded at 27 hr 45 min and yielding of the containment steel liner occurs at 47 hr. The containment pressure is 113 psia, or just 4 psi below the containment rebar yield pressure at 72 hr. Consequently, the rebar yield would be expected shortly after 72 hr unless the pressurization is mitigated.

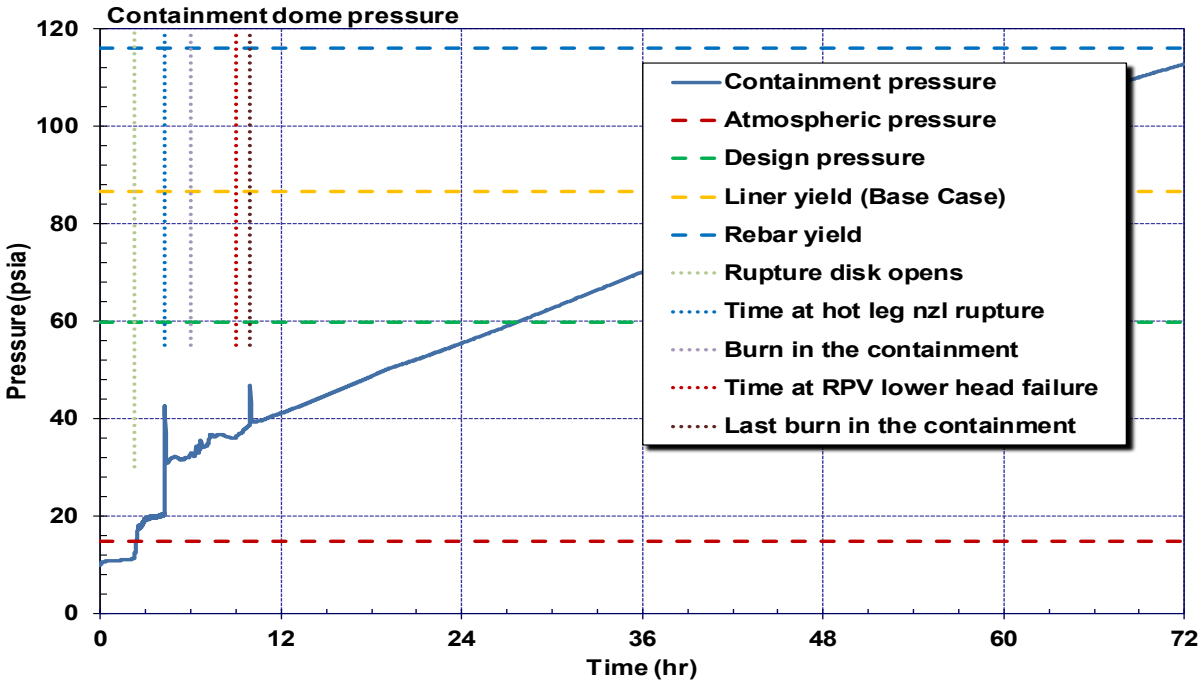

Figure 5-22 Containment Pressure (Non-SGTR Reference Realization)

The energy produced by deflagrations in containment and the compartments steam concentrations are illustrated in Figure 5-23. There are two periods of deflagrations: (1) two burns at 2 hr after hot leg nozzle creep and (2) another burn at an hour after lower head failure. The second burn is larger because it propagates to the dome. The steam concentrations throughout the containment are included on the figure and show two spikes. The first steam spike occurs when the PRT rupture disk opens at 2 hr 16 min. The second sharp increase occurs when the hot leg creep ruptures at 4 hr 17 min. The majority (i.e., >70%) of the in-vessel hydrogen production occurs between the hot leg failure and the first burn at 6 hr, which is discharged to the containment. However, most of the containment is steam-inerted after the hot leg failure until 6 hr, so there are no burns. The condensation on the cooler walls briefly drops the steam concentration below the inerting limit by 6 hr, which leads to the first combustion. The final burn occurred at 10 hr when the oxygen concentration in the cavity region increased to the combustible threshold. The burn in the cavity propagated into the other regions of the containment. However, the peak pressure was well below the liner failure pressure.[58]

[58] The combustion model was modified to allow uncertainty sampling and the incorporation of the lower flammability limit ignition model. It was determined that the combustion package modifications inadvertently allowed propagation of the flame into steam-inerted control volumes. The participating control volumes in the propagated burn had adequate oxygen and hydrogen for combustion and only the steam-inerting criterion was bypassed. The resulting response had a small effect on the results. The net effect was representative of a weakly propagating burn that progressed into regions typically not supportive of a deflagration. The strength of the propagated burn is strongly limited by the high steam concentration.

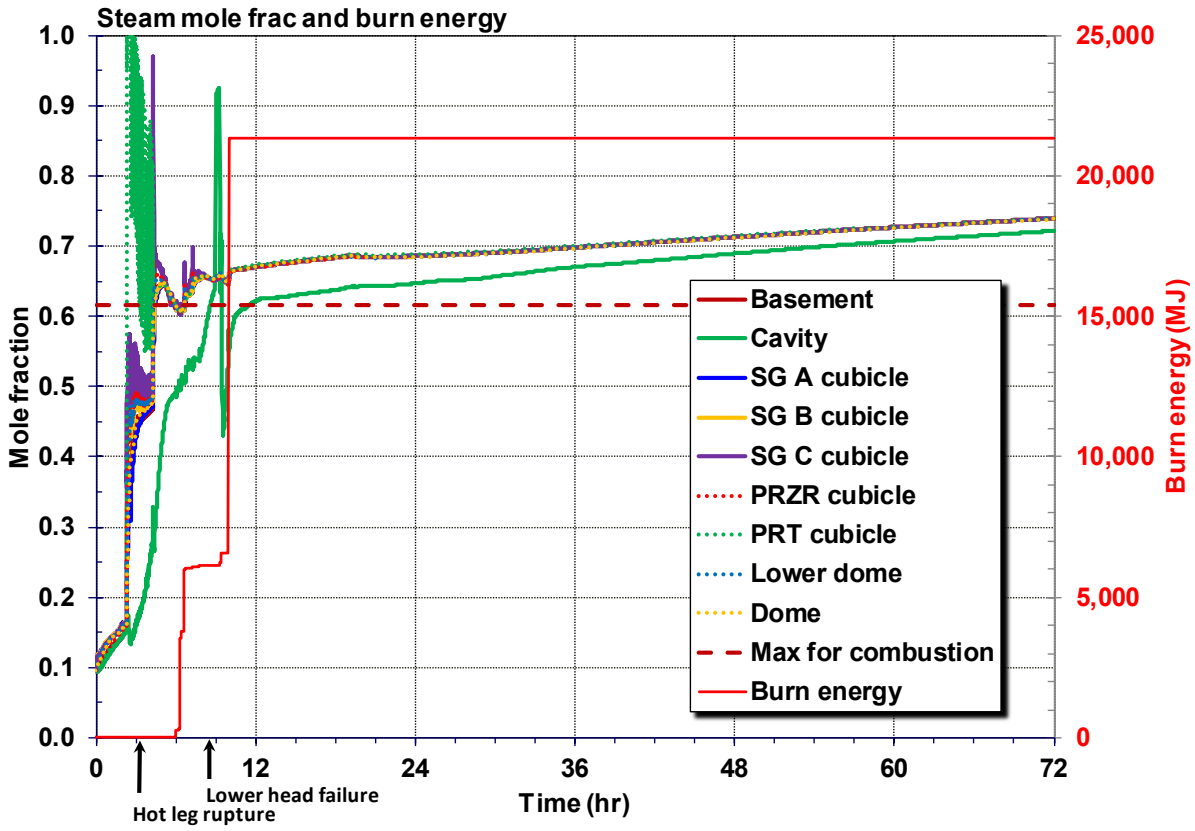

Figure 5-23 Containment Steam Mole Fraction and Energy Produced by Deflagrations (Non-SGTR Reference Realization)

The containment dome temperature can be seen in Figure 5-24. Clearly visible are three spikes corresponding to the timings of combustible gas burns and the hot leg nozzle rupture. The largest spike occurs at 4 hr 17 min when the primary system depressurizes into the containment when it is at an elevated pressure and temperature. The last burn at 10 hr started in the cavity shortly after the reactor lower head failure, which propagated into the dome region had the next largest temperature spike. Additional burns occur in the lower containment compartments between these two events but had significantly less impact on the dome temperature. After combustion is prevented by high steam concentrations and low oxygen concentrations, the containment temperature rises slowly as the containment pressurizes.

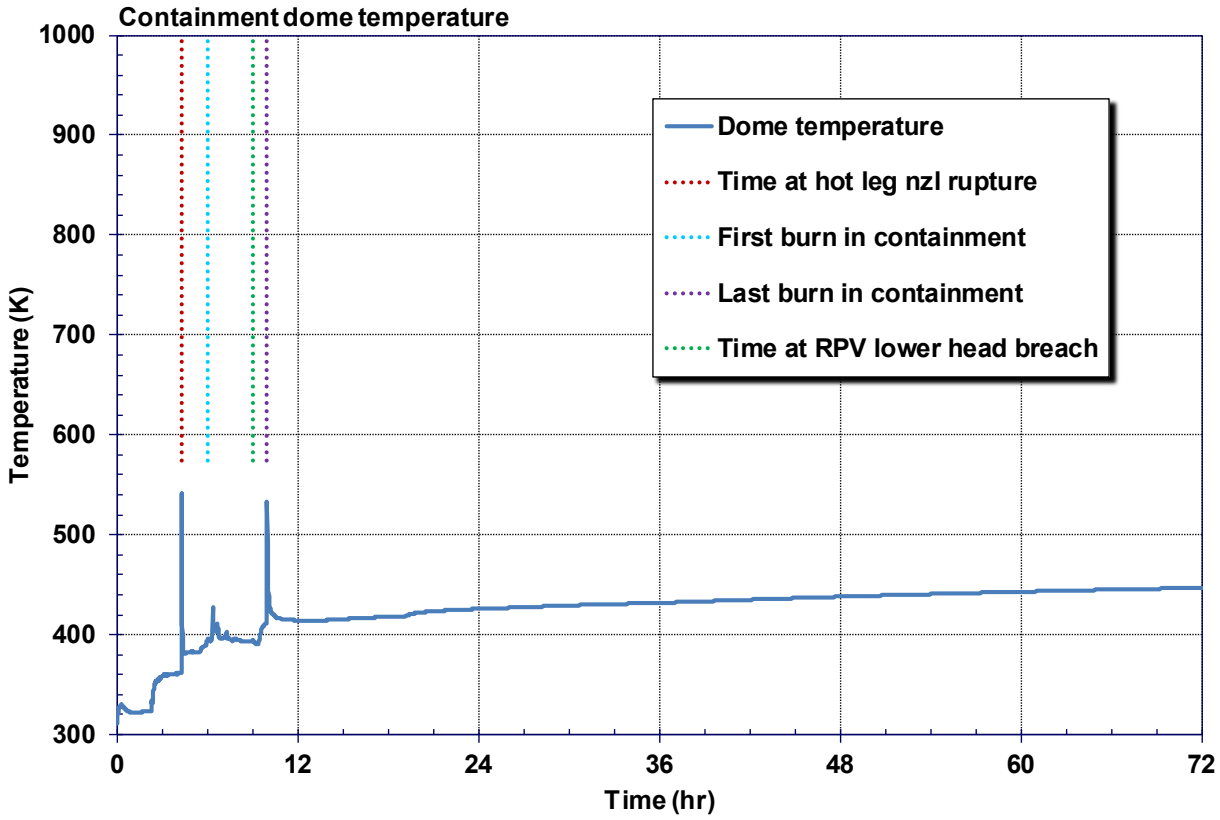

Figure 5-24 Containment Dome Temperature (Non-SGTR Reference Realization)

The non-condensable gas generation from core-concrete interaction in units of kg and kg-mol are shown in Figure 5-25 and Figure 5-26, respectively. The gas production is essentially constant after the core debris drops into the containment reactor cavity. Although the carbon monoxide mass production is larger than the hydrogen gas production, the volume of the hydrogen gas produced is much larger (see Figure 5-26).

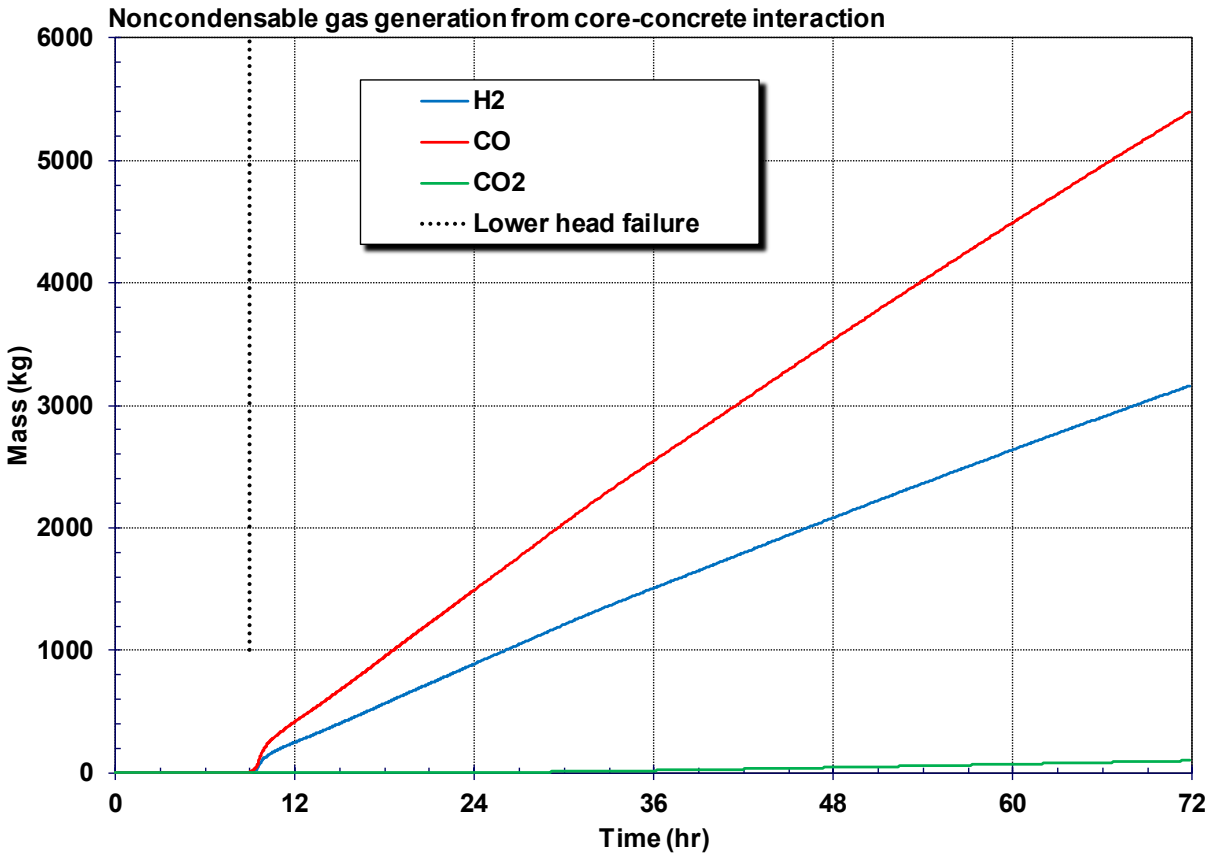

Figure 5-25 Noncondensable Gas Generation from Core-Concrete Interaction, kg (Non-SGTR Reference Realization)

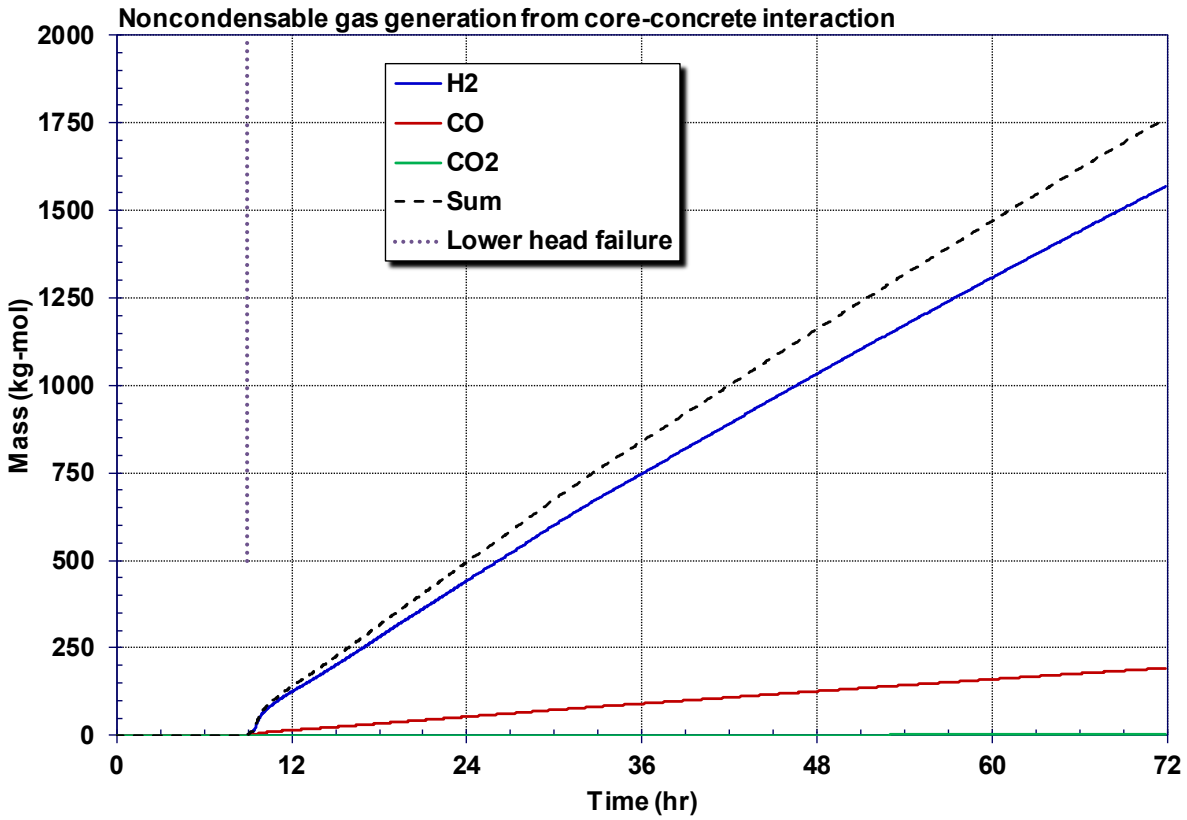

Figure 5-26 **Noncondensable Gas Generation from Core-Concrete Interaction, kg-mol (Non-SGTR Reference Realization)**

Figure 5-27 shows the partial pressures of containment atmosphere constituents. The response illustrates that the contribution of evaporated steam is the primary driver for the overall containment pressurization. As shown in Figure 5-28, over 220 mt of water are discharged into the containment from the primary system through the RCP seal leakage, the failed hot leg, and spillage from the PRT after the rupture disk opening. The water from the primary system also includes the injected water from the three accumulators. The hot gases from the ex-vessel CCI heats the water on the containment floor, which steadily evaporates and saturates the atmosphere. The partial pressure of the hydrogen from the core-concrete interactions eventually exceeds the nitrogen concentration. Although the carbon monoxide mass produced in the ex-vessel core-concrete interaction is significant, its impact on the containment pressure is relatively small.

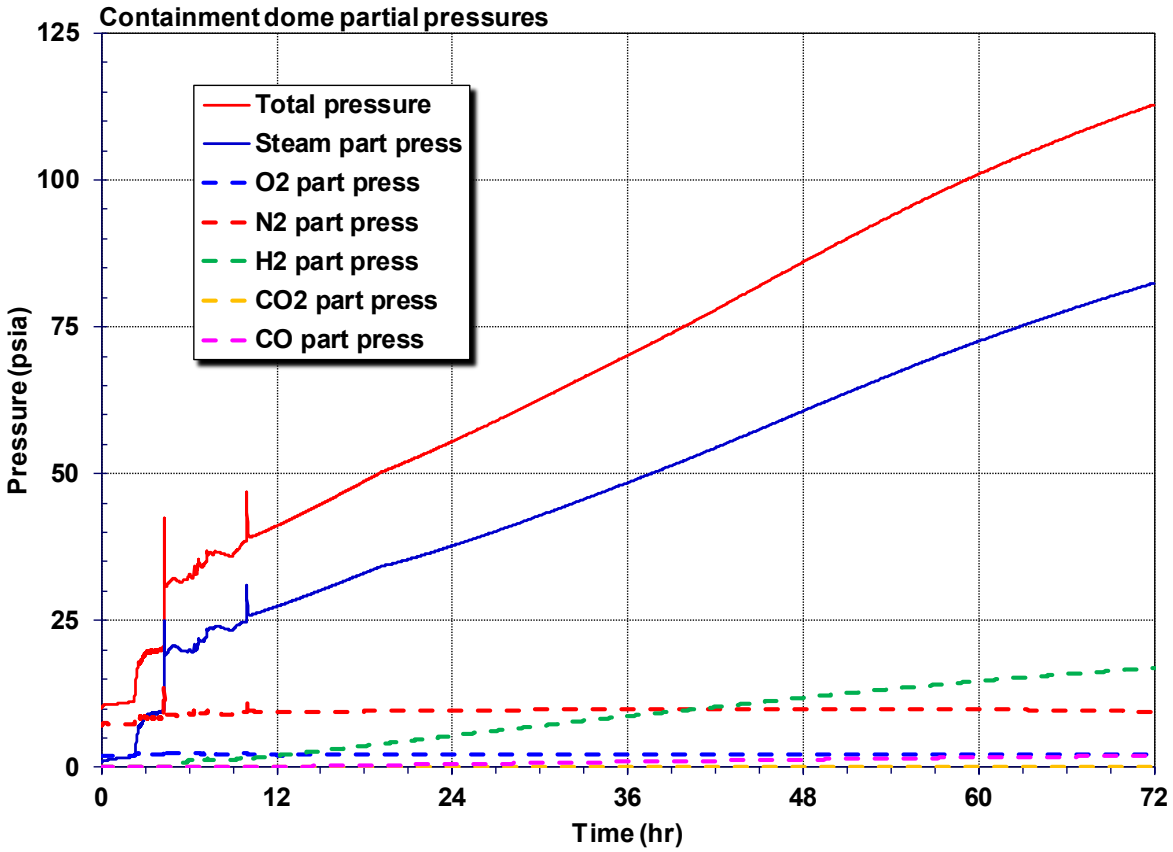

Figure 5-27 Containment Dome Partial Pressures (Non-SGTR Reference Realization)

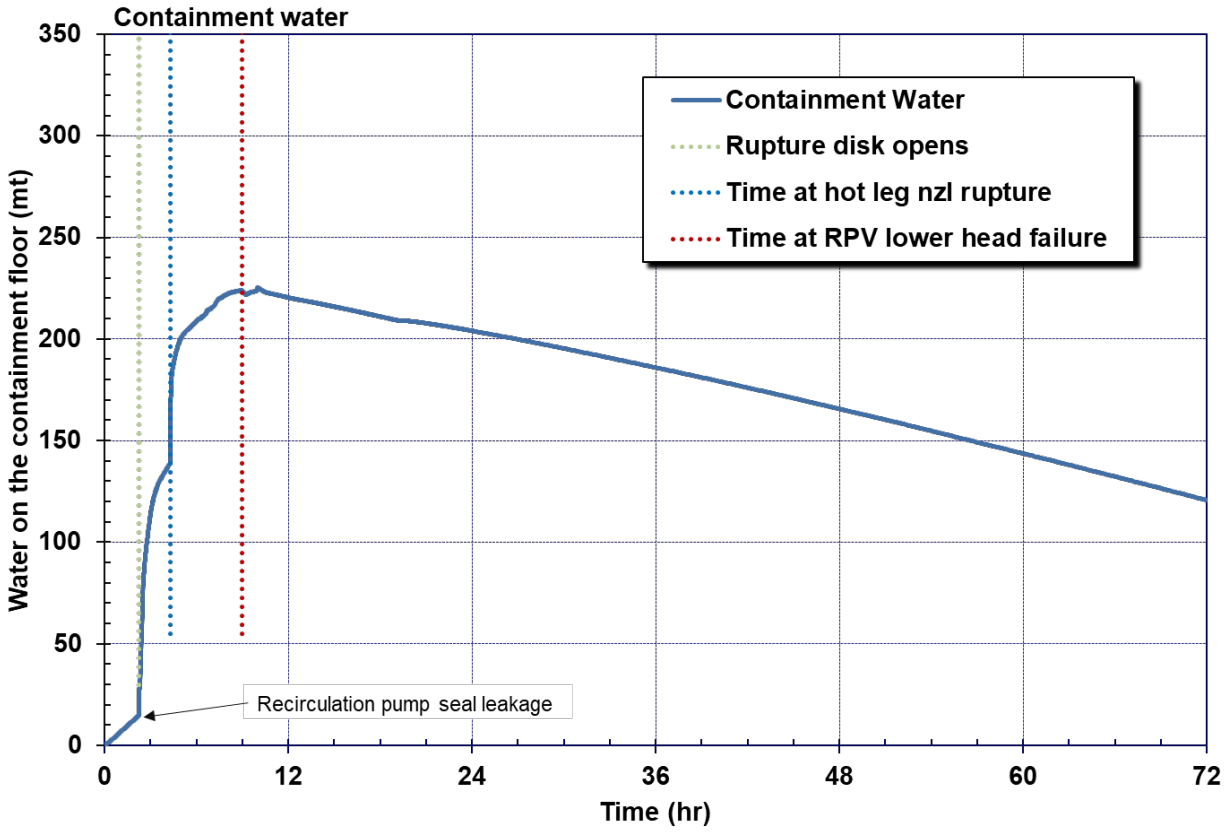

Figure 5-28 Water on the Containment Floor (Non-SGTR Reference Realization)

The rate of gas leakage from containment to the environment is presented in Figure 5-29. The leakage is negligible until the containment liner failure occurs at 47 hr. The subsequent leakage is the primary radionuclide release pathway.

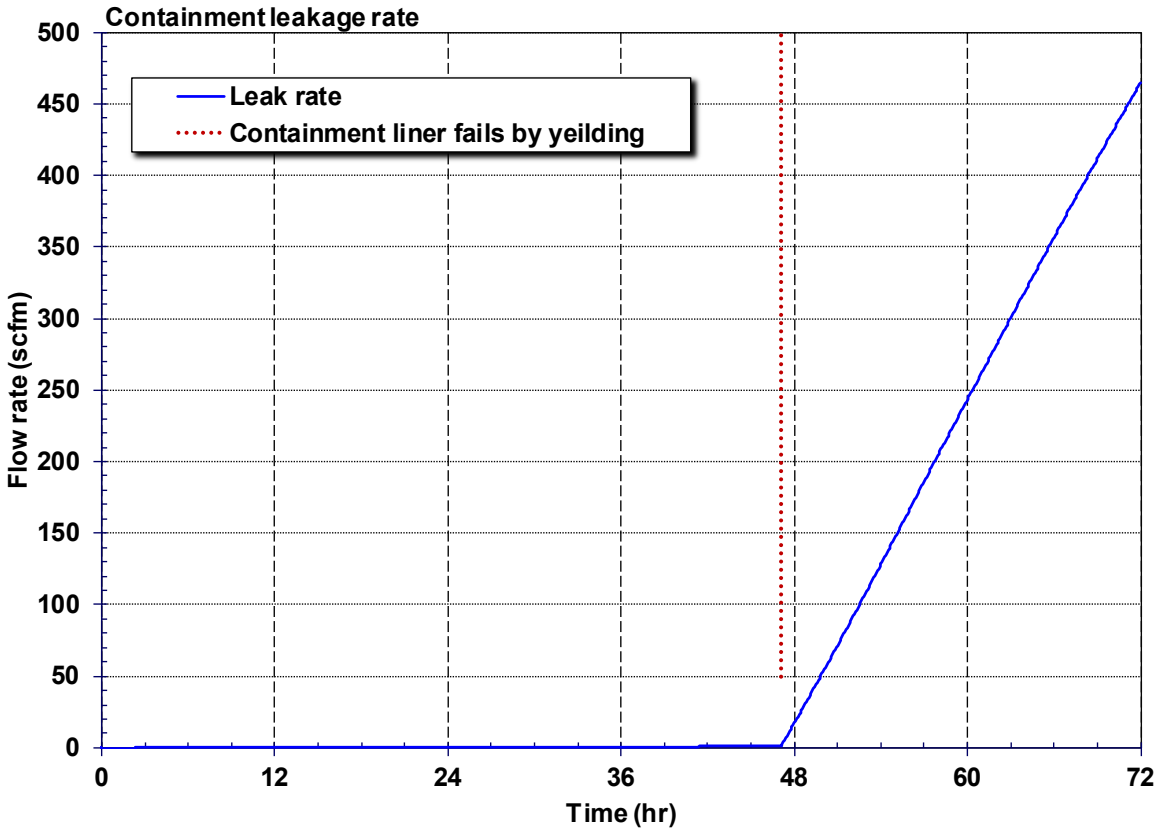

Figure 5-29 Containment Leakage Rate (Non-SGTR Reference Realization)

Figure 5-30 shows the hot leg nozzles and the SG tube temperature responses at the inlet to the steam generators where the creep rupture evaluations are made[59]. The three SG tube locations include the region where the hottest portion of the thermal plume from the core enters the steam generator, the hot upflow region, and a tube temperature representative of the region outside of the hot plume entry into the steam generator. The temperature responses in the various steam generators show slight variations based on other factors such as MSIV leakage (i.e., see Section 4.1.1.7) and the maximum hot plume temperature (i.e., see Section 4.1.1.5) but are generally grouped as described above. Following the hot leg failure, the primary system immediately depressurizes, and the tube temperatures decrease in response to the system depressurization and subsequent accumulator injection.

Figure 5-31 shows the creep damage accumulation in the three tube locations of SGs A, B and C and the hot leg nozzles. The accumulated creep in the SG tubes is a function of the tube temperature, the differential pressure across the tube, and the flaw depth. Each of the

[59] The temperature response for the hottest tube after the hot leg failure is not shown (i.e., the model is not used after the hot leg failure).

monitored locations has separately sampled flaw depths and unique temperature conditions. The differential pressures also vary slightly but those differences have a negligible impact on the creep evaluation. The maximum creep accumulation occurs in the hottest region of SG C but is more than an order of magnitude below the assumed failure condition. The hottest region of SG C had a maximum flaw depth of 0.35 whereas monitored hottest tube in SGs A and B did not have a flaw.

The hot leg nozzle C heats slightly faster than loops B and C due to the pressurizer SV flow (i.e., the pressurizer is located on loop C). The creep accumulates steadily until the carbon structure yields, which only leaves the stainless steel liner as the primary structural component. The stainless-steel liner fails shortly after, which causes the gross failure of the hot leg.

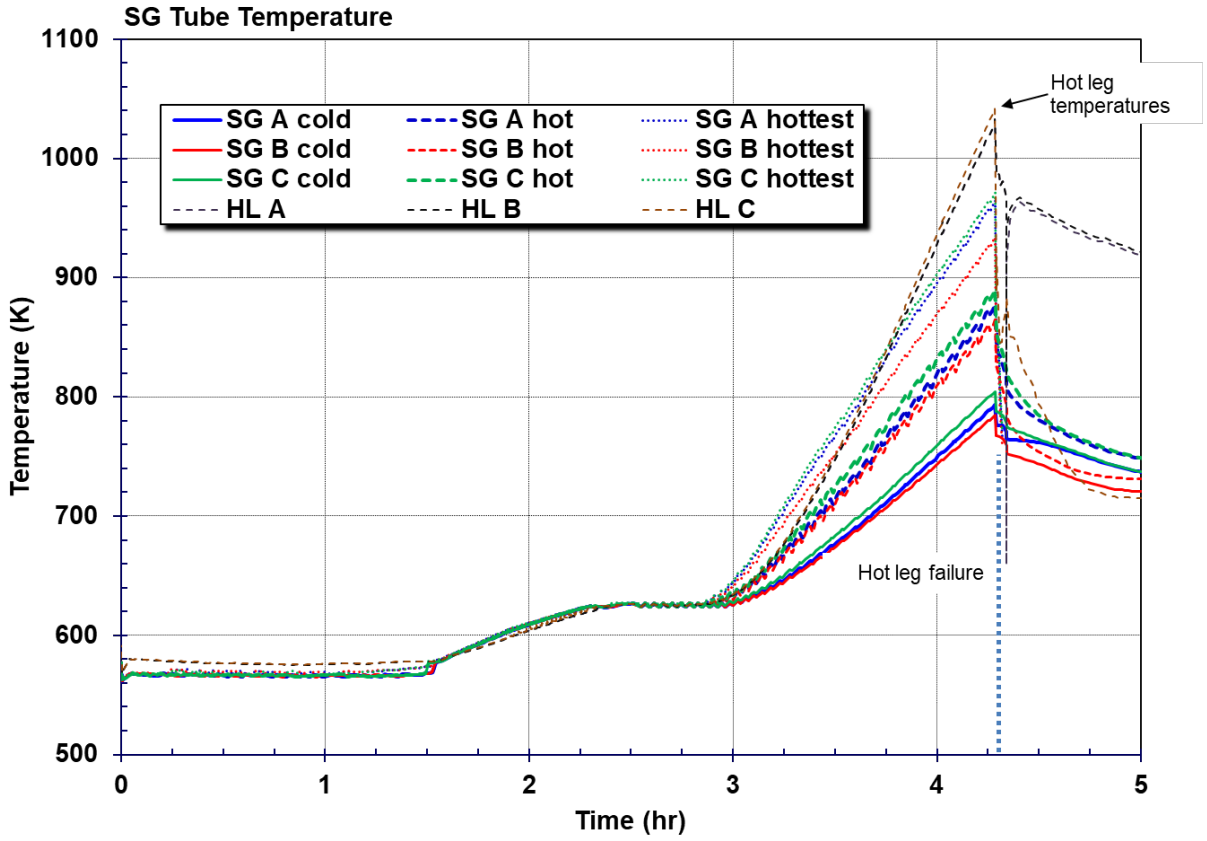

Figure 5-30 SG Tube Temperature Response (Non-SGTR Reference Realization)

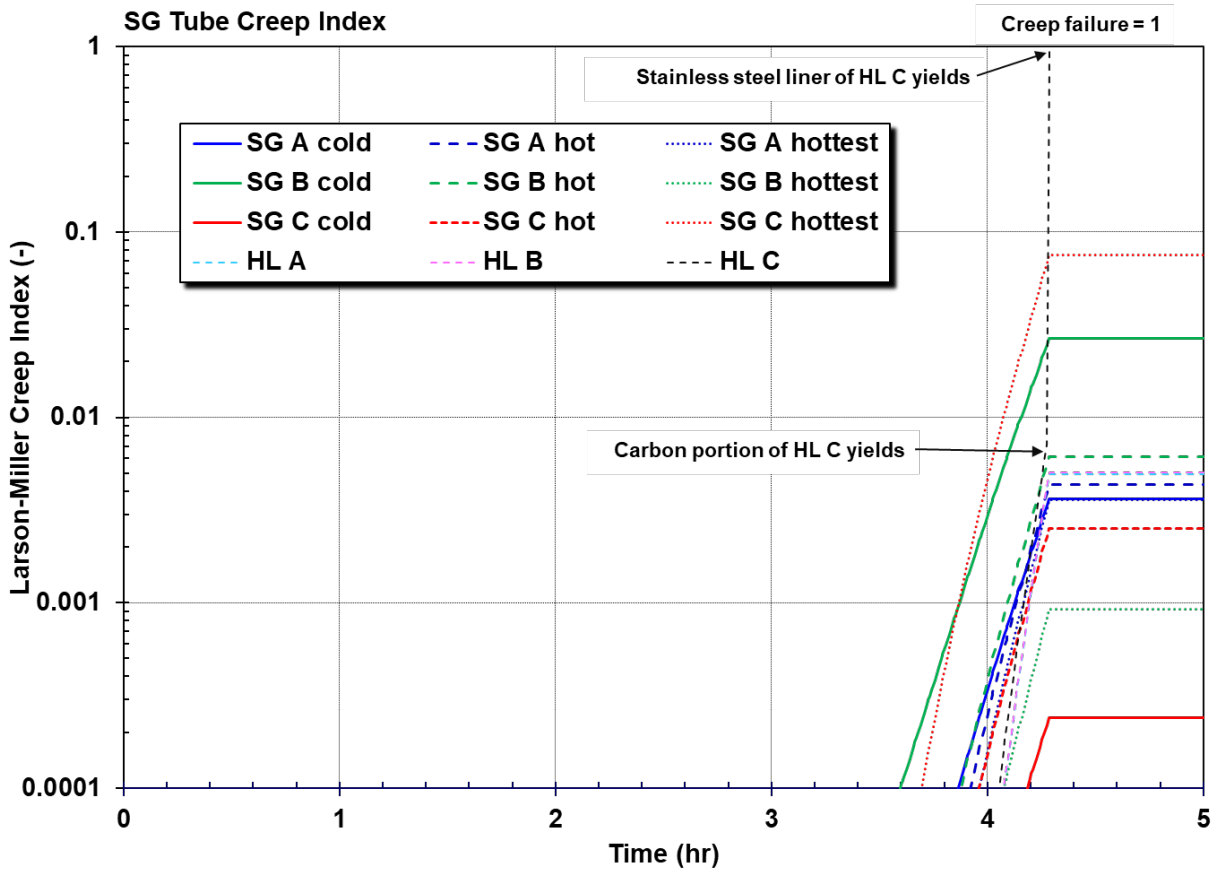

Figure 5-31 **SG Tube and HL Creep Damage Accumulation (Non-SGTR Reference Realization)**

Figure 5-32 and Figure 5-33 show the fractional distribution of elemental gaseous iodine and cesium-iodide aerosol in the RCS, PRT, containment, and environment. Relatively little iodine is released prior to the hot leg failure. Consequently, the PRT has little iodine from the pressurizer SV cycling. The small amount of airborne iodine in the RCS is immediately discharged into the containment at hot leg failure. The subsequent increase in released iodine occurs after the hot leg failure during the second core heatup. Most of the iodine released during the second fuel heatup flows out the failed hot leg location. There is also some very slow revaporization of iodine deposited in the RCS, evidenced by the gradual decrease of the RCS primary side mass fraction after 12 hr. The total iodine release to the environment was 0.028% at 72 hours, which was composed of gaseous iodine and cesium iodide aerosols.

The gaseous iodine available for release to the environment includes the initial gaseous mass released from the fuel gap (i.e., ~0.15% of the total iodine in realization 459) and any revolitized iodine from previously deposited cesium iodide. All the gaseous iodine can slowly leak to the environment whereas the aerosols can eventually settle. Only 5.4% of the gaseous iodine had been released to the environment at 72 hr. Consequently, the remaining 94.6% of the gaseous iodine and any new revolitized iodine can continue to slowly leak after 72 hr. However, the gaseous portion is only a very small fraction of the total iodine at 72 hr (i.e., <1%).

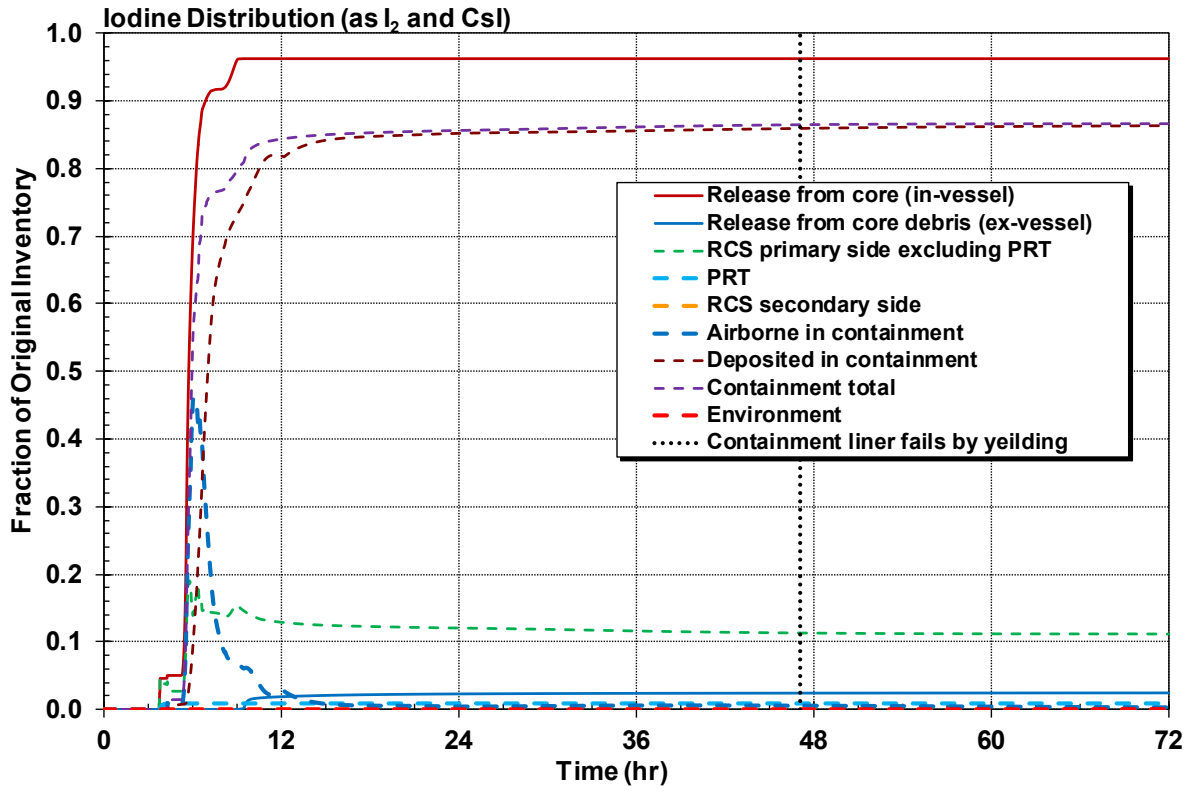

Figure 5-32 Iodine Distribution (as I_2 and CsI, Non-SGTR Reference Realization)

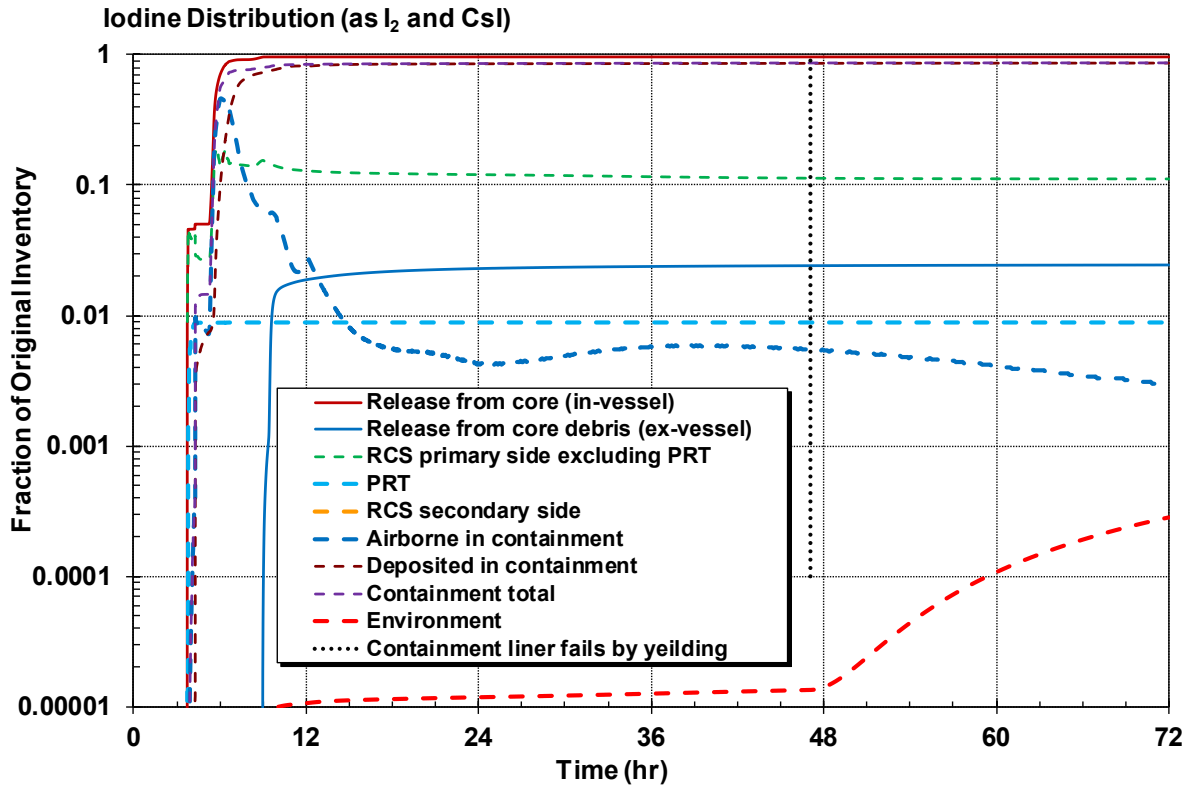

Figure 5-33 Iodine Distribution (Log, as I_2 and CsI, Non-SGTR Reference Realization)

Figure 5-34 and Figure 5-35 show the same information as Figure 5-32 and Figure 5-33 but for cesium rather than iodine. The fraction of cesium released and transported is reported as the combined contributions of cesium hydroxide, cesium iodide and cesium molybdate. The same general trends as observed in the iodine figures are also seen for cesium. As with the iodine release to the environment, there was also very little Cs release to the environment by 72 hr (0.003%). Unlike the iodine releases, there is no significant gaseous component in the containment. Consequently, the small release of cesium to the environment is from the very small sized airborne aerosols in the containment that have not settled (see log-scale in Figure 5-35). These small aerosols represent a very small portion of the total cesium but will remain airborne within the containment for days. Consequently, the small airborne aerosols could continue to release after 72 hr. However, the total airborne mass in the containment was less than 0.02% of the cesium inventory and would not significantly change the magnitude of the cesium source term to the environment.

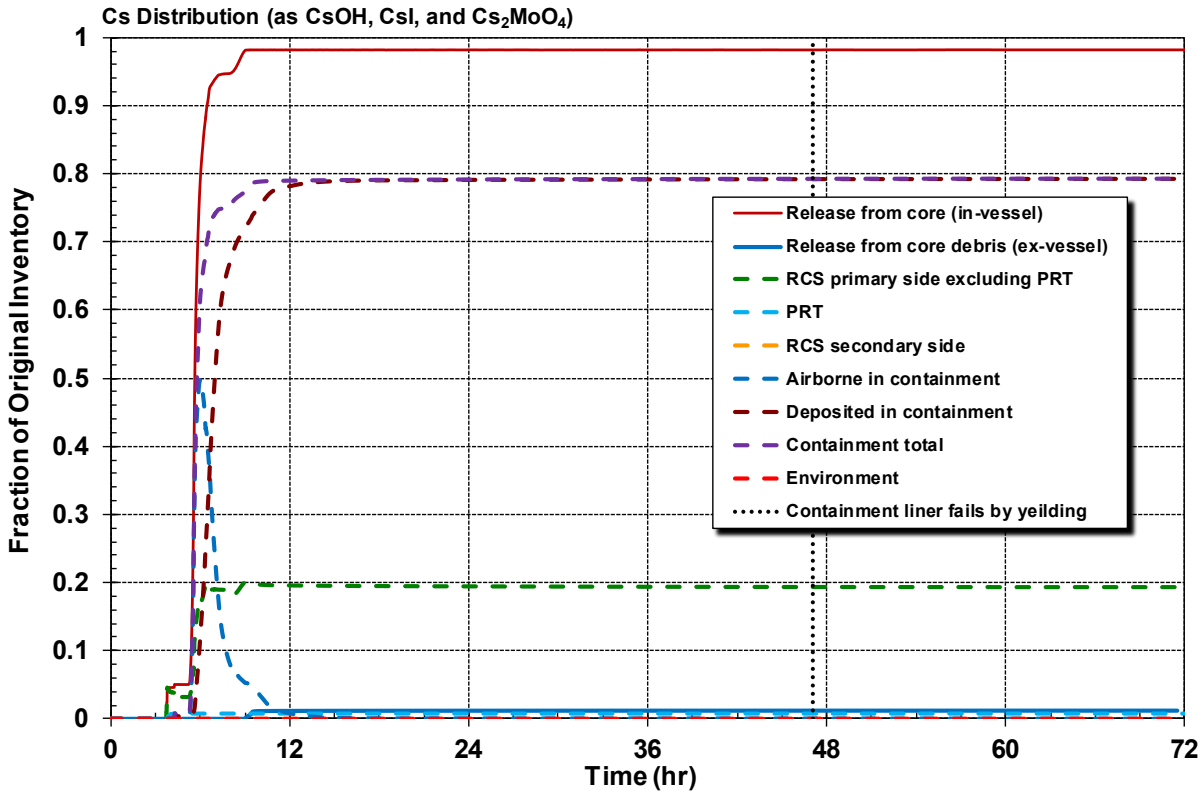

Figure 5-34 Cs Distribution (as CsOH, CsI, and Cs2MoO4, Non-SGTR Reference Realization)

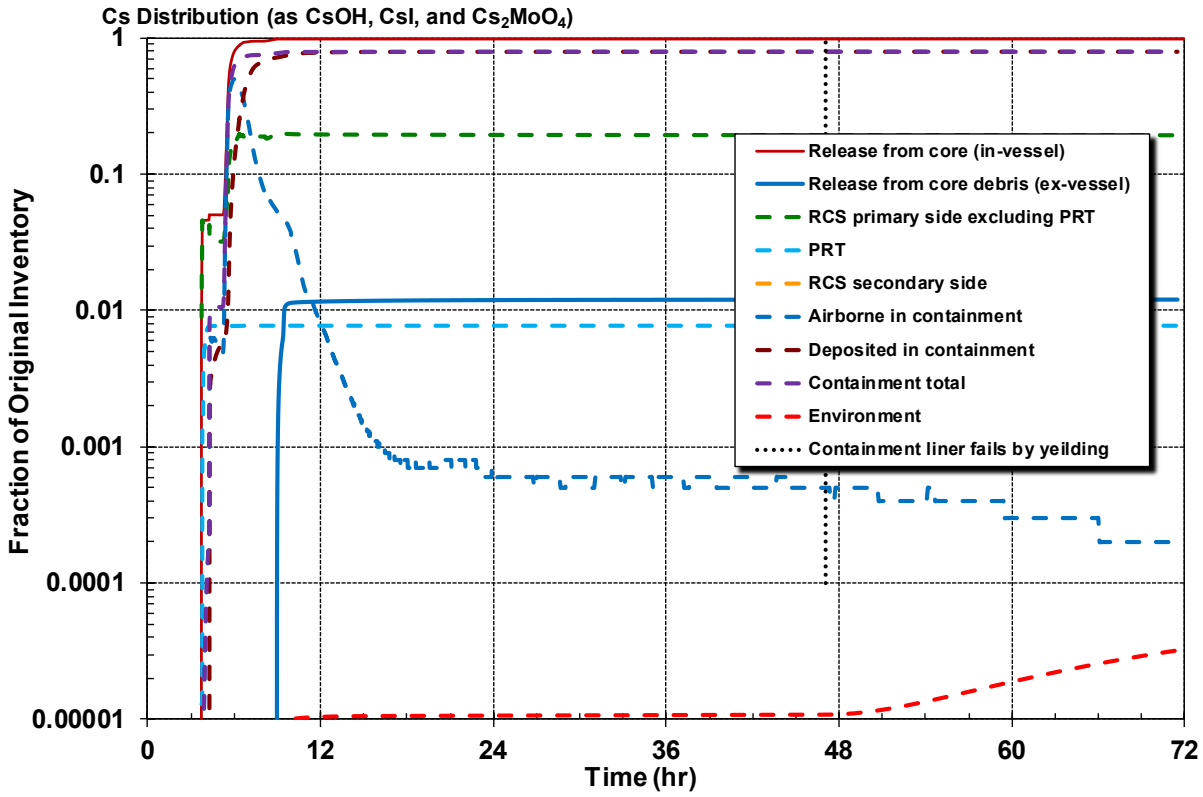

Figure 5-35 **Cs Distribution (Log, as CsOH, CsI, and Cs2MoO4, Non-SGTR Reference Realization)**

The central and peripheral fuel temperatures at low and high regions in the core are shown in Figure 5-36[60]. The fuel temperature trends reflect the steady heat removal by the SGs until the SG inventory is depleted at 1 hr 30 min. The fuel heats up with the water in the primary system to near the saturation temperature until 2 hr 50 min. As the two-phase core water level decreases below the top of the core, the fuel at the top and middle of the periphery of the core begins to heatup (Level 17). The middle of the core (Level 13) starts heating almost simultaneously due to the higher relative power at this location. The fuel near the bottom of the core (Level 8) starts to heat up 30 min later. Like the top of the core, the high-powered fuel in Ring 1 heats faster than the low-powered peripheral fuel in Ring 5. There is complete quenching of the fuel from a peak of 1429 K following the hot leg failure and accumulator discharge. Approximately 15 min later, a second heatup occurs that accelerates due to steam oxidation above approximately 1300 K. The fuel degrades and collapses during the second heatup. The temperature drops to zero when the fuel collapses from its intact geometry into the debris. The bulk of the hydrogen generation and fission product release occurs during the second heatup.

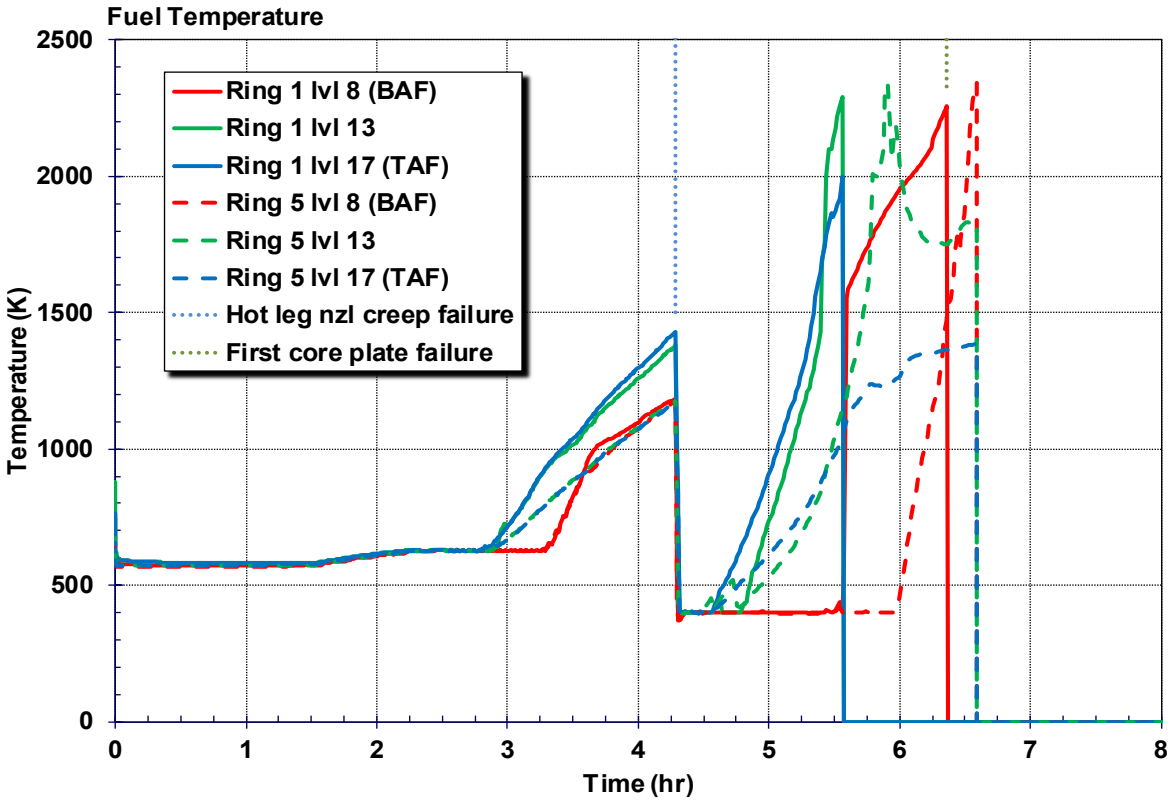

Figure 5-36 Fuel Temperature (Non-SGTR Reference Realization)

[60] The fuel temperature for Ring 1 (i.e., center of the core), Level 8 (near the bottom of the core) shows a sharp increase in temperature at 5.8 hr due to the arrival of hot relocated debris and molten Zircaloy from degrading fuel above this elevation. When the previously intact fuel collapses, MELCOR transfers the materials to the debris field. Figure 5-36 only shows the intact fuel temperatures for Ring 1 Levels 13 and 17 going to 0 K (i.e., the intact component does not exist at this elevation anymore) when the fuel temperature at Level 8 rapidly increases.

The debris behavior in the reactor cavity below the failed vessel is shown in Figure 5-37. There is a small of amount of water discharged into the reactor cavity following the hot leg failure at 4 hr 17 min. The water in the cavity is rapidly boiled off following the vessel lower head failure when the core debris drops into the reactor cavity. The concrete ablation proceeds at a vigorous and steady rate. The debris has ablated 1.3 m downward into the concrete by 72 hr. The debris and ablation materials rise 0.8 m above the initial floor elevation.

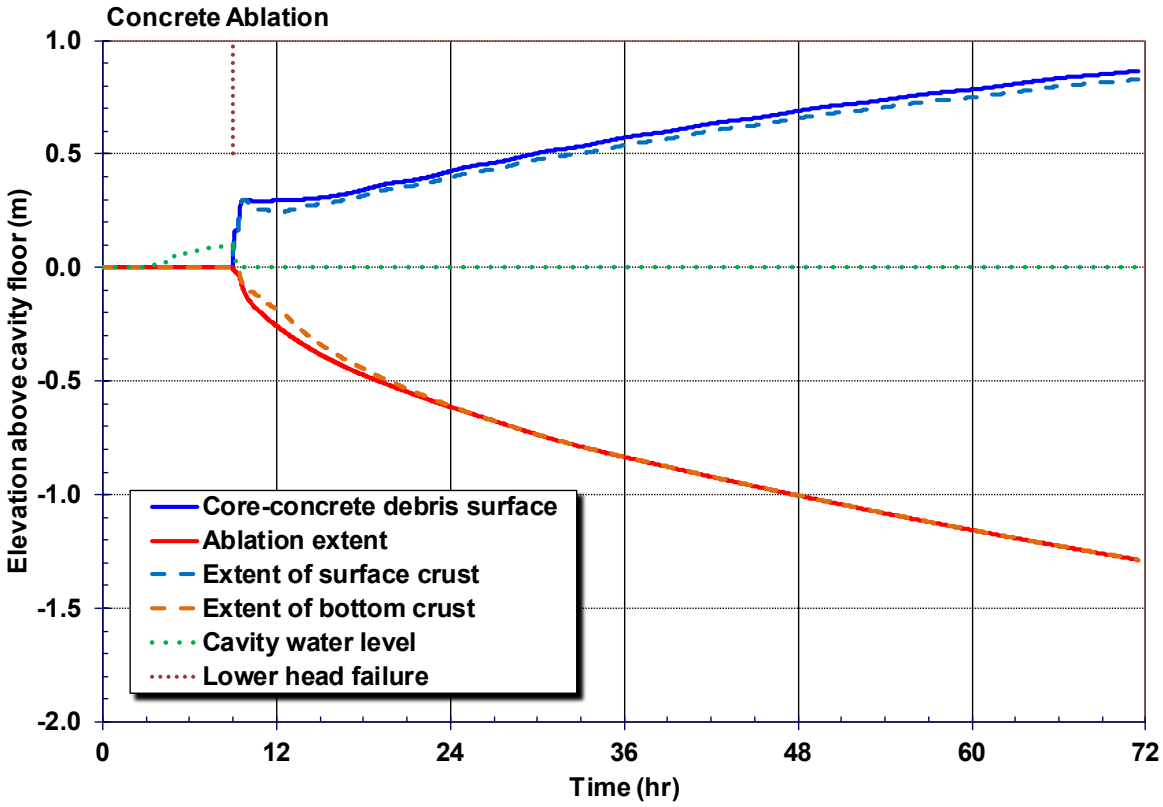

Figure 5-37 Concrete Ablation and Cavity Water Depth (Non-SGTR Reference Realization)

5.2.2 Reference STSBO Realization with a SGTR

The key event times for reference realization 39, which progressed with a SGTR are listed in Table 5-17. The settings of the key uncertain parameters are summarized in Table 5-15. The timings and key calculated responses of the Realization 39 accident progression are summarized in Figure 5-38 through Figure 5-64. The attributes of the figures are discussed below.

Table 5-17 Key Event Timing in the Reference STSBO Realization with a SGTR

Event	Time (hh:mm)
STSBO – loss of all AC and DC electrical power, AFW unavailable	00:00
Reactor trips Main steam isolation valves (MISVs) close RCP seal leakage initiates at 21 gpm/pump	00:00
SG dryout	01:32
PRT rupture disk breaks	02:16
RPV water level reduces to TAF	02:16
First fission product gap release	03:43
SGTR in SG A in the cold region	04:01
Release of elemental iodine to the environment exceeds 1.0%	04:06
Loop C hot leg nozzle rupture	04:17
Accumulators begin discharging	04:18
Accumulators empty	04:19
Release of noble gases to the environment exceeds 1.0%	05:37
Core debris mass exceeds 5%	05:46
1st hydrogen burn	06:09
Initial core plate failure	06:36
RPV lower head breach	09:13
End of containment hydrogen burns	10:12
Containment pressure reaches design (45 psig)	32:15
Containment liner yields	57:55
End of calculation	72:00

The primary system pressure for the SGTR reference realization is shown in Figure 5-38. The initial primary system response is similar to the non-SGTR realization. The heat removal from the SGs causes the pressure to decrease until all the SGs water inventory is boiled away. The primary system pressure subsequently rises until the SV opens. The primary system cycles as the pressurizer SVs open and close until 4 hr 1 min, when a SGTR occurs. The energy release through the SGTR stops the pressurizer SV cycling but does not depressurize the primary system. The hot nozzle fails by creep rupture at 4 hr 17 min, which corresponds to 16 min of high-pressure flow from the primary system to the SG through the SGTR. Following hot leg failure, the primary system completely depressurizes, which effectively stops any significant SGTR flow.

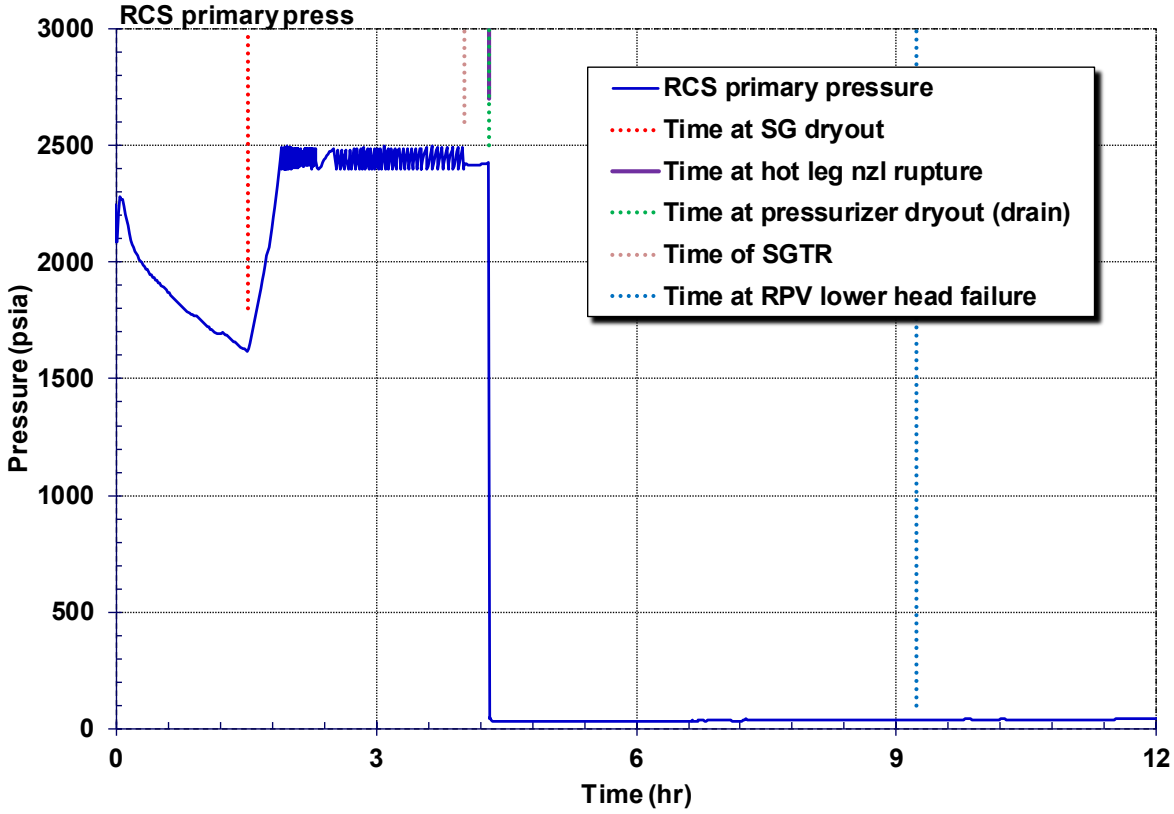

Figure 5-38 RCS Primary Pressure (SGTR Reference Realization)

Figure 5-39 shows SG pressure history. The SG pressure rises quickly to the SV setpoint following the closure of the MSIVs and termination of the feedwater flow. The SG system pressure cycles with the SV opening and closings to remove heat transferred from the primary system to the secondary. Following the dryout of the SGs at 1.5 hr due to venting steam out the cycling SVs, the system pressure begins to slowly decrease. The subsequent pressure response is primarily controlled by leakage past the MSIVs. The initial differences in the depressurization rates following the SG dryout are attributed to the various sampled leakages (i.e., 0.57, 0.43, and 0.67 in^2 for the MSIVs on SGs A, B, and C, respectively). The impact of the SGTR and the subsequent hot leg failure are evident in the SG A pressure response. The SGTR pressurizes SG A until the hot leg failure. After the primary system depressurizes at 4 hr 17 min, the SG A depressurizes backwards through the SGTR into the primary system and through MSIV leakage to the environment. By approximately 5 hr 15 min, the SG A pressure has reduced to atmospheric pressure.

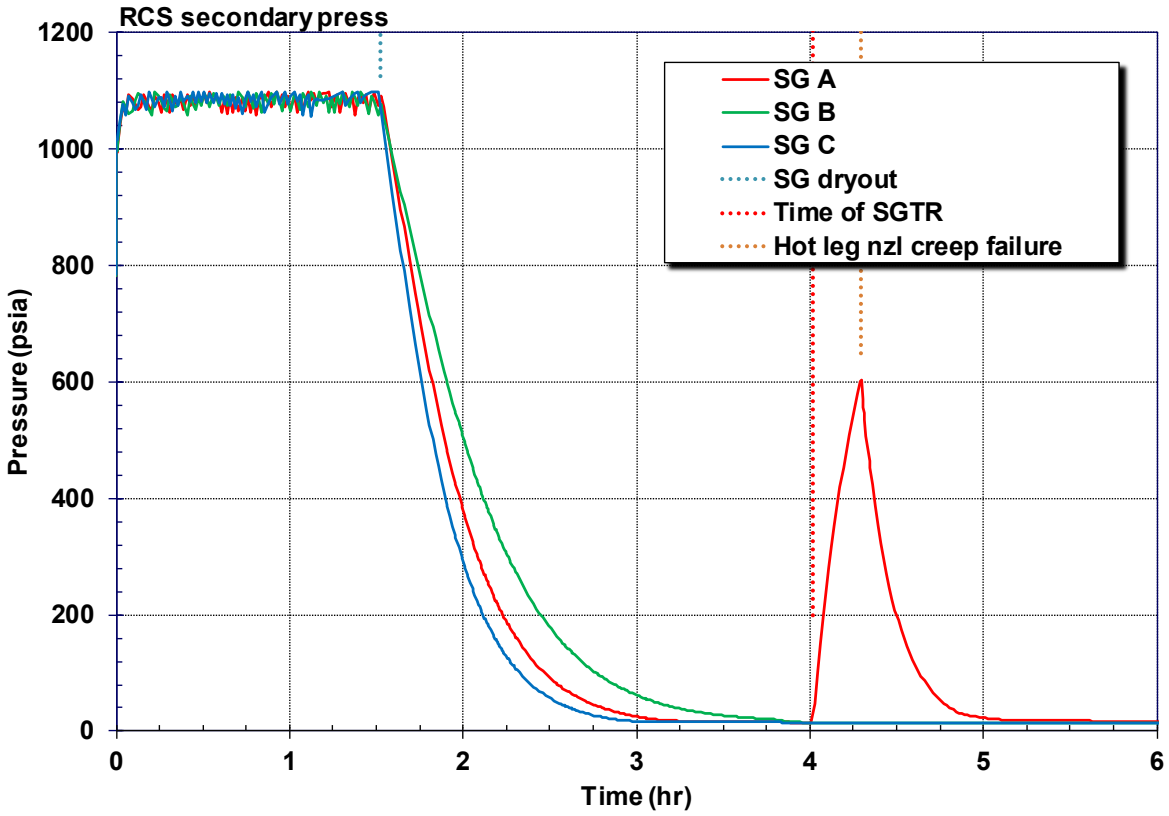

Figure 5-39 RCS Secondary Pressure (SGTR Reference Realization)

The SG A MSIV and SGTR leakages are shown in Figure 5-40. The sampled hole size for the SG A MSIV leakage was 0.57 in^2, which leaked about 7300 scfm at full secondary pressure. Following the SG dryout at 1 hr 30 min, the secondary systems depressurized due to the MSIV leakage. At the time SGTR of at 4 hr 1 min, the MSIV leakage was near zero. The SGTR pressurized the SG A secondary and the leakage increased to 3000 scfm until the hot leg nozzle creep rupture failure. The double-ended SGTR leakage rate to the secondary was about 4600 scfm until the primary system rapidly depressurized. The SGTR was negative until 4 hr 50 min when the SG pressure decreased below the coupled primary system and containment pressure. The long-term SGTR leakage is compared to the containment leakage, which is shown later in Figure 5-52.

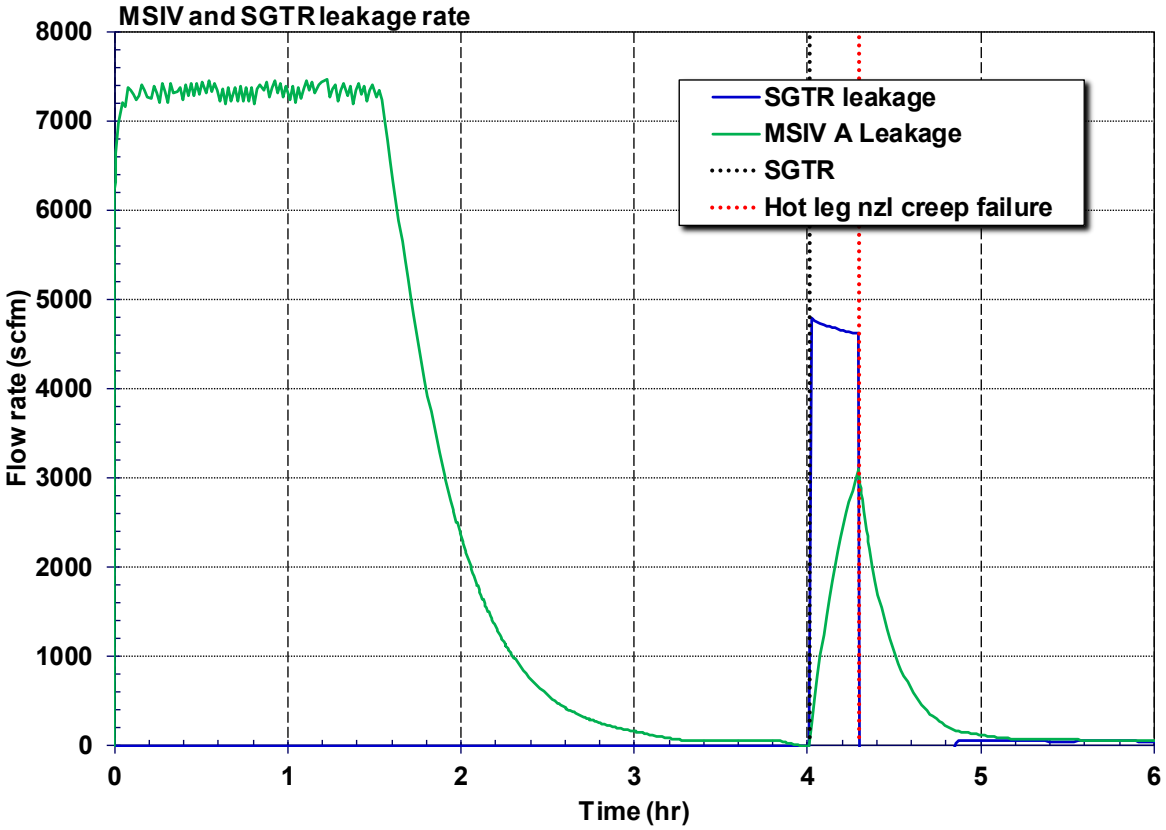

Figure 5-40 SG A MSIV and the SGTR Leakage (SGTR Reference Realization)

The RCS level response is shown in Figure 5-41. Like Realization 459, there is water holdup in the pressurizer prior to the pressurizer SV failure to close even though the hot leg is dry. The accumulator injection is evident. However, there is no significant impact of the SGTR at 4 hr 1 min.

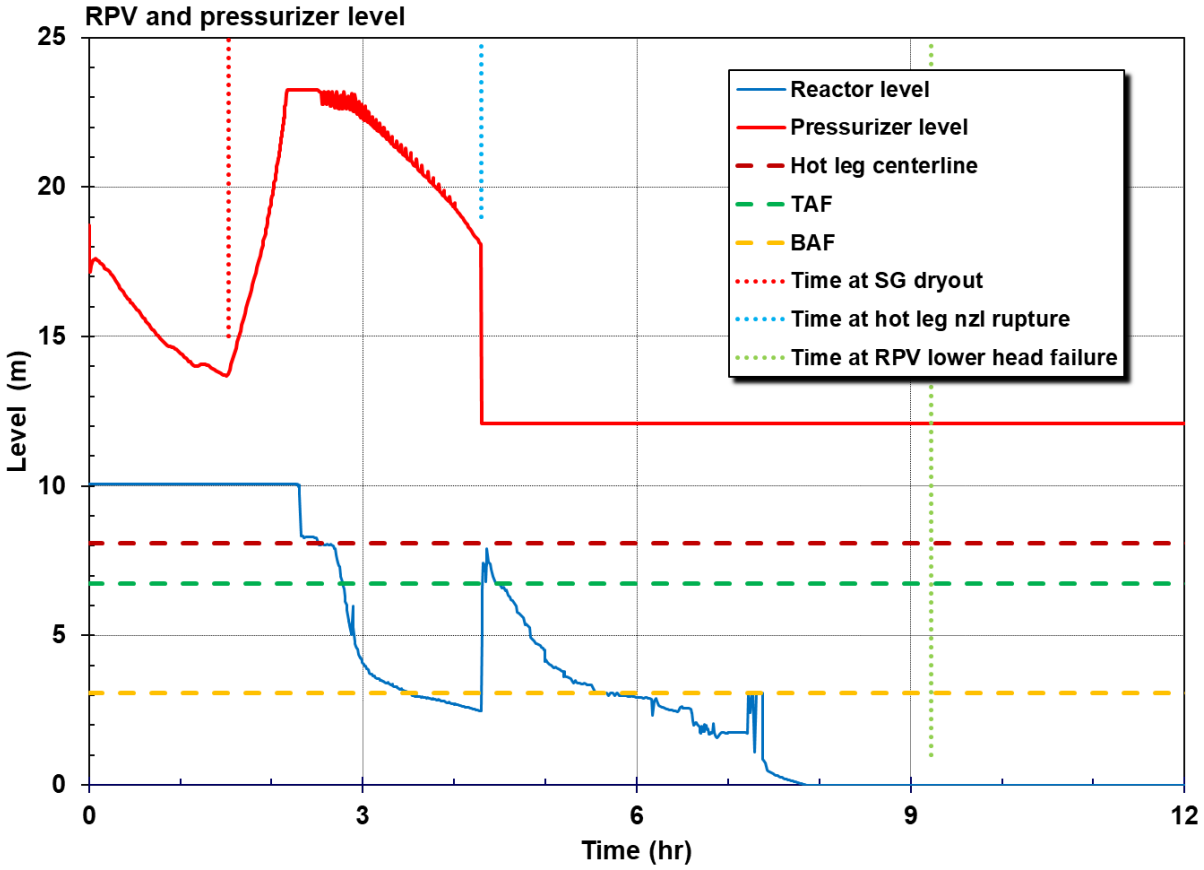

Figure 5-41 RCS Primary Level (SGTR Reference Realization)

Figure 5-42 shows the history of combined leakage from the RCS through the RCP seals. Note that there is no damage assumed to result to the seals during the base calculation. The seals simply continue to leak at the nominal amount of 21 gpm/pump (at normal operating conditions). There was no significant impact of the SGTR on the seal leakage rate.

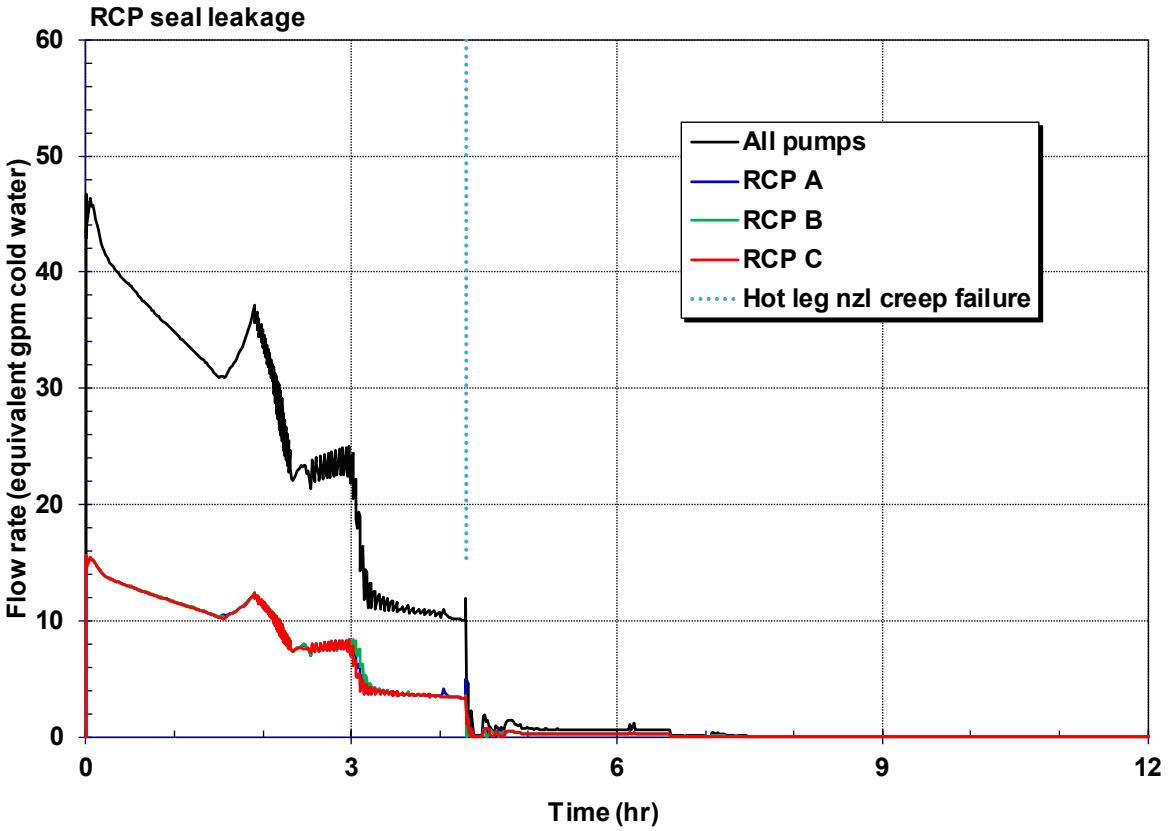

Figure 5-42 RCP Seal Leakage (SGTR Reference Realization)

The SG level response is shown in Figure 5-43. All three SGs have essentially the same water level trend. The water level decreases continuously in the absence of any feedwater delivery. SG C does not contain any water at the time of the SGTR.

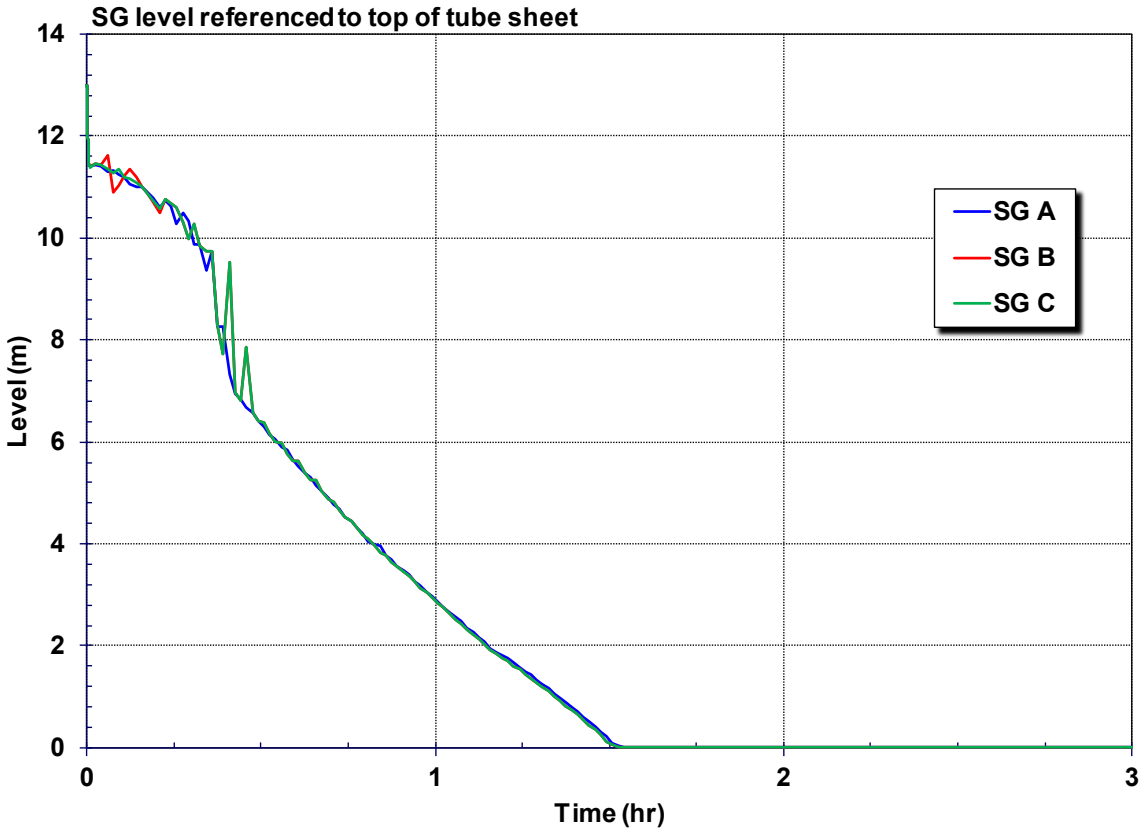

Figure 5-43 SG Level Referenced to Top of Tube Sheet (SGTR Reference Realization)

Figure 5-44 shows the hydrogen produced inside the RPV through oxidation of fuel cladding and steel. The figure shows the total hydrogen production is dominated by zircaloy oxidation rather than steel oxidation. The large surface area of the zircaloy cladding on the fuel rods dominates oxidation reactions until after the fuel degrades into debris geometry. There is about 50 kg of steel oxidation after the collapse of the core. The total hydrogen production initially increases until the hot leg nozzle failure, which depressurizes the primary system and discharges the accumulator water into the core. There is only 35 kg of hydrogen produced at the time of the hot leg failure. After the injected water boils away, the second heatup of the core creates approximately 300 kg of hydrogen. The hydrogen production slows after the core starts degrading into debris geometry. By the time of lower head failure, all the core debris is discharged to the containment (see Figure 5-45) and the in-vessel oxidation phase is over. The hydrogen response and total generation is very similar to Realization 459 without a SGTR.

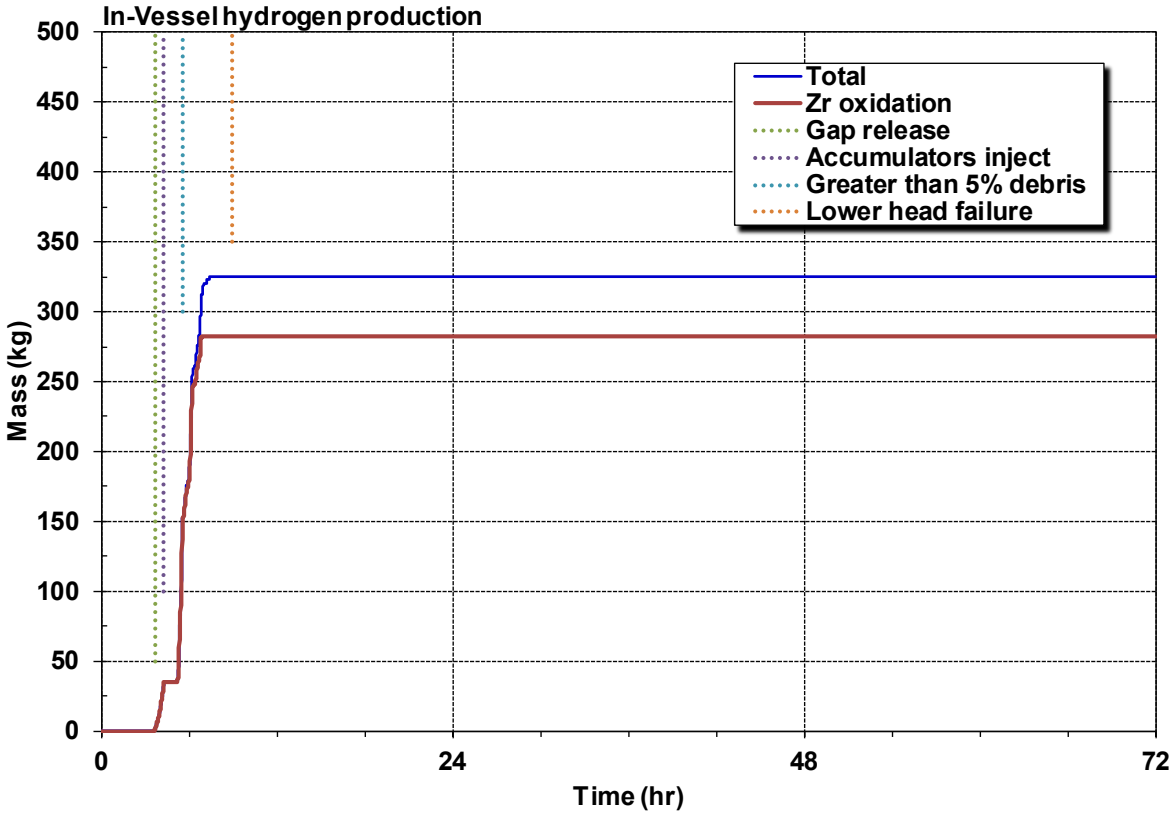

Figure 5-44 In-Vessel Hydrogen Production (SGTR Reference Realization)

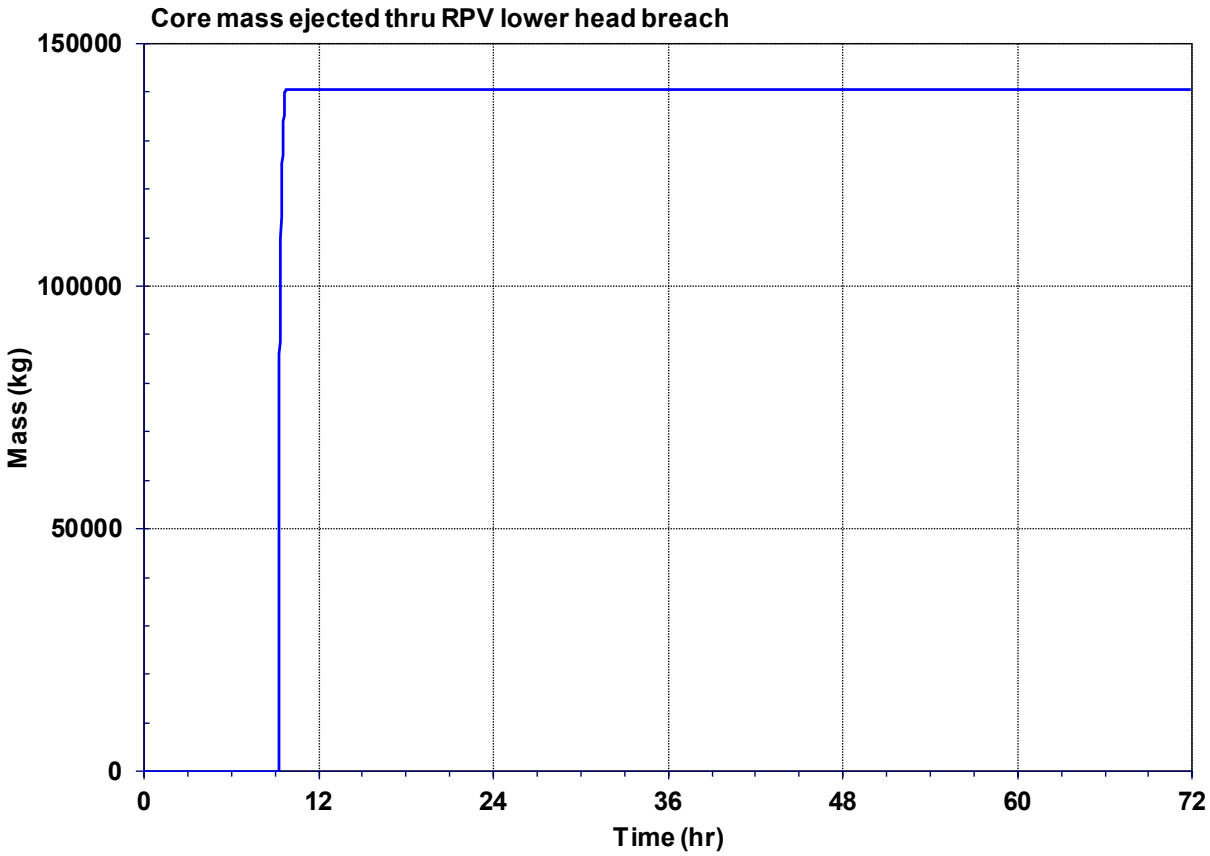

Figure 5-45 Core Mass Relocated to the Reactor Cavity (SGTR Reference Realization)

Figure 5-46 shows the containment pressure response. The SGTR reference realization response is very similar to the non-SGTR response described in Figure 5-22. The presence of a SGTR has an impact on the containment pressurization rate, which is evident when comparing the responses of Realization 459 and 39. The design pressure of containment is exceeded at 27 hr 45 min in the non-SGTR reference realization versus 32 hr 15 min in the SGTR calculation. Similarly, the yielding of the containment steel liner occurs at 47 hr in the non-SGTR reference realization versus 57 hr 55 min in the reference SGTR calculation. Finally, the containment pressure is 113 psia at 72 hr, or just 4 psi below the containment yield pressure in the non-SGTR realization but only 101 psia in the SGTR calculation, or 16 psi below the containment yield pressure. Some of the differences cited above are due to the specifications of the uncertain values. However, since the containment pressure was used in the criteria to select the reference realizations, the comparison of the non-SGTR and SGTR reference realizations is characteristic of the median impact of the SGTR leakage pathway on the containment pressure response.

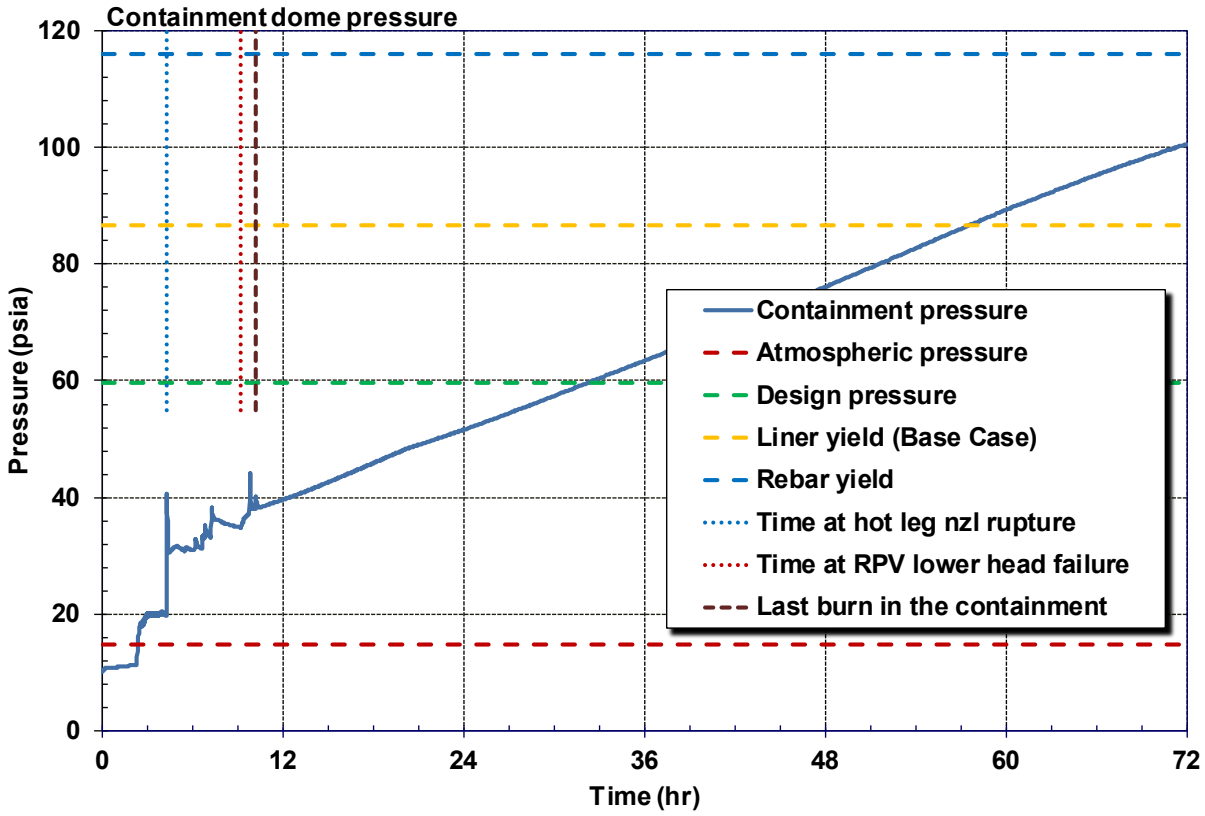

Figure 5-46 Containment Pressure (SGTR Reference Realization)

The energy produced by deflagrations in containment and the room steam concentrations are illustrated in Figure 5-47. There are three large deflagrations, one almost 3 hr after hot leg nozzle creep and two at 45 min after lower head failure. The second burn is largest because it propagates to the dome (see Footnote 58). The total burn energy is similar to the non-SGTR reference realization (see Figure 5-23) with 18,700 MJ in the SGTR reference realization versus 21,300 MJ in the non-SGTR reference calculation. Both reference realizations become steam-inerted and oxygen-limited shortly after the vessel lower head failure and the start of core-concrete interactions in the reactor cavity.

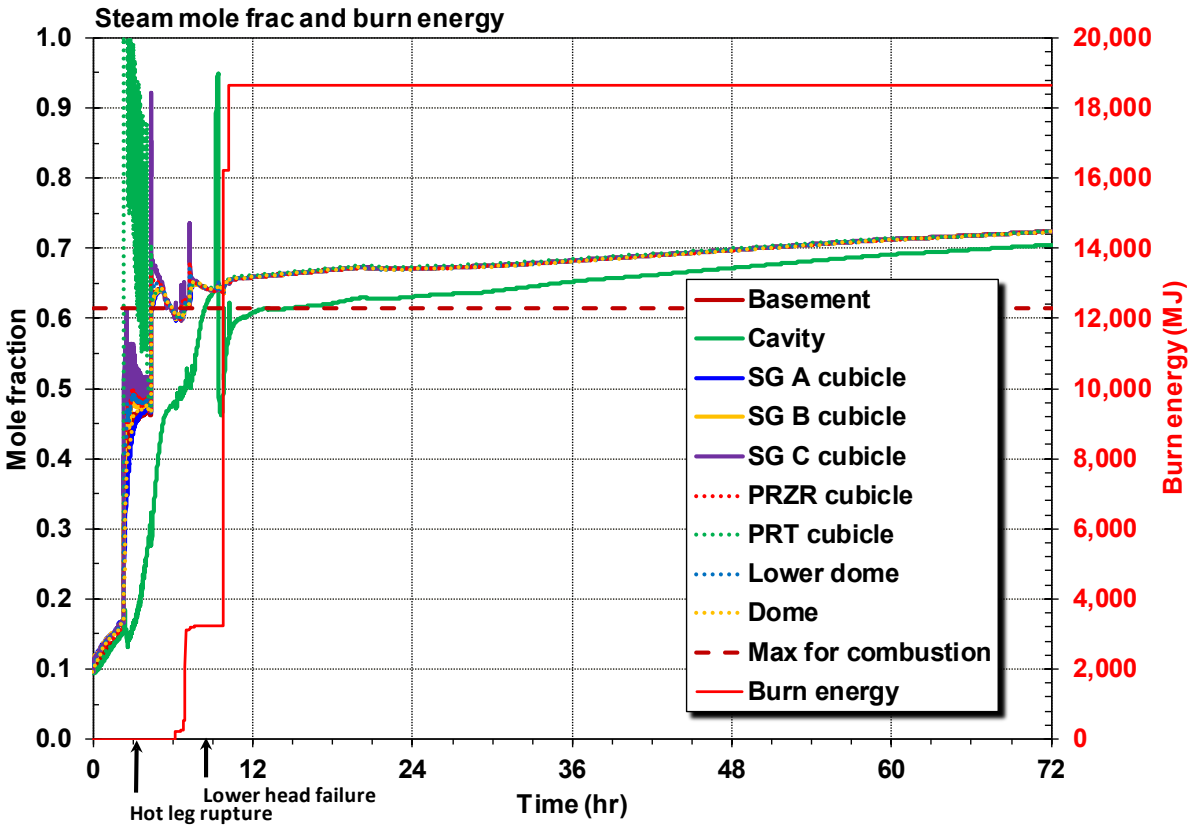

Figure 5-47 Containment Steam Mole Fraction and Energy Produced by Deflagrations (SGTR Reference Realization)

Similar to the non-SGTR reference realization containment dome temperature response in Figure 5-24, the largest temperature spike occurs when the primary system depressurizes into the containment from high pressure and temperature. The second large burn at 9 hr 45 min, which propagated into the dome region was the next largest temperature spike. Some small burns occur in the lower containment compartments between and after these two larger burns but had little impact on the dome temperature. After combustion is prevented by high steam concentrations and low oxygen concentrations, the containment temperature rises slowly as the containment pressurizes.

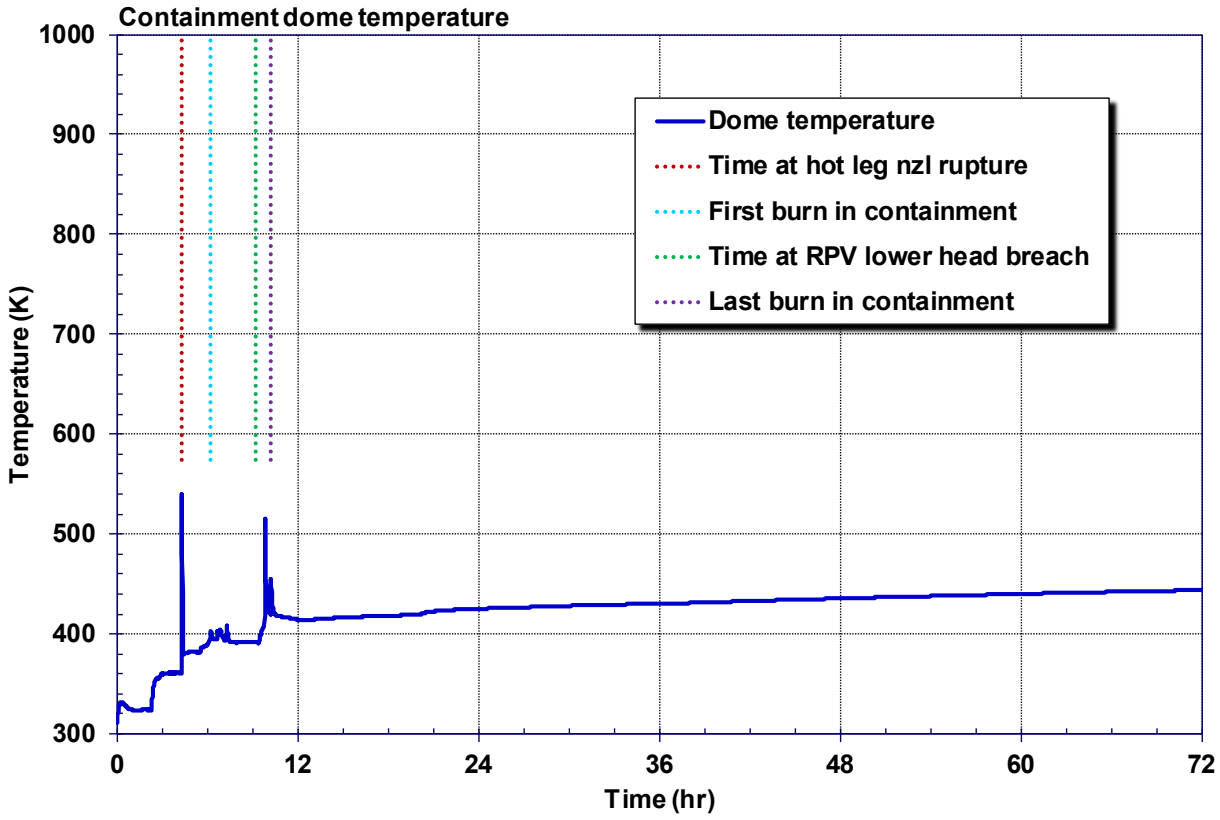

Figure 5-48 Containment Dome Temperature (SGTR Reference Realization)

The non-condensable gas generation from core-concrete interaction in units of kg and kg-mol are shown in Figure 5-49 and Figure 5-50, respectively. The gas production is essentially constant after the core debris drops into the containment reactor cavity. Although the carbon monoxide mass production is larger than the hydrogen gas production, the volume of the hydrogen gas produced is much larger (see Figure 5-50). The ex-vessel gas productions from the concrete ablation in the two reference realizations are very similar due to the similar timings of the vessel failure, the mass discharged to the cavity, and the decay heat levels. For example, both reference realizations had 3,170 kg of hydrogen production and 5,400 kg of carbon-monoxide production at 72 hr.

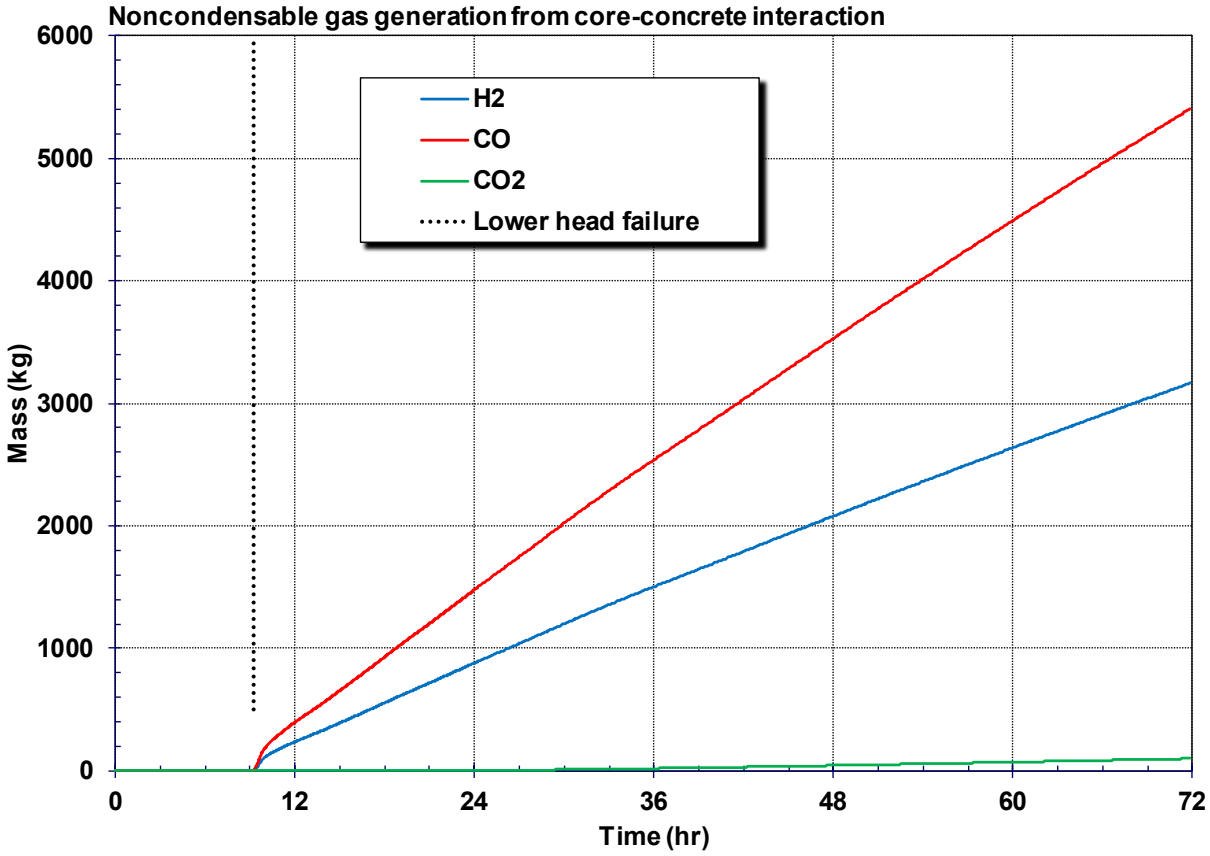

Figure 5-49 Noncondensable Gas Generation from Core-Concrete Interaction, kg (SGTR Reference Realization)

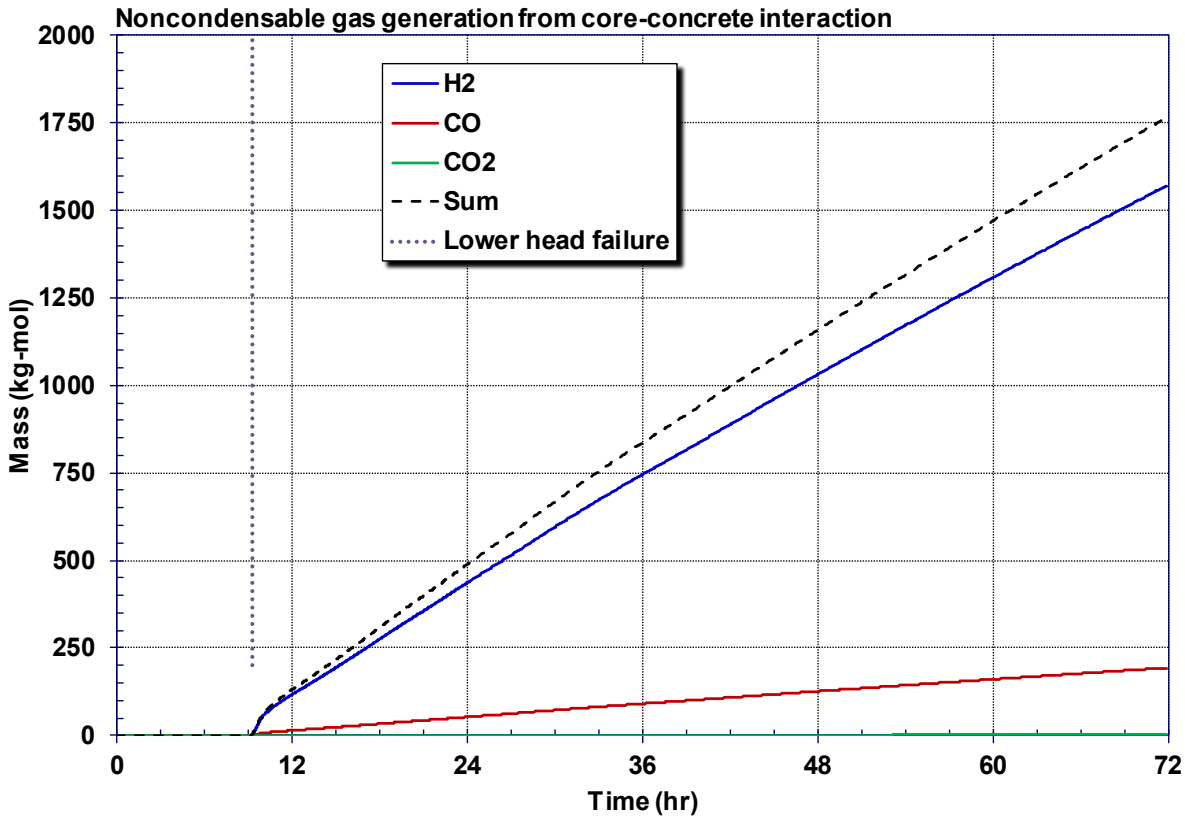

Figure 5-50 Noncondensable Gas Generation from Core-Concrete Interaction, kg-mol (SGTR Reference Realization)

As previously shown in the non-SGTR reference realization (see Figure 5-27), the containment pressurization is primarily due to the evaporation and heating of the water from the primary system in the containment, which is also true in the SGTR reference realization (see Figure 5-51). The partial pressure of the steam at the 72 hr is 72% of the total steam pressure in both cases.

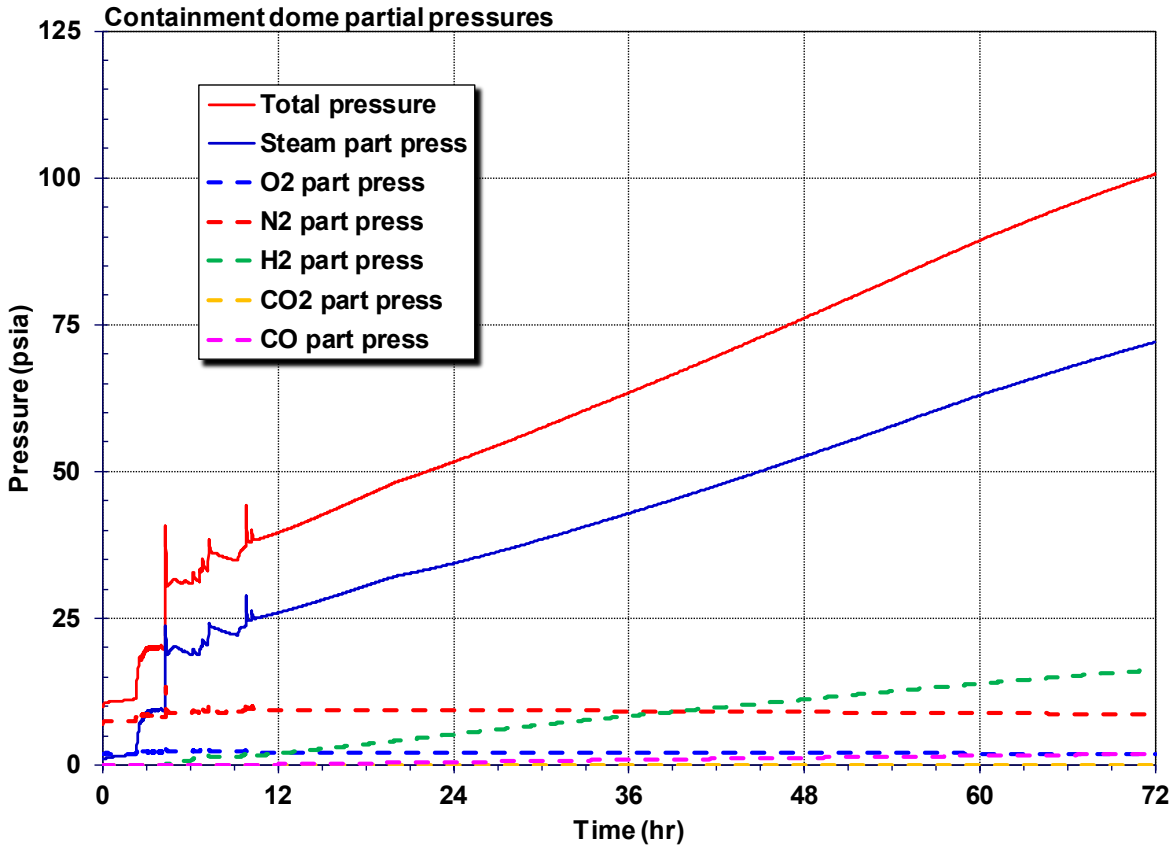

Figure 5-51 Containment Dome Partial Pressures (SGTR Reference Realization)

The rate of gas leakage from containment to the environment and from the primary system to the environment are shown in Figure 5-52. The SGTR occurs at 4 hr 1 min and begins leaking from the primary system to the secondary side of the steam generator and then past the MSIV. After the initial high leakage while the primary system was pressurized, the SGTR leakage follows the containment pressure response (see Figure 5-46) and steadily increases from 50 scfm to 215 scfm. The containment leakage from the liner yield doesn't start until 57 hr 55 min and increases to 175 scfm at 72 hr. The magnitude and duration of the SGTR leakage is larger than the containment yielding leakage, which directly contributes to the slower containment pressurization in the SGTR realizations.

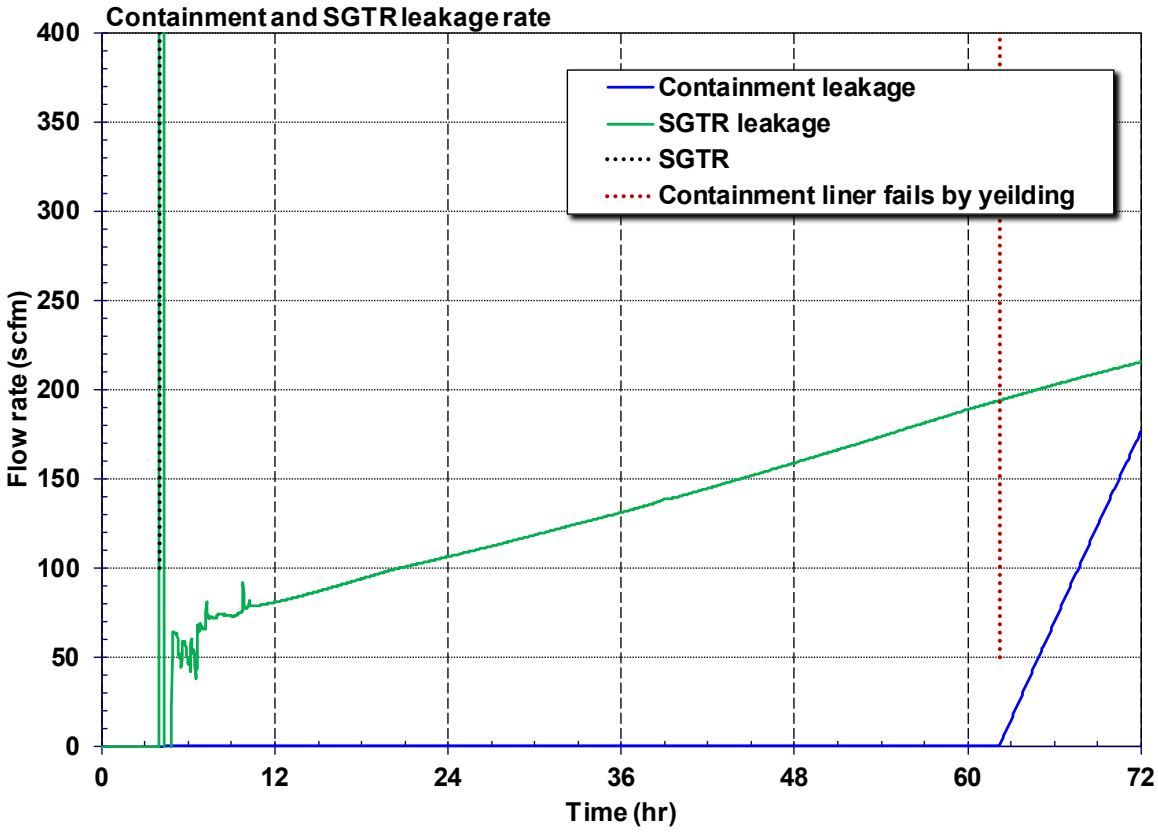

Figure 5-52 Containment and SGTR Leakage Rate (SGTR Reference Realization)

Figure 5-53 shows the tube temperature responses at the inlet to the steam generators and the hot leg nozzles where the creep rupture evaluations are made. The three tube locations include the region where the hottest portion of the thermal plume from the core enters the steam generator (i.e., the hottest tubes), the hot upflow region at the inlet to the steam generator, and a tube temperature representative of the region outside of the hot plume entry into the steam generator (i.e., the cold tubes). Figure 5-54 shows the corresponding creep damage accumulation in the three tube locations of SGs A, B and C and the hot leg nozzles. The accumulated creep is a function of the tube temperature, the differential pressure across the tube, and the flaw depth. The SGTR reference realization had a very severe non-dimensional flaw depth in the cold tube region of SG A. The creep accumulation increased much faster in this tube than the other monitored locations until its failure at 4 hr 1 min. No other tube is close to failure prior to the hot leg nozzle rupture at 4 hr 17 min. Similar to the response of the non-SGTR reference realization, the hot leg C nozzle fails shortly after the carbon steel nozzle weakened.

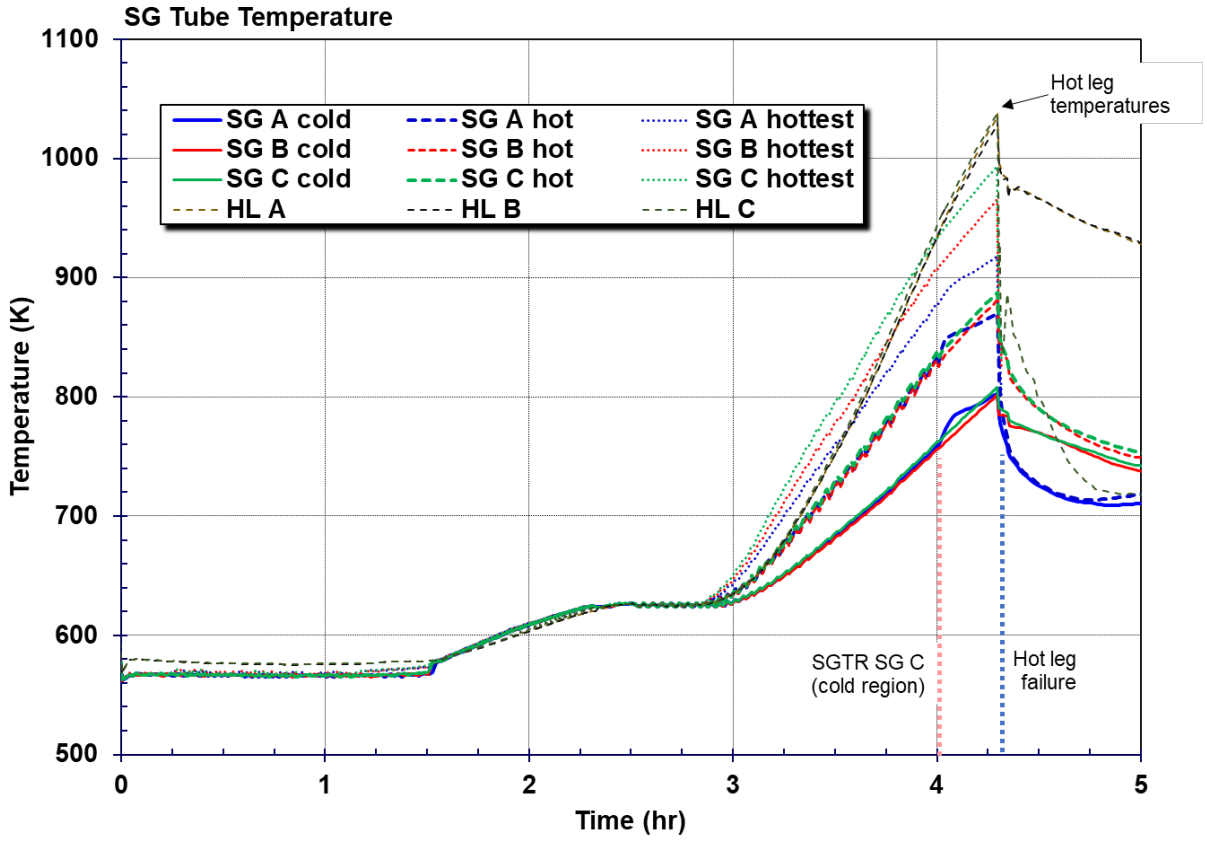

Figure 5-53 SG Tube Temperature Response (SGTR Reference Realization)

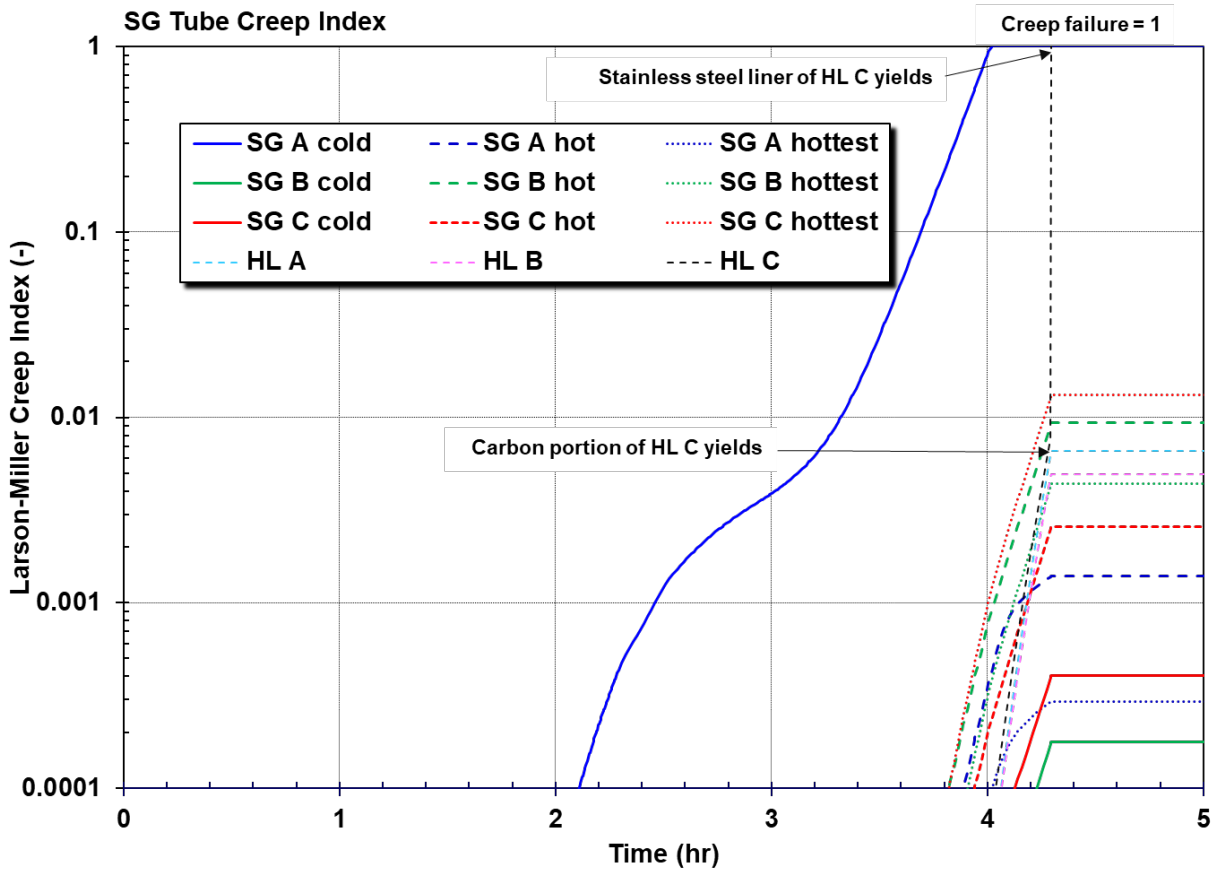

Figure 5-54 SG Tube Creep Damage Accumulation (SGTR Reference Realization)

Figure 5-55 and Figure 5-56 show the fractional distribution of elemental gaseous iodine and cesium-iodide aerosol in the RCS, PRT, containment, and environment. At the time of the hot leg failure, only 4.6% of the iodine inventory had been released. Consequently, the amount available for leakage through the SGTR was relatively small. However, 93% of the gaseous iodine was released from Rings 1, 2, 3, and 4 of the failed fuel claddings in the core prior to the hot leg nozzle failure. In the 16 min between the SGTR and the hot leg nozzle failure, 8% of the gaseous iodine is released to the environment. The gaseous iodine release exceeded 1% of the total gaseous inventory at 5 min after the SGTR (i.e., 4 hr 6 min). Although this is a significant percentage of the gaseous iodine, it was only 0.015% of the total iodine.

Most of the iodine release from the fuel occurs after the hot leg failure when the iodine is released during the second fuel heatup (see Figure 5-56). Almost all the remaining iodine is released from the fuel during the second heatup through vessel failure at 9 hr 13 min. There is a steady increase in the environmental release through 12 hr during and after the high release phase from the fuel. Although much of the iodine flows out the failed hot leg into the containment, a portion of the released iodine transports to the SGTR. The gaseous iodine leakage through the SGTR slowly increases to 27% of the gaseous inventory by 72 hr. The total gaseous and aerosol iodine release to the environment was 1.42% at 72 hours.

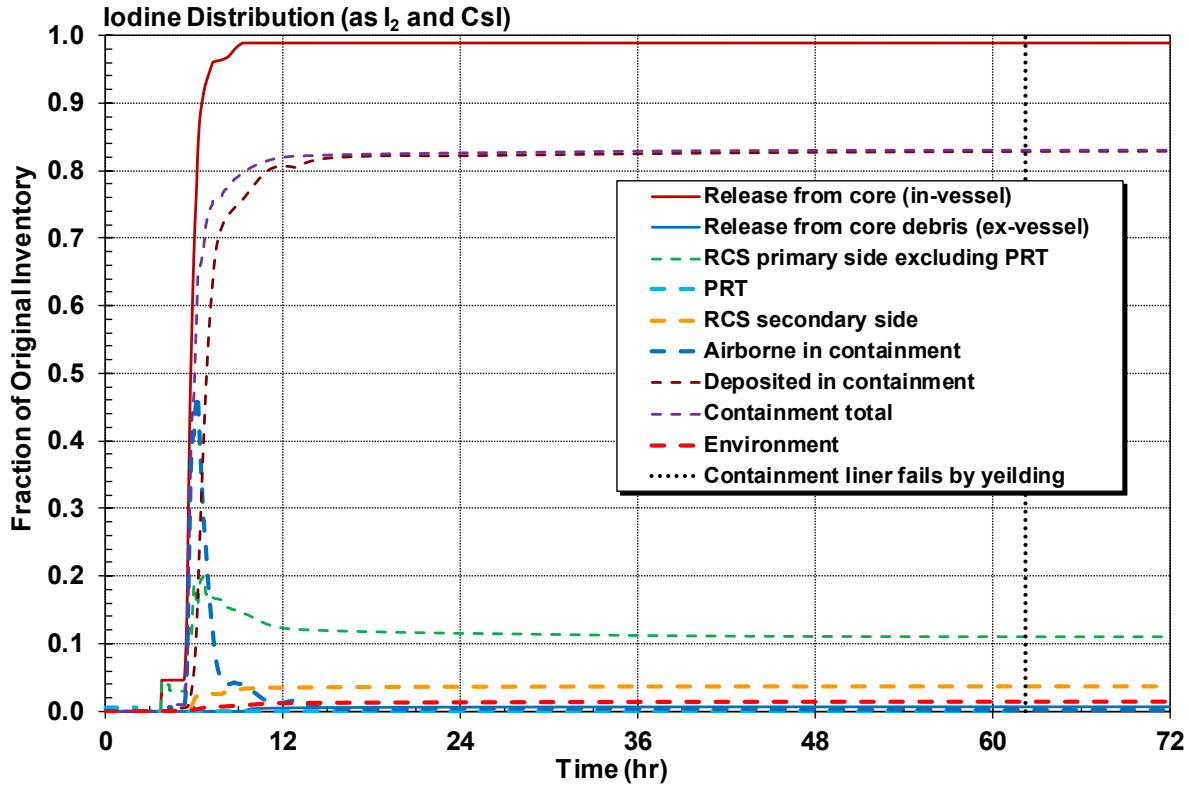

Figure 5-55 Iodine Distribution (as I2 and CsI, SGTR Reference Realization)

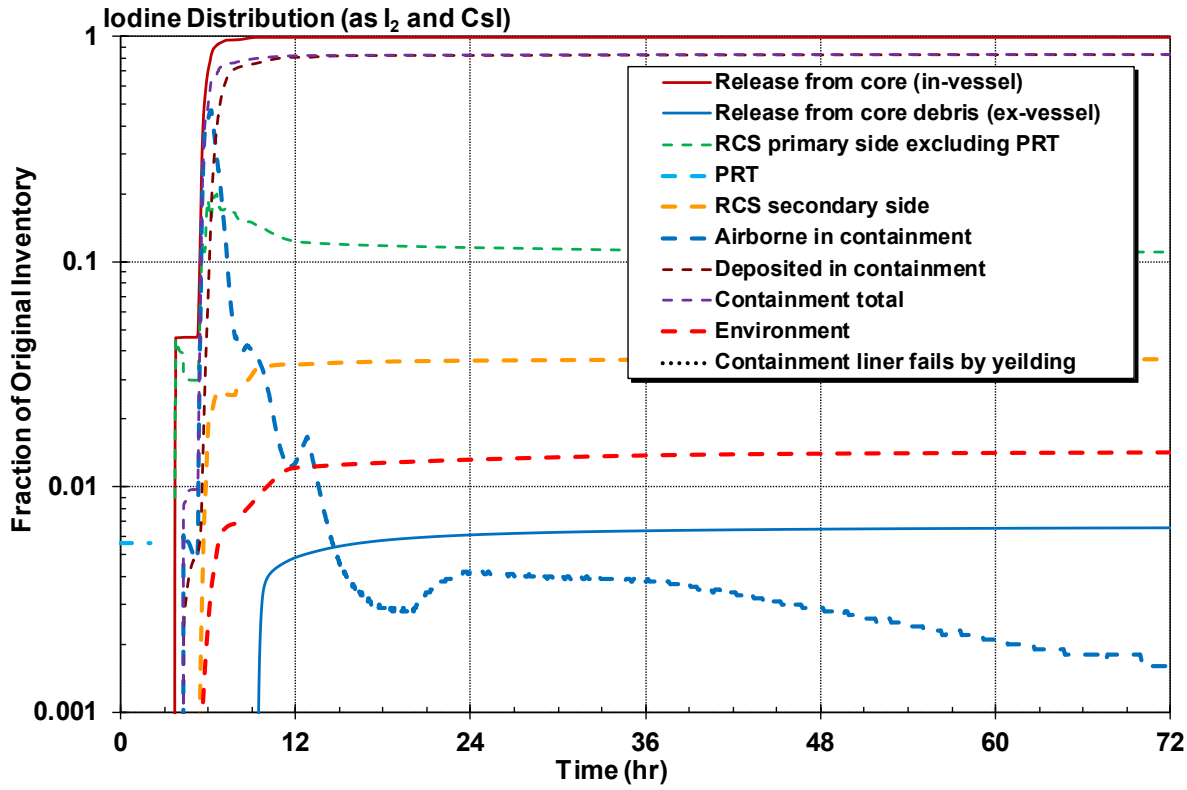

Figure 5-56 Iodine Distribution (Log, as I2 and CsI, SGTR Reference Realization)

Figure 5-57 and Figure 5-58 show the same information as Figure 5-55 and Figure 5-56 but for cesium rather than iodine. The reported cesium results show the combined behavior of cesium hydroxide, cesium iodide and cesium molybdate. The same general trends as observed in the iodine figures are also seen for cesium. However, no gaseous forms of cesium are expected away from the core except in very hot locations. Unlike the iodine response through the SGTR, only very small aerosols are expected to transport through the secondary side of the SG (see Section 4.1.4.4 for a further discussion). For example, the cesium hydroxide, cesium iodine, and cesium molybdate released to the environment through the SGTR prior to the hot leg failure were 0.05%, 0.02%, and 0.001%, respectively, versus 8.2% of the gaseous iodine. If the environmental releases are scaled by the amount released from the fuel through the timing of the hot leg failure rather than the total inventory, the respective numbers are 0.2%, 0.5%, 1.7%, and 8.8%, which also shows diminished releases for aerosol versus gaseous radionuclides.

The gaseous iodine is not only quickly readily released from the fuel cladding gap during the fuel damage but also transports essentially without any deposition. In contrast, there is significantly more deposition of the cesium aerosols. The cesium release to the environment at 72 hr was 0.92% of the cesium inventory as compared to only 0.003% in the non-SGTR reference calculation. Since most of the airborne cesium in the containment had settled by the time of the containment liner failure, there is a negligible impact on the environmental release.

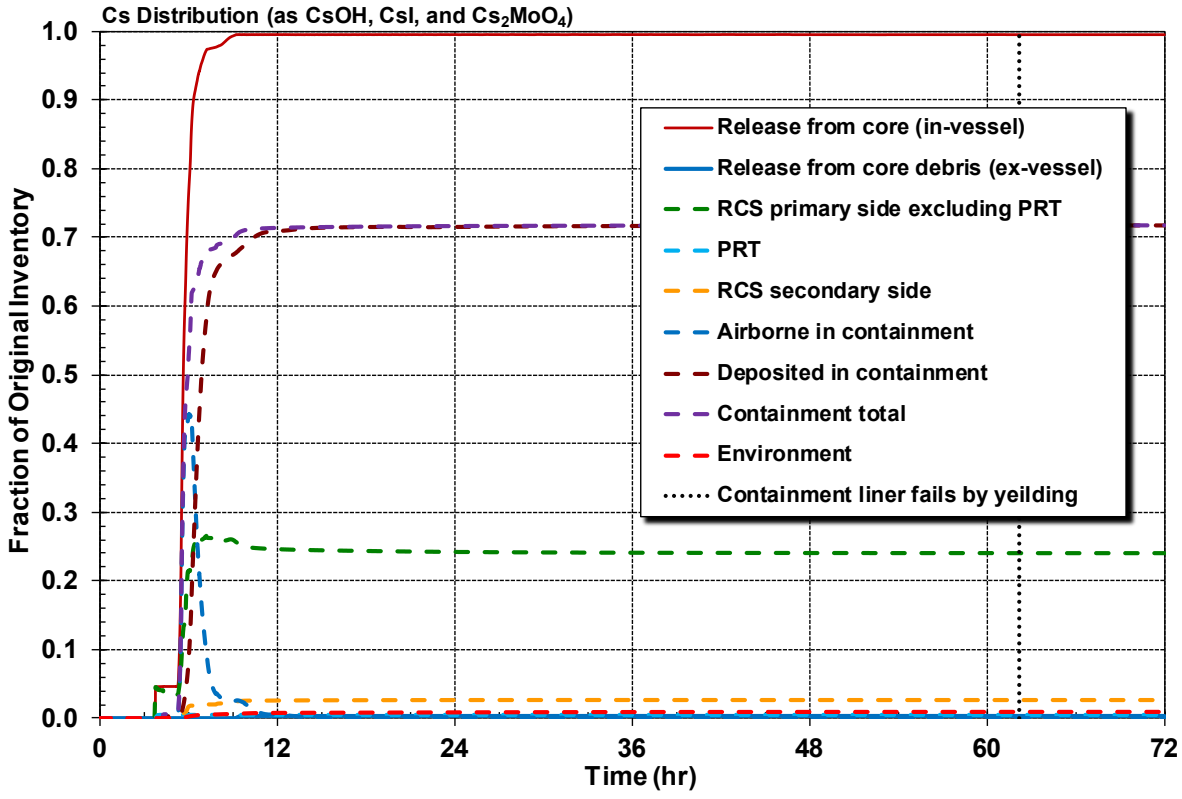

Figure 5-57 Cs Distribution (as CsOH, CsI, and Cs2MoO4, SGTR Reference Realization)

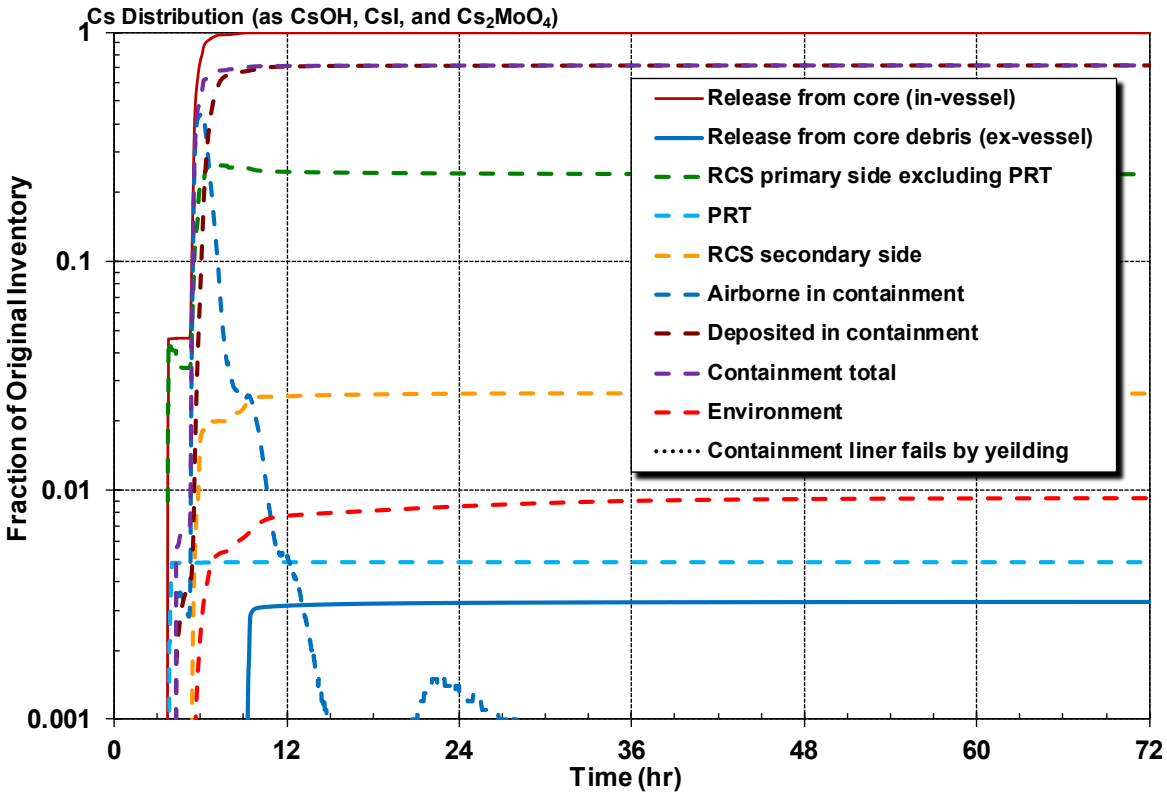

Figure 5-58 **Cs Distribution (Log, as CsOH, CsI, and Cs2MoO4, SGTR Reference Realization)**

Figure 5-59 shows the calculated time-dependent aerosol sectional decontamination factors in SG A following the SGTR. As described in Section 4.1.4.4, a size-dependent aerosol decontamination factor is applied to the releases exiting the SGTR into the secondary side of the tube bundle. The MELCOR model discretizes the aerosols into size ranges, called sections. The ten sections are uniformly spaced logarithmic intervals from a minimum of 0.1 microns to a maximum of 50 microns. The larger aerosols in Sections 5 through 10 have very large decontamination factors and are effectively retained in the SG. Large aerosols are more likely to deposit on the surrounding tubes and be captured in the tube grid spacers. However, the smaller aerosols in sections 1 through 4 more closely follow the gas streamlines through the tube region and out the MSIV leakage pathway.

The integral SG decontamination factors of key chemical groups exiting through the SGTR are shown in Figure 5-60. The retention of the noble gases (i.e., characterized by the xenon radionuclide class) and the elemental iodine gas are contrasted with the predominantly aerosol release of the various cesium compounds and the combined aerosol and iodine gas.[61] The gas decontamination factors go to one as the gases pass through the tube bundle and exit out the MSIV leak path. In contrast, the total iodine and cesium decontamination factors trend towards 1.5 and 1.9 at 5 hr, respectively.

After the hot leg failure at 4.25 hr, the secondary side of the steam generator leaks inward to the primary system and outward through the MSIV leak path until fully depressurized (i.e., see Figure 5-39 and Figure 5-40). The backwards leakage into the primary system changes the shape of the integral decontamination factor after 5 hr (see Figure 5-61). Although the 72-hr values of the total iodine and cesium decontamination factors in the SG are 3.5 and 3.8, respectively, the total leakage through the SGTR is significant. 99.9% and 99.8% of the total Cs and I released to the environment comes through the SGTR pathway versus due to containment leakage.

The SGTR leakage during the high flow rate phase prior to the hot leg failure and primary system depressurization is not the dominant release phase to the environment. For example, only 2.7% and 5.0% of the total cesium and iodine is released via the SGTR to the environment by 5 hr (see Figure 5-62). The bulk of the release to the environment (i.e., 97.3% and 95% of the cesium and iodine released to the environment) occurs after 5 hr. This was primarily due to more significant releases from the fuel occurring during the second fuel heatup after the hot leg failure and accumulator discharge at 4.3 hr. However, 69% and 62% of the total cesium and iodine release to the environment, respectively, occurred by vessel failure at 9.2 hr.

100% of the elemental iodine is in the gap between the fuel and the cladding. The iodine gas is released in a puff following the cladding failures in the various rings. Due to the rapid and complete release of the elemental iodine, 57% of the total environmental release occurs by 5 hr. In contrast, most of the xenon gas is tied up in the fuel matrix, which releases over time as the fuel heats and degrades. The percentage of the xenon gas released to the environment is only 29% at vessel failure. The subsequent release occurs very slowly as xenon flows back into the RCS from the containment and out the SGTR leakage pathway. The long-term shape of the xenon release via the SGTR is driven by the steady containment pressurization (e.g., see Figure 5-46 for the containment pressure response).

---

[61] The total cesium decontamination factor includes all forms of cesium including cesium hydroxide, cesium molybdate, and cesium iodide. The total iodine decontamination factor includes the two forms of iodine, which are elemental iodine (i.e., gas) and cesium iodide.

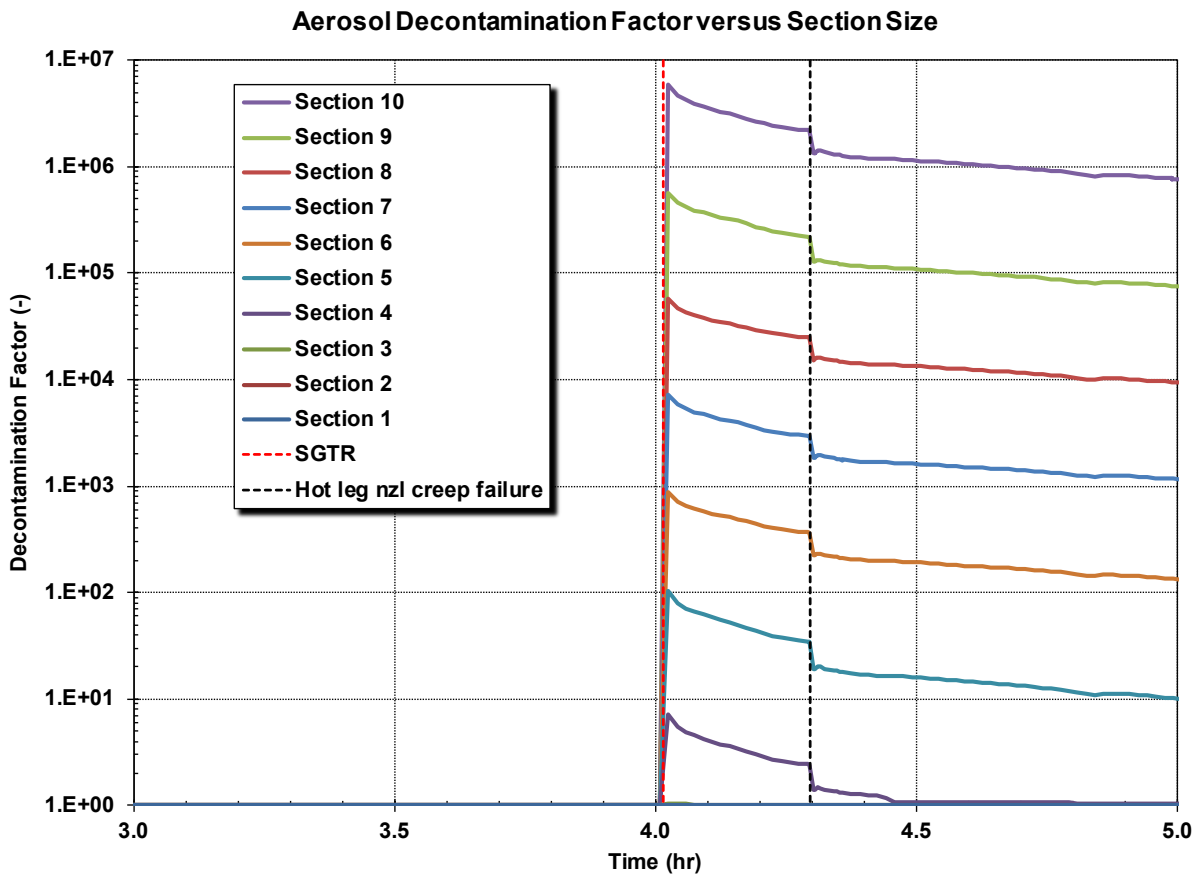

Figure 5-59 Aerosol Decontamination in the SG Secondary following the SGTR (SGTR Reference Realization)

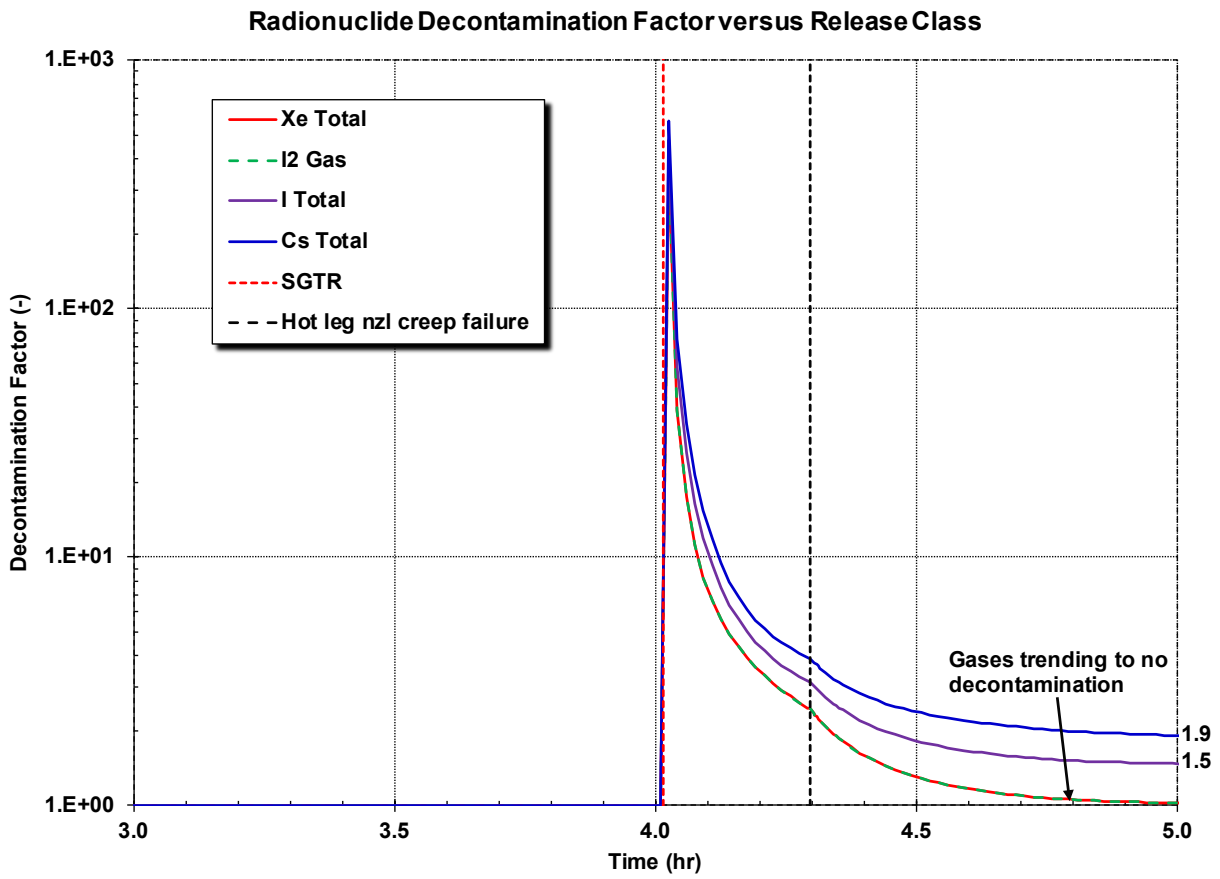

Figure 5-60 **Comparison of the Short-Term Xenon, Iodine Gas, Total Iodine, and Total Cesium Time-Dependent Decontamination Factor in the SG (SGTR Reference Realization)**

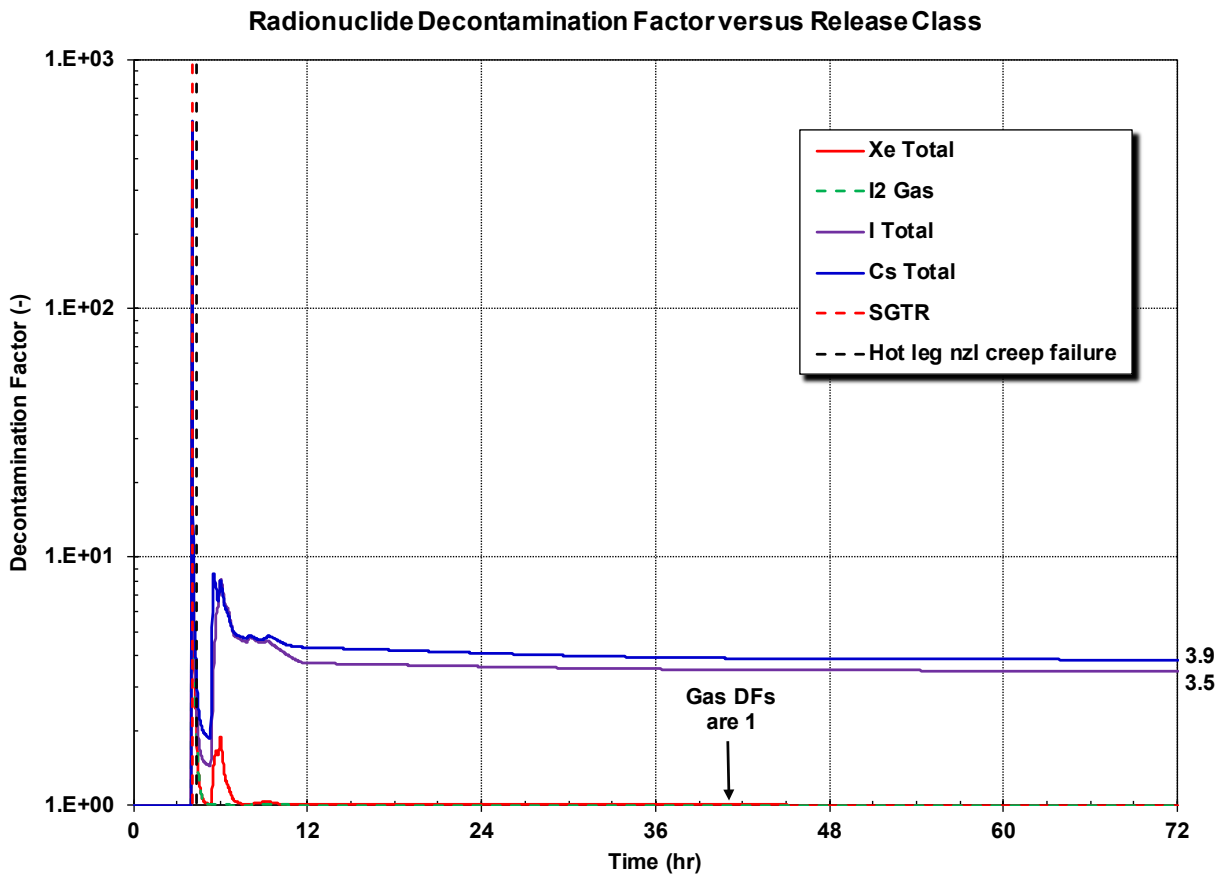

Figure 5-61 **Comparison of the Long-Term Xenon, Iodine Gas, Total Iodine, and Total Cesium Time-Dependent Decontamination Factor in the SG (SGTR Reference Realization)**

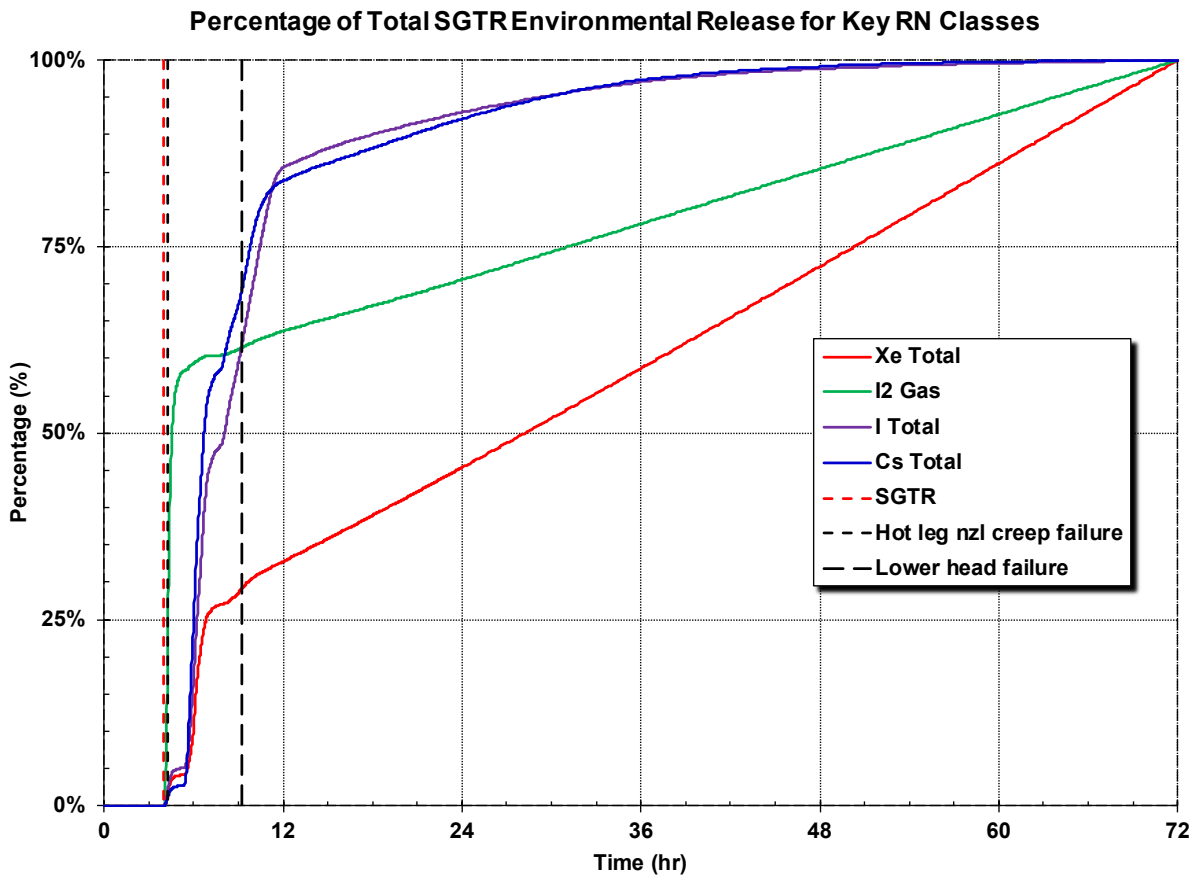

Figure 5-62 **Comparison of the Long-Term Xenon, Iodine Gas, Total Iodine, and Total Cesium Environmental Release via the Time-Dependent in the SG (SGTR Reference Realization)**

The central and peripheral fuel temperatures at low and high regions in the core are shown in Figure 5-63. The temperature trends are like the responses shown in the non-SGTR realization (see Figure 5-36). The peak fuel temperatures are slightly higher than the non-SGTR reference realization due to the high sampled effective eutectic melting temperature. There is complete quenching of the fuel from a peak of 1403 K following the hot leg failure and accumulator discharge. The peak temperature prior to the hot leg failure is very close the 1430 K value in the non-SGTR calculation. There appears to be a small cooling effect from the SGTR, which induces more flow and heat removal from the core. Approximately 15 min later, a second heatup occurs that accelerates due steam oxidation. As the fuel degrades and collapses, the temperature drops to zero as the intact fuel is converted into debris (i.e., the debris component temperature is not shown). The bulk of the hydrogen generation and fission product release occurs during the second heatup, which is after the SGTR leakage had reduced substantially (see Figure 5-40).

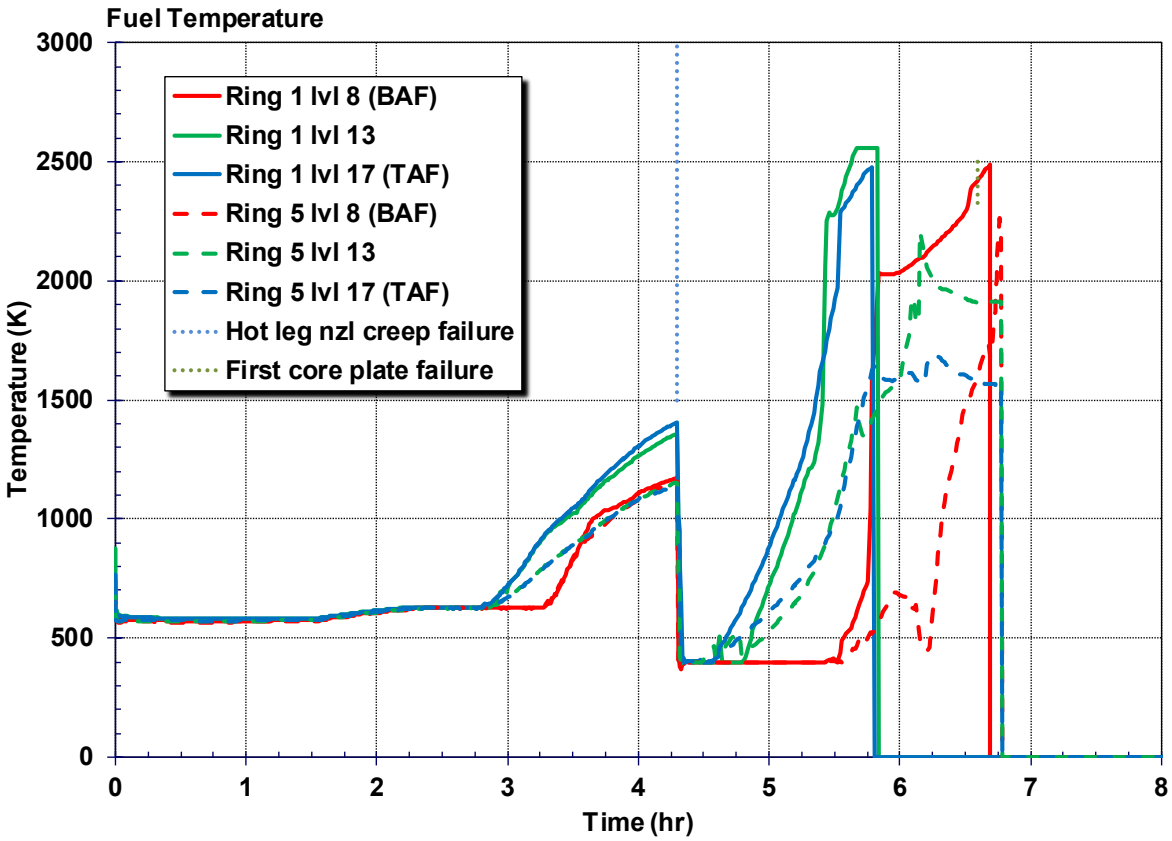

Figure 5-63 Fuel Temperature (SGTR Reference Realization)

The long-term core-concrete response is very similar to the non-SGTR reference calculation. The gas generation (see Figure 5-49) and erosion (see Figure 5-64) are very similar between the two reference realizations. Both realizations showed steady erosion through 72 hr with a maximum erosion depth of approximately 1.3 m.

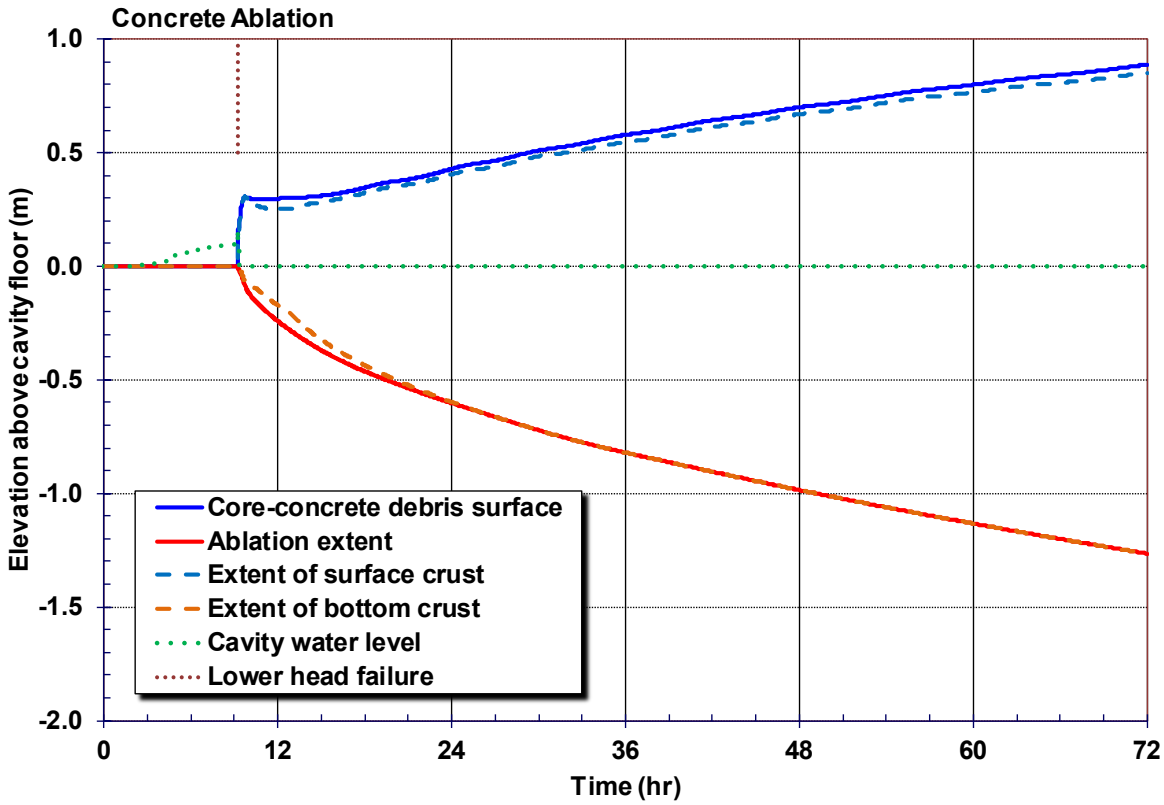

Figure 5-64 Concrete Ablation and Cavity Water Depth (SGTR Reference Realization)

5.3 Select MELCOR Realization Detailed Analyses

The individual realizations were investigated to identify phenomena influencing important responses including the occurrence of a SGTR, the magnitude and timing of fission product releases to the environment and the amount of hydrogen produced in-vessel. The realizations investigated and the reason for investigating them, i.e., the results metric satisfied, are identified in Table 5-18. The values of sampled parameters in these realizations are identified in Table 5-19 through Table 5-23. Table 5-24 and Table 5-25 present the timing of key events in the realizations and Table 5-26 and Table 5-27 present various important attributes in the realizations including the magnitudes of Cs and I releases to the environment by 72 hr, and the amounts of hydrogen produced in-vessel.

Table 5-18 Result Metrics Considered in selecting UA Realizations for Detailed Analysis and the Qualifying Cases

Results Metric	Rlz
Reference non-SGTR Rlz	459
Reference SGTR Rlz	37
Largest Cs release (by mass)	237
Earliest fission product release to the environment[1]	19
Earliest SGTR	777
Largest Cs release without a SGTR	837
Earliest lower head melt through	148
Earliest containment failure (liner tearing)	1062
A late fission product release	504
Smallest Cs release	1170
A realization where the PRT boils dry	499
A realization without hot leg rupture[2]	935
Earliest hot leg rupture	122
Most in-vessel hydrogen production	999

[1] Earliest time at which elemental iodine release to the environment exceeds 1% of initial fuel-cladding gap inventory
[2] Only 1 Rlz (Rlz 935) did not suffer a hot leg rupture

Rlz	RCP leakage			SG tube NFD									
	A	B	C	Cold 1 A	Cold 2 A	Cold 3 A	Hot Upflow A	Hottest A	Cold 1 B	Cold 2 B	Cold 3 B	Hot Upflow B	Hottest B
459	21	21	21	0.37	0.32	0.65	0.44	0.00	0.38	0.74	0.68	0.51	0.00
37	21	21	21	0.32	0.49	0.85	0.41	0.00	0.46	0.38	0.39	0.47	0.00
237	21	182	21	0.90	0.36	0.36	0.34	0.00	0.51	0.42	0.85	0.87	0.00
19	182	21	182	0.33	0.42	0.87	0.34	0.00	0.34	0.34	0.47	0.31	0.00
777	21	182	182	0.37	0.35	0.39	0.90	0.00	0.40	0.54	0.35	0.45	0.00
837	21	21	21	0.38	0.45	0.67	0.33	0.00	0.35	0.32	0.54	0.36	0.00
148	182	480	76	0.33	0.43	0.37	0.32	0.00	0.38	0.42	0.36	0.83	0.00
1062	182	21	182	0.38	0.31	0.36	0.33	0.00	0.51	0.31	0.34	0.31	0.63
504	21	21	21	0.30	0.33	0.39	0.34	0.00	0.35	0.39	0.50	0.37	0.00
1170	21	21	182	0.30	0.34	0.39	0.36	0.00	0.35	0.34	0.38	0.44	0.00
499	21	21	21	0.30	0.35	0.35	0.34	0.42	0.82	0.47	0.40	0.34	0.00
935	21	21	21	0.47	0.37	0.37	0.46	0.00	0.39	0.38	0.48	0.34	0.00
122	182	182	182	0.38	0.49	0.35	0.31	0.00	0.37	0.39	0.39	0.39	0.00
999	21	182	21	0.44	0.41	0.35	0.34	0.00	0.40	0.38	0.45	0.45	0.00

Table 5-19 Sampled Values in the Realizations Identified for Detailed Analysis (Inputs #1)

Rlz	SG tube NFD					Hottest SG tube normalized temperature			Zr breakout temperature	UO_2-ZrO eutectic melting temperature	Zr drain rate	Containment relative fractional leak area
	Cold 1 C	Cold 2 C	Cold 3 C	Hot Upflow C	Hottest C	A	B	C				
459	0.46	0.40	0.31	0.34	0.35	0.42	0.36	0.41	2411.2	2391.5	0.13	0.221
37	0.42	0.37	0.49	0.34	0.00	0.33	0.42	0.49	2307.3	2560.4	0.48	0.166
237	0.90	0.36	0.40	0.36	0.00	0.43	0.42	0.37	2474.5	2558.7	0.18	0.370
19	0.45	0.34	0.45	0.33	0.00	0.41	0.47	0.51	2341.0	2375.8	0.19	0.131
777	0.34	0.43	0.39	0.36	0.00	0.37	0.46	0.42	2269.3	2468.6	0.21	0.134
837	0.46	0.38	0.36	0.37	0.00	0.44	0.48	0.41	2270.4	2378.3	0.13	8.566
148	0.31	0.34	0.35	0.40	0.00	0.53	0.49	0.46	2331.4	2499.9	0.16	0.289
1062	0.45	0.33	0.34	0.31	0.00	0.42	0.48	0.42	2317.6	2579.8	0.26	0.106
504	0.32	0.37	0.34	0.35	0.00	0.40	0.33	0.46	2360.1	2547.2	0.33	0.129
1170	0.36	0.39	0.32	0.32	0.00	0.39	0.46	0.45	2416.8	2439.2	0.51	0.124
499	0.32	0.38	0.37	0.58	0.00	0.38	0.40	0.43	2343.1	2428.7	0.23	0.433
935	0.47	0.36	0.37	0.36	0.00	0.46	0.42	0.44	2426.7	2420.4	0.17	0.150
122	0.36	0.33	0.38	0.50	0.00	0.44	0.39	0.47	2358.1	2589.2	0.40	0.284
999	0.39	0.34	0.43	0.47	0.00	0.50	0.45	0.49	2425.6	2441.0	0.11	0.860

Table 5-20 **Sampled Values in the Realizations Identified for Detailed Analysis (Inputs #2)**

Rlz	Containment rupture pressure multiplier	Burn location (e.g., ceiling, floor)	SGTR A elevation	SGTR B elevation	SGTR C elevation	Aerosol shape factor	Condensation multiplier	Oxidation model	MSIV A leak area (in^2)	MSIV B leak area (in^2)	MSIV C leak area (in^2)	ORIGEN Day
459	1.56	1	2	5	3	1.95	1.72	1	0.32	0.25	0.80	400
37	1.71	1	7	7	6	1.12	1.43	1	0.58	0.43	0.67	300
237	1.39	3	7	6	4	2.08	1.35	1	0.44	0.07	0.62	500
19	1.57	2	3	4	1	1.05	1.79	0	0.63	0.32	0.96	500
777	1.65	3	6	6	6	1.56	1.2	0	0.36	0.39	0.58	400
837	1.53	2	6	6	5	1.47	1.12	1	0.61	0.06	0.98	550
148	1.46	2	7	5	2	2.14	1.4	1	0.26	0.71	0.35	400
1062	1.25	2	6	7	6	2.05	1.22	1	0.15	0.01	0.34	550
504	1.69	2	1	4	5	2.01	1.74	1	0.55	0.51	0.37	100
1170	1.61	3	6	1	7	1.47	1.43	1	0.31	0.57	0.30	25
499	1.48	1	7	7	5	1.68	1.59	1	0.87	0.47	0.73	450
935	1.66	2	4	7	6	2.58	1.28	1	0.61	0.61	0.23	200
122	1.75	1	7	7	6	2.15	1.56	1	0.28	0.82	0.15	350
999	1.52	2	7	5	7	1.99	1.51	1	0.16	0.45	0.74	0.5

Table 5-21 Sampled Values in the Realizations Identified for Detailed Analysis (Inputs #3)

Rlz	Fuel-clad gap I2 gas fraction	Fraction of Cs as Cs_2MoO_4	Pressurizer SV cycles to FTC			Pressurizer SV FTC area fraction			MSL SV cycles to FTC		
			SV 1	SV 2	SV 3	SV 1	SV 2	SV 3	MSL A	MSL B	MSL C
459	0.0015	0.89	415	34	55	0.09	0.01	0.92	912	671	344
37	0.0019	0.76	107688	19466	366266	0.31	0.04	0.00	16506	4277	7089
237	0.0045	0.61	5223	13466	25267	0.01	0.06	0.29	223529	31646	3294
19	0.0038	0.77	567	232	443	0.05	0.14	0.09	43	45	232
777	0.0279	0.68	128	132	51	0.78	0.06	0.96	5895	315	3196
837	0.0072	0.48	72	138	90	0.01	0.01	0.94	611	105	677
148	0.0072	0.78	76	64	11	0.06	0.05	0.21	977	430	2747
1062	0.0167	0.83	6854	65877	75164	0.03	0.94	0.09	667	2548	1
504	0.0021	0.70	3521	1	1747	1.00	0.99	0.95	991	9149	4131
1170	0.0081	0.90	4	15	1	0.04	0.03	0.40	1730	14	495
499	0.0008	0.73	1	1	66	0.04	0.35	0.19	4	23	123
935	0.0254	0.67	17	643	473	0.90	0.98	0.01	921	690	159
122	0.0007	0.66	1	210	341	0.10	0.93	0.89	9691	8503	3844
999	0.0085	0.42	932	2039	1952	0.25	0.99	0.01	111	448	133

Table 5-22 **Sampled Values in the Realizations Identified for Detailed Analysis (Inputs #4)**

Table 5-23 Sampled Values in the Realizations Identified for Detailed Analysis (Inputs #5)

	MSL SV FTC area fraction		
Rlz	MSL A	MSL B	MSL C
459	0.09	0.01	0.92
37	0.31	0.04	0.00
237	0.01	0.06	0.29
19	0.05	0.14	0.09
777	0.78	0.06	0.96
837	0.01	0.01	0.94
148	0.06	0.05	0.21
1062	0.03	0.94	0.09
504	1.00	0.99	0.95
1170	0.04	0.03	0.40
499	0.04	0.35	0.19
935	0.90	0.98	0.01
122	0.10	0.93	0.89
999	0.25	0.99	0.01

Table 5-24
Key Timings in the Realizations Identified for Detailed Analysis (Outputs #1)

Event / Rlz	Reference non-SGTR Rlz	Reference SGTR Rlz	Largest Cs release	Earliest release	Earliest SGTR	Largest Cs release w/o a SGTR	Earliest lower head melt thru
	459	37	237	19	777	837	148
STSBO – loss of all AC and DC electrical power, AFW unavailable	0:00	0:00	0:00	0:00	0:00	0:00	0:00
Reactor trips	0:00	0:00	0:00	0:00	0:00	0:00	0:00
MSIVs close	0:00	0:00	0:00	0:00	0:00	0:00	0:00
RCP seal leakage initiates at 21 gpm/pump	0:00	0:00	0:00	0:00	0:00	0:00	0:00
RCP seal failure	-	0:13	0:13	0:13	0:13	-	0:13
MSL SV FTC	-	-	-	0:58	-	-	-
SG dry out	1:28	1:29	1:29	1:05	1:30	1:26	1:27
PRT rupture disk breaks	2:16	2:16	2:11	2:15	-	2:15	-
RPV water level reduces to TAF	2:46	2:45	2:31	2:16	2:18	2:45	1:52
Hot leg natural circulation established	2:52	2:52	2:37	2:22	2:24	2:51	1:58
Pressurizer SV FTC	-	-	-	-	-	-	-
First fission product gap release	3:43	3:42	3:54	3:15	3:33	3:42	2:43
Time elemental iodine release to environment exceeds 1% of initial fuel-cladding gap inventory	55:48	4:06	4:03	3:30	3:45	30:31	60:12
SGTR	-	4:00	3:16	3:25	2:58	-	-
Hot leg nozzle rupture	4:22	4:17	4:43	4:19	4:24	4:17	3:45
1st hydrogen burn	6:08	6:08	4:43	8:57	4:24	10:04	3:45
Accumulator discharge	4:17	4:17	4:44	4:19	4:24	4:17	3:46
Accumulators exhausted	4:18	4:19	4:45	4:21	4:26	4:18	3:47
RPV lower head breach	8:57	9:13	9:24	8:48	8:52	9:24	7:32
PRT dry	-	-	-	-	-	-	-
H2 deflagrations end	9:57	10:12	10:12	10:58	10:11	10:44	9:14
Containment pressure reaches design (45 psig)	27:40	32:20	35:45	34:25	33:30	27:55	35:55
Containment steel liner yields (and tears)	47:04	62:11	56:35	57:33	58:36	49:09	52:49
Containment rebar yields/concrete fractures	-	-	-	-	-	-	-
End of calculation	72:00	72:00	72:00	72:00	72:00	72:00	72:00

Event / Rlz	Earliest containment failure (liner tearing)	A late release	Smallest Cs release	A realization where the PRT boils dry	A realization w/o hot leg rupture	Earliest hot leg rupture	Most in-vessel H2 production
	1062	**504**	**1170**	**499**	**935**	**122**	**999**
STSBO – loss of all AC and DC electrical power, AFW unavailable	0:00	0:00	0:00	0:00	0:00	0:00	0:00
Reactor trips	0:00	0:00	0:00	0:00	0:00	0:00	0:00
MSIVs close	0:00	0:00	0:00	0:00	0:00	0:00	0:00
RCP seal leakage initiates at 21 gpm/pump	0:00	0:00	0:00	0:00	0:00	0:00	0:00
RCP seal failure	0:13	-	0:13	-	-	0:13	0:13
MSL SV FTC	0:02	-	0:23	1:04	-	-	-
SG dry out	1:26	1:29	0:41	0:31	1:27	1:25	2:03
PRT rupture disk breaks	2:22	2:18	2:20	2:06	2:10	2:48	-
RPV water level reduces to TAF	2:20	2:49	2:43	2:42	2:40	2:05	5:15
Hot leg natural circulation established	2:26	2:56	2:50	2:48	2:45	2:12	5:39
Pressurizer SV FTC	-	-	2:29	1:52	2:09	2:20	-

Table 5-25 **Key Timings in the Realizations Identified for Detailed Analysis (Outputs #2)**

Table 5-25
Key Timings in the Realizations Identified for Detailed Analysis (Outputs #2) Continued

Event / Rlz	Earliest containment failure (liner tearing)	A late release	Smallest Cs release	A realization where the PRT boils dry	A realization w/o hot leg rupture	Earliest hot leg rupture	Most in-vessel H2 production
	1062	504	1170	499	935	122	999
	3:26	3:50	3:49	3:26	3:13	2:55	12:21
release to environment exceeds 1% of initial fuel-cladding gap	42:08	71:58	-	54:09	67:59	65:36	-
	-	-	-	-	-	-	-
Hot leg nozzle rupture	4:12	4:24	4:27	4:10	-	3:42	15:18
1st hydrogen burn	9:42	9:51	10:30	4:10	10:36	3:42	15:18
Accumulator discharge	4:12	4:24	4:27	4:10	3:28	3:42	13:03
Accumulators exhausted	4:14	4:25	4:29	4:11	7:18	3:44	15:19
RPV lower head breach	9:19	9:39	10:17	9:05	10:14	8:35	42:28
PRT dry	-	-	-	66:12	7:22	-	-
H2 deflagrations end	10:35	10:17	11:43	10:12	10:36	9:07	42:29
Containment pressure reaches design (45 psig)	26:10	31:50	37:00	27:30	31:25	31:15	-
Containment steel liner yields (and tears)	34:29	61:26	68:44	45:18	58:57	57:51	-
Containment rebar yields/concrete fractures	-	-	-	-	-	-	-
	72:00		72:00	72:00	72:00	72:00	72:00

Attribute / Rlz	Reference non-SGTR Rlz	Reference SGTR Rlz	Largest Cs release	Earliest release	Earliest SGTR	Largest Cs release w/o SGTR	Earliest lower head melt thru
	459	37	237	19	777	837	148
PRZR SV aggregate openings	66	61	66	14	12	65	0.
PRZR SV combined open fraction	0.00	0.00	0.00	0.00	0.00	0.00	0.00
Peak containment pressure during 1st burn (psig)	18.19	17.13	14.21	20.15	17.89	32.93	24.01
In-Vessel H2 production (kg)	321.01	325.09	438.23	282.12	334.21	293.15	589.09
H2 vented to containment prior to 1st burn (kg)	256.38	220.13	28.34	286.68	31.44	387.51	226.63
Fractional I release by 72 hr	2.82E-04	1.42E-02	6.94E-02	1.62E-02	2.77E-02	1.14E-03	5.10E-04
Fractional Cs release by 72 hr	3.25E-05	9.24E-03	4.60E-02	1.08E-02	1.41E-02	5.19E-04	8.38E-05
I mass release by 72 hr (kg)	4.34E-03	1.93E-01	1.19E+00	2.79E-01	4.24E-01	2.05E-02	7.82E-03
Cs mass release by 72 hr (kg)	7.30E-03	1.85E+00	1.15E+01	2.68E+00	3.16E+00	1.34E-01	1.88E-02

Table 5-26 Key Timings in the Realizations Identified for Detailed Analysis (Outputs #3)

Attribute / Rlz	Earliest containment failure (liner tearing)	A late release	Smallest Cs release	A realization where the PRT dries out	A realization w/o hot leg rupture	Earliest hot leg rupture	Most in-vessel H_2 production
	1062	**504**	**1170**	**499**	**935**	**122**	**999**
PRZR SV aggregate openings	12	66	16	7	17	1	0
PRZR SV combined open fraction	0.00	0.00	0.04	0.39	0.91	0.10	0.00
Peak containment pressure during 1st burn (psig)	31.34	28.64	27.19	21.36	38.87	19.82	24.79
In-Vessel H2 production (kg)	304.96	333.96	343.72	391.54	376.25	425.26	777.03
H2 vented to containment prior to 1st burn (kg)	378.63	358.18	362.19	122.55	443.07	146.63	189.36
Fractional I release by 72 hr	3.71E-03	4.11E-05	1.92E-05	1.99E-04	5.44E-04	6.78E-05	8.89E-05
Fractional Cs release by 72 hr	5.43E-05	1.14E-05	7.52E-06	4.74E-05	2.69E-05	2.54E-05	7.04E-05
I mass release by 72 hr (kg)	6.67E-02	4.24E-04	1.74E-04	3.22E-03	6.45E-03	9.76E-04	7.26E-04
Cs mass release by 72 hr (kg)	1.41E-02	1.73E-03	1.00E-03	1.12E-02	4.74E-03	5.39E-03	8.98E-03

Table 5-27 **Key Timings in the Realizations Identified for Detailed Analysis (Outputs #4)**

Comparisons follow between contrasting select individual realizations of the UA to illustrate the influence of key phenomena. Dependencies of the phenomena on the uncertain parameters considered in the UA are identified. Several comparisons are made to the reference realizations presented in the previous section.

5.3.1 Largest Cs Release – Rlz 237

All the UA realizations that experienced a SGTR resulted in relatively large releases of Cs to the environment. This includes Rlz 237 which had the largest release by mass. The release amounted to 11.4560 kg by 72 hr compared to a median value for the UA of 0.0083 kg and a median value in SGTR realizations of 2.1222 kg. The release was 4.6% of the initial core inventory of Cs. Notable is that Rlz 237 did not experience the largest Cs release to the environment by percent of original inventory. The largest release by percent was 7.3% in Rlz 1200.

Rlz 237 was one of the rare realizations in the UA that experienced the rupture of more than one steam generator tube. Rlz 237 experienced two ruptured tubes as did five other UA realizations. In Rlz 237, a tube ruptured in SG C at 3 hr and 16 min and a tube ruptured in SG A at 3 hr and 24 min. In contrast to the other single tube rupture realizations, RCS pressure reduced in Rlz 237 in response to two tubes rupturing. The primary system depressurization reduced the stress in the hot leg nozzles and slowed the accumulation of creep damage. Consequently, an extended period passed between the tube ruptures and hot leg rupture when a still pressurized RCS was venting to the secondary sides of SGs A and C through the ruptured tubes. The venting carried fission products to the secondary sides of the SGs where they were available to release to the environment via leakage past MSIVs.

The contrast between RCS pressure response given one ruptured steam generator tube or two ruptured tubes is evidenced in the differences between Figure 5-65 and Figure 5-66. Figure 5-65 is for Rlz 237 and Figure 5-66 is for the reference SGTR realization (i.e., Rlz 37). Rlz 37 experienced the rupture of one SG tube. Labeled in these plots of RCS pressure and hot leg creep damage is the “period of heightened fission product release” from the RCS to SG secondary sides. The difference in the duration of this period is the cause of Cs release being higher in Rlz 237 than in other SGTR realizations in the UA. The duration was 1 hr and 27 min which was 86th percentile. A late sampled 85th percentile ORIGEN day (500 days) contributed to Rlz 237 being the highest release realization (due to the greater Cs inventory associated with later ORIGEN day) as probably did a low sampled 15th percentile Cs_2MoO_4 fraction due to the greater mobility of Cs in the form of CsOH than in the form of Cs_2MoO_4.

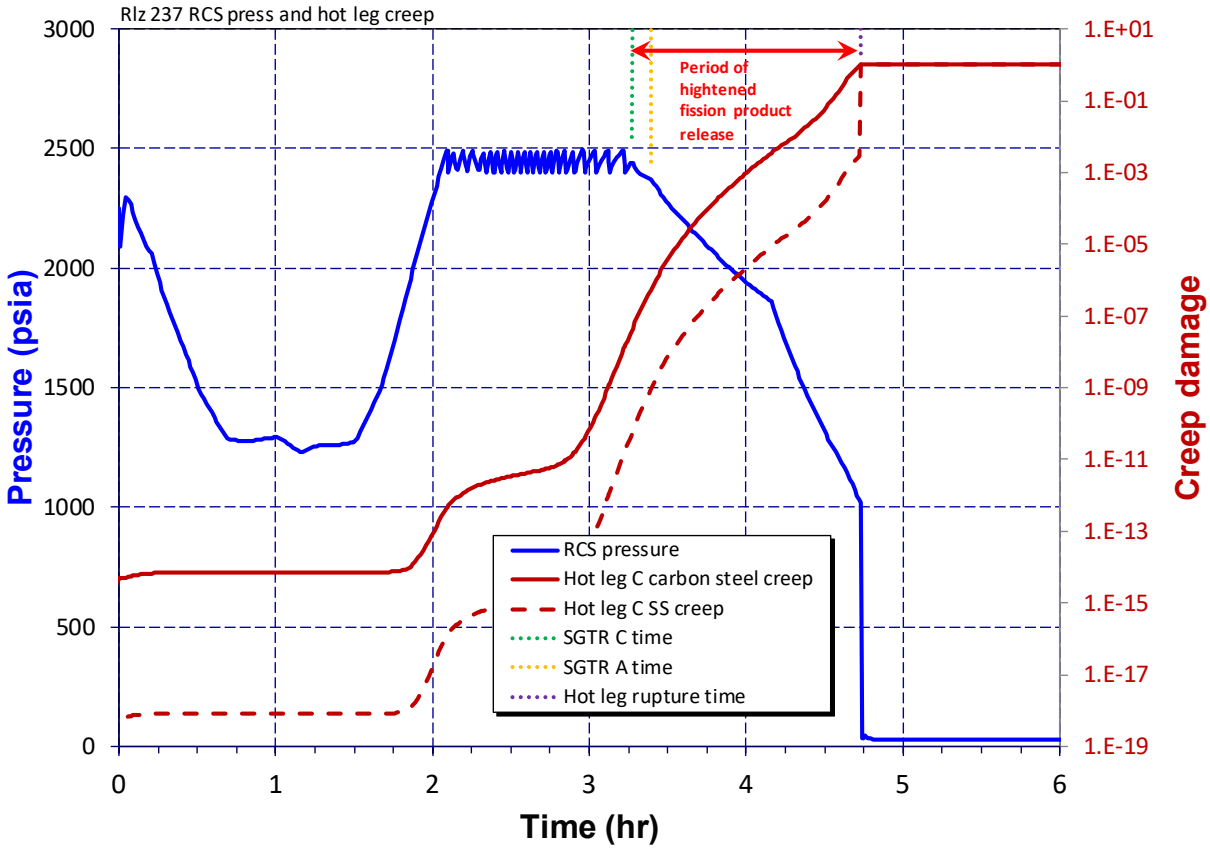

Figure 5-65 Rlz 237 RCS Pressure and Hot Leg Nozzle Creep Damage

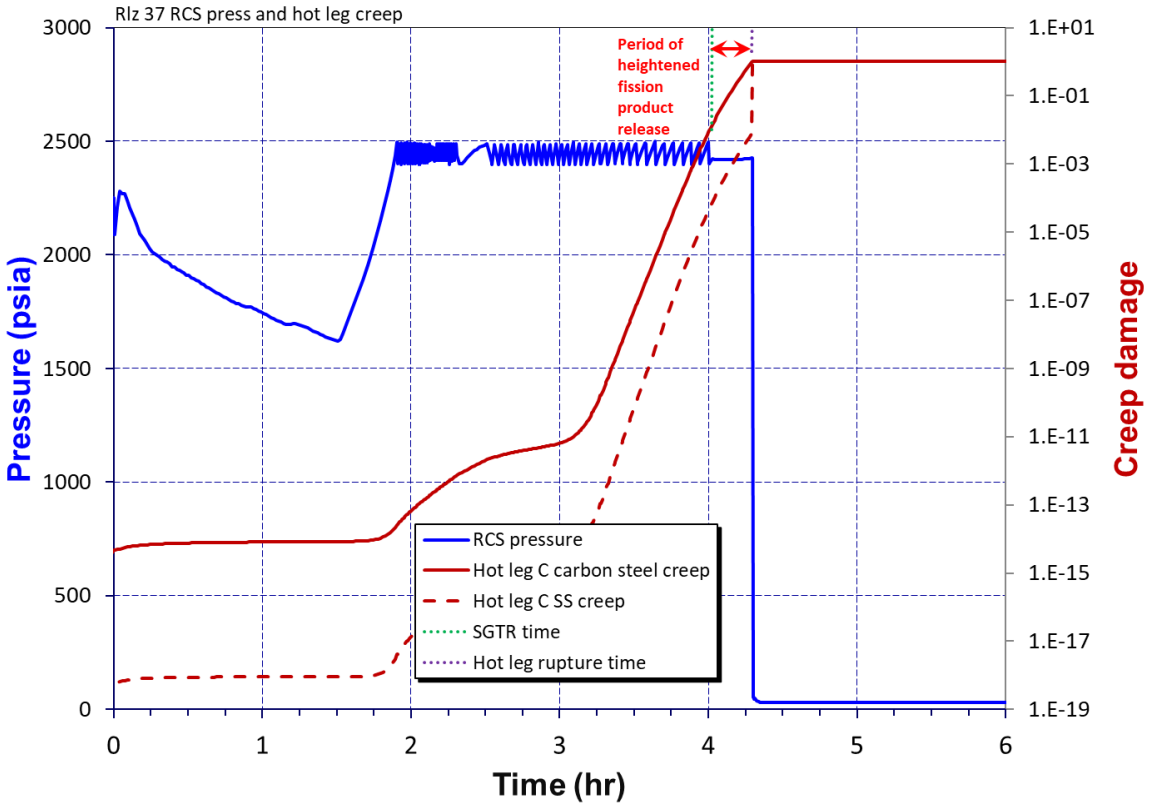

Figure 5-66 Rlz 37 RCS Pressure and Hot Leg Nozzle Creep Damage

5.3.2 Earliest Fission Product Release to the Environment – Rlz 19

The timing of elemental gaseous iodine released to the environment exceeding 1% of the initial inventory in the fuel pins served as a metric in the UA for earliest fission product release to the environment. The metric is simply a convenient relative measure between the accident progression calculations but having no specific alignment to consequences. The time to 1% I_2 release was earliest in Rlz 19 where the metric was reached at 3 hr and 30 min compared to a median time of 56 hr and 14 min excluding the 74 realizations that did not reach 1% within 72 hr.

Rlz 19 suffered a SGTR in SG A. It experienced a MSL SV FTC but not on MSL A. Sampled MSIV leakage associated with SG A was 61st percentile, I_2 fuel-cladding gap fraction was 57th percentile and ORIGEN day was 85th percentile (at 500 days).

The SGTR in Rlz 19 was early (7th percentile at 3 hr and 25 min), but it was not the earliest SGTR in the UA. The earliest SGTR occurred in Rlz 777 at 2 hr and 58 min. Although Rlz 777 had the earliest SGTR, it did not have the earliest 1% I_2 release. The differences are due to the timing of initial fuel-cladding gap release. The initial cladding failure in Rlz 19 was at an early 4th percentile value of 3 hr 15 min. This preceded the SGTR in Rlz 19 by 15 min. In contrast, the initial cladding failure in Rlz 777 was at 3 hr and 33 min, which was 35 min after the SGTR, 18 min after initial cladding failure in Rlz 19 and 8 min after the SGTR in Rlz 19. So I_2 resided in the RCS outside of the fuel pins at the time a SG tube ruptured in Rlz 19 while all I_2 remained confined in the fuel pins when a SG tube ruptured earlier in Rlz 777.

The earliest 1% I_2 release to the environment occurred in Rlz 19 because it had the earliest initial fuel cladding failure of the realizations that experienced a SGTR. The accelerated timing to cladding the failure was enhanced by two 181 gpm RCP seal failures, which led to an early cladding failure. Although Rlz 19 had the earliest 1% gaseous iodine release, 11 other realizations reached this value within 10 min of Rlz 19. Consequently, it was typical of other realizations with cladding gap failure prior to the SGTR.

5.3.3 Earliest SGTR – Rlz 777

Rlz 777 experienced the earliest SGTR in the UA realizations. The rupture occurred 2 hr and 59 min into the calculation. This compares to a median time to SGTRs of 3 hr and 50 min and a maximum time to a SGTR of 23 hr and 25 min. The rupture occurred in SG A in the "hot" intermediate-temperature region of the tube bundle as opposed to in the hottest or cooler regions. In considering Rlz 777 as to what resulted in its early SGTR, comparisons are made below of this realization to the reference SGTR realization Rlz 37.

Over the course of the UA, the factors seen to influence the occurrence of a SGTR were:

- Overheating of SG tubes
- Increased pressure differentials across SG tubes
- Substantially initially weakened SG tubes

The variables in the UA realizations primarily affecting these factors were found to be the:

- Degree of initial degradation of SG tubes (flaw depth)
- Function of the pressurizer SVs (per design vs. FTC)
- Function of the MSL SVs (per design vs. FTC)
- Magnitude of RCP seal leakage
- Magnitude MSIV leakage
- Variation between the hottest and average gas temperatures in a SG tube bundle

Table 5-28 presents information on the above key variables for Rlz 777 and Rlz 37 (i.e., the SGTR reference realization). Standing out as different between the two realizations is RCP seal leakage.

Table 5-28 Key Sampled Variable Values in Rlzs 777 and 37

Rlz	SGTR location (region)	SGTR time (hr:min)	Pressurizer SV FTC (Yes/No)	RCP seal leakage (percentile)	MSL-A SV FTC (Yes/No)	MSIV-A leakage (percentile)
37	SG-A cold	4:01	No	0th	No	56th
777	SG-A hot	2:59	No	89th	No	35th

Rlz	SGTR location (region)	SG-A hottest region NFD (percentile)	SG-A hot upflow region NFD (percentile)	SG-A cold region NFD (percentile)	SG-A hottest norm tube temp (percentile)
37	SG-A cold	0th	76th	98th	1st
777	SG-A hot	0th	100th	33th	8th

Figure 5-67[62] through Figure 5-72 are horsetail plots showing how the results of Rlzs 777 and 37 compare to the population of the first 600 UA realizations with respect to the key variables

affecting the occurrence of a SGTR.[62] Figure 5-67shows the history of SG A pressure, which is color-coded by the sampled MSIV A leak area. The pressure comes down earlier as leak area increases, which enhances the differential pressures across steam generator tubes and increases the stress on tubes. The earlier depressurization exhibited in this figure for Rlz 37 reflects the larger leak area sampled for Rlz 37 than for Rlz 777. However, the leakage was larger in Rlz 37 but the SGTR in Rlz 777 occurs earlier. Consequently, the MSIV leakage rate and associated higher differential pressure across the tube was not a dominant factor in determining the earlier timing for the STGR in Rlz 777.

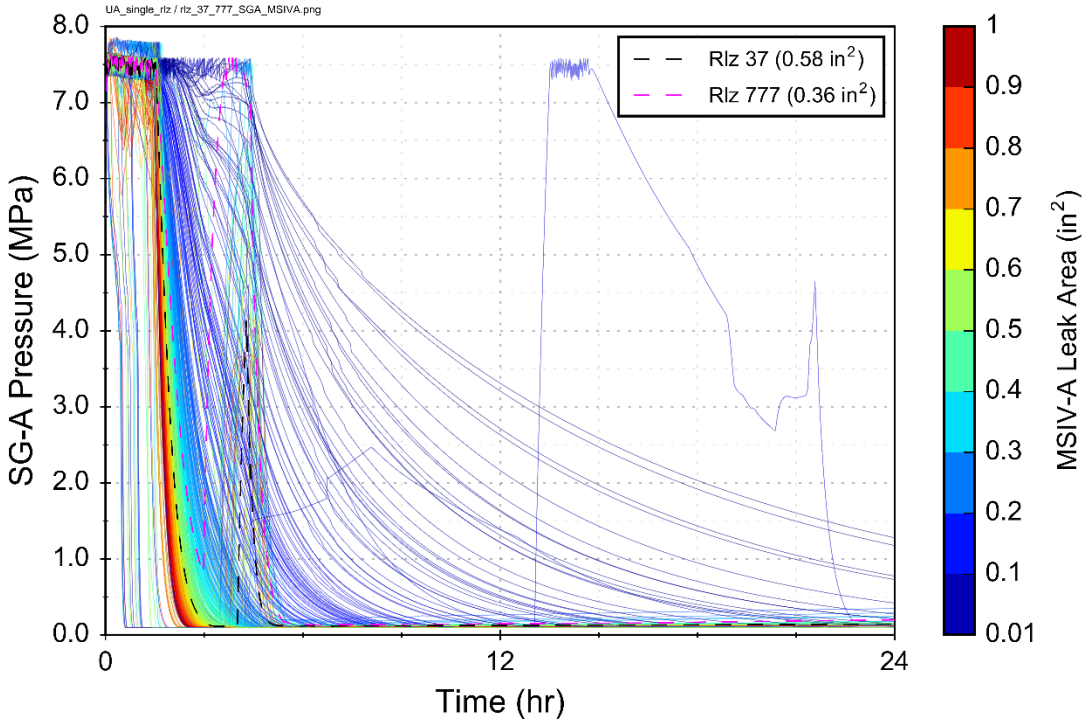

Figure 5-67 SG A Pressure Versus MSIV A Leak Area in the 1st 600 UA Realizations

[62] The color trends were better resolved when only 600 realization are shown.

Figure 5-68[62] shows the history of RCS pressure colored by the sampled RCP seal leakage parameter. Notice how relatively large leakages depressurize the RCS sooner and realize that higher RCS pressures relate to greater differential pressures across steam generator tubes and hence aggravated stress on the tubes. The primary system pressure persisted at the setpoint of the lowest-setpoint pressurizer SV in Rlz 777 up to the time of tube rupture and in Rlz 37 through the time of tube rupture maximizing tube stress in both cases.

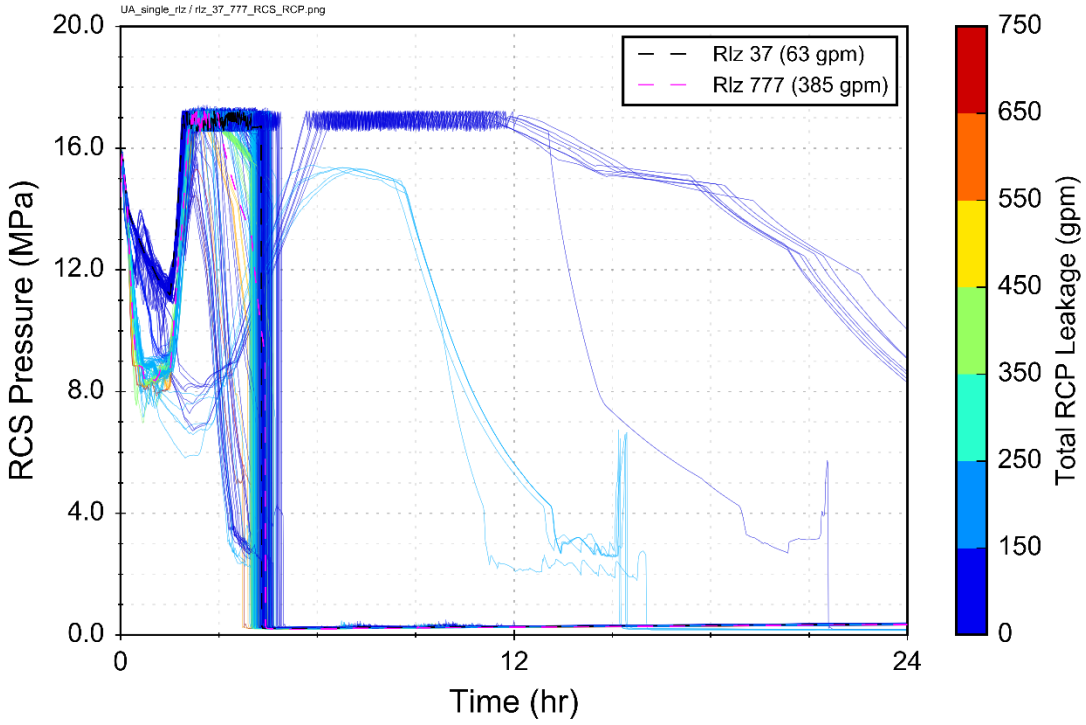

Figure 5-68 RCS Pressure Versus RCP Seal Leakage Rate in the 1st 600 UA Realizations

Figure 5-69[62] shows the history of RCS pressure colored by the aggregate stuck-open fractional area of the three pressurizer SVs. Zero values of open fraction in this plot are indicative of no SV FTC. Notice how larger values of fractional open area relate to lower RCS pressures and realize that lower RCS pressures relate to reduced differential pressures across steam generator tubes and hence reduced tube stress. Rlzs 777 and 37 did not experience a SV FTC so pressure persisted at the setpoint of the lowest-setpoint SV maximizing tube stress in both cases.

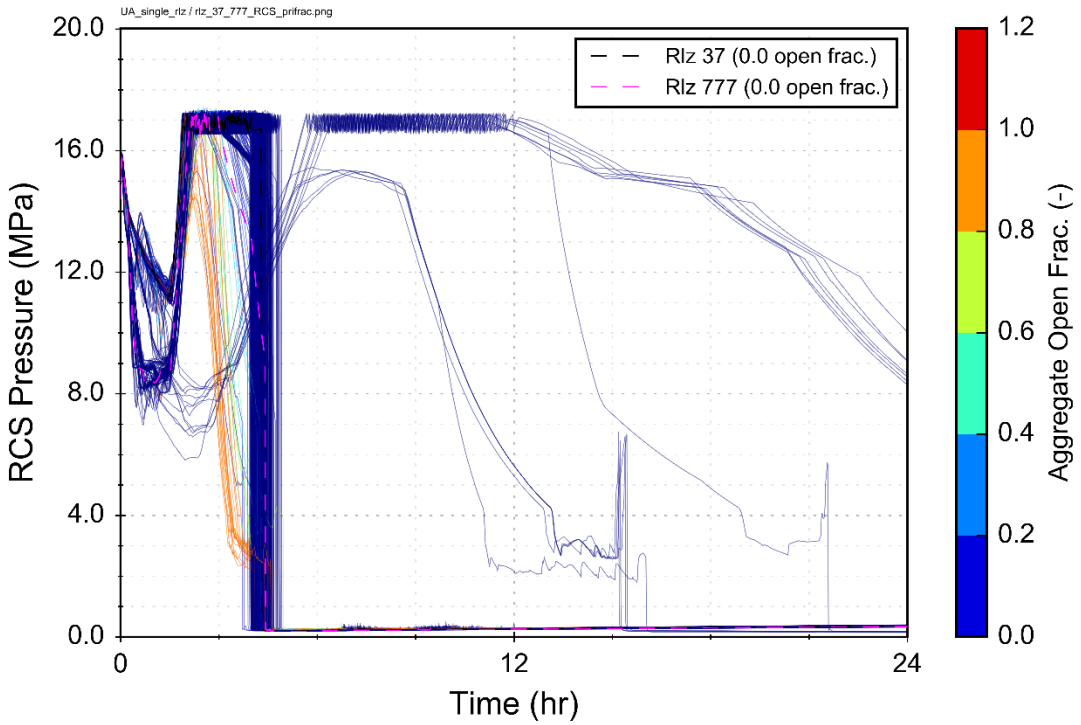

Figure 5-69 RCS Pressure Versus Aggregate Pressurizer Open Area Fraction in the 1st 600 UA Realizations

Figure 5-70[62] shows the history of SG A pressure colored by the stuck-open fractional area of the lowest MSL A SV. Zero values of open fraction in this plot are indicative of no SV FTC. Notice how large open fractions depressurize the SG relatively early resulting in greater differential pressure across the SG A tubes and hence greater stress in them. Neither Rlz 777 nor Rlz 37 experienced a SG A SV FTC suggesting that SG depressurization via a stuck-open SV FTC is not a necessary condition for a SGTR to occur.

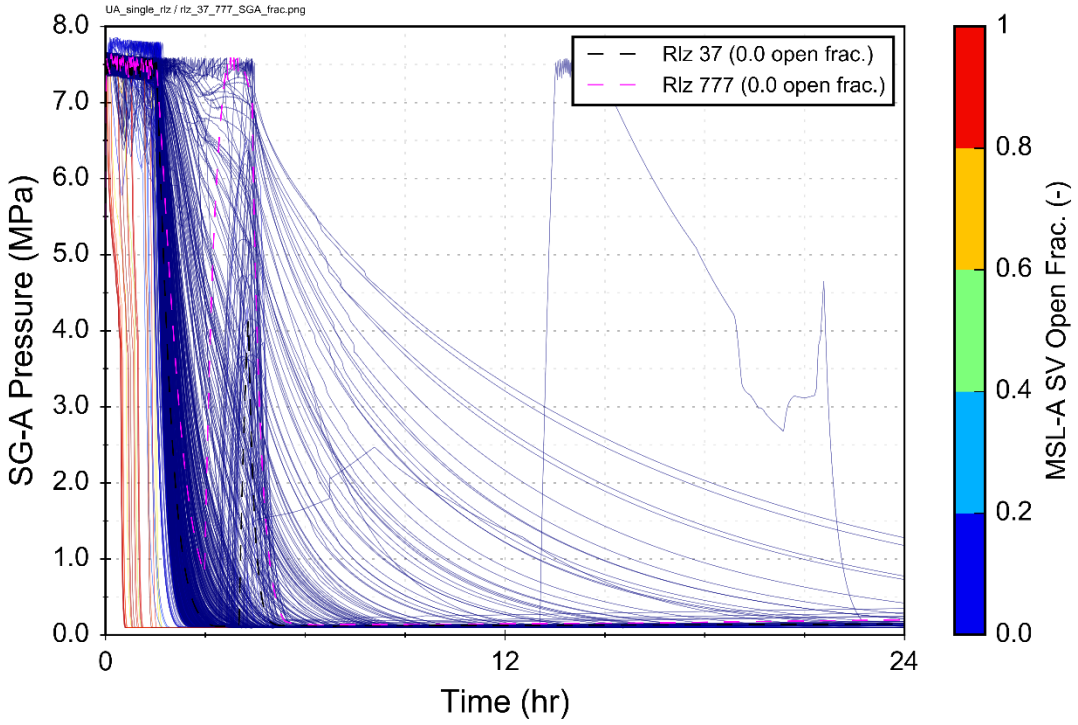

Figure 5-70 SG A Pressure Versus MSL A SV Open Area Fraction in the 1st 600 UA Realizations

Shown in Figure 5-71[62] is the history of creep damage accrued in the hot upflow region (as opposed to the hottest or cold tube regions) of the SG A tube bundle colored by sampled NFD in that region. Small flaws resulted in little damage as seen in this figure while large flaws resulted in the opposite. The sampled hot-region NFD value of 0.41 in Rlz 37 led to inconsequential tube creep damage in the hot upflow region while the sampled value of 0.89 in Rlz 777 led to a tube rupture.[63]

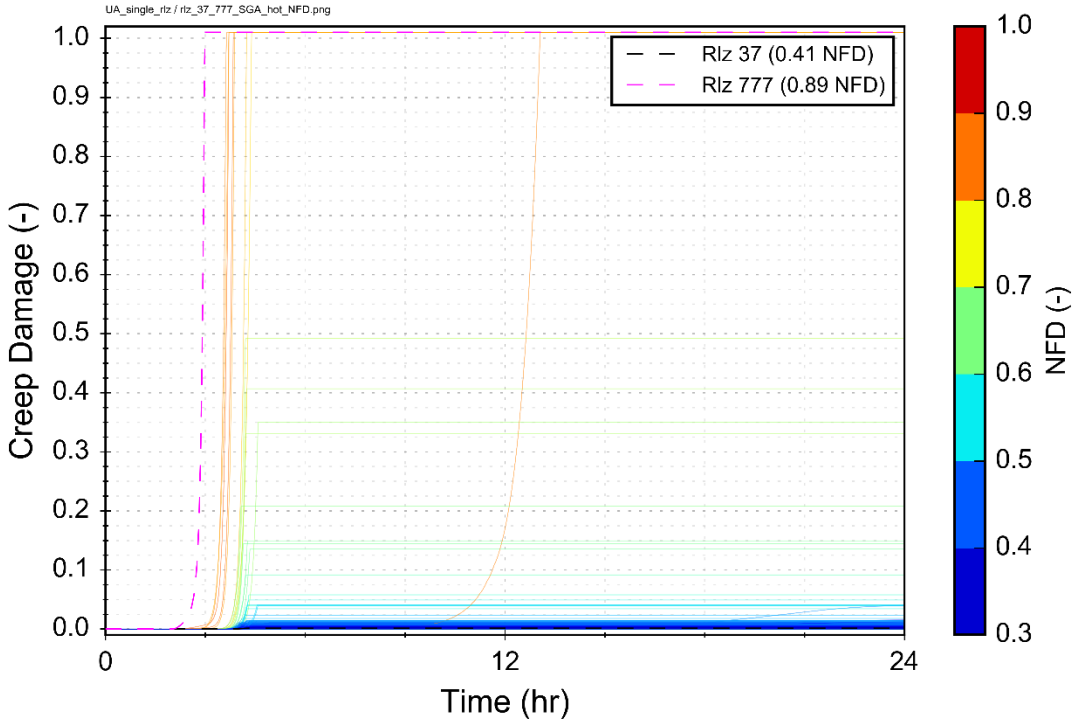

Figure 5-71 SG A Hot Upflow Tube Creep Versus SG A Hot Upflow Tube Flaw Severity (NFD) in the 1st 600 UA Realizations

[63] The SGTR in Rlz 37 occurred in the cold section of the SG A. Consequently, the creep in the SG A upflow region was not expected to reach the failure threshold.

The history of creep damage accrued in the hottest region of the SG A tube bundle is shown in Figure 5-72[62] colored by sampled value of hottest tube normalized gas temperature. Evidenced in this figure is a modest dependence of elevated creep damage with higher values of the sampled parameter. Rlzs 37 and 777 both had sampled parameter values on the low end suggesting that large values of this parameter are not necessary for a SGTR to occur.

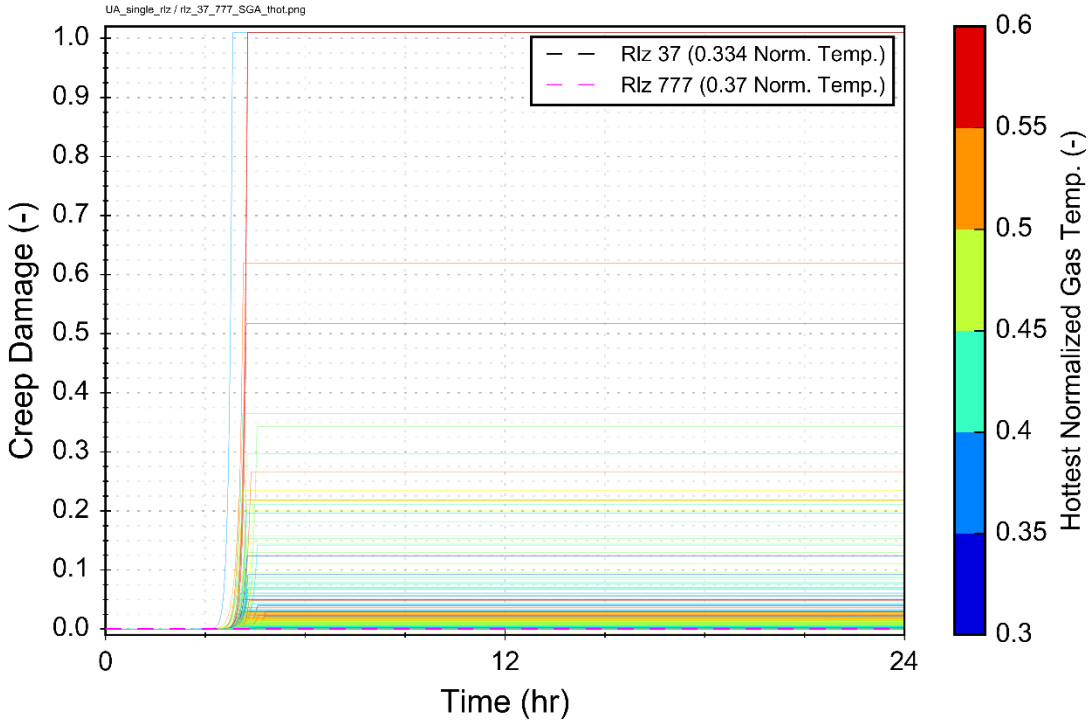

Figure 5-72 SG A Hottest Tube Creep Versus SG A Hot Tube Normalized Gas Temperature in the 1st 600 UA Realizations

The large RCP seal leakage and the largest sampled value of NFD combined to rupture a SG tube early in Rlz 777. The seal leakage was large enough to significantly speed the depletion of RCS coolant inventory relative to other UA realizations but not large enough to reduce RCS pressure below the setpoint of lowest-setpoint pressurizer SV. The early depletion of inventory resulted in early onset of hot leg natural circulation and concurrent early overheating of SG tubes. With RCS pressure remaining high, the maximally damaged SG tube in the hot upflow region of SG A accumulated creep damaged to the point of rupturing at the earliest time of all the UA realizations that experienced a SGTR. Figure 5-73 through Figure 5-75 show the progression of pressure, natural circulation thresholds and SG tube creep damage between Rlz 777 and Rlz 37 respectively.

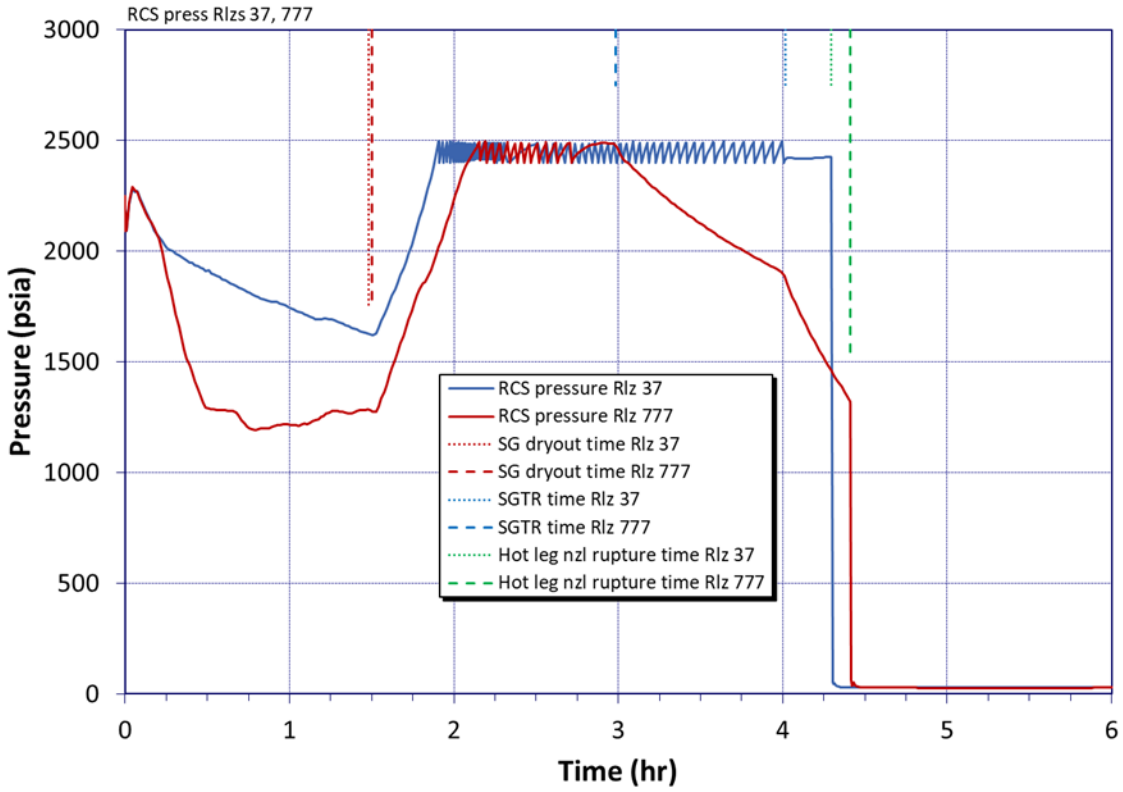

Figure 5-73 RCS Pressure Comparison Between Rlz 777 (Earliest SGTR) and Rlz 37 (SGTR Reference Realization)

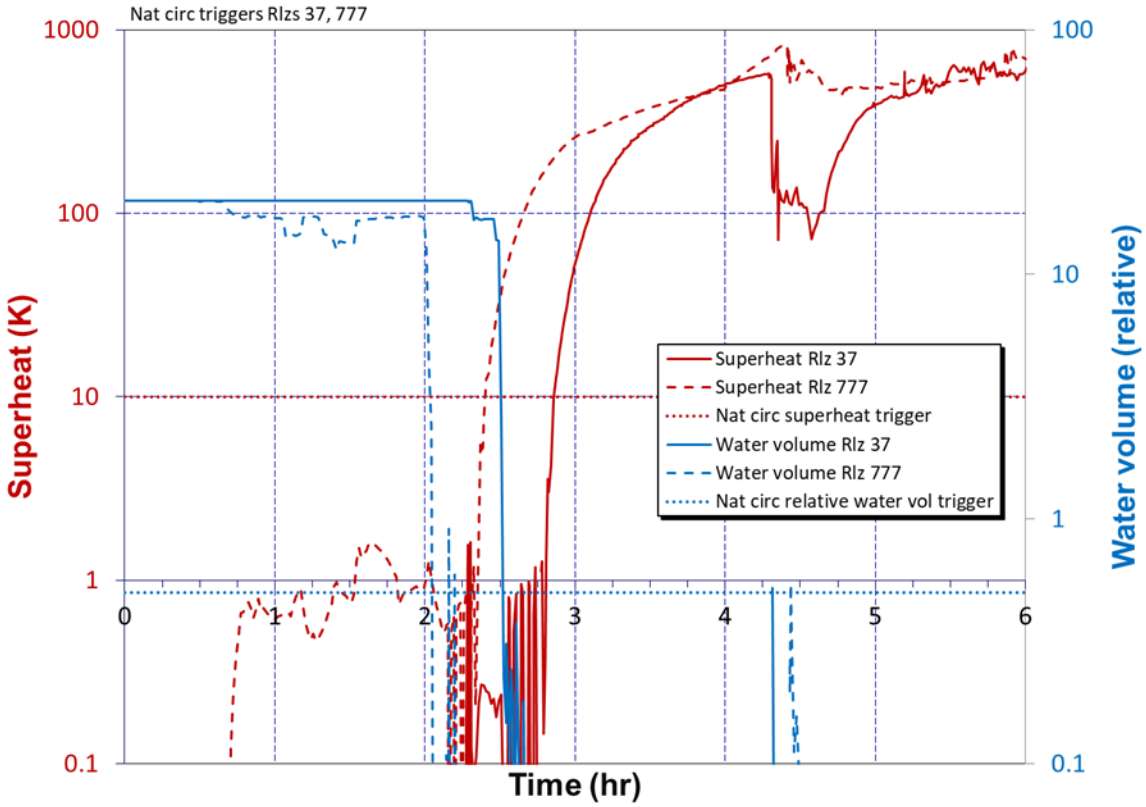

Figure 5-74 Comparison of Natural Circulation Thresholds Between Rlz 777 (Earliest SGTR) and Rlz 37 (SGTR Reference Realization)

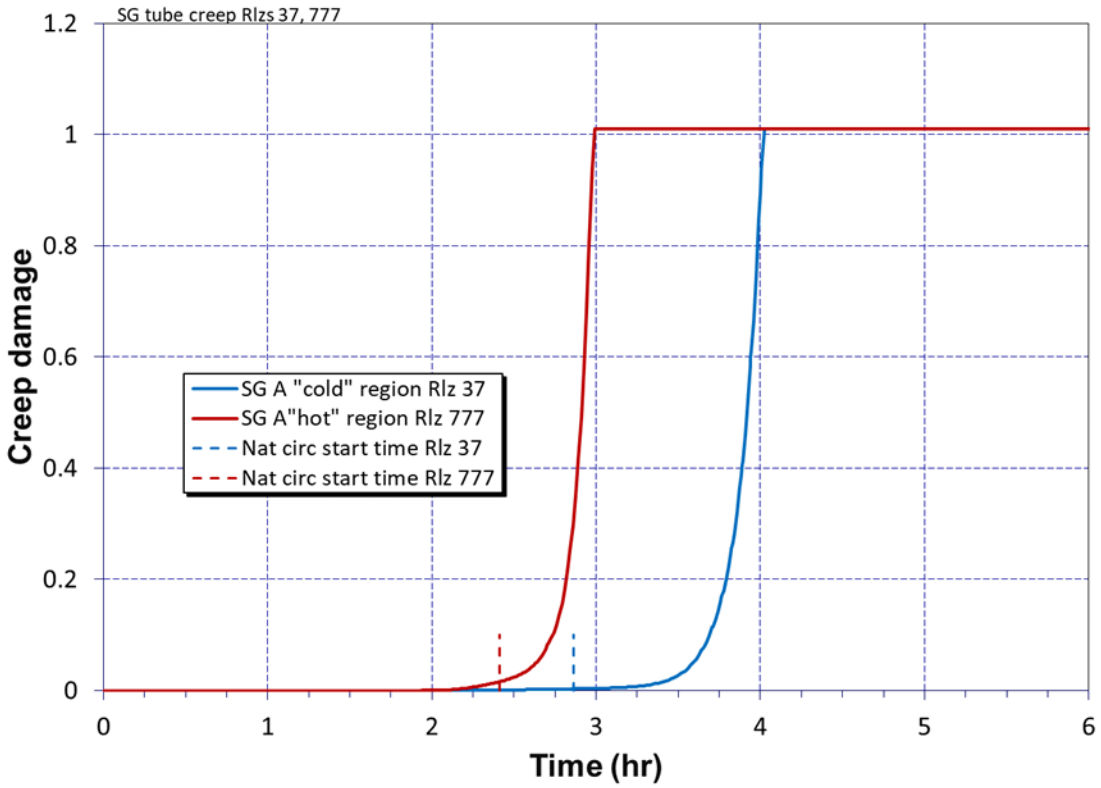

Figure 5-75 SG Tube Creep Damage Comparison Between Rlz 777 (Earliest SGTR) and Rlz 37 (SGTR Reference Realization)

5.3.4 Largest Cs Release without a SGTR – Rlz 837

The largest Cs release to the environment by mass that occurred in calculations that did not experience a SGTR was in Rlz 837. Candidate sampled values of uncertain parameters in Rlz 837 potentially important with respect to this metric are:

- A latest possible 95th percentile ORIGEN day (550 days)
- A relatively very large 98th percentile containment leakage rate (22.5 times greater than the median value)
- A low 3rd percentile Cs_2MoO_4 fraction
- A middling 46th percentile containment rupture pressure (liner failure)
- A middling 45th percentile aerosol shape factor

Most all the Cs release to the environment in Rlz 837 came before 12 hr. In considering this, it is informative to compare with Rlz 459 the reference non-SGTR realization. Figure 5-76 shows containment leakage rate and fractional Cs release to the environment in the two realizations. Notice the very large difference in containment leakage rate and consequential very large difference in release over in the first 12 hours. These differences evidence how the largest Cs release in non-SGTR realizations of the UA primarily materialized in Rlz 837 – through relatively very large containment leakage. The relatively large initial inventory of Cs in this realization associated with the late sampled ORIGEN day likely also contributed to its largest-release status.

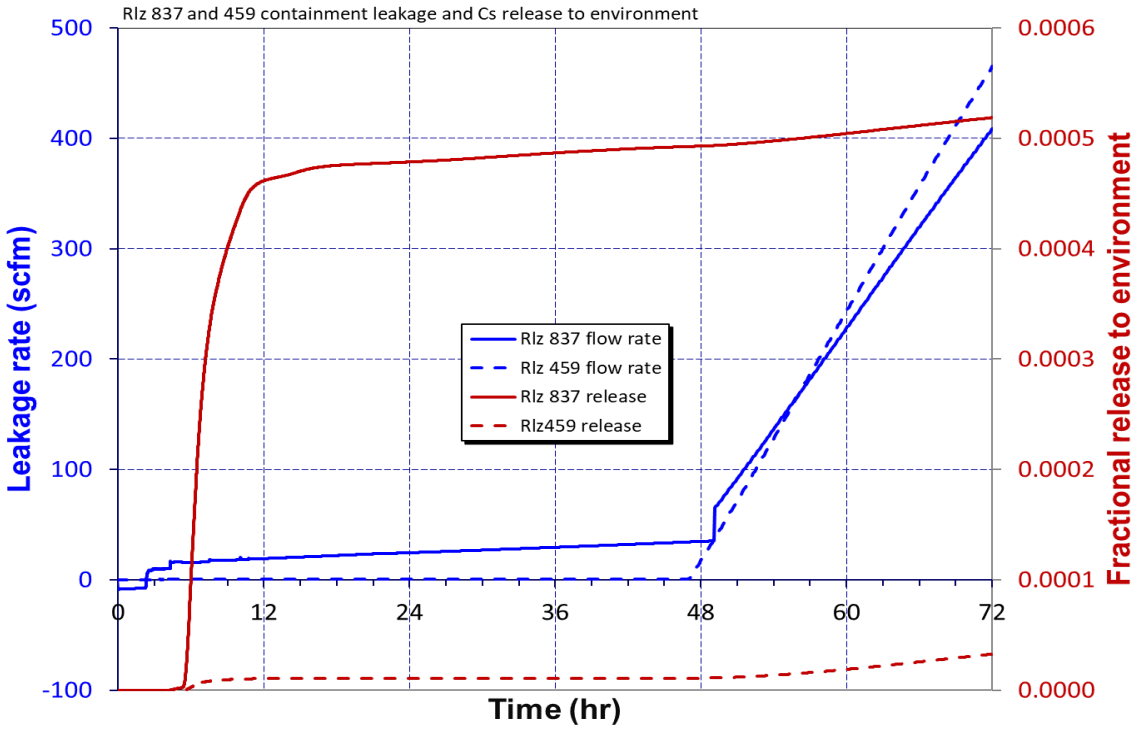

Figure 5-76 Rlz 837 and Rlz 459 Containment Leakage Rate and Cs Release to the Environment

5.3.5 Earliest Lower Head Melt through – Rlz 148

Rlz 148 experienced the earliest melting of core debris through the RPV lower head at 7 hr and 32 min. This compares to a median time of 9 hr and 13 min and to 5 realizations where the lower head did not fail within 72 hr. Lower head failure timing is important because core concrete interaction initiates then contributing to containment pressurization. Rlz 148 had a middling 66th percentile (400 day) ORIGEN day. It did not experience a SGTR. The realization had no pressurizer SV FTC and no MSL SV FTC either of which would have hurried the core drying out and overheating. The realization did, however, have a combined leakage through the RCP seals greater than in any other UA calculation. The combined sampled leakage was 738 gpm (at rated pressure) compared to a minimum and median sampled value of 63 gpm and 118 gpm, respectively. The very large leakage in Rlz 148 was the driving factor in this realization failing the lower head earliest. Figure 5-77 and Figure 5-78 illustrate this in their comparisons of RCS pressure and RPV water level between Rlz 148, Rlz 658 and Rlz 459. Rlz 658 is a realization where the lowest-setpoint SV on the pressurizer failed 98% open on 1st demand and where RCP leakage was a minimal 63 gpm. Rlz 459 is the reference non-SGTR realization with no SV FTC and minimal RCP leakage of 63 gpm. Note how pressure after a few hours is somewhat similar between Rlz 148 with large RCP leakage and Rlz 658 with an immediately failed-open SV and quite different between these Rlzs and the reference calculation. This suggests that with respect to RCS depressurization, maximal RCP leakage has fairly the same (large) effect as a stuck-open SV. Notice that no SV ever even lifted in the case of large RCP leakage. Figure 5-78 shows how RPV inventory was exhausted earliest in Rlz 148 apparently as a consequence of the very large RCP seal leakage. Early drying out of the RPV (0th percentile) led to early relocation of core debris to the RPV lower head and early failure of the head.

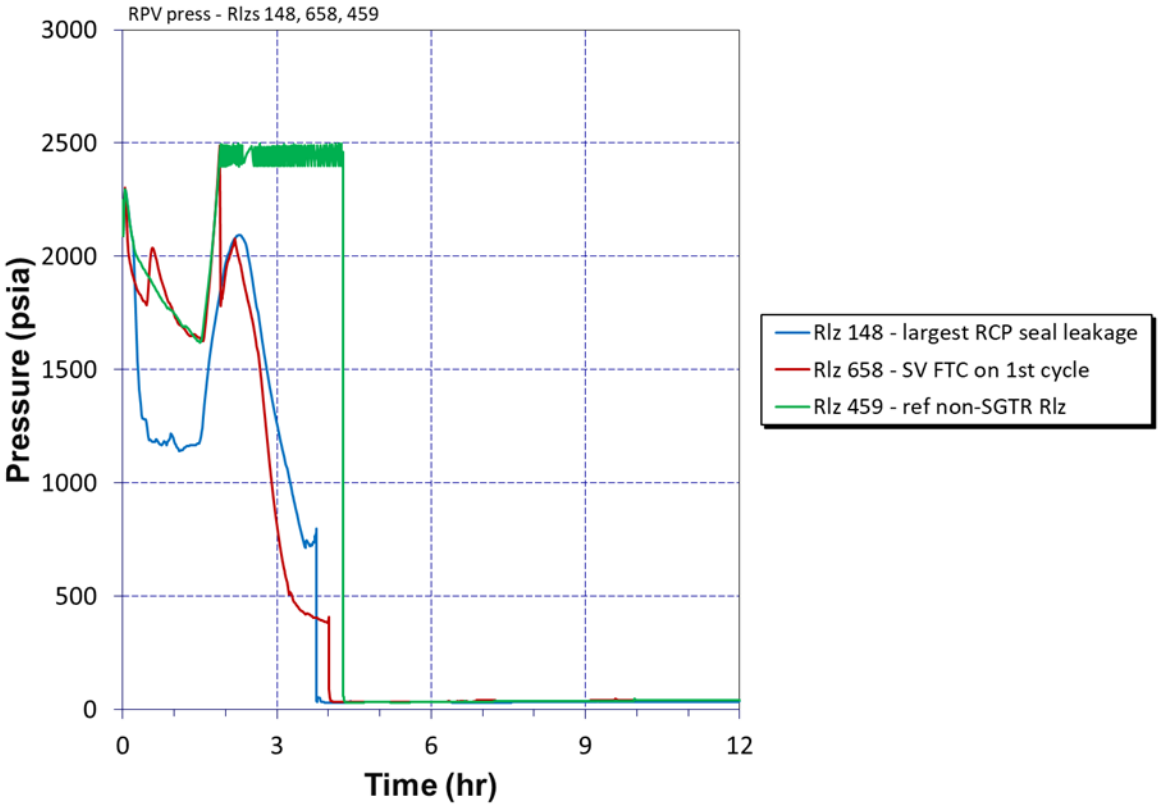

Figure 5-77 Pressure Histories of Rlzs 148, 658 and 459

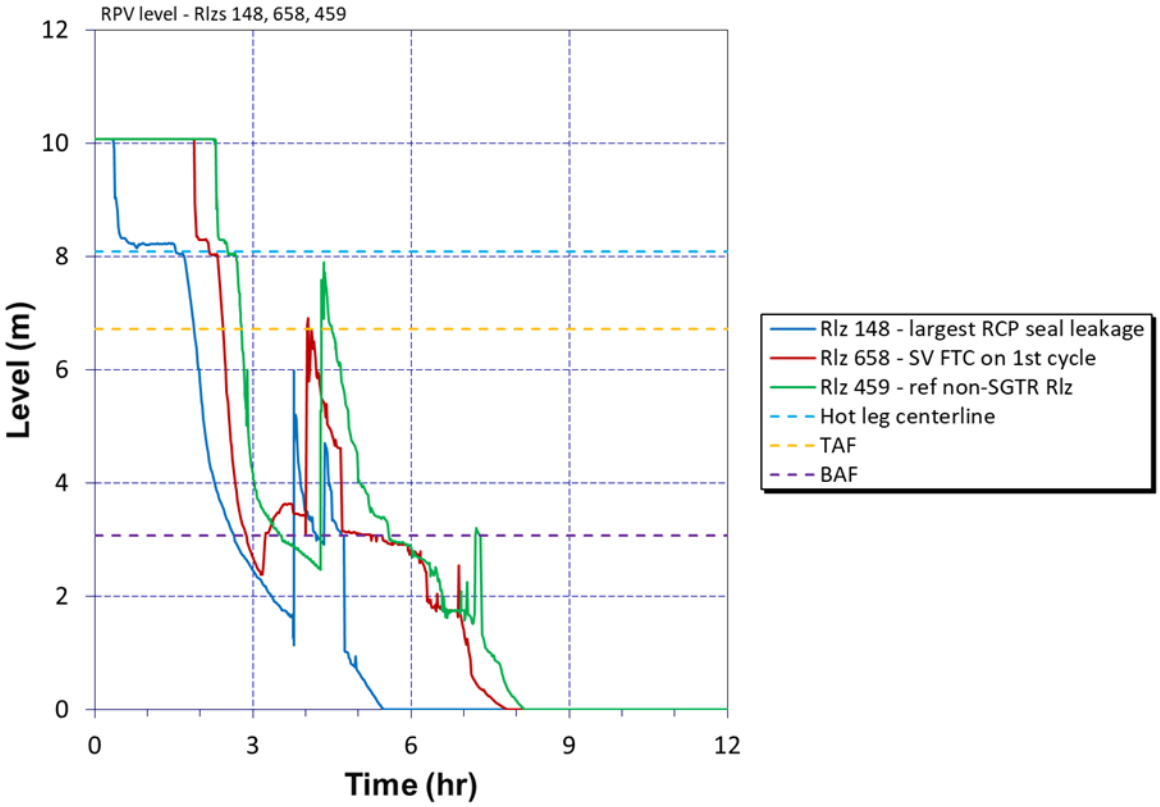

Figure 5-78 RPV Water Level Histories of Rlzs 148, 658 and 459

5.3.6 Earliest Containment Failure (Liner Tearing) – Rlz 1062

The earliest containment steel liner tearing occurred in Rlz 1062 at 34 hr and 29 min. This compares to a median time at tearing of 50.058 hr. A very low 1st percentile sampled value of containment rupture pressure combined with a latest 95th percentile sampled ORIGEN day to result in this earliest failure. The elevated heat generation rate in the larger fission product inventory associated with the late time in core life pressurized containment strongly and the low containment failure pressure was reached early.

5.3.7 A Late Fission Product Release – Rlz 504

A realization of the UA with late 1% I_2 release to the environment was Rlz 504. The metric was reached just shy of 72 hr. This compares to a median time of 56 hr and 14 min and 74 realizations that did not reach 1% within 72 hr.

Several factors combined to delay I_2 release to the environment in Rlz 504. Firstly, Rlz 504 did not experience a SGTR so there was no early bypass of containment. Secondly, sampled containment leakage rate was a low 8th percentile so leakage was relatively small as containment pressurized. Thirdly, sampled rupture pressure was a high 88th percentile so containment failure required a relatively high pressure. Fourthly, ORIGEN day was an early 16th percentile (100 days) so overall heating and pressurization of containment from steam generation and non-condensable gas production from core-concrete interaction was relatively slow. High sampled rupture pressure and early sampled ORIGEN day combined in Rlz 504 such that the containment liner tore at a late 88th percentile time of 61 hr and 27 min. Such a late time of containment failure translated to a late time of 1% I_2 release. Lastly, sampled steam

condensation rate on heat structures was a high 87th percentile which would slow increases in steam partial pressure as containment heated.

5.3.8 Smallest Cs Release – Rlz 1170

No occurrence of a SGTR and sampled values of multiple uncertain parameters conducive to small releases to the environment combined predictably in Rlz 1170 to yield the realization with the smallest release of Cs by mass. Notably:

- An early 3rd percentile ORIGEN day (25 days) availed relatively little initial Cs mass and relatively weak containment pressurization
- A small 8th percentile containment leakage kept early releases relatively low
- A fairly high 70th percentile containment rupture pressure contributed to a very late tearing of the containment liner
- A 92nd Cs_2MoO_4 fraction availed most Cs in the less volatile/less transportable form.

5.3.9 A Realization where the PRT Boils Dry – Rlz 499

The PRT was a location of substantial deposition and retention of fission products in the UA realizations. The degree of fission product retention in the tank was strongly influenced by whether the tank boiled dry. In all but two of the 56 realizations in the UA that experience a failure to close of a pressurizer SV in a substantially open position (>0.36 open area fraction), the PRT boiled dry. Figure 5-79 shows this dependence. Zero values in this figure indicate no valve failure, i.e., the pressurizer SVs operated per design. Heat released in the decay of fission products is what boiled the PRT dry. The fission products were vented to the PRT through the pressurizer SVs as core damage proceeded. The fission products deposited in the water pool that is normally maintained in the PRT. In a realization with a stuck-open SV, more fission products were vented to the PRT. This is evidenced in Figure 5-80 showing the radionuclide content of the water in the PRT in Rlz 499, a realization where the PRT boiled dry, and reference non-SGTR realization Rlz 459. Notice the much larger content in Rlz 499. Figure 17 shows the resulting water level history in the PRT in the two cases. The time to boiling dry in Rlz 499 of ~72 hr was late relative to the median time of ~10 hr in the 54 realizations that experienced a boiling dry of the PRT, meaning the radionuclides vented to the PRT in other realizations that boiled the PRT dry were in larger amounts than that shown for Rlz 499 in Figure 5-81.

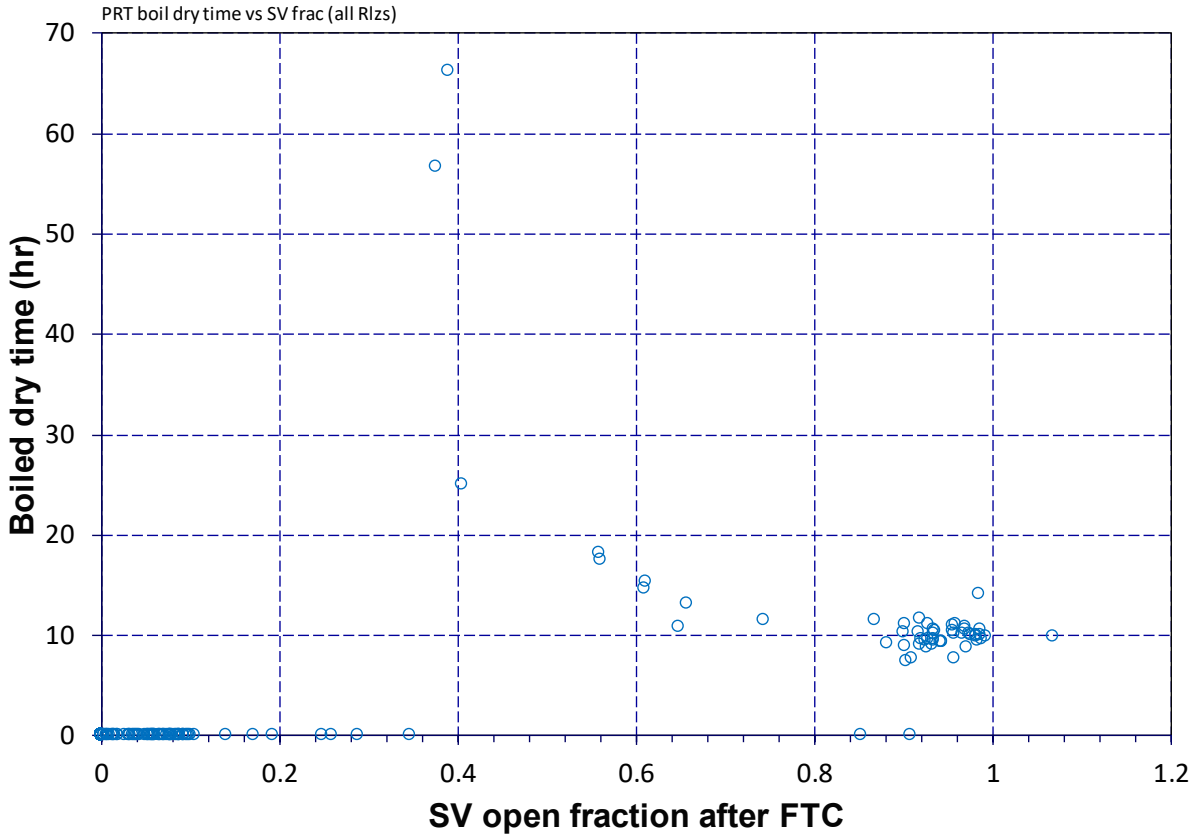

Figure 5-79 Time of PRT Boiling Dry Versus Pressurizer SV FTC Open Fraction

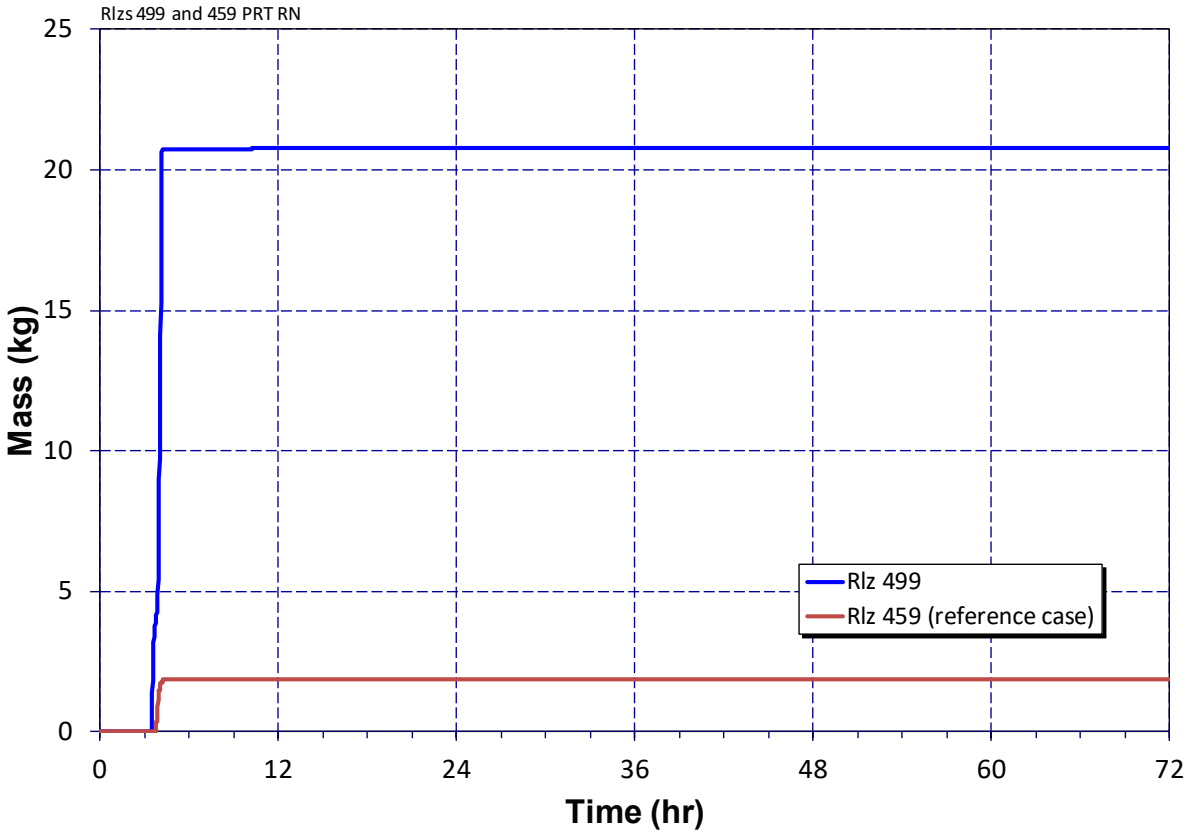

Figure 5-80 Rlzs 499 and 459 Radionuclide Mass in the PRT Water

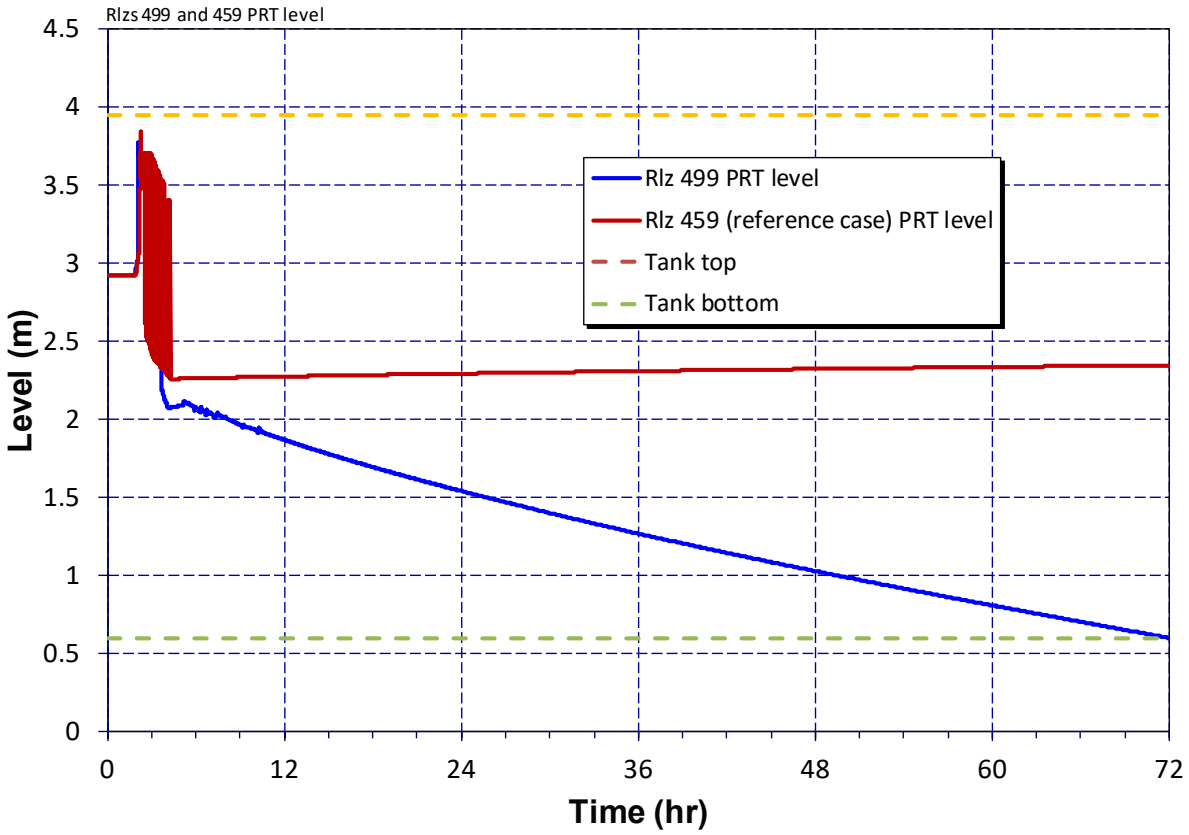

Figure 5-81 Rlzs 499 and 459 PRT Water Level

The two realizations in Figure 5-79 that experienced a failure to close of a pressurizer SV in a substantially open position that didn't boil the PRT dry, Rlz 934 and Rlz 1016, had clear reasons for differing. In Rlz 934 the valve failure came very late such that radionuclide venting to the PRT was relatively modest. In Rlz 1016, sampled RCP leakage was a large 89th percentile and the leakage relieved the venting that occurred to the PRT.

Notable in the realizations that experienced a drying out of the PRT is the dramatic heating of the tank following its becoming dry. Rlz 459 doesn't inform well in this regard because of the drying out coming so late in the realizations. Another calculation, Rlz 761, informs much better. Figure 5-82 shows the temperature excursion in the tank associated with drying out in Rlz 761. Figure 5-83 shows the corresponding history of the three chemical forms of Cs resident in the tank. Note the large steep drops in tank inventories of CsOH and CsI when the tank dries out indicating substantial vaporization of these chemical forms and venting of the vapor to containment. The venting reduces the fission produce decay power in the tank and the tank subsequently cools putting an end to the vaporization. Note also that the Cs_2MoO_4 form of Cs is stable throughout this process due to its lesser volatility. Interestingly, the Cs associated with the CsOH form in Figure 5-83 that remained in the PRT after dry-out is reported by MELCOR as having chemisorbed from CsOH into the steel of the tank.

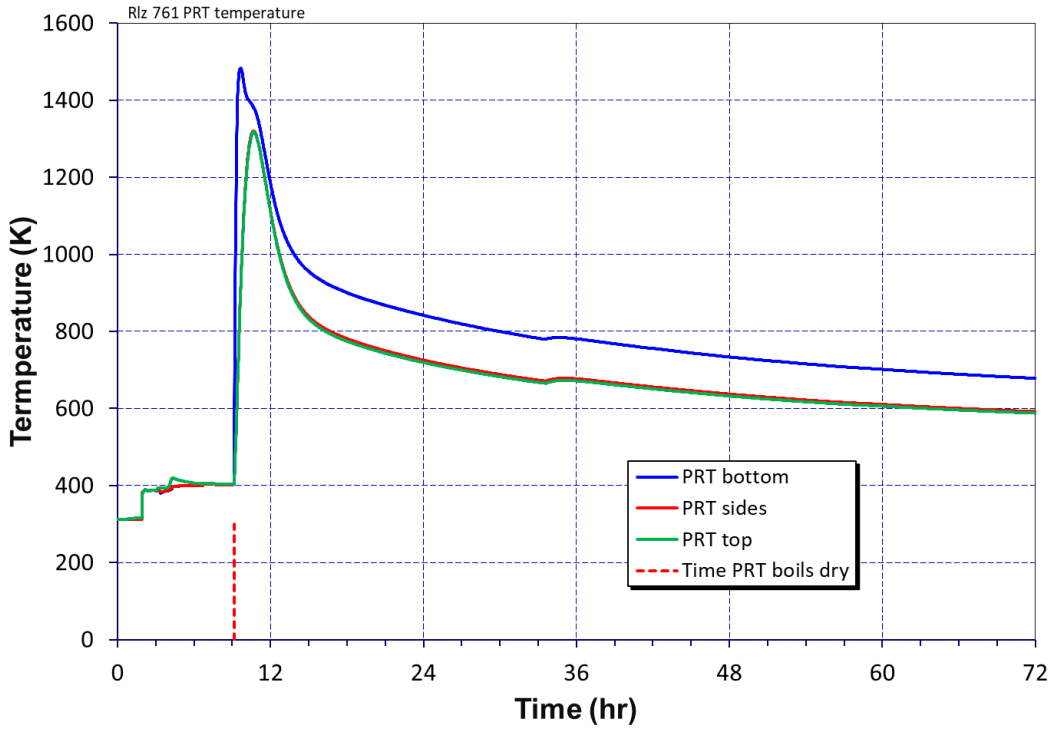

Figure 5-82 Rlz 761 PRT Temperature

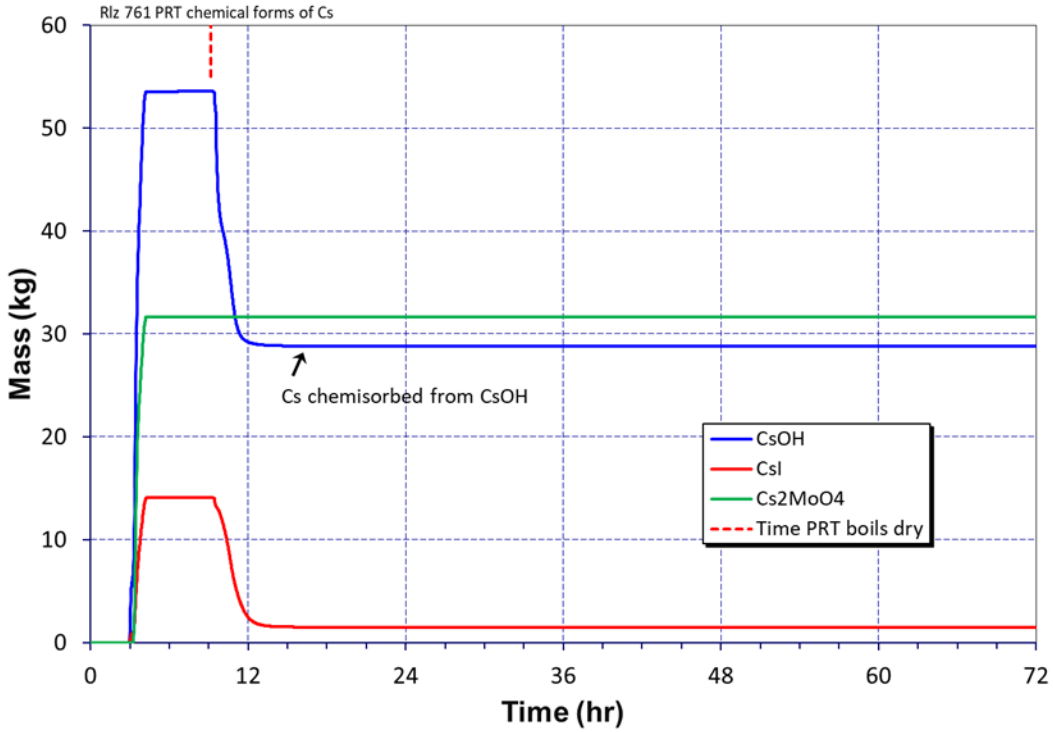

Figure 5-83 Rlz 761 Chemical Forms of Cs Resident in the PRT

5.3.10 A Realization without Hot Leg Rupture – Rlz 935

One realization in the UA, Rlz 935, did not experience a rupture of a hot leg nozzle. The reason for this is not fully clear but informative is a comparison of the contributors to nozzle creep damage between this realization and non-SGTR reference realization Rlz 459. Specifically, comparing RCS pressure and hot leg temperature is informative. Figure 5-84 and Figure 5-85 show the histories of RCS pressure and hot leg nozzle creep damage in Rlzs 459 and 935, respectively. Figure 5-86 shows the histories of hot leg nozzle temperature in the two realizations. While the temperature histories between the realizations are not largely different, the pressure histories are quite different suggesting that differences in creep damage accumulation between the realizations are due to pressure differences rather than temperature differences. Rlz 935 suffered an early failure of a pressurizer SV to close and a largely open position of the valve after the failure. Rlz 459 did not suffer a SV FTC. Apparently then, an early pressurizer SV FTC reduced RCS pressure in Rlz 459 such that creep damage sufficient to fail a hot leg nozzle never materialized. Why this happened in Rlz 459 and did not happen in the 26 other realizations in the UA that experienced similar SV FTC occurrences, is unclear, but subtle differences in accumulator water delivery to the core in these reduced-pressure realizations are suspected of playing a role.

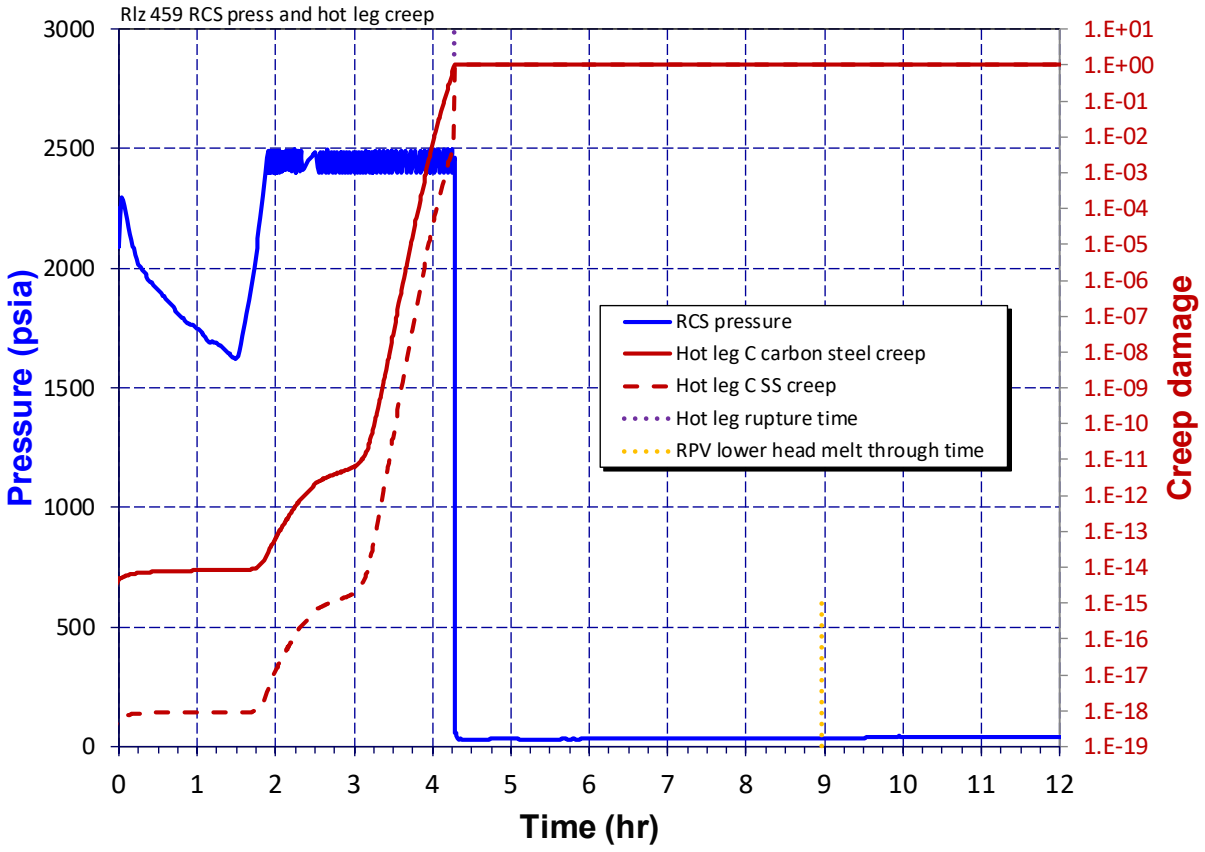

Figure 5-84 Rlz 459 RCS Pressure and Hot Leg Creep Damage

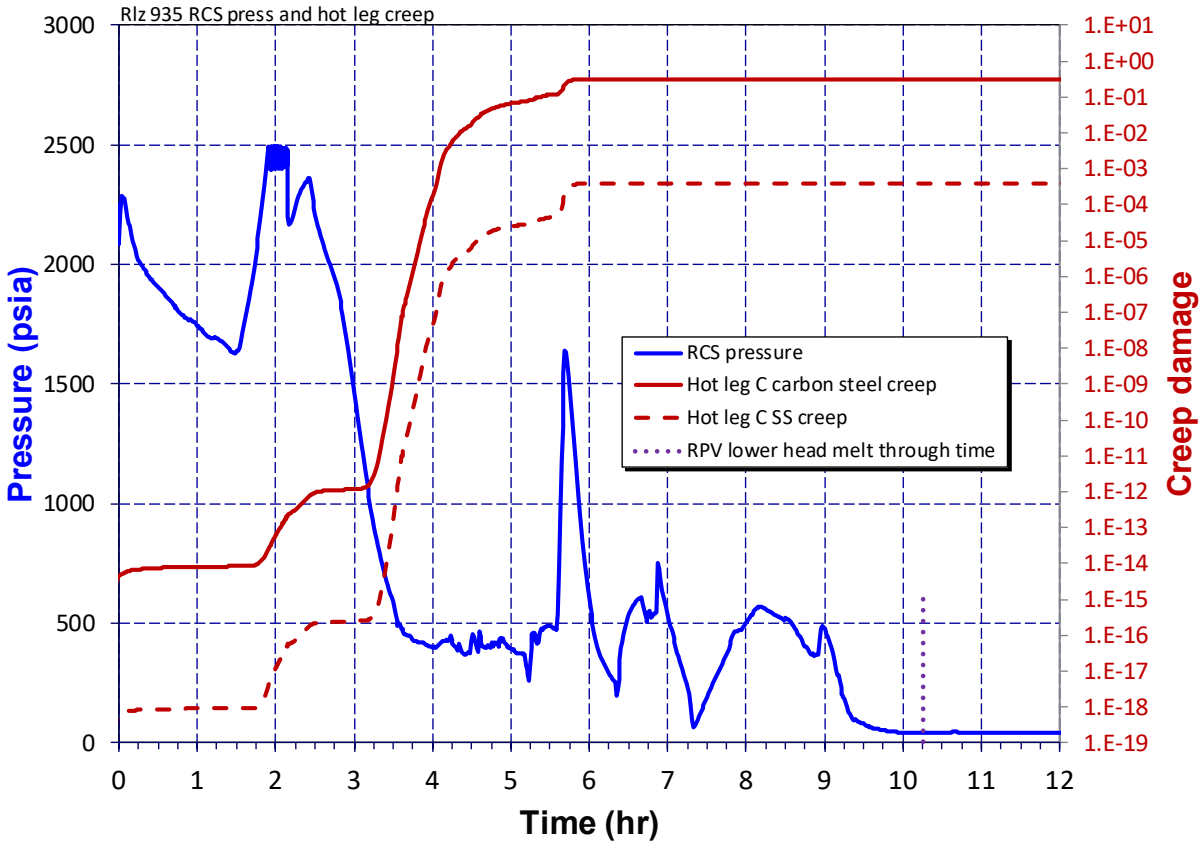

Figure 5-85 Rlz 935 RCS Pressure and Hot Leg Creep Damage

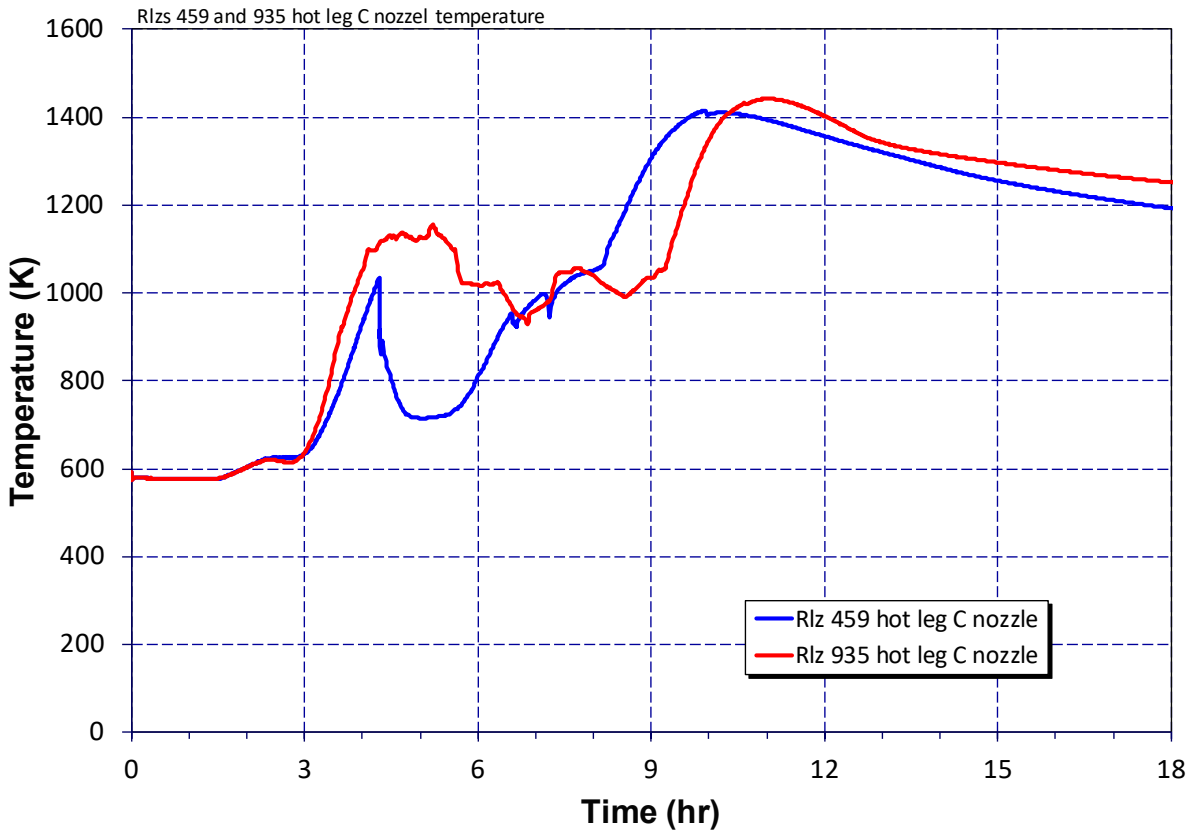

Figure 5-86 Rlzs 459 and 935 Hot Leg Nozzle Temperature

5.3.11 Earliest Hot Leg Rupture - Rlz 122

The earliest rupture of a hot leg nozzle in the UA occurred in Rlz 122. Like in nearly all of the realizations the rupture was in the loop C nozzle. Notable in this realization is that it had very large 99th percentile sampled RCP seal leakage. Also, the realization experienced a FTC of the lowest set-point pressurizer SV on the 1st cycle but with the valve left a small 0.096 fraction open. While these aspects served to reduce RCS pressure and hence the stress on the hot leg nozzles, they more importantly leaked RCS coolant relatively rapidly. The rapid loss of coolant resulted in a relatively early overheating of the fuel rods and the open SV kept a continuous flow of hot gas moving through the loop C hot leg nozzle. Creep damage accumulation in the nozzle started early and proceed steadily to where the nozzle ruptured earlier than in any other realization in the UA. The characteristics of the early progression to hot leg rupture in Rlz 122 are evidenced in Figure 5-87, Figure 5-88, and Figure 5-89, where responses in this realization are shown together with responses from non-SGTR reference realization (i.e., Rlz 459). Figure 5-88 shows the hot leg creep damage and RCS pressure while Figure 5-87 shows hot leg C nozzle temperature. Figure 5-89 shows RCS water level.

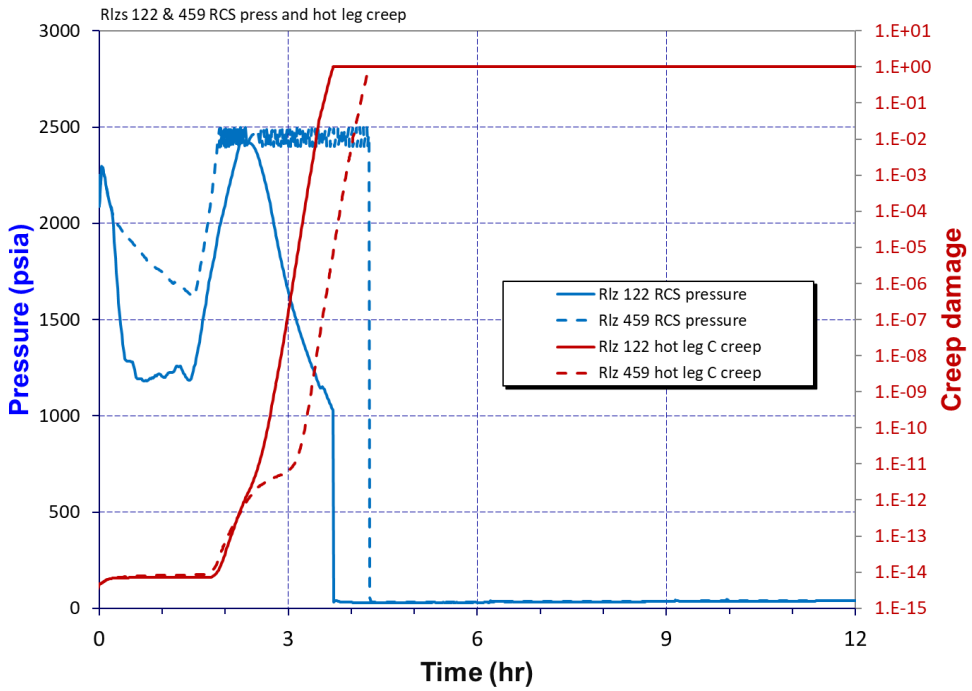

Figure 5-87 Rlzs 122 and 459 RCS Pressure and Hot Leg Creep Damage

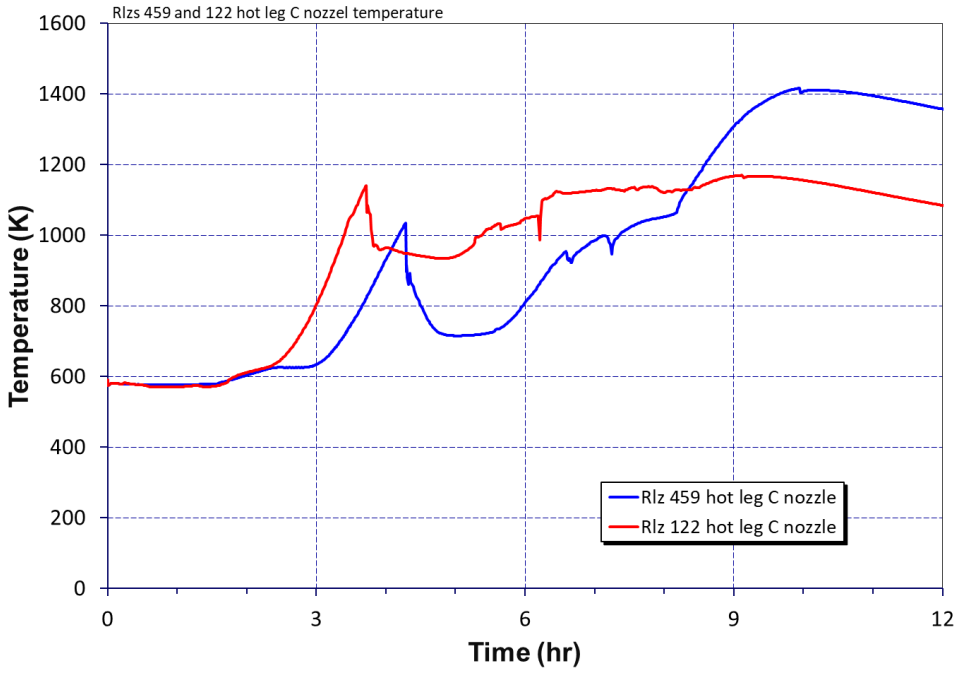

Figure 5-88 Rlzs 122 and 459 hot leg nozzle temperature

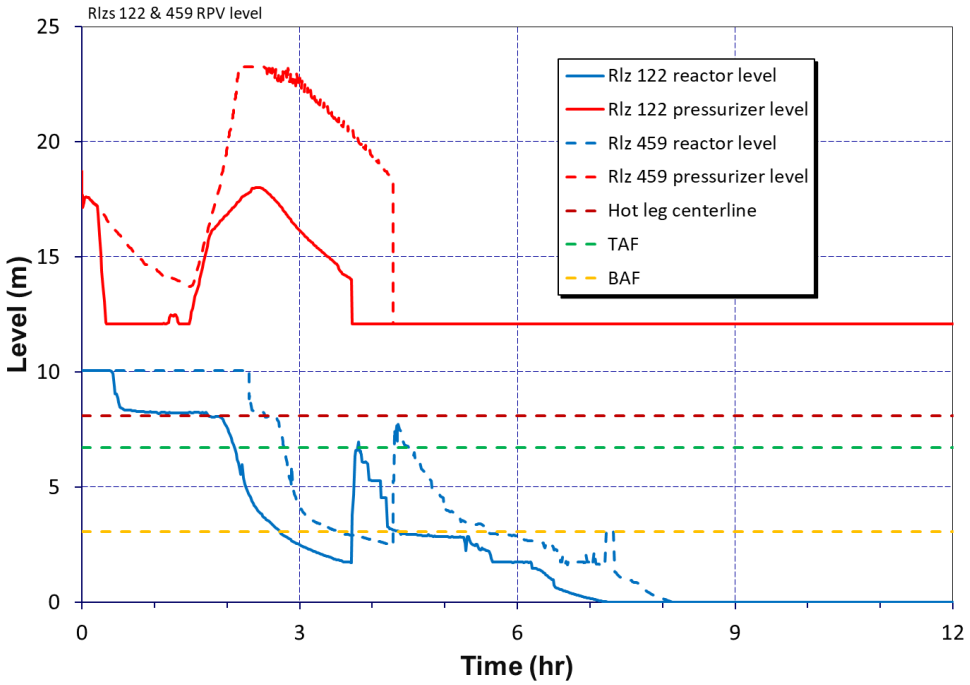

Figure 5-89 Rlzs 122 and 459 RCS level

5.3.12 Most In-Vessel Hydrogen Production - Rlz 999

The most hydrogen production in-vessel from fuel cladding and steel oxidation reactions occurred in Rlz 999. This was a realization with:

- No pressurizer SV FTC,
- No MSL SV FTC,
- No SGTR, and
- A RCP leakage rate near the median (224, gpm, 51st percentile).

All the above served to maintain RCS pressure and steam availability (for oxidation reactions) during core degradation. Additionally, the realization had:

- A lowest 0th percentile sampled ORIGEN day (0.5 days)
- A high 81st percentile sampled Zr breakout temperature
- A lowest 0th percentile sampled Zr drain rate

All three of these samplings would have served to extend the period over which an efficient (generally intact) core geometry existed for oxidation. The high Zr breakout temperature and low Zr drain rate would have supported oxidation by delaying and slowing the draining of cladding (Zr) from standing fuel pins. This influence was probably modest, however, compared to the large effect of the very low fission product decay power associated with the early ORIGEN day. The low power dramatically slowed the overheating and dismantling of the core which greatly prolonged the period that standing fuel pins experienced oxidation. Realization 999 also included a large contribution from stainless steel oxidation between 24 hours and core plate failure, starting at 28 hr. The prolonged oxidation period is reflected in the following timings in Rlz 999 relative to the overall UA:

- A very late 98th percentile (12.36 hr) time to initial fuel-cladding failure
- A very late 98th percentile time (23.64 hr) to 90% core relocation
- A very long 96th percentile (11.28 hr) elapsed time between initial fuel-cladding failure and 90% core relocation
- Large stainless-steel oxidation due to the delayed core plate failure.

Rlz 999 had a somewhat low 31st percentile sampled value of fuel-zirconium oxide melting temperature. The low fuel melting temperature and associated collapse would have served to limit in-vessel hydrogen production by triggering a relatively early collapse of fuel pins. This influence was evidently overwhelmed in Rlz 999 by the very low fission product decay power defined in the calculation.

Rlz 999 used the Leistikov-Schanz/Prater-Courtright oxidation correlation. However, the choice of the oxidation model was not identified as an important parameter in the UA.

6 SOARCA PARAMETER UNCERTAINTY ANALYSES

The uncertainty in the source term for the MELCOR realizations is described in Section 6.1 and the uncertainty in the offsite consequences for the MACCS realizations is described in Section 6.2.

6.1 Source Term Parameter Uncertainty Analysis

There were 23 MELCOR parameters that were selected for sampling in the UA. Sandia used a high-performance computing cluster to execute a Monte Carlo simulation with 1200 MELCOR runs, of which 1147 were successful. Each run is identified with a unique realization number. In the 1147 successful realizations, the following results were observed within the 72 hour run time:

- A SGTR occurred in 144 realizations; this number does not reflect a best-estimate of SGTR frequency due to the use of exploratory distributions;
- A hot leg nozzle rupture occurred in all but one realization;
- In every realization that a SGTR occurred, a hot leg nozzle rupture also occurred. The hot leg failure terminated the high leakage flow rate through the SGTR;
- A failure of one or more RCS secondary side safety valves (SG safety valves) to close occurred in 297 realizations;
- All three of the RCS secondary side safety valves failed to close in 9 realizations;
- One or more SVs on the RCS primary side (on the pressurizer) failed to close in 121 realizations; 10 of the realizations had 2 SV failures; No realizations had 3 SV failures;
- The steel containment liner yielded in 1091 realizations; and
- Containment concrete rebar yielded (and the concrete fractured) in 16 realizations.

Regression analyses were performed on the full set of realizations, a set with only SGTRs, a set without SGTRs (e.g., the non-SGTR set), and a set with all realizations as identified in Table 6-1. The figures-of-merit considered in the analysis were the iodine and cesium masses released to the environment, the time of containment failure, and in-vessel hydrogen production. In addition, tube creep results were treated as figures-of-merit to facilitate the study of steam generator tube rupture. Regression results for each of the figures-of-merit were reviewed against the accident progression phenomenology. The separate analyses were performed to identify separately the parameters driving uncertainty given a SGTR or given no SGTR and the parameters driving the occurrence of SGTR. Because of the magnitude difference between SGTR and non-SGTR realizations for most figures-of-merit, regression results on the total population fail to identify drivers of uncertainty within SGTR (or within non-SGTR) realizations.

Table 6-1 Summary of the MELCOR Accident Progression Regression Analyses

Figure-of-Merit Regressions Summary Data set used based on occurrence of SGTR										
Released Cesium			Released Iodine			Containment Failure Timing			In-Vessel Hydrogen Production	Creep (SGA and SGB, all tubes)
SGTR	Non-SGTR	All	SGTR	Non-SGTR	All	SGTR	Non-SGTR	All	All	All

Regression tables provide summaries of the analysis. The first four major columns in the tables are labeled with the regression technique used to create the results. The last two columns contain weighted average values of the main (individual, independent) contribution of the parameter on the figure-of-merit and the conjoint influence[64] of the parameter on the result metric. These are calculated as arithmetic averages of the overall contributions from the four regression techniques as described in Section 3. Values of main contribution greater than 0.02 and conjoint contributions greater than 0.1 are considered potentially significant and are highlighted. The parameters in the first column of the tables are ordered by the values in the column labeled Main Contribution, thus the most important parameters appear in rank order at the top of the table. This ranking assumes that all four model types are equally appropriate for the data but accounts for weaker models based on the R^2 values. For example, a linear regression model is not assumed to be any more or any less appropriate for the data than a quadratic regression model, but the effect of the linear model on the ranking will be stronger than the effect of the quadratic model if it has a higher overall R^2 value.

For some of the parameters, the sampled value is only used under certain circumstances that do not always occur (e.g., valve open area fraction is only used if a valve fails) so it was more desirable to include a post-calculated parameter in the regression calculations that more meaningfully captures the translation of the sampled input to reactor system behavior. Several parameters were post-calculated (see key regression variables in Table 6-2) for use in regressions, based on both the sampled input and actual behavior. Additionally, some parameters were excluded from the regression due to correlations. This correlation occurred due to the dependence between leakage parameters and valve cycling behavior on the primary and secondary sides. The leakage parameters were included, and the results are interpreted using scatter plots of the cycle parameters to evaluate their influence. Also included are those parameters for which the input is slightly different than the description in Chapter 4.

Sections 6.1.1 through 6.1.4 and Appendix E present the results of the regressions cited in Table 6-2.

[64] Conjoint influence is the influence of two or more input parameters acting together, which may have synergistic effects that would not be uncovered by studying the influence of each parameter separately and individually.

Table 6-2 Summary of Key Regression Parameters

#	Parameter Name	Description	Notes
1	priSVfrac	Overall open fraction of the 3 primary SV system at 72 hours	Value is 0 if there are no SV failures and the sum of the sampled open fractions for any SVs that fail if at least one SV fails partially open
2	priSVcyc	Number of cycles experienced by the 3 primary SV system	If a valve experiences the sampled number cycles-to-failure prior to depressurization then the valve fails, and the value of the parameter is the sampled number of cycles, otherwise it is the number of cycles experienced by the valve up to depressurization (by a mode other than the valve failing to close). The values for the three valves are combined to define a single parameter using addition.
3	secSVfrac	Open area fraction of the lowest setpoint secondary side valve if it failed to close (secSVfrac1)	Value is 0 if the SV did not fail and it is the sampled open area fraction for that SV if it did fail
4	secSVcyc	Number of cycles experienced by the lowest setpoint valve before depressurization or valve failure (secSVcyc1)	If valve experiences the sampled number cycles-to-failure prior to depressurization then the valve fails, and the value of the parameter is the sampled number of cycles, otherwise it is the number of cycles experienced by the valve up to depressurization (by a mode other than the valve failing to close)
5	Time-in-Cycle	Integral decay energy at 72 hours, representing time at cycle	The calculation of the integral energy separates out the decay heat aspect of time at cycle from the change in radionuclide inventory portion and for each sampled day, the nearest day for which an ORIGEN calculation was available was used
6	designLeakLa	The amount of containment design leakage in La, where 1.0 La is technical specification for the allowable leakage rate, see Section 4.1.3.2.	There were no changes applied to this regression parameter. The sampling is from the distribution presented in Section 4.1.3.2.
7	RCP_Leak	Reactor coolant pump seal leakage (gpm/RCP)	The value was sampled independently for three pumps and the sum of these values is used in regression
8	tubeColdA_max tubeColdB_max tubeColdC_max	Maximum non-dimensional flaw depth over the three cold tubes modeled in the SG for each loop.	Three flaw samples were made for the cold tubes in each SG based on the discussion in Section 4.1.1.5. Because the cold tubes in a SG are modeled in the same way, only the maximum flaw is used in the MELCOR creep and the subsequent regression evaluations.
9	tubeUpflowA_NFD tubeUpflowB_NFD tubeUpflowC_NFD	Non-dimensional flaw depth for the Upflow region tube modeled in the SG for each loop.	There were no changes applied to this regression parameter. The sampling is from the distribution presented in Section 4.1.1.6.

Table 6-2 Summary of Key Regression Parameters (Continued)

#	Parameter Name	Description	Notes
10	tubeHotA_NFD tubeHotB_NFD tubeHotC_NFD	Non-dimensional flaw depth for the hot upflow region tube modeled in the SG for each loop.	There were no changes applied to this regression parameter. The sampling is from the distribution presented in Section 4.1.1.6.

6.1.1 Iodine Release to Environment

Iodine is a volatile fission product, and can be released as an elemental gas, or bound together with cesium as CsI, an aerosol. Because of its volatility, a portion of the iodine transports to the fuel-cladding gap, leading to early releases when the cladding gap failure occurs. Although iodine is released and tracked as an element or a compound, the released iodine includes many different nuclides of iodine that are formed from the fission process. I-131 is one of the most important nuclide forms of iodine due to its importance for thyroid cancer and can dominate early health effects. There is a relatively high inventory of I-131 at shutdown. However, I-131 has a relatively short half-life (i.e., high specific activity) compared to other fission products with a half-life of 8 days. Consequently, its impact is short-lived.

Typical of severe accident analyses, the iodine release from fuel is near 100 percent of its total inventory. The reason environmental releases are much lower is due to hold-up and deposition in both the primary system and in containment. However, any released gaseous iodine remains airborne and is available for release to the environment (see Section 4.1.4.1 for a discussion of the chemical form of iodine). Additionally, there can be events in which containment is bypassed (e.g., SGTRs in this UA) and the environmental releases are typically much higher. However, only a small portion of the total iodine is gaseous. The CsI form of iodine experiences natural deposition processes that limit its overall release. Consequently, the impact of the potentially higher gaseous iodine release to the environment is limited.

6.1.1.1 *Comparison to SOARCA and Horsetail Plot*

The environmental release mass of iodine by 72 hours is a primary figure-of-merit for the analysis. Figure 6-1 shows time-dependent release of iodine mass to the environment with the reference realization results from Section 5.2. There is a clear bifurcation in the results, with the higher release masses representing SGTR realizations, and the remainder of the realizations having much lower releases. The non-SGTR realizations are all below 0.125 kg. At 72 hours, the results are well distributed, with no clear bifurcations except the SGTRs. However, the iodine mass released is still increasing at 72 hours in some of the realizations while it remains relatively constant in others. As described in detail in a subsequent section, late increases in release masses come after containment overpressure failure. This is evident in some of the non-SGTR realizations that plateau for a period of hours before increasing more rapidly (i.e., especially evident on a semi-log figure). The impact of containment failure (i.e., at approximately 45-55 hr for most realizations) is a significant increase in the late environmental release with a large portion of non-SGTR realizations showing an order of magnitude or more increase in the released iodine masses.

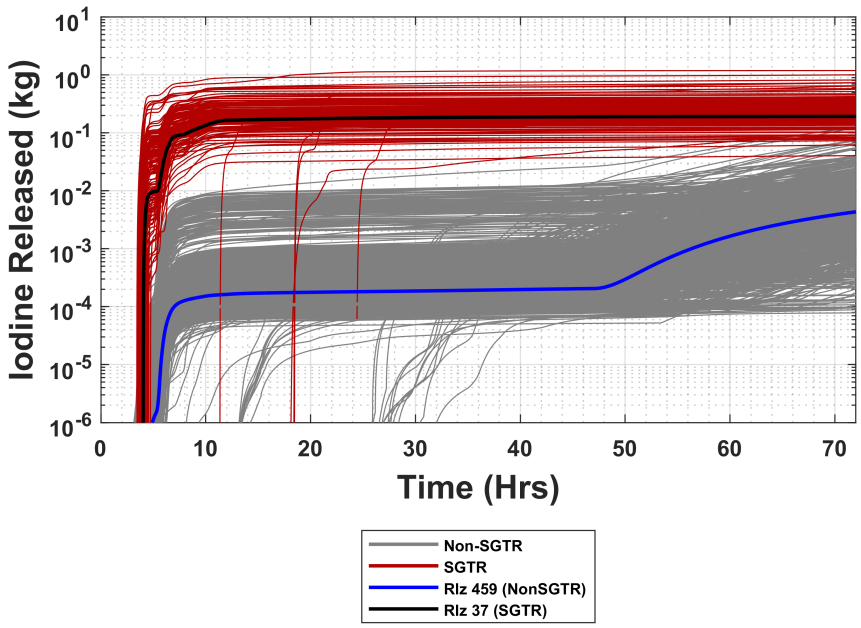

Figure 6-1 SGTR and Non-SGTR Iodine Release Masses to the Environment with the Corresponding Reference Realizations

Figure 6-2 illustrates the cumulative probability for the mass of iodine released by 72 hours. The cumulative probability to 0.9 is primarily due to the non-SGTR realizations and the highest releases in the cumulative probability from 0.9 to 1.0 are primarily due to the SGTR realizations. The 0.0 to 0.9 cumulative probability range shows a S-shaped characteristic with 70% of the cumulative probability of releases between 0.001 and 0.02 kg. Similarly, approximately 8% of the top 10% of the cumulative probability of releases between 0.11 to 0.14 kg, which is primarily SGTR realizations (see Figure 6-1).

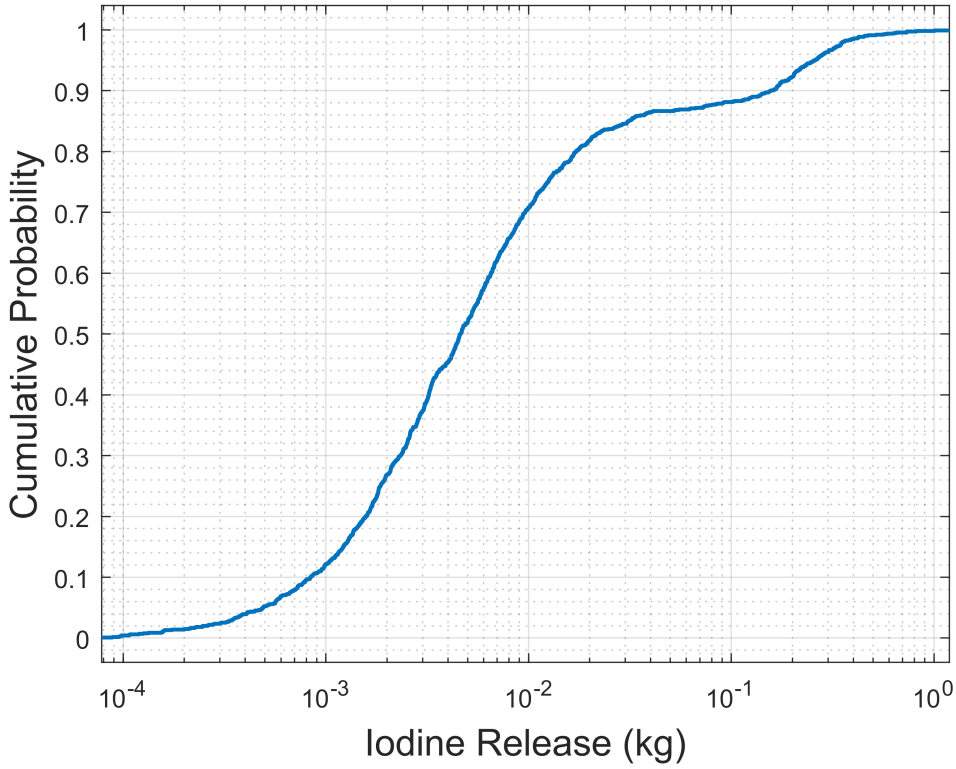

Figure 6-2 Cumulative Probabilities for the Mass of Iodine Release for Selected Time Intervals

Figure 6-3 compares the UA iodine environmental release masses for non-SGTR UA realizations to the non-SGTR SOARCA STSBO from the 2012 Surry SOARCA analysis (Reference [3]). Until containment failure at about 25.5 hours, the SOARCA release mass is comparable to the non-SGTR release mass mean. However, the SOARCA release mass rapidly increases following containment failure. At 72 h, the SOARCA STSBO iodine release mass is 0.156 kg which is nearly an order of magnitude higher than the 95th percentile of non-SGTR UA realizations.

The major differences between the original Surry SOARCA [3] result and the new realizations included (1) an error in the concrete type in the original SOARCA evaluation, (2) the variable nominal containment leakage modeling in the UA, (3) the modifications to the containment failure model for the UA, (4) the variable time at cycle in the UA versus at the end of cycle in SOARCA, and (5) the inclusion of gaseous iodine in the new UA. A comparative analysis was presented on many of these items in Appendix A of the draft Surry UA [8]. However, due to changes in the uncertainty parameter distributions between the draft and final Surry UA, there are some new factors affecting the differences between the original SOARCA response and the current UA realizations. Each of the key differences are discussed next.

In the original SOARCA analysis, limestone concrete was specified for the reactor cavity floor. Subsequent fact checking after SOARCA showed the actual concrete is basaltic. The impact of the change in concrete composition resulted in different chemistry and gas production quantities in the ex-vessel debris ablation of the concrete. Researchers at CEA Cadarache cite the

following differences between limestone and silica-rich (i.e., basaltic) concrete [53]. The ablation of limestone-rich concretes is almost isotropic whereas the ablation of silica-rich (i.e., basaltic) concretes is much faster towards the sides than towards the bottom of the cavity; limestone concretes liberate about twice as much gas at a given ablation rate than siliceous concretes; limestone concrete has a higher liquidus temperature than siliceous concrete; and the molten limestone concrete has a larger diffusion coefficient and can more easily dissolve a corium crust than siliceous melt. The net effect was a much slower pressurization of the containment in the new UA using basaltic concrete, which is shown in the comparative analysis in Appendix A from the draft UA [8].

The range of design leakage for the new UA spanned from 10% of the SOARCA value to 10 times the SOARCA value (see Section 4.1.3.2). However, 90% of the leakage probability was less than the SOARCA value. Consequently, most UA realizations have a smaller nominal leakage rate than the SOARCA calculation. The nominal leakage is more important earlier in the accident prior to the containment liner failure. After the containment liner failure, the leakage rate is much larger than the design leakage after containment failure. Since the UA liner failure is delayed relative to the SOARCA result, the airborne concentration of aerosols available for leakage due to natural gravitational settling. The overall effect was a higher release of radionuclides prior to containment liner failure in SOARCA due to higher design leakage than 90% of the UA realizations and higher leakage after the containment liner failure due to less time for gravitational settling.

The containment failure curve was also modified for the UA. Figure 6-4 displays the curve for the original Surry SOARCA [3] run on the left, with the modified UA curve on the right. Both curves use three of the same data points, which were scaled from containment testing at Sandia. However, the original SOARCA model did not include the liner plate yield point and fit a parabolic function to the remaining three data points, which results in the enhanced failure leakage initiating at a higher containment pressure. With the liner plate yield point included and a linear fit between the four points, the Surry UA model starts enhanced leakage at a lower pressure. However, the SOARCA approach has a sharp increase in leakage flow when the enhanced failure leakage starts. These differences were significantly less important than the much higher concrete ablation rate and gas generation from limestone concrete in the SOARCA model that led to a rebar yield condition much earlier (also described in Appendix A in the draft Surry UA [8]).

The SOARCA calculations used an end of cycle decay heat power whereas the new UA sampled the decay heat from the beginning of cycle to the end of the cycle (see Section 4.1.2.4). The end of cycle decay heat and radionuclide inventory are largest at the end of the cycle. Consequently, the SOARCA calculation was most consistent with the highest samples from the Surry UA. The accident progression and containment pressurization (see Figure 5-14) in the SOARCA calculation is more consistent with the limiting value in the UA.

Finally, the UA included gaseous iodine in the released radionuclides. After its release, the gaseous iodine remains airborne with very little deposition. The gaseous iodine will continue to leak for the duration of the sequence whereas the airborne aerosol leakage will diminish as settling occurs. In contrast, SOARCA assumed all iodine bound with cesium to form cesium iodide. Cesium iodide is an aerosol at typical containment temperatures and therefore settles over time. Consequently, the mobility of the iodine was expected to be lower in the SOARCA.

Although some of the previously listed factors are compensating, the most important factor contributing to the higher releases in the SOARCA calculation is the faster pressurization rate

due to the limestone concrete and the earlier transition to a rebar yield failure at 25.5 hr. In contrast, most liner failures occurred after 48 hours in the UA simulations (e.g., primarily due to the smaller gas generation from the basaltic concrete).

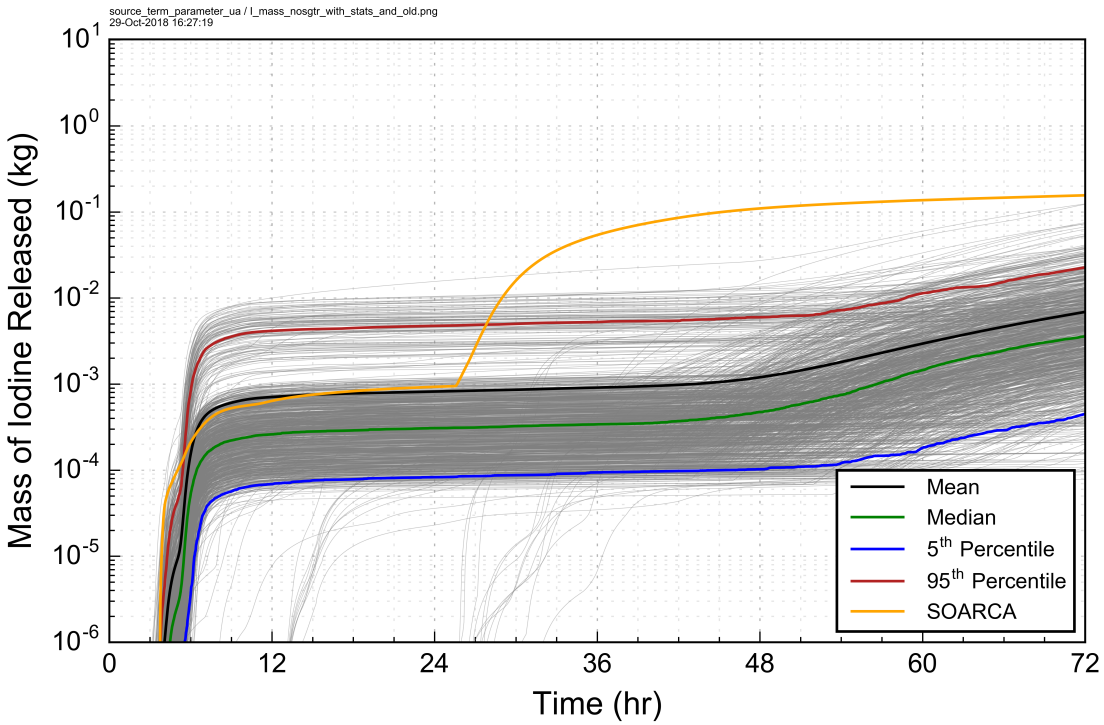

Figure 6-3 Comparison of Iodine Release Mass in the Original SOARCA STSBO (Non-SGTR) to the Calculated Values of all Successful Realizations without a SGTR

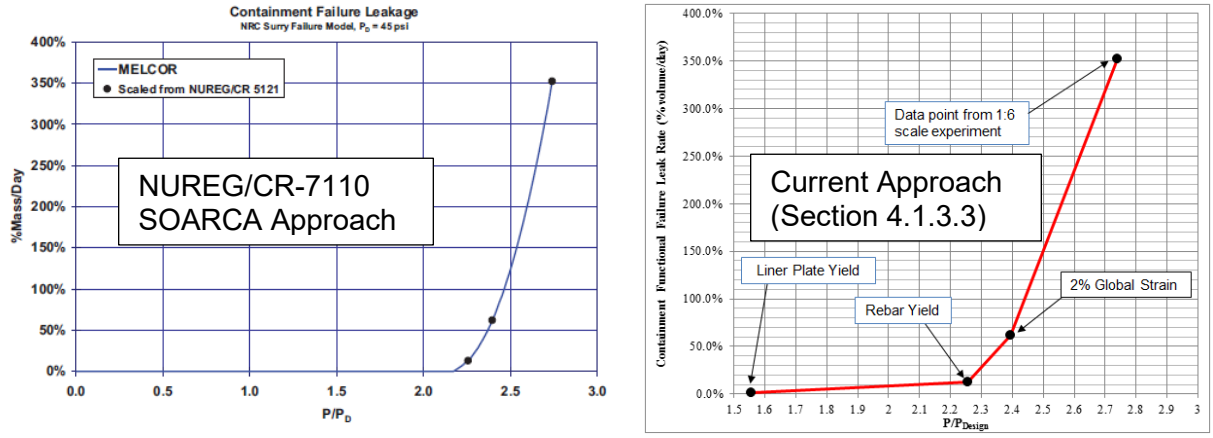

Figure 6-4 Comparison of Containment Failure Models Used for the Original SOARCA STSBO and the UA Realizations

6.1.1.2 Regression Tables and Scatterplots

Regression analyses were performed with all successful realizations. Three sets were done: one for all realizations, one for SGTR realizations, and one for non-SGTR realizations. The SGTR parameters dominated the regression results for all realizations. Consequently, the results in this section were limited to the non-SGTR regressions while Section 6.1.4 and Appendix E address the SGTR results.

The regressions on the non-SGTR realizations are shown in Table 6-3. The I_2 gas gap fraction is identified by each regression technique as explaining much of the overall variance for iodine release masses. Notably, the rank regression model ranks the time-in-cycle (ORIGENDay) as the most important parameter and the gas gap fraction as the second most important parameter. The gas gap fraction is also identified as having a high conjoint contribution, indicated by the yellow highlighting. The remaining parameters identified as important occur in essentially the same order for each of the models with one exception (MARS ranks the design leakage parameter just above the rupture parameter). The technical rationale as to why they may contribute to uncertainty in iodine release masses is explored for each of the top parameters in Section 6.1.1.3, as well as other parameters of interest.

Table 6-3 Regression Analysis of Iodine Release Mass for Non-SGTR Realizations

	Rank Regression		Quadratic		Recursive Partitioning		MARS		Main Contribution	Conjoint Contribution
Final R^2	0.81		0.94		0.81		0.93			
Input	R2 contr.	SRRC	Si	Ti	Si	Ti	Si	Ti		
I2GasGapFraction	0.20	0.48	0.44	0.61	0.82	0.89	0.54	0.72	0.444	0.131
ORIGENDay	0.49	0.54	0.11	0.21	0.07	0.10	0.14	0.25	0.193	0.077
rupture	0.07	-0.26	0.05	0.09	0.02	0.09	0.07	0.12	0.049	0.046
designLeakLa	0.04	0.20	0.05	0.08	0.03	0.03	0.08	0.13	0.045	0.029
EU_melt_T	0.00	0.06	0.01	0.07	---	---	0.01	0.04	0.004	0.032
RCP_Leak	---	---	0.00	0.16	---	---	0.00	0.02	0.001	0.054
secSVfrac1	0.00	0.07	---	---	---	---	---	---	0.001	0.000
priSVfrac	---	---	0.00	0.10	---	---	---	---	0.001	0.031

** highlighted if main contribution larger than 0.02 or conjoint contribution larger than 0.1*

6.1.1.3 Key Parameters for Non-SGTR Realizations

Scatterplots were produced for the parameters ranked most important by the weighted arithmetic average of the regression techniques. Such plots are useful for verifying relationships between the parameter input values and iodine release masses indicated by the regressions. They can also identify when a result from one of the regression models is spurious. The scatterplots of most interest are displayed next in the respective parameter discussion sections below.

I_2 Gas Gap Fraction (I2GasGapFraction)

This parameter determines the initial gaseous iodine mass present in the gap with the remaining iodine mass assumed to be chemically bound to cesium. The sampling is described in detail in Section 4.1.4.1 and, in brief, consists of sampling a log-normal distribution for each ORIGENDay sample. The separate log-normal distributions account for increases in both iodine inventory from fission in the fuel and gaseous iodine present in the gap from diffusion out of the fuel; these factors results in a higher likelihood of higher sampled fractions with increasing ORIGENDay.

The parameter has greatest influence on iodine release masses in three of the four regression techniques, with Rank Regression placing it second behind ORIGENDay. It also has the highest main and conjoint contributions among all the non-SGTR parameters as shown in Table 6-3. Based on the described range dependence on time at cycle sampling, the high conjoint contribution is expected and may indicate that analysis of iodine release masses should consider time at cycle in tandem with the gas gap fraction.

The iodine release masses for non-SGTR realizations exhibit a noticeably increase with increasing I2 gas gap fraction as shown on Figure 6-5. A clustering of release masses exists around the gas gap fraction's empirical mean and the release masses show a strong decade-for-decade relationship with the gas gap fraction in this cluster. Due to the higher mobility of gaseous iodine relative to cesium iodide, the iodine release to the environment is correlated with the specified gaseous mass.

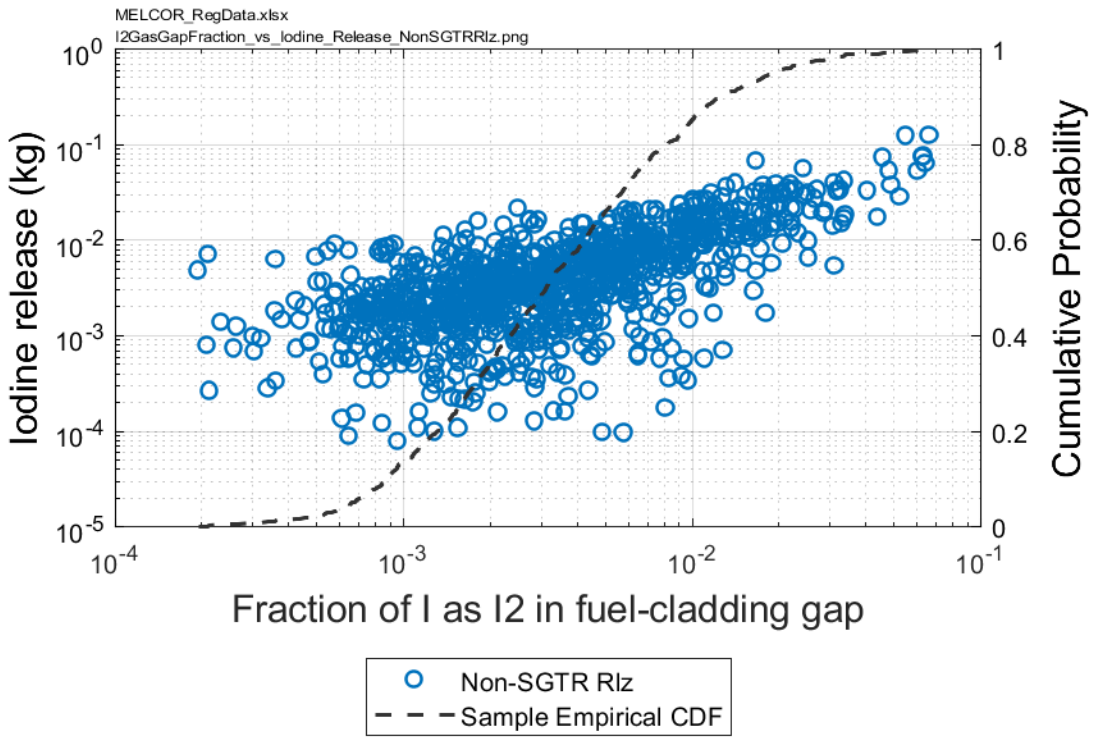

Figure 6-5 Scatterplot of Iodine Release Mass Versus the Mass of Iodine as Gaseous Iodine in Fuel-Cladding Gap

Time at Cycle (ORIGENDay)

This parameter determines the burn-up of the core, which in turn affects integral decay heat and radionuclide inventories. For iodine specifically, the time at cycle impacts the magnitude of the sampled gaseous iodine mass and the overall core decay heat. In total, fourteen values for time at cycle were sampled. Each of the regression techniques lists time at cycle as one of the most important parameters for iodine release masses. The scatterplot (Figure 6-6) clearly shows the trend of increasing iodine release mass as time at cycle increases.

The more rapid increase in iodine release for time at cycle less than 100 days compared to the rest of the time at cycle range is primarily caused by the magnitude of the sampled iodine mass. The time at cycle not only impacts the total inventory of iodine (i.e., kg) but also the magnitude of the sampled fraction that is gaseous (see Section 4.1.4.1). A second impact is the magnitude of the decay heat power pressurizing the containment. The decay heat power trends lower towards the beginning of the cycle with the sample at 0.5 days being significantly lower (see Figure 4-23).

For time at cycle values greater than 100 days, the primary difference is the sampling of gaseous iodine amount once iodine inventory in the fuel reaches an equilibrium value (see Figure 4-22). It is noted that MELCOR models chemisorption of gaseous iodine on stainless steel structures. However, possible iodine release from pools and containment walls was not modelled. Therefore, there may be an under-prediction of iodine mass in the containment due to

the lack iodine pool and wall chemical reactions. The precise effect of these modeling choices was not explored in this UA. However, the original SOARCA study concluded that a persistent equilibrium airborne concentration from the deposited iodine (e.g., like observed in the French Phebus tests) was insignificant to the amount released otherwise over the simulated time frame (48 hours) [3].

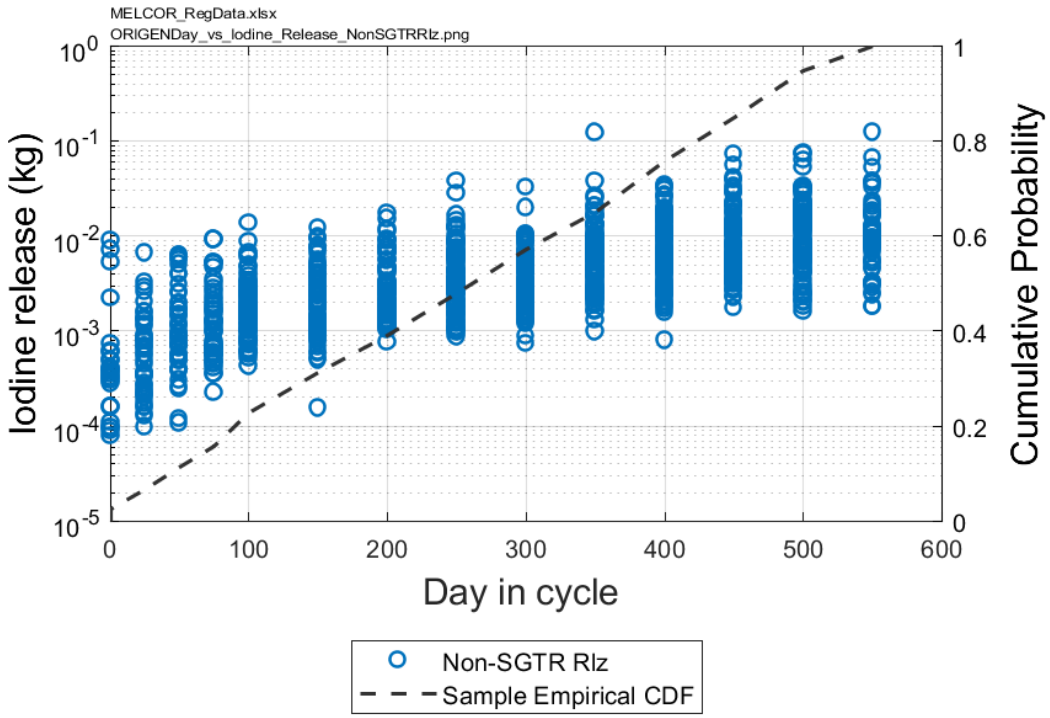

Figure 6-6 Scatterplot of Iodine Release Mass Versus Integrated Decay Energy Time at Cycle Input Values

Containment Failure (rupture)

The rupture uncertainty parameter represents the ratio of actual containment pressure to design pressure at which liner plate yield occurs. The rupture parameter characterizes the uncertainty in the liner failure pressure, which represents the pressure where leakage begins to increase significantly above the allowable amount of leakage as described in Section 4.1.4.2. A low sample of this parameter corresponds to containment liner failure at lower pressures. The rupture variable was identified as the third most important parameter by all regression techniques, except MARS regression which listed it fourth. RUPTURE has some conjoint influence, most likely with time at cycle since this drives the containment pressurization. The SRRC[65] in rank regression indicates that there is a negative trend with iodine releases decreasing as this parameter increases. The scatterplot, Figure 6-7, does give confirmation with a clear trend spanning the domain of the ratio.

[65] Standardized rank regression coefficients (SRRC) display the rank regression coefficients after they have been standardized to take out the unit influence. The rank regression coefficient is an indication of the strength of the influence.

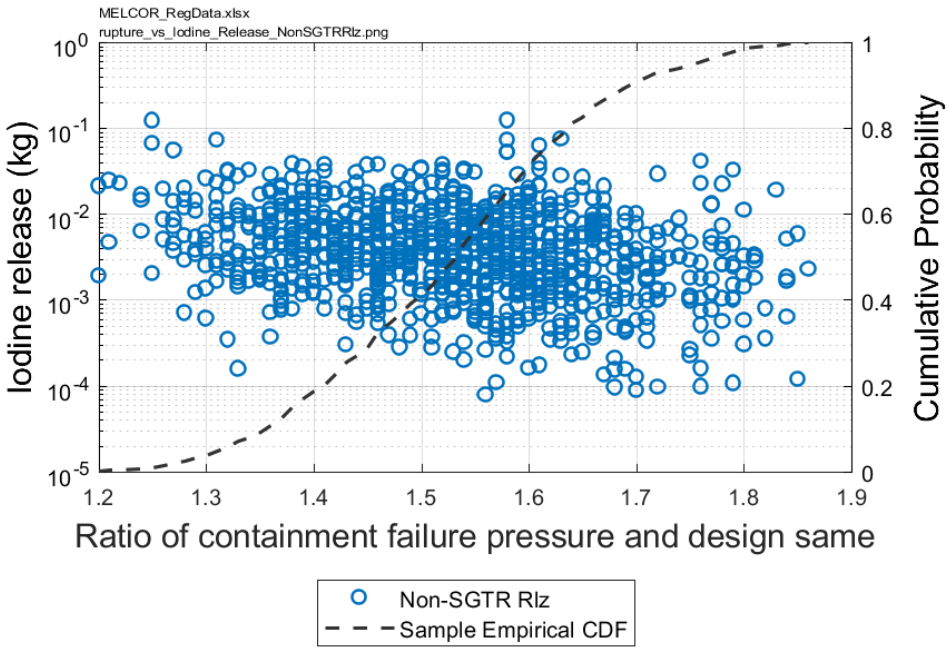

Figure 6-7 Scatterplot of Iodine Release Mass Versus Containment Failure Input Values

Containment Leakage (designLeakLa)

The amount of nominal leakage from the containment is a sampled parameter. Prior to enhanced leakage due to containment liner yield, this is the only release path for radionuclides to the environment, excluding bypass events like a SGTR. The containment leakage was identified by all of the regression techniques as having an influence on iodine release uncertainty, although the strength of the effect is fairly small compared to the top two parameters. Figure 6-8 shows a negligible impact of the iodine release between the design leakage values of 0 and 1, where the sampling density of leakage rate is on a log scale. For the smaller design leakages, there is more spread in the releases that is likely attributed to other parameters having greater influence. The higher leakages above 1 show a slight increasing trend with more leakage and no realizations with iodine releases less than 1E-3. The higher releases are also more clustered, indicating a stronger influence with more leakage.

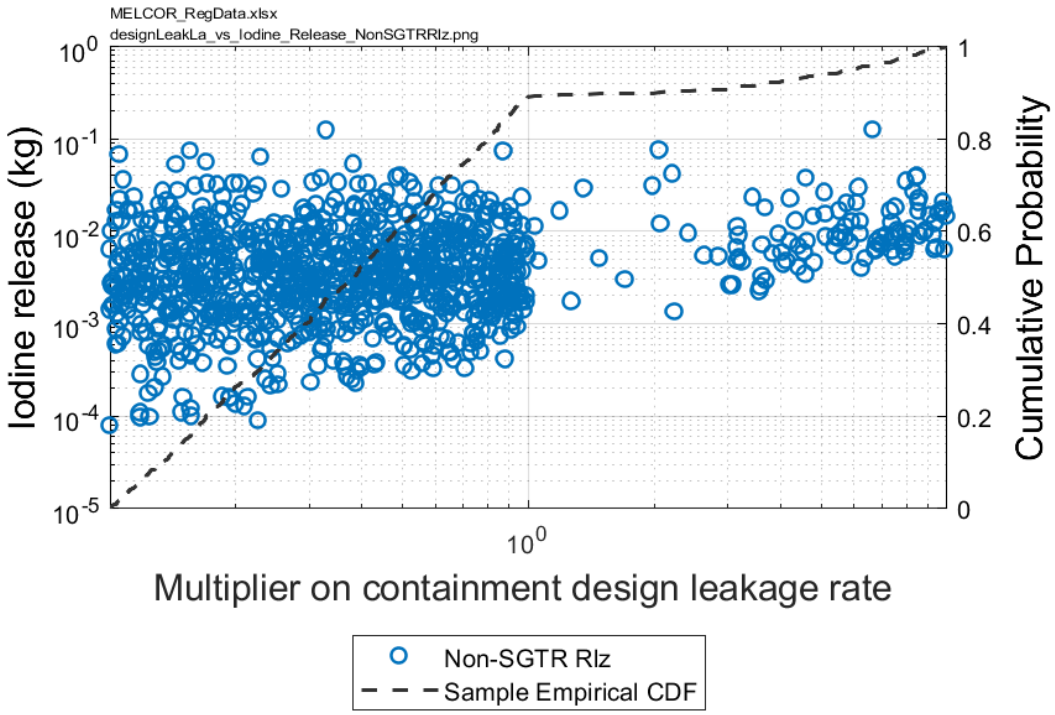

Figure 6-8 Scatterplot of Iodine Release Mass Versus Containment Leakage Input Values

Parameter Interaction

As discussed above, a correlation exists between the gaseous iodine mass present in the gap and the burn-up of the core. Because an increase in either is expected to increase the iodine release mass, the highest releases of iodine generally coincide with realizations that have a high I_2 gas gap fraction and a late time at cycle. Figure 6-9 shows the anticipated relationship. The highest releases clustered in the upper right-hand side of the graph occur when the gas gap fraction and time at cycle are highest. Additionally, the lowest releases are located near the beginning of cycle when the range of sampled gas fractions are smaller. Since the gaseous iodine remains airborne, it will eventually leak. Consequently, larger inventories of gaseous iodine will contribute to a larger iodine releases to the environment.

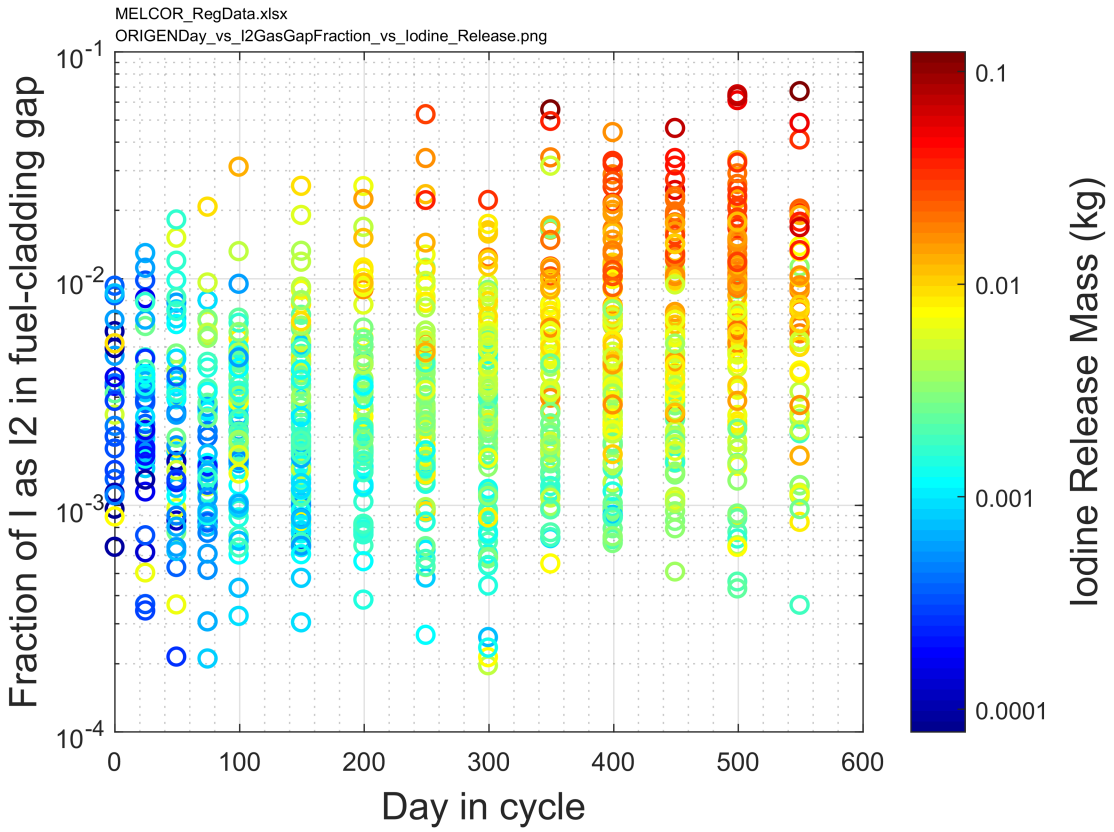

Figure 6-9 Scatter Plot Illustrating the Relationship Between the Day in Cycle, Fraction of I as I2 in Fuel-Cladding Gap, and the Iodine Release Mass

Other Parameters

When reviewing the regression results for all realizations rather than separating by occurrence of SGTR, the results were completely dominated by the severity of the flaw depths within the SG tubes. The flaw parameters relate to the frequency of SGTRs. The sampled non-dimensional flaw depth acts as a stress multiplier on the creep rupture evaluation and since the secondary is usually depressurized, it is the primary determinant on whether a SGTR occurs. Once there is a SGTR, the sampled area fraction for MSIV design leakage is usually the only environment bypass leakage path. However, if a SV failed open on the same line as the SGTR, then the failed valve is also an environment bypass leakage path. The SGTR results are described in much more detail in Section 6.1.4 but are mentioned here due to their dominance over regression results when all realizations are considered versus only the non-SGTR results. Although only 13% of the realizations progressed with SGTRs, the much higher release rates to the environment (i.e., 1 to 2 orders of magnitude larger) substantially skewed the regression results on all realizations.

There are no other parameters that were outside the top parameters that still had a significant contribution to uncertainty in iodine release masses, nor is there a parameter that was expected to be important for iodine that does not appear.

6.1.1.4 Timing and Other Effects

As observed in Figure 6-1, almost all realizations show the onset of iodine release occurring three to seven hours into the accident with the SGTR realizations dominating the early portion of the same time frame. Some realizations, both SGTR and non-SGTR, show later onsets of release in the twenty to thirty-hour range. These are the 0.5 ORIGENDay realizations whose lower power results in less aggressive containment pressurization. Almost all of the releases are steady between about 10 and 40 hours. After this time, the majority of releases start to increase again due to liner failure. These are the only clear splits observed from the horsetail results, aside from the SGTR realizations, which have releases that are 1 to 2 orders of magnitude higher.

In addition to the horsetail plots produced for the key metrics of Cs and I release and in-vessel hydrogen production, a horsetail plot was produced for containment pressure. Figure 6-10 illustrates a bifurcation starting at about 2 hours. The lower (blue) traces are the 0.5 ORIGENDay realizations, which have a substantially lower decay heat power (see Figure 4-23). The magnitude of the decay power impacts the containment pressurization through the heating of the containment atmosphere, the rate the water on the containment vaporizes, and the rate noncondensable gases are generated in the core concrete interaction. Lower decay powers in the UA realizations slow these effects and hence have weaker pressurizations.

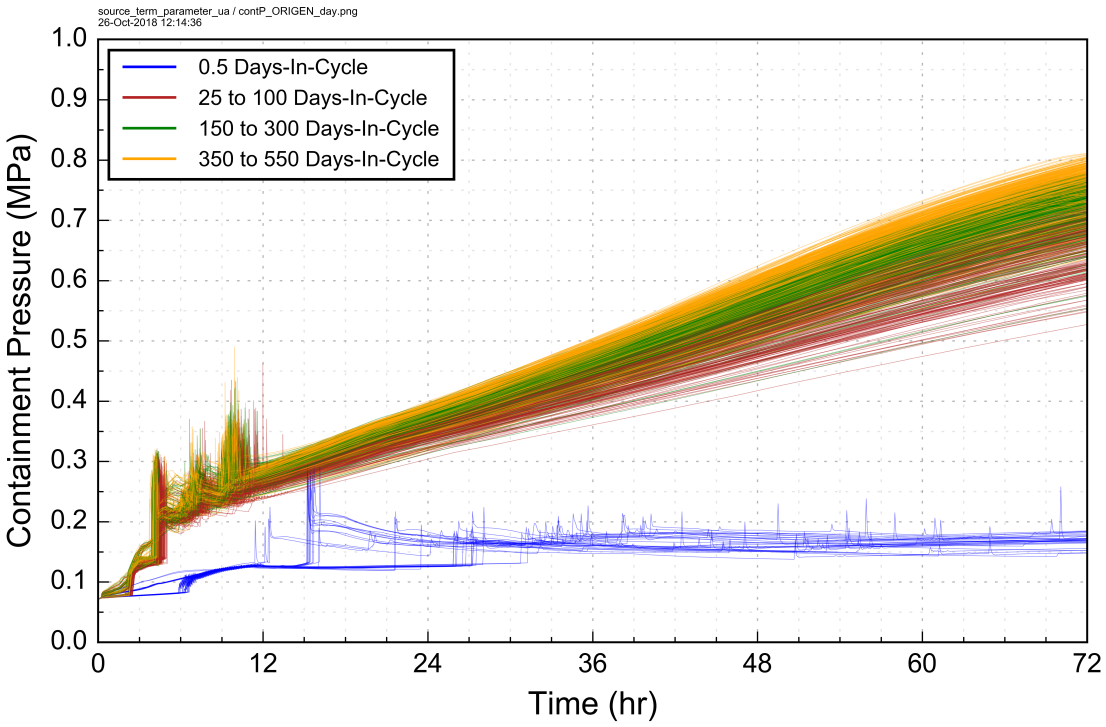

Figure 6-10 Containment Pressure Over 72 hours

6.1.1.5 Iodine Release Mass to Environment – Conclusions

The mean UA non-SGTR iodine environmental release mass is comparable to the original SOARCA calculation prior to the containment liner failure in the SOARCA calculation at 25.5 hr. Some differences were expected due to the variable time at cycle in the new UA versus just the

end of cycle, the inclusion of gaseous iodine in the UA, the error in the concrete type in the original SOARCA evaluation, the variance in the nominal containment leakage modeling in the UA, and the modifications to the containment failure model for the UA. The end-of-simulation iodine mass to the environment from the original SOARCA analysis is 0.156 kg higher than all of the UA non-SGTR results. The most important factor is the early containment liner yield time of 25.5 hours due to the more rapid containment pressurization from the limestone concrete (i.e., see Appendix A of Reference [8] for a full discussion and comparison).

There is a large split between SGTR and non-SGTR realizations, in that SGTRs have one to two orders of magnitude higher release masses. For non-SGTRs (87% of realizations), the spread of release masses, excluding low outliers, is over an order of magnitude. The most important parameters for the non-SGTR realizations are the I_2 gas gap fraction and the time at cycle. The time at cycle is important because it impacts the decay heat power and the associated containment pressurization rate as well as the sampling range for the I_2 gas gap fraction. The sampled I_2 gas gap fraction is important because the iodine gas transports without any significant deposition to the environment versus an aerosol form of iodine. As expected, the parameters affecting flow rates to environment, both the design leakage and the containment liner failure pressure, also played a dominant role. The iodine release increases with increasing design leakage and a decreasing liner failure pressure.

6.1.2 Cesium Release Mass to Environment

Cesium is very volatile and binds with other elements to form aerosols. Specifically, it is known to bind with iodine as CsI, molybdenum as Cs_2MoO_4, and water as CsOH. Because of its volatility, a portion of cesium transports to the fuel-cladding gap, leading to early releases to the RCS upon the occurrence of the cladding failure. Key cesium nuclides formed in fission reactions at high concentrations have relatively long half-lives (e.g., approximately 30 years for Cs-137 and 2 years for Cs-134) and dominate latent health effects. Although the cesium release from fuel is near 100 percent of its total inventory, the environmental releases is relatively low due to hold-up and deposition in the primary system and in containment. For the SGTR realizations, the environmental releases are higher due to the more direct release pathway but still have considerable attenuation in the SG, primary system, and containment.

There is an expected correlation between cesium and iodine environmental releases, since a portion of cesium bonds with iodine, and many of the same factors drive release of both (e.g., containment leakage area and liner failure pressure). Figure 6-11 shows the release mass of iodine as a function of the cesium release. The cesium iodide releases appear as strong linear correlation. The remaining scatter above the linear correlation at low releases of cesium is due to the release gaseous iodine. At such low absolute values of the releases, the small but highly mobile release of gaseous iodine is readily evident. Nevertheless, the parameters with high importance to iodine releases would also be expected to have importance to cesium releases.

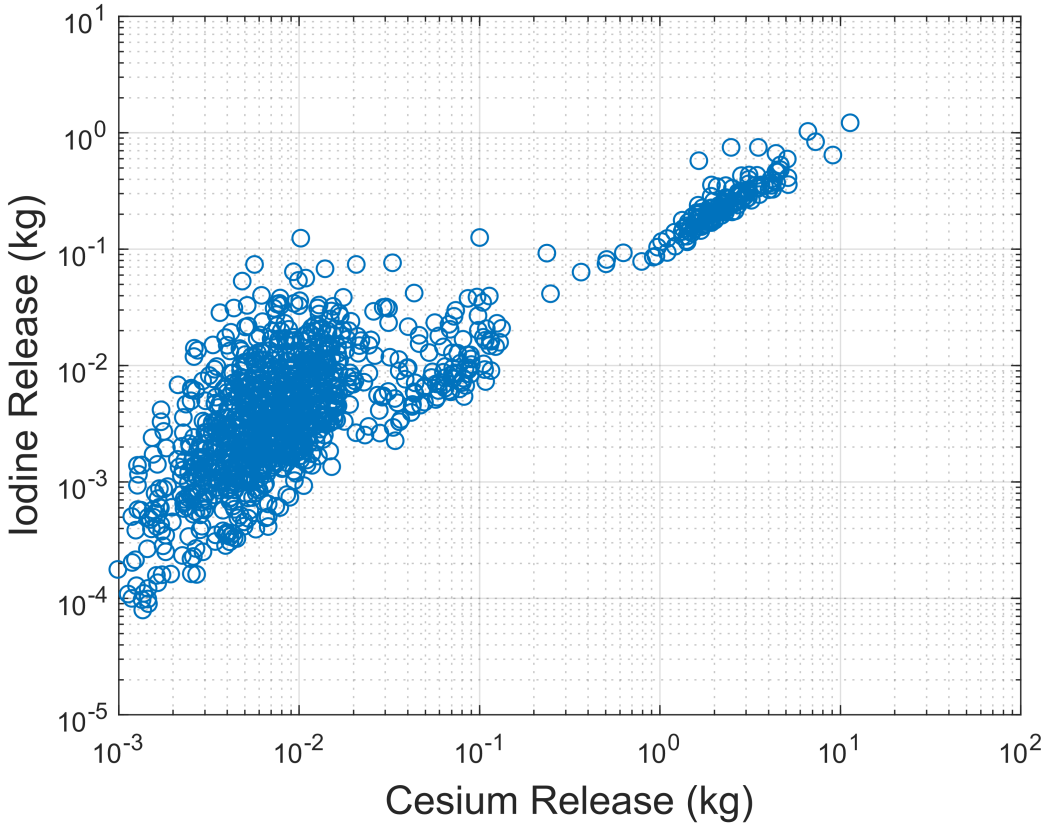

Figure 6-11 Comparison of Cesium and Iodine Environmental Release Masses at 72 Hours

6.1.2.1 Comparison to SOARCA and Horsetail Plot

The environmental release mass of cesium at 72 hours is a primary figure-of-merit for the analysis. Figure 6-12 shows the time dependent release masses for all successful realizations, as well as the two reference realizations described in Section 5.2 There is a clear bifurcation in the results, with the higher release masses representing SGTR realizations, and the remainder of the realizations having much lower releases. The release masses for non-SGTR realizations are all below 0.14 kg at 72 hours while the SGTR realizations range between 0.24 kg and 11.46 kg released to the environment. The results are well distributed, with no clear splits except between the non-SGTRs and the SGTRs. The cesium release is still increasing at 72 hours in some of the realizations while others remain relatively constant.

As described in detail in subsequent sections, late increases in release masses are primarily due to containment liner yield, which is driven by pressurization from the decay heat in the ex-vessel core debris. This is evident in the many realizations where cesium release plateaus for a period of hours before increasing further near the end of the calculation.

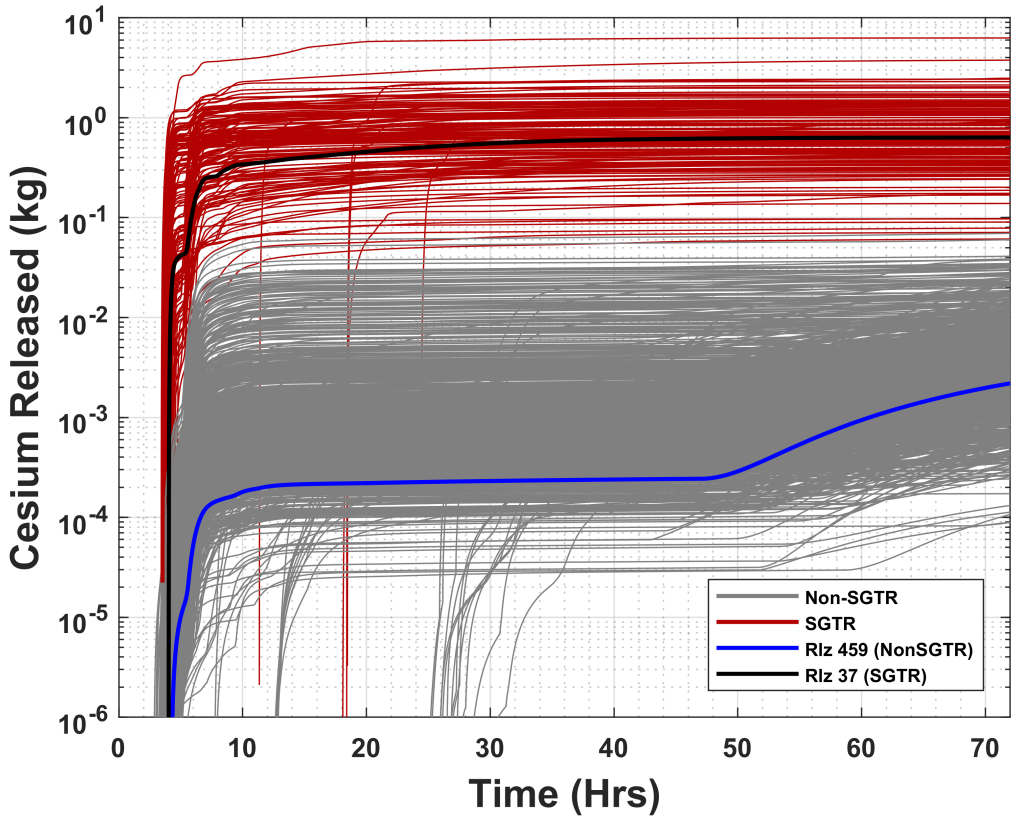

Figure 6-12 **Cesium Release Masses Over 72 Hours with Realizations Identified Near the Central Tendencies for Further Investigation**

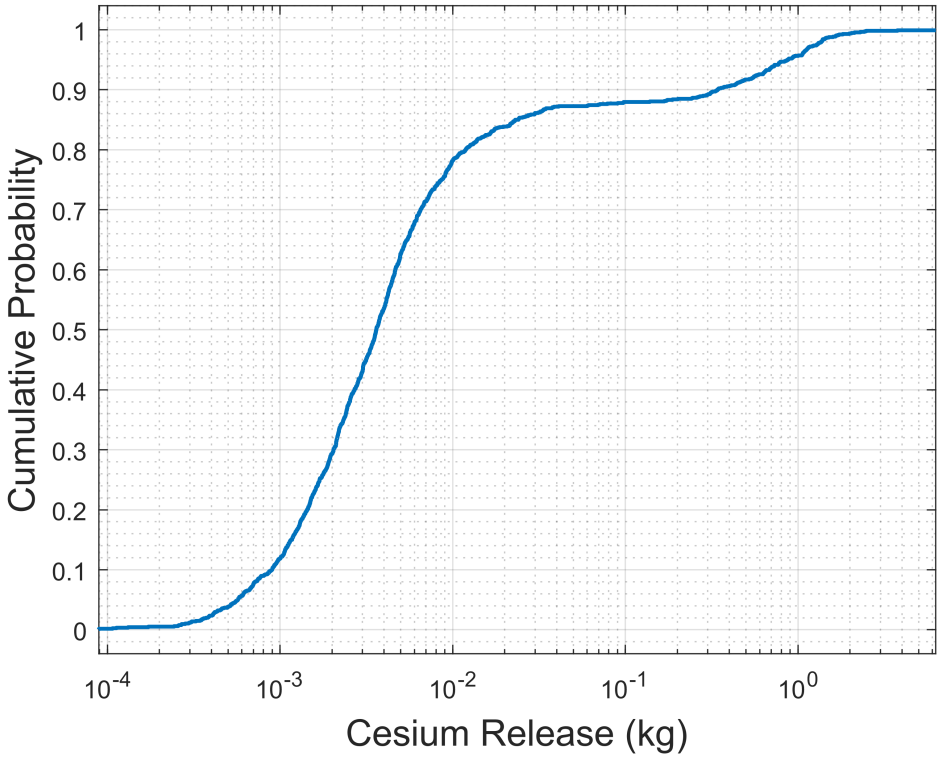

Figure 6-13 Cumulative Probability for the Cesium Release Mass after 72 Simulation Hours

As shown in Figure 6-14, the environmental release mass of cesium at 72 hours in the SOARCA STSBO run is 0.282 kg, which is above the 95th percentile of the non-SGTR results. The major differences between the Surry SOARCA model [3] and the new realizations affecting the iodine release were discussed in Section 6.1.1.1. The key differences are also applicable to release of cesium. Of course, the inclusion of iodine gas in the UA does not impact the cesium release. The differences in the cesium releases are also impacted by the variable chemical forms of cesium used in the new UA analysis versus predominantly cesium molybdate in the original SOARCA analysis. The new UA includes uncertainty sampling to specify between 20% to 100% of the remaining cesium after the combination with iodine as cesium molybdate. Any remaining cesium is cesium hydroxide (see Section 4.1.4.2). In contrast, the SOARCA analysis assumed 100% cesium molybdate after the combination with iodine and specification of the mass in the gap between the fuel and the cladding. Consequently, the new UA can have significantly more cesium hydroxide (e.g., up to 80% of the remaining cesium), which is significantly more volatile than cesium molybdate.

Similar to the iodine discussion, the previously cited factors are compensating. However, the most important factor contributing to the higher releases in the SOARCA calculation is the faster pressurization rate and earlier transition to a rebar yield failure at 25.5 hr. In contrast, most liner failures occurred after 48 hours in the UA simulations (e.g., primarily due to the lower decay heat powers and small gas generation by the basaltic concrete).

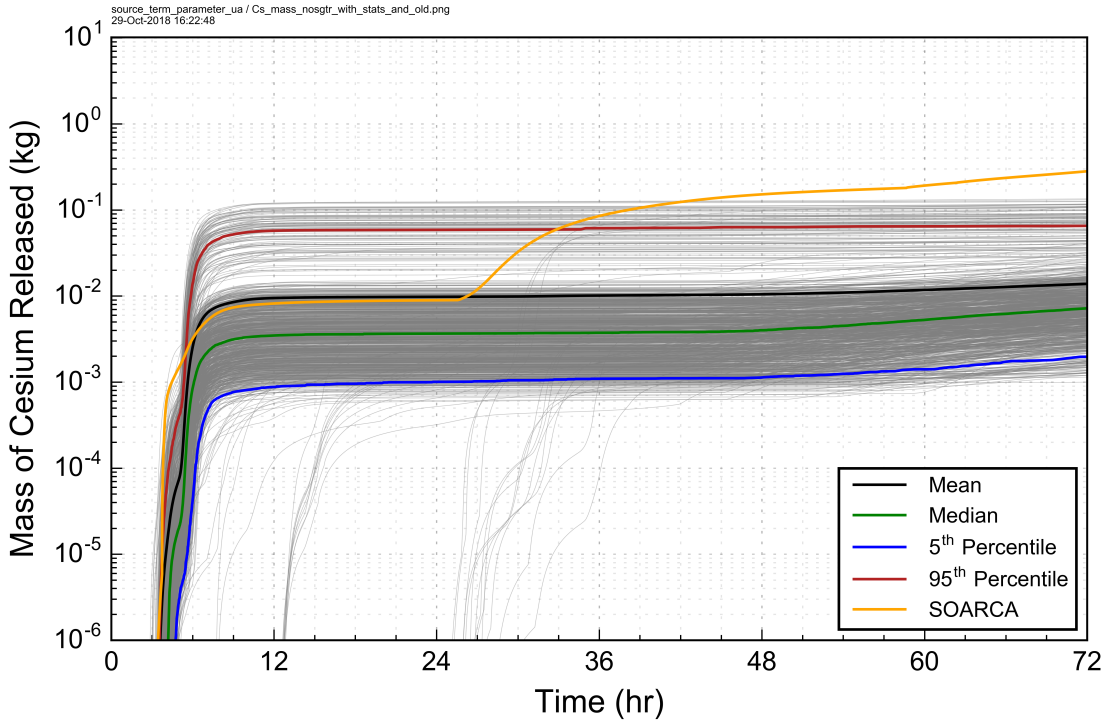

Figure 6-14 Comparison of Cesium Release Mass in the Original SOARCA STSBO to the Calculated Values of all Successful Realizations with a SGTR

6.1.2.2 Regression Tables and Scatterplots

Three sets of regression analyses were performed, one for all realizations, one for just SGTR realizations, and one for non-SGTR realizations. SGTR parameters dominated the regression results for all realizations due to the large bifurcation in cesium mass release between the SGTR and non-SGTR realizations. Since SGTR results have a unique section elsewhere in this report (Section 6.1.5), Table 6-4 just shows the results for the non-SGTR realizations.

The design leakage is the most important parameter by all the regression techniques. The next parameter identified as important in Table 6-4 is time at cycle although its importance is significantly lower. Section 6.1.2.3 discuses the technical rationale regarding the phenomenology behind the numerical effects of parameters detected in the regressions.

Table 6-4 Regression Analysis of Cesium Release Mass in Non-SGTR Realizations

	Rank Regression		Quadratic		Recursive Partitioning		MARS		Main Contribution	Conjoint Contribution
Final R^2	0.82		0.96		0.94		0.97			
Input	R2 contr.	SRRC	Si	Ti	Si	Ti	Si	Ti		
designLeakLa	0.50	0.70	0.94	0.96	0.96	0.99	0.92	0.96	0.800	0.027
ORIGENDay	0.21	0.46	0.02	0.04	0.02	0.04	0.02	0.06	0.068	0.024
rupture	0.05	-0.22	---	---	0.00	0.01	0.00	0.01	0.015	0.005
shapeFactor	0.03	0.18	0.01	0.02	---	---	0.01	0.01	0.011	0.005
Cs2MoO4Fraction	0.03	-0.16	---	---	---	---	0.01	0.01	0.008	0.000
Zr_brkout_T	0.00	-0.04	0.00	0.01	---	---	---	---	0.000	0.005

** highlighted if main contribution larger than 0.02 or conjoint contribution larger than 0.1*

6.1.2.3 Key Parameters for Non-SGTR Realizations

Containment Leakage (designLeakLa)

The nominal leakage rate from containment is a sampled variable. Prior to increased leakage due to containment liner yield, this is the only release path for radionuclides to the environment, excluding bypass events like a SGTR. The design (or nominal) leakage was identified by each regression technique as the largest contributor to uncertainty, accounting for at least 50% of the variance explained by the model in each case. Its influence was primarily independent, with little conjoint contribution. This is a logical result, as the majority of these realizations have late or no containment liner yield, leaving this leakage as the only release pathway for cesium. The scatterplot (Figure 6-15) shows a clear trend of increasing release mass with increasing design leakage.

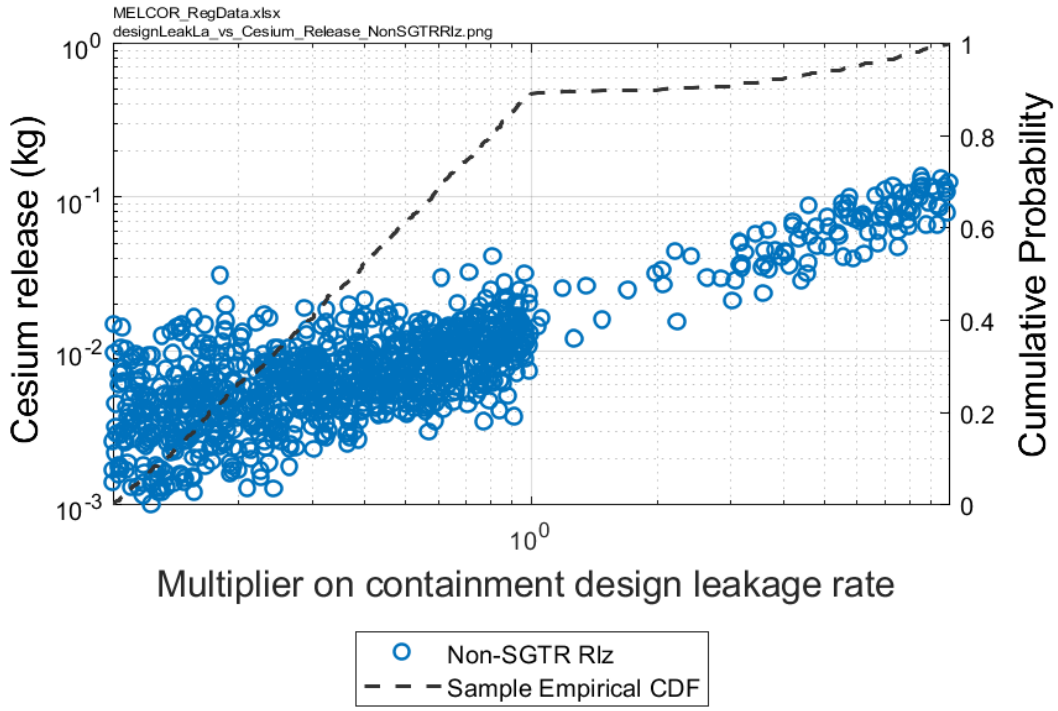

Figure 6-15 Scatterplot of Cesium Release Mass Versus Containment Leakage Input Values

Time at Cycle (ORIGENDay)

The ORIGENDay parameter specifies the time in the cycle and therefore the burn-up of the core. As the cycle progresses from the start-up, the decay power initially increases rapidly during the first 25 days and then slowly increases until the end of the cycle (e.g., see Figure 4-23). However, the cesium inventory increases steadily over the entire cycle (see Figure 4-22). The time at cycle impacts the timing of fuel heat-up, which in turn causes initial radionuclide releases, and later in the accident progression, the rate of containment pressurization. Each regression technique identified time at cycle as the second largest contributor to uncertainty, though in all but linear regression any detected effect is low.

The scatterplot in Figure 6-16 shows cesium release as a function of ORIGENDay. A clear bifurcation shows at ~0.03 kg suggesting a strong influence by some other sampled parameter. Figure 6 17, a colored enhancement of Figure 6-16, suggests that the other parameter is design leakage. The coloring in Figure 6 17 is by design leakage and it clearly shows that larger releases are associated with larger values of design leakage. Considering just the region in this figure below the bifurcation shows well that cesium release increases as ORIGENDay increases. The release of cesium to the environment then, in the UA MELCOR realizations, is clearly dependent upon the sampled parameters ORIGENDay and designLeakLA.

The dependence of cesium release on ORIGENDay is due to initial radionuclide class loading and associated fission product decay power. There is 128 kg of cesium at ORIGENDay 0.5 but twice that by day 550. The integral decay energy over the transient is 1,070 GJ for the

ORIGENDay 0.5-day realizations but 3,638 GJ by 550 days. A higher decay heat energy leads to stronger pressurization of the containment and increased leakage. Gross containment failure and associated release rate increases occur earlier with higher decay heat. The effect of containment pressure is described in more detail in a later section (Section 6.1.2.5).

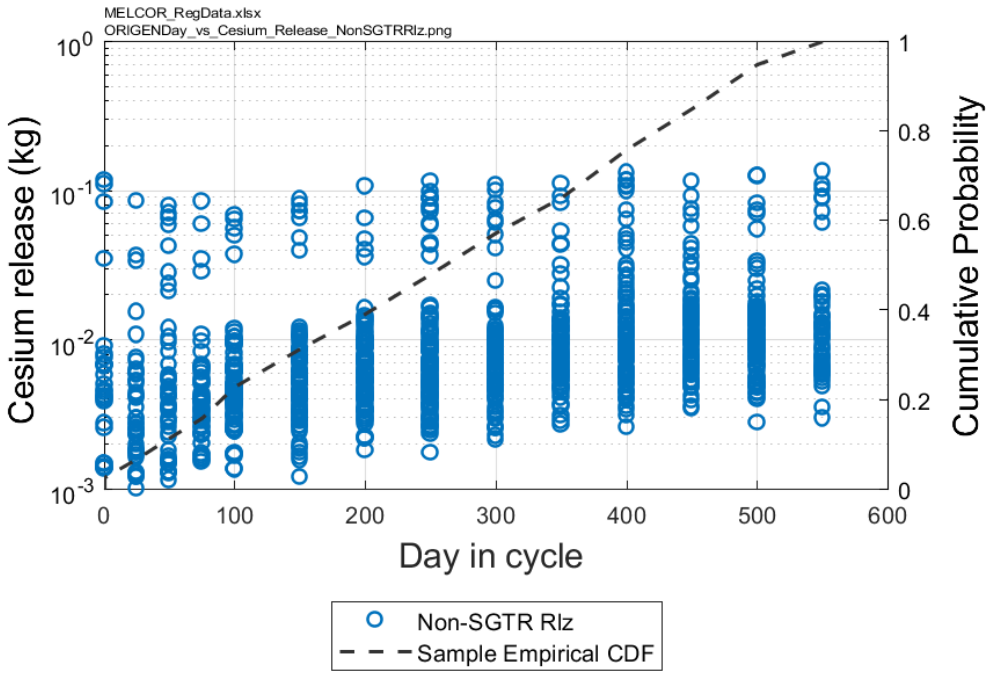

Figure 6-16 Scatterplot of Cesium Release Mass Versus Day in Cycle

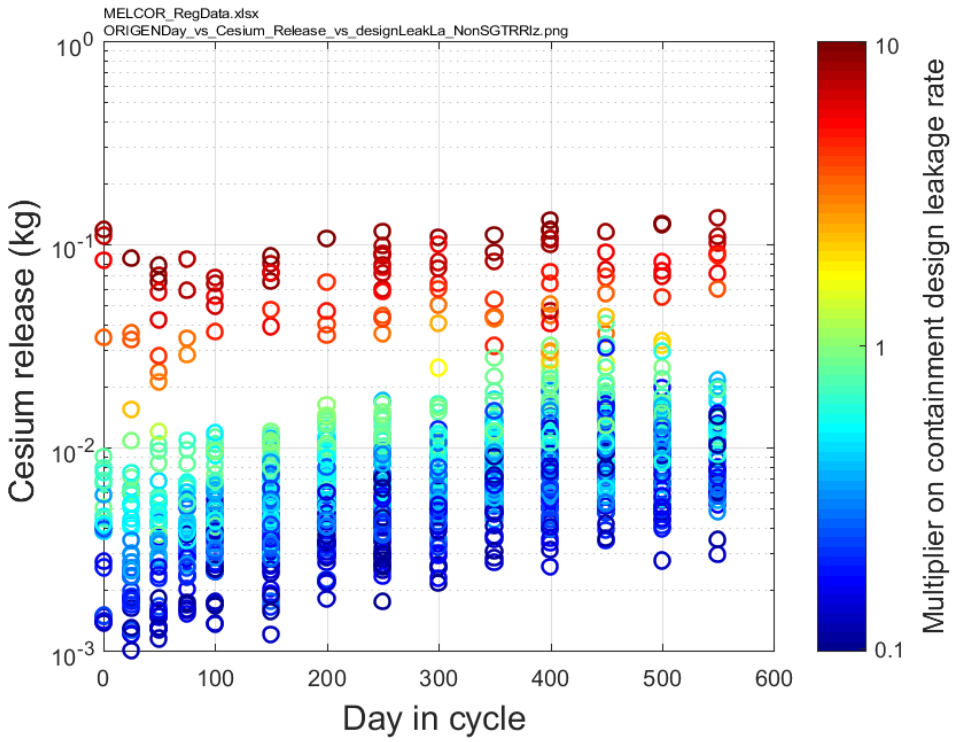

Figure 6-17 Scatter Plot Illustrating the Relationship Between Day in Cycle, Cesium Release, and the Multiplier on Containment Design Leakage

Other Parameters

When looking at the regression results for all successful realizations rather than separating by occurrence of SGTR, the results were completely dominated by the severity of flaw depths within the SG tubes. These flaw parameters relate to the frequency of SGTRs. The sampled flaw depth acts as a stress multiplier on the creep rupture equation, and since the secondary is always depressurized, it is the primary determinant on whether a SGTR occurs. Once there is a SGTR, MSIV leakage is the primary environment bypass leakage path. If a SV failed open on the same line as the SGTR, the failed valve at its sampled open area fraction is also treated as an environment bypass leakage path. The SGTR results are described in detail in Section 6.1.4 but are mentioned here due to their dominance over regression results for all realizations and the fact that those releases are 1 to 2 orders of magnitude larger in their fission product releases.

6.1.2.4 Timing and Other Effects

The considerations presented in Section 6.1.1.4 with respect to the timing of I release to the environment are fully applicable to the timing of Cs release. Almost all of the releases are steady between about 10 and 40 hours (see Figure 6-12). After this time, the majority of releases start to increase again due to liner failure. The magnitude and timing of the cesium release is strongly impacted by the decay heat power (i.e., time at cycle). The magnitude of the decay power impacts the containment pressurization through the heating of the containment atmosphere, the rate the water on the containment vaporizes, and the rate noncondensable gases are generated in the core concrete interaction. Lower decay powers in the UA realizations slow down these effects and hence have weaker pressurizations.

6.1.2.5 Release Mass to Environment – Conclusions

The non-SGTR cesium environmental release mass released to the environment at 72-hr of 0.281 kg in the original SOARCA calculation is above the non-SGTR range from the UA results. Some differences were expected due to the variable time at cycle in the new UA versus using the end of cycle in the SOARCA calculation, the variable distributions of cesium molybdate and cesium hydroxide in the UA versus primarily cesium molybdate in SOARCA, the error in the concrete type in the original SOARCA evaluation, the variance in the nominal containment leakage modeling in the UA versus only design leakage in SOARCA, and the modifications to the containment failure model for the new UA. The most important factor is the earlier liner yield time of 25.5 hours due to the more rapid containment pressurization from the limestone concrete (i.e., see Appendix A of Reference [8] for a full discussion and comparison). The strong pressurization from the ablation of the limestone concrete caused a much earlier and large release in the SOACRA calculation versus the UA results. The concrete type was corrected to basaltic composition for the UA, which had significantly less non-condensable gas production.

There is a large split between SGTR and non-SGTR realizations, with SGTRs having one to two orders of magnitude higher release masses. For non-SGTRs (87% of realizations), the spread of release masses, excluding low outliers, is one order of magnitude. As expected, there is a very strong correlation between the parameters with highest importance for iodine releases and those for cesium releases. The most important parameter for the non-SGTR realizations is nominal containment leakage, which provides a pathway to the environment and slightly influences the timing of containment liner yield. The time at cycle explains a significant portion of the remaining uncertainty, i.e., determining containment pressurization rates and fission product inventories. Releases increase with containment liner yield, and especially rebar yield and concrete rupture, but no 0.5-day decay heat realizations reach either failure within 72 hours. For the remaining decay heat curves, the containment liner yield becomes more important and rebar yield is occasionally reached (i.e., 16 realizations out of 1147). However, these effects do not significantly change time at cycle independent regression results. The relative lower importance of containment failure mechanism suggests little cesium is airborne at the containment failure and there is not any significant amount of cesium revaporization. The chemical form of cesium, while always in the top six parameters, never contributed to a significant amount of the uncertainty.

6.1.3 Hydrogen Production

The in-vessel hydrogen production in the Surry model is primarily due to oxidation reactions of the Zircaloy fuel cladding, although there is also some hydrogen produced by oxidation of stainless steel structures. The cladding oxidation continues at rapid rate until the Zircaloy interior of the zirconium oxide shell melts, breaks through the oxide layer, and relocates. The released molten zircaloy relocates downward until it freezes on cooler surfaces or reaches debris blockage. Eventually, the fuel rods collapse, which creates a debris bed. The amount of in-vessel zircaloy oxidation rate is relatively low following the core degradation due to the inability of steam to flow freely into the debris bed and reduced amount of open surface area.

The onset of hydrogen release and total production are indicators of the start and magnitude of the fuel damage, respectively. The release of hydrogen is also an indicator for radionuclide releases as these occur during the fuel damage progression. The amount of hydrogen produced in-vessel, along with the ex-vessel production of hydrogen and other NCGs during CCI, are also the primary influences on whether combustible conditions are reached in containment. The prediction of hydrogen combustion is important for the pressure increases that augment

containment leakage and fission product releases to environment and possibly challenge the containment integrity.

6.1.3.1 Comparison to SOARCA and Horsetail Plot

The total amount of hydrogen produced at 72 hours is the primary figure-of-merit for the analysis. Figure 6-18 shows the time dependent hydrogen production for all the realizations (i.e., both the SGTRs and the non-SGTRs). The reference realizations that were described in Section 5.2 are also identified in the figure. The total hydrogen production is between about 200 and 700 kg, with one realization above the overall population at 777 kg. Figure 6-20 illustrates the cumulative probability for the quantity of hydrogen produced. The trend is generally smooth compared to the cesium and iodine mass release horsetails because there is not a significant difference in hydrogen production between the SGTR and non-SGTR realizations. Sections 5.3.12 describes the realization with the highest in-vessel hydrogen production.

It is also evident that the SGTR and non-SGTR reference realizations are good representatives of central tendency in the total population of realizations. The reference realizations were selected to be near the median for hydrogen productions as well as other figures-of-merit in their respective groupings (i.e., non-SGTR or SGTR). The behavior of SGTR and non-SGTR reference realizations with respect to hydrogen production is practically indistinguishable. For most realizations, the hydrogen production begins within four hours of the transient and ceases by 10 hours. However, there is a subset of realizations that do not begin hydrogen production until after four hours with some having no production until 25 hours into the sequence. As illustrated in Figure 6-19, all of these late-time hydrogen generation realizations belong the 0.5-day decay heat curve set. As discussed in Section 5.3, the slow heatup in the 0.5 day decay heat curve realizations also led to some of the largest hydrogen generations (see Figure 6-19).

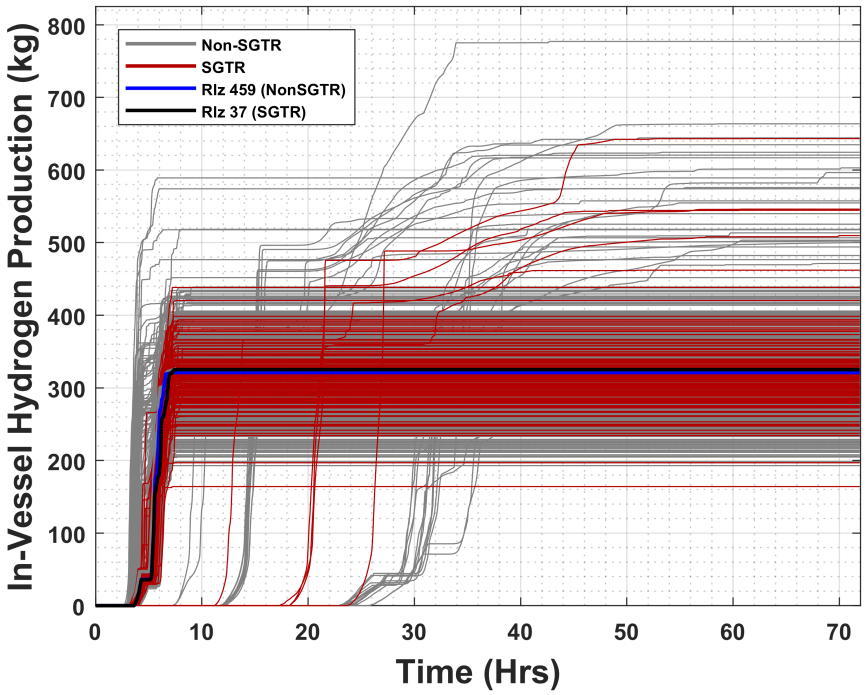

Figure 6-18 Total Hydrogen Production Over 72 Hours with Reference Realizations Identified for Single Realization Analysis

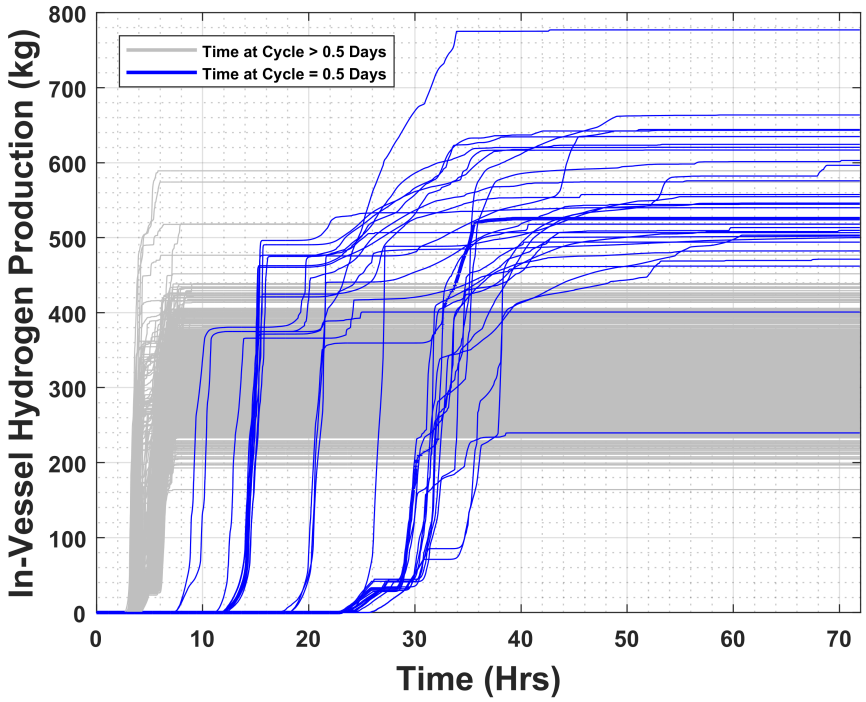

Figure 6-19 **Total Hydrogen Production Over 72 Hours Demonstrating that Realizations with Hydrogen Production Beginning after 6 Hours have a Sampled Time at Cycle Value of 0.5 Days**

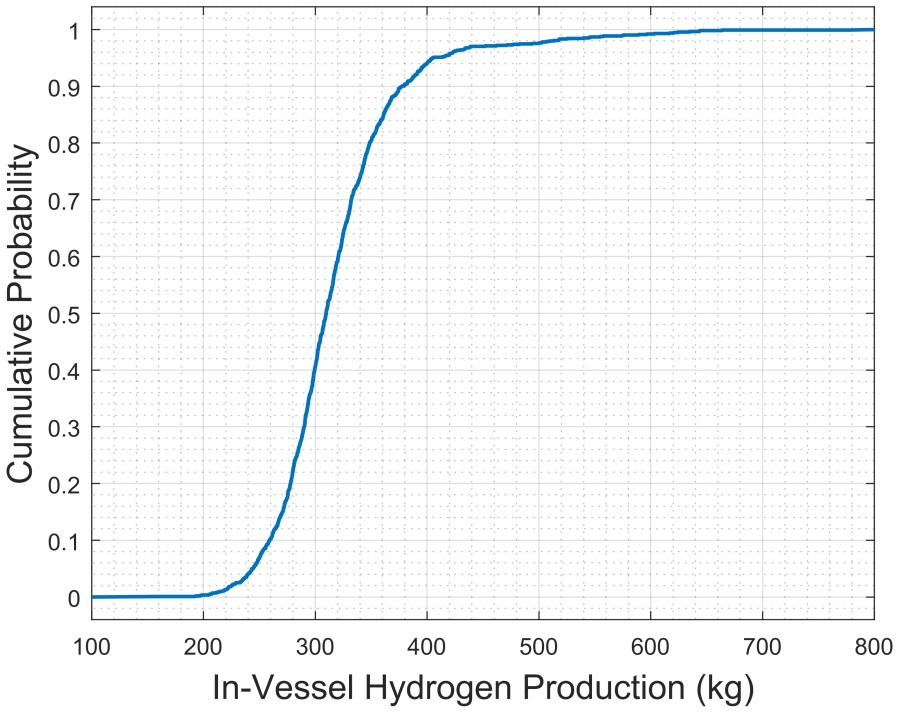

Figure 6-20 **Cumulative Probabilities for the Quantity of Hydrogen Produced for Selected Time Intervals**

Figure 6-21 shows the total amount of hydrogen produced in the original SOARCA STSBO run was 349 kg, which is slightly above the mean and median from the UA results but below the 95th percentile. For the first hour of the release, the original SOARCA results follows the 95th percentile curve. The SOARCA in-vessel hydrogen production stops shortly after lower head failure and core debris discharge into the containment (i.e., debris transfer occurs from 7 hr 16 min to ~8 hr). Most of the realizations show similar signature to the SOARCA result with a relatively discrete stopping point for hydrogen production once fuel relocation occurs.

The earlier rise in the hydrogen production in the SOARCA calculation is due to the higher decay heat power (i.e., the SOARCA calculation used a high burn-up EOC whereas the UA sampled from BOC to EOC). After the earlier rise in the SOARCA calculation, there were two key changes and a code modification that contributed to the higher total in-vessel hydrogen production in the SOARCA result. First, the sampled fuel melting temperature was lower in UA, which led to an earlier collapse of the fuel rods. The SOARCA value is at the 100th percentile of the UA distribution (see Section 4.1.2.3). Second, the SOARCA molten zircaloy breakout temperature was at approximately the 70th percentile. Once the molten zircaloy is released, the oxidation stops. Consequently, the SOARCA oxidation continued longer due to the higher molten zircaloy breakout temperature. Finally, MELCOR 2.2 code used in the UA calculations included some improvements to the post-accumulator quench model that impacted the late-phase stainless steel hydrogen production (e.g., see [7]).

The UA also included some parameters that could increase hydrogen production. For example, the UA included oxidation model sampling that included a correlation with a higher oxidation kinetics rate constant at high temperatures. However, the impact of the oxidation correlation can be non-intuitive as it can also promote an earlier collapse of the fuel. The UA also includes variable time at cycle (i.e., decay heat sampling) and stuck-open pressurizer SVs, which can also increase hydrogen production. Overall, the impact of the parameters that could increase the hydrogen production had a lower influence than the previous cited parameters that decreased the hydrogen production.

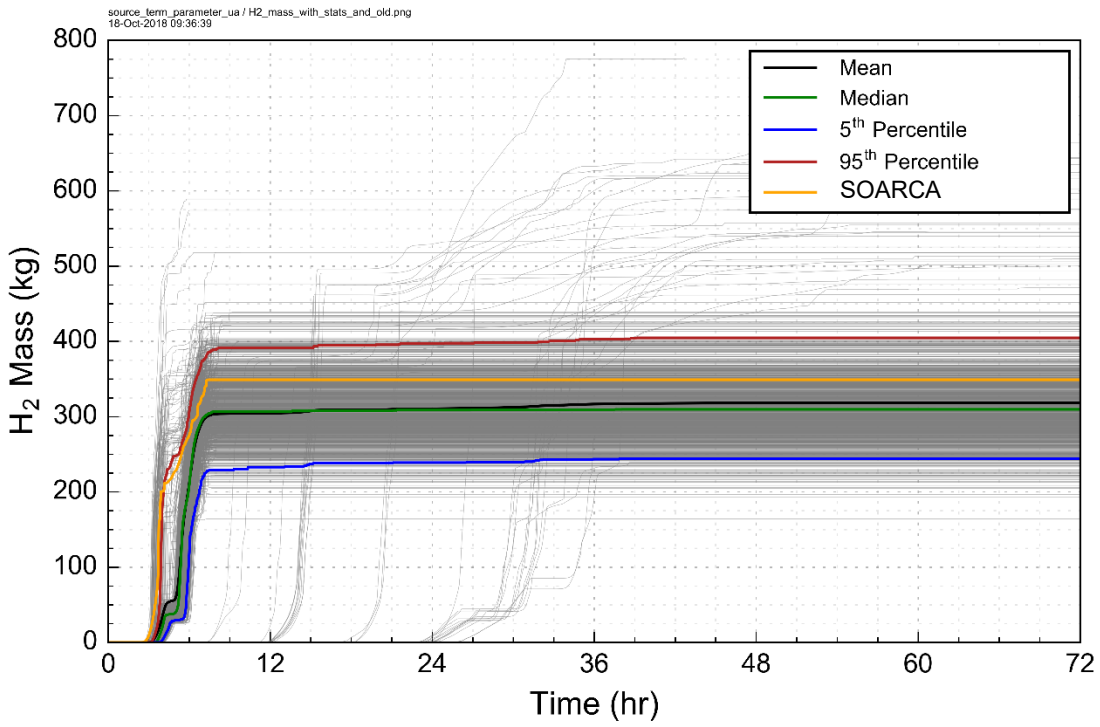

Figure 6-21 Comparison of Hydrogen Production in the Original SOARCA STSBO to the Calculated Values of all Successful Realizations

6.1.3.2 Regression Tables and Scatterplots

Regression analyses were performed with all successful realizations. It was not necessary to look at the SGTR and non-SGTR realizations separately for hydrogen production as there is no significant difference in the hydrogen production between the two populations. In the following section, the technical rationale is provided to explain the phenomenology that drives the importance of Key Parameters identified by the regression analysis as well as other parameters of interest in contributing to uncertainty in in-vessel hydrogen production.

The main result from the regression analysis is that the time in cycle continues to be an important parameter just as it was for cesium and iodine release masses. The regression methods disagree on the ranking of the two most important parameters, with the eutectic melt temperature being identified first by two regression models and time in cycle being identified first by the other two. The models agree that zirconium melt breakout temperature is the third most important parameter and generally agree on the importance of primary valve behavior and RCP seal leakage. High RCP leakage promotes an earlier uncovery of the core at higher decay heat power.

Table 6-5 Regression Analysis of Hydrogen Production in all Realizations

	Rank Regression		Quadratic		Recursive Partitioning		MARS		Main Contribution	Conjoint Contribution
Final R^2	0.40		0.44		0.76		0.61			
Input	R2 contr.	SRRC	Si	Ti	Si	Ti	Si	Ti		
ORIGENDay	0.02	-0.14	0.27	0.27	0.51	0.53	0.42	0.43	0.195	0.006
EU_melt_T	0.23	0.46	0.34	0.39	0.20	0.31	0.26	0.30	0.172	0.043
Zr_brkout_T	0.10	0.29	0.11	0.14	0.05	0.16	0.08	0.11	0.057	0.038
priSVfrac	0.03	0.33	0.10	0.12	0.05	0.06	0.10	0.10	0.043	0.007
RCP_Leak	0.00	0.08	0.10	0.10	0.02	0.03	0.07	0.08	0.026	0.004
Zr_drn_rate	0.02	-0.14	0.02	0.02	0.01	0.05	0.03	0.03	0.013	0.011
Ox_model	0.01	0.09	---	---	0.00	0.02	0.01	0.01	0.003	0.005
tubeHotA_NFD	---	---	---	---	0.01	0.01	0.00	0.01	0.002	0.003

** highlighted if main contribution larger than 0.02 or conjoint contribution larger than 0.1*

6.1.3.3 Key Parameters

Time at Cycle (ORIGENDay)

The time at cycle determines the burnup of the core, which has two main effects: the magnitude of the decay heat and the radionuclide inventories. The integrated decay energy at 72 hours is shown in Figure 6-22 and summarizes the decay heat load increase as a function of the time at cycle. The amount of decay heat is the primary factor in initial core heat up and the time to onset of oxidation. There is nearly a factor of three increase in net energy output between 0.5 days and 25 days of irradiation. The incremental increases in net energy become smaller with more time at cycle to a maximum of approximately 3,600 GJ. The three more complex regression techniques (i.e., Quadratic, Recursive Partitioning, and MARS) indicated time at cycle was the first or second most important parameter in explaining uncertainty.

Although oxidation starts earlier with increased burn-up, the scatterplot (Figure 6-23) shows that there is a slight trend of lower total hydrogen production with higher burn-up. The reason for the trend is an accelerated core melt progression that leads to a faster collapse of the fuel and earlier lower head failure, which ends the in-vessel oxidation phase. At the other end of the spectrum, the lowest decay heat level promoted a very slow heat up of the fuel. The subsequent oxidation phase was much longer, which led to significantly higher integrated hydrogen generation totals. Similar to the shape of the integrated decay heat curve in Figure 6-22, the impact of the reduction in the integral hydrogen generation is relatively small after first time at cycle value.

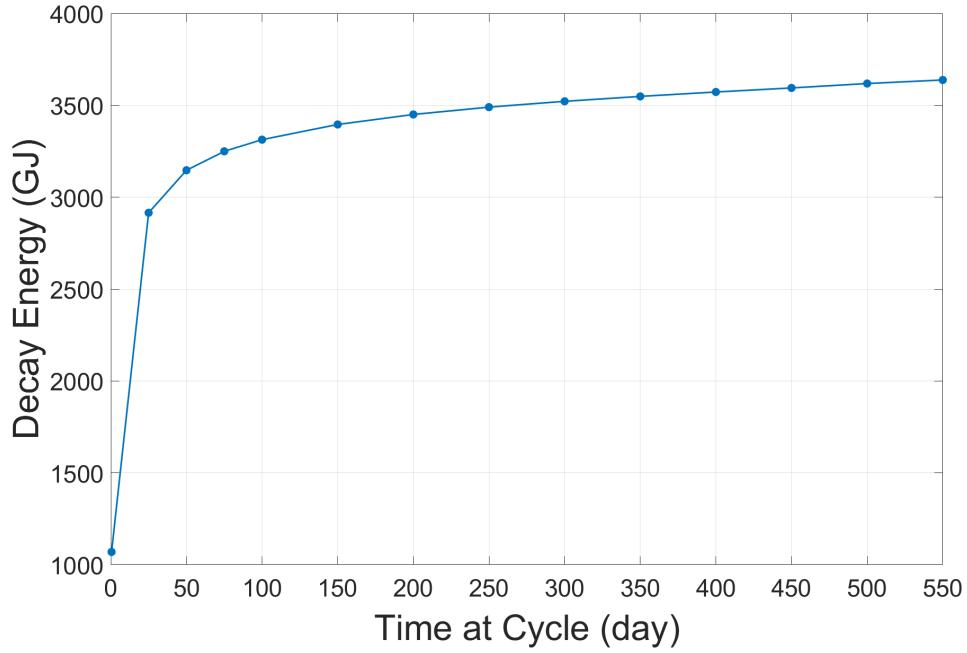

Figure 6-22 Plot of Integrated Decay Energy at 72 Hours for Each Time at Cycle

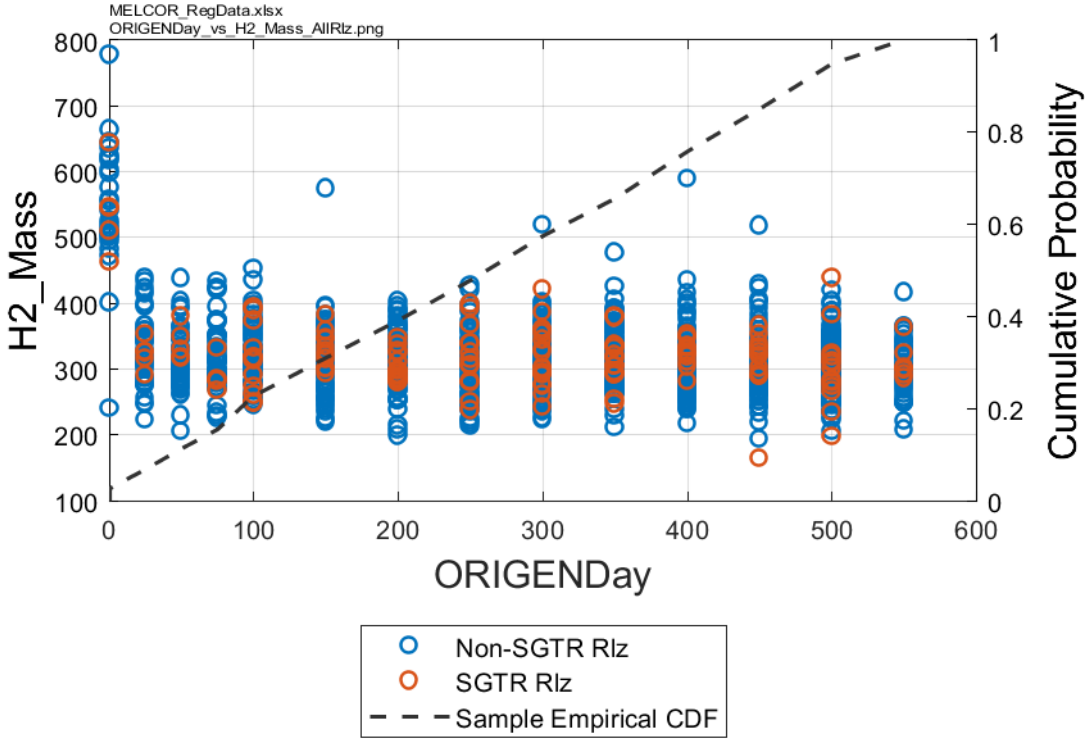

Figure 6-23 Scatterplot of In-Vessel Hydrogen Production Versus Time at Cycle

Temperature at which the Eutectic Formed from UO_2 and ZrO_2 Melts (Eu_Melt_T)

The effective eutectic melting temperature is a surrogate for a number of chemical reactions that lead to fuel melting and relocation. It specifies the temperature where the eutectic formed from UO_2 and ZrO_2 melts, which also specifies the timing of the fuel collapse. The Eu_Melt_T parameter was identified as the first or second most important parameter by the four regression methods. The scatterplot (Figure 6-24) shows a linearly increasing trend for hydrogen production as a function of the eutectic melt temperature. As the eutectic temperature increases, the intact fuel oxidation phase extends longer and to higher temperatures. These two factors directly contributed to more hydrogen production. There was no observable sensitivity for SGTR versus non-SGTR hydrogen totals or profiles for this parameter. These factors support combining all realizations for the analysis of uncertainty in the hydrogen production.

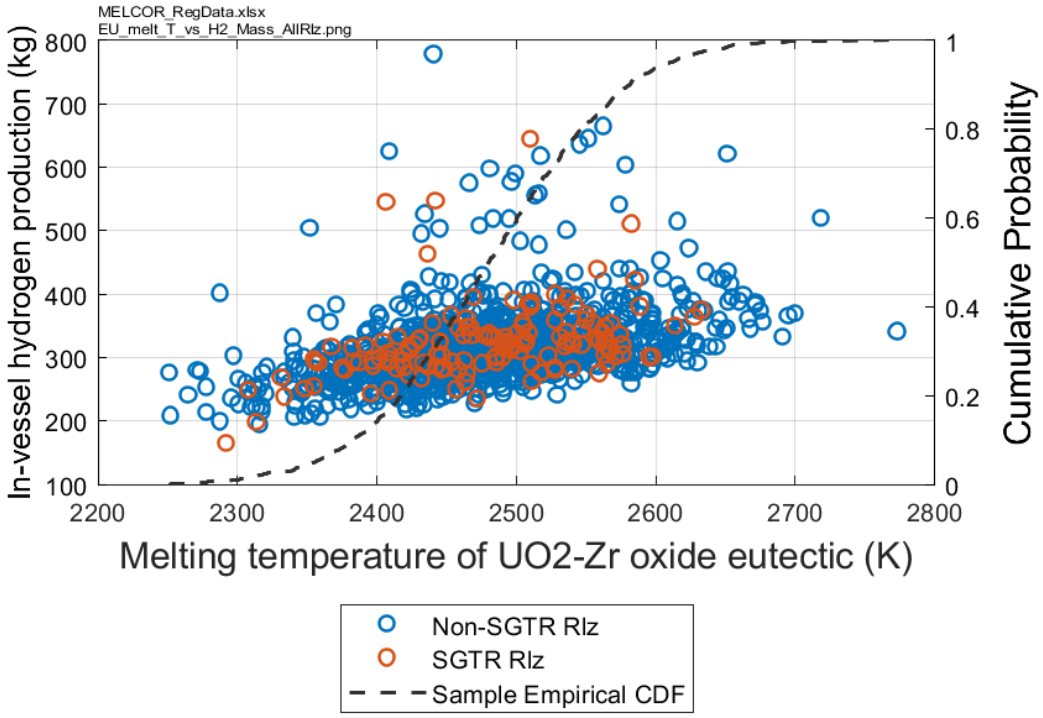

Figure 6-24 Scatterplot of In-Vessel Hydrogen Production Versus Eutectic Melt Temperature Input Values

Zircaloy Breakout Temperature (Zr_brkout_T)

The Zr_brkout_T parameter determines the temperature at which molten Zircaloy breaks through the oxide layer. Following the failure of the oxide shell, the molten Zircaloy relocates and freezes at lower elevations. Any subsequent oxidation of the relocated conglomerate Zircaloy is usually very small relative to the intact fuel oxidation phase. The open lattice of the intact fuel is much more conducive to oxidation than the relocated conglomerate. The rank regression identifies this parameter as second most important parameter while the other three calculated a lower contribution to the uncertainty. The scatterplot in Figure 6-25 shows a small

trend toward more hydrogen production with higher temperatures. This would be an expected result since higher temperatures allow more time for oxidation. The correlation is likely impacted because the fuel could collapse prior to the breakout of the molten zircaloy. The range of the effective melting temperature of the fuel and the fuel collapse overlaps the upper range of the zircaloy breakout temperature. Consequently, some realizations progress with a collapse of the fuel rods prior to the release of the molten zircaloy. These realizations fall in the shaded areas of Figures 6-26 and 6-27 which show hydrogen production as a function of eutectic melting temperature and Zr breakout temperature with 0.5-day time-in-cycle realizations removed. Noteworthy in these figures is that hydrogen production:

- trends higher with increasing eutectic melting temperature combined with increasing Zr breakout temperature,
- increases with Zr breakout temperature for a given eutectic melting temperature,
- varies sporadically with eutectic melting temperature for a given Zr breakout temperature, and that
- the cases with lowest hydrogen production associate with fuel rods collapsing before Zr breakout has an opportunity to occur.

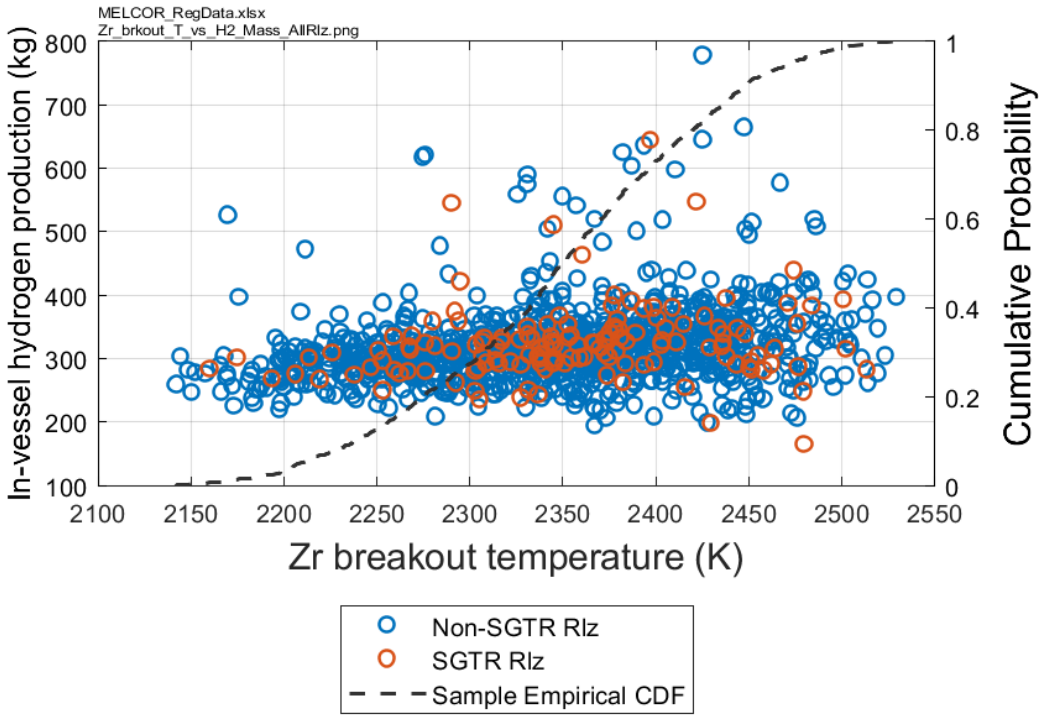

Figure 6-25 Scatterplot of In-Vessel Hydrogen Production Versus Zircaloy Breakout Temperature Input Values

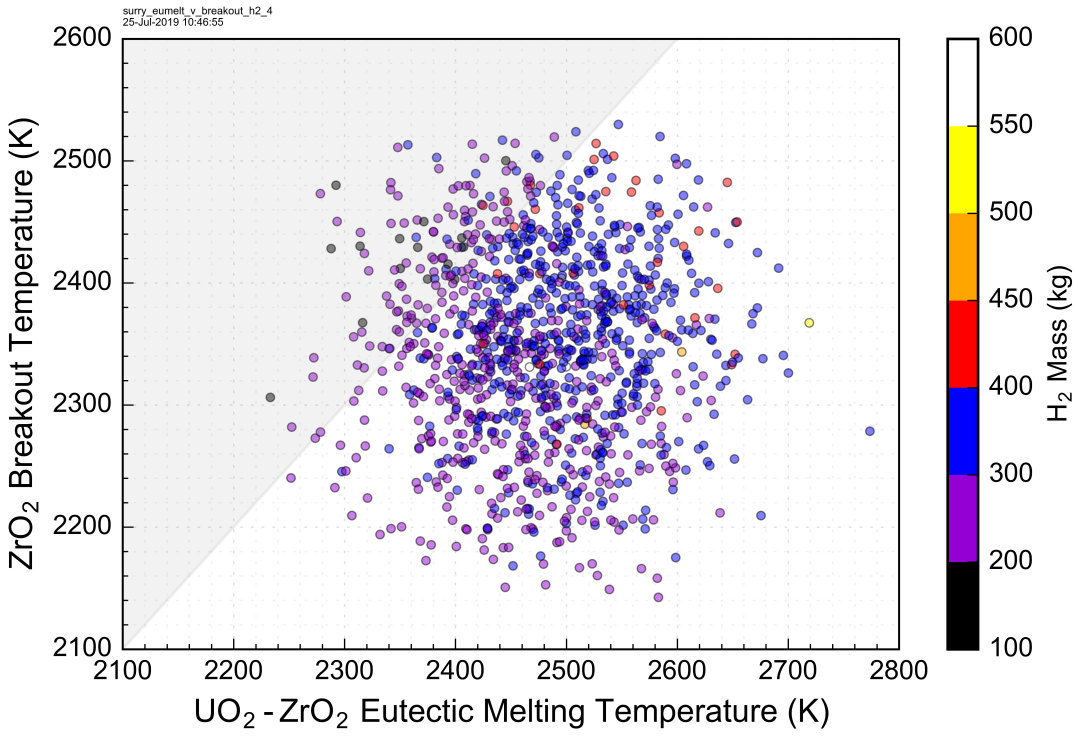

Figure 6-26 Scatterplot of In-Vessel Hydrogen Production Versus Eutectic Melting Temperature and Zircaloy Breakout Temperature (Full Color Scale)

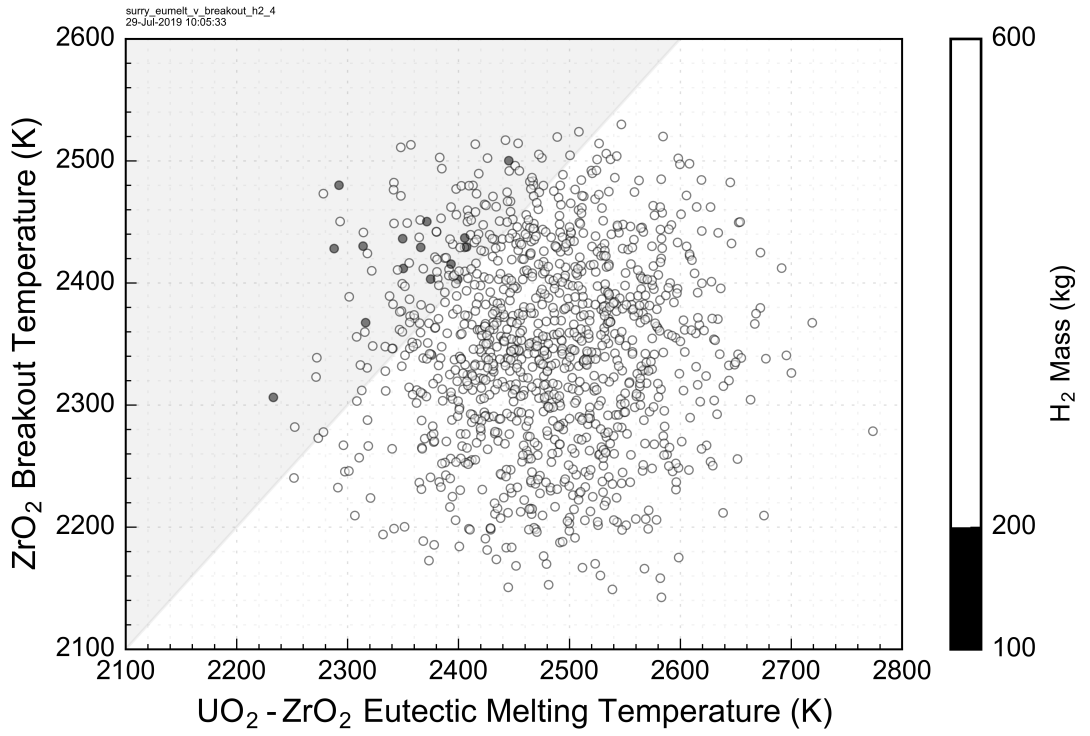

Figure 6-27 Scatterplot of In-Vessel Hydrogen Production Versus Eutectic Melting Temperature and Zircaloy Breakout Temperature (Limited Color Scale)

Pressurizer SV Open Fraction (priSVfrac)

This parameter indicates the open fraction of the primary SV system at 72 hours. The open fraction identifies the valve failure area if it reached the sampled failure cycle during the transient. The failure cycle is randomly sampled from the distribution described in Section 4.1.1.2. If one SV experienced a cycling failure, then the failed valve open fraction is used. If multiple SVs experience cycling failure, then the open fractions are summed.

The open fraction was identified by the three more advanced regression techniques (i.e., Quadratic, Recursive Partitioning, and MARS), as having the third or fourth most important contribution to uncertainty in hydrogen production. The rank regression had a low importance of the valve open fraction. Since most of the realizations did not have a valve failure, the majority of the realizations are located on the y-axis and show no correlation with the valve area (Figure 6-28). The remaining realizations with non-zero failure areas show a possible parabolic trend, with hydrogen production peaking at an open fraction of 0.5. However, due to the limited number of non-zero realizations, it is impossible to conclude whether the few data points between 0.2 and 0.8 exhibit a meaningful trend.

Although the priSVfrac parameter was used instead of the priSVcyc parameter, the two parameters are interrelated. The priSVcycle parameter gives the number of normal cycles until a primary SV fails to fully close. If a SV failed, then the parameter is simply the number of cycles to failure; however, if the first SV failed with a small open area fraction and a second SV failed as a result, then the parameter is the sum of all cycles to failure. In most of the realizations, the

sampled number of cycles is great enough that no SV failures occur. The priSVcycle parameter is assigned to the number of cycles that occurred over all valves when there is no valve failure.

The priSVcycle scatterplot (Figure 6-29) shows potentially high hydrogen generation rates when the valve fails on or near the first opening. However, several of these high hydrogen realizations also occurred with an early time at cycle and leakage through the RCP seals that also limited pressurizer cycling. There is another large spread near 40 cycles, which occurs near the start of the fuel heatup. If the valve fails at the start of the heatup, then the subsequent blowdown during this phase can delay the heatup and allow for higher hydrogen generation totals. The majority of the realizations continued without any valve failures until the hot leg creep rupture near 70 cycles. In these realizations, the majority of the hydrogen generation occurred after the hot leg creep rupture (i.e., see the reference realizations in Section 5.2). The decay heat power or the eutectic melting temperature better explains the distribution at high end of the primary SV cycles.

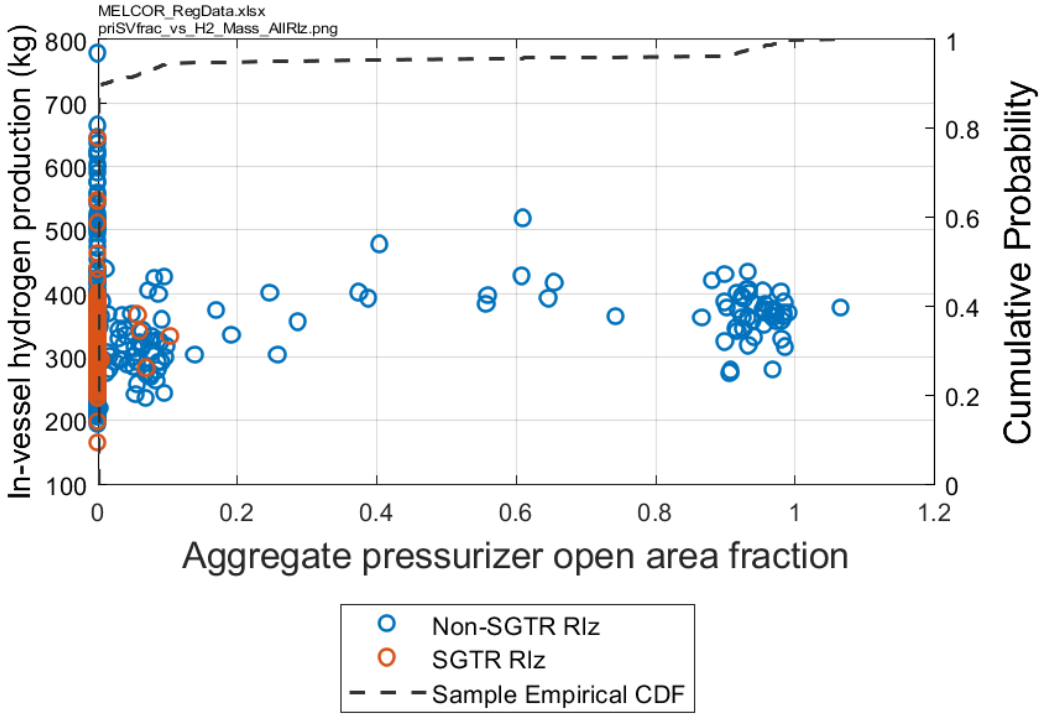

Figure 6-28 Scatterplot of In-Vessel Hydrogen Production Versus SV 72-Hour Post-Calculated Aggregate Open Area Fraction

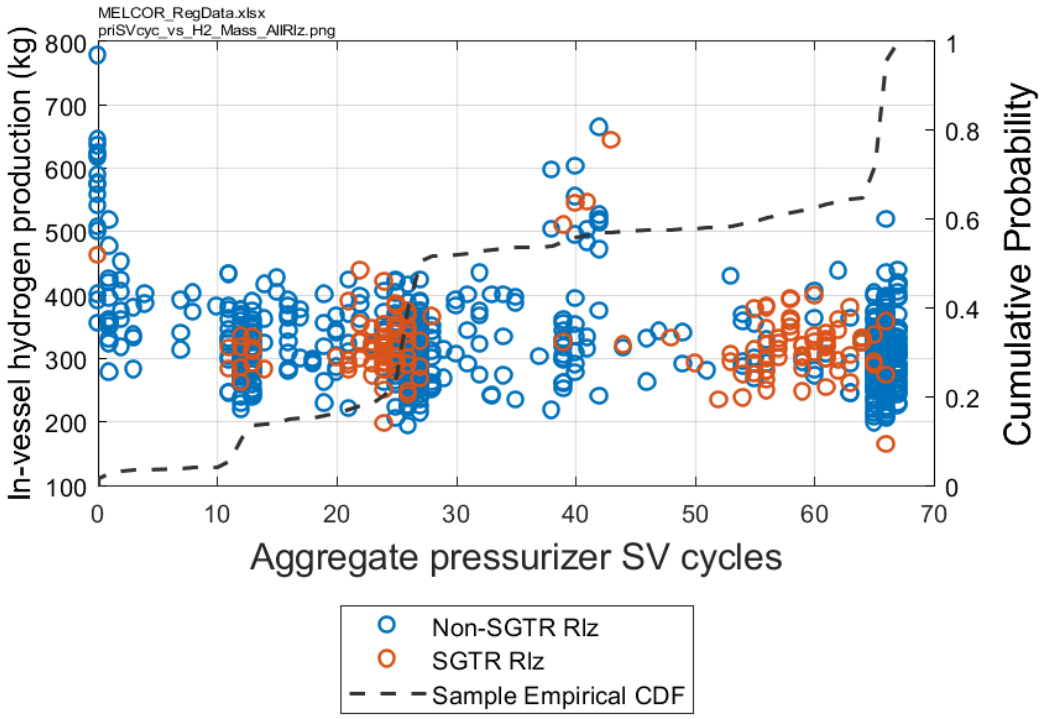

Figure 6-29 Scatterplot of In-Vessel Hydrogen Production Versus Aggregate Primary SV Cycles

RCP Seal Leakage

The RCP seal leakage has a minor contribution to hydrogen uncertainty, which is comparable to that of the aggregate primary SV open area fraction. The RCP seal leakage may contribute to the primary system's depressurization and inventory loss if seal failures occur at 13 min.[66] Although it occurred infrequently, very high combined RCP seal leakages totals above 500 gpm showed a trend for increasing hydrogen production. The high leakage promoted a faster inventory loss and earlier onset of hydrogen generation with higher decay power. The RCP leakage amounts above 500 gpm only had one realization with less than 300 kg of total hydrogen generation. However, this was not a strong correlation since the range of the more prevalent smaller RCP leakage rates also encompassed the higher RCP leakage rate distributions.

[66] The RCP seals leak following the loss of the seal cooling injection flow when the onsite power is lost. The seal chambers fill with the hot primary system fluid within 13 min and are susceptible to failure. The RCP leakage uncertainty parameter samples on the increased leakage from seal failures at 13 minutes. Due to the construction of the seal package, various modes of seal failures may occur that lead to varying amounts of addition leakage. Note that Surry has replaced their pump seals with low leakage Flowserve N-9000 seals (see Section 4.1.1.4). Consequently, Surry would respond better than the lowest sampled leakage values with respect to this uncertain parameter.

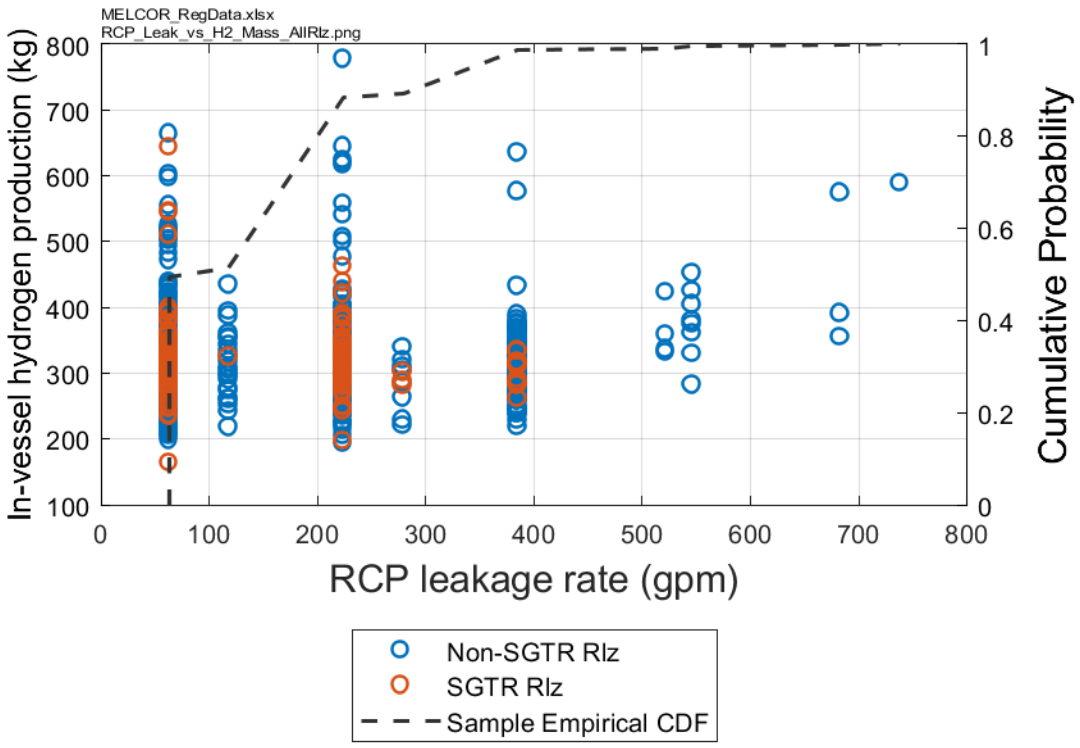

Figure 6-30 Scatterplot of In-Vessel Hydrogen Production Versus the RCP Seal Leakage Rate Combined Over All Seals

Other Parameters

The molten clad drainage rate and the oxidation model are not listed in the top six most important parameters, although each has a very minor conjoint contribution. The drainage rate places a maximum on the flow rate of molten material following the failure of a flow blockage. However, the duration of the molten zircaloy drainage is relatively fast and did not significantly impact the results. The oxidation model showed the highest importance in the Sequoyah UA [7] and was also expected to have some impact on Surry UA. The low importance of the oxidation model is believed to be related to the more continuous sampling of time at cycle in the Surry UA. In the Sequoyah UA, a significant fraction of the realizations (i.e., 1/6 in the Sequoyah UA versus 1/14 in the Surry UA) were assigned to a beginning of cycle decay heat (i.e., 6 days at cycle for Sequoyah). The low decay heat and slower heatup would increase the impact for the various oxidation models, especially in the high temperature phase (i.e., particularly the higher oxidation kinetics in the Leistikov-Schanz/Prater-Courtright model). No other parameters had an independent contribution to hydrogen production uncertainty, nor are there any other parameters that were expected to have a significant contribution that didn't.

6.1.3.4 Timing and Other Effects

There is an observed timing difference in the onset of hydrogen production, shown in the horsetail in Figure 6-19. There is a clear split between the majority of hydrogen time series, in which hydrogen production starts between 3 and 6 hours and ends before 10 hours, and the realizations with later initiation of hydrogen production starting between about 7 hours 26 hours and ending between 10 and 68 hours. As shown in Figure 6-19, all of the realizations with later

hydrogen production are the realizations with earliest time in cycle (0.5 days). The same bifurcation due to time at cycle is evident in the RPV water level, as show in Figure 6-31.

Specifically, the time at cycle determines the first initiation of hydrogen production. All realizations with a time at cycle greater than or equal to 25 days of irradiation begin hydrogen generation at approximately the same time while all 0.5-day realizations begin production several hours later and with a much larger variability in onset times. The decay heat, therefore, has the dominant influence on timing by affecting the boildown rates, SV cycling frequency, and oxidation rates. Then, for a given decay heat curve, variation in the hold-up parameters, the eutectic and Zircaloy breakout temperatures, influence the total amount of hydrogen generation by changing the amount of time the fuel remains intact and oxidizing. The remaining parameters indicated as significant, primary SV failure open fraction and RCP leakage rate, determine the depressurization and water level decrease rate of the primary system. However, as discussed in the previous section, the time at cycle and the eutectic melting temperature had the highest importance to the uncertainty in the total hydrogen generation.

The realizations with shortest time at cycle and the highest eutectic melting temperature generate the largest amounts of hydrogen produced. However, the highest decay heat (i.e., a late time at cycle) and the largest valve failure areas or RCP leakage had the earliest timing to the start of hydrogen production. Consequently, the factors that influenced the total magnitude of the hydrogen production were different than the factors that drove the earliest timing. Since the regression analysis was based on the total hydrogen generation rather than the start of the core degradation and hydrogen production, parameters that delayed the fuel collapse had higher importance (e.g., a low time at cycle and high eutectic temperature). The remaining parameters such as depressurization parameters (SV open fraction and RCP leakage) had a lower contribution to uncertainty in the hydrogen production.

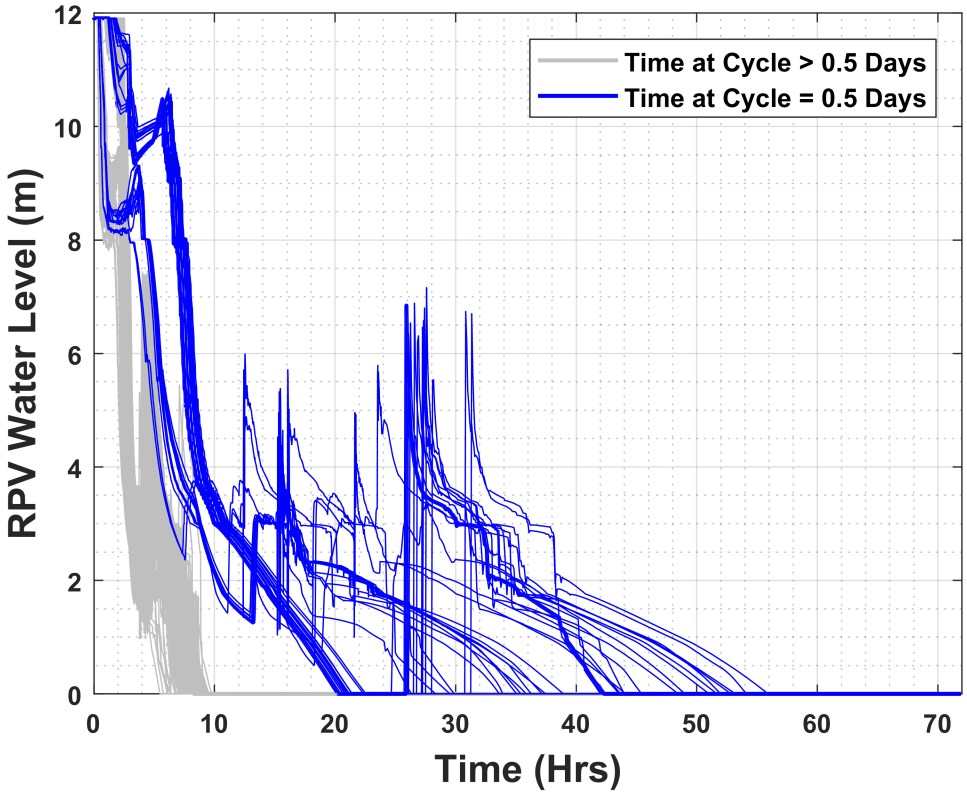

Figure 6-31 Plot of the RPV Water Level Over Time Showing the Effects of Time at Cycle

6.1.3.5 Hydrogen Production Conclusions

The total in-vessel hydrogen production at 72 hours for all realizations is in good agreement with the original SOARCA STSBO run for Surry. The range of total production is generally bounded between 200 kg and 700 kg, with a few realizations below 200 kg and one realization above 700 kg while the SOARCA calculation generated 349 kg. The regression results for hydrogen uncertainty are essentially the same, regardless as to whether there is a SGTR or not. Consequently, the hydrogen regression results included all the realizations (i.e., non-SGTR and SGTR realizations).

The two most important phenomena for the in-vessel hydrogen production are time at the cycle and the effective eutectic melting temperature. The regression analysis shows that a longer time at cycle that has more decay heat hastens heat-up and core degradation. The net effect was less time for oxidation before the core collapsed. In contrast, the shortest time at cycle (i.e., 0.5 day) had a very slow heatup that could generate very large amounts of hydrogen due to the slower accident progression. The 0.5 day time at cycle realizations were significantly slower than the other realizations due to the very low decay heat at the start of the cycle relative to the other times at cycle (e.g., see Figure 6-22).

The effective eutectic melting temperature had the second most overall importance. The oxidation rate significantly slows following the collapse of the fuel. A high eutectic melting temperature allowed the fuel to remain intact longer and allow oxidation to continue to higher

temperatures. Both of these factors led to higher hydrogen production. The collapse of the fuel into a debris bed also limited flow through the core. Consequently, any factors that delayed the core collapse increased the efficiency of the steam penetration to unoxidized locations in the core.

Several other parameters had a smaller importance including the Zircaloy breakout temperature, the primary SV failure area, and the RCP seal leakage. A higher Zircaloy breakout temperature kept the zircaloy in the intact fuel geometry longer, which promotes more oxidation. Once the zircaloy is discharged from the fuel rod, it relocates and freezes to lower locations and is not effectively oxidized thereafter. The primary SV failure area and the RCP seal leakage impacted the early primary system depressurization prior to a hot leg failure. The primary system depressurization delayed the hot leg failure due to the lower system pressure while accelerating the core damage due to the inventory loss. The primary system depressurization also enhanced steam flow through the core as it degraded. This had a small impact of increasing hydrogen production relative to cycling on the pressurizer SV at high pressure with a very rapid blowdown following the hot leg failure. The subsequent oxidation phase at low pressure from a high-pressure blowdown is not as effective due to the low steam density at low pressure. There is not always agreement between the four regression techniques, emphasizing the benefit of using multiple techniques.

6.1.4 Steam Generator Tube Rupture

To understand drivers of uncertainty in steam generator tube rupture, regression analyses were performed on creep for cold tubes, a hot upflow tube, the hottest tubes, and an unflawed tube in the hottest tube region. The analysis was performed for the tubes in SG A and SG B because parameters are sampled independently for each steam generator. The comparison of results between steam generators shows the same phenomenology for tube damage and ultimately rupture in each of the steam generators.

Results for each figure of merit are presented below and results for the different steam generators are grouped to facilitate comparison. Recall that the parameter for aggregate pressurizer safety valve cycles was not included in the regression due to correlation with the pressurizer SV failure open fraction. However, the aggregate pressurizer open area fraction was included so the effects of the pressurizer SVs could still be reflected in the regression models. The total RCP seal leakage rate is also related to these two parameters as a metric for primary system depressurization. However, RCP seal leakage was maintained as a regression parameter due to differences in its impact of the system response (e.g., initially a water release versus a steam release).

6.1.4.1 Cold Tube Creep

The parameters that account for the most uncertainty in cold tube damage are the maximum flaw depth among the cold tubes (tubeColdA_max), the MSIV leak area (msiv_leak_a), and behavior of the pressurizer safety valves (priSVfrac, priSVcyc). Of these, the maximum flaw depth among the cold tubes is, by far, the dominant factor. The other parameters contributing to the magnitude of the pressure difference across the tube also had importance. These parameters included the MSIV leakage and the secondary SV failure area, which impacted the pressure on the secondary side of the SG tubes. Similar, the priSVfrac and RCP leakage parameters impacted the pressure on the primary system side of the tube. However, the impact of these secondary parameters was dominated by the MSIV leakage on the secondary side and whether a pressurizer SV stuck open on the primary side (i.e., the priSVfrac parameter). The time at cycle (ORIGENDay) parameter also showed up having a very small impact to the rank regression.

The cold tube creep regressions for SG A and SG B are summarized in Table 6-6 and Table 6-7. The parameters that account for the most uncertainty in cold tube damage are the maximum flaw depth among the cold tubes (tubeColdA_max), the MSIV leak area (msiv_leak_a), and behavior of the pressurizer safety valves (priSVfrac, priSVcyc). Of these, the maximum flaw depth among the cold tubes is, by far, the dominant factor. This effect is shown in Figure 6-32Figure , which shows that tubes with flaws at least 80% through-wall experience multiple orders of magnitude more damage than tubes with less severe flaws. This is consistent with occurrence of SGTR in SG A, as approximately 84% of realizations with a maximum cold tube flaw depth above 0.8 experienced rupture of a cold tube, whereas no realizations with a maximum cold tube flaw depth less than 0.8 experienced a cold tube rupture.

The cold tube creep scatter plots as a function of the cold tube flaw depth, MSIV leakage, and primary SV failure fraction are shown in Figure 6 32 through Figure 6 34. 140 of the 144 realizations had operating pressurizer SVs, which is indicated at x= 0 and y=100 (i.e., 1) on Figure 6 34. The 4 SGTR realizations with a stuck-open pressurizer SV occurred when the SV failure area when very small or the failure area was small and the SV stuck open close to the time of the SGTR.

The cold tube creep recursive partitioning regression trees for SG A and B are shown in Figure 6-35. The regression trees illustrate the strong threshold effect of the minimum cold tube flaw depth on the creep magnitude. The cold tubes with flaws with 80% through wall or greater experience multiple orders of magnitude more damage than tubes with less severe flaws.

Table 6-6 Regression Results for Cold Tube Creep in SG A

	Rank Regression		Quadratic		Recursive Partitioning		MARS		Main Contribution	Conjoint Contribution
Final R2	0.64		0.87		0.95		0.95			
Input	R2 contr.	SRRC	Si	Ti	Si	Ti	Si	Ti		
tubeColdA_max	0.36	0.57	0.97	0.99	1.00	1.00	0.94	1.00	0.760	0.022
msiv_leak_a	0.15	0.40	---	---	---	---	0.01	0.06	0.040	0.017
priSVfrac	0.10	-0.57	---	---	---	---	---	---	0.025	0.000
secSVfrac1	0.02	0.25	---	---	---	---	0.00	0.01	0.004	0.004
ORIGENDay	0.01	-0.10	---	---	---	---	---	---	0.003	0.000
RCP_Leak	0.01	0.08	---	---	---	---	0.00	0.02	0.001	0.007

**** highlighted if main contribution larger than 0.02 or conjoint contribution larger than 0.1***

Table 6-7 Regression Results for Cold Tube Creep in SG B

	Rank Regression		Quadratic		Recursive Partitioning		MARS		Main Contribution	Conjoint Contribution
Final R2	0.63		0.73		0.86		0.95			
Input	R2 contr.	SRRC	Si	Ti	Si	Ti	Si	Ti		
tubeColdB_max	0.38	0.62	0.88	0.98	0.86	1.00	0.65	0.98	0.595	0.170
msiv_leak_b	0.11	0.35	0.00	0.03	0.01	0.08	0.01	0.18	0.032	0.083
priSVfrac	0.11	-0.60	0.01	0.06	---	---	0.00	0.05	0.027	0.029
secSVfrac2	0.01	0.21	---	---	---	---	---	---	0.003	0.000
ORIGENDay	0.01	-0.11	---	---	---	---	---	---	0.003	0.001
RCP_Leak	0.00	0.04	0.00	0.02	---	---	0.00	0.01	0.002	0.005
condensation_X	---	---	0.00	0.01	0.00	0.08	---	---	0.001	0.025

* highlighted if main contribution larger than 0.02 or conjoint contribution larger than 0.1

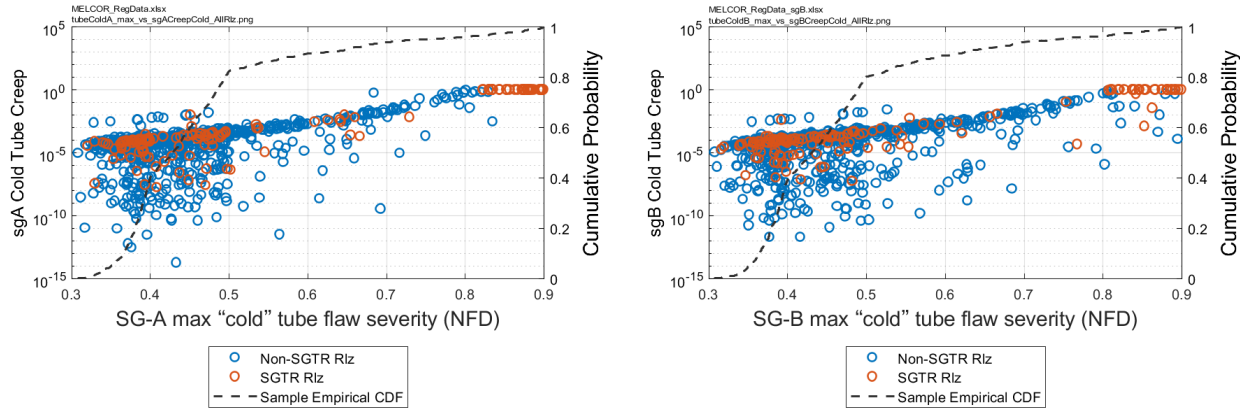

Figure 6-32 Scatter Plots of Maximum Cold Tube Flaw Severity vs. Cold Tube Creep for SGs A and B

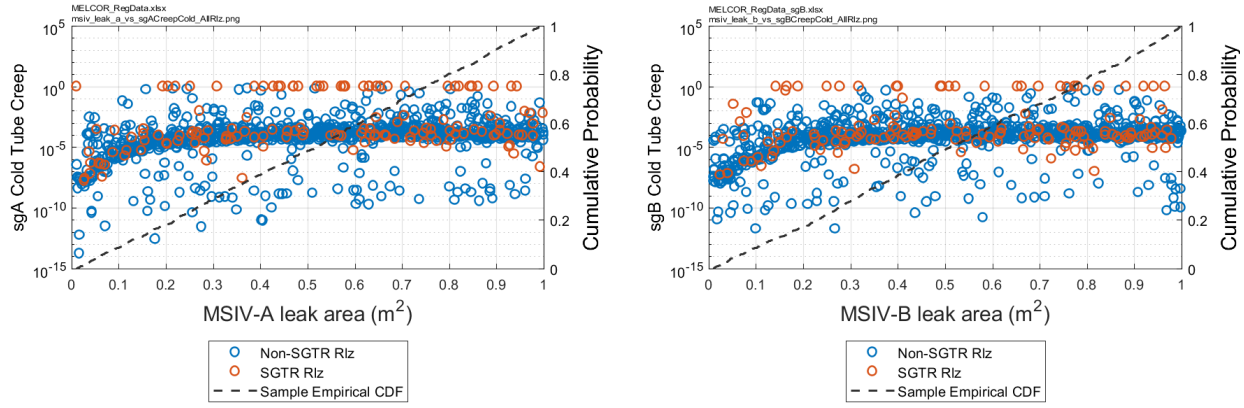

Figure 6-33 Scatter Plots of MSIV Leak Area vs. Cold Tube Creep for SGs A and B

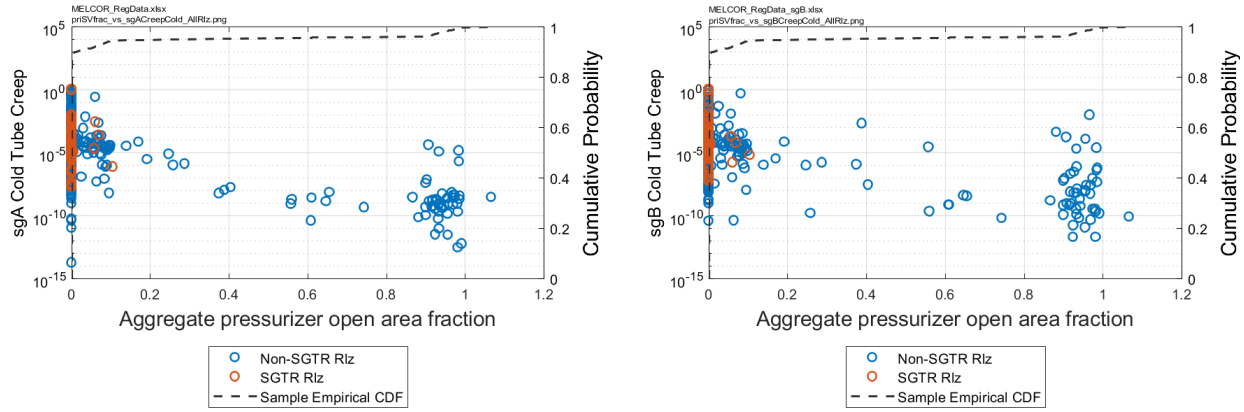

Figure 6-34 Scatter Plots of aggregate Pressurizer SV Open Area Fractions vs. Cold Tube Creep for SGs A and B

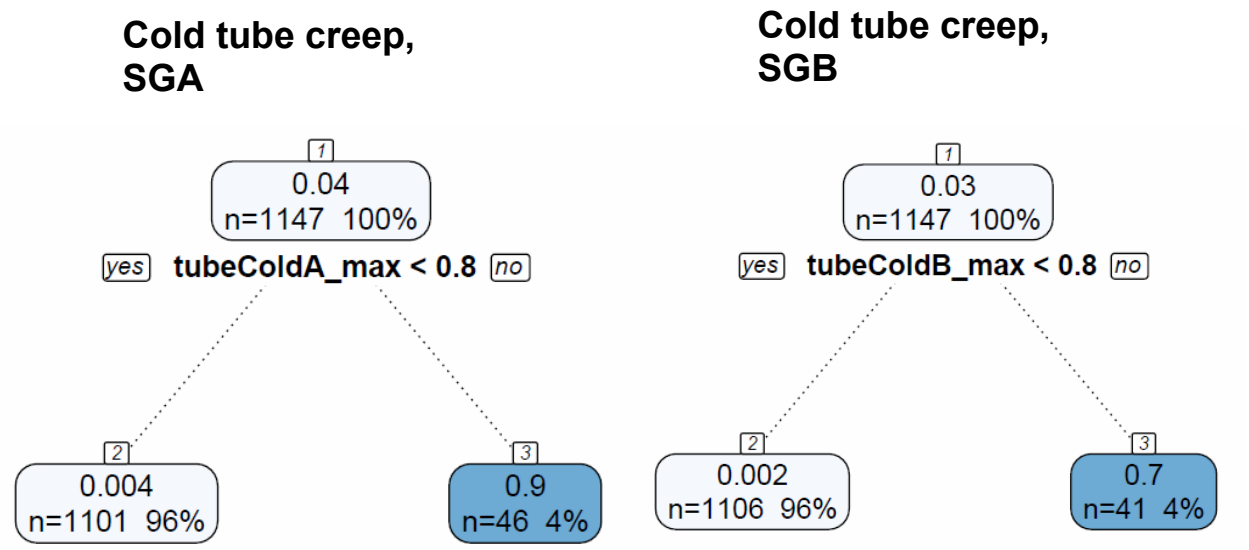

Figure 6-35 Recursive Partitioning Regression Trees for Cold Tube Creep in SGs A and B

6.1.4.2 Hottest Tube Creep

As with the cold tubes, the parameter that accounts for most of the uncertainty in the hottest tube damage is the flaw depth. In contrast, smaller flaws are sufficient to increase the extent of damage due to the higher temperatures. The rate of creep is impacted by both the mechanical stress from the pressure difference across the tube and the temperature of the tube. The hottest tube also included the hot tube normalized gas temperature to address uncertainty in the maximum thermal plume temperature. The hottest tube creep showed this parameter also has a significant effect.

The hottest tube creep regressions for SG A and SG B are summarized in Table 6-7 and Table 6-8. The hottest tube creep scatter plots as a function of the tube flaw depth, the normalized hot tube gas temperature, and the MSIV leakage is shown in Figure 6-36 through Figure 6-38, respectively.

The hottest tube creep recursive partitioning regression trees for SG A and B are shown in Figure 6-39 and Figure 6-40. The regression trees illustrate the strong threshold effect of the minimum hottest tube flaw depth on the creep magnitude but also importance of the normalized hot tube inlet temperature. In SG A, about 24% of hottest tubes with a flaw depth greater than 0.42 ruptured but only 0.09% with a flaw depth less than 0.42 ruptured (see Figure 6-39). In SG B, 12% of hottest tubes with a flaw depth greater than 0.43 (see Figure 6-40) ruptured, and none with a flaw depth less than 0.43 ruptured.

Table 6-8 Regression Results for Hottest Tube Creep in SG A

	Rank Regression		Quadratic		Recursive Partitioning		MARS		Main Contribution	Conjoint Contribution
Final R2	0.59		0.88		0.77		0.85			
Input	R2 contr.	SRRC	Si	Ti	Si	Ti	Si	Ti		
tubeHotA_NFD	0.18	0.72	0.64	0.89	0.78	0.97	0.70	0.90	0.485	0.179
ThotA_norm	0.19	0.42	0.03	0.16	0.03	0.20	0.02	0.27	0.063	0.152
msiv_leak_a	0.14	0.39	0.01	0.09	0.00	0.02	0.00	0.00	0.038	0.029
priSVfrac	0.05	-0.47	0.01	0.05	---	---	0.02	0.02	0.016	0.012
secSVfrac1	0.03	0.31	0.00	0.02	---	---	0.00	0.02	0.007	0.009
RCP_Leak	0.02	0.15	0.00	0.05	---	---	---	---	0.005	0.014

** highlighted if main contribution larger than 0.02 or conjoint contribution larger than 0.1*

Table 6-9 Regression Results for the Hottest Tube Creep in SG B

	Rank Regression		Quadratic		Recursive Partitioning		MARS		Main Contribution	Conjoint Contribution
Final R2	0.60		0.88		0.76		0.98			
Input	R2 contr.	SRRC	Si	Ti	Si	Ti	Si	Ti		
tubeHotB_NFD	0.18	0.74	0.70	0.95	0.95	0.99	0.57	0.96	0.520	0.209
ThotB_norm	0.18	0.45	0.03	0.14	0.01	0.07	0.03	0.20	0.059	0.105
msiv_leak_b	0.14	0.40	0.01	0.03	---	---	0.00	0.21	0.038	0.075
priSVfrac	0.06	-0.50	0.01	0.06	---	---	0.00	0.02	0.017	0.020
secSVfrac2	0.02	0.28	0.00	0.01	---	---	---	---	0.006	0.001
RCP_Leak	0.01	0.12	0.01	0.08	---	---	---	---	0.005	0.021

* highlighted if main contribution larger than 0.02 or conjoint contribution larger than 0.1

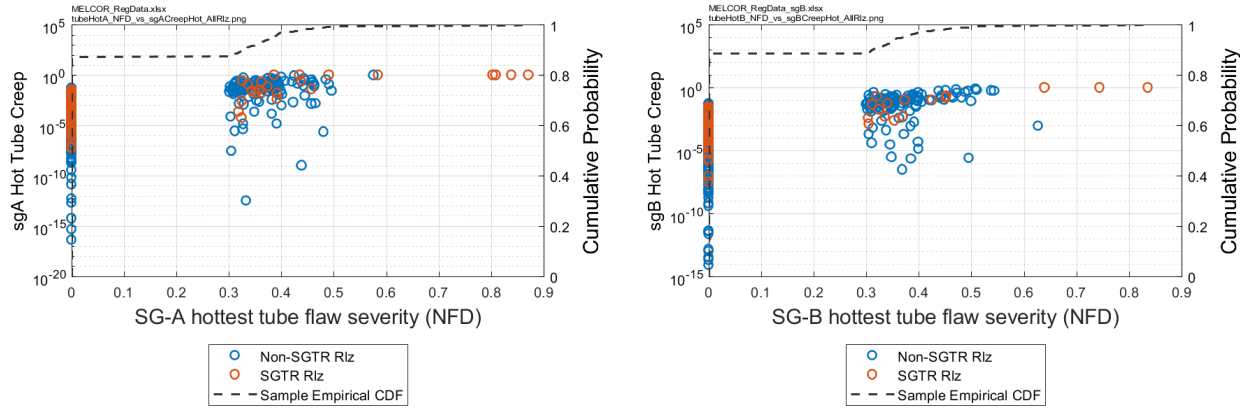

Figure 6-36 Scatter Plot of Tube Flaw Severity in the Hottest Tube vs. Hottest Tube Creep for SGs A and B

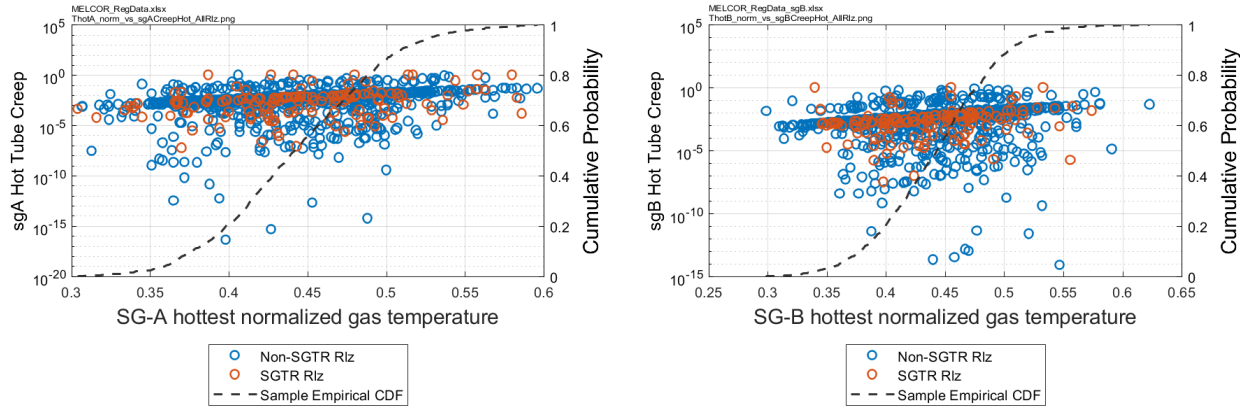

Figure 6-37 Scatter Plot of Hot Tube Normalized Gas Temperature vs. Hottest Tube Creep for SGs A and B

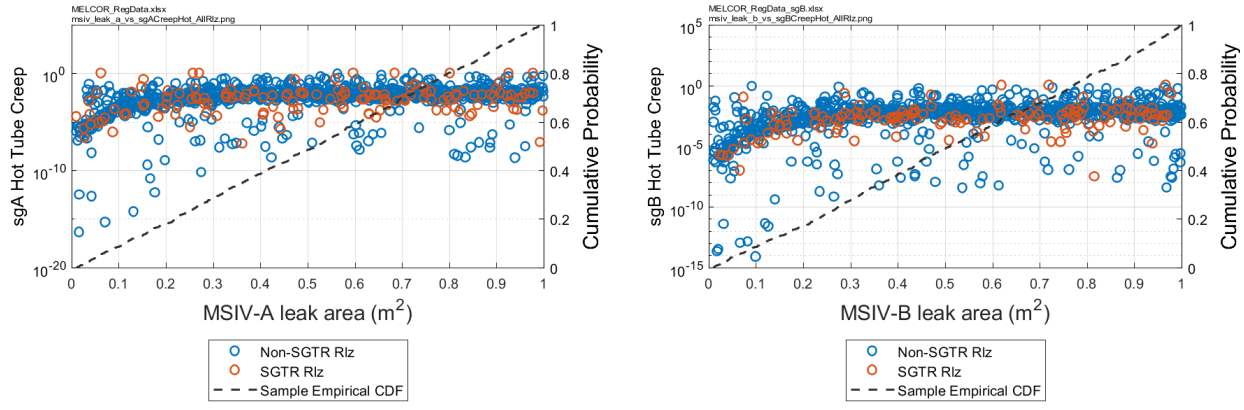

Figure 6-38 Scatter Plot of MSIV Leak Area vs. Hottest Tube Creep for SGs A and B

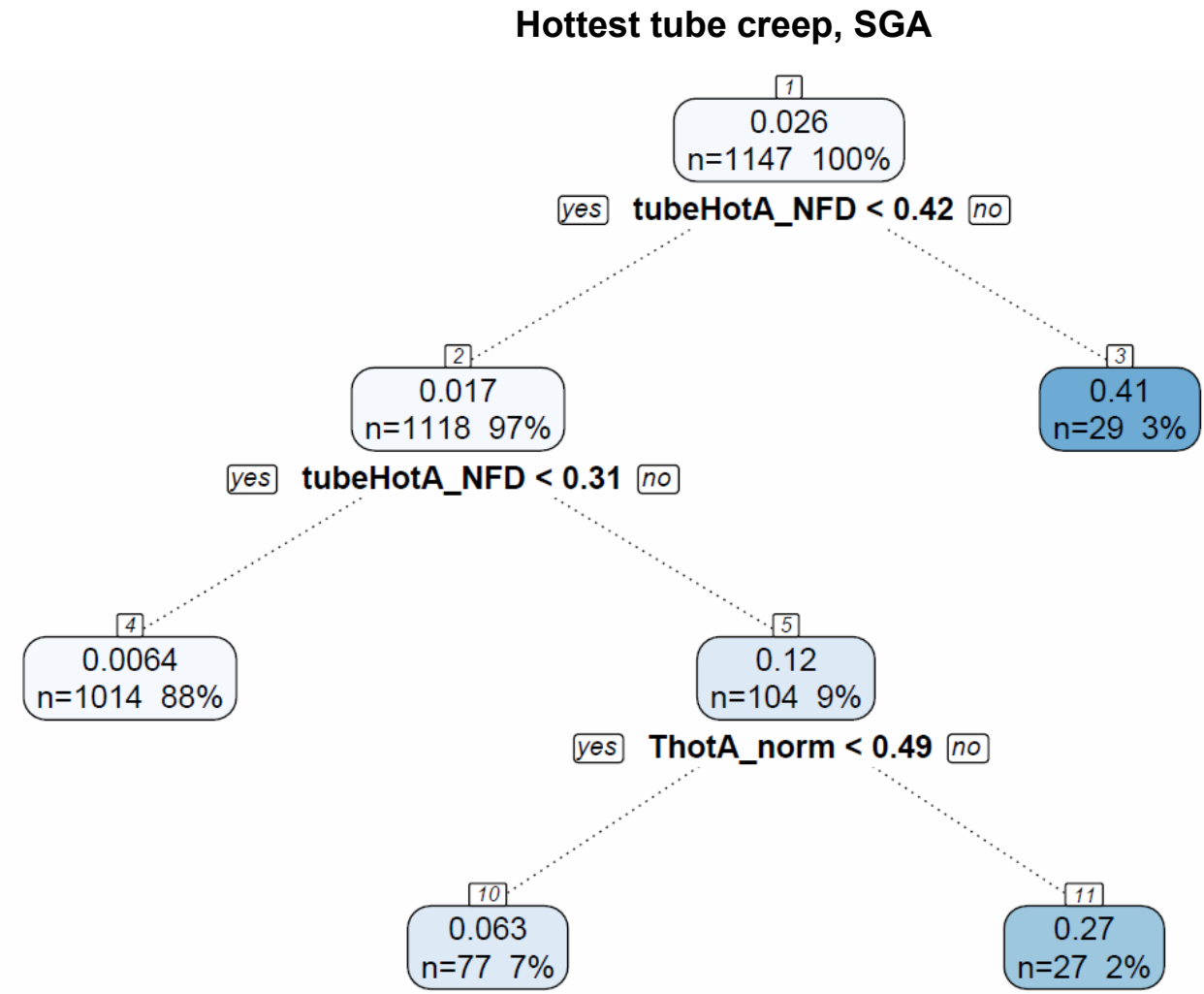

Figure 6-39 Recursive Partitioning Tree for the Hottest Tube Creep in SG A

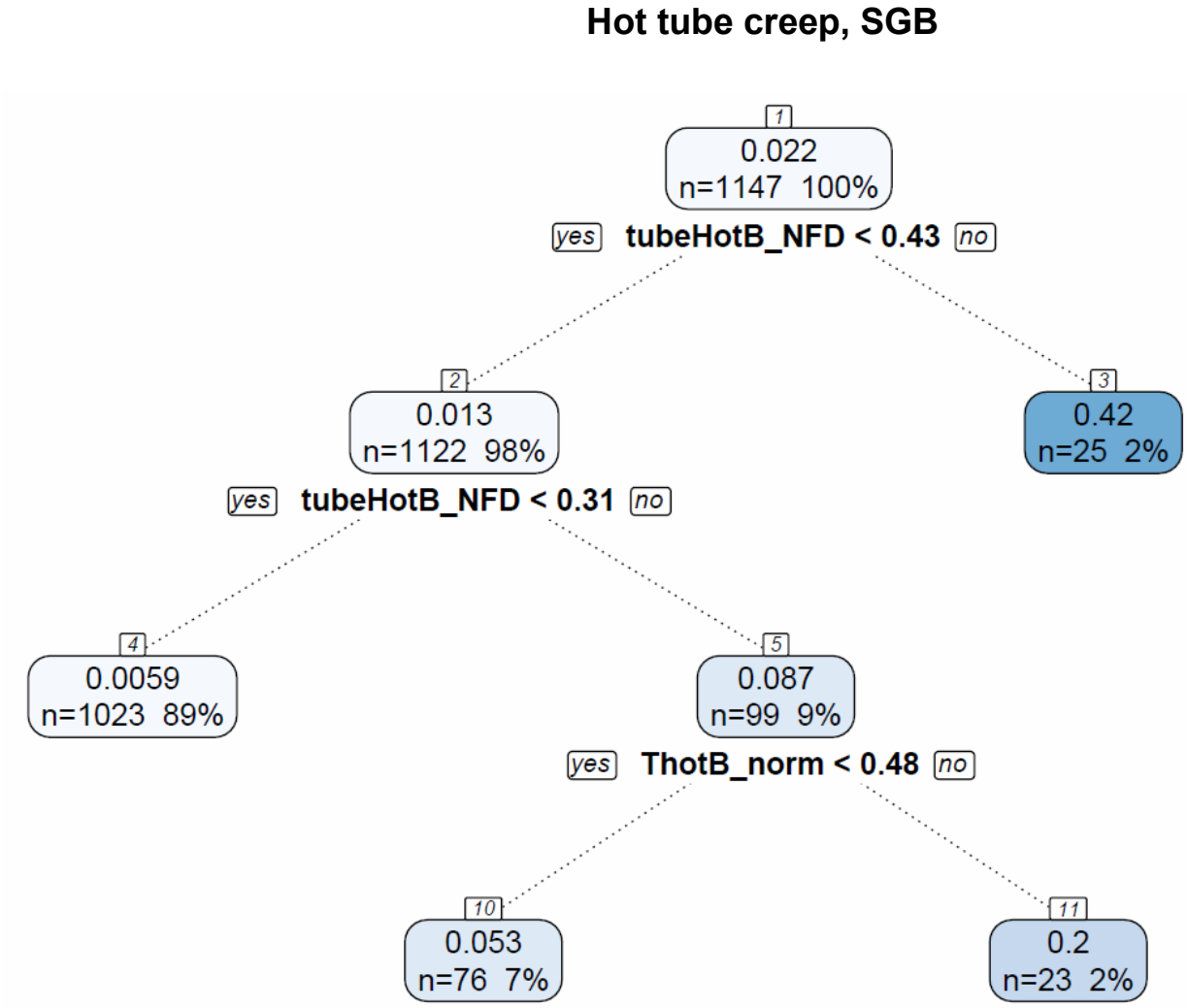

Figure 6-40 Recursive Partitioning Tree for the Hottest Tube Creep in SG B

6.1.4.3 Unflawed Hottest Tube Creep

The next regression examines an unflawed tube in the hottest region of the SG. The unflawed regression allows resolution of more subtle factors other than the flaw depth by using an unflawed creep parameter as the figure of merit. Since no unflawed tubes were predicted to fail in the UA, the parameters that maximize the tube creep can be isolated. Table 6-10 and Table 6-11 show the regression results for the unflawed hottest tube creep in SG A and SG B, respectively. The uncertainty in creep for the unflawed hottest tube is dominated by the second most important parameter, the hot tube normalized gas temperature. The hot tube normalized gas temperature for unflawed tubes is significantly more important than predicted in the flawed tube correlation, which illustrates its importance increases when flaws no longer dominate the uncertainty. The remaining parameters that showed some importance included MSIV leakage, the primary SV failure area, and the RCP seal leakage. These parameters are also consistent with the previous flawed tube regressions.

The supporting scatter plots for this regression are shown in Figure 6-41 through Figure 6-44. The strong correlation for the hot tube normalized gas temperature is well shown in Figure 6-41. The importance of the MSIV leakage being greater than ~0.25 in^2 is also slightly more evident in Figure 6-42 than previously observed in Figure 6-38. The remaining scatter plots do not show strong correlation patterns.

The unflawed hottest tube regression tree is illustrated in Figure 6-45. The highest creep magnitudes occur when both the gas temperature is greater than about 0.5 and the MSIV leak area is greater than 0.24 to 0.28 in^2. While these parameters affect creep, the unflawed hottest tubes did not rupture in any realizations, further supporting the importance of flaw depth when flaws are present.

Table 6-10 Regression Results for the Unflawed Hottest Tube Creep in SG A

	Rank Regression		Quadratic		Recursive Partitioning		MARS		Main Contribution	Conjoint Contribution
Final R2	0.56		0.79		0.81		0.76			
Input	R2 contr.	SRRC	Si	Ti	Si	Ti	Si	Ti		
ThotA_norm	0.29	0.52	0.62	0.73	0.60	0.60	0.62	0.76	0.435	0.120
msiv_leak_a	0.18	0.44	0.15	0.23	0.17	0.17	0.16	0.29	0.139	0.103
priSVfrac	0.04	-0.44	0.05	0.08	0.01	0.01	0.05	0.08	0.032	0.017
RCP_Leak	0.02	0.18	0.03	0.06	---	---	0.03	0.03	0.017	0.013
secSVfrac1	0.03	0.32	0.00	0.01	---	---	0.00	0.01	0.007	0.009

**** highlighted if main contribution larger than 0.02 or conjoint contribution larger than 0.1***

Table 6-11 Regression Results for the Unflawed Hottest Tube Creep in SG B

	Rank Regression		Quadratic		Recursive Partitioning		MARS		Main Contribution	Conjoint Contribution
Final R2	0.59		0.82		0.83		0.80			
Input	R2 contr.	SRRC	Si	Ti	Si	Ti	Si	Ti		
ThotB_norm	0.29	0.56	0.57	0.70	0.61	0.80	0.66	0.80	0.448	0.127
msiv_leak_b	0.17	0.44	0.13	0.20	0.15	0.31	0.13	0.24	0.125	0.095
priSVfrac	0.06	-0.53	0.03	0.08	0.02	0.05	0.04	0.07	0.033	0.030
RCP_Leak	0.03	0.18	0.04	0.12	0.01	0.04	0.03	0.03	0.022	0.029
secSVfrac2	0.02	0.30	0.01	0.03	---	---	---	---	0.009	0.007

* highlighted if main contribution larger than 0.02 or conjoint contribution larger than 0.1

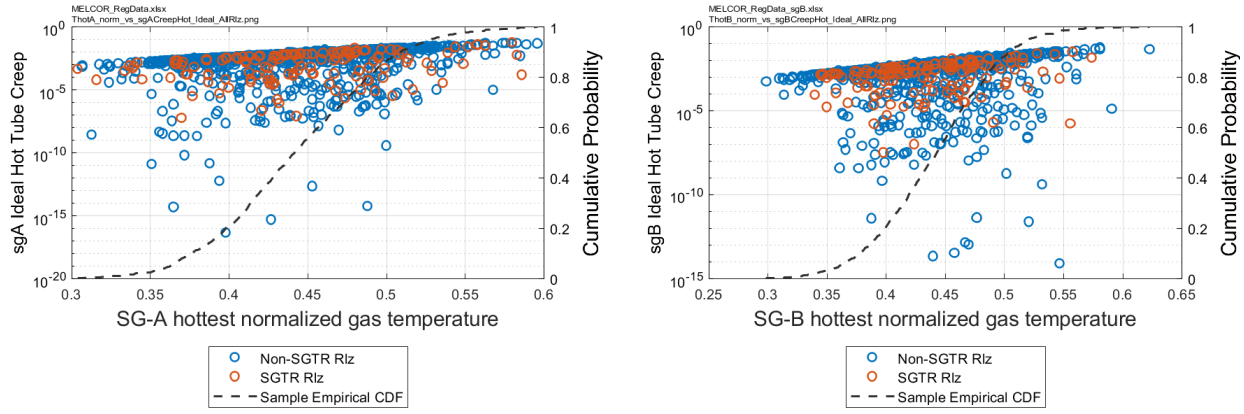

Figure 6-41 Scatter Plot of Hot Tube Normalized Gas Temperature vs. Creep for an Unflawed Hottest Tube in SGs A and B

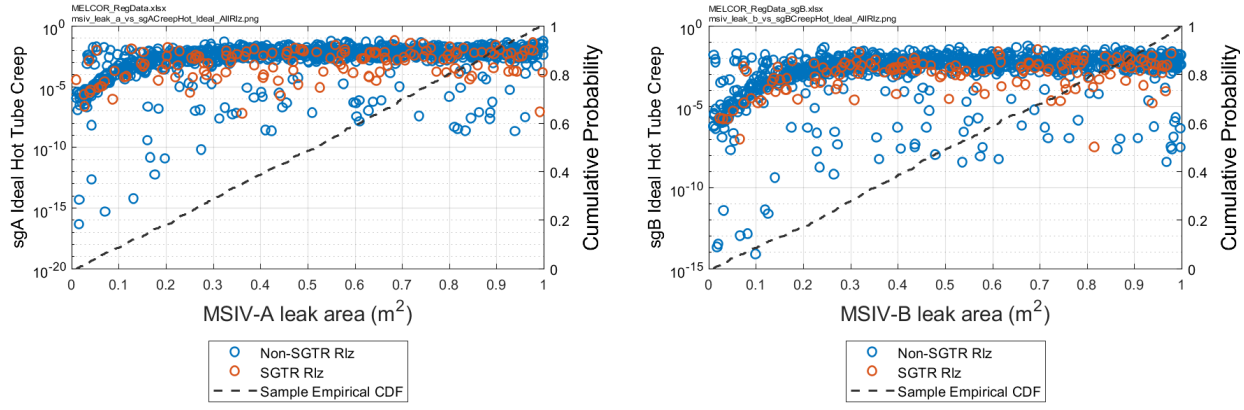

Figure 6-42 Scatter Plot of MSIV Leak Area vs. Creep for an Unflawed Hottest Tube in SGs A and B

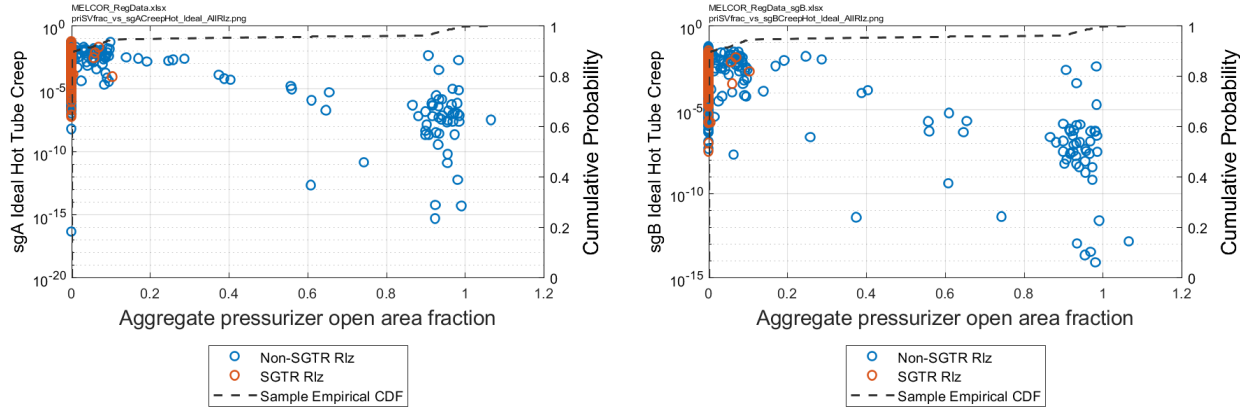

Figure 6-43 Scatter Plot of Aggregate Pressurizer SV Open Area Fraction vs. Creep for an Unflawed Hottest Tube in SGs A and B

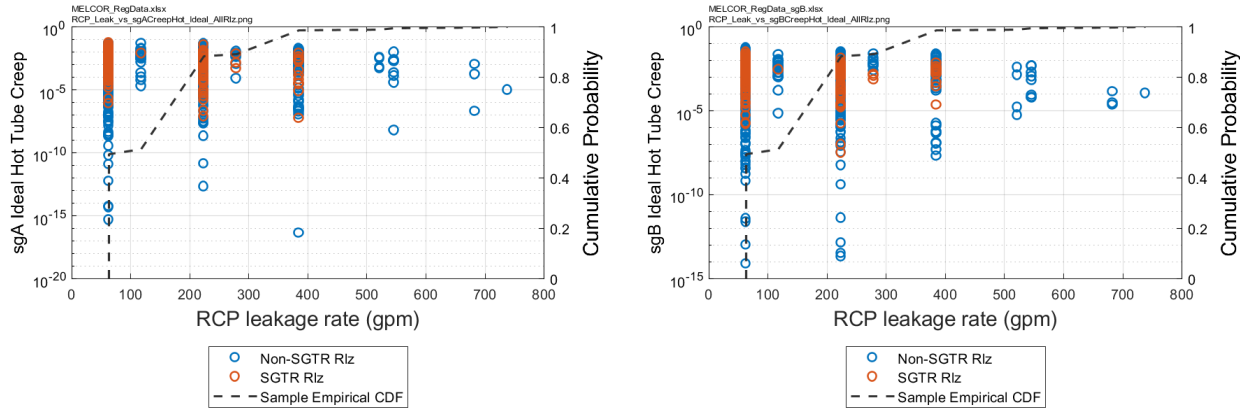

Figure 6-44 Scatter Plot of RCP Leakage vs. Creep for an Unflawed Hottest Tube in SGs A and B

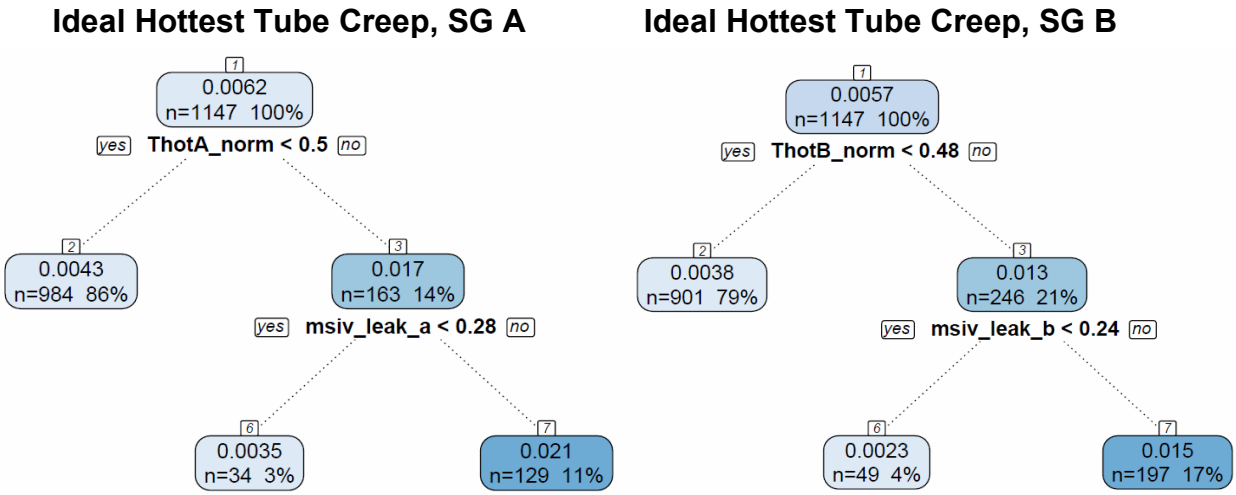

Figure 6-45 Recursive Partitioning Tree for Unflawed Hottest Tube Creep in SGs A and B

6.1.4.4 Hot Upflow Tube Creep

Consistent with the previous creep evaluations, the regressions for the flawed tubes in the hot upflow region of the SG identified the non-dimensional flaw depth as the most important parameter. As shown in Table 6-12 and Table 6-13, there were small contributions from MSIV leakage and pressurizer SV valve behavior for SG A and B, respectively.

The flawed upflow tube creep scatter plots are shown in Figure 6-46 through Figure 6-48 for the various important parameters. The responses are consistent with the cold and hottest tube

creep responses. There are significantly more flawed tube samples in the upflow region than for the hottest tube.[67]

The recursive partitioning trees for creep in the upflow tubes are shown in Figure 6-49. The recursive partitioning regression for SG A identified flaw depths greater than 69% through wall and the regression for SG B identified flaw depths greater than 67% through wall as leading to more severely damaged tubes. With respect to tube ruptures, about 79% of upflow region tubes with a flaw depth greater than 69% in SG A ruptured, and about 62% of upflow region tubes with a flaw depth greater than 67% in SG B ruptured.

Table 6-12 Regression Results for Upflow Tube Creep in Steam Generator A

	Rank Regression		Quadratic		Recursive Partitioning		MARS		Main Contribution	Conjoint Contribution
Final R2	0.56		0.92		0.93		0.96			
Input	R2 contr.	SRRC	Si	Ti	Si	Ti	Si	Ti		
tubeUpflowA_NFD	0.26	0.51	0.89	0.97	1.00	1.00	0.92	1.00	0.724	0.052
msiv_leak_a	0.18	0.44	0.00	0.05	---	---	0.00	0.03	0.046	0.021
priSVfrac	0.08	-0.56	0.00	0.04	---	---	0.01	0.03	0.022	0.021
secSVfrac1	0.02	0.29	0.00	0.00	---	---	0.00	0.00	0.006	0.000
tubeColdA_max	0.01	-0.09	---	---	---	---	0.01	0.01	0.003	0.000

** highlighted if main contribution larger than 0.02 or conjoint contribution larger than 0.1*

Table 6-13 Regression Results for Upflow Tube Creep in SG B

	Rank Regression		Quadratic		Recursive Partitioning		MARS		Main Contribution	Conjoint Contribution
Final R2	0.58		0.89		0.85		0.95			
Input	R2 contr.	SRRC	Si	Ti	Si	Ti	Si	Ti		
tubeUpflowB_NFD	0.32	0.55	0.95	0.99	1.00	1.00	0.88	0.96	0.710	0.036
msiv_leak_b	0.16	0.40	---	---	---	---	0.00	0.06	0.041	0.018
priSVfrac	0.10	-0.58	0.00	0.01	---	---	0.00	0.02	0.025	0.009
RCP_Leak	0.00	0.06	0.00	0.01	---	---	0.05	0.05	0.011	0.004
tubeColdB_max	0.01	-0.07	0.00	0.03	---	---	---	---	0.001	0.008

* highlighted if main contribution larger than 0.02 or conjoint contribution larger than 0.1

[67] Only 15% of the samples had a flawed tube in the hottest plume location versus always having a flawed tube in the upflow region. Consequently, there was a much lower likelihood of having a hottest flawed tube with a primary system SV failure. See the discussion in Section 4.1.1.6 for the hottest tube versus the upflow flaw distributions.

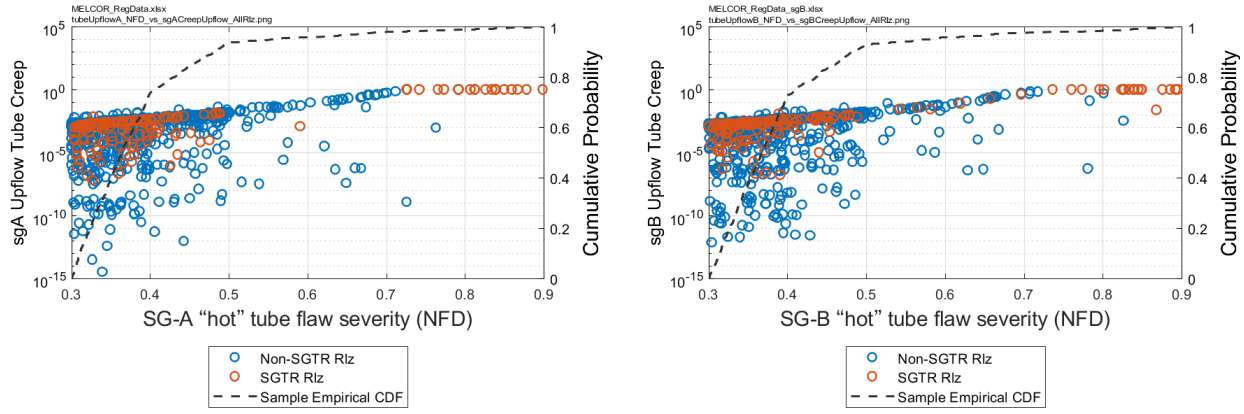

Figure 6-46 Scatter Plot of Flaw Severity vs. Creep for a Tube in the Upflow Region for Steam Generators A and B

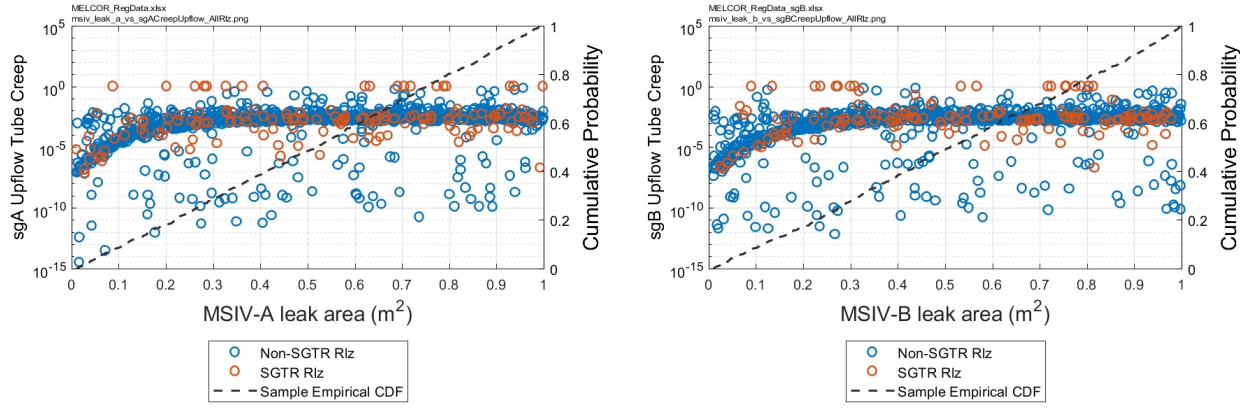

Figure 6-47 Scatter Plot of MSIV Leak vs. Creep for a Tube in the Upflow Region for Steam Generators A and B

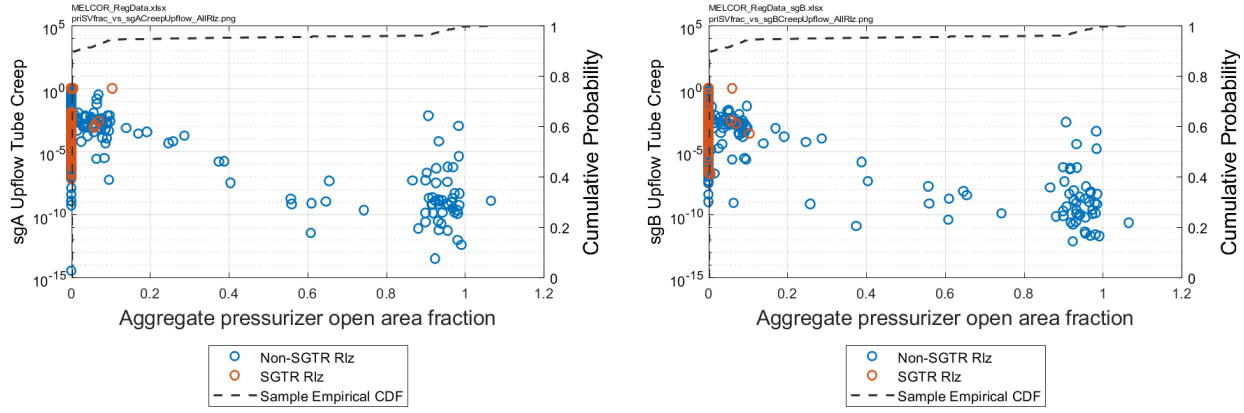

Figure 6-48 Scatter Plot of Aggregate Pressurizer SV Open Area Fraction vs. Creep for a Tube in the Upflow Region for SG A and B

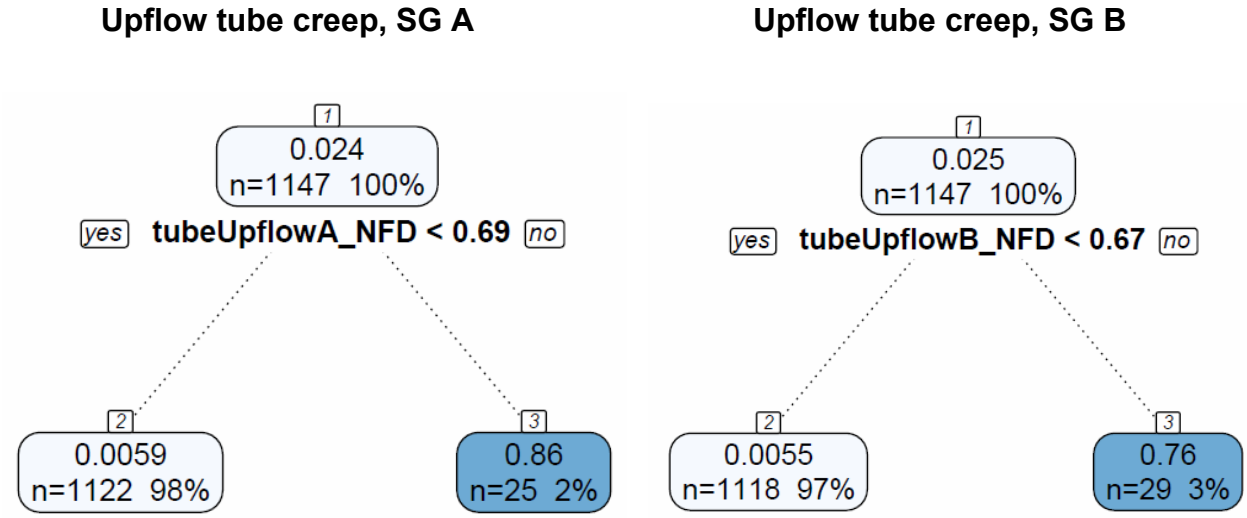

Figure 6-49 Recursive Partitioning Trees for Upflow Tube Creep in SGs A and B

6.1.4.5 Comparison to SOARCA

In the original SOARCA calculation for Surry [3], there was a STSBO scenario that included induced (forced) SGTRs. A sensitivity analysis was also done to vary the flow area, representative of one or two failed tubes. In these runs, a secondary SV was stuck open at 3 hours and then a SGTR was modeled to occur when the creep damage index exceeded 5 percent, which occurred at 3 hr 33 min [3]. The SOARCA calculations [3] had 14 minutes between the induced SGTR and hot leg creep rupture. Figure 6-50 shows the environmental release masses for cesium and iodine for 1 and 2 tube SGTRs. In comparison to the SGTR realizations in the cesium and iodine horsetails (Figure 6-1 and Figure 6-12), the SOARCA results fall within the spread, although on the lower side in both cases (i.e., the single tube SGTR SOARCA results are shown but the magnitude of the source term was similar).

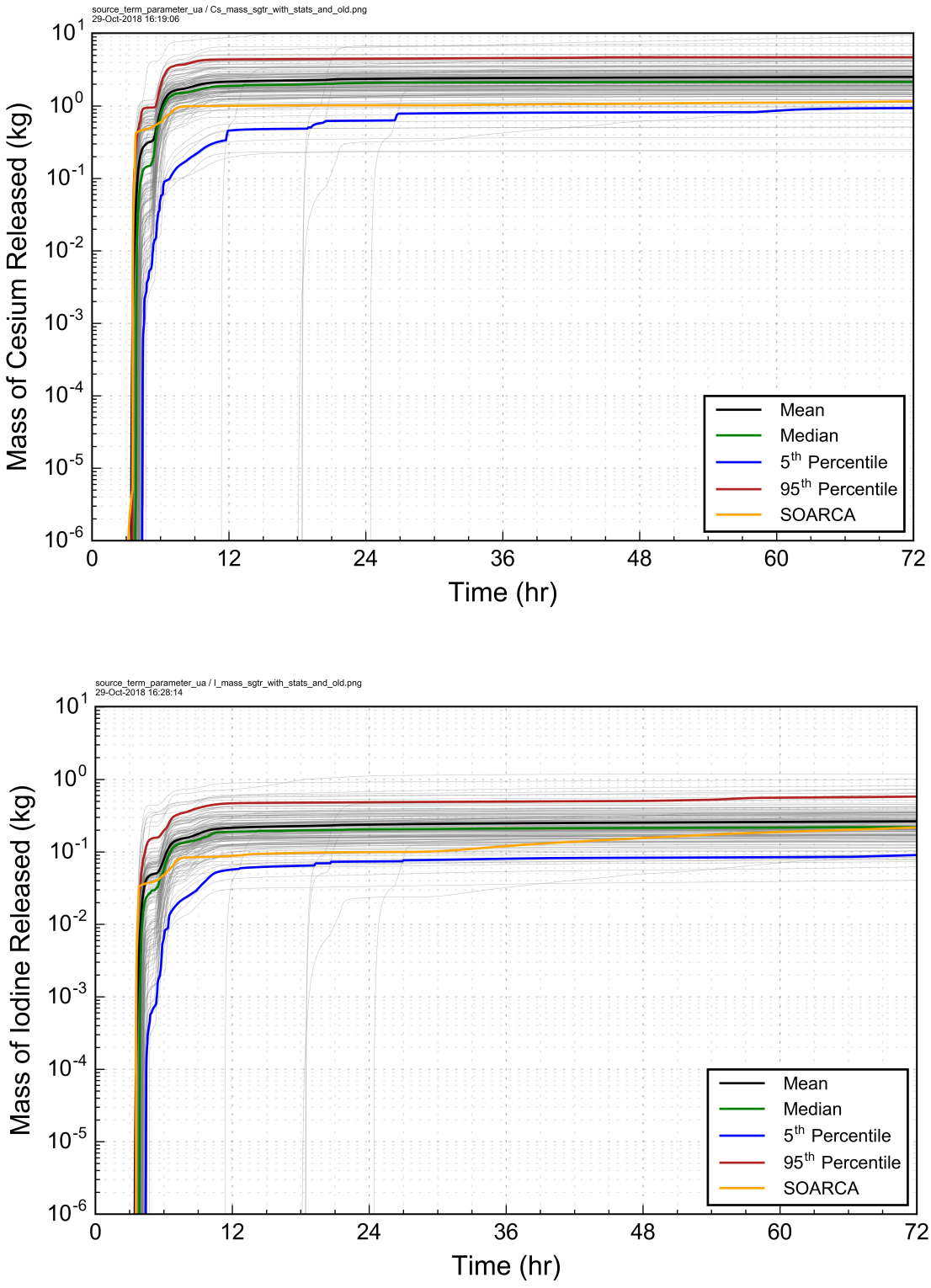

Figure 6-50 Cesium and Iodine Environmental Release Fractions from Original SOARCA SGTR Sensitivities

In addition to the model enhancements since the original SOARCA SGTR calculations (e.g., see summary in Section 3.1.1), there are three primary differences between the Surry SOARCA [3] SGTRs and those in the uncertainty realizations. First, the flow area to the environment is different in the UA. The Surry SOARCA [3] assumed a secondary SV failed fully open. Although the UA realizations with SGTRs have stuck open secondary SVs, the open fraction is varied and often the only leakage is through the MSIVs. Second, the Surry SOARCA [3] calculation had a prescribed secondary DF of 7 applied to all aerosol size bins. With the UA realizations, the secondary decontamination factor was enhanced to include variable aerosol decontamination based on the scaled velocity, the break location, and the aerosol size. The SG decontamination correlations are described in Section 4.1.4.4. In one spot-checked SGTR example, total DFs for smallest particles were less than 2, while those for the larger particle bins ranged from 4 to 1E6. Differences in the break location can have an even larger impact based on the power factor. Third, due to the sampling of numerous parameters that influence core temperatures and primary system depressurization, the timing of hot leg creep varies somewhat between realizations, as does the timing of the SGTR based on time at cycle, tube temperature, and other parameters. This yields a wider range of times between SGTR and hot leg creep. As will be described in more detail in the timing section, this difference has a large impact on total releases.

6.1.4.6 Steam Generator Tube Rupture Conclusions

Environmental release masses from SGTR realizations are 1 to 2 orders of magnitude larger than the remainder of the uncertainty realizations. A key result is the determination that SGTRs only occur with significant flaws in the tubes. No unflawed tubes failed in the UA realizations. The flaw depth analysis revealed,

- The likelihood of a SGTR from a cold tube flaw significantly increased when the non-dimensional flaw depth is >0.80;

- The likelihood of a SGTR from a hot upflow tube flaw significantly increased when the non-dimensional flaw depth is >0.68; and

- The likelihood of a SGTR in the hottest tube significantly increased when the non-dimensional flaw depth is (a) >0.42 or (b) >0.31 with a maximum normalized hot plume temperature >0.48 (i.e., >75th percentile of the maximum normalized plume temperature distribution).

The individual steam generator cold and hot upflow tube regression analyses also showed that the magnitude of the MSIV leakage and the flow area of a stuck-open pressurizer SV (most important when zero) as factors influencing the cold tube creep but significantly less important relative to the flaw depth. A large MSIV leakage increased the pressure difference across the tube to increase creep whereas a failed pressurizer SV, and then a larger area if failed, decreased the pressure difference to decrease creep.

The regression on the unflawed hottest tube also showed that the maximum normalized plume inlet temperature is important. The maximum plume temperature was the second most important parameter but significantly less important relative to the flaw depth. The MSIV leakage rate was also an important parameter for the hottest tube but the pressurizer SV failure area was slightly below the criterion for high importance.

The SOARCA [3] SGTR calculation had the same modeling differences as noted in Sections 6.1.1.1 and 6.1.2.1. The SOARCA work did not include the current sophistication of

flaw modeling and monitoring multiple locations in the SG. Instead, a SGTR was specified following the full depressurization of the connected steam generator by a 100% stuck-open SV during the initial heat-up [3]. Although the in the containment pressurization rate was faster and timing of the liner failure was earlier, the SGTR source term is dominated by the magnitude of the early SGTR releases (e.g., see Figure 6-1 and Figure 6-12).

6.2 Offsite Consequences

The results of the consequence analyses are presented in terms of risk to the public for the set of source terms analyzed. The reported risk metrics are individual latent cancer fatality (LCF) and early-fatality risk to residents within circular and annular regions centered on the reactor site. They are averaged over the entire population within each region. The risk values represent the predicted number of fatalities divided by the population for the linear, no-threshold, dose-response model. These risk metrics account for the distribution of the population within the circular or annular region and for the interplay between the population distribution and the wind rose probabilities.

All results are presented as conditional risks, which are the risks assuming that the accident occurs. The absolute risk is the product of the core damage frequency for the accident scenario and the conditional risk for that scenario and is discussed where applicable. The absolute risk is expressed as the likelihood of receiving a latent fatal cancer or early fatality for an average individual living within specified radii of the plant per year of plant operation (i.e., LCF risk per reactor year (pry) and early-fatality risk pry).

6.2.1 Latent Cancer Fatality Risk

This section describes the primary results for the uncertainty analysis of LCF risk. LCF risks are calculated based on the linear no-threshold (LNT) assumption for dose response. Unlike the previous SOARCA studies, other dose-response options are not examined.

Table 6-14 and Table 6-15 show statistical results from the MACCS uncertainty analysis for mean, individual, LCF risk conditional on a STSBO accident occurring at nine spatial intervals representing concentric circles and annular areas, all centered on the Surry site. In these tables, all results represent means over weather variability. In the tables, mean indicates that results are also averaged over the spatial interval and over the set of 1147 realizationsEach of the statistics in the table represents the overall epistemic (state of knowledge) uncertainty for the groups of MELCOR (Level 2) and MACCS (Level 3) inputs that were treated as uncertain (cf., Sections 4.1 and 4.2). The results show that mean conditional risks are on the order of 10^{-5} and diminish with distance from the plant.

Figure 6-51 and Figure 6-52 show the CCDFs for the same circular and annular areas summarized in Table 6-14 and Table 6-15. The points on the curves represent the mean LCF risk over variable weather for each of the 1147 realizations representing epistemic uncertainty in this UA and are conditional on a STSBO occurring. The curves show that the conditional risks span the range of 10^{-8} to 10^{-3} per event. The curves display a distinct shoulder at a probability of 0.125. This represents the transition from events with no SGTR above the shoulder to events with SGTR below the shoulder.

Table 6-14 Mean, Individual LCF Risk using LNT Dose Response, Conditional on a STSBO Occurring, for Five Circular Areas Centered on Surry Site

	0-10 miles	0 to 20 miles	0 to 30 miles	0 to 40 miles	0 to 50 miles
Mean	3.22E-05	2.20E-05	1.62E-05	1.14E-05	9.02E-06
Median	2.22E-06	1.16E-06	7.45E-07	4.59E-07	3.41E-07
5th Percentile	3.22E-07	1.76E-07	1.14E-07	7.17E-08	5.35E-08
95th Percentile	2.07E-04	1.49E-04	1.14E-04	8.05E-05	6.34E-05

Table 6-15 Mean, Individual LCF Risk using LNT Dose Response, Conditional on a STSBO Occurring for Four Annular Areas Centered on Surry Site

	10 to 20 miles	20 to 30 miles	30 to 40 miles	40 to 50 miles
Mean	1.77E-05	9.34E-06	6.16E-06	4.02E-06
Median	7.05E-07	2.52E-07	1.42E-07	9.17E-08
5th Percentile	1.18E-07	4.11E-08	2.35E-08	1.51E-08
95th Percentile	1.24E-04	6.76E-05	4.18E-05	2.63E-05

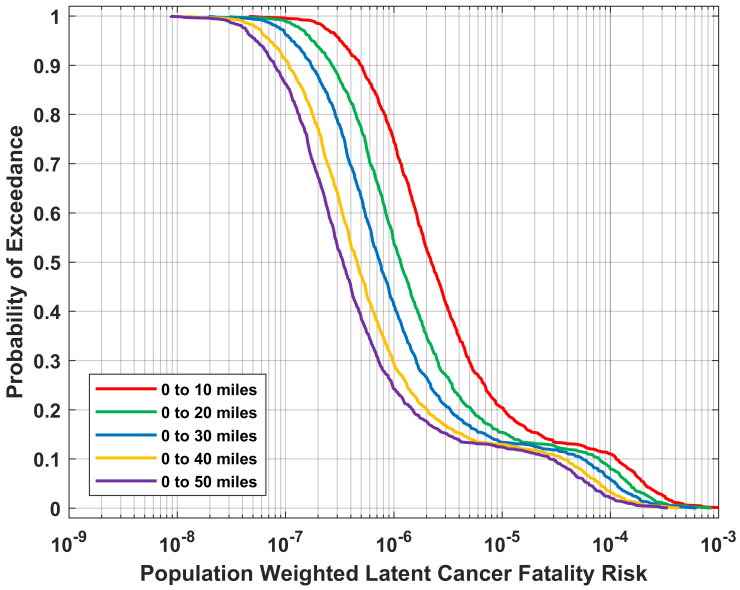

Figure 6-51 Complementary Cumulative Distribution Functions of Mean, Population-Weighted LCF Risk (Based on LNT Dose Response) Conditional on a STSBO Occurring for Five Circular Areas Centered on the Surry Site

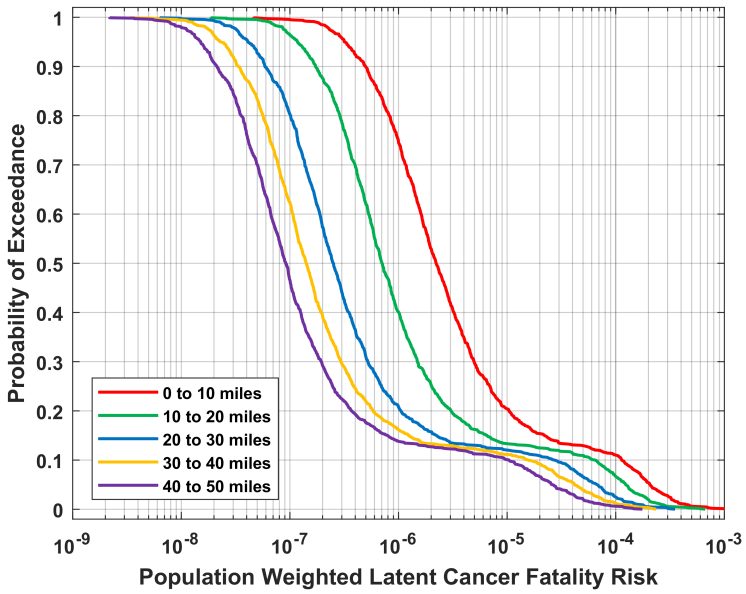

Figure 6-52 Complementary Cumulative Distribution Function of Mean, Population-Weighted LCF Risk (Based on LNT Dose Response) Conditional on a STSBO Occurring for Five Annular Areas Centered on the Surry Site

The emergency phase used in this analysis is the first seven days following the beginning of release into the environment. A 1-year intermediate phase follows the emergency phase. A long-term phase immediately follows the intermediate phase and extends to 50 years.

Figure 6-53 shows the fraction of the total risk from the emergency phase for the set of LCF risk results shown in Figure 6-52. Two key features are apparent from this figure. First, the large majority of the LCF risk based on the linear no-threshold dose response is from the long-term phase at all five distance intervals, even for the realizations with SGTR. The mean values from the five distributions are 0.01, 0.15, 0.17, 0.16, and 0.16 for distance intervals 0 to 10, 10 to 20, 20 to 30, 30 to 40, and 40 to 50 miles, respectively. Less than 30 of the 1147 realizations have emergency-phase contributions to risk that exceed those from the long-term phase. Second, the curve for the distance range from 0 to 10 miles has a very different character than those for the other distance ranges because evacuation is very effective in reducing risk during the emergency phase for the population living within the EPZ. Most of the emergency-phase risk within 10 miles is to the 0.5 percent of the public that is assumed to not evacuate; however, some of the risk is to the slowly evacuating cohorts for the realizations with relatively early releases, mainly the ones with SGTR.

The core damage frequency for a STSBO at Surry provided in NUREG/CR-7110 Volume 2 is 2×10^{-6} pry. Thus, the absolute risk of a STSBO based on a LNT dose-response model, including the possibility of an induced SGTR, is estimated to be about 6×10^{-11} pry (2×10^{-6} pry · 3×10^{-5} conditional risk from Table 6-14) to a member of the population living within 10 miles of the reactor site. For comparison, the absolute risk for a STSBO with and without SGTR in the original SOARCA study was about 3×10^{-10} pry, about a factor of 5 higher.

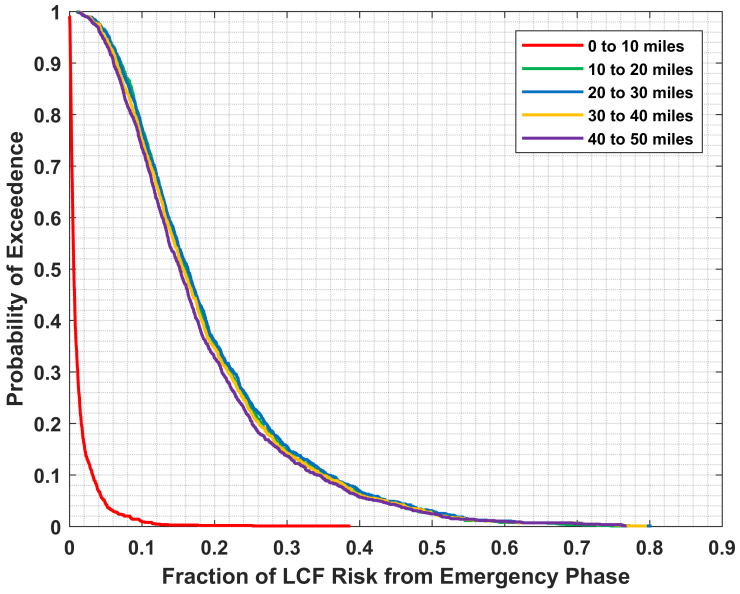

Figure 6-53 Complementary cumulative distribution functions of fraction of the population-weighted LCF risk (based on LNT dose response) from the emergency phase for residents within five annular areas centered on the Surry site

6.2.2 Early Fatalities

Only one realization had a nonzero risk for early fatalities. Within this realization, only a single weather trial, with a probability of about $1 \cdot 10^{-3}$ that this weather pattern would occur at the time of an accident, had doses large enough to exceed the dose threshold for early fatalities. The mean (over weather variability) risk for this realization was approximately $6 \cdot 10^{-8}$ for the population within a 2-mile radius of the site. Thus, accounting for the fact that no early fatality risk was predicted for all but one realization, the likelihood that an early fatality might occur, given the occurrence of a STSBO accident sequence at Surry, is only about $5 \cdot 10^{-11}$ for the population living within 2 miles of the site. The risk is even lower at longer distances. This estimated early fatality risk is so small that it is essentially zero.

6.2.3 Regression Analysis

As part of the statistical analysis of the MACCS UA, a series of regression methods were applied to determine which input parameters most affect LCF risk. Because early-fatality risk was found to be nonzero only for one realization, a regression analysis on early-fatality risk was not possible. The four regression methods, rank regression, quadratic regression, recursive partitioning, and MARS, are described in Section 3.3.2.

6.2.3.1 Regression Analysis of Latent Cancer Fatality Risk Using LNT

Each of the four regression techniques was applied to the 1147 realizations that were evaluated in this UA. Regression analyses for nine distance intervals were performed. Five circular areas with outer radii of 10, 20, 30, 40, and 50 miles were evaluated; annuli (rings) from 10 to 20 miles, 20 to 30 miles, 30 to 40 miles, and 40 to 50 miles were also evaluated. The combination

of regression techniques and distance intervals resulted in a set of 36 results. A complete set of regression analyses were also performed on the subset of the realizations that did not involve induced SGTRs and those that did involve SGTRs. This resulted in a total of 108 regression results. A subset of these results is discussed in this section. The results that are not discussed here have similar trends to those that are included and provide consistent insights.

6.2.3.1.1 All Cases

Table 6-16 through Table 6-18 show the regression results for mean LCF risks from the complete set of 1147 realizations. The results are based on the LNT dose-response model and are shown for three distance intervals from the site: 0 to 10 miles, 10 to 20 miles, and 0 to 50 miles. The word “mean” in the table titles indicates a statistical mean over variable weather and over the population within the spatial interval. Since each realization is a data point in the analysis, mean does not imply a mean over the set of realizations for this purpose.

The first four major columns in the tables are labeled with the regression technique used to create the results. The last two columns contain average values of the main (individual, independent) contribution of the parameter on the result metric and the conjoint influence of the parameter on the result metric. These are calculated as averages of the overall contributions from the four regression techniques (R^2 from rank regression and S_i from the others) weighted by the Final R^2 for that technique and an average of the values of (Final R^2) * (T_i – S_i) for the three nonlinear regression techniques (i.e., all but rank regression), respectively. More details on the regression techniques are provided in Section 3.3.2.

Values of main contribution greater than 0.02 are considered significant, are highlighted, and are discussed in subsequent paragraphs. Conjoint contributions greater than 0.1 are also considered significant and are highlighted. The parameters in the first column of the tables are ordered by the value in the column labeled Main Contribution, so the most important parameters appear in rank order in the table.

The first three parameters in all three regression tables are tubeColdA_max, the maximum flaw depth in the downflow (cold) tubes of SG A, tubeUpflowA_NFD, the maximum flaw depth in the upflow (hot) tubes of SG A, and tubeColdC_max, the maximum flaw depth in the downflow (cold) tubes of SG C. These parameters are important because they strongly influence the likelihood of a SGTR. Thus, they have a critical influence on both the magnitude and timing of the release and directly influence LCF risk. All three parameters are positively correlated with risk because risk increases when the flaw depth is large.

The fourth parameter in all three tables is designLeakLa, which defines the flow area for containment design leakage. The flow area is proportional to the leakage rate prior to containment failure. This parameter has a significant influence on the magnitude of the source term, mainly for realizations that do not include SGTR. This parameter correlates positively with LCF risk, indicating that risk increases when containment design leakage area is relatively large.

The fifth parameter in all three tables is GSHFAC_2, which is the groundshine shielding factor for normal activity during the emergency phase. This parameter is fully rank-correlated with the value of groundshine shielding factor used for the long-term phase. Normal activity is averaged for the population over a normal week of activity, including time spent indoors at home, at work, outdoors, and commuting. Groundshine is not a particularly important dose pathway during the emergency phase, but it is the dominant dose pathway during the long-term phase. Since the groundshine dose received by any individual during the long-term phase is proportional to the

long-term groundshine shielding factor, it is important for latent cancer risk. This is especially so when the long-term-phase dominates over the emergency-phase contribution to risk, which it does for most of the realizations, as shown in a previous section. This parameter is positively correlated with LCF risk, which indicates that risk increases as the parameter value gets larger (which corresponds to less shielding).

Table 6-16 Mean, Individual, LCF Risk Regression Results within a 10-Mile Circular Area for all Realizations Based on LNT

	Rank Regression		Quadratic		Recursive Partitioning		MARS		Main Contribution	Conjoint Contribution
Final R^2	0.49		0.62		0.50		0.58			
Input	R^2 contr.	SRRC	S_i	T_i	S_i	T_i	S_i	T_i		
tubeColdA_max	0.01	0.09	0.21	0.28	0.35	0.43	0.31	0.37	0.122	0.039
tubeUpflowA_NFD	---	---	0.09	0.21	0.28	0.28	0.19	0.35	0.101	0.056
tubeColdC_max	0.01	0.07	0.12	0.20	0.13	0.15	0.14	0.20	0.056	0.031
designLeakLa	0.16	0.38	---	---	0.01	0.01	---	---	0.041	0.000
GSHFAC_2	0.13	0.37	---	---	0.00	0.02	0.01	0.05	0.034	0.011
CFRISK_8	0.03	0.19	0.03	0.18	0.01	0.09	0.04	0.18	0.019	0.073
ORIGENDay	0.08	0.26	0.00	0.03	---	---	---	---	0.019	0.006
tubeHotC_NFD	---	---	0.02	0.05	0.04	0.04	0.03	0.07	0.016	0.014
rupture	0.02	-0.13	---	---	---	---	0.00	0.03	0.006	0.005

** highlighted if main contribution larger than 0.02 or conjoint contribution larger than 0.1*

Table 6-17 Mean, Individual, LCF Risk Regression Results within a 10- to 20-Mile Annular Area for all Realizations Based on LNT

	Rank Regression		Quadratic		Recursive Partitioning		MARS		Main Contribution	Conjoint Contribution
Final R^2	0.47		0.60		0.49		0.68			
Input	R^2 contr.	SRRC	S_i	T_i	S_i	T_i	S_i	T_i		
tubeColdA_max	0.01	0.09	0.29	0.37	0.42	0.50	0.27	0.33	0.143	0.043
tubeUpflowA_NFD	---	---	0.08	0.17	0.24	0.26	0.11	0.18	0.079	0.037
tubeColdC_max	0.00	0.06	0.12	0.18	0.12	0.15	0.18	0.37	0.065	0.058
designLeakLa	0.15	0.38	0.00	0.03	0.00	0.01	---	---	0.038	0.008
GSHFAC_2	0.10	0.32	0.01	0.03	---	---	0.01	0.05	0.028	0.013
ORIGENDay	0.09	0.29	0.00	0.04	---	---	0.01	0.08	0.024	0.023
CFRISK_8	0.03	0.19	0.01	0.15	0.01	0.13	0.02	0.19	0.015	0.083
tubeHotC_NFD	---	---	0.01	0.03	0.04	0.04	0.03	0.05	0.015	0.007
VDEPOS_1	0.01	0.10	0.00	0.04	0.03	0.05	0.01	0.02	0.008	0.014

** highlighted if main contribution larger than 0.02 or conjoint contribution larger than 0.1*

Table 6-18 Mean, Individual, LCF Risk Regression Results within a 50-Mile Circular Area for all Realizations Based on LNT

	Rank Regression		Quadratic		Recursive Partitioning		MARS		Main Contribution	Conjoint Contribution
Final R^2	0.48		0.60		0.48		0.65			
Input	R^2 contr.	SRRC	S_i	T_i	S_i	T_i	S_i	T_i		
tubeColdA_max	0.01	0.09	0.23	0.35	0.40	0.52	0.30	0.32	0.133	0.049
tubeUpflowA_NFD	---	---	0.09	0.15	0.21	0.24	0.08	0.19	0.070	0.039
tubeColdC_max	0.00	0.07	0.10	0.15	0.11	0.11	0.18	0.39	0.058	0.057
designLeakLa	0.15	0.38	---	---	0.00	0.03	---	---	0.039	0.005
GSHFAC_2	0.11	0.34	0.02	0.08	---	---	0.01	0.05	0.033	0.020
ORIGENDay	0.09	0.28	---	---	---	---	0.02	0.07	0.024	0.011
tubeHotC_NFD	---	---	0.00	0.03	0.04	0.05	0.03	0.03	0.012	0.008
CFRISK_8	0.03	0.19	0.00	0.13	0.00	0.12	0.02	0.22	0.011	0.088
VDEPOS_1	0.01	0.10	0.01	0.03	0.04	0.04	---	---	0.009	0.004

** highlighted if main contribution larger than 0.02 or conjoint contribution larger than 0.1*

The sixth parameter showing as significant in Table 6-17 and Table 6-18 is ORIGENDay. This parameter represents the time during the fuel cycle when the accident occurs and directly affects the MELCOR source term calculation through decay heat and it directly affects the MACCS consequence analysis through fission product inventory. Of all the sampled parameters, this is the only one that has such a dual role. The activities of shorter lived isotopes increase with burnup only until secular equilibrium is established; however, the activities of longer lived isotopes, like Cs-137, can nearly double from early to late in the fuel cycle. Because the longer lived isotopes have a significant effect on LCF risk, especially in the long-term phase, this parameter is significant for LCF risk. The correlation between ORIGENDay and predicted risk is positive, indicating that consequences are greater when the accident occurs later in the fuel cycle.

The scatter plots provided in Figure 6-54 through Figure 6-59 show the trends for the six most important inputs for LCF risk discussed in the preceding paragraphs. These scatter plots are for the 50-mile circular area. The trends in these figures are very similar for the other circular and annular areas that were evaluated in this study. The plots qualitatively show the sign and strength of the correlation between the parameters and LCF risk, although the trend is sometimes hard to distinguish by eye because of the density of the dots. Additionally, these plots show the bimodal nature of the source terms: the points at the top of each plot generally correspond to realizations with an induced SGTR (red circles); the points below generally correspond to realizations with no SGTR (blue circles). Scatter plots in which the group of points corresponding to SGTR is shifted right or left indicate a correlation between the variable and the occurrence of a SGTR. The black dashed line on these plots show the cumulative probability function of the sample parameter values.

Figure 6-54 through Figure 6-56 show positive correlations between tubeColdA_max, tubeUpflowA_NFD, and tubeColdC_max, the three steam generator tube flaw depths, with LCF risk, primarily because the cluster of points representing SGTR is shifted to the right in each of these plots. Figure 6-57 shows a positive correlation between designLeakLa, the containment design leakage area, for realizations without SGTR; the correlation is much weaker for realizations with SGTR. Figure 6-58 shows a positive correlation between GSHFAC_2, representing the long-term groundshine shielding factor, with LCF risk. The correlation is relatively independent of whether a SGTR occurs or does not occur, as expected. Figure 6-59

shows a positive correlation between ORIGENDay, the day the accident occurs during the fuel cycle, and LCF risk, mainly for cases where a SGTR does not occur; there is no apparent trend when a SGTR does occur. The cases with SGTR are not shifted to the right noticeably, indicating that a SGTR can occur over the entire fuel cycle. A positive correlation indicates that risk increases when the accident occurs later in the fuel cycle.

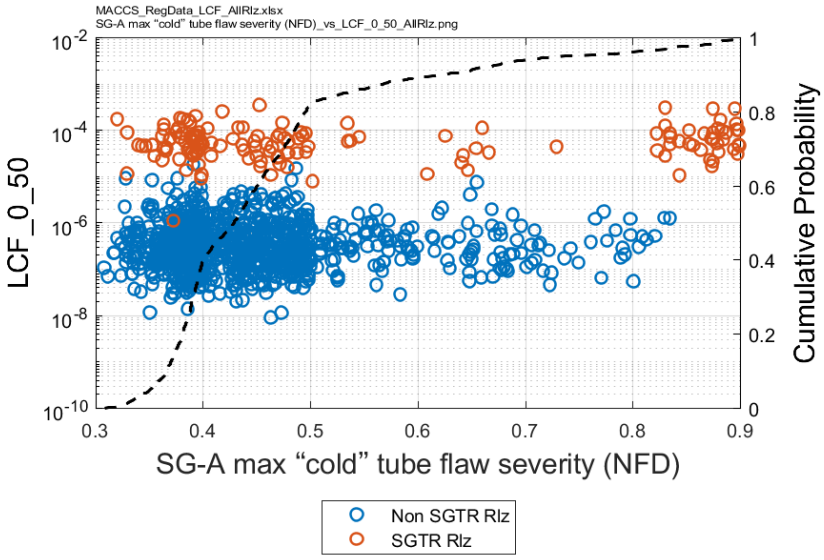

Figure 6-54 Scatter Plot of Mean, Individual, LCF Risk within a 50-Mile Circular Area for all Realizations Versus tubeColdA_max, Conditional on a STSBO Accident

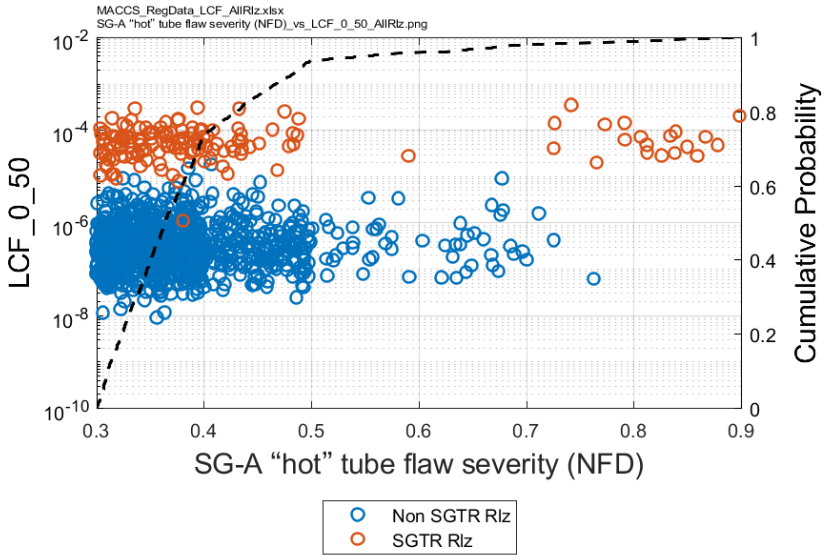

Figure 6-55 **Scatter Plot of Mean, Individual, LCF Risk within a 50-Mile Circular Area for all Realizations Versus tubeUpflowA_NFD, Conditional on a STSBO Accident**

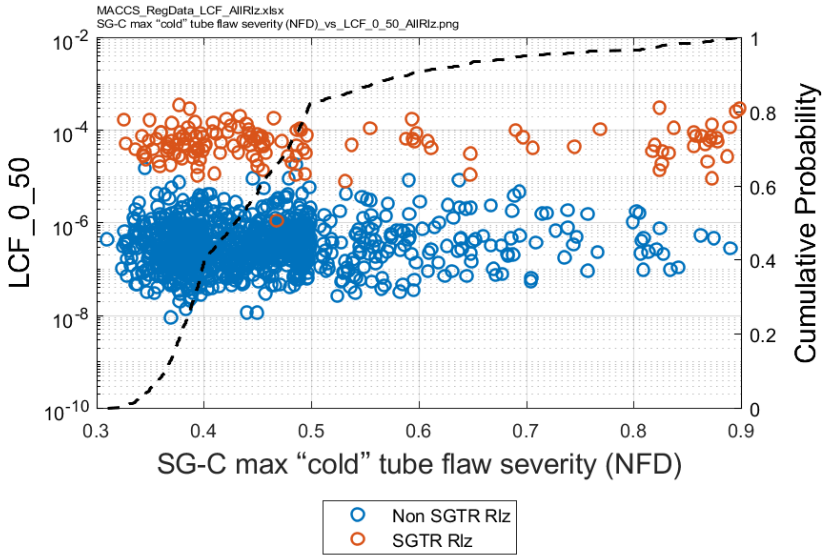

Figure 6-56 **Scatter Plot of Mean, Individual, LCF Risk within a 50-Mile Circular Area for all Realizations Versus tubeColdC_max, Conditional on a STSBO Accident**

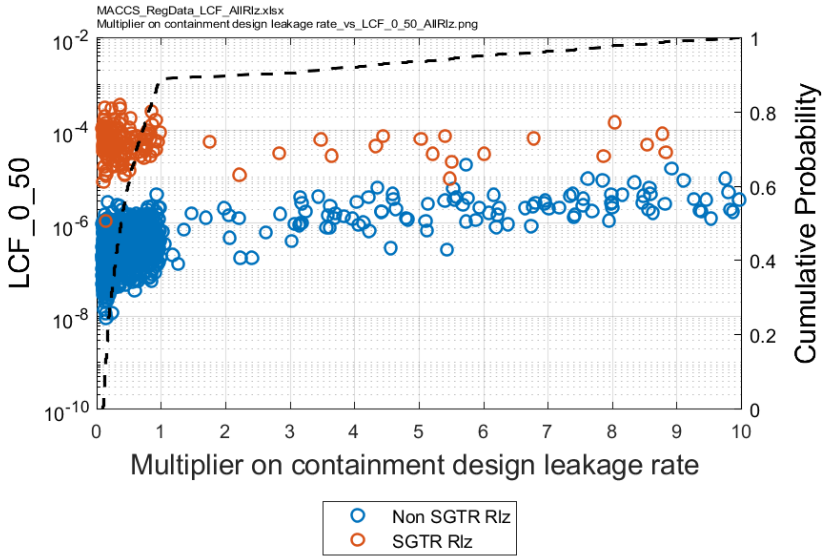

Figure 6-57 **Scatter Plot of Mean, Individual, LCF Risk within a 50-Mile Circular Area for all Realizations Versus designLeakLa, Conditional on a STSBO Accident**

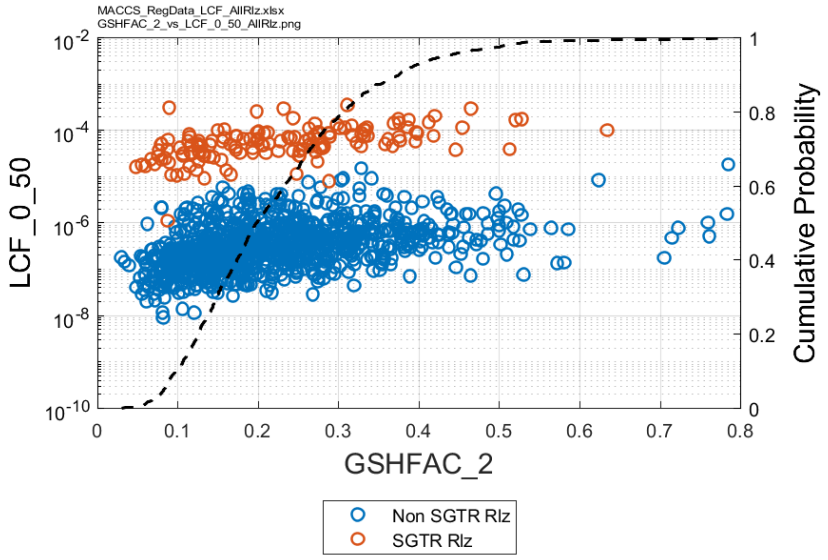

Figure 6-58 **Scatter Plot of Mean, Individual, LCF Risk within a 50-Mile Circular Area for all Realizations Versus GSHFAC_2, Conditional on a STSBO Accident**

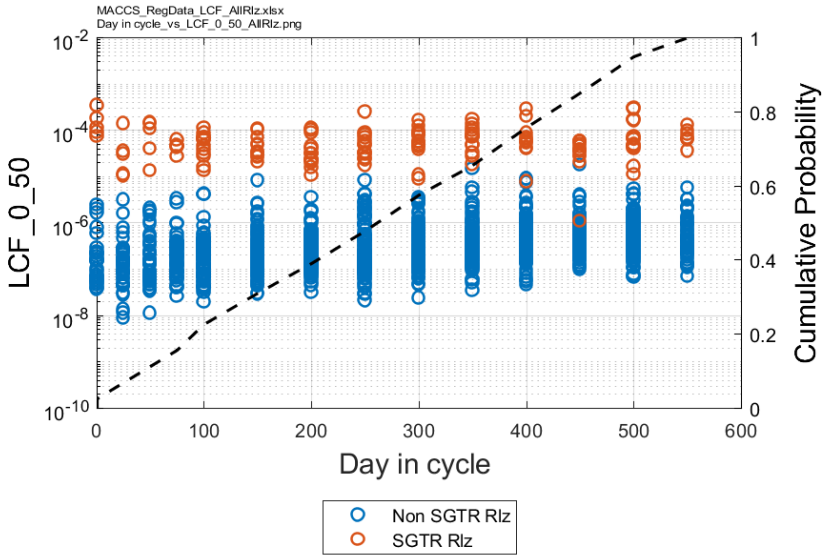

Figure 6-59 Scatter Plot of Mean, Individual, LCF Risk within a 50-Mile Circular Area for all Realizations Versus ORIGENDay, Conditional on a STSBO Accident

6.2.3.1.2 Cases Involving Steam Generator Tube Rupture

The subset of realizations in which SGTR occurs are described in this section. The MELCOR parameters that control SGTR do not dominate in this set of realizations because SGTR is a precondition for the set of realizations that are evaluated; however, one of these MELCOR parameters does appear on the list of important parameters and is discussed below.

Table 6-19 through Table 6-21 show the important input parameters identified by the regression analyses at the same three radial intervals shown in the preceding section. Three parameters are highlighted as being important at all three of the distance ranges, although the order is different in Table 6-19 than it is in the other two tables: (1) groundshine shielding factor (GSHFAC_2), primarily representing groundshine shielding during the long-term phase; (2) the risk factor for residual latent cancer fatalities (CFRISK_8); and (3) the risk factor for colon cancer fatalities (CFRISK_7). Groundshine shielding factor is important, especially during the long-term phase, for the same reasons described in the previous section. The cancer fatality risk factor for residual cancers is the largest of the risk factors and represents all of the cancer types not specifically treated. Risk increases with this parameter, as expected. Similarly, the risk factor for colon cancer is one of the larger risk factors. Even though the risks in SOARCA do not include the ingestion pathway, some of the inhaled contamination is captured in the upper respiratory system and is swallowed and transferred to the digestive system, resulting in risk of colon cancer.

Three additional parameters are identified as important for one or two of the three distance intervals: the dynamic shape factor used in MELCOR (shapeFactor), the containment design leakage area (RCP_Leak), and the dose and dose-rate reduction factor for residual cancers (DDREFA_8). The dynamic shape factor affects aerodynamic drag and thus affects gravitational settling and inertial impaction. A larger value of the dynamic shape factor corresponds to less deposition within the reactor coolant system and thus to larger release fractions, so a larger value corresponds to higher risks. However, the dynamic shape factor is only treated in

MELCOR in this UA; the deposition velocities in MACCS are independent of this parameter. The containment leakage area corresponds to design leakage rate from the containment and correlates positively with risk even for the case when a SGTR occurs, although, as noted above, it has a larger effect for cases with no SGTR. Finally, the dose and dose-rate effectiveness factor for residual cancers is in the denominator of the expression for risk at the low dose range, so the correlation is negative, indicating that risk is larger for smaller values of this parameter. This parameter is synergistic with the residual cancer fatality risk factor, as indicated by the relatively large conjoint contribution factors for the two parameters.

Interestingly, dose and dose-rate effectiveness factor for residual cancers is more important within the 10-mile EPZ than at longer distances. This is likely because the inhalation pathway is significantly less important for the population who evacuate and thus are not directly exposed to the plume during the emergency phase. On the other hand, dynamic shape factor and containment leakage area are more important beyond the 10-mile EPZ. These parameters can have an effect on the release fractions in the MELCOR calculation and the dynamic shape factor should cause the particle size distribution of the released aerosols to be biased toward larger sizes. Both of these influences should increase ground deposition throughout the 50-mile region. So, it is not entirely clear why they have a stronger effect on risk beyond the 10-mile EPZ than within the EPZ. The most likely explanation is that the risks are mitigated to a greater extent at shorter distances, where doses are higher and trigger protective actions, than at longer distances, where doses are lower and do not meet the threshold for mitigative measures.

Table 6-19 Mean, Individual, LCF Risk Regression Results within a 10-Mile Circular Area for Realizations with SGTR Based on LNT

	Rank Regression		Quadratic		Recursive Partitioning		MARS		Main Contribution	Conjoint Contribution
Final R^2	0.58		0.77		0.52		0.76			
Input	R^2 contr.	SRRC	S_I	T_I	S_I	T_I	S_I	T_I		
CFRISK_8	0.18	0.44	0.19	0.34	0.41	0.67	0.31	0.44	0.193	0.118
CFRISK_7	0.08	0.25	0.37	0.44	0.10	0.15	0.37	0.42	0.174	0.040
GSHFAC_2	0.19	0.47	0.07	0.11	0.07	0.13	0.04	0.05	0.077	0.024
DDREFA_8	0.05	-0.22	0.07	0.29	0.10	0.31	0.07	0.24	0.053	0.134
RCP_Leak	0.02	0.16	0.03	0.04	---	---	---	---	0.009	0.004
DDREFA_5	0.03	0.17	---	---	0.01	0.01	---	---	0.008	0.000
burn_dir	0.02	0.18	0.01	0.04	---	---	0.00	0.02	0.008	0.013
I_134_ICH_1	---	---	---	---	---	---	0.02	0.03	0.004	0.004
priSVfrac	0.01	0.27	---	---	---	---	---	---	0.003	0.000

** highlighted if main contribution larger than 0.02 or conjoint contribution larger than 0.1*

Table 6-20 Mean, Individual, LCF Risk Regression Results within a 10- to 20-Mile Annular area for Realizations with SGTR Based on LNT

	Rank Regression		Quadratic		Recursive Partitioning		MARS		Main Contribution	Conjoint Contribution
Final R^2	0.61		0.99		0.51		0.56			
Input	R^2 contr.	SRRC	S_i	T_i	S_i	T_i	S_i	T_i		
GSHFAC_2	0.28	0.53	0.06	0.12	0.24	0.34	0.16	0.16	0.138	0.035
CFRISK_7	0.07	0.24	0.03	0.21	0.46	0.49	0.39	0.53	0.137	0.091
CFRISK_8	0.14	0.35	0.04	0.19	0.18	0.26	0.25	0.39	0.103	0.086
shapeFactor	0.06	0.18	---	---	---	---	0.07	0.07	0.024	0.000
SGTRC_loc	0.00	0.08	0.05	0.26	---	---	---	---	0.014	0.068
La_140_ICH_1	---	---	0.03	0.09	---	---	0.01	0.02	0.010	0.023
burn_dir	0.01	0.17	0.01	0.14	---	---	0.00	0.01	0.006	0.043
I2GasGapFraction	---	---	0.02	0.06	0.00	0.02	---	---	0.005	0.016
Te_127_ICH_1	---	---	0.02	0.06	---	---	0.00	0.00	0.005	0.014

** highlighted if main contribution larger than 0.02 or conjoint contribution larger than 0.1*

Table 6-21 Mean, Individual, LCF Risk Regression Results within a 50-Mile Circular Area for Realizations with SGTR Based on LNT

	Rank Regression		Quadratic		Recursive Partitioning		MARS		Main Contribution	Conjoint Contribution
Final R^2	0.59		0.93		0.54		0.62			
Input	R^2 contr.	SRRC	S_i	T_i	S_i	T_i	S_i	T_i		
GSHFAC_2	0.35	0.61	0.07	0.11	0.29	0.39	0.20	0.21	0.173	0.032
CFRISK_7	0.07	0.27	0.06	0.10	0.44	0.48	0.34	0.49	0.143	0.049
CFRISK_8	0.11	0.35	0.05	0.40	0.13	0.22	0.21	0.34	0.088	0.155
shapeFactor	0.06	0.27	0.01	0.02	0.01	0.02	0.10	0.10	0.035	0.002
RCP_Leak	---	---	0.08	0.21	---	---	0.00	0.01	0.024	0.041
SGTRB_loc	---	---	0.03	0.35	---	---	0.01	0.02	0.010	0.101
SGTRC_loc	---	---	0.03	0.04	---	---	---	---	0.008	0.005
CWASH1	---	---	0.02	0.21	---	---	---	---	0.005	0.060
msiv_leak_c	---	---	0.01	0.06	---	---	0.00	0.02	0.004	0.019

** highlighted if main contribution larger than 0.02 or conjoint contribution larger than 0.1*

The scatter plots provided in Figure 6-60 through Figure 6-64 show the trends between the six most important inputs and LCF risks, as discussed in the preceding paragraphs. The trends in these figures are for the 50-mile circular area, but they are very similar for the other circular and annular areas that were evaluated in this study. The plots indicate the sign of the correlation between the parameters and LCF risk, although the trend is sometimes hard to distinguish by visual inspection alone.

The risk coefficient for residual cancers is positively correlated with LCF risk, as shown in Figure 6-60. Similarly, the correlation between the risk factor for colon cancers is positively correlated with LCF risk, as shown in Figure 6-61, indicating that a larger value of this risk factor increases the LCF risk. The MACCS parameter for groundshine shielding factor affects doses from the groundshine pathway, which dominates the long-term health effect risk. The groundshine shielding factor (GSHFAC_2) is positively correlated with risk because a higher value increases doses through this pathway (Figure 6-62). Figure 6-63 shows that the dose and dose-rate reduction factor for residual cancers (DDREFA_8) has a small negative correlation with LCF risk within 50 miles, but it has a larger correlation within 10 miles, as described above. Finally, Figure 6-64 shows that there is a significant positive correlation between the dynamic shape factor (shapeFactor) used in MELCOR and LCF risk. A larger value of shape factor

corresponds to less deposition within the reactor coolant system and containment and, therefore, more release into the atmosphere. Furthermore, it should bias the aerosol size distribution toward larger sizes since gravitational settling diminishes as this parameter increases in the MELCOR treatment of aerosol transport. Both of these influences should result in increased deposition in the MACCS calculation, leading to higher groundshine exposures. Thus, a larger value of shape factor corresponds to a larger LCF risk.

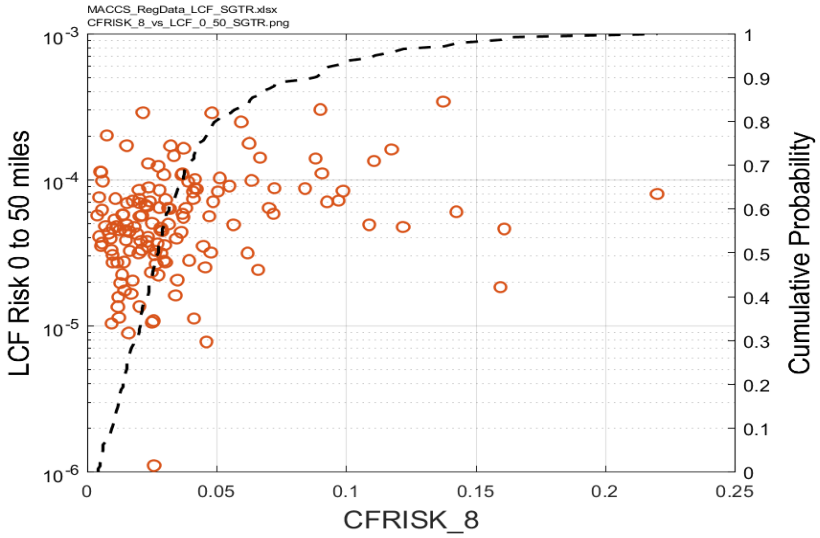

Figure 6-60 Scatter Plot of Mean, Individual, LCF Risk within a 50-Mile Circular Area for Realizations Involving SGTR, Conditional on a STSBO Accident, CFRRISK_8

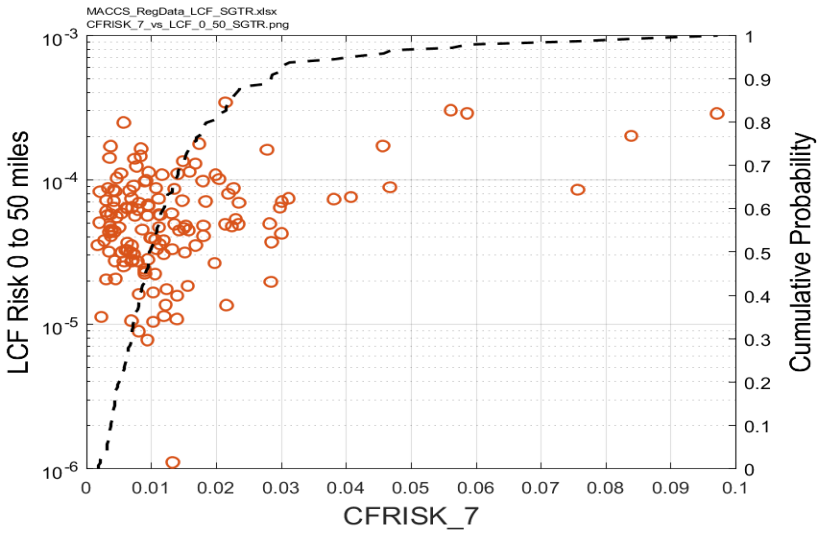

Figure 6-61 Scatter Plot of Mean, Individual, LCF Risk within a 50-Mile Circular Area for Realizations involving SGTR, Conditional on a STSBO Accident, Versus CFRISK_7

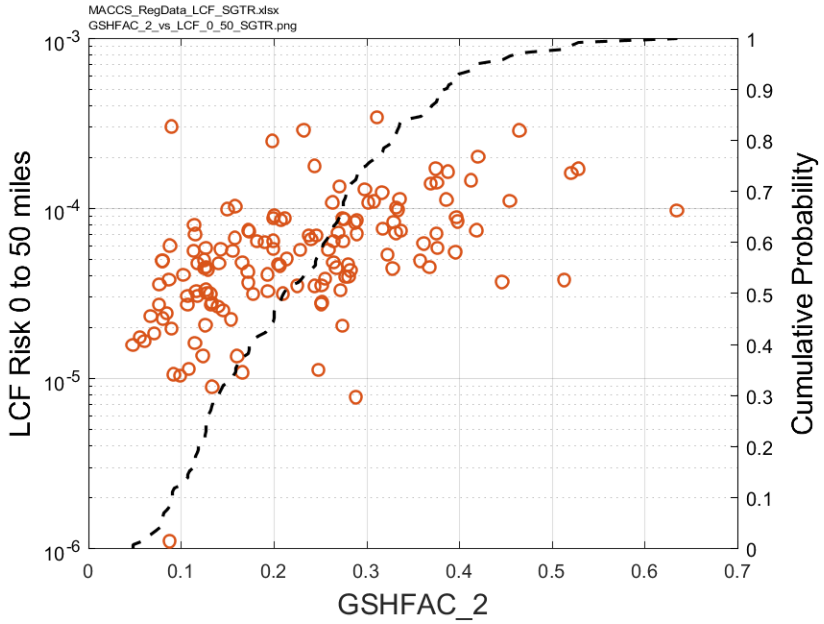

Figure 6-62 **Scatter Plot of Mean, Individual, LCF Risk within a 50-Mile Circular Area for Realizations with SGTR, Conditional on a STSBO Accident, Versus Groundshine Shielding Factor for Normal Activity during the Emergency Phase, GSHFAC_2**

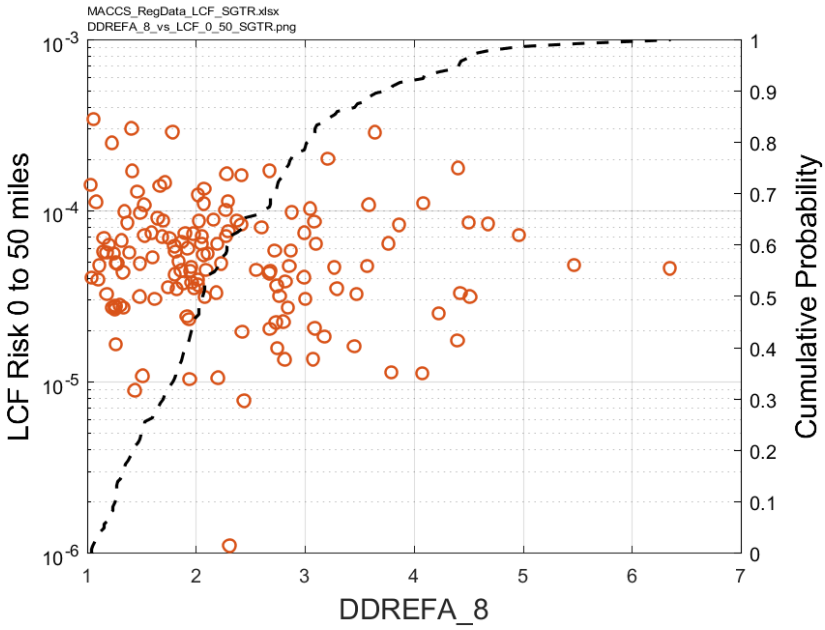

Figure 6-63 **Scatter Plot of Mean, Individual, LCF Risk within a 50-Mile Circular Area for Realizations with SGTR, Conditional on a STSBO Accident, Versus DDREFA_8**

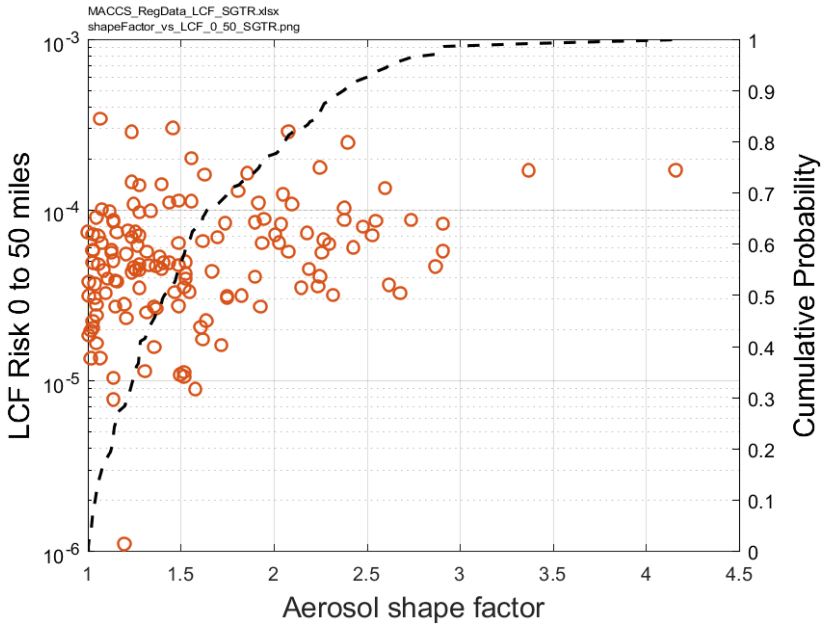

Figure 6-64 Scatter Plot of Mean, Individual, LCF Risk within a 50-Mile Circular Area for Realizations involving SGTR, Conditional on a STSBO Accident, Versus the Aerosol Shape Factor (shapeFactor)

6.2.3.1.3 Cases Not Involving Steam Generator Tube Rupture

The subset of realizations in which a SGTR does not occur is described in this section. The MELCOR parameters that control the occurrence of a steam generator tube rupture do not dominate in this set of cases because SGTR is eliminated from the set of realizations that are evaluated.

Table 6-22 through Table 6-24 show the important input parameters identified by the regression analyses at the same three radial intervals shown in the two preceding sections. The four most important parameters appear in the same order for all three distance intervals. The most important input parameter is the containment design leakage area, designLeakLa, which controls the rate of release prior to containment failure. This parameter has an elevated importance for the cases without a SGTR because containment leakage is the dominant release pathway. Second is the groundshine shielding factor for normal activity during the emergency phase, GSHFAC_2, which is fully correlated and is a surrogate for the groundshine shielding factor for the long-term phase. The third most important parameter is the time during the fuel cycle at which the accident occurs, ORIGENDay. The fourth most significant parameter at all three distance intervals is cancer fatality risk factor for residual cancers, CFRISK_8. Residual cancers (the ones not specifically modeled) are larger than any of the individual cancer types that are modeled and thus this parameter is more important than the other cancer risk factors.

Table 6-22 Mean, Individual, LCF Risk (Based on LNT) Regression Results within a 10-Mile Circular Area for Realizations that do Not Involve SGTR

	Rank Regression		Quadratic		Recursive Partitioning		MARS		Main Contribution	Conjoint Contribution
Final R^2	0.79		0.95		0.75		0.95			
Input	R^2 contr.	SRRC	S_i	T_i	S_i	T_i	S_i	T_i		
designLeakLa	0.27	0.51	0.48	0.77	0.53	0.86	0.49	0.80	0.399	0.271
GSHFAC_2	0.20	0.46	0.08	0.20	0.08	0.38	0.07	0.19	0.100	0.152
ORIGENDay	0.13	0.35	0.03	0.07	0.02	0.02	0.03	0.05	0.048	0.022
CFRISK_8	0.04	0.20	0.03	0.14	0.01	0.01	0.04	0.15	0.027	0.067
rupture	0.03	-0.17	0.01	0.01	0.00	0.02	---	---	0.011	0.007
DDREFA_8	0.02	-0.12	0.01	0.05	0.00	0.15	0.01	0.02	0.007	0.055
CYSIGA_1	0.02	-0.16	---	---	---	---	0.01	0.01	0.007	0.002

** highlighted if main contribution larger than 0.02 or conjoint contribution larger than 0.1*

Table 6-23 Mean, Individual, LCF Risk (Based on LNT) Regression Results within a 10- to 20-Mile Annular Area for Realizations that do Not Involve SGTR

	Rank Regression		Quadratic		Recursive Partitioning		MARS		Main Contribution	Conjoint Contribution
Final R^2	0.76		0.94		0.72		0.95			
Input	R^2 contr.	SRRC	S_i	T_i	S_i	T_i	S_i	T_i		
designLeakLa	0.26	0.50	0.44	0.77	0.54	0.87	0.52	0.79	0.390	0.269
GSHFAC_2	0.15	0.40	0.06	0.23	0.06	0.32	0.06	0.21	0.078	0.162
ORIGENDay	0.16	0.37	0.03	0.04	0.03	0.07	0.02	0.02	0.055	0.015
CFRISK_8	0.04	0.20	0.04	0.09	0.01	0.01	0.03	0.08	0.027	0.032
rupture	0.04	-0.19	---	---	0.00	0.01	0.00	0.01	0.010	0.007
CYSIGA_1	0.02	-0.17	0.01	0.02	0.00	0.00	0.00	0.05	0.008	0.019
DDREFA_8	0.01	-0.12	0.01	0.03	0.00	0.16	0.00	0.03	0.007	0.050

** highlighted if main contribution larger than 0.02 or conjoint contribution larger than 0.1*

Table 6-24 Mean, Individual, LCF Risk (Based on LNT) Regression Results within a 50-Mile Circular Area for Realizations that do Not Involve SGTR

	Rank Regression		Quadratic		Recursive Partitioning		MARS		Main Contribution	Conjoint Contribution
Final R^2	0.77		0.94		0.74		0.95			
Input	R^2 contr.	SRRC	S_i	T_i	S_i	T_i	S_i	T_i		
designLeakLa	0.27	0.50	0.45	0.78	0.57	0.88	0.53	0.80	0.404	0.265
GSHFAC_2	0.17	0.43	0.07	0.23	0.06	0.38	0.08	0.20	0.089	0.166
ORIGENDay	0.15	0.37	0.02	0.03	0.02	0.03	0.03	0.04	0.055	0.006
CFRISK_8	0.04	0.20	0.04	0.13	0.00	0.04	0.03	0.12	0.026	0.064
rupture	0.04	-0.18	0.01	0.02	0.00	0.00	0.00	0.03	0.011	0.014
DDREFA_8	0.01	-0.12	0.01	0.07	0.00	0.14	0.01	0.04	0.008	0.064

** highlighted if main contribution larger than 0.02 or conjoint contribution larger than 0.1*

The scatter plots provided in Figure 6-65 through Figure 6-68 show the trends between the four most important of the uncertain inputs and LCF risk, as discussed in the preceding paragraph. The trends in these figures are for the 50-mile circular area, but they are very similar for the other circular and annular areas that were evaluated in this study. The plots indicate the sign and degree of the correlation between the parameters and LCF risk, although the trend is sometimes hard to distinguish by visual inspection alone. The sign of the correlations are also indicated by the signs of SRRC in the above tables. All four of the most important parameters have positive signs in the tables.

Figure 6-65 shows that the containment design leakage area, designLeakLa, which is proportional to the leakage rate, has a clear positive correlation with the LCF risk. That indicates that higher leakage rates lead to higher LCF risk, as expected.

Similarly, Figure 6-66 shows a clear trend between groundshine shielding factor for normal activity during the emergency phase, GSHFAC_2 (which is correlated with a coefficient of 1.0 with groundshine shielding factor during the long-term phase) and LCF risk. The value during the long-term phase has a greater influence on risk than the value during the emergency phase because of the extended period over which groundshine contributes to dose (50 years versus 1 week). An increases in the shielding factor corresponds to an increase in groundshine dose and, thus, to an increase in LCF risk.

Figure 6-67 shows a clear trend between time during the fuel cycle (ORIGENDay) and LCF risk. The trend indicates a positive correlation, which indicates that LCF risk increases with fuel burnup. Cs-137 activity nearly doubles from beginning of cycle to end of cycle, and this isotope is a dominant contributor to long-term groundshine doses, as shown in a subsequent section. The plot indicates that the trend flattens toward the end of cycle, which is likely because many of the important isotopes reach secular equilibrium sometime during the fuel cycle.

Finally, Figure 6-68 indicates that the residual cancer fatality risk factor, CFRISK_8, is positively correlated with LCF risk. Thus, cancer risk increases when this factor increases, as expected. While all of the cancer risk factors should be positively correlated with LCF risk, residual cancers are the largest single contributor and thus this risk factor is more important than the other ones.

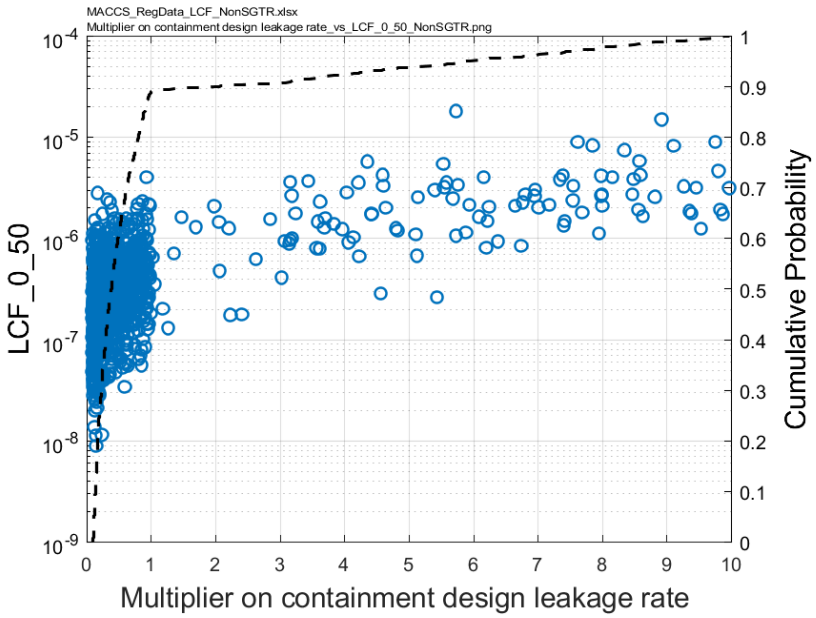

Figure 6-65 Scatter Plot of Mean, Individual, LCF Risk (Based on LNT) within a 50-Mile Circular Area for Realizations that do Not Involve SGTR, Conditional on a STSBO Accident, Versus Containment Design Leak Area, designLeakLa

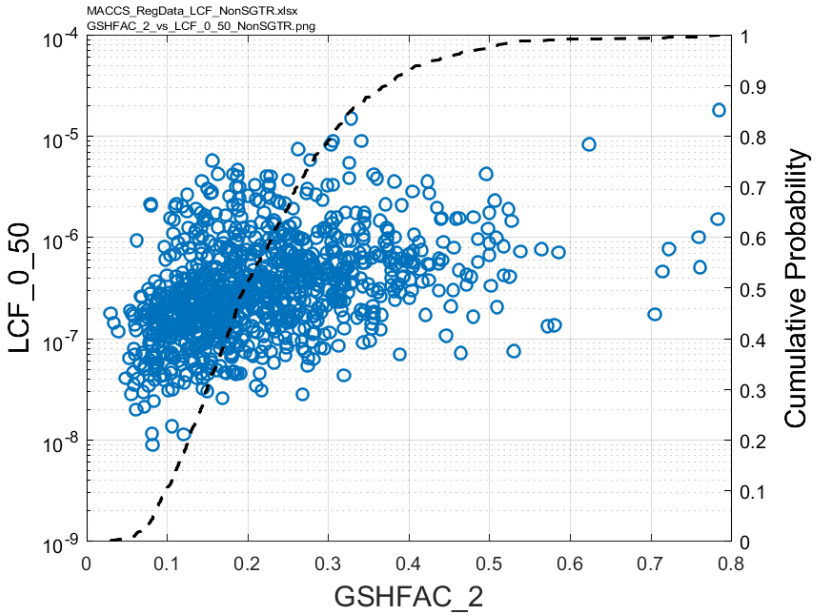

Figure 6-66 **Scatter Plot of Mean, Individual, LCF Risk (Based on LNT) within a 50-Mile Circular Area for Realizations that do Not Involve SGTR, Conditional on a STSBO Accident, Versus Groundshine Shielding Factor for Normal Activity during the Emergency Phase, GSHFAC_2**

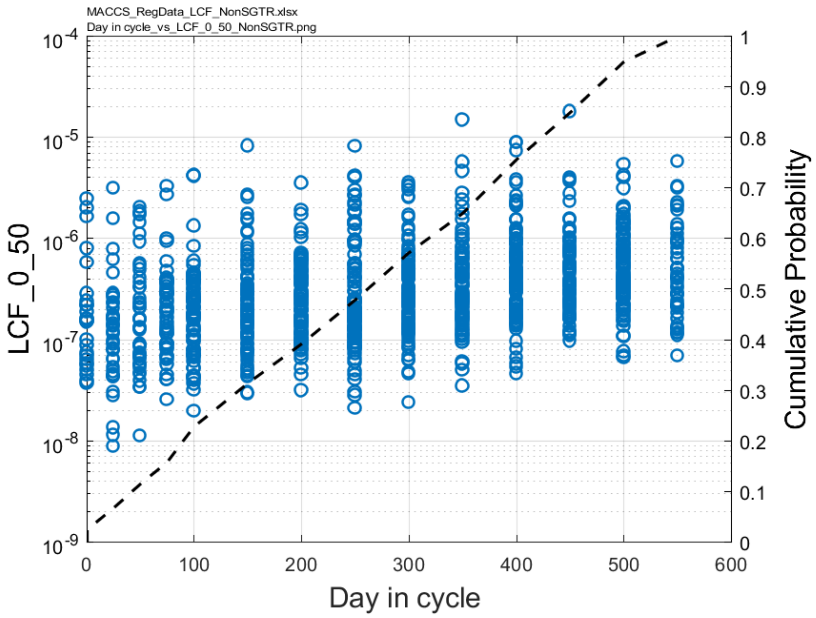

Figure 6-67 **Scatter Plot of Mean, Individual, LCF Risk (Based on LNT) within a 50-Mile Circular Area for Realizations that do Not Involve SGTR, Conditional on a STSBO Accident, Versus Time during the Fuel Cycle, ORIGENDay**

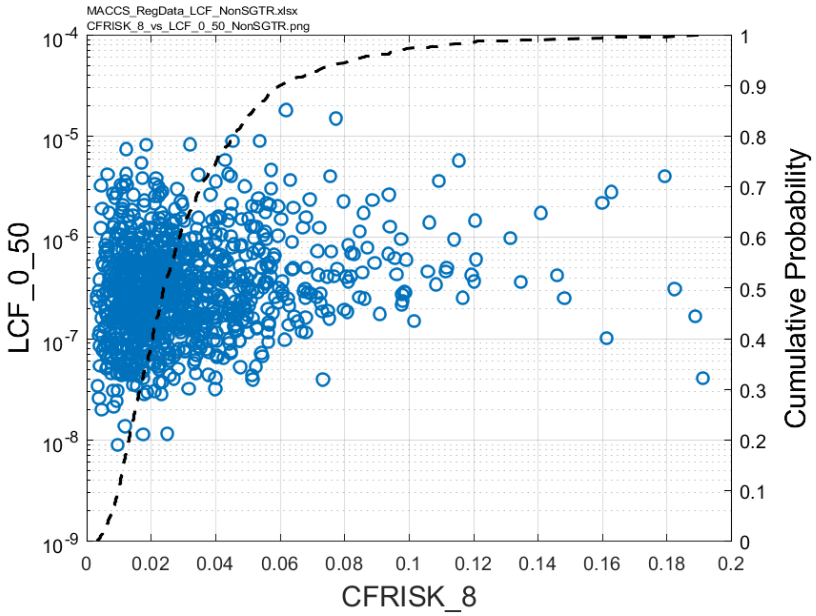

Figure 6-68 Scatter Plot of Mean, Individual, LCF Risk (Based on LNT) within a 50-Mile Circular Area for Realizations that do Not Involve SGTR, Conditional on a STSBO Accident, Versus Residual Cancer Fatality Risk Factor, CFRISK_8

6.2.3.2 Regression Analysis of Early Fatality Risk

Because a nonzero result was only predicted for a single realization, it was not possible to perform a regression analysis on early fatality risk for this Surry UA.

6.2.4 Analysis of Single Realizations

This section evaluates six individual realizations from the uncertainty analysis in greater detail to identify the influences affecting the predicted consequences. The six realizations are

(1) the reference SGTR (Realization 37),
(2) the reference non-SGTR (Realization 459),
(3) the earliest release (Realization 19),
(4) the largest release of cesium mass (Realization 237),
(5) the earliest containment failure (Realization 1062), and
(6) the earliest SGTR (Realization 777).

This is a subset of the realizations that are discussed in terms of MELCOR accident progression and source term in Section 5.3. Masses of released cesium for these realizations are shown in Figure 6-69. Realization 237 has the largest release of cesium, followed by Realization 777, the earliest SGTR. The earliest release, Realization 19, is next followed by the reference SGTR, Realization 37. The other two realizations, the reference non-SGTR and the earliest containment failure, both have very small and late cesium releases. In both cases, the containment fails by gradual over-pressurization that leads to an increased release rate later in the accident.

Each of these realizations are discussed further in the following sections. The most significant of the sampled MACCS input parameters for these six realizations, as determined by the regression analyses shown in Section 6.2.3, are displayed in Table 6-25.

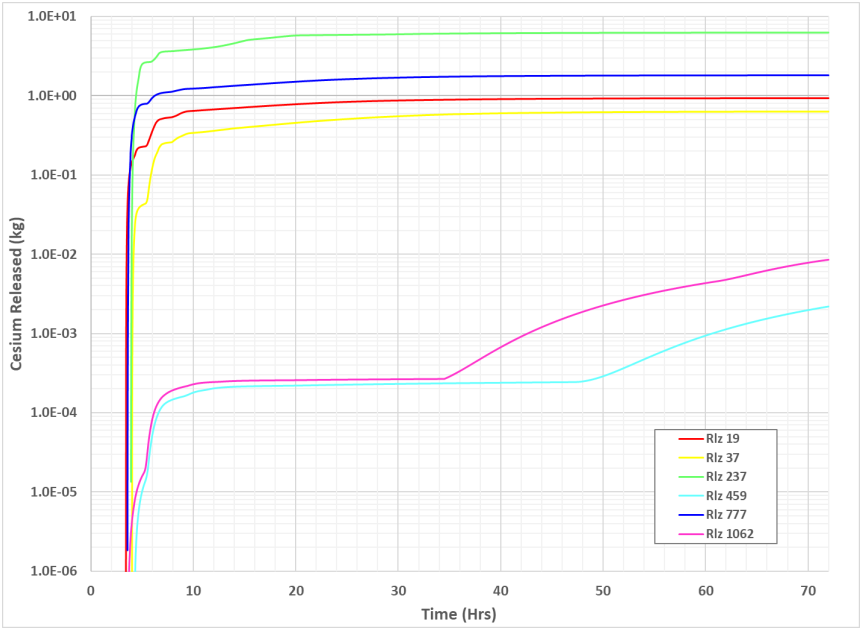

Figure 6-69 Cesium Release (Mass) Histories for Six Realizations

Table 6-25 Most Significant Sampled Input Parameters in the Six Individual Realizations

Realization		Parameter Description and Name					
		Groundshine Shielding Factor	Risk Factor for Colon Cancer (1/Sv)	Risk Factor for Residual Cancers (1/Sv)	Dose and Dose-Rate Effectiveness Factor for Residual Cancers	Time During Cycle (d)	Estimated Bias from Sampled MACCS Parameters
No.	Description	GSHFAC_2	CFRISK_7	CFRISK_8	DDREFA_8	ORIGEN Day	
37	Reference SGTR	0.346	0.0180	0.0062	2.88	300	0.82
459	Reference non-SGTR	0.480	0.0356	0.0977	3.52	400	6.52
19	Earliest Release	0.056	0.0104	0.0173	1.27	500	0.40
237	Largest Cs Release	0.226	0.0587	0.0217	1.79	500	3.37
1062	Earliest CF	0.178	0.0050	0.0373	1.30	550	2.35
777	Earliest SGTR	0.424	0.0840	0.0078	3.21	400	5.27
Mean of Sampled Values		0.219	0.0144	0.0324	2.24	281	1.00

Many of the sampled input parameters used in these six realizations are within a factor of 2 of the mean of all of the sampled values, as shown in Table 6-25; however, there are some exceptions. Realization 19 has a value of groundshine shielding factor that is about a factor of 4 lower than the mean; realizations 459 and 777 have groundshine shielding factors that are about a factor of 2 higher than the mean. Higher values of the groundshine shielding factor result in higher cancer fatality risk, all else being equal. For the two cancer fatality risk factors, realizations 19, 37, and 1062 have values of one or both factors that are relatively low, which correspond to lower LCF risks; realizations 237 and 459 have values that are relatively high, which should give higher LCF risks. Dose and dose-rate effectiveness factor is in the denominator for health effect risk, so a lower value leads to a higher risk, all else being equal. The values for realizations 19 and 1062 are about a factor of 2 below the mean; none of the

realizations have values that are as much as a factor of 2 above the mean. Finally, all of the selected realizations have values of time during cycle that are above the mean, but by no more than a factor of 2.

An equation that approximately expresses the influence of the five parameters shown in Table 6-25, other things being equal, on the results for the six selected realizations is the following:

$$Risk \propto \frac{GSHFAC\_2}{GSHFAC\_2(mean)} \times \frac{CFRISK\_7 + CFRISK\_8 \times \frac{DDREF\_8(mean)}{DDREF\_8}}{CFRISK\_7(mean) + CFRISK\_8(mean)} \times \frac{ORIGENDay}{ORIGENDay(mean)}$$

The factor from this equation is shown in the final column of the table to provide an expectation of the relative influence of the sampled MACCS input parameters on the calculated risk; the other major contributor to the LCF risk is the source term from MELCOR. Only one of the values in the last column of the table is between 0.5 and 2.0. Four of the six realizations are expected to be significantly biased on the high side because of the sampled MACCS input parameters; only one of the six realizations is expected to be significantly biased on the low side because of the sampled MACCS input parameters.

6.2.4.1 Reference SGTR

The results for the reference SGTR realization (Realization 37) are shown in Figure 6-70 and Figure 6-71. The results are of population-weighted, LCF risk. Probability in the figures represents the aleatory uncertainty from weather variability. The square symbol on each of the curves shows the mean of the distributions.

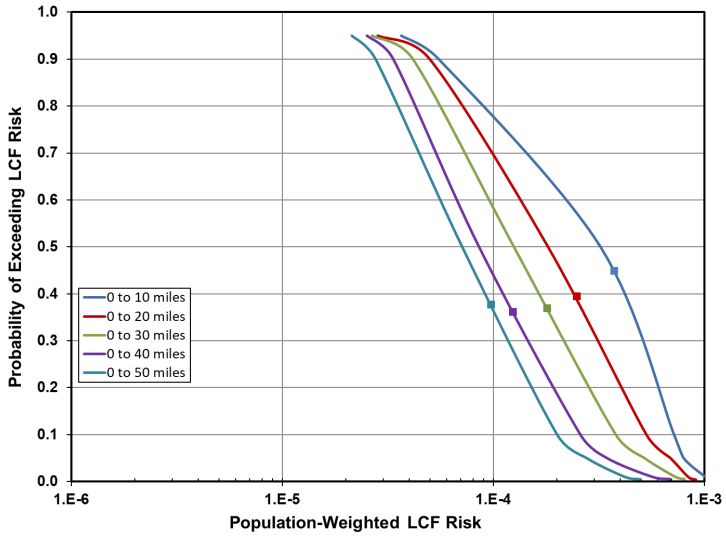

Figure 6-70 Complementary Cumulative Distribution Function of Population-Weighted LCF Risk within Five Circular Areas Centered on the Surry Site for the Reference SGTR Realization

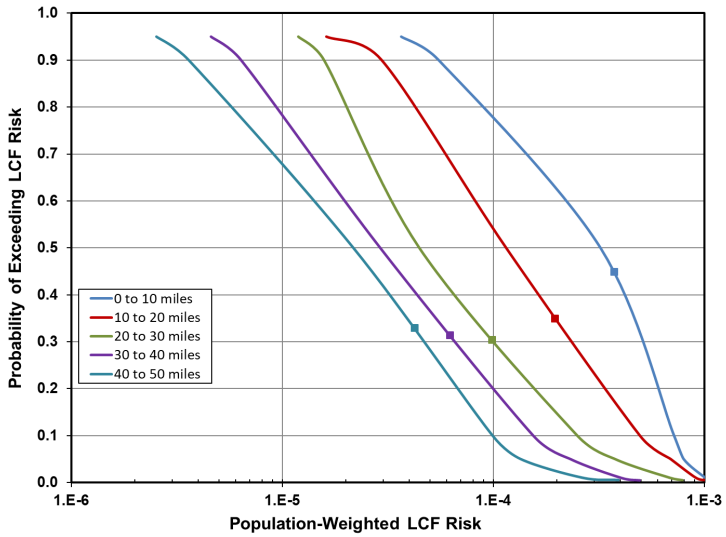

Figure 6-71 Complementary Cumulative Distribution Function of Population-Weighted LCF Risk within Five Annular Areas Centered on the Surry Site for the Reference SGTR Realization

The risks shown in these figures are representative of the values shown in Figure 6-51 and Figure 6-52 for the portion of the curves that represent SGTR (to the right of the shoulder in the CCDF curves). The ranges of risks from weather variability are about one and one-half orders of magnitude for the circular areas and about two orders of magnitude for the annular areas, especially for the larger radii. This realization is relatively unbiased because of the sampled MACCS input parameters, as shown in Table 6-25; it is biased toward the high end of the risk spectrum by virtue of the relatively large source term calculated by MELCOR for this SGTR sequence, as shown in Figure 6-69.

6.2.4.2 Reference Non-SGTR

The results for the reference non-SGTR single realization (Realization 459) are shown in Figure 6-72 and Figure 6-73. The results are of population-weighted, LCF risk. Probability in the figures represents the aleatory uncertainty from weather variability. The square symbol on each of the curves shows the mean of the distributions.

The risks shown in these figures are representative of the values shown in Figure 6-51 and Figure 6-52 for the portion of the curves that represent non-SGTR (to the left of the shoulder in the CCDF curves). The risks are about two orders of magnitude lower than the ones shown in the previous section. The risks for this realization are biased toward the high side by the MACCS input parameters assigned to this realization by nearly an order of magnitude, as shown in Table 6-25. The risks are influenced to be low by the small and late cesium release calculated by MELCOR for this realization, as shown in Figure 6-69. The ranges of risks from weather variability are about one order of magnitude for the circular areas and about one and one-half orders of magnitude for the annular areas, especially for the larger radii.

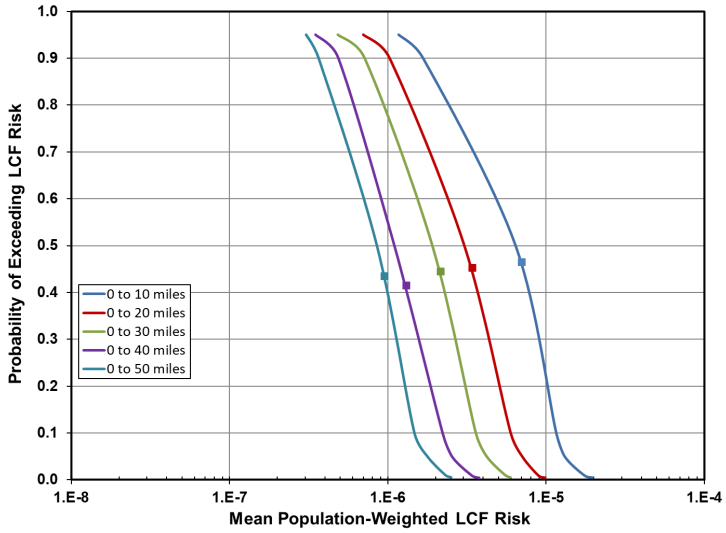

Figure 6-72 Complementary Cumulative Distribution Function of Population-Weighted LCF Risk within Five Circular Areas Centered on the Surry Site for the Reference Non-SGTR Realization

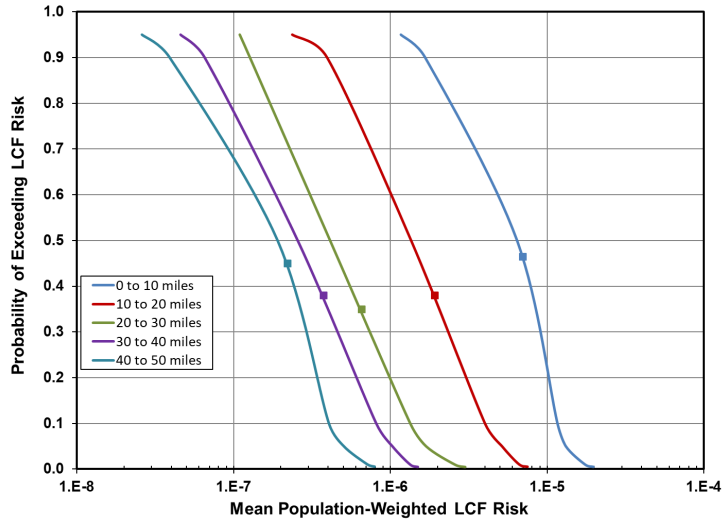

Figure 6-73 Complementary Cumulative Distribution Function of Population-Weighted LCF Risk within Five Annular Areas Centered on the Surry Site for the Reference Non-SGTR Realization

6.2.4.3 Earliest Release

The results for the realization with the earliest release (Realization 19) are shown in Figure 6-74 and Figure 6-75. The results are of population-weighted, LCF risk. Probability in the figures represents the aleatory uncertainty from weather variability. The square symbol on each of the curves shows the mean of the distributions.

The risks shown in these figures are intermediate between those shown in the previous two sections. The risks are biased toward the low side by the MACCS input parameters assigned to this realization, as shown in Table 6-25. The source term is for a SGTR and is similar to but slightly larger than the one for the reference SGTR reported above. The ranges of risks from weather variability are about one and one-half orders of magnitude for the circular areas and about two orders of magnitude for the annular areas, especially for the larger radii.

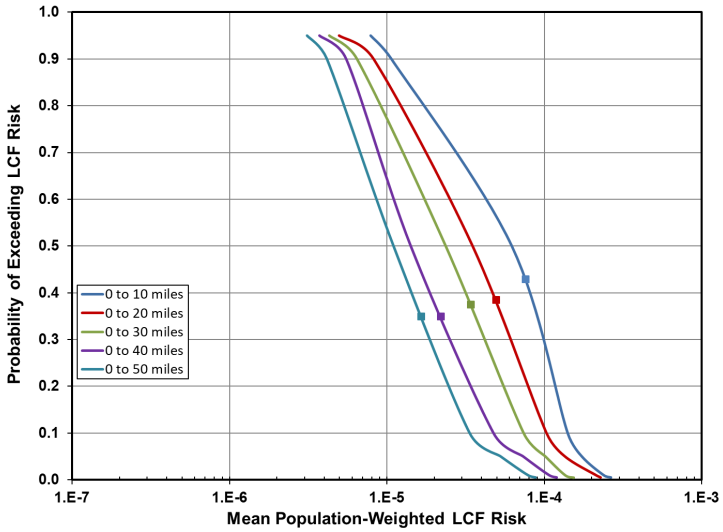

Figure 6-74 Complementary Cumulative Distribution Function of Population-Weighted LCF Risk within Five Circular Areas Centered on the Surry Site for the Realization with the Earliest Release

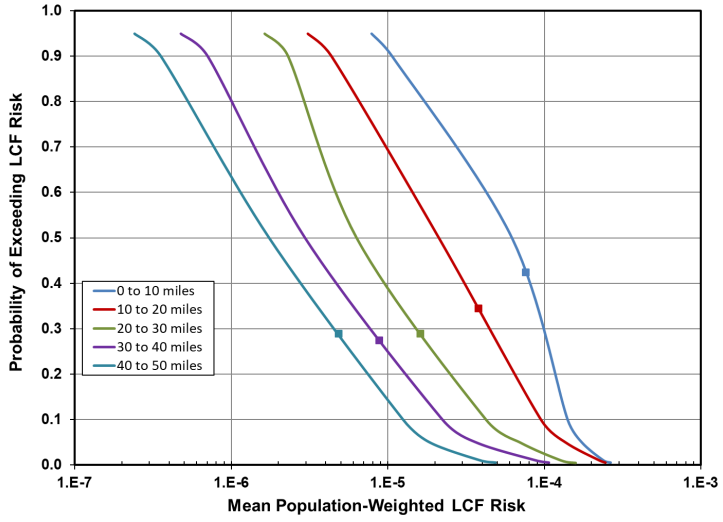

Figure 6-75 Complementary Cumulative Distribution Function of Population-Weighted LCF Risk within Five Annular Areas Centered on the Surry Site for the Realization with the Earliest Release

6.2.4.4 Largest Cs Release

The results for the realization with the largest cesium release (Realization 237) are shown in Figure 6-76 and Figure 6-77. The results are of population-weighted, LCF risk. Probability in the figures represents the aleatory uncertainty from weather variability. The square symbol on each of the curves shows the mean of the distributions.

The risks shown in these figures are the largest of all the risks shown in the section. They are biased toward the high side by the MACCS input parameters sampled for this realization, as shown in Table 6-25. Furthermore, the source term for this realization is for a SGTR and is similar to but about an order-of-magnitude larger than the one for the reference SGTR reported above. The combination of the sampled MACCS input parameters and the source term make the risks for this realization very close to the maxima of the values shown in Figure 6-51 and Figure 6-52. The ranges of risks from weather variability are about one and one-half orders of magnitude for the circular areas and about two orders of magnitude for the annular areas, especially for the larger radii.

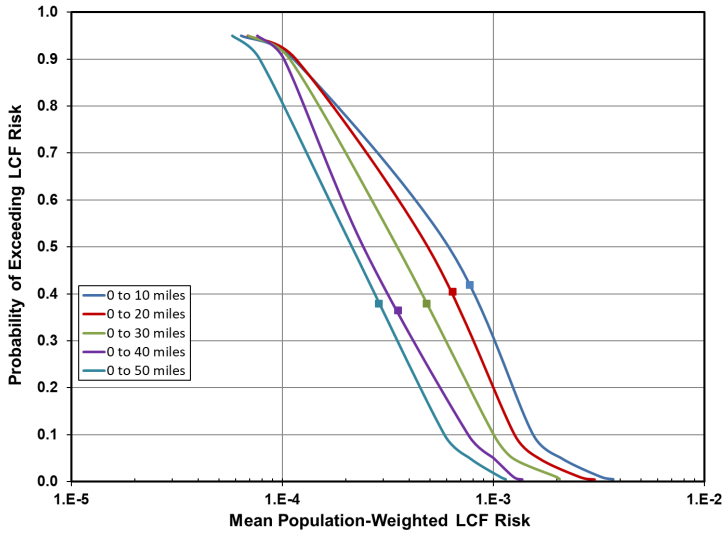

Figure 6-76 Complementary Cumulative Distribution Function of Population-Weighted LCF Risk within Five Circular Areas Centered on the Surry Site for the Realization with the Largest Cs Release

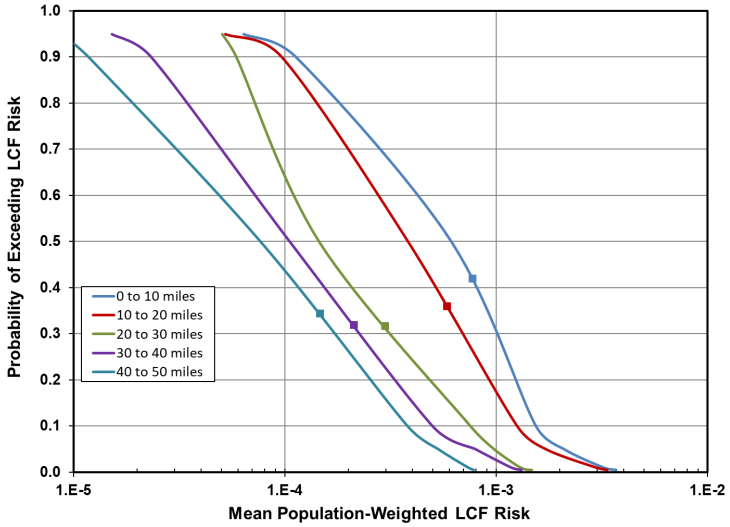

Figure 6-77 Complementary Cumulative Distribution Function of Population-Weighted LCF Risk within Five Annular Areas Centered on the Surry Site for the Realization with the Largest Cs Release

6.2.4.5 Earliest Containment Failure

The results for the realization with the earliest containment failure (Realization 1062) are shown in Figure 6-78 and Figure 6-79. The results are of population-weighted, LCF risk. Probability in the figures represents the aleatory uncertainty from weather variability. The square symbol on each of the curves shows the mean of the distributions.

The risks shown in these figures are very similar to those for the reference non-SGTR realization shown in Figure 6-72 and Figure 6-73. Comparing the source terms for these two realizations, Realization 459 for the reference non-SGTR with Realization 1062 for the earliest containment failure, shows that the more significant portion of the cesium release (corresponding to containment failure) for the earliest containment failure realization starts about 15 hours earlier and that the total release of cesium is about four times higher than for the reference non-SGTR. The difference in timing is not that significant from the standpoint of evacuation; both cases have very little release until well beyond the completion of evacuation. The difference in the ultimate cesium release is largely compensated by the bias from the randomly sampled MACCS input parameters, as shown in Table 6-25. Ultimately, the CCDFs for the two realizations end up being very similar. The ranges of risks from weather variability are about one order of magnitude for the circular areas and about one and one-half orders of magnitude for the annular areas, especially for the larger radii.

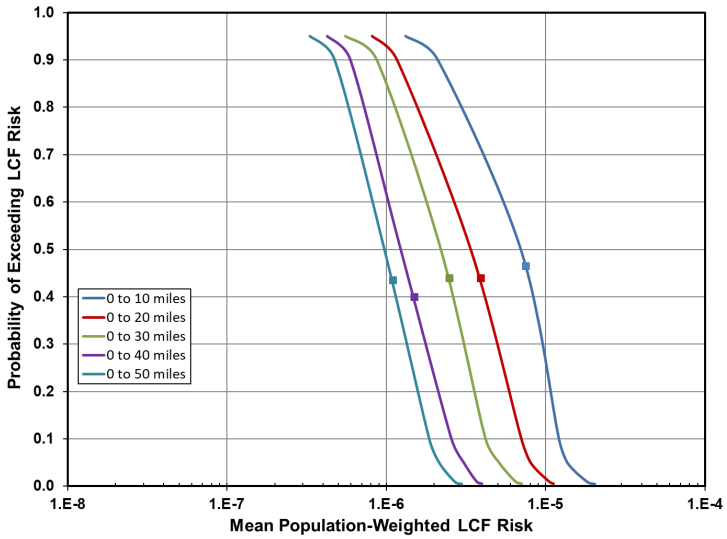

Figure 6-78 Complementary Cumulative Distribution Function of Population-Weighted LCF Risk within Five Circular Areas Centered on the Surry Site for the Realization with the Earliest Containment Failure

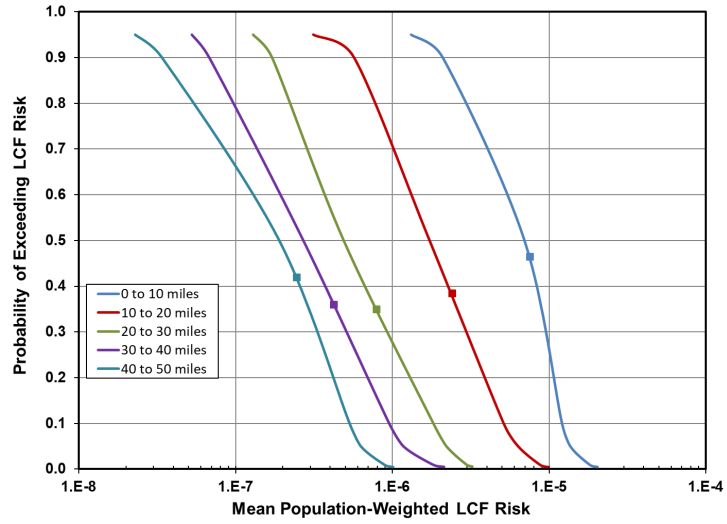

Figure 6-79 Complementary Cumulative Distribution Function of Population-Weighted LCF Risk within Five Annular Areas Centered on the Surry Site for the Realization with the Earliest Containment Failure

6.2.4.6 Earliest SGTR

The results for the realization with the earliest SGTR (Realization 777) are shown in Figure 6-80 and Figure 6-81. The results are of population-weighted, LCF risk. Probability in the figures represents the aleatory uncertainty from weather variability. The square symbol on each of the curves shows the mean of the distributions.

The risks shown in these figures are between those for the reference SGTR realization (Realization 37) shown in Figure 6-72 and Figure 6-73 and those for the largest cesium release (Realization 237) shown in Figure 6-76 and Figure 6-77. These three realizations have similar release timing and some of the largest cesium releases considered in this section, but differ in ultimate cesium release by about an order of magnitude, as shown in Figure 6-69. Each of these realizations also have sampled MACCS inputs that bias the results toward higher risk, as shown in Table 6-25. By comparison, Realization 19 has a larger cesium release than Realization 37, but that realization happens to be paired with other MACCS inputs that bias the result toward lower risk. The ranges of risks from weather variability are about one and one-half orders of magnitude for the circular areas and almost two orders of magnitude for the annular areas, especially for the larger radii.

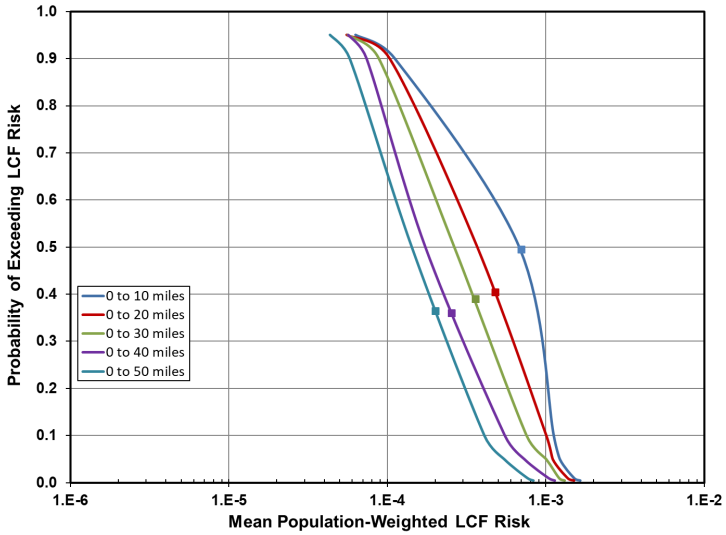

Figure 6-80 Complementary Cumulative Distribution Function of Population-Weighted LCF Risk within Five Circular Areas Centered on the Surry Site for the Realization with the Earliest SGTR

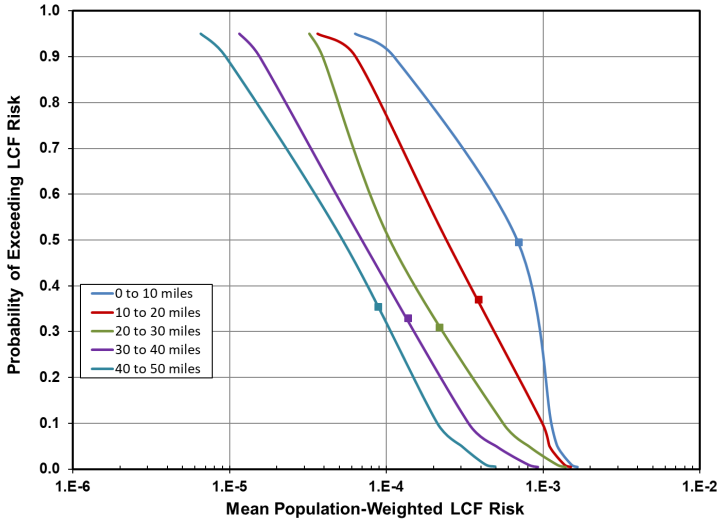

Figure 6-81 Complementary Cumulative Distribution Function of Population-Weighted LCF Risk within Five Annular Areas Centered on the Surry Site for the Realization with the Earliest SGTR

6.2.5 Sensitivity Study of Chemical Groups

Three MACCS sensitivity evaluations were performed to investigate the importance of the released chemical groups and isotopes. One evaluation was performed using the reference non-SGTR source term (Realization 459) and two using the reference SGTR source term (Realization 37). These evaluations were performed using the standard set of DCFs and nominal values for all of the other uncertain MACCS input parameters. The nominal values are chosen to be modes for parameters that use a triangular distribution or median values for the other distribution types.

Figure 6-82 shows the relative contributions of each chemical group to LCF risk using the reference non-SGTR source term. Contributions are split into those for the emergency phase and for the intermediate and long-term phases. The cesium group contributes most of the overall LCF risk, about 84.5%. Of that, about 83.7% is from the intermediate and long-term phases and about 0.8% is from the emergency phase. The second largest contributor overall is the iodine group. Its contribution is about 5.5% overall, and of that 3% is from the intermediate and long-term phases and 2.5% is from the emergency phase. The third largest contributor is the tellurium group. Its contribution is 3.4% overall; of that about 2.5% is to the emergency phase and about 0.8% is to the intermediate and long-term phases. The fourth largest contributor is the xenon/krypton group. It contributes about 3.3% of the risk, and all of that is from exposures during the emergency phase. Finally, the fifth most significant contributor is from the molybdenum group. Its total contribution is about 2.2%, which is divided into 1.7% from the intermediate and long-term phases and 0.5% from the emergency phase. Each of the other groups contribute less than 1% overall; combined, they contribute about 1.1% of the risk, and this contribution is about equally divided between the emergency phase and the intermediate and long-term phases. Overall, exposures during the intermediate and long-term phases represent about 90% of the LCF risk and those during the emergency phase represent about 10% of the risk.

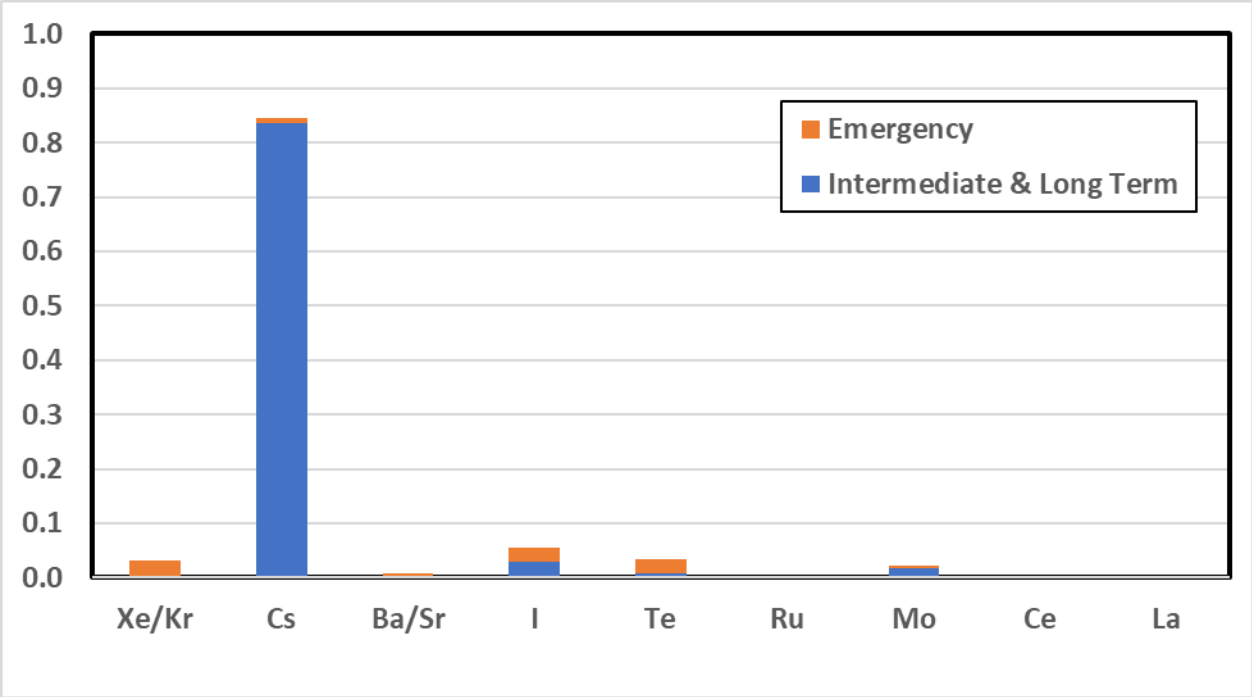

Figure 6-82 Relative Contribution of the Chemical Groups for LCF Risk within 50 Miles of the Site using the Reference Non-SGTR Source Term (Realization 459)

Figure 6-83 shows the relative contributions of each chemical group to LCF risk using the reference SGTR source term. The contributions are only slightly different that for the reference non-SGTR case. Again, each of the contributions is separated into the part from exposures during the emergency phase and the part from exposures during the intermediate and long-term phases. The cesium group contributes most of LCF risk overall, about 87.9%, which is slightly more than for the reference non-SGTR case. Of that, about 86.4% is from the intermediate and long-term phases and about 1.5% is from the emergency phase. The second largest contributor is the tellurium group. Its contribution is 4.5% overall; of that about 4.1% is to the emergency phase and about 0.4% is to the intermediate and long-term phases. The third most significant contributor is from the molybdenum group. Its total contribution is about 4.0%, which is divided into 2.5% from the intermediate and long-term phases and 1.5% from the emergency phase. The fourth largest contributor overall is the iodine group. Its contribution is about 2.6% overall, and of that 0.8% is from the intermediate and long-term phases and 1.9% is from the emergency phase. The xenon/krypton group contributes very little to risk in this case, about 0.3%. The only other group that contributes at least 0.1% is the ruthenium group, which contributes about 0.6%, mostly from the emergency phase. Overall, exposures during the intermediate and long-term phases represent about 90% of the LCF risk and those during the emergency phase represent about 10% of the risk for this case.

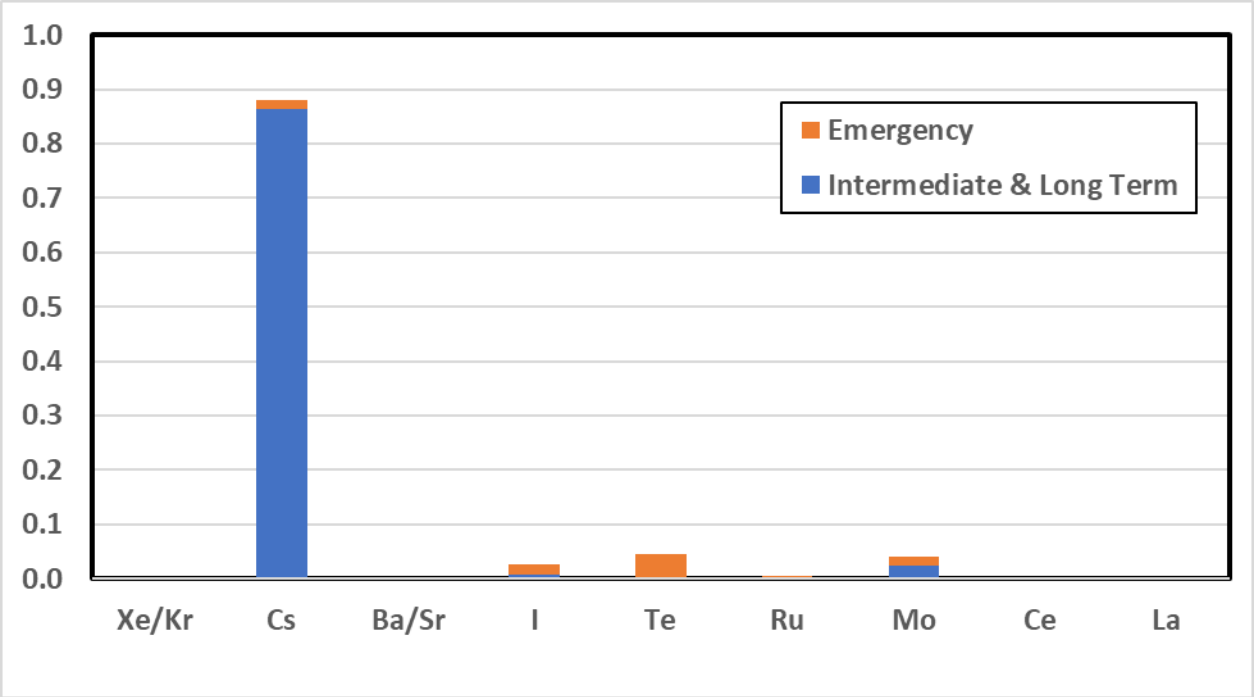

Figure 6-83 Relative Contribution of the Chemical Groups for LCF Risk within 50 Miles of the Site using the Reference SGTR Source Term (Realization 37)

Figure 6-84 and Figure 6-85 show the relative contributions of individual isotopes to LCF risk using the reference SGTR source term. Figure 6-84 shows the results on a linear scale and the contributions from only five of the isotopes are visible on that scale. The largest contributor is Cs-137, which contributes 64.5% overall, of which 64.1% is from exposures during the intermediate and long-term phases. Second in importance is Cs-134, which contributes 25.1% overall, of which 24.3% is from contributions during the intermediate and long-term phases. Third in significance is Te-132 and it contributes 3.9% overall, of which 3.5% is from exposures during the emergency phase. Fourth is Nb-95, a member of the molybdenum group, which contributes 3.1% overall, and of that 2.3% is from exposures during the intermediate and long-term phases. Finally, I-131 is the fifth largest contributor, which contributes 1.9% overall, and of that 1.2% is from exposures during the emergency phase. Figure 6-85 shows the results on a logarithmic scale and it shows that seven other isotopes contribute between 0.4% and 0.04% each. Nearly all of the 1.5% contribution for the seven isotopes combined is to the emergency phase. All of the other isotopes, to the accuracy of this sensitivity study, do not contribute to LCF risk. Other isotopes can contribute significantly when different conditions prevail during fuel degradation and fission product release, especially those that involve highly reducing or oxidizing conditions.

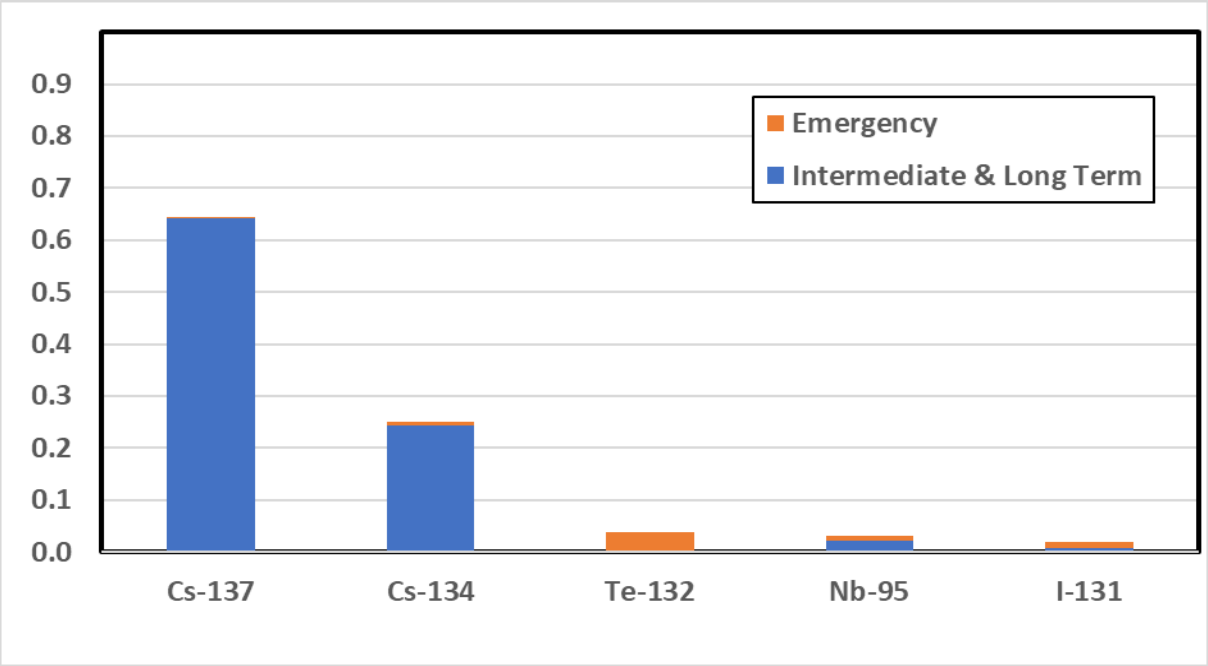

Figure 6-84 **Relative Contribution of the Individual Isotopes for LCF Risk within 50 Miles of the Site using the Reference SGTR Source Term (Realization 37) shown on a Linear Scale**

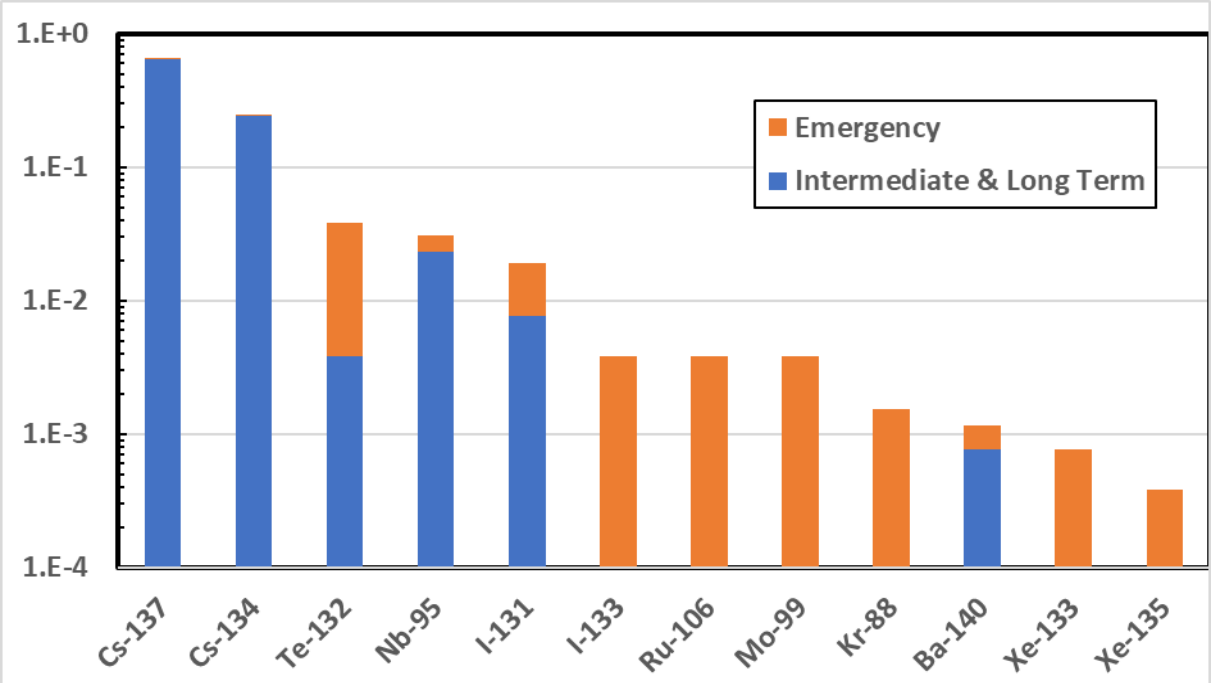

Figure 6-85 **Relative Contribution of the Individual Isotopes Groups for LCF Risk within 50 Miles of the Site using the reference SGTR Source Term (Realization 37) shown on a Log Scale**

6.2.6 Summary of Consequence Results

Mean (over epistemic uncertainty and weather variability), individual, LCF risks assuming LNT dose response, conditional on the occurrence of a STSBO accident at Surry, are very low, approximately 3×10^{-5} within 10 miles and lower at longer distances. This is about a factor-of-three lower than the risk evaluated in the original SOARCA study for a STSBO without SGTR, which was 9×10^{-5}. The primary reason for this reduction is that refinements in the MELCOR model, primarily in treatment of the containment, have led to later and smaller source terms. Most of the risks, 99% within the 10-mile EPZ and about 83% to 85% beyond 10 miles from the plant, are from exposures following the emergency phase. Early fatality risks for this scenario are essentially zero.

Regression analyses of the UA results were performed to determine the uncertain inputs that most affect the LCF risks. No regression analysis was performed for early fatality risks because only one realization displayed a risk greater than zero and even this risk is extremely small. The regression analyses were performed for three sets of realizations: the full set, only those with a SGTR, and those without a SGTR.

When the full set of realizations was evaluated, the most important input variables identified were consistently the MELCOR parameters specifying the flaw depths in the steam generator tubes, the containment design leakage area, the long-term groundshine shielding factor, and the day at which the accident occurs during the operating cycle (cf., Table 6-16 through Table 6-18). The flaw depths significantly influence the likelihood that a SGTR (a containment bypass event) occurs. The containment design leakage area is proportional to the containment leakage rate, which is more important when a SGTR does not occur and plays a more minor role when it does occur. Most of the LCF risk is from the long-term phase and the dominant exposure pathway during this phase is groundshine. Since groundshine doses are proportional to the groundshine shielding factor, this parameter is one of the most important of the uncertain MACCS parameters. The day when the accident occurs during the operating cycle directly influences core degradation through decay heat and additionally influences doses to individuals through the isotopic inventories in core, so this parameter is influential for LCF risk.

For the cases involving a SGTR, the most important of the uncertain input parameters are the MACCS cancer fatality risk factors for residual and colon cancers and groundshine shielding factor (cf. Table 6-19 through Table 6-21). Additional parameters that are important at some of the distance ranges are the dose and dose-rate effectiveness factor corresponding to residual cancers, the MELCOR parameter for dynamic shape factor for the aerosols, and containment leakage area.

For the cases excluding the occurrence of SGTR, the most important of the uncertain input parameters are design leakage area of the containment, long-term groundshine shielding factor, the day the accident occurs during the fuel cycle, and the cancer fatality risk factor for residual cancers (cf. Table 6-22 through Table 6-24).

The sensitivity studies for the importance of the chemical groups is similar for the reference source terms with and without SGTR. For the case with SGTR, the sensitivity analysis of LCF

risk estimates that the cesium group contributes about 88% of the risk, mostly from exposures during the intermediate and long-term phases. Of the 88%, about 64% is from Cs-137 and most of the remainder is from Cs-134. The large majority of the exposures from the cesium group is from groundshine during the intermediate and long-term phases. Next, the tellurium group contributes about 4.5% of the LCF risk, and most of that is from Te-132. Most of the tellurium contribution is from exposures during the emergency phase. Third in importance is the molybdenum group, and the major contributor to that group is Nb-95. Exposures from the molybdenum group are more from the intermediate and long-term phases than from the emergency phase. Fourth is the iodine group, which contributes about 2.6%. The majority of that is from I-131, but I-133 also contributes significantly. Most of the iodine exposures occur during the emergency phase. Other isotopes, Ru-106, Mo-99, Kr-88, Ba-140, Xe-133, and Xe-135 combined contribute about 1% to the overall risk, and this is almost exclusively from exposures during the emergency phase.

For the reference non-SGTR source term, about 84.5% of the LCF risk is from the cesium group, 5.5% is from the iodine group, 3.4% is from the tellurium group, 3.3% is from the xenon/krypton group, and 2.2% is from the molybdenum group. The barium and ruthenium groups contribute a combined total of 1.1%. The other two groups cerium and lanthanum, do not contribute to risk to the precision of the calculation. The major difference between the SGTR and non-SGTR cases is that the noble gases contribute significantly more when the source term is small. This is because the noble gases are generally released in large fraction even when other chemical groups are not. Thus, the relative contribution of the noble gases is greater for smaller source terms.

7 SUMMARY OF RESULTS AND CONCLUSIONS

Through the application of modern analysis tools and techniques, the SOARCA project [1] developed a body of knowledge regarding the realistic outcomes of theoretical severe nuclear reactor accidents with best estimate analyses of selected accident scenarios with specific boundary conditions for nuclear power plants at Peach Bottom and Surry. SOARCA efforts have continued with an integrated UA of the unmitigated LTSBO at Peach Bottom [2], the integrated deterministic and uncertainty analyses at Sequoyah, and the UA presented herein of the Surry unmitigated STSBO. The Surry UA follows the approach developed for the Peach Bottom and Sequoyah UAs investigating the same figures of merit, which for MELCOR includes environmental release fractions of cesium and iodine, in-vessel hydrogen production, and release timing, and for MACCS includes individual LCF risk and early fatality risk at specified distances. The SOARCA analyses were completed for specific accident scenarios at specific plants. Thus, the application of results must be tempered with the understanding of the reactor type, scenario for which results were produced, and site-specific characteristics.

One of the original objectives of the Surry UA was to quantify the robustness of the Surry best estimate results for the unmitigated STSBO [3]. However, since the completion of the Surry SOARCA study [3], there have been many model enhancements and updates to all of the severe accident codes making a direct comparison less meaningful. This UA provides a comparison of the results of the Surry best estimate analysis [3] with the current, more advanced, severe accident modeling systems applied in an uncertain framework. Additional objectives included:

- Determining whether the Surry UA results corroborate the general conclusions and insights from the original SOARCA best estimate study.

- Developing insights into the overall sensitivity of SOARCA results to uncertainty in selected modeling inputs.

- Identifying influential input parameters contributing to accident progression and offsite consequences through application of an uncertainty analysis methodology.

- Informing the NRC's Site Level 3 PRA and post-Fukushima activities including Tier 3 items.

To accomplish the final objective above, the Level 3 PRA staff supported the Surry parameter development meetings and were presented with early Surry UA results. The project team interacted with Level 3 PRA staff on key issues of interest throughout the project.

This Surry UA modeled distributions for parameter values that historically were modeled with fixed values and applied multiple regression techniques to support an understanding of the results. The analysis produced substantial information that is described in detail in this document.

In addition, like the Peach Bottom and Sequoyah UAs [2] did, the results of this Surry UA corroborate the conclusions from the SOARCA project [1]:

- Public health consequences from severe nuclear accident scenarios modeled are smaller than those projected in NUREG/CR-2239.

- The delay in releases calculated provides more time for emergency response actions (such as evacuating or sheltering).

- "Essentially zero" absolute early fatality risk is projected.

7.1 MELCOR Accident Progression Conclusions

The key conclusions from the Surry UA MELCOR accident progression calculations include,

- The parameters found to influence source term in the original SOARCA Surry study were found to similarly influence source term in the SOARCA Surry UA.
  - The influences of these parameters are further characterized as a result of the UA.
- A significant number (12.5%) of the realizations included SG tube ruptures.
  - There were 144 realizations with SGTRs. 6 of those realizations had 2 SGTRs.
  - The largest and earliest releases of I and Cs to the environment occurred in realizations with a SGTR.
  - A substantial tube flaw was necessary for a tube rupture to occur. The flaw depth largely dictated the vulnerability of a SG tube to a SGTR.
  - Interestingly, the threat of a SGTR was not limited to the small subset of the hottest tubes in a SG tube bundle but instead existed for all tubes in the steam generator. The flaw depth analysis revealed,
    - The likelihood of a SGTR from a cold tube flaw significantly increased when the non-dimensional flaw depth is >0.80;
    - The likelihood of a SGTR from a hot upflow tube flaw significantly increased when the non-dimensional flaw depth is >0.68; and
    - The likelihood of a SGTR in the hottest tube significantly increased when the non-dimensional flaw depth is (a) >0.42 or (b) >0.31 with a maximum normalized hot plume temperature >0.48 (i.e., >75th percentile of the maximum normalized plume temperature distribution).
  - No SGTR was predicted in the unflawed SG tubes in any realization.
  - The SVs on the pressurizer usually functioned without failure in realizations with a SGTR. If a pressurizer SV sticks open, the RCS depressurized, which reduced the pressure difference across the SG tubes and hence the stress developed in the tubes.
    - 4 of the 144 realizations had a stuck-open pressurizer SV. However, a SGTR only occurred when (a) the SV failure area when very small or (b) the failure area was small and the SV stuck open close to the time of the SGTR.
  - Also important to the occurrence of a SGTR was the degree of leakage past the RCP seals and the MSIVs. Larger values of these sampled variables decreased or increased the magnitude of the pressure difference across the SG tubes, respectively.
  - The largest cesium release occurred in a realization with two SGTRS (i.e., two falied tubes) and high reactor coolant pump seal leakage. The depressurization from these events delayed hot leg failure such that a pressurized bypass of containment existed for a substantial period (i.e., ~1½ hr).

- Predictably, the containment leak tightness was important with respect to the timing and magnitude of fission product releases to the environment.
- The elapsed time since refueling to the onset of the SBO significantly influenced the rate of containment pressurization and hence the timing of fission product release to the environment.
- The realizations at the earliest time at cycle (i.e., 0.5 days) had significantly different behavior than the other realizations.
    - The earliest sampled time at cycle had a significantly lower containment pressurization rate and did not have containment failure within 72 hr.
    - The slow fuel heatup at the earliest time at cycle also led to higher in-vessel hydrogen production, including the realization with the highest hydrogen generation.
- There developed no threat to the sub-atmospheric containment from hydrogen deflagrations.

7.2 MACCS Consequence Conclusions

Mean (over epistemic uncertainty and weather variability), individual, LCF risks, conditional on the occurrence of an accident, estimated in this uncertainty analysis of the Surry STSBO are very low, approximately 3×10^{-5} within 10 miles and lower at longer distances. This is about a factor-of-five lower than the risk evaluated in the original SOARCA study. The primary reason for the reduction in estimated risk is that refinements in the MELCOR model, primarily in treatment of the containment, have led to smaller and later source terms. Most of the risks, about 99% within the 10-mile EPZ and 84% beyond 10 miles from the plant, are from exposures following the emergency phase. Early fatality risks for this scenario are essentially zero.

Regression analyses of the UA results were performed to determine the uncertain inputs that most affect the LCF risks. No regression analysis was performed for early fatality risks because only one realization estimated a risk greater than zero and even this risk is extremely small. The regression analyses on LCF risk were performed for three sets of realizations: the full set, only those with a SGTR, and those without a SGTR.

When the full set of realizations was evaluated, the most important input variables identified were consistently the MELCOR parameters specifying the flaw depths in the steam generator tubes and the containment design leakage area. Also, the MACCS parameter for the long-term groundshine shielding factor and the day at which the accident occurs during the refueling cycle, which directly affects both MELCOR and MACCS inputs, are important. The flaw depths significantly influence the likelihood that a SGTR occurs. The containment design leakage area is proportional to the containment leakage rate, which is an important release path when a SGTR does not occur. Long-term groundshine exposures are responsible for most of the long-term doses, are proportional to the groundshine shielding factor, and as a result, this factor is the most important of the uncertain MACCS input parameters. The day when the accident occurs during the operating cycle directly influences core degradation through decay heat in MELCOR and doses to individuals through the isotopic inventories in core in MACCS, and this parameter contributes significantly to LCF risk.

For the realizations with a SGTR, the most important of the uncertain input parameters are MACCS parameters for cancer fatality risks for residual and colon cancers and groundshine shielding factor. Additional parameters that are important at some of the distance ranges are the

dose and dose-rate effectiveness factor for residual cancers, the MELCOR parameter for dynamic shape factor of the aerosols, and containment leakage area.

For the realizations without the occurrence of a SGTR, the most important of the uncertain input parameters are design leakage area of the containment, long-term groundshine shielding factor, the day the accident occurs during the refueling cycle, and the cancer fatality risk factor for residual cancers.

MACCS Sensitivity Analyses

The sensitivity studies for the importance of the chemical groups is similar for the reference source terms with and without SGTR. For the case with SGTR, the sensitivity analysis of LCF risk estimates that the cesium group contributes about 88% of the risk, mostly from exposures during the intermediate and long-term phases. Of the 88%, about 64% is from Cs-137 and most of the remainder is from Cs-134. The large majority of the exposure from the cesium group is from groundshine during the intermediate and long-term phases. Next, the tellurium group contributes about 4.5% of the LCF risk, and most of that is from Te-132. Most of the tellurium contribution is from exposures during the emergency phase. Third in importance is the molybdenum group and the major contributor to that group is Nb-95. Exposures from the molybdenum group are more from exposures during the intermediate and long-term phases than from the emergency phase. Fourth is the iodine group, which contributes about 2.6%. The majority of that is from I-131, but I-133 also contributes significantly. Most of the iodine exposures occur during the emergency phase. Other isotopes, Ru-106, Mo-99, Kr-88, Ba-140, Xe-133, and Xe-135, combined contribute about 1% to the overall risk and this is almost exclusively from exposures during the emergency phase. To the accuracy of the sensitivity analysis, the other isotopes do not contribute to LCF risk.

For the reference non-SGTR source term, about 84.5% of the LCF risk is from the cesium group, 5.5% is from the iodine group, 3.4% is from the tellurium group, 3.3% is from the xenon/krypton group, and 2.2% is from the molybdenum group. The barium and ruthenium groups contribute a combined total of 1.1%. The other two groups cerium and lanthanum, do not contribute to risk to the precision of the calculation.

The major difference between the SGTR and non-SGTR cases is that the noble gases contribute significantly more when the source term is small. This is because the noble gases are generally released in large fraction even when other chemical groups are not. Thus, the relative contribution of the noble gases is greater for smaller source terms.

8 REFERENCES

[1] NUREG/CR-1935, "State-of-the-Art Reactor Consequence Analyses (SOARCA) Report," ML12332A057, U.S. Nuclear Regulatory Commission, Washington, DC, November 2012.

[2] NUREG/CR-7155, "State-of-the-Art Reactor Consequence Analyses Project, Uncertainty Analysis of the Unmitigated Long-Term Station Blackout of the Peach Bottom Atomic Power Station," Draft Report. ML13189A145, U.S. Nuclear Regulatory Commission, Washington, DC, 2013.

[3] NUREG/CR-7110 Volume 2, Rev. 1, "State-of-the-Art Reactor Consequence Analysis Project Volume 2: Surry Integrated Analysis," U.S. Nuclear Regulatory Commission, Washington, DC, August 2013.

[4] SECY-12-0092, “State-of-the-Art Reactor Consequence Analyses – Recommendation for Limited Additional Analysis,” U.S. Nuclear Regulatory Commission, Washington, DC, July 5, 2012.

[5] NUREG/CR-2239, “Technical Guidance for Siting Criteria Development,” Nuclear Regulatory Commission: Washington DC. 1982.

[6] NUREG/CR-7009, "MACCS2 Best Practices as Applied in the State-of-the-Art Reactor Consequence Analyses (SOARCA) Project,” U.S. Nuclear Regulatory Commission, Washington, DC, 2014.

[7] NUREG/CR-7245, U.S. Nuclear Regulatory Commission, “State-of-the-Art Reactor Consequence Analyses Project: Sequoyah Integrated Deterministic and Uncertainty Analysis,” October, 2019.

[8] U.S. Nuclear Regulatory Commission, “State-of-the-Art Reactor Consequence Analyses Project: Uncertainty Analysis of the Unmitigated Short-Term Station Blackout of the Surry Power Station,” Draft Report. (ADAMS Accession No ML15224A001) 2016.

[9] NUREG-1493, “Performance-Based Containment Leak-Test Program,” Draft Report for Comment. U.S. Nuclear Regulatory Commission, Washington, DC, January 1995.

[10] NUREG-2195, “Consequential SGTR Analysis for Westinghouse and Combustion Engineering Plants with Thermally Treated Alloy 600 and 690 Steam Generator Tubes,” draft, U.S. Nuclear Regulatory Commission, Washington, DC, May 2016

[11] Stickler, L. A., et al., “Calculations to Estimate the Margin to Failure in the TMI-2 Vessel.” NUREG/CR 6196, March 1994.

[12] Rempe, J. L., et al., “Light Water Reactor Lower Head Failure Analysis.” NUREG/CR-5642, October 1993.

[13] Lind, T., and A. Dehbi, “The Final Summary Report of the ARTIST II Project Severe Accident Tests,” TM-42-11-25; ARTIST-95-11, Paul Scherrer Institute, 2012.

[14] NUREG/CR-6119, "MELCOR Computer Code Manuals, Vol. 2: References Manuals, Version 1.8.5." Revision 3. U.S. Nuclear Regulatory Commission, Washington, DC, 2005.

[15] NUREG/CR-6119, "MELCOR Computer Code Manuals, Vol. 1: Primer and User's Guide, Version 1.8.5." Revision 2. U.S. Nuclear Regulatory Commission, Washington, DC, 2000.

[16] NUREG-1150, "Severe Accident Risks: An Assessment for Five U.S. Nuclear Power Plants," U.S. Nuclear Regulatory Commission, Washington, DC, 1990.

[17] Bixler, N.E., et al., "Software Regression Quality Assurance for MACCS2 Version 2.5.0.0 through Version 2.5.0.9," SAND2012-6333, Sandia National Laboratories, Albuquerque, NM. July 2012.

[18] "State-of-the-Art Reactor Consequence Analyses Project Uncertainty Analysis of the Unmitigated Short-Term Station Blackout of the Surry Power Station," Draft Report, ML15224A001, U.S. Nuclear Regulatory Commission, Washington, DC, June 2015.

[19] Regulatory Guide 1.174, "An Approach for Using Probabilistic Risk Assessment in Risk-Informed Decisions on Plant-Specific Changes to the Licensing Basis." U.S. Nuclear Regulatory Commission, Washington, DC, 1998.

[20] NUREG/CR-6953 Volume 2, "Review of NUREG-0654, Supplement 3, 'Criteria for Protective Action Recommendations for Severe Accidents' Focus Groups and Telephone Survey," U.S. Nuclear Regulatory Commission, Washington, DC, October 2008.

[21] Kaplan, S. and B.J. Garrick, "On the Quantitative Definition of Risk," Risk Analysis, 1(1): p. 11-27, 1981.

[22] Sobol', I. "Sensitivity Estimates for Nonlinear Mathematical Models," Mathematical Modeling and Computational Experiment, 1, 407-414. 1993.

[23] Helton, J.C., et al., "Survey of Sampling-based Methods for Uncertainty and Sensitivity Analysis," Reliability Engineering & System Safety, 91(10-11): p. 1175-1209, 2006.

[24] Storlie, C.B. and J.C. Helton, "Multiple predictor smoothing methods for sensitivity analysis: Description of techniques," Reliability Engineering & System Safety, 93(1): p. 28-54, 2008.

[25] Helton, J.C. "Uncertainty and Sensitivity Analysis in the Presence of Stochastic and Subjective Uncertainty," Journal of Statistical Computation and Simulation 1997; Volume 57: pages 3-76.

[26] Helton, J.C. Johnson, J.D, Oberkampf W.L. Sallaberry C.J. "Representation of Analysis Results Involving Aleatory and Epistemic Uncertainty," International Journal of General Systems; 39(6): 605-646, 2010.

[27] Helton JC, Sallaberry CJ. “Uncertainty and Sensitivity Analysis: From Regulatory Requirements to Conceptual Structure and Computational Implementation.” IFIP Advances in Information and Communication Technology; 377 AICT: 60-76, 2012.

[28] Helton JC, Johnson JD, Sallaberry CJ. “Quantification of Margins and Uncertainties: Example Analyses from Reactor Safety and Radioactive Waste Disposal Involving the Separation of Aleatory and Epistemic Uncertainty.” Reliability Engineering and System Safety; 96(9): 1014-1033. 2011.

[29] Storlie, C.B., et al., "Implementation and evaluation of nonparametric regression procedures for sensitivity analysis of computationally demanding models," Reliability Engineering & System Safety, 94(11): p. 1735-1763, 2009.

[30] Metropolis, N. and Ulam S., “The Monte Carlo Method,” Journal of the American Statistical Association; 44(247):335-341, 1949.

[31] McKay, M.D., Beckman, R.J., and Conover, W.J., “A Comparison of Three Methods for Selecting Values of Input Variables in the Analysis of Output from a Computer Code,” Technometrics 21(2): 239-245, 1979.

[32] Sallaberry CJ, Helton JC, Hora SC. “Extension of Latin Hypercube Samples with Correlated Variables.” Reliability Engineering and System Safety; 93: 1047-1059. 2008.

[33] Helton J.C. and Davis F.J., “Latin hypercube sampling and the propagation of uncertainty in analyses of complex systems” Reliability Engineering and System Safety 81 (1) 23-69, 2003.

[34] Efron B. and Tibshirani R.J., “An Introduction to the Bootstrap” Monographs on Statistics and Applied Probability 57 - Chapman & Hall/CRC – ISBN 0-412-04231-2, 1993.

[35] NUREG/CR-7037, “Industry Performance of Relief Valves at U.S. Commercial Nuclear Power Plants through 2007,” U.S. Nuclear Regulatory Commission, Washington, DC, March 2011.

[36] NUREG-1022, Rev. 3, “Event Report Guidelines 10 CFR 50.72 and 50.73 – Final Report,” U.S. Nuclear Regulatory Commission, Washington DC, January 2013.

[37] NUREG-1570, “Risk Assessment of Severe Accident-Induced Steam Generator Tube Rupture,” U.S. Nuclear Regulatory Commission, Washington, DC, March 1998.

[38] NUREG/CR-6995, “SCDAP/RELAP5 Thermal-Hydraulic Evaluations of the Potential for Containment Bypass During Extended Station Blackout Severe Accident Sequences in a Westinghouse Four-Loop PWR,” U.S. Nuclear Regulatory Commission, Washington, DC, March 2010.

[39] Stewart, W.A., Pieczynski, A.T., and Srinivar, V., "Natural Circulation Experiments for PWR Degraded Core Accidents," EPRI Report NP 6324 D, 1989.

[40] Stewart, W.A., Pieczynski, A.T., and Srinivar, V., "Natural Circulation Experiments for PWR High Pressure Accidents," EPRI Report TR 102815, 1993.

[41] Eide, S., T. Wierman, et al., “Industry-Average Performance for Components and Initiating Events at U.S. Nuclear Power Plants,” INL/EXT-01-01623, Idaho National Laboratory 2007.

[42] Fuller, E. L., G. Hannaman, and M. Kenton. “Steam Generator Management Project Risks from Severe Accidents Involving Steam Generator Tube Leaks or Ruptures,” Volume 2. EPRI Report TR-106194-V2. October 1997.

[43] M. Zhu and A. Lu, “The Counter-intuitive Non-informative Prior for the Bernoulli Family”, *Journal of Statistics Education*, 12:2, 2004.

[44] NUREG/CR-6928, "Industry-Average Performance for Components and Initiating Events at U.S. Commercial Nuclear Power Plants,” U.S. Nuclear Regulatory Commission, Washington, DC, 2007.

[45] Ang AH-S, Tang WH. “Probability Concepts in Engineering,” 2nd edition. Hoboken, NJ: Wiley; 2007.

[46] NUREG/CR-6823, "Handbook of Parameter Estimation for Risk Assessment,” U.S. Nuclear Regulatory Commission, Washington, DC, 2003.

[47] NUREG/CR-4294, "Leak Rate Analysis of the Westinghouse Reactor Coolant Pump,” U.S. Nuclear Regulatory Commission, Washington, DC, July 1985.

[48] Westinghouse Electric Company, LLC. “WOG 2000 Reactor Coolant Pump Seal Leakage Model for Westinghouse PWRs.” Revision 1. Pittsburgh, PA. May 2002.

[49] NUREG-1953, "Confirmatory Thermal-Hydraulic Analysis to Support Specific Success Criteria in the Standardized Plant Analysis Risk Models – Surry and Peach Bottom,” U.S. Nuclear Regulatory Commission, Washington, DC, September 2011.

[50] NUREG-1781, C. F. Boyd, K. Hardesty, "CFD Analysis of 1/7th Scale Steam Generator Inlet Plenum Mixing During a PWR Severe Accident," U.S. Nuclear Regulatory Commission, Washington, DC, October 2003.

[51] NUREG-1788, "CFD Analysis of Full-Scale Steam Generator Inlet Plenum Mixing During a PWR Severe Accident," U.S. Nuclear Regulatory Commission, Washington, DC, May 2004.

[52] NUREG-1922, C.F. Boyd, K.W. Armstrong, "Computational Fluid Dynamics Analysis of Natural Circulation Flows in a Pressurized-Water Reactor Loop under Severe Accident Conditions," U.S. Nuclear Regulatory Commission, Washington, DC, March 2010.

[53] C. Journeau, J. F. Haquet, P. Piluso, J. M. Bonnet, “Differences between Silica and Limestone Concretes that may Affect their Interaction with Corium,” Proceedings of the 2008 International Congress on Advances in Nuclear Power Plants, ICAPP ’08, Anaheim, CA USA, June 8-12, 2008, Paper 8059.

[54] N. Girault, F. Payot, “Insights into iodine behavior and speciation in the Phebus Primary circuit.” Institut de Radioprotection et de Surete Nucleaire, PSN-RES/SAG, Cadarache Center. St. Paul lez Durance, France. Annals of Nuclear Energy 61 143-156. 2013

[55] R.O. Gauntt, N. Bixler, and K.C. Wagner, "An Uncertainty Analysis of the Hydrogen Source Term for a Station Blackout Accident in Sequoyah Using MELCOR 1.8.5 (Draft For Review)," Sandia National Laboratories, Albuquerque, NM, 2003.

[56] Y. Pontillon, et al., "Lessons learnt from VERCORS tests. Study of the active role played by UO2–ZrO2–FP interactions on irradiated fuel collapse temperature," Journal of Nuclear Materials 344, pp. 265–273 (2005).

[57] P. Hofmann et al., "ZrO_2 Dissolution by Molten Zircaloy and Cladding Oxide Shell Failure. New Experimental Results and Modeling," Wissenschaftliche Berechte, INV-CIT(98)-P026, December 1999.

[58] NUREG/CR 7008, "MELCOR Best Practices as Applied in the State-of-the-Art Reactor Consequence Analyses (SOARCA) Project," U.S. Nuclear Regulatory Commission, Washington, DC, August 2014.

[59] R. K. Kumar, "Flammability of Limits of Hydrogen-Oxygen-Diluent Mixtures," Journal of Fire Sciences, Vol. 3, July/August 1985.

[60] ANSI/ANS-5.1-2005, "American National Standard Decay Heat Power in Light Water Reactors." American Nuclear Society, La Grange Park, Illinois. April 1, 2005.

[61] NUREG-1493, "Performance-Based Containment Leak-Test Program," Draft Report for Comment. U.S. Nuclear Regulatory Commission, Washington, DC, January 1995.

[62] NUREG/CR-5121, "Experimental Results from Pressure Testing a 1:6 Scale Nuclear Power Plant Containment," U.S. Nuclear Regulatory Commission, Washington, DC, January 1992.

[63] Duhanyan N, Roustan Y. "Below-Cloud Scavenging by Rain of Atmospheric Gases and Particulates," Atmospheric Environment 2011; 45(39): 7201-7217. 2011.

[64] Wang X, Zhang L, Moran MD. Uncertainty Assessment of Current Size-Resolved Parameterizations for Below-Cloud Particle Scavenging by Rain," Atmospheric Chemistry and Physics 2010; 10(12): 5685-5705. 2010.

[65] Sportisse B. "A Review of Parameterizations for Modelling Dry Deposition and Scavenging of Radionuclides," Atmospheric Environment 2007; 41(13): 2683-2698. 2007.

[66] Andronache C. "Estimated Variability of Below-Cloud Aerosol Removal by Rainfall for Observed Aerosol Size Distributions," Atmospheric Chemistry and Physics 2003; 3(1): 131-143. 2003.

[67] Baklanov A, Sorensen JH. "Parameterisation of Radionuclide Deposition in Atmospheric Long-Range Transport Modelling," Physics and Chemistry of the Earth, Part B: Hydrology, Oceans and Atmosphere 2001; 26(10): 787-799. 2001.

[68] NUREG/CR-6244, "Summary of Objectives, Approach, Application, and Results for the Dispersion and Deposition Uncertainty Assessment," U.S. Nuclear Regulatory Commission, Washington, DC, 1994.

[69] Leadbetter SJ, Hort MC, Jones AR, Webster HN, Draxler RR. “Sensitivity of the Modelled Deposition of Caesium-137 from the Fukushima Dai-ichi Nuclear Power Plant to the Wet Deposition Parameterisation in NAME,” Journal of Environmental Radioactivity 2014.

[70] Saito K, Shimbori T, Draxler R. “JMA's Regional Atmospheric Transport Model Calculations for the WMO Technical Task Team on Meteorological Analyses for Fukushima Daiichi Nuclear Power Plant Accident.” Journal of Environmental Radioactivity 2014; In press.

[71] Brenk H. D., Vogt K.J., “The Calculation of Wet Deposition from Radioactive Plumes,” Nuclear Safety 1981; 22(3): 362-371. 1981.

[72] McMahon TA, Denison PJ. “Empirical Atmospheric Deposition Parameters: A Survey,” Atmospheric Environment - Part A General Topics 1979; 13(5): 571-585. 1979.

[73] NUREG/CR-7161, Rev. 1, "Synthesis of Distributions Representing Important Non-Site-Specific Parameters in Off-Site Consequence Analysis," U.S. Nuclear Regulatory Commission, Washington, DC, 2013.

[74] NUREG/CR-4551, Vol. 2, Rev. 1, Part 7, “Evaluation of Severe Accident Risks: Quantification of Major Input Parameters,” U.S. Nuclear Regulatory Commission, Washington, DC, 1990.

[75] Gregory, J.J., et al., "Task 5 Letter Report: MACCS2 Uncertainty Analysis of EARLY Exposure Results," Sandia National Laboratories, Albuquerque, NM, September 2000.

[76] Eckerman, K., "Radiation Dose and Health Risk Estimation: Technical Basis for the State-of-the-Art Reactor Consequence Analysis (SOARCA) Project," Oak Ridge National Laboratory, Oak Ridge, TN, 2011.

[77] NUREG/CR-6526, “Probabilistic Accident Consequence Uncertainty Analysis, Uncertainty Assessment for Deposited Material and External Doses,” U.S. Nuclear Regulatory Commission, Washington, DC, December 1997.

[78] NUREG/CR-6953, Vol. 1, "Review of NUREG-0654, Supplement 3, ‘Criteria for Protective Action Recommendations for Severe Accidents’," U.S. Nuclear Regulatory Commission, Washington, DC, December 2007.

[79] D.J. Pawel, Leggett, R.W., Eckerman, K. F., and Nelson C.B., “Uncertainties in Cancer Risk Coefficients for Environmental Exposure to Radionuclides,” ORNL/TM-2006/583, Oak Ridge National Laboratory, Oak Ridge, TN, 2007.

[80] NUREG/CR-6613, "Code Manual for MACCS2: Volume 1, User's Guide," U.S. Nuclear Regulatory Commission, Washington, DC, 1997.

[81] NUREG/CR-6853, "Comparison of Average Transport and Dispersion Among a Gaussian, a Two-Dimensional, and a Three-Dimensional Model," U.S. Nuclear Regulatory Commission, Washington, DC, October 2004.

[82] NUREG-75/014, (WASH-1400) “Reactor Safety Study: An Assessment of Accident Risks in U.S. Commercial Nuclear Power Plants. Appendix VI,” U.S. Nuclear Regulatory Commission, Washington, DC, 1975.

[83] NUREG/CR-7003, “Background and Derivation of ANS-5.4 Standard Fission Product Release Model,” U.S. Nuclear Regulatory Commission, Washington, DC, January, 2010.

[84] International Atomic Energy Agency (IAEA). “Actions to Protect the Public in an Emergency due to Severe Conditions at a Light Water Reactor.” Emergency Preparedness and Response. Vienna, Austria. May, 2013.

[85] NUREG/CR-6864, “Identification and Analysis of Factors Affecting Emergency Evacuations,” U.S. Nuclear Regulatory Commission, Washington, DC, January 2005.

[86] Surry Power Station Development of Evacaution Time Estimates. Rev. 1. (ML13037A63) KLD, 2012.

[87] NUREG/CR-6525, Rev. 1, “SECPOP2000: Sector Population, Land Fraction, and Economic Estimation Program,” U.S. Nuclear Regulatory Commission, Washington, DC, 2003.

[88] Wolshon, Brian, J. Jones, and F. Walton. "The Evacuation Tail and Its Effect on Evacuation Decision Making," Journal of Emergency Management. January/February 2010, Volume 8, Number 1. 201.

[89] Environmental Protection Agency (EPA). “PAG Manual Protective Action Guides and Planning Guidance for Radiological Incidents.” Draft for Interim Use and Public Comment. Washington, DC, March 2013.

[90] NUREG/CR-7002, “Criteria for Development of Evacuation Time Estimate Studies.” Washington, DC.: NRC. November 2011.

[91] NUREG/CR-6863, “Development of Evacuation Time Estimate Studies for Nuclear Power Plants,” U.S. Nuclear Regulatory Commission, Washington, DC, January 2005.

[92] NUREG/CR-6981, “Assessment of Emergency Response Planning and Implementation for Large Scale Evacuations,” U.S. Nuclear Regulatory Commission, Washington, DC, October 2008.

[93] Mitchell, Jerry T., et al., “Evacuation behavior in response to the Graniteville, South Carolina, Chlorine Spill,” Quick Response Research Report 178. Boulder, CO: Natural Hazards Center, University of Colorado. 2005.

[94] Mitchell, J.T., S.L. Cutter, and A.S. Edmonds. “Improving shadow evacuation management: Case study of the Graniteville, South Carolina, chlorine spill,” Journal of Emergency Management. 5(1): 28-34. 2007.

[95] NUREG/CR-7032, “Developing an Emergency Risk Communication (ERC)/Joint Information Center (JIC) Plan for a Radiological Emergency,” U.S. Nuclear Regulatory Commission, Washington, DC, February 2008.

[96] NUREG/CR-7110 Volume 1, Rev. 1, "State-of-the-Art Reactor Consequence Analysis Project Volume 1: Peach Bottom Integrated Analysis," U.S. Nuclear Regulatory Commission, Washington, DC, March 2013.

[97] NUREG/CR-7160, "Emergency Preparendess Significance Quantification Process: Proof of Concept," U.S. Nuclear Regulatory Commission, Washington, DC, 2012.

[98] Regulatory Guide 1.23, Rev.1, “Meteorological Monitoring Programs for Nuclear Power Plants,” U.S. Nuclear Regulatory Commission, Washington, DC, March 2007.

[99] Cardoni, J.N., “Radionuclide Inventory and Decay Heat Quantification Methodology for Severe Accident Simulations,” SAND2014-17667, Sandia National Laboratories, Albuquerque, NM 2014

[100] Oak Ridge National Laboratory, “Scale: A Comprehensive Modeling and Simulation Suite for Nuclear Safety Analysis and Design,” ORNL/TM-2005/39, Version 6.1, June 2011.

[101] Gauntt, R.; D. Kalinich, J. Cardoni, J. Phillips, et al. “Fukushima Daiichi Accident Study Status as of April 2012,” SAND2012-6173. July 2012.

[102] Cardoni, J., R. Gauntt, D. Kalinich, J. Phillips. “MELCOR Simulations of the Severe Accident at the Fukushima 1F3 Reactor,” 2012 ANS Winter Meeting and Nuclear Technology Expo. SAND2012-5866C. November, 2012.

[103] P. Hofmann et al., “ZrO_2 Dissolution by Molten Zircaloy and Cladding Oxide Shell Failure. New Experimental Results and Modeling,” Wissenschaftliche Berechte, INV-CIT(98)-P026, December 1999.

[104] T.J. Haste et al., “In-Vessel Core Degradation in LWR Severe Accidents, European Commission,” EUR16695EN, 1996.

[105] Holser, J., “Relief Valve Thermal Analysis: Development of a Transient Thermal/Mechanical Model of a Crosby Relief Valve,” Electric Power Research Institute (EPRI), Palo Alto, CA. EPRI-1006934. 2002.

[106] DeGarmo, E.P., J.T. Black, and R.A. Kohser, “Materials and Processes in Manufacturing” 9th ed. New Jersey: John Wiley & Sons, Inc. 2003.

[107] NUREG/CR-6920, "Risk-Informed Assessment of Degraded Containment Vessels," U.S. Nuclear Regulatory Commission, Washington, DC, June 2006.

[108] NUREG/CR-6906, "Containment Integrity Research at Sandia National Laboratories, An Overview," U.S. Nuclear Regulatory Commission, Washington, DC, March 2006.

[109] NUREG/CR-6433, "Containment Perrformance of Prototypical Reactor Containments Subjected to Severe Accident Conditions," U.S. Nuclear Regulatory Commission, Washington, DC, August 1996.

[110] NUREG/CR-7149, "Effects of Degradation on the Severe Accident Consequences for a PWR Plant with a Reinforced Concrete Containment Vessel," U.S. Nuclear Regulatory Commission, Washington, DC, June 2013.

[111] NUREG/CR-6533, “Code Manual for CONTAIN 2.0: A Computer Code for Nuclear Reactor Containment Analysis,” U.S. Nuclear Regulatory Commission, Washington, DC, December 1997.

[112] Helton JC, Iman RL, Johnson JD, Leigh CD. “Uncertainty and Sensitivity Analysis of a Model for Multicomponent Aerosol Dynamics.” Nuclear Technology; 73: 320-342. 1986.

[113] Helton JC, Iman RL, Johnson JD, Leigh CD. “Uncertainty and Sensitivity Analysis of a Dry Containment Test Problem for the MAEROS Aerosol Model.” Nuclear Science and Engineering; 102: 22-42. 1989.

[114] Nuclear Regulatory Commission (NRC). Tills, J., Notafrancesco, A., and Murata, K., “An Assessment of CONTAIN 2.0: A Focus on Containment Thermal Hydraulics (Including Hydrogen Distributions),” SMSAB-02-02, (ML022140438). July 2002.

[115] F. Kreith and W. Z. Black, “Basic Heat Transfer,” pg. 15. Harper & Row, Publishers, New York, 1980.

[116] Kasper, G., T. Niida, and M. Yang, ”Measurements of viscous drag on cylinders and chains of sphere with aspect ratios between 2 and 50,” J. Aerosol Science, **16** (6), 535-556. Great Britain 1985.

[117] Hinds, W. C., “Aerosol Technology.” Wiley, 1982.

[118] Brockmann, J. E., et al, Appendix F, “Uncertainty in Radionuclide Release Under Specific LWR Accident Conditions,” in “Range of Possible Dynamic and Collision Shape Factors,” Sandia National Laboratories, Albuquerque, New Mexico, SAND84-0410 Volume 2, 1985.

[119] Kissane, M.P., “On the nature of aerosols produced during a severe accident of a water-cooled nuclear reactor”, Nuclear Engineering and Design, 238, 2792-2800, 2008.

[120] NUREG/CR-4691. Vol. 2. “MELCOR Accident Consequence Code System (MACCS) Model Description,” U.S. Nuclear Regulatory Commission, Washington, DC, February, 1990.

[121] NUREG/CR-1465. “Accident Source Terms for Light-Water Nuclear Power Plants,” Final Report. U.S. Nuclear Regulatory Commission, Washington, DC, February, 1995.

[122] Electric Power Research Institute, “Modeling of Molten Corium-Concrete Interaction,” EPRI NP-5403, Palo Alto, CA, 1987.

[123] Ghosh, S.T., et al., “Estimating Safety Valve Stochastic Failure-to-Close Probabilities for the Purpose of Nuclear Reactor Severe Accident Analysis,” NRC2017-3538, Proceedings of the Thirteenth NRC/ASME Symposium on Valves, Pumps, and In-Service Testing for Operating and New Reactors, July, 2017.

[124] NUREG/CR-6365, “Steam Generator Tube Failures,” U.S. Nuclear Regulatory Commission, Washington, DC, 1996.

[125] NUREG-1771, “U.S. Operating Experience With Thermally Treated Alloy 600 Steam Generator Tubes,” U.S. Nuclear Regulatory Commission, Washington, DC, February 2003.

[126] NUREG-2188, “U.S. Operating Experience With Thermally Treated Alloy 600 Steam Generator Tubes,” U.S. Nuclear Regulatory Commission, Washington, DC, February 2016.

[127] NUREG/CR-6995, “SCDAP/RELAP5 Thermal-Hydraulic Evaluations of the Potential for Containment Bypass During Extended Station Blackout Severe Accident Sequences in a Westinghouse Four-Loop PWR,” U.S. Nuclear Regulatory Commission, Washington, DC, March 2010.

[128] NUREG/CR-6365, “Steam Generator Tube Failures,” U.S. Nuclear Regulatory Commission, Washington, DC, 1996.

[129] NUREG-2195, “Consequential SGTR Analysis for Westinghouse and Combustion Engineering Plants with Thermally Treated Alloy 600 and 690 Steam Generator Tubes,” draft, U.S. Nuclear Regulatory Commission, Washington, DC, May 2016.

[130] U.S. Nuclear Regulatory Commission, “Virginia Electric and Power Company Surry Power Station Unit 1 Steam Generator In-service Inspection Report for the Fall 2013 Refuel Outage,” (ADAMS Accession No ML14135A365) 2013.

[131] U.S. Nuclear Regulatory Commission, “Virginia Electric and Power Company Surry Power Station Unit 1 Steam Generator In-service Inspection Report for the Spring 2015 Refuel Outage,” (ADAMS Accession No ML15324A014) 2015.

[132] U.S. Nuclear Regulatory Commission, “Virginia Electric and Power Company Surry Power Station Unit 1 Steam Generator In-service Inspection Report for the Fall 2016 Refuel Outage,” (ADAMS Accession No ML1712A378) 2016.

[133] U.S. Nuclear Regulatory Commission, “Virginia Electric and Power Company Surry Power Station Unit 2 Steam Generator In-service Inspection Report for the Fall 2012 Refuel Outage,” (ADAMS Accession No ML14150A137) 2012.

[134] U.S. Nuclear Regulatory Commission, “Virginia Electric and Power Company Surry Power Station Unit 2 Steam Generator In-service Inspection Report for the Spring 2014 Refuel Outage,” (ADAMS Accession No ML14294A449) 2014.

[135] U.S. Nuclear Regulatory Commission, “Virginia Electric and Power Company Surry Power Station Unit 2 Steam Generator In-service Inspection Report for the Fall 2015 Refuel Outage,” (ADAMS Accession No ML1614A117) 2015.

[136] U.S. Nuclear Regulatory Commission, “State-of-the-Art Reactor Consequence Analyses Project: Uncertainty Analysis of the Unmitigated Short-Term Station Blackout of the Surry Power Station,” Draft Report. (ADAMS Accession No ML15224A001) 2016.

[137] NUREG/CR-6791, “Eddy Current Reliability Results from the Steam Generator Mock-up Analysis Round-Robin,” U.S. Nuclear Regulatory Commission, Revision 1, October 2009.

[138] J. Birchley, L. Fernandez-Moguel, “Simulation of air oxidation during a reactor accident sequence: Part 1 – Phenomenology and model development,” Annals of Nuclear Energy, Volume 40, Issue 1, February 2012, Pages 163-170, ISSN 0306-4549.

[139] M. Steinbrück, et al., “Status of studies on high-temperature oxidation and quench behaviour of Zircaloy-4 and E110 cladding alloys,” The 3rd European Review Meeting on Severe Accident Research (ERMSAR-2008).

[140] M. C. Billone, “Steam Oxidation Kinetics of Zirconium Alloys ADAMS Accession No. ML021680052.

[141] L. Fernandez-Moguel, J. Birchley, “Simulation of air oxidation during a reactor accident sequence: Part 2 – Analysis of PARAMETER-SF4 air ingress experiment using RELAP5/SCDAPSIM,” Annals of Nuclear Energy, Volume 40, Issue 1, February 2012, Pages 141-152, ISSN 0306-4549.

[142] E. Beuzet, et al., “Cladding oxidation during air ingress. Part II: Synthesis of modeling results”, The 7th European Review Meeting on Severe Accident Research (ERMSAR-2015) Marseille, France, 24-26 March 2015.

[143] T. Yamashita, “Steam Oxidation of Zircaloy in the ORNL Fission Product Tests,” NUREG/CR-4477, Oak Ridge National Laboratory, March 1988.

[144] Prater, J.T., Courtright, E.L., “High-temperature Oxidation of Zircaloy-4 in Steam and Steam-Hydrogen Environments,” NUREG/CR-4476, Pacific Northwest Laboratory, March 1988.

[145] 602nd meeting of the Advisory Committee on Reactor Safeguards (ADAMS Accession No ML13067A219), March 7, 2013.

[146] “Type C Containment Isolation Valve Performance,” EPRI Report Number 1022599, (ADAMS Accession No ML110970450) March 2011.

[147] “Surry Power Station, Unit 2, Issuance of Amendment Regarding Revision of Technical Specification 4.4 Pertaining to the Containment Leakage Rate Testing Program,” (ADAMS Accession No ML083180243) December 18, 2008.

[148] NUREG/CR-4220, “Reliability Analysis of Containment Isolation Systems,” Pacific Northwest Labs., Richland, WA, March 1985.

[149] Gauntt, R.O., Radel, T., Salay, M.A, and Kalinich, D.A., “Analysis of Main Steam Isolation Valve Leakage in Design Basis Accidents Using MELCOR 1.8.6 and RADTRAD”, SAND2008-6601, Oct. 2008.

[150] “Transcript of the February 2, 2016 Advisory Committee on Reactor Safeguards, Regulatory Policies and Practices,” Nuclear Regulatory Commission, ADAMS Accession Number ML16049A510, February 2, 2016.

[151] “Virginia Electric and Power Company (Dominion) Surry Power Station Unit 1 Compliance Letter in Response to he March 12, 2012 Commission Order Modifying Licenses with Regard to Requirements for Mitigating Strategies for Beyond-Design-Basis External Events (Order Number EA-12-0490,” Adams Ascension Number ML15209A503, February 28, 2016.

APPENDIX A
GLOSSARY OF UNCERTAINTY ANALYSIS TERMS

Note that this glossary defines terms as they are used in this study, and the same terms may be used differently in other studies.

Additive Model – A regression technique where an estimation of the regression line is formed by a summation of a collection of one-dimensional arbitrary basis functions. An additive model considers the influence of the variables themselves and does not consider any possible interaction.

Aleatory – Inherent randomness in the properties or behavior of the system under study. Aleatory uncertainty cannot be reduced based on increased knowledge of the system under study.

Basis Function – Elementary elements used in the decomposition of a function in a specific space. Every continuous function can be constructed as a linear combination of basis functions. For example, a quadratic polynomial has basis functions of $\{1, x, x^2\}$. Every quadratic polynomial has the form:

$$y = a * 1 + b * x + c * x^2$$

where 1, x, and x^2 are the basis functions and a, b, and c are coefficients of the basis functions that define the unique polynomial.

Beta Distribution – A family of continuous probability distributions defined on the interval [0,1] parameterized by two positive shape parameters (α and β) that control the shape of the distribution. Its probability density function is expressed as follows:

$$f(t) = \frac{\Gamma(\alpha + \beta)}{\Gamma(\alpha)\Gamma(\beta)} t^{\alpha-1}(1-t)^{\beta-1}$$

where Γ represents the gamma function:

$$\Gamma(w) = \int_0^\infty x^{w-1} e^{-x} dx$$

Beta distributions can serve as a model for the probability that a system or component is in operation for at least *t* units of time. Sometimes, two parameters (min and max) are added to the beta function parameters. These parameters scale the domain of definition from [0,1] to [min,max]. See illustrations below.

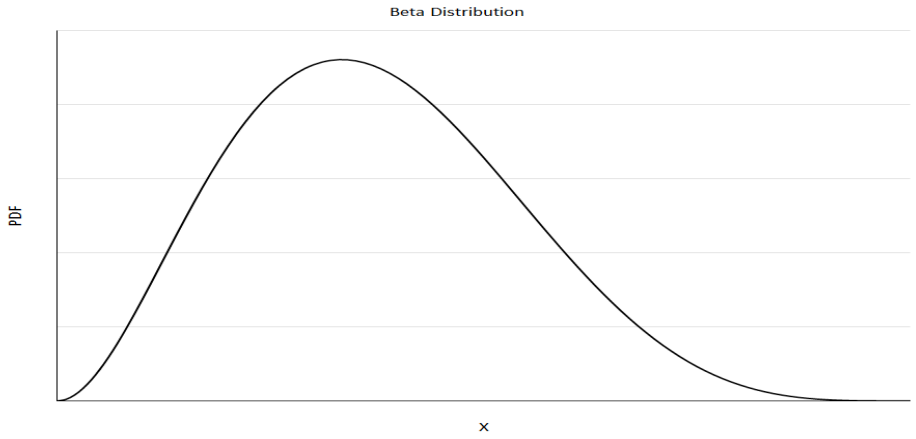

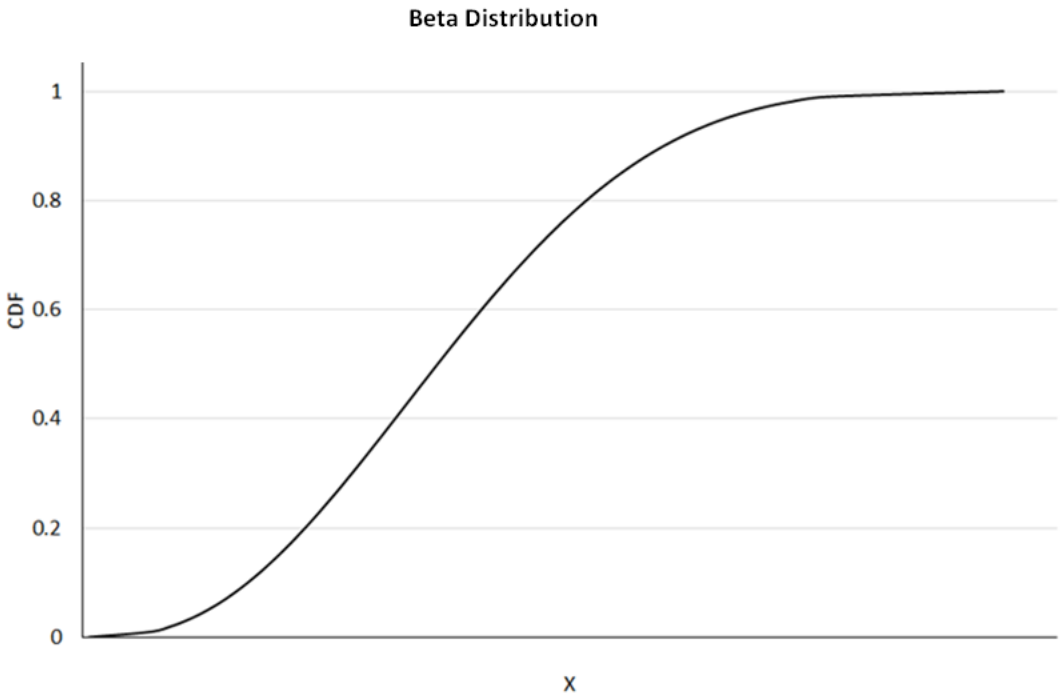

Cliff-Edge Effects – An instance in which a small change in an input can lead to a large change in the response of the system.

Coefficient of Determination – This coefficient (noted as R^2) estimates the proportion of the variance of the output that is explained by the regression model under consideration. Thus, this coefficient provides an indication of how well a regression model replicates the observed outcomes.

Complementary Cumulative Distribution Function (CCDF) – This function represents the probability for a value sampled from a probability distribution to be greater than a given quantile value. Given a real-valued random variable X and a threshold value x for a metric of interest, the complementary cumulative distribution function $\bar{F}(x)$ is defined as:

$$\bar{F}(x) = P(X > x) = 1 - F(x)$$

where $F(x)$ is the cumulative distribution function (CDF) defined by $F(x) = P(X \leq x)$.

Conjoint Influence – The influence of two or more input parameters acting together. This influence may have synergistic effects that would not be uncovered by studying the influence of each parameter individually.

Correlation – A possible dependence between two random variables. Positive correlation between two variables implies that a high value (or low value) for one variable is more likely to be associated with a respectively high value (low value) for the other. Negative correlation will reverse this relation, meaning that low values of one variable will be associated with high values of the other. Correlation does not imply causation. Correlation determines the existence of a trend but does not assess the magnitude of the change in output with respect to the change in input.

Cumulative Distribution Function (CDF[68]) - This function represents the probability for a value sampled from a probability distribution to be equal to or less than a given quantile value. For continuous variables, this function is the integral of the probability density function and is given by:

$$F(x) = \int_{-\infty}^{x} f(x)dx$$

where $F(x)$ is the cumulative distribution function and $F(x) = P(X \leq x)$.

Deterministic – Describing a system in which no randomness is involved in the calculation of a given response. A set of constant inputs definitively predict the output.

Discrete Distribution – A probability distribution where the random variable can have a set of distinct, finite values.

Epistemic – Uncertainty related to the lack of knowledge or confidence about the system under analysis. This type of uncertainty is produced by a lack of knowledge regarding the inputs or models under consideration. Epistemic uncertainty is usually considered as reducible uncertainty because increased knowledge should reduce it. Also called “state-of-knowledge” uncertainty.

Kaplan/Garrick Ordered Triplet Representation for Risk – This representation of risk poses three questions:

1) What can go wrong?
2) How likely is it to go wrong?
3) What are the consequences if the event occurs?

This representation is used to assess inherent randomness in the system (i.e., aleatory uncertainty). Potential lack of knowledge (i.e., epistemic uncertainty) adds a fourth question to the original triplet which is:

4) How much confidence do we have in the answers to the first three questions?

The exploration of these questions is the basis for Probabilistic Risk Assessment (PRA) (see ‘Probabilistic Risk Assessment’ below.) The Kaplan/Garrick ordered triplet representation is typically the NRC’s definition of the term “risk.”

---

[68] Not to be confused with core damage frequency (CDF) from a level 1 probabilistic risk assessment.

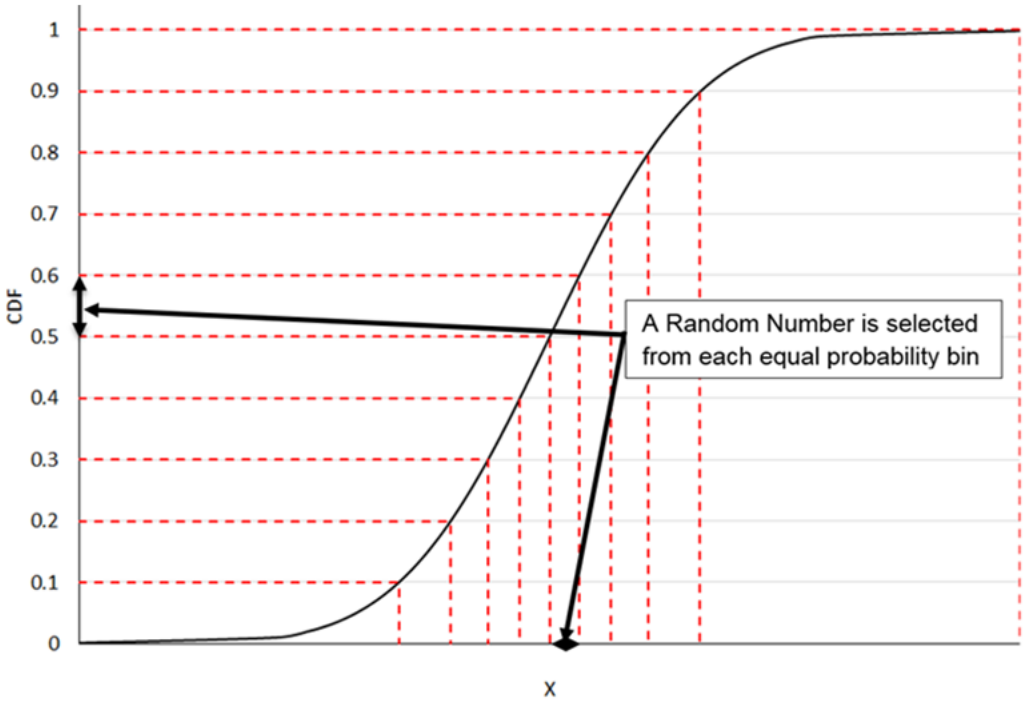

Latin Hypercube Sampling (LHS) – A sampling technique in which each input variable is sampled in a stratified way in order to guarantee that all portions of the range of the variable's distribution are represented. LHS samples a probability density function (PDF) by first dividing the PDF of each variable into N bins of equal probability where N is the sample size per variable chosen ahead of time. One value is then sampled from the random variable's PDF in each of the N bins. Thus, if there are n random input variables, the input space is partitioned into $n \times N$ hypercubes from which N will be selected such that each variable will have exactly one value sampled in each of its defined strata (PDF interval). See illustrations below for one (x) and two (x, y) variables, where the red marks on the 2nd illustration represent one possible Latin Hypercube Sample of size N = 6.

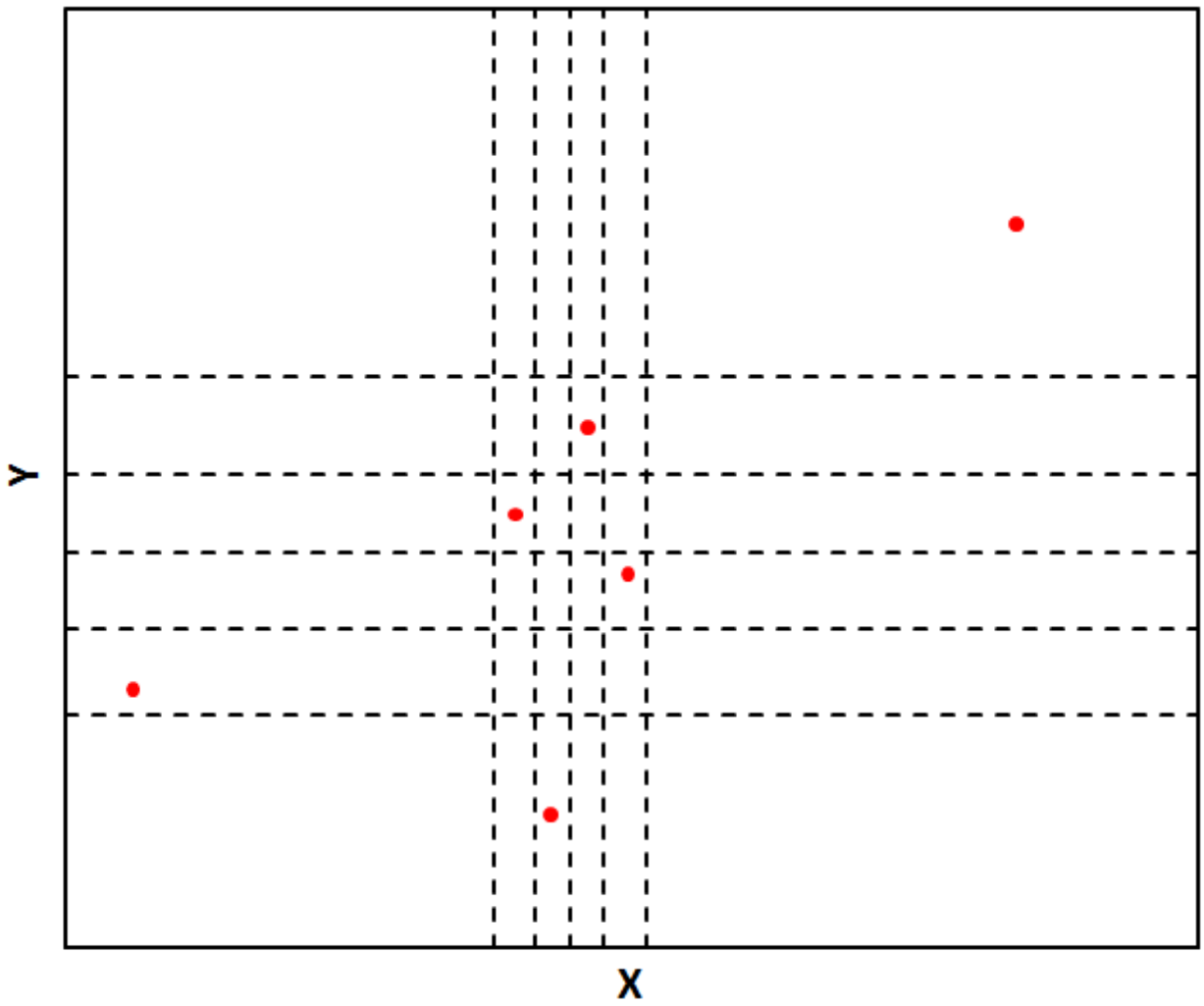

Least Squares – An optimization technique that select the parameters of a model such that the difference between the estimation and empirical values (derived from observations or another model) is minimized according to the L^2-norm (i.e., the square root of the sum of square differences is minimized).

Lognormal Distribution – A normal distribution over the logarithm of the random variable.

Log Triangular Distribution – A triangular distribution over the logarithm of the random variable. See illustrations under '**Triangular Distribution**' below, where the only difference is that "log(x)" replaces "x" on the x axis.

Log Uniform Distribution – A uniform distribution over the logarithm of the random variable. See illustrations under '**Uniform Distribution**' below, where the only difference is that "log(x)" replaces "x" on the x axis.

Mean – Estimates the expected value of a distribution of values. The mean value of a random variable is the arithmetic average of possible values as described by its probability density function. See illustration below for 'mean,' '**median**,' and '**mode**,' all of which are measures of central tendency, though they are all different.

Median – The median of a probability distribution corresponds to the middle value that separates a sample or a distribution into halves of equal likelihood. A random variable is equally

likely to take on a value greater than the median or less than the median. In other words, the CDF(Median value) = CCDF(Median value) = 0.5. See illustration below for '**mean**,' 'median,' and '**mode**,' all of which are measures of central tendency, though they are all different.

Mode – The most likely value for an uncertain variable. For a discrete distribution, the mode represents the most common (most likely) value in a set of n values. For a continuous distribution, the mode represents the value at which the probability density function reaches its maximum. See illustration below for '**mean**,' '**median**,' and 'mode,' all of which are measures of central tendency, though they are all different.

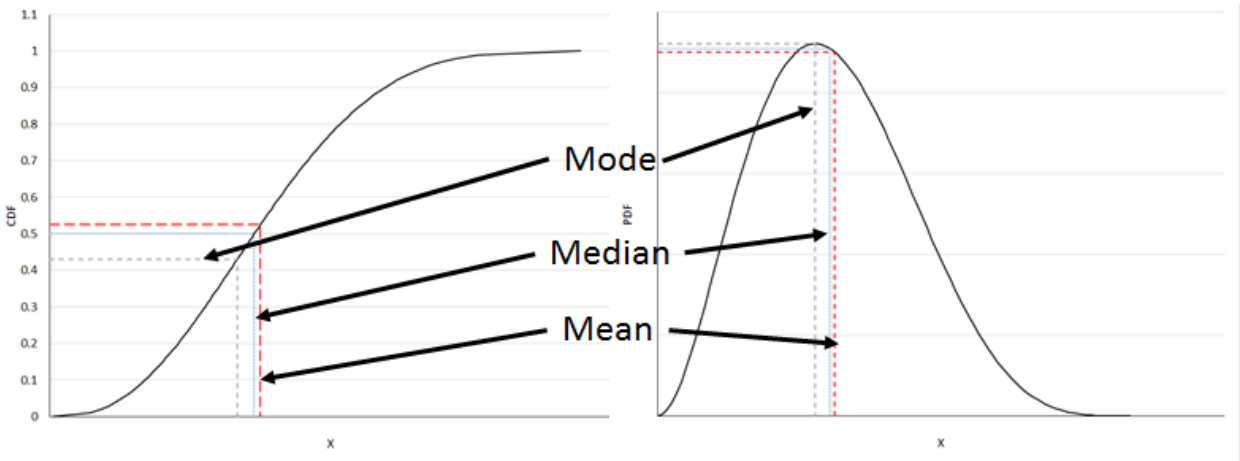

Monotonic – A monotonic function is a function which is either solely non-increasing or solely non-decreasing. A monotonic function cannot increase with increasing values of a dependent variable in one range and then decrease with increasing values of a dependent variable in a different range.

Monte Carlo Simulation – A numerical technique that covers the uncertain input space (multidimensional space where each dimension represents a different random variable with its associated distribution) by sampling each probability distribution using random, or pseudo-random, numbers. This method is preferred over a direct discretization when the number of inputs is large because a regular discretization in each direction would lead to an impractically large number of simulations. The system model is then run repeatedly using a single set of values for the input variable vector at each repetition. With this process, Monte Carlo simulation produces a distribution of system model outputs (results) based on the input variable uncertainty as described by the input space.

(Multiplicative) Interaction Term – In regression models, interaction (or higher order) terms are basis functions that do not solely depend on one parameter. They can involve interactions amongst just two parameters up to interactions that involve all parameters under study. They can be as simple as a multiplication of two parameters or fairly complex (division, power, log, etc.). These terms are ignored by additive regression models.

Normal Distribution – The normal distribution is one of the most common probability distributions. As demonstrated by the central limit theorem, the normal distribution can be used to represent the distribution of the sum of random variables (if they follow the same distribution) or the distribution of the mean value. The normal distribution's probability density function is defined from $-\infty$ to $+\infty$ and has a bell shape:

$$f(x|\mu,\sigma) = \frac{1}{\sigma\sqrt{2\pi}} e^{-\frac{(x-\mu)^2}{2\sigma^2}}$$

Where μ and σ represent respectively the mean and standard distribution and are the traditional parameters used to define a normal distribution.

Percentile – Specific form of quantile for which the value is reported as a percentage (e.g. the 0.01 quantile is the same as the 1st percentile). See **'quantile'** for additional description.

Piecewise Uniform Distribution – A distribution formed by distinct uniform distributions over intervals of the range of the probability density function. See illustration below.

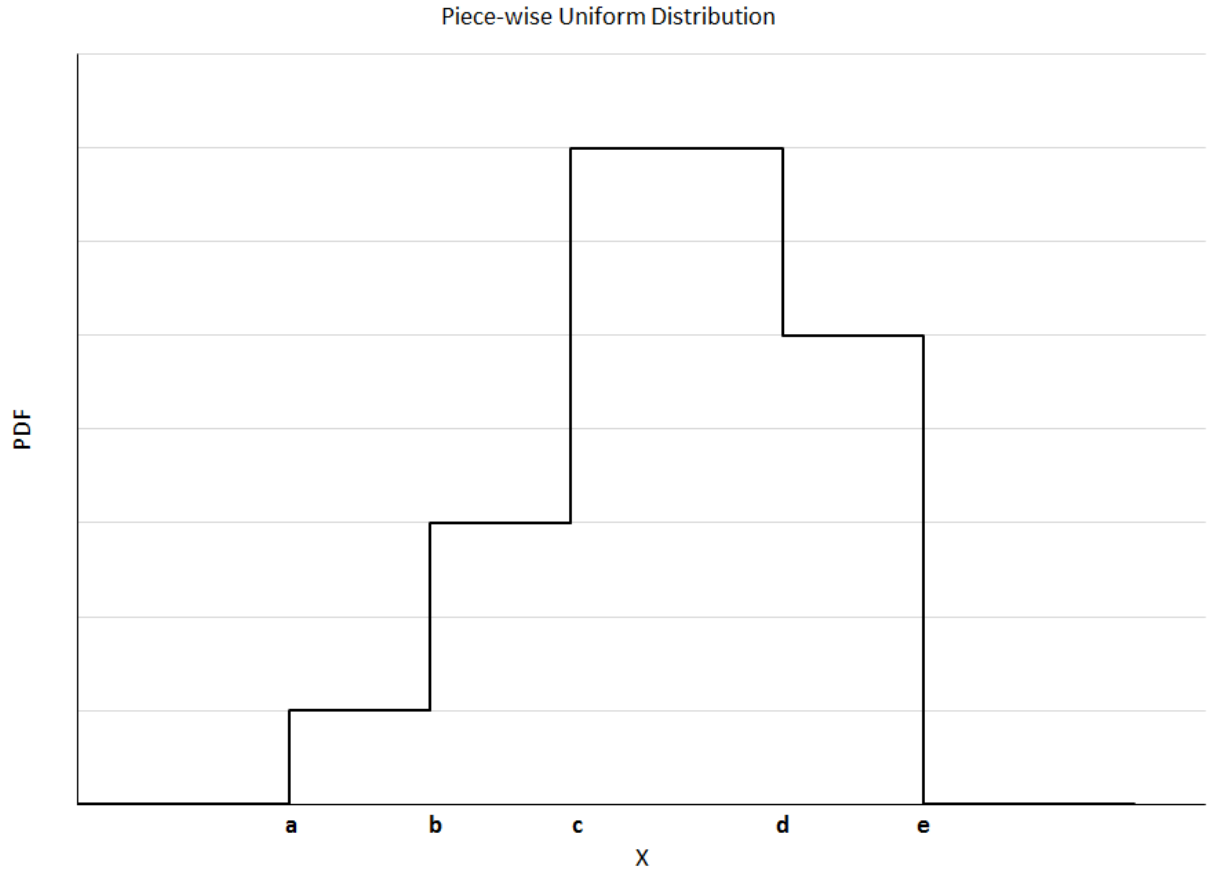

Probabilistic Risk Assessment (PRA) – A systematic method for assessing three questions that the NRC uses to define "risk." These questions consider (1) what can go wrong, (2) how likely it is, and (3) what its consequences might be. (See '***Kaplan/Garrick ordered triplet representation for risk***' above.) These questions allow the NRC to understand likely outcomes, sensitivities, areas of importance, system interactions, and areas of uncertainty, which the staff can use to identify risk-significant scenarios. The NRC uses PRA to determine a numeric estimate of risk to provide insights into the strengths and weaknesses of the design and operation of a nuclear power plant.

Probability Density Function (PDF) – A function that describes the likelihood that a continuous random variable takes on a value in an interval. A PDF has the properties that 1) a value on the function is greater than or equal to 0 and 2) the total integral probability is 1.

$$f(t) \geq 0$$

$$\int_{-\infty}^{\infty} f(t)dt = 1$$

Probability Distribution – A mathematical representation of the uncertainty of a random variable in a probabilistic framework. Specification of a probability distribution can be done via probability density (or mass for discrete variable) function or a cumulative distribution function for instance.

Probability Mass Function (PMF) – A function that is equivalent to the probability density function for discrete variables (and for which integral is replaced with a regular sum).

Quantile – A quantile x_q is the value of a random variable such that there is a probability q that a sampled value will be equal or lower to x_q. Specific quantiles include the median (for which $q = 0.5$), quartiles (where q =0.25 and 0.75 and represents the 1st and 3rd quartiles, respectively) and percentiles (in which q is expressed as a percent from 0 to 100 instead of a probability between 0 and 1).

Rank Correlation Coefficient – Also known as Spearman Correlation Coefficient, the rank correlation coefficient measures the degree of linearity in the relationship between two random variables after they have been rank-transformed (see **'rank transformation'**).

Rank Regression – Rank regression is a linear regression applied to rank values. The linear regression builds a linear function model between outputs and inputs using a least squares approach. Often, linear and rank regressions use a stepwise approach such that new parameters are added to the model only if they increase the strength of the regression model significantly enough such that the complexity of adding a parameter is overcome by the increase in variance explained. Rank Regression is solely used to estimate the influence of uncertainty in the input parameters on the output uncertainty and is not used for prediction.

Rank Transformation – Rank transformation consists of replacing the actual value of a random variable by its rank in the total sample. Regression methods become non-parametric when working with rank values instead of with raw data. This allows for monotonic relations to be captured instead of simple linear relations and reduces the effect of outliers.

Realization – An individual calculation using one sample of values for the input variable vector in Monte Carlo simulation. In other words, a Monte Carlo simulation where the system model is run N times has N realizations. Within a realization, the model is usually run deterministically and returns a unique set of output values.

Regression – A measure of the relation between one variable (e.g., output or results of a model) and corresponding values of other variables (e.g., inputs to a model). Regression methods attempt to find a mathematical relationship between input variables and the output variable(s) of interest.

Regression Analysis – An analysis that determines the importance of input variables to outputs of interest by examining how sensitive an output is to a given input or set of inputs. Regression analysis in this study used the results of Monte Carlo simulation. Regression results quantify how much the uncertainty in each analysis input contributes to the variance in the output under consideration.

Sensitivity Analysis – A set of studies that exercise a complex system under different conditions in order to 1) validate some assumptions, 2) explore alternative conceptual models or address differences in opinion, or 3) study one particular aspect of the complex system in greater detail. These studies are different from Monte Carlo simulations in that they require changing some options that have been considered to be constants in the study of reference and

may study only one variable or conceptual model in isolation. Such studies can be completed through either deterministic or probabilistic means.

Simple Random Sampling (SRS) – A random sampling technique where for each time sampled, the probability that a particular value of a variable is chosen is proportional to the probability density function of the variable at that particular value. No further requirements are imposed on the sampling (unlike Latin Hypercube Sampling).

Stochastic – A random occurrence. A stochastic simulation refers to a simulation in which randomness in uncertain input variables is used to calculate a system response.

Stochastic Failure – A failure that is caused by random processes.

Sum of Square Error (SSE) – The total sum of the squares of the differences between estimated and empirical values (i.e., observations, measurements, or an empirical model).

$$SSE = \sum_i \left(y_i - f(x_i)\right)^2$$

A small SSE indicates a good fit between the predicted and observed values.

Triangular distribution – A continuous distribution that takes the form of a triangle. The probability density for the range [*a*,*b*] reaches its mode at the location c and forms a triangular shape:

$$f(x) = \begin{cases} 0 & for\ x < a \\ \dfrac{2(x-a)}{(b-a)(c-a)} & for\ a \le x < c \\ \dfrac{2}{b-a} & for\ x = c \\ \dfrac{2(b-x)}{(b-a)(b-c)} & for\ c < x \le b \\ 0 & for\ x > b \end{cases}$$

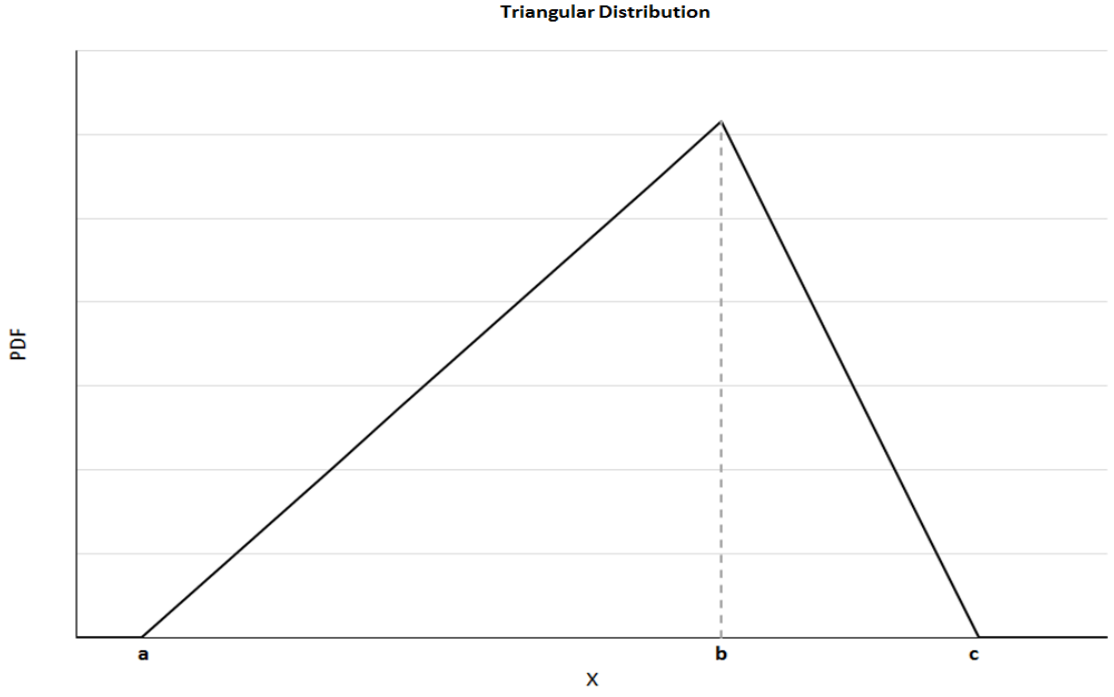

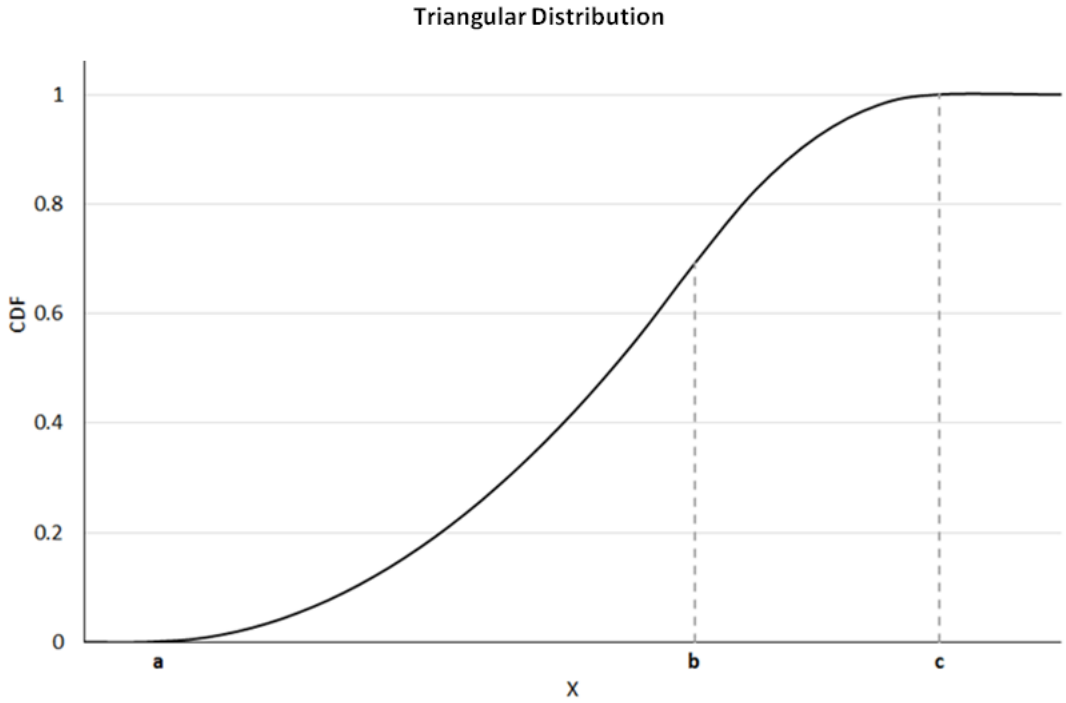

Uncorrelated – A situation in which no linear dependence between sampled values for two variables is observed.

$$f(x) = \begin{cases} \dfrac{1}{b-a} & \text{for } x \in [a, b] \\ 0 & \text{otherwise} \end{cases}$$

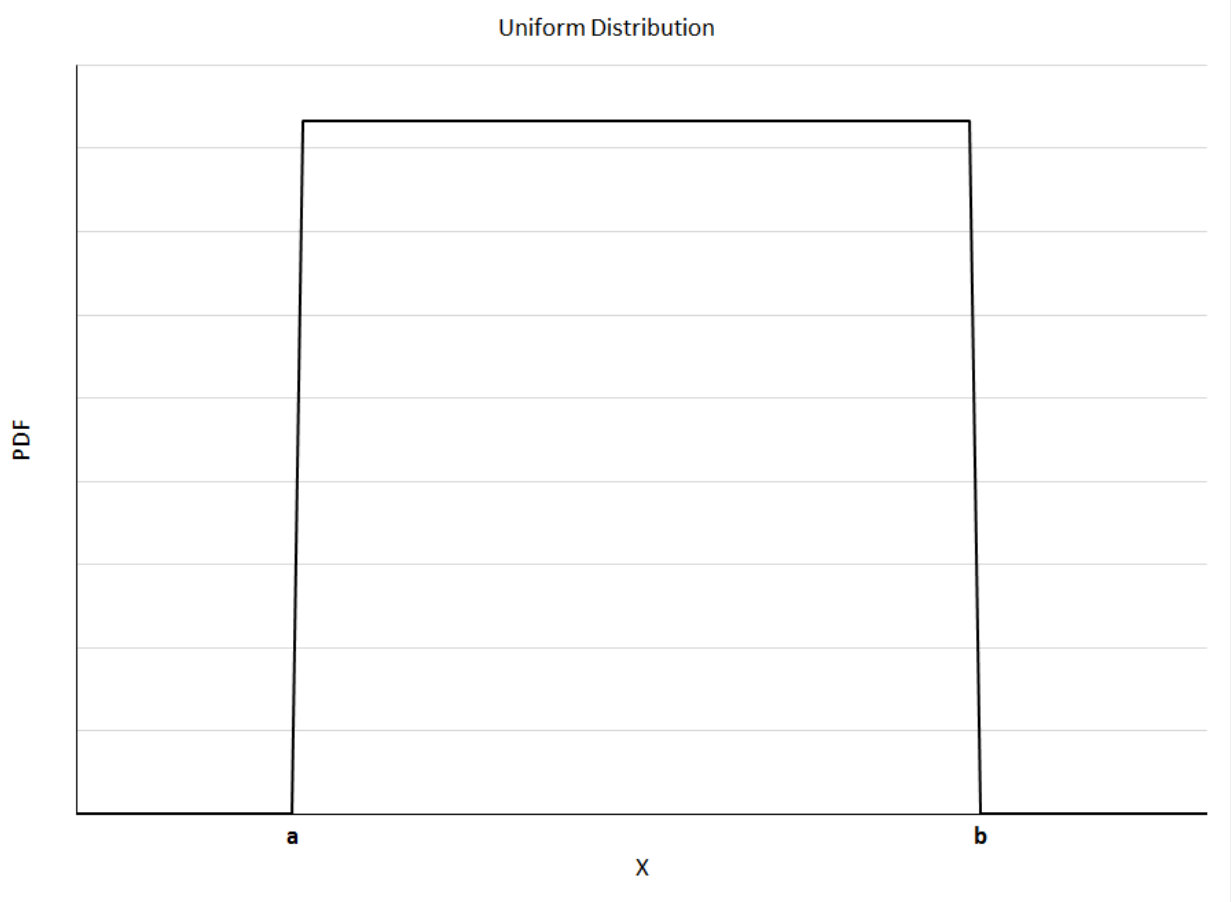

Uniform Distribution – A distribution used when any value for a random variable defined on a range [*a*,*b*] is equally likely. The uniform probability density function forms a rectangle and is given by:

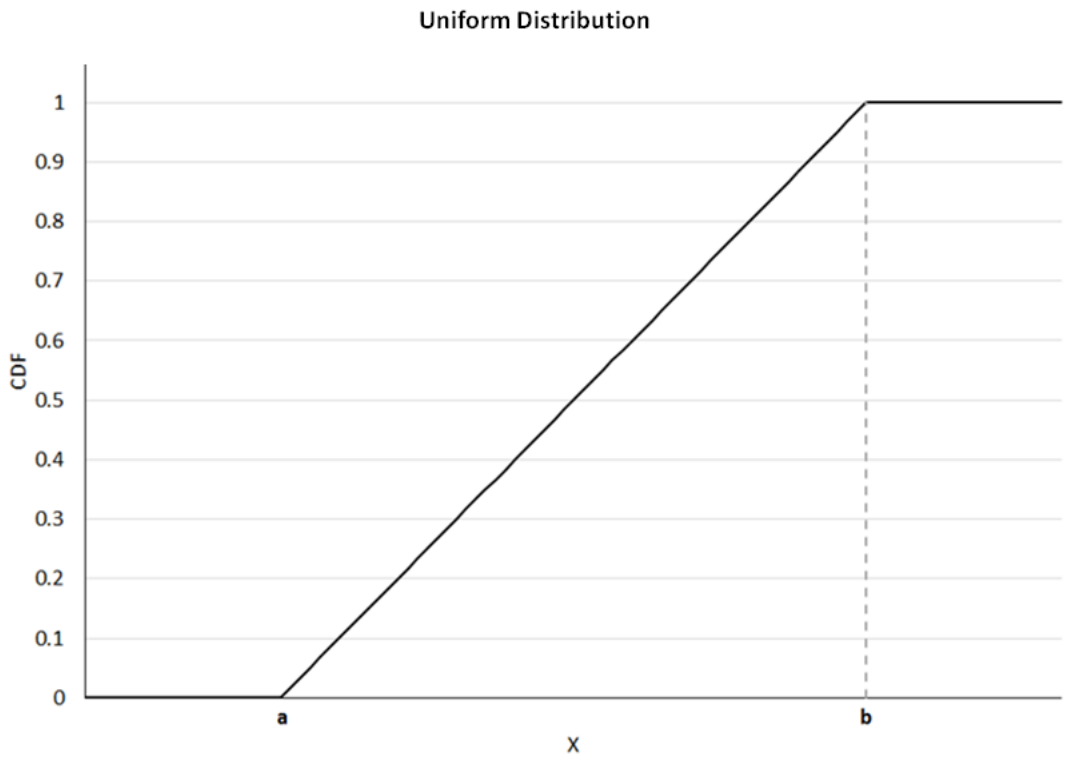

Variance – A measure of the dispersion of data about a mean, given by:

$$V = \sigma^2 = \frac{\sum_{i=1}^{N}(Y_i - \mu)^2}{N}$$

where Y_i is a particular data point, μ is the mean, and N is the number of data points. The variance characterizes the average spread squared of the data set.

APPENDIX B
COMPARISON OF THICK AND THIN-WALLED STRESS EVALUATIONS

The thick-walled stress pipe stress equation in MELCOR is:

$$\text{Pipe-Str}_{\text{MELCOR}} = \frac{\left(r_o^2 + r_i^2\right)P_i - 2\,r_o^2\,P_o}{(r_o + r_i)(r_o - r_i)} = \frac{\left(r_o^2 + r_i^2\right)P_i - 2\,r_o^2\,P_o}{\left(r_o^2 - r_i^2\right)}$$

Relative flaw depth may be taken as

$$\widehat{\Delta r}_{\text{flaw}} = \frac{r_{\max} - r_{\text{flaw}}}{r_{\max} - r_{\min}} = \frac{\Delta r_{\text{flaw}}}{\Delta r_{\max}}$$

If all of the total wear is assigned to the outer diameter with r_{flaw} taken to be r_o and $r_{\min}$ be $r_i$for consistency. The pipe stress equation can then be written as

$$\text{Pipe-Str}_{\text{o}} = \frac{\left([r_{\max} - \Delta r_{\text{flaw}}]^2 + r_{\min}^2\right)P_i - 2\,[r_{\max} - \Delta r_{\text{flaw}}]^2\,P_o}{(r_{\max} + r_{\min} - \Delta r_{\text{flaw}})(\Delta r_{\max} - \Delta r_{\text{flaw}})}$$

A more general definition of flaw depth is defined as the sum of the difference between the maximum inner and outer radii and their flawed values:

$$\widehat{\Delta r}_{\text{flaw}} = \frac{(r_{\max} - r_{\text{o}}) + (r_{\text{i}} - r_{\min})}{r_{\max} - r_{\min}} = \frac{(r_{\max} - r_{\min}) - (r_{\text{o}} - r_{\text{i}})}{r_{\max} - r_{\min}} = \frac{\Delta r_{\max} - \Delta r}{\Delta r_{\max}} = \frac{\Delta r_{\text{flaw}}}{\Delta r_{\max}}$$

There is an implicit assumption in this formula that the flaw is always ablative in nature from both sides, and therefore, the outer and inner radii will always be less and greater than their extrema, respectively. A complication is introduced because the relative flaw depth now incorporates both radii and doesn't offer the clean compatibility conditions from the previous definition and a closure for apportionment must be introduced if a single relative flaw depth sample will be used:

$$r_o = r_{\max} - \alpha \cdot \Delta r_{\text{flaw}}$$
$$r_i = r_{\min} + (1 - \alpha) \cdot \Delta r_{\text{flaw}}$$

where $\alpha \in [0,1]$.

$$\text{Pipe-Str}_{\alpha} = \frac{([r_{\max} - \alpha\,\Delta r_{\text{flaw}}]^2 + [r_{\min} + (1 - \alpha) \cdot \Delta r_{\text{flaw}}]^2)P_i - 2\,[r_{\max} - \alpha\,\Delta r_{\text{flaw}}]^2\,P_o}{(r_{\max} + r_{\min} + [1 - 2\alpha]\Delta r_{\text{flaw}})(\Delta r_{\max} - \Delta r_{\text{flaw}})}$$

It is noted that, albeit by construction, this form matches $\text{Pipe-Str}_{\text{o}}$with $\alpha = 1$.

Several evaluations of Pipe-Str_{α} are presented in Figure B-1. The maximum relative difference across the parametrizations exceeds 5% beyond 40% relative flaw depth and peaks at

approximately 11% after 95% (higher evaluations of relative flaw depth were not taken since the evaluations begin to significantly diverge toward infinity).

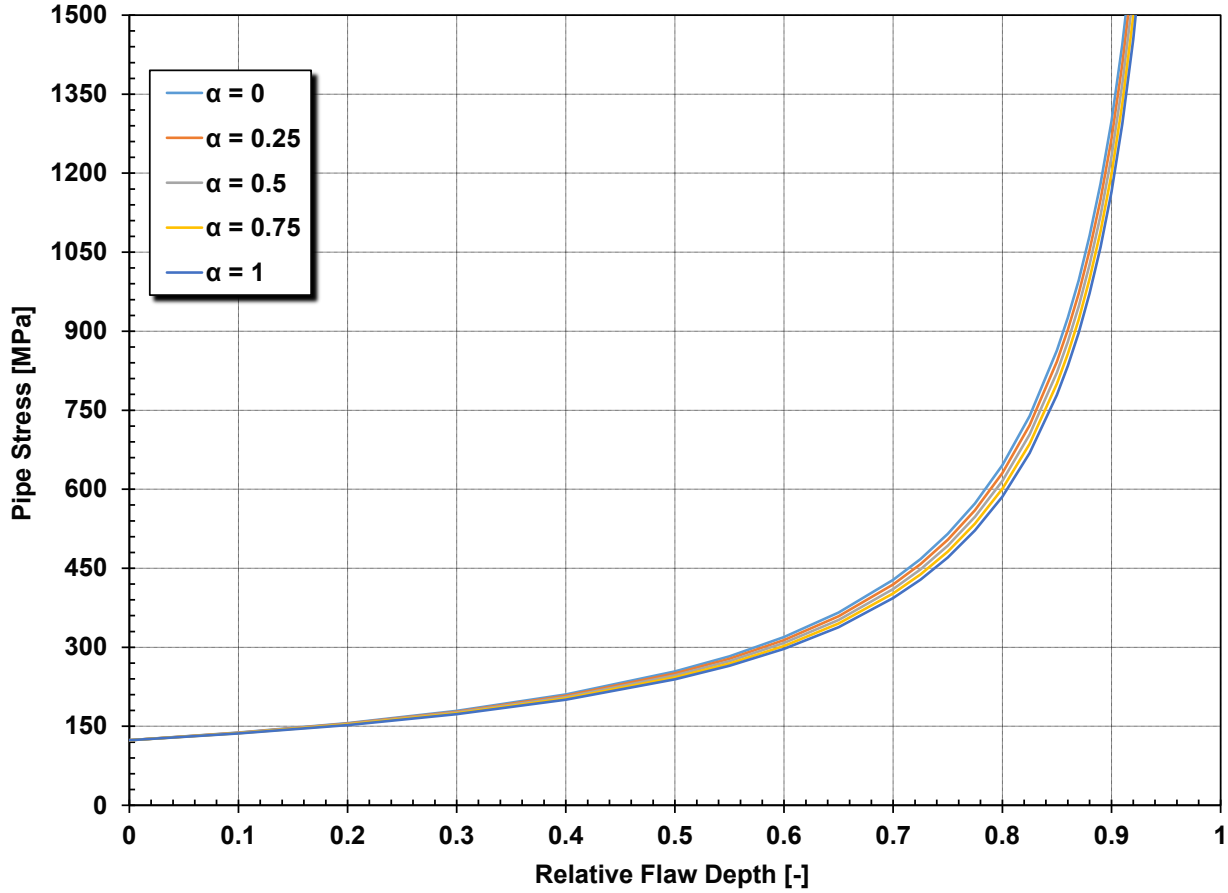

Figure B-1 **Pipe Stress Versus Relative Flaw Depth Parametrized by the Apportionment Factor α. The Maximum and Minimum radii are 11.11 mm and 9.843 mm, respectively. The Inner and Outer Pressures are 15 MPa and 101,325 Pa, respectively**

APPENDIX C
SUMMARY OF RECENT LERS FOR PWR MSIV ISSUES

Date	Description	Location	LER Number	Mode	Power Level	Mention of Partial or Non-Closure (event or possible)
2001	MSIVs were not tested in mode 3 as required.	Braidwood, Unit 2	2001-002-00	1	96	
2001	Two surveillance requirements for the MSIVS were not tested in Mode 3 as required, resulting in missed technical specifications surveillance requirements on all 4 MSIVs on each unit.	Byron, Unit 1,2	2001-002-00	1	100	
2001	Human error event; recorded stroke time from Mode 3 test was 4.09s. Corrected during review to 5.09s, which it outside tech spec.	Seabrook	01-004-00	3	0	
2004	Stroking of 1SM-1 (D SG MSIV) introduced valve stem scoring. Scoring was indicative of conditions which probably prevented the valve from fully closing. Attributed to high valve friction due to main poppet tripping and plowing of the guide rib, actuator stem misalignment, stem side loading, and abnormal packing friction.	McGuire, Unit 1	2005-002-01	4	0	Yes
2005	2SM-1 2D steam generator MSIV failed to stroke closed during testing. Attributed to binding caused by insufficient clearance between the valve stem and cover brushing due to excessive corrosion growth, thermal binding, and extrusion of the packing into the clearance gap.	McGuire, Unit 2	2005-005-00	3	0	Yes
2006	MSIV inoperable for 20 hours due to both power supply fuses in the MSIV control cabinet being open. Deemed random failure of the MSIV control module printed circuit board.	Seabrook	2006-005-00	1	100	Yes
2006	MSIVs A and B inoperable due to scaffolding interfering with closure. Scaffolding removed and operability restored within 6 hours of detection. Estimated inoperability time was >16 hours.	Beaver Valley, Unit 2	2006-003-01	1	60	Yes

Date	Description	Location	LER Number	Mode	Power Level	Mention of Partial or Non-Closure (event or possible)
2006	Unit 1 downstream MSIVs failed to fully stroke closed. Valve A closed approx. 70%, B and C did not move from full open position. After cooldown (~6 hours) valve A was found 90% closed and would not move open or closed. B was found 75% open and was closed by repeated mechanical agitation. Valve C was found full open and was closed by a single application of mechanical agitation. Following completion of cooldown, all three valves would stroke both open and closed. Attributed to inadequate preventative maintenance on shaft load-bearing components, improper valve assembly, omission of relevant info in the procedure, and turbulence in the downstream valves resulting in a more severe duty condition than in the upstream valves.	Joseph M. Farley, Unit 1	2006-002-00	3	0	Yes
2006	Scaffolding prevented the #1 SG MSIV 2-MS-64A valve from fully closing during surveillance testing. Scaffold in place for 44 days.	Millstone, Unit 2	2006-006-01	3	0	Yes
2007	MSIV 181 actuator train A inoperable from 7/31 through 10/27.	Palo Verde, Unit 2	2007-004-00	1	100	
2009	MSIV 1D discovered inoperable due to restricted movement that kept it from being closed completely. Root cause: inadequate procedures for scaffold installation.	South Texas, Unit 1	2009-002-1	1	100	Yes
2009	Personnel found steam leaking from the bottom of the 3C MSIV in the area where the weld boss joins the valve body. The leak was from a weld and structural integrity was impacted. The 3A and 3B MSIVs closed, but the 3C MSIV did not close on demand. It closed approximately 1 hour later. Cause of the MSIV failure "inadequate guidance for verification of post maintenance tests for returning equipment to service".	Turkey Point, Unit 3	2009-002-01	2	2	Yes

Date	Description	Location	LER Number	Mode	Power Level	Mention of Partial or Non-Closure (event or possible)
2011	B MSIV position indicator lights on the main control board flickered and went out (June 11, 2011). A fire water booster pump auto-started and the lights indicating that the B MSIV was open turned on. After pump secured, lights turned off. A fuse clip in the control circuit was determined to be not making contact with the fuse. Suspected relay actuation from the booster pump vibrated the fuse clip causing it to make contact (August 23). It was established that the fuse clip for the B train actuation circuit was damaged, potentially since June 11. Cause is the use of fuse blanks for hanging clearance tags causing excessive bending of the fuse clips.	R.E. Ginna	2001-002-0	1	100	
2012	MSIV SGE-UV-180 A actuator train was inoperable for 23 days due to nitrogen leak.	Palo Verde, Unit 1	2012-003-00	1	100	
2013	Actions to close and deactivate MSIV-170 did not meet operability requirements, so the requirement to place the unit in Mode 2 within 6 hours was not completed.	Palo Verde, Unit 1	2013-004-00	1	100	
2013	Spurious closure of 1b MSIV in Mode 1, 100% power. Interference between the internal tail link and the valve body prevented the valve disc from fully opening. This allowed unintentional loading of internal parts resulting in the failure of the valve's lower shear pin. Pin failure led to spindle/disc separation and inadvertent closure of the valve. Internal interference was caused by an oversized tail link supplied by the valve manufacturer.	St. Lucie, Unit 1	2013-001-00	1	100	
2015	Air-line fitting failure, MSIV-191B actuator train inoperable.	Palo Verde, Unit 3	2015-004-01	1	100	
2015	Review identified two occurrences in three years where a single MSIV actuator train was inoperable and not restored within 8 hr requirement.	Braidwood, Unit 1	2015-001-00	1	100	

Date	Description	Location	LER Number	Mode	Power Level	Mention of Partial or Non-Closure (event or possible)
2015	One of the associated redundant actuator trains was inoperable; there were two previous occurrences in three years when an actuator train for an MSIV was inoperable and not restored within the 8 hr time frame.	Byron, Unit 1	2015-001-00	1	100	
2015	SCRAM due to indications that the Loop 3 MSIV had starting drifting in the closed direction. Troubleshooting identified a loose termination associated with the Loop 3 MSIV hand switch that would result in a slow loss of air pressure and cause the MSIV to drift in the closed direction. Direct cause determined to be a loose electrical connection on the MSIV hand switch.	Sequoyah, Unit 1	2015-004-01	1	100	Yes
2016	MSIV 171 train A actuator inoperable due to nitrogen leak from 7/30 to 8/9, exceeding 7 day required action completion time.	Palo Verde, Unit 2	2016-001-00	1	100	
2012	Two MSIVs declared inoperable during surveillance test. Root cause was unexpected long-term corrosion of the valve piston rings. The A MSIV closed in under five seconds; B MSIV closed in 1 hour 14 mins; C MSIV closed in 4 hours 37 mins.	Shearon Harris, Unit 1	2012_001_00	4	0	Yes
2015	MSIV spuriously closed due to failure of the hydraulic dump solenoid valve and loss of hydraulic control pressure.	Vogtle, Unit 2	2015_001_00	1	100	
2014	Control room operators received a Loop 1 Train B MSIV trouble annunciator followed by the MSIV not fully open annunciator. Cause was a failed o-ring on the Loop 1 Train B MSIV lower manifold-to-cylinder mating surface resulting in a loss of hydraulic oil pressure. Root cause was misalignment of the lower manifold_-to-cylinder mating surface during valve reassembly. The MSIV drifted closed to its fail safe position.	Vogtle, Unit 1	2014_002_00	1	28	

Date	Description	Location	LER Number	Mode	Power Level	Mention of Partial or Non-Closure (event or possible)
2008	MSIV (A) did not open on demand, but opened shortly after when the ASD had already been opened. Unclear how long the MSIV did not respond.	Callaway, Unit 1	2008_003_00	4	0	
2000	Unplanned closure of MSIV as a result of a blown fuse in the positive side of the circuit. Investigation found no electrical ground in the circuit of evidence of an overcurrent condition. No water or visible damage. Review of valve history showed the negative side fuse in the MSIV circuit had blown and been replaced during testing in previous outage. Unclear if related, no clear cause.	Vogtle, Unit 1	2000_002_00	1	100	
2017	Loop 1 MSIV drifted closed due to failure of an o-ring on the MSIV lower manifold pressure boundary, causing loss of hydraulic pressure on the MSIV and subsequent drifting. O-ring failed from extrusion because of radial misalignment.	Vogtle, Unit 1	2017_001_00	1	100	
2010	MSIV failed to fully close on demand, but fully closed after locally isolating instrument air to the valve. Cause was determined to be two solenoid operated shuttle valves failing to fully realign to vent air after de-energizing. One of the SOVs was found stuck in its energized position and the other in an intermediate position. A portion of the air was trapped in the valve actuator, preventing the valve from fully closing.	Harris, Unit 1	2010_002_01	1	100	
2011	During testing, the C MSIV failed its stroke test due to an out-of-tolerance stroke time and was closed. No explanation included for causes of test failure.	VC Summer, Unit 1	2011_003_01	3	0	

Date	Description	Location	LER Number	Mode	Power Level	Mention of Partial or Non-Closure (event or possible)
2016	Unplanned 1A MSIV closure caused by failure of its test solenoid in conjunction with other air system leakage, which vented air pressure from the 1A MSIV actuator. The preventative maintenance task of the test solenoid valve had been deactivated in 2004.	Joseph M. Farley, Unit 1	2016_002_00	1	99	
2003	Inadvertent closure of the C MSIV. The west air cylinder rupture disk on the MSIV was damaged due to human error (it was torn with a pole) during installation of scaffolding in the area below the MSIV. The rupture disk failed, venting the instrument are pressure resulting in closure of the MSIV.	Beaver Valley, Unit 1	2003_001_00	1	100	

APPENDIX D
DESCRIPTION OF THE INITIAL RADIONUCLIDE INVENTORY SPECIATION

RADIONUCLIDE DISTRIBUTION AND SPECIATION

As discussed in Section 4.1.2.4, each realization's radionuclide inventory is defined by a representative ORIGEN fission product inventory determined by a sampled time-in-cycle. The ORIGEN fission product inventory and power distribution are used to define the realization's initial fission product inventory and distribution between the fuel and gap across the core. There are two parameters of interest for this fission product loading: elemental iodine gas initially in the gap and the initial fractional speciation of cesium in the fuel between elemental cesium (Cs), cesium iodide (CsI), and cesium molybdate (Cs2MoO4). The following section discusses how the iodine and cesium in the fuel are speciated and classed for use in MELCOR's Radionuclide Package.

DETAILED SPECIATION PROCESS

Following the selection of the sampled iodine gas and cesium molybdate fractions as described in Sections 4.1.4.1 and 4.1.4.2, the initial fission product speciation can be determined. The elemental masses from ORIGEN and their respective decay powers are organized into the appropriate classes shown in Table D-1 as defined by MELCOR's Radionuclide Package. Also shown on the table is the representative element for each class. For the purposes of the following discussion, all references to individual elements are references to the classes those elements represent (e.g., the class 2 mass is referred to as the mass of cesium unless explicitly stated otherwise). Cesium hydroxide is handled directly by class 2 when that cesium is released from the fuel.

The initial assignment of the ORIGEN inventory is into MELCOR Classes 1 through 15, which include all the elements identified. Two of the classes not populated after the initial summation from ORIGEN data are class 16 and class 17[69]; these are classes that represent CsI and Cs_2MoO_4. (i.e., other chemical compounds of the respective elements defined in Classes 1 through 12). CsI and Cs_2MoO_4 are referred to as combination classes since they are composed of more than one constituent and require additional bookkeeping in the speciation process.

The speciation process begins with the unspeciated masses of cesium, iodine, and molybdenum (i.e., classes 2, 4, and 7). Using several defined or sampled fractions, these masses are then speciated between cesium, iodine, molybdenum, CsI, and Cs2MoO4 (i.e., classes 2, 4, 7, 16, and 17) with both in-fuel and in-gap (as gas) fractions. The symbols used in the equations are delineated in Table D-2.

[69] Classes 14 and 15 also exist but are immaterial to this section.

Table D-1 MELCOR's Radionuclide Class Structure

MELCOR Class Number [a]	Class Name	Representative	Element Members
1	Noble Gases	Xe	He, Ne, Ar, Kr, Xe, Rn, H, N
2	Alkali Metals	Cs	Li, Na, K, Rb, Cs, Fr, Cu
3	Alkaline Earths	Ba	Be, Mg, Ca, Sr, Ba, Ra, Es, Fm
4	Halogens	I_2	F, Cl, Br, I, At
5	Chalcogens	Te	O, S, Se, Te, Po
6	Platinoids	Ru	Ru, Rh, Pd, Re, Os, Ir, Pt, Au, Ni
7	Early Transition Elements	Mo	V, Cr, Fe, Co, Mn, Nb, Mo, Tc, Ta, W
8	Tetravalents	Ce	Ti, Zr, Hf, Ce, Th, Pa, Np, Pu, C
9	Trivalents	La	Al, Sc, Y, La, Ac, Pr, Nd, Pm, Sm, Eu, Gd, Tb, Dy, Ho, Er, Tm, Yb, Lu, Am, Cm, Bk, Cf
10	Uranium	UO_2	U
11	More Volatile	Cd	Cd, Hg, Zn, As, Sb, Pb, Tl, Bi
12	Less Volatile Main	Ag	Ga, Ge, In, Sn, Ag
13	Boron	BO_2	B, Si, P
16	Cesium Iodide [b]	CsI	Classes 2 and 4
17	Cesium Molybdate [b]	Cs_2MoO_4	Classes 2 and 7

a. Classes 14 and 15 do not contain fission products and are not relevant to this section.
b. Masses are derived from the speciation process and are not initially populated by the ORIGEN data.

Table D-2 Symbol Table for the Speciation Process

Symbol	Meaning	Value
$m_{c,0}$	Unspeciated, initial mass of class c	From ORIGEN
m_c	Speciated, initial mass of class c	Calculated
$m_{c,\mathrm{fuel}}$	Speciated, initial mass of class c in the fuel	Calculated
$m_{c,\mathrm{gap}}$	Speciated, initial mass of class c in the gap	Calculated
$m_{e,c}$	Mass of speciated element e in speciated class c	Calculated
$r_{s,u}$	Mass ratio of speciated class s to unspeciated class u [1]	Calculated
$P_{c,0}$	Unspeciated decay power of class c	From ORIGEN
P_c	Speciated decay power of class c	Calculated
$f_{\mathrm{I,CsI}}$	Molecular weight ratio of iodine to CsI	0.489
$f_{\mathrm{Cs,CsI}}$	Molecular weight ratio of cesium to CsI	0.512
$f_{\mathrm{Cs,Cs_2Mo}}$	Molecular weight ratio of cesium to Cs_2Mo [2]	0.735
$f_{\mathrm{Mo,Cs_2Mo}}$	Molecular weight ratio of cesium to Cs_2Mo [2]	0.265
$f_{\mathrm{Cs,gap,all}}$	Fraction of all cesium allowed in the gap (classes 2 and 16)	0.05
$f_{\mathrm{I,gap,all}}$	Fraction of all iodine allowed in the gap (classes 4 and 16)	0.05
$f_{\mathrm{I,gap,gas}}$	Fraction of iodine in gap as gaseous iodine	Sampled
$f_{\mathrm{Cs_2Mo}}$	Fraction of non-CsI mass that is Cs_2Mo in the fuel	Sampled
MW_e	Molecular weight of element e	Data

[1] For the combination classes CsI and Cs_2Mo, there are separate ratios for each of the classes' constituents relative to the corresponding unspeciated class.

[2] This is MELCOR's expected elemental composition of class 17. Upon release from fuel, the oxygen mass is added.

Determination of Speciated Iodine and Cesium Iodide Masses

The speciation begins by defining the mass of iodine in the gap. The sampled parameter species the amount of gaseous iodine mass, which is located in the gap of Class 4 (halogens):

$$m_{\mathrm{I,gap}} = f_{\mathrm{I,gap,gas}} \cdot m_{\mathrm{I},0}$$

$$m_{\mathrm{I,fuel}} = 0$$

$$m_{\mathrm{I}} = m_{\mathrm{I,gap}}$$

The remaining iodine mass is assumed to be present as CsI, so the total mass of CsI and its constituents are found through stoichiometry:

$$m_{\mathrm{I,CsI}} = \left(1 - f_{\mathrm{I,gap,gas}}\right) \cdot m_{\mathrm{I,0}}$$
$$m_{\mathrm{CsI}} = \frac{m_{\mathrm{I,CsI}}}{f_{\mathrm{I,CsI}}}$$
$$m_{\mathrm{Cs,\,CsI}} = f_{\mathrm{Cs,CsI}} \cdot m_{\mathrm{CsI}}$$

With m_{CsI} being the total mass of CsI, the fraction of CsI in the gap is determined from the constraint that a maximum of 5% of the unspeciated iodine mass is initially present in the gap. However, since the gaseous iodine gap fraction is sampled, it may exceed this limit since no explicit truncation was introduced into the sampling. To account for this situation, the sampled gaseous iodine gap fraction will be used even if it exceeds 5%, and the gap mass fraction of CsI will have a minimum of zero if the gaseous iodine gap fraction exceeds 5%:

$$m_{\mathrm{CsI,gap}} = \mathrm{Max}\left(0\,, \frac{f_{\mathrm{I,gap,all}} \cdot m_{\mathrm{I,0}} - m_{\mathrm{I,gap}}}{f_{\mathrm{I,CsI}}}\right)$$
$$m_{\mathrm{CsI,fuel}} = m_{\mathrm{CsI}} - m_{\mathrm{CsI,gap}}$$

Determination of Speciated Cesium and Cesium Molybdate Masses

The masses of cesium hydroxide and cesium molybdate are now determined from the CHEMFORM Cs sampled parameter $f_{\mathrm{Cs_2Mo}}$. The definition of this fraction is the mass fraction of cesium that is not present as CsI that is bound to molybdenum. This definition is simple and directly relates the masses of the two classes to a single, samples number.
The total mass of cesium that is not present as CsI is,

$$m_{\mathrm{Cs}^{\dagger}} = m_{\mathrm{Cs,0}} - f_{\mathrm{Cs,CsI}} \cdot m_{\mathrm{CsI}}\,,$$

where $m_{\mathrm{Cs}^{\dagger}}$ denotes the mass of cesium that is not CsI. Using the sampled CHEMFORM Cs mass fraction, the speciation of cesium is completed as follows:

$$m_{\mathrm{Cs,Cs_2Mo}} = f_{\mathrm{Cs_2Mo}} \cdot m_{\mathrm{Cs}^{\dagger}}$$
$$m_{\mathrm{Cs}} = \left(1 - f_{\mathrm{Cs_2Mo}}\right) \cdot m_{\mathrm{Cs}^{\dagger}}$$

Following recommended NUREG-1465 gap release fractions [1], the total mass of cesium in the gap is taken to be 5% of all cesium produced within the fuel from fission. Since there is already a non-zero mass of cesium already in the gap in the form of cesium iodide to match NUREG-1465's 5% Halogen loading, the remaining balance of the 5% cesium mass gap loading will be present as cesium hydroxide. However, since the total mass of cesium hydroxide is determined separately from the gap mass of cesium hydroxide, there may be cases on the extremes of the CHEMFORM I2 and CHEMFORM Cs distributions where there is not enough mass to satisfy the NUREG-1465 5% Alkali Earth loading.

To account this situation, if there is not enough cesium hydroxide to make up the balance of the 5% Alkali Earth, the totality of Class 2 will be assigned to the gap and none to the fuel:

$$m_{\mathrm{Cs,gap}} = \mathrm{Min}(m_{\mathrm{Cs}}, f_{\mathrm{Cs,gap,all}} \cdot m_{\mathrm{Cs,0}} - f_{\mathrm{Cs,CsI}} \cdot m_{\mathrm{CsI,gap}})$$

$$m_{\mathrm{Cs,fuel}} = m_{\mathrm{Cs}} - m_{\mathrm{Cs,gap}}$$

$$m_{\mathrm{Cs_2Mo}} = \frac{m_{\mathrm{Cs,Cs_2Mo}}}{f_{\mathrm{Cs,Cs_2Mo}}}$$

The determination of the speciated molybdenum mass is also independent of the CHEMFORM Cs method and is derived from the mass of cesium present as cesium molybdate:

$$m_{\mathrm{Mo,Cs_2Mo}} = f_{\mathrm{Mo,Cs_2Mo}} \cdot m_{\mathrm{Cs_2Mo}}$$

$$m_{\mathrm{Mo}} = m_{\mathrm{Mo,0}} - m_{\mathrm{Mo,Cs_2Mo}}$$

Determination of Speciated Decay Powers

With all the speciated masses determined, the power for each speciated class is determined from the ratio of the speciated masses to the unspeciated masses:

$$r_{\mathrm{I,I}} = \frac{m_{\mathrm{I,I}}}{m_{\mathrm{I,0}}}$$

$$r_{\mathrm{Cs,Cs}} = \frac{m_{\mathrm{Cs}}}{m_{\mathrm{Cs,0}}}$$

$$r_{\mathrm{CsI,I}} = \frac{m_{\mathrm{I,CsI}}}{m_{\mathrm{I,0}}}$$

$$r_{\mathrm{Mo,Mo}} = \frac{m_{\mathrm{Mo}}}{m_{\mathrm{Mo,0}}}$$

$$r_{\mathrm{CsI,Cs}} = \frac{m_{\mathrm{Cs,CsI}}}{m_{\mathrm{Cs,0}}}$$

$$r_{\mathrm{Cs_2Mo,Cs}} = \frac{m_{\mathrm{Cs,Cs_2Mo}}}{m_{\mathrm{Cs,0}}}$$

$$r_{\mathrm{Cs_2Mo,Mo}} = \frac{m_{\mathrm{Mo,Cs_2Mo}}}{m_{\mathrm{Mo,0}}}$$

The speciated decay heat powers are then

$$P_{\mathrm{Cs}} = r_{\mathrm{Cs,Cs}} \cdot P_{\mathrm{Cs,0}}$$

$$P_{\mathrm{I}} = r_{\mathrm{I,I}} \cdot P_{\mathrm{I,0}}$$

$$P_{\mathrm{Mo}} = r_{\mathrm{Mo,Mo}} \cdot P_{\mathrm{Mo,0}}$$

$$P_{\mathrm{CsI}} = r_{\mathrm{CsI,I}} \cdot P_{\mathrm{I,0}} + r_{\mathrm{CsI,Cs}} \cdot P_{\mathrm{Cs,0}}$$

$$P_{\mathrm{Cs2Mo}} = r_{\mathrm{Cs_2Mo,Cs}} \cdot P_{\mathrm{Cs,0}} + r_{\mathrm{Cs_2Mo,Mo}} \cdot P_{\mathrm{Mo,0}}$$

References

[1] NUREG-1465, “Accident Source Terms for Light-Water Nuclear Power Plants,” U.S. Nuclear Regulatory Commission, Washington, DC, February 1995.

[2] NUREG/CR-7110 Volume 2, Rev. 1, "State-of-the-Art Reactor Consequence Analysis Project Volume 2: Surry Integrated Analysis," U.S. Nuclear Regulatory Commission, Washington, DC, August 2013.

APPENDIX E
REGRESSION TABLES FOR SGTR REALIZATIONS

Most figures-of-merit showed a strong bifurcation depending on the occurrence of SGTR. For example, higher cesium and iodine releases occurred in SGTR realizations than in non-SGTR realizations. As a result, regression models on the set of all realizations struggle to characterize both the within-population and the between-populations variance in the data so the populations were analyzed separately. For non-SGTR realizations, the sample size is sufficiently large to build reasonable regression models. However, the small number of SGTR realizations relative to the number of uncertain inputs leads to poorer quality regression models for SGTR realizations. These regression tables are presented here for completeness and can be interpreted with care.

Cesium Release for SGTR Realizations

	Rank Regression		Quadratic		Recursive Partitioning		MARS		Main Contribution	Conjoint Contribution
Final R2	0.29		0.39		0.38		0.40			
Input	R2 contr.	SRRC	Si	Ti	Si	Ti	Si	Ti		
shapeFactor	0.29	0.54	0.65	0.74	0.70	0.81	0.67	0.67	0.270	0.026
ORIGENDay	---	---	0.17	0.25	0.01	0.05	0.25	0.25	0.057	0.015
I2GasGapFraction	---	---	---	---	0.12	0.22	---	---	0.015	0.013
SGTRC_loc	---	---	---	---	---	---	0.08	0.08	0.011	0.000
Ox_model	---	---	0.01	0.19	0.02	0.06	---	---	0.005	0.028
priSVfrac	---	---	---	---	---	---	0.00	0.01	0.000	0.001
ThotB_norm	---	---	---	---	0.00	0.03	---	---	0.000	0.003

* highlighted if main contribution larger than 0.02 or conjoint contribution larger than 0.1

Iodine Release for SGTR Realizations

	Rank Regression		Quadratic		Recursive Partitioning		MARS		Main Contribution	Conjoint Contribution
Final R2	0.40		0.54		0.60		0.57			
Input	R2 contr.	SRRC	Si	Ti	Si	Ti	Si	Ti		
I2GasGapFraction	0.13	0.26	0.53	0.53	0.67	0.72	0.52	0.52	0.279	0.010
shapeFactor	0.23	0.37	0.26	0.26	0.20	0.26	0.25	0.25	0.158	0.012
ORIGENDay	0.04	0.24	0.21	0.21	0.04	0.10	0.15	0.15	0.066	0.013
SGTRC_loc	---	---	---	---	---	---	0.07	0.07	0.014	0.000

* highlighted if main contribution larger than 0.02 or conjoint contribution larger than 0.1

Containment Failure Time for SGTR Realizations

	Rank Regression		Quadratic		Recursive Partitioning		MARS		Main Contribution	Conjoint Contribution
Final R^2	0.70		0.93		0.74		0.86			
Input	R^2 contr.	SRRC	S_i	T_i	S_i	T_i	S_i	T_i		
ORIGENDay	0.31	-0.53	0.03	0.03	0.46	0.55	0.51	0.51	0.278	0.020
rupture	0.35	0.59	0.03	0.05	0.42	0.52	0.43	0.44	0.264	0.031
SGTRC_loc	---	---	0.20	0.67	---	---	0.01	0.02	0.067	0.147
EU_melt_T	0.03	-0.16	---	---	0.01	0.03	0.02	0.02	0.012	0.006
SGTRA_loc	0.02	0.14	0.01	0.01	---	---	0.03	0.03	0.011	0.001
secSVfrac3	---	---	0.03	0.22	---	---	---	---	0.009	0.060
SGTRB_loc	---	---	0.02	0.21	---	---	---	---	0.006	0.059

* highlighted if main contribution larger than 0.02 or conjoint contribution larger than 0.1

NRC FORM 335
(12-2010)
NRCMD 3.7

U.S. NUCLEAR REGULATORY COMMISSION

BIBLIOGRAPHIC DATA SHEET

(See instructions on the reverse)

1. REPORT NUMBER
(Assigned by NRC, Add Vol., Supp., Rev., and Addendum Numbers, if any.)

NUREG/CR-7262

2. TITLE AND SUBTITLE

State-of-the-Art Reactor Consequence Analyses Project: Uncertainty Analysis of the Unmitigated Short-Term Station Blackout of the Surry Power Station

3. DATE REPORT PUBLISHED

MONTH	YEAR
December	2022

4. FIN OR GRANT NUMBER

5. AUTHOR(S)

Severe Accident Analysis Department

6. TYPE OF REPORT

Technical

7. PERIOD COVERED (Inclusive Dates)

8. PERFORMING ORGANIZATION - NAME AND ADDRESS (If NRC, provide Division, Office or Region, U. S. Nuclear Regulatory Commission, and mailing address; if contractor, provide name and mailing address.)

Sandia National Laboratories
PO Box 5800 MS-0748
Albuquerque, NM 87185-0748

9. SPONSORING ORGANIZATION - NAME AND ADDRESS (If NRC, type "Same as above", if contractor, provide NRC Division, Office or Region, U. S. Nuclear Regulatory Commission, and mailing address.)

Division of System Analysis
Office of Nuclear Regulatory Research
U.S. Nuclear Regulatory Commission
Washington, D.C. 20555-0001

10. SUPPLEMENTARY NOTES

11. ABSTRACT (200 words or less)

The State of the Art Reactor Consequence Analyses (SOARCA) project published best estimate analyses for select accident scenarios at the Peach Bottom Atomic Power Station and Surry Power Station in 2012. This work was followed by an integrated uncertainty analysis (UA) performed on the unmitigated long-term station blackout (LTSBO) scenario for Peach Bottom, a draft UA on the unmitigated short-term station blackout (STSBO) scenario for Surry, and a UA on the unmitigated STSBO scenario for Sequoyah. The approach developed for the Peach Bottom UA was further enhanced for application to the subsequent UAs. Consequently, the current Surry UA not only benefits from additional knowledge gained since the original Surry SOARCA best-estimate calculation but also the other UAs. The UA projects include an integrated Monte Carlo analysis using the MELCOR and MACCS codes. Regression analyses, separate sensitivity analyses, and single realization analyses were conducted to understand the contributions of uncertain input parameters to the uncertainty in key figures of merit, such as radionuclide release to the environment and individual latent cancer fatality risk to the offsite public. Like the previous UAs, the analyses herein corroborate the conclusions of the original SOARCA study and further extend the body of knowledge on severe reactor accidents.

12. KEY WORDS/DESCRIPTORS (List words or phrases that will assist researchers in locating the report.)

SOARCA, severe accident, environmental consequence, MELCOR, MACCS, uncertainty

13. AVAILABILITY STATEMENT

unlimited

14. SECURITY CLASSIFICATION

(This Page)
unclassified

(This Report)
unclassified

15. NUMBER OF PAGES

16. PRICE

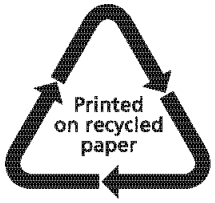

Federal Recycling Program

UNITED STATES
NUCLEAR REGULATORY COMMISSION
WASHINGTON, DC 20555-0001

OFFICIAL BUSINESS

NUREG/CR-7262

State-of-the-Art Reactor Consequence Analyses Project
Uncertainty Analysis of the Unmitigated Short-Term Station Blackout of the Surry Power Station

December 2022